batteries

Special Issue Reprint

Thermal Management System for Lithium-Ion Batteries

2nd Edition

Edited by
Jinsheng Xiao, Hengyun Zhang and Tianqi Yang

mdpi.com/journal/batteries

MDPI

Thermal Management System for Lithium-Ion Batteries: 2nd Edition

Thermal Management System for Lithium-Ion Batteries: 2nd Edition

Guest Editors

Jinsheng Xiao
Hengyun Zhang
Tianqi Yang

MDPI

Basel • Beijing • Wuhan • Barcelona • Belgrade • Novi Sad • Cluj • Manchester

Guest Editors

Jinsheng Xiao
School of Automotive Engineering
Wuhan University of Technology
Wuhan
China

Hengyun Zhang
School of Mechanical and Automotive Engineering
Shanghai University of Engineering Science
Shanghai
China

Tianqi Yang
School of Automotive Engineering
Wuhan University of Technology
Wuhan
China

Editorial Office
MDPI AG
Grosspeteranlage 5
4052 Basel, Switzerland

This is a reprint of the Special Issue, published open access by the journal *Batteries* (ISSN 2313-0105), freely accessible at: https://www.mdpi.com/journal/batteries/special_issues/LBFX04817B.

For citation purposes, cite each article independently as indicated on the article page online and as indicated below:

Lastname, A.A.; Lastname, B.B. Article Title. *Journal Name* **Year**, *Volume Number*, Page Range.

ISBN 978-3-7258-7623-5 (Hbk)
ISBN 978-3-7258-7624-2 (PDF)
https://doi.org/10.3390/books978-3-7258-7624-2

Contents

About the Editors

Jinsheng Xiao

Jinsheng Xiao is a full professor at the School of Automotive Engineering, Wuhan University of Technology, China, and a visiting professor at the Hydrogen Research Institute, University of Quebec at Trois-Rivieres, Canada. He obtained his M.S. in 1986 in Marine Engineering, Wuhan University of Technology, and his Ph.D. in 1999 in Engineering Thermophysics, Tsinghua University. His recent research interests include the simulation and optimization of hydrogen production, storage, and fuel cell systems, and battery thermal management systems.

Hengyun Zhang

Hengyun Zhang is a distinguished professor at Shanghai University of Engineering Science, a Senior Member of IEEE, Senor Member of China Automotive Society, and the Co-Chairman of the ICSEE 2024–2026 and ICEMAT2023 International Conference Organizing Committee. He obtained a B.E. from the University of Science and Technology of China in 1994 and a PhD from Nanyang Technological University in 2001. He has led and strongly participated in four National Natural Science Foundation projects and three provincial projects, among others. His main research interests include the characterization of thermal and electrical parameters and the thermal management of new energy vehicle batteries. He has published over 180 papers, and one key national book. He is the reviewer of more than thirty prestigious journals. He has been granted more than a dozen invention patents and has won the Innovation and Entrepreneurship Award from the China Invention Association. Prof. Zhang was also elected as the Global Top 2% Scientist and China highly cited scholar (Elsevier) continuously from 2023 to 2025.

Tianqi Yang

Tianqi Yang is an associate professor at the School of Automotive Engineering, Wuhan University of Technology. He received his Master's degree in Marine Engineering from the same university in 2007, and his Ph.D. in Automotive Application Engineering in 2011. His recent research interests include hydrogen purification, storage, refueling, and hydrogen safety, as well as battery thermal management, thermal runaway, and thermal safety.

Preface

Lithium-ion batteries (LIBs) have been widely used as power sources for the automotive and energy storage industries due to their high energy density, high power output, low self-discharge rate, and minimal memory effect. However, the performances of LIBs are greatly affected by their operating temperature. Various studies on the thermal management and thermal performance enhancement of LIBs have thus been carried out to address their ever-increasing application scenarios. This Special Issue, "Thermal Management System for Lithium-Ion Batteries: 2nd Edition", aims to present and disseminate the most recent advances in the thermal management of LIBs under various application conditions. Thirteen high-quality papers on the different aspects of the thermal management of lithium ion batteries are included in this Special Issue. Among them, seven papers are devoted to the thermal cooling of battery modules, of which four address the cooling of single battery modules using liquid cooling channels and immersion cooling. Three papers consider hybrid cooling in contrast to cooling-related research, one paper is devoted to low-temperature heating strategies for batteries under subzero conditions, and another centers on the development of polymer-based thermal interface materials (TIMs) for enhancing interfacial heat transfer. For battery thermal runaway and safety, three studies are conducted: one investigates the overcharge-induced thermal runaway behavior of lithium iron phosphate (LFP) batteries under the coupled effects of charging rate and ambient temperature, one systematically discusses the multi-factor degradation influences on lithium-ion batteries throughout their first and second life cycles, and another analyzes the intrinsically high thermal stability of lithium-rich manganese-based cathode materials that endow high safety performance.

The editors would like to congratulate all the authors for publishing their excellent original work in this Special Issue. The editors would also like to express special gratitude to the reviewers, who selflessly devoted their time and expertise to provide comments and suggestions for the improvement of the quality of papers. The second editor would like to acknowledge the support from the Natural Science Foundations of China (52476079, 12272217), as well as the Qinghai Kunlun Talent Plan. We hope that the papers in this Special Issue will benefit readers and add new knowledge to the academic community in this important area.

Jinsheng Xiao, Hengyun Zhang, and Tianqi Yang
Guest Editors

batteries

MDPI

Article

Experimental Investigation of Phase Change Material-Based Battery Pack Performance Under Elevated Ambient Temperature

Mohammad J. Ganji, Martin Agelin-Chaab * and Marc A. Rosen

Faculty of Engineering and Applied Science, Ontario Tech University, Oshawa, ON L1G 0C5, Canada; mohammadjavad.ganji@ontariotechu.ca (M.J.G.); marc.rosen@ontariotechu.ca (M.A.R.)
* Correspondence: martin.agelin-chaab@ontariotechu.ca

Abstract: This study experimentally assesses the thermal performance of a proposed phase change material (PCM)-based battery pack under elevated ambient temperatures. In addition, the novel approach of the research addresses scenarios where the ambient temperature reaches the PCM's melting point while maintaining the initial temperature at the ideal operating point of 22 °C. The experiments employed nine 2500 mAh 18650 lithium-ion cells connected in series and subjected to constant-current discharges of 1C and 3C, with a conventional air-cooled system as the baseline and paraffin as the PCM. The results indicate that as the ambient temperature reached the PCM's melting point, approximately 98% utilization of the PCM around the heating cell was achieved. Additionally, the PCM demonstrates noticeable advantages over the baseline by stabilizing the temperature profile and reducing the maximum temperature increase rate from over 18 °C in the baseline system to around 7 °C. Notably, under a high-load (3C) discharge rate, the PCM-based system successfully maintained battery temperatures below 42 °C, demonstrating its effectiveness under demanding operational scenarios. These findings establish a critical baseline for PCM-based BTMSs operating under elevated ambient temperatures and up to the melting point of the PCM, thereby informing future research and development of more efficient PCM-based thermal management solutions.

Keywords: hybrid battery thermal management system; phase change material; ambient temperature; thermal performance; experimental analysis; Li-ion cylindrical cells

1. Introduction

Lithium-ion batteries (LIBs) have emerged as the dominant energy storage solution for electric and hybrid vehicles due to their high specific energy, extended life cycle, and low self-discharge rates [1,2]. However, heat generation during charging and, more critically, during discharging poses significant safety risks and limits their effectiveness. Elevated temperatures can lead to thermal runaway, capacity degradation, and even fires, especially when the operational temperature exceeds the optimal range of 20 to 40 °C [3,4]. Uneven temperature distribution and inadequate thermal dissipation within battery packs further diminish LIB performance and efficiency.

To address these challenges, recent advancements in battery thermal management systems (BTMSs) aim to reduce maximum temperatures and achieve uniform temperature distribution while minimizing cooling energy consumption [5–8]. BTMSs are typically classified as active or passive based on their energy requirements. Active cooling utilizes

external energy sources to dissipate heat through heat exchangers. At the same time, passive methods, such as phase change materials (PCMs), rely on natural heat transfer mechanisms without external energy input [9–11]. Although passive methods are generally simpler, lighter, and more cost-effective, their applications are constrained by their thermal performance, especially under varying ambient temperatures.

Ambient temperature, referred to as inlet coolant temperature, can vary significantly due to factors such as geographic location, time of day, or cooling system failures, potentially raising the ambient temperature above the standard room temperature of 23 °C. The thermal performance of the PCMs quantified in this study as the temperature difference between cases with and without PCMs (Equation (3)) exhibits significant sensitivity to variations in ambient temperature [12]. Landini et al. [12] reported that PCMs may exhibit limitations under extreme operational conditions of LIBs, such as high ambient temperatures and high discharge rates. However, the current study focuses on assessing the PCM's capabilities under highly demanding conditions, where active cooling becomes unfavorable and heats up the system rather than dissipating the heat. Under these conditions, the PCM must utilize its stored energy to mitigate both the heat generated within the cells and the elevated ambient temperature affecting the cooling air ducts.

Extensive research has been conducted on PCM-based BTMSs as a primary cooling option for battery packs [13–16]. During phase transitions, PCMs can maintain a constant temperature profile until fully melted, which helps keep battery temperatures within safe limits. This provides extensive energy storage at the safe threshold of batteries, keeping the batteries below the melting point to ensure safety in high operational conditions. However, unfavorable cooling systems could hinder this effectiveness and affect the safety of batteries. Several studies have focused on optimizing PCM placement and enhancing heat dissipation through design modifications. Suo et al. [17] evaluated different PCM placements in prismatic battery modules combined with air cooling, finding that an optimized configuration reduced PCM volume significantly with minimal impact on temperature reduction. Dey et al. [18] investigated various fin designs in a cylindrical PCM-based BTMS, demonstrating that optimal fin configurations could maintain maximum temperatures under critical limits even at high discharge rates and simulated short circuit conditions with a resistance of 0.5 Ω.

Other researchers have introduced novel designs to improve thermal performance. Zhang et al. [19] developed new branch fin designs coupled with PCMs around a single battery module, while Khaboshan et al. [20] examined the efficacy of combining PCMs with metal foam and fins. Their findings indicated that integrating metal foam with PCMs substantially enhanced melting time and temperature uniformity. Sharma et al. [21] assessed fin designs combined with PCMs under high ambient temperatures, achieving superior cooling efficiency and preventing the PCM from melting during multiple charge/discharge cycles.

The effectiveness of composite PCMs (CPCMs) has also been explored. Wang et al. [22] evaluated a CPCM in a battery pack under various initial and ambient temperatures, finding that temperature control improved with higher ambient temperatures and discharge rates. Li et al. [23] implemented a novel passive thermal regulator based on PCMs, demonstrating an automatic natural thermal regulation mechanism that enhanced heat dissipation as temperatures rose. Wu et al. [24] introduced a flexible CPCM to maximize contact surface area with cylindrical cells, reducing maximum temperatures and ensuring better operating flexibility.

Integrating active cooling methods with PCM-based BTMSs has been shown to further improve thermal performance. Luo et al. [25] evaluated snowflake fins with liquid channels in a PCM-based cylindrical BTMS, achieving significant reductions in maximum

temperature and improved temperature uniformity under high ambient temperatures and discharge rates. Xie et al. [26] incorporated micro-heat pipe arrays into a PCM-based BTMS, resulting in enhanced cooling performance and energy density.

Chen et al. [27] developed forked flow cooling channels in conjunction with a PCM–fin-based BTMS, identifying optimal configurations that balanced thermal performance and cooling power consumption. Zheng et al. [28] proposed a two-way wavy cooling plate coupled with a PCM-based BTMS, finding that certain flow direction strategies improved temperature uniformity without significantly increasing flow rates.

Shahid et al. [29] introduced a novel hybrid BTMS using stationary water channels and circulating air duct cooling integration with PCMs, which are in direct contact with the battery cells. The results revealed that the battery surface temperature reached the PCM melting temperature after the fifth discharge cycle. Moreover, after the seventh cycle, the temperature uniformity started to change as the PCM melting percentage exceeded 2.3%. In another study [30], the authors replaced water channels with cold plates. The results revealed that using cold plates instead of water channels decreased the maximum temperature by 1.5 °C, preventing the PCM from reaching its melting temperature. Also, maximum temperature uniformity was reduced from 3.2 °C to 1.2 °C. Further investigations [31] showed that increasing the height of the air duct and Reynolds number by more than 6 mm and 1950, respectively, does not significantly improve cooling performance. The present study experimentally examines the thermal performance using a similar air duct and water channels but without any water in the proposed BTMS. Natural air circulation is proposed instead of stationary water inside the cylindrical channels due to battery safety measures and simplicity.

The comprehensive review and experimental insights underscore the critical role of thermal management in enhancing the safety, performance, and lifespan of LIBs, particularly under varying operational conditions. Ambient operating temperatures can elevate significantly due to cooling system failures, and such elevated temperature conditions can consequently affect the thermal performance of PCMs and BTMSs, potentially compromising battery safety and efficiency. Despite prior advancements in PCM-based BTMSs, the existing literature has a limited scope of performance of ambient temperatures up to 30 °C.

The present study aims to address this gap by experimentally evaluating the effectiveness of a PCM-based BTMS at elevated ambient temperatures up to 42 °C, which is beyond what currently exists in the literature. Additionally, the study extends the evaluation of the elevated ambient temperature up to the melting point of the PCM to provide new insights into PCM performance under its operational limit. Thus far, no study has evaluated the performance of the PCM at its melting point temperature. Furthermore, the study aims to maintain the initial temperature at an ideal operating point of 22 °C for all tested experiments to ensure a consistent starting behavior of the PCM during the experiments. The rationale is to replicate scenarios in which a cooling system fails or, if there are any other contributing factors, leads to heating the system rather than dissipating heat. Consequently, this also allows for the assessment of the material's capacity for stored latent heat and regulates the maximum battery temperature at both low and high discharge rates and under both favorable and unfavorable cooling conditions (i.e., 22–42 °C ambient temperature). Furthermore, the study quantifies the degree of PCM melting and assesses how effectively stored energy is utilized to mitigate ambient temperature rise. By analyzing the effects of elevated ambient temperatures and PCMs' latent heat utilization, this research provides valuable insights into the thermal management of LIBs under varying operational conditions. The findings are expected to provide a baseline for PCM-based BTMSs under

elevated ambient temperatures for future research and the development of more efficient thermal management solutions.

2. Methodology

2.1. Experimental Setup

Nine cylindrical lithium-ion Samsung INR18650-25R batteries were utilized. Each battery had a capacity of 2500 mAh and a nominal voltage of 3.7 V. The batteries were arranged in series within a cuboid battery pack, with each battery spaced 6 mm apart to maintain consistency with previous research by Shahid et al. [29]. The battery pack was constructed using a medium-density fiberboard (MDF) with a thickness of 6.5 mm, assembled and sealed with high-temperature-resistant sealant glue. MDF was selected for its availability and suitability for precise laser cutting. The internal dimensions of the battery pack were 7.5 cm in width and 5.5 cm in height, accommodating the INR18650-25R batteries (18 mm diameter, 65 mm height). An isometric visualization of the battery pack is presented in Figure 1a.

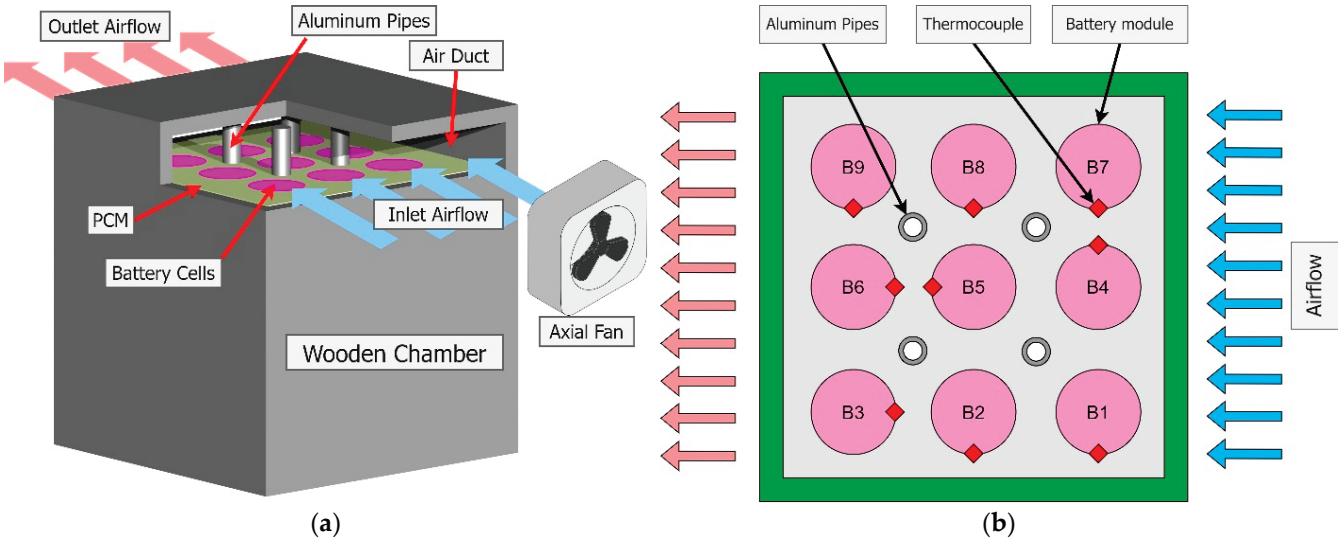

Figure 1. (**a**) Isometric view of the battery pack configuration for Phase 1, and (**b**) top view of the battery pack showing the thermocouple placement.

The batteries were interconnected using nickel strips measuring 5 mm in width, 4 cm in length, and 0.5 mm in thickness. Four vertical air pipes with an outer diameter of 6 mm and a wall thickness of 1 mm were installed between the battery cells to facilitate heat dissipation. These air pipes were strategically placed to ensure efficient heat dissipation from the battery cells, thereby maintaining the desired operating temperature. The chosen air pipe geometry was selected based on its consistency with previous research, as well as its symmetry, simplicity, and ease of assembly, in contrast to more complex rectangular or irregular geometries. Aluminum was used for the air pipes. An air duct, matching the length and width of the battery chamber and with a height of 1.9 cm, was placed above the battery pack to dissipate heat from the air pipes. An axial AC fan (GDSTIME 1203) was employed to ensure steady airflow through the duct, achieving an inlet speed of 2.1 $\pm$ 0.1 m/s, as measured by a Proster anemometer. The inlet air temperature was controlled using a 227 L (8 cubic feet) thermal chamber (SD-508, Associated Environmental Systems) with an accuracy of $\pm$0.5 °C. The walls of the battery pack were assumed to be adiabatic, implying that all heat dissipation relied exclusively on the air duct. Real images of the thermal chamber and the experimental setup installed inside it are shown in Figure 2.

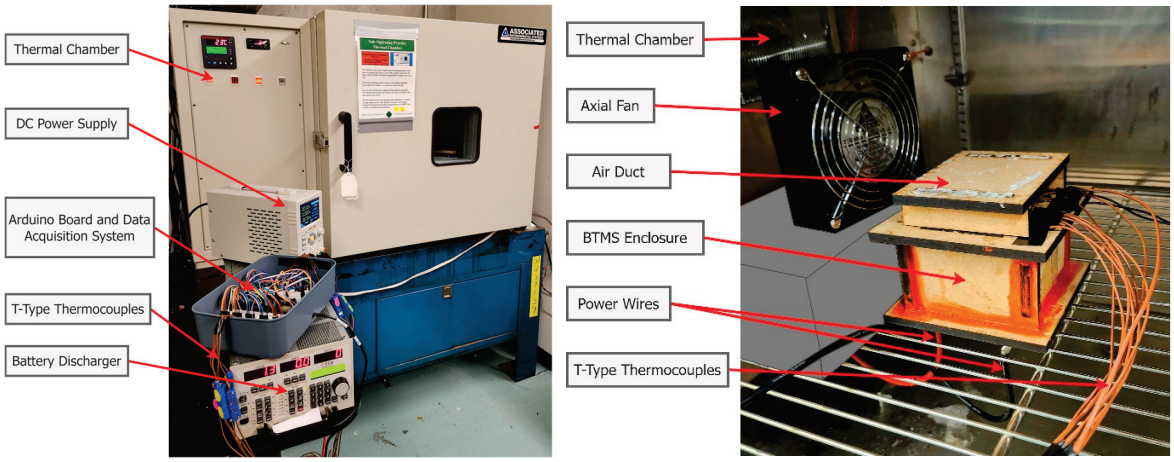

Figure 2. (**a**) Real image of the experimental equipment, and (**b**) real image of the experimental setup installed inside the thermal chamber.

T-type thermocouples (5TC-TT-T-24-72 Omega), with a reported accuracy of ±0.5 °C, were installed to monitor the temperature distribution within the battery pack. Nine thermocouples were attached to the surface of the batteries at the center of the total height, capturing temperature data from all sides of the batteries, as depicted in Figure 1b. Each thermocouple was connected to an Adafruit 3263 temperature sensor (±0.075 °C reported accuracy) and interfaced with an Arduino Mega microcontroller (Elegoo MEGA 2560 R3). The temperature readings were transmitted to a computer via the Arduino terminal connection for real-time monitoring and data logging. A schematic of the data acquisition and electrical setup is provided in Figure 3.

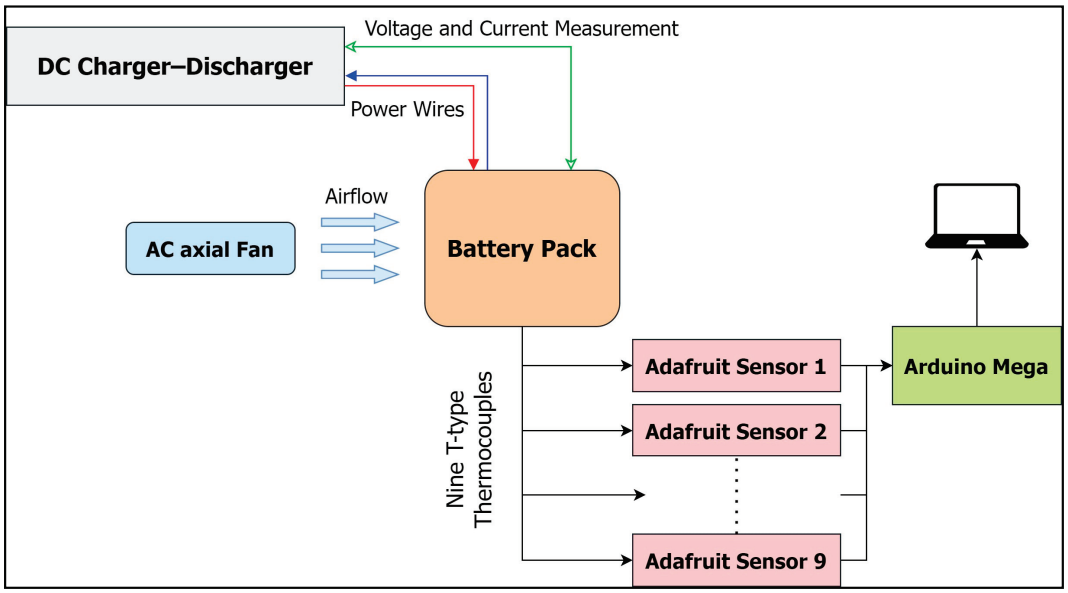

Figure 3. Schematic of the data acquisition and electrical setup.

Paraffin wax, with a melting temperature range of 40–42 °C, was selected as the working PCM. Despite its flammability, paraffin offers an optimal balance of cost, thermal storage capacity, chemical stability, and availability across various melting points. The flammability concern can be mitigated later through appropriate system design and encapsulation. While the optimal temperature range for many lithium-ion cells is typically

30–35 °C, the batteries are designed to withstand operating temperatures of up to 40 °C. Consequently, paraffin 40–42 °C was chosen to maintain battery temperatures below this point. Paraffin with a lower melting point was deemed unsuitable, as the scope of this research aims to simulate higher temperatures and test the batteries up to their safe threshold of 40 °C. The manufacturer's temperature specifications for the PCM were validated through multiple thermal experiments conducted before and after the study to ensure its thermophysical stability. The corresponding average results of the melting experiments are presented in Figure 4, illustrating the melting and solidification temperature profiles of the paraffin 40–42 PCM, confirming a melting temperature of 41 ± 1 °C. To improve comparative visualization, the x-axis has been normalized in time. As anticipated, the solidification process takes approximately twice as long as the melting process. The physical properties of the materials used in this study are provided in Table 1. Based on the dimensions of the battery pack and the available volume for PCM storage, 177 ± 1 mL of molten paraffin was poured into the battery pack, corresponding to 136 ± 1 g of material. The volume of the PCM was measured using a precise graduated syringe, with repeated measurements ensuring consistency and accuracy.

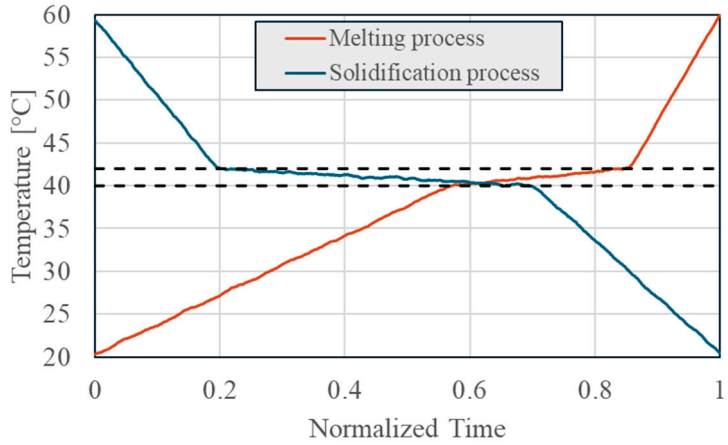

Figure 4. Paraffin 40–42 PCM temperature profiles of melting and solidification (time axis is normalized for better visualization of the temperature profile).

Table 1. Physical properties of materials used in experiment *.

Property	Unit	Wood [31]	Aluminum [31]	Nickel [32]	PCM (Solid–Liquid) ** [33]	Air [31]
Specific Heat at Constant Pressure (C_p)	J/kg · K	2310	871	444	2150–2250	1006
Thermal Conductivity (k)	W/m · K	0.173	202.4	90.9	0.21–0.18	0.026
Density (ρ)	kg/m^3	700	2719	8908	880–770	1.225
Latent Heat of Fusion (L_f)	kJ/kg	-	-	-	245	-
Liquidus Temperature (T_l)	°C	-	-	-	42	-
Solidus Temperature (T_s)	°C	-	-	-	39	-
Electrical Resistivity (ρ_e)	Ω · m	-	2.65×10^{-8} [32]	6.84×10^{-8}	-	-

* The physical properties provided are measured at 25 °C and 1 bar [31–33]. ** The PCM used in this study is 40–42 paraffin wax.

2.2. Experimental Procedure

The battery pack was installed inside the thermal chamber, where the ambient temperature within the chamber was controlled with an accuracy of ±0.5 °C. The initial temperature of the battery pack was maintained at 22 ± 0.1 °C for all experiments. Consequently, variations in ambient temperature only affected the air duct flow temperature. Five ambient temperatures were studied, ranging from 22 °C to 42 °C in increments of 5 °C.

The batteries were configured in a series arrangement and initially charged using a constant current (CC) of 4 ± 0.01 A until the overall voltage reached a cutoff of 37.8 ± 0.005 V, corresponding to 4.2 V per cell, using the DC Power Supply OWON SP6103 with specified accuracy. Subsequently, the charging process continued with a constant voltage (CV) of 37.8 ± 0.005 V until the charging current decreased to 0.1 ± 0.01 A, defined as the cutoff current according to the manufacturer's specifications.

For the discharging procedure, the series-connected batteries were subjected to constant current discharges at rates of 1C and 3C, corresponding to currents of 2.5 ± 0.01 A and 7.5 ± 0.01 A, respectively, using the Multifunctional Load TDI RBL488 with specified accuracy. The discharge process continued until the total voltage dropped to 22.5 ± 0.01 V, corresponding to 2.5 V per cell. Thereafter, discharging proceeded with a constant voltage of 22.5 ± 0.01 V until the discharge current fell to 0.1 A, designated as the cutoff current per the manufacturer's specifications. The discharge power usage profiles of the battery modules during the experiments are illustrated in Figure 5, where the horizontal axis is normalized by the total discharge times to facilitate better comparison between different discharge rates. The total discharge times for 1C and 3C discharge rates are approximately 66 min and 25 min, respectively.

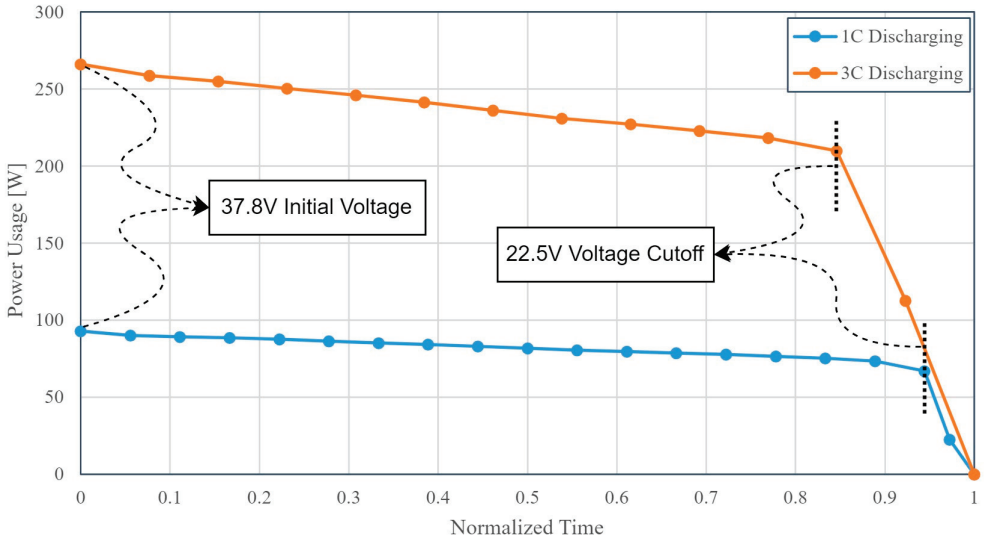

Figure 5. Discharge power usage profile of the battery modules.

2.3. Consistency and Uncertainty Analysis

The methodology proposed by Moffat (1988) [34] was employed to quantify the uncertainties associated with the experimental results. In this study, two primary sources of uncertainty were identified: bias error and precision error. Bias errors represent systematic deviations inherent to the measurement system, while precision errors represent random fluctuations observed during repeated measurements. Both types of errors were quantified to ensure the reliability of the experimental results.

The bias error originates from the measurement instruments used in the experiments. In this case, thermocouples and Adafruit sensors were employed for temperature measurements. According to the manufacturers' specifications, the thermocouples have an accuracy of ±0.5 °C (δT_{TC}), while the Adafruit sensors have an accuracy of ±0.075 °C (δT_S). Since both devices were used in series, their combined uncertainty was calculated using the RSS method [35]:

$$\text{Absolute Bias Error } (^\circ\text{C}) \; \delta T = \sqrt{(\delta T_{TC})^2 + (\delta T_S)^2} \approx 0.5056\ ^\circ\text{C} \tag{1}$$

The resulting absolute bias error for the temperature measurements was determined to be ±0.5056 °C, which is consistent across all experimental conditions, as the bias error depends solely on the instrumentation.

The precision error was assessed based on the variability of the repeated temperature measurements. Precision error is quantified using the maximum discrepancy of data from the mean value, expressed in the same unit as the measurement. The maximum discrepancy is the largest deviation observed between an individual measurement and the mean value of the repeated data for each experiment. This measure provides a straightforward representation of the worst-case scenario for the absolute precision error.

Each experiment was repeated multiple times according to the discharge power usage shown in Figure 5. Figure 6 presents the maximum temperature deviations from the mean values, referred to as the absolute precision error, for each tested condition. The results indicate a maximum absolute precision error of ±0.29 °C, highlighting the consistency of the experimental data.

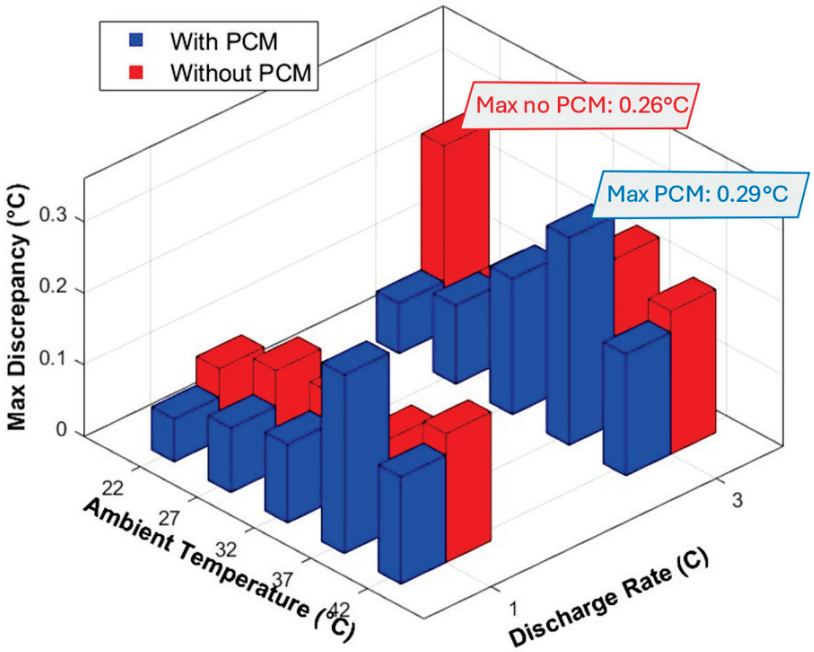

Figure 6. Maximum temperature deviation from the average in repeated experiments.

The total uncertainty of the measurements was determined by combining the relative bias error and the relative precision error using the RSS method:

$$\text{Total Uncertainty } (\%) = \sqrt{(\text{RelativeBiasError})^2 + (\text{RelativePrecisionError})^2} \quad (2)$$

The results are summarized in Table 2 for the minimum and maximum temperatures measured in the experiment. The table highlights the bias error, maximum precision error, and maximum total uncertainty.

Table 2. Errors and total uncertainty of the experiments.

Parameters	Reference Value	Absolute Bias Error (°C)	Relative Bias Error (%)	Max Absolute Precision Error (°C)	Max Relative Precision Error (%)	Max Total Uncertainty (%)
Min. Temperature	20 °C	±0.5056	2.53	±0.29	1.45	2.91
Max. Temperature	55 °C	±0.5056	0.92	±0.29	0.52	1.06

The combined analysis of bias error, precision error, and total uncertainty ensures the reliability and accuracy of the experimental results, providing the validity of the measurements and the overall experimental methodology.

3. Results and Discussion

3.1. Temperature Uniformity Analysis

The surface temperature of all nine battery cells in distinct orientations was measured using nine thermocouples attached to the center of each battery, as depicted in Figure 1b. The thermocouples were strategically positioned to capture a comprehensive range of orientations, including facing the outer wall parallel and perpendicular to the inlet flow, facing the center of the chamber, and being adjacent to others. Each orientation was accurately monitored by a corresponding thermocouple. Figure 7 illustrates the temperature data for the baseline 1C discharge rate at an ambient temperature of 22 °C. The figure reveals that all recorded temperatures exhibit a variance of less than 0.1 °C. This value is below the estimated inherent experimental error in the measurement, demonstrating a high degree of temperature uniformity across the batteries. This consistent behavior was observed in other experiments as well across all tested ambient temperatures. Accordingly, only the temperature measured by thermocouple T1 will be presented and analyzed in subsequent analyses; any reference to temperature henceforth specifically pertains to T1 measurements.

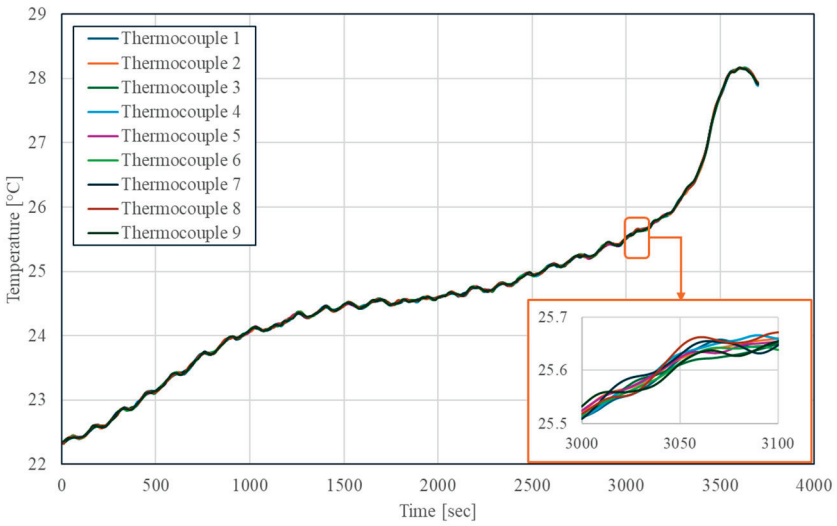

Figure 7. Temperature uniformity analysis across installed thermocouples.

3.2. Temperature Analysis

Figure 8a,b presents the temperature profiles of the batteries, as measured by Thermocouple 1, during the discharge period at 1C and 3C rates, respectively, with and without the PCM under various ambient temperatures. For ease of comparison, both figures are normalized by 3700 and 1400 s, respectively. At a 1C discharge rate and ambient temperatures of 22 °C and 27 °C, incorporating the PCM has minimal impact on both the temperature profile and the maximum temperature, showing the underutilization of current PCM under a 1C discharge rate and favorable ambient temperatures. This result stems from the ambient temperatures being significantly lower than the PCM's melting point (40–42 °C), preventing it from undergoing phase change and utilizing its latent heat absorption capabilities.

However, at higher ambient temperatures of 32 °C and 37 °C, the PCM effectively reduces the rate of temperature rise during discharge, lowering the maximum temperature by approximately 2.5 °C and 2.1 °C, respectively. Moreover, the effect of the PCM is even

more pronounced at an ambient temperature of 42 °C, achieving a thermal performance comparable to the baseline condition at 37 °C without a PCM. This indicates that the PCM becomes more effective as the system temperature nears its melting point.

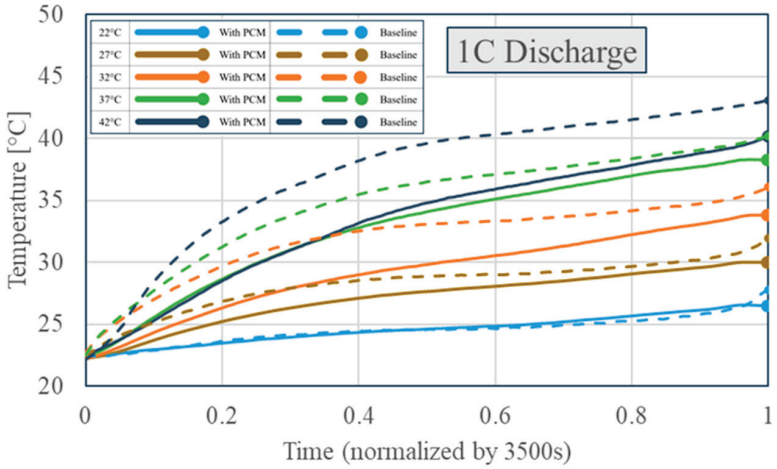

(**a**)

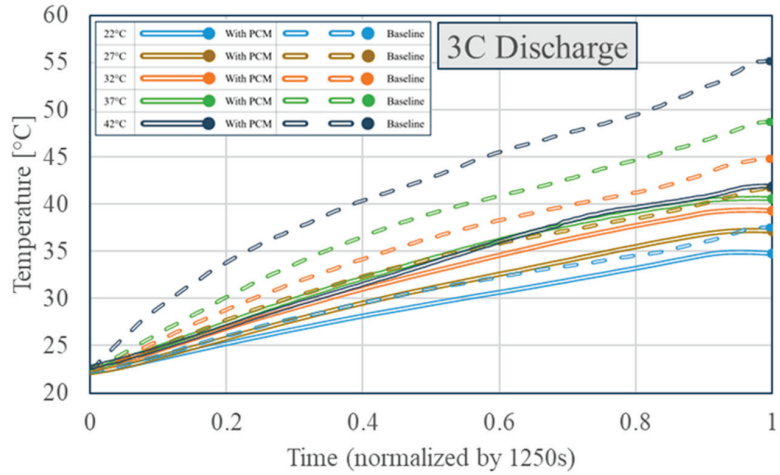

(**b**)

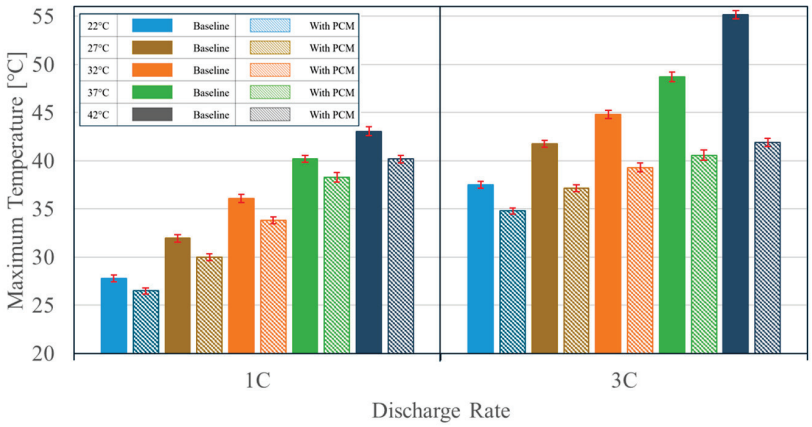

(**c**)

Figure 8. Temperature profile of batteries during constant current discharge at (**a**) 1C and (**b**) 3C, and (**c**) maximum temperature bar chart for each experiment.

As anticipated from the literature, the benefits of using PCMs are more evident at higher discharge rates. Nevertheless, there is a lack of comprehensive understanding of how ambient temperatures approaching the melting point of the PCM affect performance under varying discharge rates, from normal levels (1C) to higher rates (3C).

At a discharge rate of 3C, employing the PCM significantly enhances thermal management, reducing the maximum temperature by approximately 2.6 to 13.3 °C across the tested ambient temperatures. In contrast, under a 1C discharge rate, the maximum temperature was notably decreased by values ranging from 1.6 to 2.5 °C. This underscores the PCM's increased efficacy at higher discharge rates, which generate greater heat and accelerate the PCM's latent heat activation.

Figure 8b shows that with the implementation of the PCM, the maximum temperature remained below 42 °C, which is the melting temperature of the PCM. However, at 27 °C, where the PCM did not reach its melting point, the maximum temperature was reduced by 4.5 °C, which is double the reduction compared to the same ambient temperature at a 1C discharge rate. Additionally, the PCM usage at a 3C discharge rate with a higher ambient temperature (e.g., 42 °C, 37 °C, or 32 °C) exhibits similar cooling performance to the case without the PCM at an ambient temperature of 27 °C. For example, in Figure 8b, the temperature profile at 42 °C with the PCM and at 27 °C without the PCM are identical.

Figure 8c presents the maximum battery temperature measured under each experimental condition, with error bars indicating measurement uncertainties. The data show that, in the absence of a PCM, increases in ambient temperature led to a nearly constant upward trend in the maximum temperature for both the 1C and 3C discharge cases. By contrast, integrating PCM substantially moderates this temperature rise, especially once the system reaches the PCM's melting range. This mitigating effect becomes more pronounced at higher discharge rates, where the batteries generate enough heat to activate the PCM's latent heat storage capacity. Consequently, the maximum temperatures in PCM-equipped setups remain comparatively lower, underscoring the PCM's effectiveness in stabilizing thermal behavior under demanding operational conditions.

3.3. PCM Performance Analysis

Hybrid cooling systems are employed to dissipate heat from batteries and to maintain the maximum temperature below the PCM's melting point. Although incorporating a PCM reduces the equivalent thermal conductivity between the cells and the environment, it provides latent cooling energy storage that becomes active at the PCM's melting point, thereby preventing system overheating [1,36,37]. During the discharge period, the battery cells are assumed to produce a consistent heat flux profile according to the discharge rates. Given the consistent cooling properties, the equivalent thermal conductivity can also be considered constant [38]. Consequently, variations in ambient temperature primarily impact the rate at which the PCM releases stored energy, thereby affecting the system's thermal performance.

Figure 9 presents the temperature reduction performance of the PCM under different ambient temperatures for both 1C and 3C discharge rates. The cooling performance is quantified by comparing the temperature reduction to the baseline case without a PCM, as defined by Equation (3). To assess the PCM's performance per unit of energy stored and account for its dependence on the quantity inside the pack, Equation (3) has been normalized by the PCM's latent heat of fusion (L_f) and its mass (m_{PCM}).

$$\text{PCM Performance } [^\circ\text{C/kJ}] = \frac{T_{without\ PCM} - T_{with\ PCM}}{L_f \,.\, m_{PCM}} \tag{3}$$

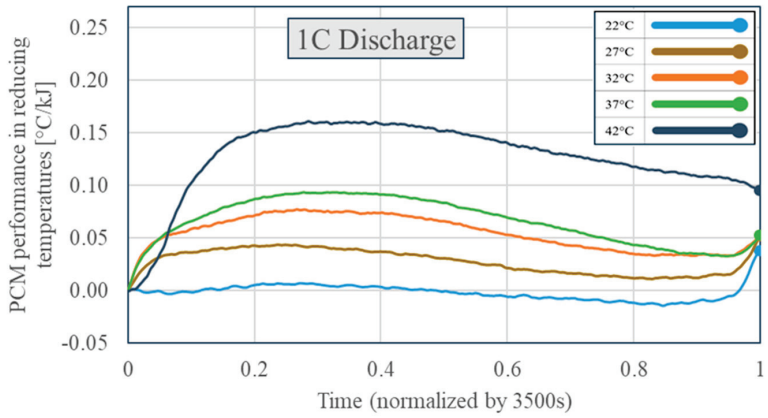

(**a**)

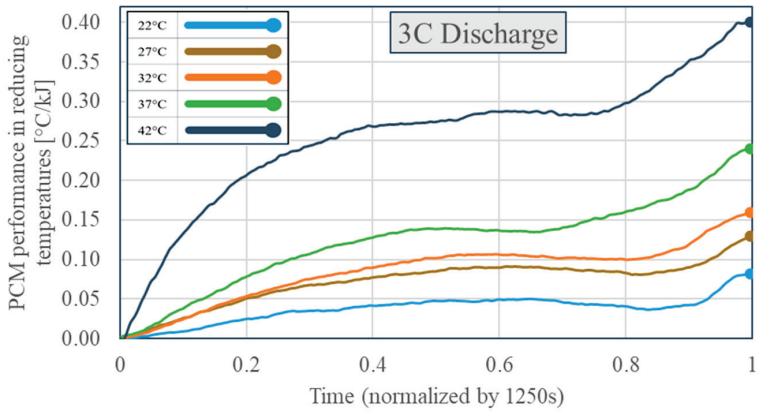

(**b**)

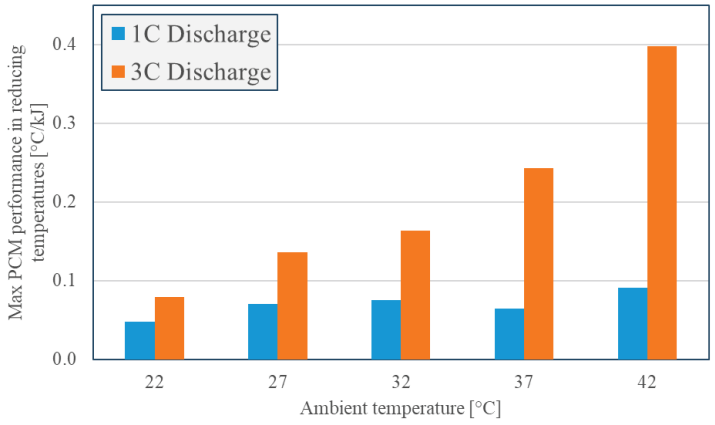

(**c**)

Figure 9. PCM performance in reducing temperatures under elevated ambient temperatures at (**a**) 1C and (**b**) 3C discharge rates and (**c**) maximum attribution of PCM in reducing temperature.

Figure 9a demonstrates the PCM performance at a 1C discharge rate for various ambient temperatures. At 22 °C, the PCM shows a minimal or even negative effect in the early stages of the discharge. This is because the ambient temperature is well below the PCM's melting point (40–42 °C), preventing the utilization of latent heat absorption. However, towards the later stages of the discharge, the PCM starts to show positive cooling effects. This late improvement in performance can likely be attributed to the sensible heat storage of the PCM rather than latent heat absorption, as the system temperature remains

below the melting point of the PCM. The PCM proves more effective for higher ambient temperatures as the system temperature approaches its melting point. However, even in these cases, the maximum temperatures during the experiment remain below the melting point of 40–42 °C, except for the cases of 37 °C and 42 °C ambient temperatures. For these two conditions, the maximum temperatures reach 38.2 °C and 40.3 °C, respectively, still slightly below the melting point of the PCM. Therefore, the cooling effect observed at the higher ambient temperatures of 27 °C, 32 °C, and 37 °C is largely influenced by the sensible heat storage. Only at 42 °C does the PCM utilize its latent heat capacity, where a significant reduction of up to 5 °C is achieved before the difference diminishes as the thermal management system reaches the ambient temperature during the second half of the experiment. Consequently, the current PCM has been underutilized under the 1C discharge rate since the maximum achieved temperature is below the melting point, and no latent heat absorption occurred at these conditions. If further reduction or stricter regulation of the maximum temperature is necessary under these conditions, a PCM with a lower melting point can be considered.

In contrast to the 1C discharge, the higher heat generation in the 3C discharge activates the PCM melting more rapidly, resulting in noticeable cooling effects early in the experiment, as illustrated in Figure 9b. At lower ambient temperatures, the PCM performance is driven primarily by sensible heat absorption since the system temperatures do not reach the melting range of the PCM. Despite this, the PCM still provides a consistent reduction in temperature throughout the discharge. As the ambient temperature increases, the system temperature approaches the PCM's melting range, leading to partial phase change and the activation of both sensible and latent heat absorption. This results in a more pronounced cooling effect as the PCM transitions into its melting phase. At the highest ambient temperature, nearly the entire PCM undergoes a phase change, maximizing its cooling potential. However, as with the 1C discharge case, the cooling effectiveness of the PCM over the case without the PCM diminishes over time due to the better utilization of traditional cooling rather than the latent capacity in the case without the PCM, indicating a limit to sustained performance.

Figure 9c illustrates the comparison of maximum PCM performance for both 1C and 3C discharge rates across varying ambient temperatures. As the ambient temperature increases, the cooling performance improves for both rates, with the 3C discharge consistently showing greater reductions due to higher heat generation and faster starting of PCM phase change. At lower ambient temperatures, the cooling effect is primarily due to sensible heat absorption. In comparison, latent heat absorption significantly enhances performance at higher temperatures as the system approaches the PCM's melting range. The results highlight the dependence of PCM efficiency on the discharge rate and ambient temperature, with the 3C discharge achieving the most substantial reductions.

3.4. PCM Phase Change Analysis

The benefits of using a PCM at high discharge rates and elevated ambient temperatures stem from harnessing the PCM's stored latent energy, which helps stabilize temperatures during the phase change process. Analyzing the melting percentage at the end of discharge is essential to understanding how effectively the PCM is utilized in the system. According to the literature [20], the simplified melting percentage of the PCM in an elemental volume is calculated as follows:

$$\text{PCM Melting Percentage} = \begin{cases} 0 & if \quad T_m < T_s \\ \frac{T_m - T_s}{T_l - T_s} & if \quad T_s < T_m < T_l \\ 1 & if \quad T_m > T_l \end{cases} \tag{4}$$

Here, T_m, T_l, and T_s denote the maximum temperature, PCM liquidus temperature, and PCM solidus temperature, respectively. The quantified value of the PCM melting percentage does not equate to the total melting fraction of the PCM contained within the chamber. Rather, it pertains specifically to the controlled volume surrounding the measuring thermocouple. Table 3 presents the PCM melting percentages at the end of the experiments. During the 1C discharge experiments, no PCM melted at an ambient temperature below the melting point, indicating that latent heat was not utilized under these conditions. However, during the 3C discharge experiments, the PCM melting commenced at an ambient temperature of 32 °C, with 12.4% of the PCM melting, and reached nearly complete utilization at 42 °C, with approximately 98% of the PCM melting.

Table 3. PCM melting percentage (in %) at the end of experiments.

Ambient Temperature (T_m) [°C]	1C Discharge Rate	3C Discharge Rate
22	0	0
27	0	0
32	0	12.4
37	0	54.3
42	46.3	97.6

Additionally, considering the 3C discharge rate, the interpolation of Figure 9 and the melting percentage data indicate that the PCM started contributing its stored cooling capacity (i.e., latent heat) to the system after achieving a 4.6 °C reduction in maximum temperature. Figure 10 illustrates the corresponding interpolation analysis. The second-degree polynomial interpolation analysis yielded R-squared values of 0.9981. From this analysis, it can be inferred that the maximum utilization of PCM at a 3C discharge rate (i.e., 100% melting) corresponds to a PCM performance of approximately 13.6 °C in maximum temperature reduction. Note that the formula derived from the 3C discharge rate results cannot be applied to the 1C analysis. Furthermore, the PCM melting percentage, as described in Equation (3), pertains solely to the close proximity of the thermocouple probes and should not be interpreted as the total melting fraction.

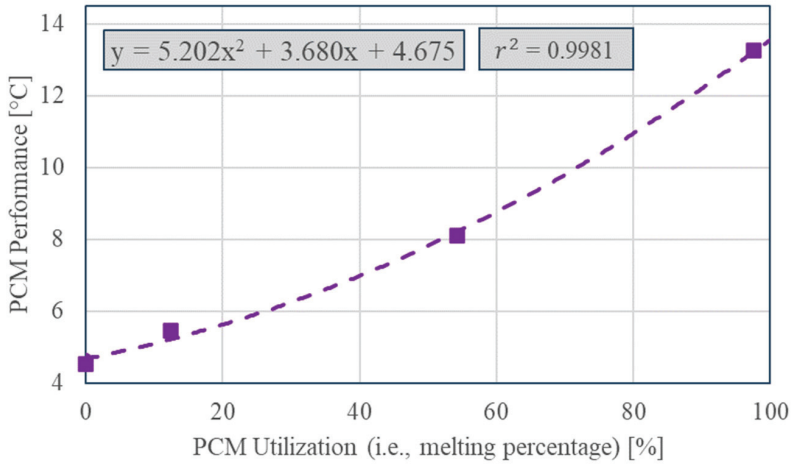

Figure 10. Interpolated PCM utilization and corresponding cooling performance in terms of maximum temperature reduction at a 3C discharge rate.

In summary, the findings demonstrate the effectiveness of the PCM in mitigating temperature rises and maintaining thermal stability within the battery pack under varied operational conditions. The PCM efficiently utilizes its stored latent heat to limit the maximum temperature, particularly at high ambient temperatures and discharge rates. While underutilized at a 1C discharge rate, it achieved a complete local phase transition at

the 3C rate and an ambient temperature of 42 °C. Despite achieving excellent temperature uniformity across the battery surfaces, with variations less than 0.1 °C, a key limitation was identified in the PCM's thermal behavior. Visual inspection revealed that only the PCM in close proximity to the battery surfaces—within approximately 1 mm—underwent phase change and melted. The PCM located farther from the batteries remained solid and was not utilized in the phase change process. This limitation is attributed to the inherently low thermal conductivity of paraffin, which restricts efficient heat transfer throughout the PCM volume. Consequently, only a fraction of the PCM's latent heat storage potential was utilized, thereby constraining its overall effectiveness under high thermal loads.

4. Conclusions

This study experimentally investigated the thermal performance of a proposed PCM-based battery pack under elevated ambient temperatures. In addition, the novel approach of the research addresses scenarios where the ambient temperature reaches the PCM's melting point while maintaining the initial temperature at the ideal operating point of 22 °C. The experiments employed nine 2500 mAh 18650 lithium-ion cells connected in series and subjected to constant-current discharges of 1C and 3C. A conventional air-cooled thermal management system served as the baseline, and paraffin with a melting temperature of 40–42 °C was selected as the integrated PCM in the battery pack, including an inlet air speed of 2.1 $\pm$ 0.1 m/s and 177 $\pm$ 1 mL of paraffin. The novelty of this research lies in the experimental evaluation of the thermal efficiency of the PCM in responding to rising ambient temperatures, reaching the PCM's melting point by quantifying the percentage of PCM's local melting and its utilization of stored energy. The following conclusions were drawn:

- At ambient temperatures approaching the PCM's melting point, the local utilization percentage of the PCM reached approximately 98% around the batteries and air pipes. This indicates the near-complete engagement of the PCM around the heating sources. However, visual inspection revealed that the PCM was not contributing to its full capacity and left a portion of its volume unmelted. This necessitates the need for further enhancements of pure PCM systems in ambient temperatures exceeding the melting point to effectively manage elevated environmental conditions while fully leveraging the PCM's latent heat storage capacity for maintaining optimal battery temperatures.
- Using the PCM diminishes the impact of rising ambient temperatures on both the maximum battery temperature and the overall temperature profile. With the PCM, the maximum temperature varied by about 7 $\pm$ 1 °C across the tested temperature range, while the baseline system without a PCM exhibited fluctuations exceeding 18 $\pm$ 1 °C. This underscores the PCM's effectiveness in stabilizing thermal performance despite rising external temperatures.
- During high-stress conditions, such as a 3C discharge rate under elevated ambient temperatures, the PCM became more suitable for thermal management. The maximum battery temperature remained below 42 °C in the PCM-integrated system, whereas the baseline system experienced a significant temperature increase from 38 °C to 55 °C. This demonstrates the PCM's effectiveness in ensuring thermal stability under demanding conditions.
- At a 1C discharge rate, the PCM achieved a modest maximum temperature reduction of up to 3.1 °C. However, at a 3C discharge rate, the PCM's performance improved considerably with rising ambient temperatures (from 22 °C to 42 °C), reducing the maximum temperature by 2.6 °C to 13.3 °C, respectively. This reinforces the PCM's enhanced thermal management capability under elevated operational and environmental stress levels.

These conclusions underscore the potential impact of using a PCM at elevated ambient temperatures, particularly under high discharge rates, on the thermal management of the battery packs. By examining ambient conditions up to the PCM's melting point and correlating local melting percentages with resulting temperature reductions, this research addresses a gap in the existing literature and provides a foundation for further advancements in PCM-based thermal management systems under a wider range of ambient operational conditions. The limitation of the study is the use of paraffin as the PCM since it is flammable. However, the flammability concern can be later mitigated through appropriate system design and packaging.

Author Contributions: Conceptualization, M.J.G., M.A.-C. and M.A.R.; methodology, M.J.G.; software, M.J.G.; validation, M.J.G., M.A.-C. and M.A.R.; formal analysis, M.J.G.; investigation, M.J.G.; resources, M.A.-C. and M.A.R.; data curation, M.J.G.; writing—original draft preparation, M.J.G.; writing—review and editing, M.J.G., M.A.-C. and M.A.R.; visualization, M.J.G.; supervision, M.A.-C. and M.A.R.; project administration, M.A.-C.; funding acquisition, M.A.-C. All authors have read and agreed to the published version of the manuscript.

Funding: This research was funded by the Natural Sciences and Engineering Research Council of Canada (NSERC), grant number RGPIN-2018-05369.

Data Availability Statement: The data presented in this study are available on request from the corresponding author due to confidentiality agreements.

Acknowledgments: The authors acknowledge with gratitude the financial support provided by the Natural Sciences and Engineering Research Council of Canada (especially the NSERC CREATE and NSERC Discovery Grant programs). The technical support of Seham Shahid, a recent graduate of Ontario Tech, is also greatly appreciated.

Conflicts of Interest: The authors declare no conflict of interest.

Nomenclature

C	Discharge rate (1/h)
C_p	Specific heat at constant pressure
k	Thermal conductivity (W/m·K)
L_f	Latent heat of fusion (kJ/kg)
T	Temperature (°C)
T_l	Liquidus temperature (°C)
T_s	Solidus temperature (°C)
Greek Symbols	
δT_S	Error of Adafruit sensor (°C)
δT_{TC}	Error of thermocouple (°C)
ρ	Density (kg/m^3)
ρ_e	Electrical resistivity (Ω·m)
Abbreviations and Acronyms	
BTMS	Battery Thermal Management System
CPCM	Composite Phase Change Material
CC	Constant Current
CV	Constant Voltage
C-rate	Current Rate
LIB	Lithium-Ion Battery
Li-ion	Lithium-Ion
MDF	Medium-Density Fiberboard
PCM	Phase Change Material

References

1. Luo, J.; Zou, D.; Wang, Y.; Wang, S.; Huang, L. Battery thermal management systems (BTMs) based on phase change material (PCM): A comprehensive review. *Chem. Eng. J.* **2022**, *430*, 132741. [CrossRef]
2. Shahid, S.; Agelin-Chaab, M. Experimental and numerical studies on air cooling and temperature uniformity in a battery pack. *Int. J. Energy Res.* **2018**, *42*, 2246–2262. [CrossRef]
3. Leng, F.; Tan, C.M.; Pecht, M. Effect of temperature on the aging rate of Li ion battery operating above room temperature. *Sci. Rep.* **2015**, *5*, 12967. [CrossRef] [PubMed]
4. Shahid, S.; Agelin-Chaab, M. A review of thermal runaway prevention and mitigation strategies for lithium-ion batteries. *Energy Convers. Manag. X* **2022**, *16*, 100310. [CrossRef]
5. Chen, K.; Wu, W.; Yuan, F.; Lin, C.; Wang, S. Cooling efficiency improvement of air-cooled battery thermal management system through designing the flow pattern. *Energy* **2019**, *167*, 781–790. [CrossRef]
6. Wang, M.; Teng, S.; Xi, H.; Li, Y. Cooling performance optimization of air-cooled battery thermal management system. *Appl. Therm. Eng.* **2021**, *195*, 117242. [CrossRef]
7. Wang, N.; Li, C.; Li, W.; Chen, X.; Yongsheng, L.; Qi, D. Heat dissipation optimization for a serpentine liquid cooling battery thermal management system: An application of surrogate assisted approach. *J. Energy Storage* **2021**, *40*, 102771. [CrossRef]
8. Jialin, L.; Gan, Y.; Li, Y. Investigation on the thermal performance of a battery thermal management system using heat pipe under different ambient temperatures. *Energy Convers. Manag.* **2018**, *155*, 1–9. [CrossRef]
9. Huang, M.; Eames, P.; Norton, B.; Hewitt, N. Natural convection in an internally finned phase change material heat sink for the thermal management of photovoltaics. *Sol. Energy Mater. Sol. Cells* **2011**, *95*, 1598–1603. [CrossRef]
10. Chen, J.; Kang, S.; E, J.; Huang, Z.; Wei, K.; Zhang, B.; Zhu, H.; Deng, Y.; Zhang, F.; Liao, G. Effects of different phase change material thermal management strategies on the cooling performance of the power lithium ion batteries: A review. *J. Power Sources* **2019**, *442*, 227228. [CrossRef]
11. Wu, W.; Liu, J.; Liu, M.; Rao, Z.; Deng, H.; Wang, Q.; Qi, X.; Wang, S. An innovative battery thermal management with thermally induced flexible phase change material. *Energy Convers. Manag.* **2020**, *221*, 113145. [CrossRef]
12. Landini, S.; Leworthy, J.; O'Donovan, T. A review of phase change materials for the thermal management and isothermalisation of lithium-ion cells. *J. Energy Storage* **2019**, *25*, 100887. [CrossRef]
13. Safdari, M.; Ahmadi, R.; Sadeghzadeh, S. Numerical investigation on PCM encapsulation shape used in the passive-active battery thermal management. *Energy* **2020**, *193*, 116840. [CrossRef]
14. Lin, C.; Xu, S.; Chang, G.; Liu, J. Experiment and simulation of a $LiFePO_4$ battery pack with a passive thermal management system using composite phase change material and graphite sheets. *J. Power Sources* **2015**, *275*, 742–749. [CrossRef]
15. Lazrak, A.; Fourmigue, J.; Robin, J. An innovative practical battery thermal management system based on phase change materials: Numerical and experimental investigations. *Appl. Therm. Eng.* **2018**, *128*, 20–32. [CrossRef]
16. Javani, N.; Dincer, I.; Naterer, G.; Rohrauer, G. Modeling of passive thermal management for electric vehicle battery packs with PCM between cells. *Appl. Therm. Eng.* **2014**, *73*, 307–316. [CrossRef]
17. Suo, Y.; Tang, C.; Jia, Q.; Zhao, W. Influence of PCM configuration and optimization of PCM proportion on the thermal management of a prismatic battery with a combined PCM and air cooling structure. *J. Energy Storage* **2024**, *80*, 110340. [CrossRef]
18. Dey, H.; Pati, S.; Randive, P.R.; Baranyi, L. Effect of finned networks on PCM based battery thermal management system for cylindrical Li-ion batteries. *Case Stud. Therm. Eng.* **2024**, *59*, 104572. [CrossRef]
19. Zhang, F.; Lu, F.; Liang, B.; Zhu, Y.; Gou, H.; Xiao, K.; He, Y. Thermal performance analysis of a new type of branch-fin enhanced battery thermal management PCM module. *Renew. Energy* **2023**, *206*, 1049–1063. [CrossRef]
20. Khaboshan, H.N.; Jaliliantabar, F.; Abdullah, A.A.; Panchal, S. Improving the cooling performance of cylindrical lithium-ion battery using three passive methods in a battery thermal management system. *Appl. Therm. Eng.* **2023**, *227*, 120320. [CrossRef]
21. Sharma, D.K.; Agarwal, P.; Prabhakar, A. Effect of fin design and continuous cycling on thermal performance of PCM-HP hybrid BTMS for high ambient temperature applications. *J. Energy Storage* **2023**, *74*, 109360. [CrossRef]
22. Wang, W.; Zhang, X.; Xin, C.; Rao, Z. An experimental study on thermal management of lithium-ion battery packs using an improved passive method. *Appl. Therm. Eng.* **2018**, *134*, 163–170. [CrossRef]
23. Li, K.; Yao, X.; Li, Z.; Gao, T.; Zhang, W.; Liao, Z.; Ju, X.; Xu, C. Thermal management of Li-ion batteries with passive thermal regulators based on composite PCM materials. *J. Energy Storage* **2024**, *89*, 111661. [CrossRef]
24. Wu, W.; Ye, G.; Zhang, G.; Yang, X. Composite phase change material with room-temperature-flexibility for battery thermal management. *Chem. Eng. J.* **2022**, *428*, 131116. [CrossRef]
25. Luo, M.; Zhang, Y.; Wang, Z.; Niu, Y.; Lu, B.; Zhu, J.; Zhang, J.; Wang, K. Thermal performance enhancement with snowflake fins and liquid cooling in PCM-based battery thermal management system at high ambient temperature and high discharge rate. *J. Energy Storage* **2024**, *90*, 111754. [CrossRef]

26. Xie, N.; Zhang, Y.; Liu, X.; Luo, R.; Liu, Y.; Ma, C. Thermal performance and structural optimization of a hybrid thermal management system based on MHPA/PCM/liquid cooling for lithium-ion battery. *Appl. Therm. Eng.* **2023**, *235*, 121341. [CrossRef]
27. Chen, X.; Su, Y.; Zhang, Y.; Shen, J.; Xu, X.; Wang, X.; Zhou, F. Performance of thermal management system based on PCM/forked liquid-cold plate for 18650 cylindrical battery. *J. Energy Storage* **2024**, *91*, 112071. [CrossRef]
28. Zheng, J.; Chang, L.; Mu, M.; Li, J.; Li, C.; Ma, C.; Du, H. A novel thermal management system combining phase change material with wavy cold plate for lithium-ion battery pack under high ambient temperature and rapid discharging. *Appl. Therm. Eng.* **2024**, *245*, 122803. [CrossRef]
29. Shahid, S.; Agelin-Chaab, M. Experimental and numerical analysis of a hybrid cooling concept for an electric battery module. *Int. J. Heat Fluid Flow* **2024**, *106*, 109320. [CrossRef]
30. Shahid, S.; Agelin-Chaab, M. Investigation of thermal properties of phase change materials for novel hybrid thermal management strategies for cylindrical Li-ion cells. *Appl. Therm. Eng.* **2024**, *242*, 122471. [CrossRef]
31. Shahid, S.; Agelin-Chaab, M. Experimental and parametric analysis of a novel hybrid thermal management strategy for cylindrical lithium-ion cells. *Heat Transfer* **2024**, *53*, 2840–2863. [CrossRef]
32. Halliday, D.; Resnick, R.; Walker, J. *Fundamentals of Physics*, 12th ed.; John Wiley Sons: Hoboken, NJ, USA, 2012.
33. Peng, P.; Wang, Y.; Jiang, F. Numerical study of PCM thermal behavior of a novel PCM-heat pipe combined system for Li-ion battery thermal management. *Appl. Therm. Eng.* **2022**, *209*, 118293. [CrossRef]
34. Moffat, R.J. Describing the uncertainties in experimental results. *Exp. Therm. Fluid Sci.* **1988**, *1*, 3–17. [CrossRef]
35. Ganji, M.; Givian, M.; Gharali, K.; Ebadi, S.; Dastjerdi, S.M. Experimental optimization of partial metallic wire mesh configuration applicable in thermal energy storage systems. *Appl. Therm. Eng.* **2023**, *218*, 119274. [CrossRef]
36. Regin, A.F.; Solanki, S.C.; Saini, J.S. Heat transfer characteristics of thermal energy storage system using PCM capsules: A review. *Renew. Sustain. Energy Rev.* **2008**, *12*, 2438–2458. [CrossRef]
37. Moaveni, A.; Siavashi, M.; Mousavi, S. Passive and hybrid battery thermal management system by cooling flow control, employing nano-PCM, fins, and metal foam. *Energy* **2024**, *288*, 129809. [CrossRef]
38. Cengel, Y.A. Heat Transfer. In *Encyclopedia of Energy Engineering and Technology—Four Volume Set*; CRC Press: Boca Raton, FL, USA, 2014; pp. 846–853.

batteries

MDPI

Article

Design Optimization of Bionic Liquid Cooling Plate Based on PSO-BP Neural Network Surrogate Model and Multi-Objective Genetic Algorithm

Jiaming Liu [1], Wenlin Yuan [1], Yapeng Zhou [2] and Hengyun Zhang [1,*]

[1] School of Mechanical and Automotive Engineering, Shanghai University of Engineering Science, Songjiang, Shanghai 201620, China
[2] China Merchants Testing Vehicle Technology Research Institute Limited Company, Chongqing 400039, China
* Correspondence: zhanghengyun@sues.edu.cn

Abstract: In this study, the particle swarm optimization (PSO) and back propagation neural network (BPNN) surrogate model in combination with a multi-objective genetic algorithm are developed for the design optimization of a bionic liquid cooling plate with a spider-web channel structure. The single-factor sensitivity analysis is first conducted based on the numerical simulation approach, identifying three key factors as design variables for optimizing design objectives such as maximum temperature (T_{max}), maximum temperature difference (ΔT_{max}), and pressure drop (ΔP). Subsequently, the PSO algorithm is used to optimize the parameters of the BPNN structure, thereby constructing the PSO-BPNN surrogate model. Next, the non-dominated sorting genetic algorithm II (NSGA-II) is employed to obtain the Pareto optimal set, and the TOPSIS with the entropy weight method is used to determine the optimal solution, eliminating subjective preferences in decision-making. The results show that the PSO-BPNN model outperforms the traditional BPNN in prediction accuracy for all three objectives. Compared to the initial structure, the T_{max} and ΔT_{max} are reduced by 1.09 °C and 0.41 °C in the optimized structure, respectively, with an increase in ΔP by 21.24 Pa.

Keywords: liquid cooling plate; particle swarm optimization; back propagation neural network; multi-objective optimization; entropy weight–TOPSIS method

1. Introduction

Due to increasingly severe energy shortages and environmental degradation, countries around the world have begun to develop more energy-efficient and environmentally friendly electric vehicles, which are gradually replacing traditional fuel vehicles and becoming the main trend of future automotive development [1,2]. Lithium-ion batteries are the core power source for electric vehicles and have become widely used in the electric vehicle sector because of their high energy density, low self-discharge rate and long cycle life [3,4]. However, the operating temperature of lithium-ion batteries significantly affects their performance and lifespan. The ideal operating temperature range is 25 °C to 40 °C, and the ΔT_{max} should be controlled within 5 °C [5]. If the temperature exceeds the maximum safety threshold of lithium-ion batteries, it may result in thermal runaway, potentially triggering serious safety accidents such as fires and explosions [6,7]. Therefore, establishing an efficient battery thermal management system (BTMS) is extremely important for ensuring the safe and stable operation of the batteries.

Battery thermal management approaches primarily consist of air cooling [8,9], liquid cooling [10,11], phase change material (PCM) cooling [12,13], and heat pipe cooling [14,15]. In the past, air cooling was widely applied due to its advantages, such as simple structure and low maintenance cost [16]. However, as the energy density of batteries rises, air cooling is unable to satisfy the heat dissipation requirements [17]. Although PCM can effectively absorb the heat generated by batteries, it has not been applied due to its poor thermal conductivity [18]. Heat pipes possess good thermal conductivity but generally need to be combined with other cooling approaches, which increases system complexity [19], thus limiting their application in BTMS. In comparison, liquid cooling remains the mainstream form of thermal management for batteries because of its outstanding heat dissipation capability [20].

Liquid cooling can be categorized into two types: direct contact cooling and indirect contact cooling [21]. In direct contact cooling, the coolant makes contact with the battery for heat exchange, providing better temperature uniformity for the battery, which, however, requires high-stability dielectric coolant and a well-sealed cooling system [22]. In comparison to direct contact cooling, indirect contact cooling employs the liquid cooling plates to establish a connection with the batteries, with thermal interface materials in between them to dissipate heat. The key design principle for the liquid cooling plate is to create a reasonable flow channel to ensure that the coolant is evenly distributed in the channels. Li et al. [23] studied the impact of two layouts of liquid cooling plates with a single channel, multiple small channels, and an S-shaped channel on the thermal management of the battery module. The results indicated that placing liquid cooling plates with multiple small channels on both sides of the battery module achieved optimal cooling performance. Sheng et al. [24] devised a liquid cooling plate with double serpentine channels, finding that the arrangement of the inlet and outlet significantly affected the temperature difference. Huang et al. [25] designed a liquid cooling plate with streamlined channels, and the results showed that it can significantly reduce $\Delta T_{\max}$ and ΔP.

Besides the conventional liquid cooling plates mentioned above, researchers have shown interest in the design of liquid cooling plates inspired by bionic structures. Wang et al. [26] designed a liquid cooling plate with a butterfly-shaped flow channel and compared its cooling performance with straight, serpentine, and leaf-shaped liquid cooling plates. The results showed that the butterfly-shaped liquid cooling plate demonstrated superior overall performance. Subsequently, further optimization of its structural parameters resulted in an optimal configuration, reducing the $T_{\max}$ to 32.72 °C and ΔP to 25.7 Pa. Liu et al. [27] proposed a bionic leaf-vein channel liquid cooling plate and studied the impact of various structural factors. It was found that the channel width and inlet velocity significantly affected the cooling performance. Fan et al. [28] designed four types of liquid cooling plates with bionic fishbone channels. Compared to the Z-shaped liquid cooling plate, the bionic fishbone channel liquid cooling plate with a single inlet and dual outlets demonstrated better cooling performance.

In most cases, the above methods for optimizing battery thermal management parameters primarily rely on numerical simulations and tedious case experiments. The diverse and complex combinations of different parameters result in the significant consumption of time and computational resources during the analysis and optimization processes. As diverse surrogate models and artificial intelligence algorithms evolve, large amounts of data can be processed quickly, improving work efficiency without human intervention. As such, many researchers have optimized BTMS using surrogate models and optimization algorithms. Due to the nonlinear characteristics of complex BTMS, the BPNN is used as a surrogate model for multi-objective optimization because of its advantages in handling

complex nonlinear mapping relationships and strong self-learning ability. Li et al. [29] used an artificial neural network to establish the relationship between battery spacing, ambient pressure, and both the T_{max} and ΔT_{max} and then improved the temperature uniformity of the battery module through optimized design. Chen et al. [30] showed that a deep learning neural network model provided more precise output predictions for the cooling performance of carbon/epoxy resin with a microchannel compared to the response surface model. Although progress has been made in performance prediction, the traditional BPNN has certain limitations as a surrogate model. The learning rate and the number of hidden nodes, which are critical hyperparameters affecting model training, are generally set based on personal experience and often require multiple human trials to optimize. Additionally, the initial weights and thresholds of the BPNN are generally initialized randomly, which would lead to the network getting stuck in local optima during training, thereby affecting the prediction performance of the model.

In response to the above issues, this paper introduces the PSO-BPNN surrogate model in combination with multi-objective genetic algorithm for the design optimization of a bionic liquid cooling plate constructed with a spider-web channel structure. The PSO algorithm can automatically optimize the number of hidden nodes, learning rate, initial weights, and thresholds without human intervention. This approach significantly enhances the prediction accuracy of the BPNN. Based on this, a novel spider-web liquid cooling plate is proposed, with the T_{max}, ΔT_{max}, and ΔP selected as optimization objectives. The optimal Latin hypercube sampling (OLHS) method is employed for sampling, and a corresponding dataset of samples is constructed through computational fluid dynamics (CFD) simulations. Based on these data, the PSO-BPNN surrogate model is established. Subsequently, the NSGA-II algorithm is adopted to perform multi-objective optimization on the spider-web cooling plate. The entropy weight method is used to determine the weight of each objective, and the TOPSIS method is applied to rank the optimal solutions, thereby obtaining the optimal structural parameters for the cooling plate.

2. Model and Validation

2.1. Model Description

A bionic liquid cooling plate with a spider-web channel is designed for battery thermal management. The prismatic lithium-ion battery used in this paper is of the model CATL2795148-51Ah. Its cathode material is $LiNi_{0.8}Co_{0.1}Mn_{0.1}O_2$, the anode material is graphite, and the electrolyte is $LiPF_6$. The detailed characteristic parameters are listed in Table 1. The geometric model of the battery liquid cooling system is shown in Figure 1, which consists of five batteries and six liquid cooling plates arranged alternately. It is noted that the liquid cooling plates are positioned on the large sides of the batteries. When prismatic lithium-ion batteries are grouped, the large sides with the highest temperature come into contact, making it difficult for the heat generated by the batteries to dissipate in time, leading to heat accumulation. As such, a side-contact cooling method is adopted to enhance the heat dissipation of the batteries. To save computational resources, a representative cooling unit will be used as the subject of subsequent simulations, namely a liquid cooling plate in direct contact with two batteries. Considering that aluminum has good thermal conductivity and lightweight properties, it is selected as the material for the liquid cooling plate. Water flows through the channels in the liquid cooling plate, absorbing heat from the batteries. The physical parameters of the liquid cooling plate and coolant are presented in Table 2.

Table 1. Parameters of prismatic lithium-ion battery.

Battery Parameters	Value
Size/mm	148 × 92 × 27
Nominal voltage/V	3.7
Nominal capacity/Ah	51
Discharge cut-off voltage/V	2.8
Charge cut-off voltage/V	4.2
Maximum continuous discharge rate/C	3
Maximum continuous charge rate/C	1
Internal resistance/mΩ	0.7
Mass/g	824.5

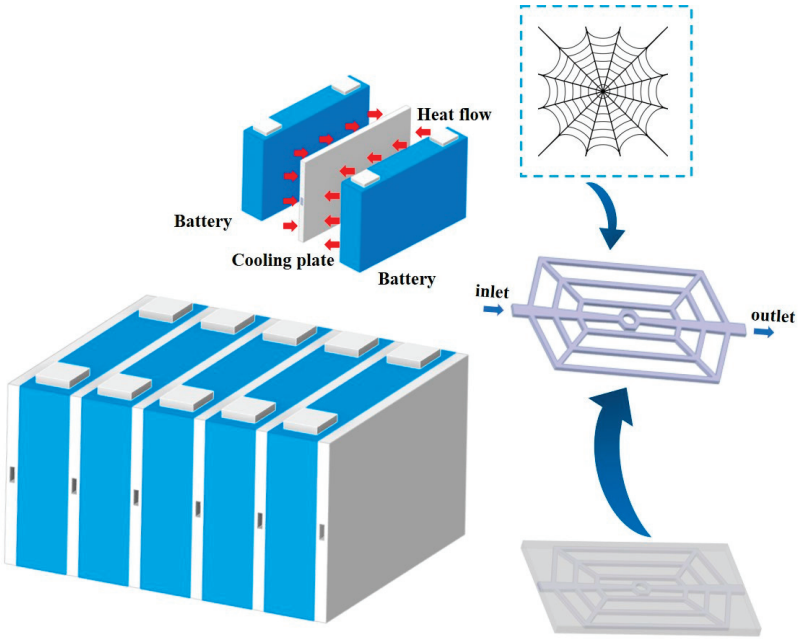

Figure 1. Schematic of battery liquid cooling system.

Table 2. Physical parameters of liquid cooling plate and coolant.

Material	Density/kg·m^{-3}	Specific Heat Capacity/J·kg^{-1}·K^{-1}	Thermal Conductivity/W·m^{-1}·K^{-1}	Viscosity/Pa·s
Liquid cooling plate (Aluminum)	2719	871	202	-
Coolant (Water)	998.2	4182	0.6	0.001003

2.2. Governing Equations and Boundary Conditions

To improve the efficiency of numerical calculations, the following assumptions are made for the model.

(1) Radiative heat transfer between the battery and the surroundings is ignored.

(2) The coolant is incompressible with steady-state flow field.

(3) The physical properties of the coolant, liquid cooling plate, and battery are unaffected by temperature.

(4) The contact thermal resistance between the battery and the liquid cooling plate is ignored.

2.2.1. Battery Governing Equation

Assuming that the battery is composed of anisotropic and uniformly distributed materials, the three-dimensional energy equation for the battery in a Cartesian coordinate system is as follows [31]:

$$\rho_{bat} c_{bat} \frac{\partial T_{bat}}{\partial t} = \lambda_x \frac{\partial^2 T_{bat}}{\partial x^2} + \lambda_y \frac{\partial^2 T_{bat}}{\partial y^2} + \lambda_z \frac{\partial^2 T_{bat}}{\partial z^2} + q \tag{1}$$

where ρ_{bat}, c_{bat}, and T_{bat} are the density, specific heat capacity and temperature of the battery, respectively. λ_x, λ_y, and λ_z are the thermal conductivity of the battery along the x, y and z directions, respectively. q is the volumetric heat generation rate of the battery.

2.2.2. Convective Boundary Between Air and Battery

The convective boundary condition between the battery and the air is as follows [32]:

$$\lambda_{bat} \frac{\partial T}{\partial n}|_{sur,bat} = -h_{sur,bat}(T_{bat} - T_a) \tag{2}$$

$$T(x, y, z, 0) = T_a \tag{3}$$

where $h_{sur,bat}$ is the convective heat transfer coefficient on the battery surface, and T_a is the ambient temperature.

2.2.3. Heat Transfer Boundary Between Battery and Liquid Cooling Plate

The heat transfer boundary condition and initial condition between the battery and the cooling plate are as follows [32]:

$$\lambda_{bat} \frac{\partial T}{\partial n}|_{sur,bat-lcp} = \lambda_{lcp} \frac{\partial T}{\partial n}|_{sur,bat-lcp} \tag{4}$$

$$T_{bat} = T_{lcp} \tag{5}$$

$$T(x, y, z, 0) = T_a \tag{6}$$

where λ_{lcp} is the thermal conductivity of the liquid cooling plate, and n is the normal direction.

2.2.4. Coolant Governing Equations and Boundary Condition

The coolant mass, energy and momentum conservation equations are as follows [33]:
Mass conservation:

$$\nabla \cdot (\rho_f \vec{v}) = 0 \tag{7}$$

Energy conservation:

$$\rho_f c_f \frac{\partial T_f}{\partial t} + \nabla \cdot (\rho_f c_f \vec{v} T_f) = \nabla \cdot (\lambda_f \nabla T_f) \tag{8}$$

Momentum conservation:

$$\frac{\partial}{\partial t}(\rho_f \vec{v}) + \nabla \cdot (\rho_f \vec{v}) \vec{v} = -\nabla P_f + \mu \nabla^2 \vec{v} \tag{9}$$

where ρ_f is the density of the coolant, $\vec{v}$ is the velocity vector, c_f is the specific heat capacity of the coolant, λ_f is the thermal conductivity of the coolant, T_f is the temperature of the

coolant, μ is the dynamic viscosity of the coolant, ∇^2 is the Laplacian operator, and P_f is the static pressure of the coolant.

The boundary condition between the liquid cooling plate and the coolant can be expressed as follows [32]:

$$\lambda_{lcp}\frac{\partial T}{\partial n}|_{sur,lcp-f} = -h_{sur,lcp-f}(T_{lcp} - T_f) \tag{10}$$

For fluid flow, the Reynolds number can be calculated by Equation (11).

$$\mathrm{Re} = \frac{\rho_f v D}{\mu} \tag{11}$$

where D is the hydraulic diameter of inlet channel. After calculation, the Reynolds number at the maximum inlet velocity and maximum hydraulic diameter is 2181, which is less than 2300. As such, for the other cases where the Reynolds number is always below 2300, the standard laminar flow model is adopted for numerical calculations.

2.3. Verification of Grid Independence

The accuracy and speed of computations are affected by the number of grids in the model. To enhance the reliability of the simulation results, the grid independence test is performed. The polyhedral grid configuration is adopted for the grid division. The $T_{\max}$ of the battery and ΔP are used as criteria for the grid independence test. The simulation results for various grid numbers are shown in Figure 2. It is indicated that with the number of grids increasing, the $T_{\max}$ and ΔP tend to stabilize, and when the number of grids is more than 448,838, the $T_{\max}$ and ΔP increase by 0.01% and 0.36%, respectively. Considering both computational accuracy and cost, the grid number at this point is ultimately selected for subsequent simulations.

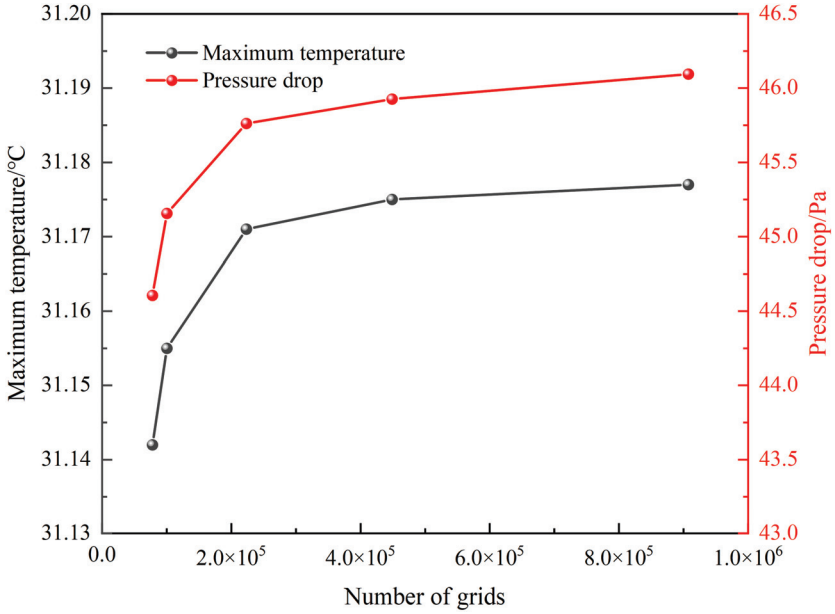

Figure 2. Results of grid independence analysis.

2.4. Experiment of Heat Generation Rate

Based on the principle of the calibrated calorimetry method [34], the heat generation rate of a 51 Ah prismatic lithium-ion battery was tested. The experimental setup for the heat generation rate test was shown in Figure 3a. The testing system mainly included the

battery, charge/discharge equipment (NEWARE CT-4008-5V60A-NFA, manufactured in China), thermostat (WBE 3SDG100L, manufactured in China), computer, and temperature data-acquisition instrument (HIOKI LR8410R, manufactured in Japan). Six thermocouples were distributed along the diagonal lines of the front and rear surfaces of the battery. The positive and negative terminals of the lithium-ion battery were connected to copper wire terminals using bolts and washers. The surface of the battery was covered with a 10 mm thick aerogel layer, which was secured with high-temperature tape to reduce heat dissipation during the experiment and establish an approximately adiabatic environment. The wrapped battery was placed in the thermostat, and all thermocouples were connected to a real-time data-acquisition instrument. The charge/discharge equipment was connected to the battery through copper wire terminals, and the computer controlled the discharging programs of the battery. Figure 3b showed the transient volumetric heat generation rate of the battery calculated using the calibrated calorimetry method under the 1C discharge rate.

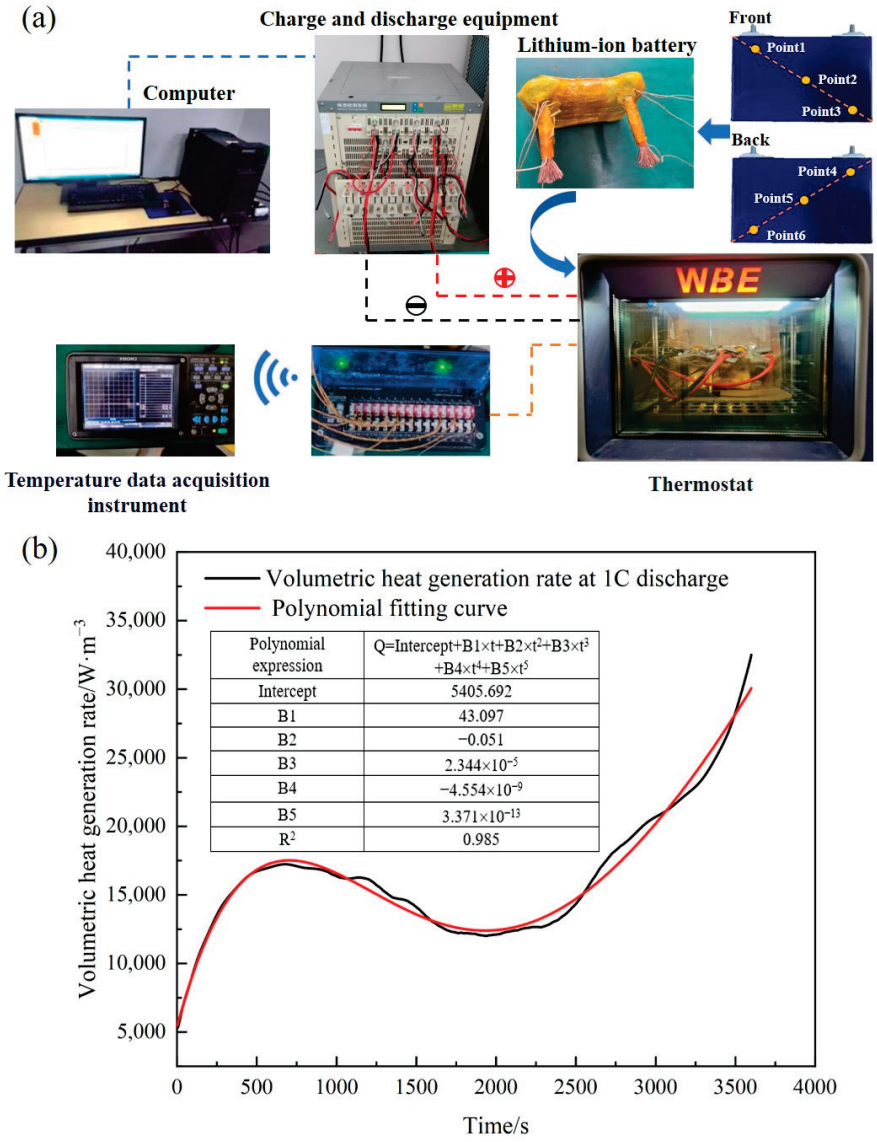

Figure 3. (**a**) Schematic of the heat generation rate testing experimental system, (**b**) volumetric heat generation rate over time.

2.5. Verification of the Thermal Model

To validate the accuracy of the battery thermal model, a numerical transient simulation is conducted on the thermal behavior of the battery under 1C discharge condition. Considering that the heat generation rate of the battery during 1C discharge varies with time, the user-defined function (UDF) compiler in Fluent 2021R1 is employed to define the battery heat source. A simulation calculation is performed for the battery discharging at 1C in an ambient temperature of 25 °C, and the calculated average surface temperature of the battery is compared with the experimental temperature data from the 1C discharge of the battery, as shown in Figure 4. The maximum relative error between the simulated temperature and the experimental temperature does not exceed 3%. The results demonstrate good consistency, indicating that the battery thermal model possesses high reliability and is suitable for simulation analysis of battery cooling.

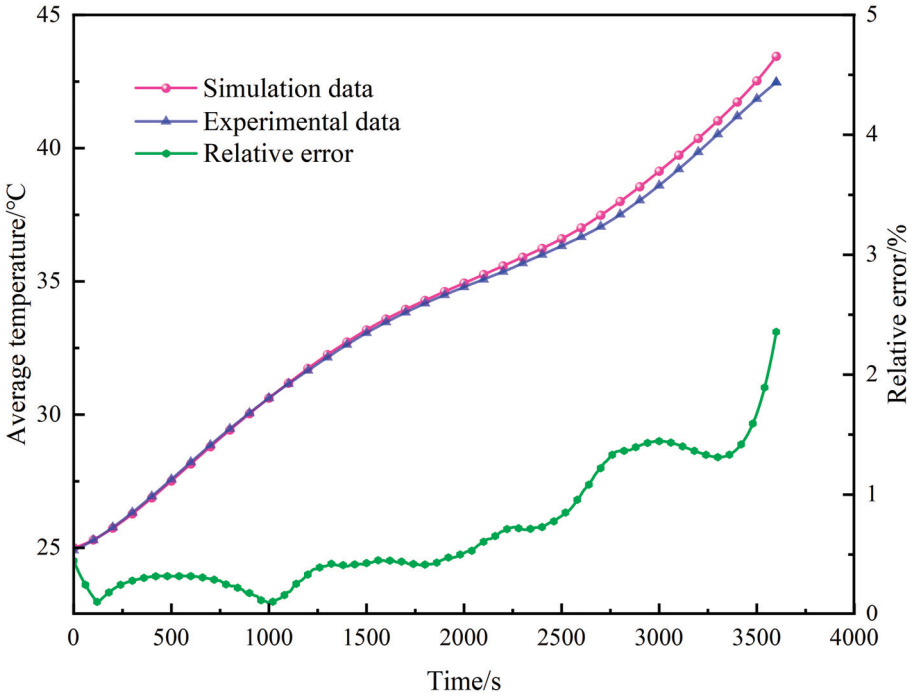

Figure 4. Average temperature comparison between simulation and experiment.

3. Optimization Procedure

3.1. Establishment of the PSO-BP Surrogate Model

3.1.1. Design of Experiment

Before establishing the surrogate model, sample points must be obtained through experimental design. Based on the sensitivity analysis of the factors, as will be discussed in the later part of this paper, the channel width (X_1), channel depth (X_2) and inlet velocity (X_3) are selected as the input variables for the experimental design, with the T_{max}, ΔT_{max}, and ΔP as the output variables. The optimal Latin hypercube sampling (OLHS) method is employed for case sampling since it allows the sample points to be more uniformly distributed across the entire sampling space, unlike the Latin hypercube sampling (LHS) method [35]. A total of 95 sample points are selected using the OLHS method, and their distribution is plotted in Figure 5, which displays relatively uniform distribution within the design range. Subsequently, numerical simulations are conducted to calculate the output response values for each sample point.

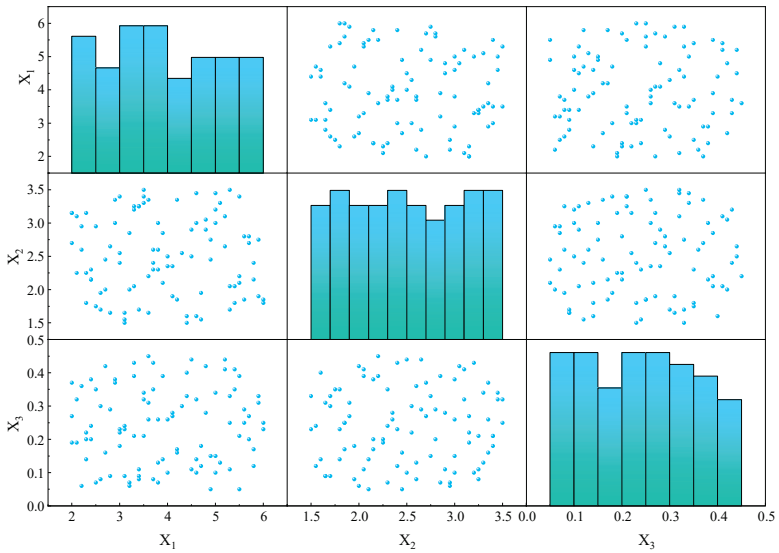

Figure 5. Distribution of optimal Latin hypercube sample points.

3.1.2. BP Neural Network Model

BPNN is a feedforward neural network trained using the back propagation algorithm, suitable for solving complex nonlinear problems. As illustrated in Figure 6, the BPNN model comprises an input layer, a hidden layer, and an output layer. The input layer includes three nodes, which are the channel width (X_1), the channel depth (X_2), and the inlet velocity (X_3). Similarly, the output layer includes three nodes, corresponding to the $T_{\max}$, $\Delta T_{\max}$, and ΔP. The number of hidden nodes is crucial for the prediction accuracy of the network. Therefore, the effect of the number of hidden nodes on prediction performance is taken into account. The number of hidden nodes, h, can be calculated by Equation (12). The output response values of the sample points obtained from numerical simulations are utilized to construct the dataset for the BPNN model, with 80% of the data allocated for training the surrogate model and 20% for testing the accuracy of the model.

$$h = \sqrt{m+n} + a \tag{12}$$

where h, m, and n are the number of nodes in the hidden layer, input layer and output layer, respectively. a is an adjusting constant ranging from 1 and 10. In order to achieve higher prediction accuracy and avoid overfitting, the optimal number of hidden nodes is determined through the PSO algorithm.

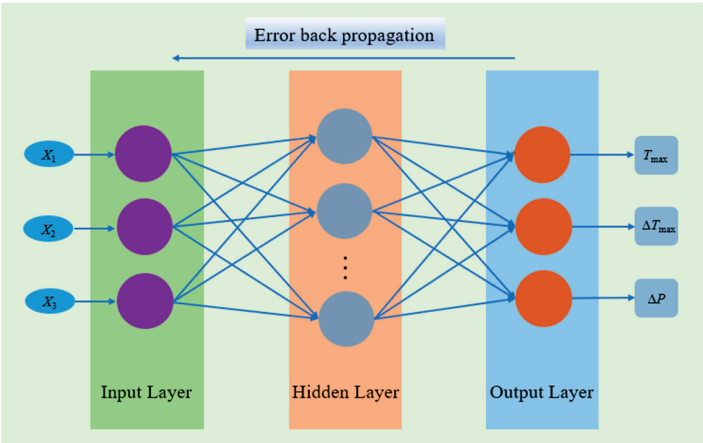

Figure 6. Diagram of BPNN topology structure.

3.1.3. Particle Swarm Optimization Algorithm

The PSO algorithm is a heuristic intelligent optimization algorithm that simulates the foraging behavior of birds through iterative updating of particles to solve problems [36]. Each particle has its own unique position and velocity. The position of a particle stands for a potential solution, and its velocity determines the direction and magnitude of movement during the iteration process. The fitness function is used to evaluate the quality of each potential solution, and the entire population moves toward the optimal solution. Through continuous iteration of the velocity and position of particles, the optimal solution is obtained. The schematic diagram of the velocity and position updates during the iteration process is shown in Figure 7, and the corresponding update formulas are as follows:

$$X_i^j(t+1) = X_i^j(t) + V_i^j(t+1) \tag{13}$$

$$V_i^j(t+1) = wV_i^j(t) + c_1r_1[p_{besti}^j - X_i^j(t)] + c_2r_2[g_{best}^j - X_i^j(t)] \tag{14}$$

where $V_i^j(t)$ and $V_i^j(t+1)$ are the velocity of the i-th particle in the j-th dimension at the t-th and $(t + 1)$-th iteration, respectively. $X_i^j(t)$ and $X_i^j(t+1)$ are the position of the i-th particle in the j-th dimension at the t-th and $(t + 1)$-th iteration, respectively. w is inertia weight, c_1 and c_2 are learning factors, and r_1 and r_2 are random values within the interval (0, 1). p_{besti}^j is the individual optimal solution of the i-th particle in the t-th iteration and g_{best}^j is the global optimal solution in the t-th iteration.

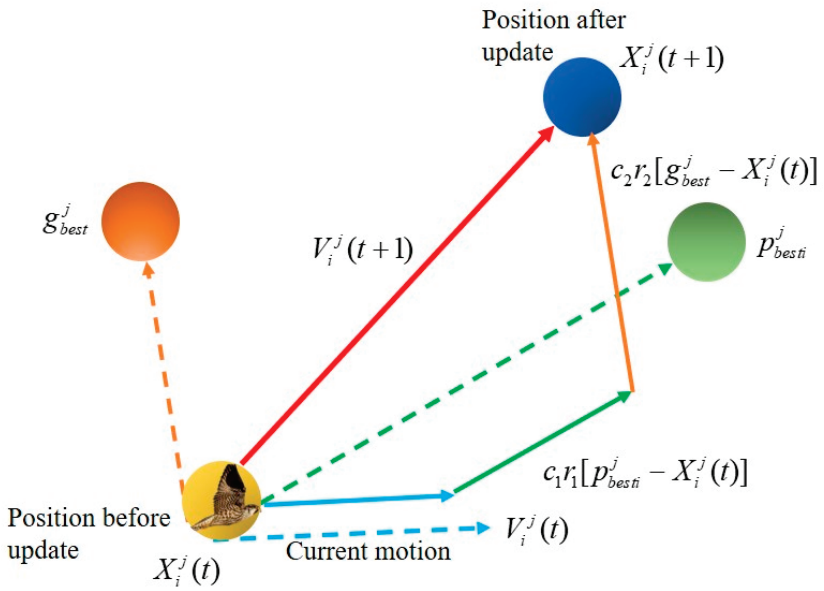

Figure 7. Particle velocity and position update diagram.

3.1.4. BPNN Model Optimized with Particle Swarm Optimization

Based on the limitations of the traditional BPNN, this paper introduces the PSO algorithm to optimize the two critical hyperparameters of the BPNN, as well as the initial weights and thresholds of the nodes. Specifically, the PSO algorithm exerts its global search capability within the search domain by utilizing the prediction error of the BPNN as the fitness function of the PSO algorithm. This process continues until the algorithm identifies the optimal combination of the number of hidden nodes, learning rate, initial weights, and thresholds that satisfy the error precision requirements. These globally

optimal solutions obtained after the algorithm terminates are assigned to the BPNN to achieve higher prediction accuracy. The specific algorithm flow is illustrated in Figure 8.

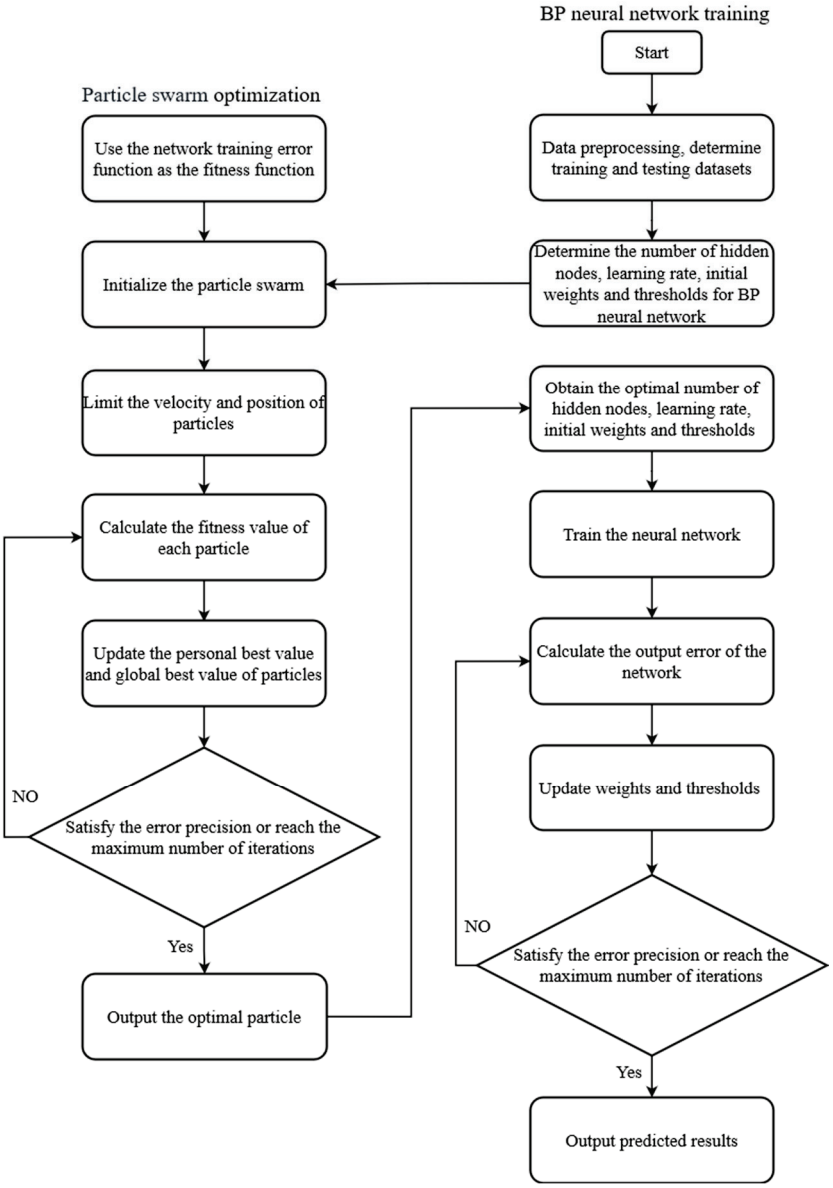

Figure 8. Flow of the PSO-BPNN algorithm.

3.2. Mathematical Model of Multi-Objective Optimization

In the design of the spider-web liquid cooling plate, numerous variables interact with each other, and thus, a comprehensive assessment of the cooling performance is necessary. However, the combinations of different variables are complex and diverse, resulting in difficulty in the analysis and optimization processes, requiring substantial computational resources and time. In such circumstances, multi-objective optimization algorithms can be resorted to identify the optimal design scheme.

Based on the previously established PSO-BPNN surrogate model, the NSGA-II algorithm is employed to optimize the parameters of the spider-web liquid cooling plate. The channel width (X_1), channel depth (X_2) and inlet velocity (X_3) are selected as the optimiza-

tion variables, while the $T_{\max}$, $\Delta T_{\max}$, and ΔP are set as the optimization objectives. The general mathematical expressions are as follows:

$$\text{find min } F(X_1, X_2, X_3) = \begin{cases} T_{\max}(X_1, X_2, X_3) \\ \Delta T_{\max}(X_1, X_2, X_3) \\ \Delta P(X_1, X_2, X_3) \end{cases} \tag{15}$$

$$\text{subject to} \begin{cases} 2.0 \le X_1 \le 6.0 \\ 1.5 \le X_2 \le 3.5 \\ 0.05 \le X_3 \le 0.45 \end{cases} \tag{16}$$

3.3. TOPSIS with the Entropy Weight Method

In order to fully consider the differences in contribution among different objectives, it is particularly important to evaluate the three optimization objectives and allocate corresponding weights to them. The TOPSIS with the entropy weight method is employed to comprehensively evaluate and rank the Pareto optimal solutions.

3.3.1. Entropy Weight Method for Determining Weights

The entropy weight method is an objective weighting method which is used to assess the importance and dispersion of the objectives [37]. A higher entropy value indicates more concentrated information and a smaller weight, while a lower entropy value indicates more dispersed information and a larger weight. By calculating the entropy values, the weights of each objective can be determined, thereby influencing the comprehensive evaluation results. The calculation procedures of the method are as follows:

(1) The initial decision matrix $A = (a_{ij})_{n\times m}$ is as follows:

$$A = \begin{bmatrix} a_{11} & a_{12} & \cdots & a_{1m} \\ a_{21} & a_{22} & \cdots & a_{2m} \\ \vdots & \vdots & \ddots & \vdots \\ a_{n1} & a_{n2} & \cdots & a_{nm} \end{bmatrix} \tag{17}$$

where a_{ij} is the value of the j-th objective in the i-th Pareto solution, n is the number of Pareto solutions, and m is the number of optimization objectives.

(2) Data normalization is calculated by Equation (18).

$$b_{ij} = \frac{\max(a_j) - a_{ij}}{\max(a_j) - \min(a_j)} \ (1 \le i \le n, 1 \le j \le m) \tag{18}$$

(3) The entropy value S_j is calculated by Equations (19) and (20).

$$p_{ij} = \frac{b_{ij}}{\sum_{i=1}^{n} b_{ij}} \ (1 \le i \le n, 1 \le j \le m) \tag{19}$$

$$S_j = -\frac{1}{\ln n} \cdot \sum_{i=1}^{n} p_{ij} \ln p_{ij} \ (1 \le i \le n, 1 \le j \le m) \tag{20}$$

where p_{ij} is the proportion of the j-th objective value for the i-th Pareto solution.

(4) The weight w_j is calculated by Equations (21) and (22).

$$G_j = 1 - S_j \tag{21}$$

$$w_j = \frac{G_j}{\sum_{j=1}^{m} G_j} \ (1 \le j \le m) \tag{22}$$

where G_j is the coefficient of variation for the j-th objective.

3.3.2. Decision-Making Using the TOPSIS Method

The TOPSIS method determines the relative priority of each Pareto solution by constructing a positive ideal solution and a negative ideal solution, which can objectively reflect the gaps between Pareto solutions and reduce the uncertainty caused by decision-makers' preferences or differences in subjective judgments, thereby effectively addressing decision-making problems within the Pareto optimal solution set [38]. The calculation procedures of the method are as follows:

(1) The weighted normalized matrix Z is as follows:

$$Z = \begin{bmatrix} w_1 b_{11} & w_2 b_{12} & \cdots & w_m b_{1m} \\ w_1 b_{21} & w_2 b_{22} & \cdots & w_m b_{2m} \\ \vdots & \vdots & \ddots & \vdots \\ w_1 b_{n1} & w_2 b_{n2} & \cdots & w_m b_{nm} \end{bmatrix} = \begin{bmatrix} Z_{11} & Z_{12} & \cdots & Z_{1m} \\ Z_{21} & Z_{22} & \cdots & Z_{2m} \\ \vdots & \vdots & \ddots & \vdots \\ Z_{n1} & Z_{n2} & \cdots & Z_{nm} \end{bmatrix} \tag{23}$$

(2) The positive ideal solution Z^+ and the negative ideal solution Z^- are determined by Equations (24) and (25).

$$Z^+ = \{\max(Z_{i1}), \max(Z_{i2}), \cdots, \max(Z_{im})\} \ (1 \le i \le n) \tag{24}$$

$$Z^- = \{\min(Z_{i1}), \min(Z_{i2}), \cdots, \min(Z_{im})\} \ (1 \le i \le n) \tag{25}$$

(3) The distances of each Pareto solution to the positive ideal solution d_i^+ and the negative ideal solution d_i^- are calculated by Equations (26) and (27).

$$d_i^+ = \sqrt{\sum_{j=1}^{m} (Z_{ij} - Z_j^+)^2} \ (1 \le i \le n) \tag{26}$$

$$d_i^- = \sqrt{\sum_{j=1}^{m} (Z_{ij} - Z_j^-)^2} \ (1 \le i \le n) \tag{27}$$

(4) The relative closeness of each Pareto solution f_i is calculated by Equation (28).

$$f_i = \frac{d_i^-}{d_i^+ + d_i^-} \tag{28}$$

where a higher f_i value means a better Pareto solution.

4. Results and Analysis

4.1. Comparison of Cooling Performance of Different Cooling Plates

To verify the performance advantages of the spider-web liquid cooling plate, a comparison is made with straight and serpentine liquid cooling plates. The geometric shapes of the three flow channels are shown in Figure 9. The cooling performance of liquid cooling plates can be influenced by various parameters of the internal flow channel structure, including

inlet size, channel depth, channel width, and the cross-sectional area of the flow channels. As such, to better compare the cooling performance of different liquid cooling plates, it is necessary to ensure that the dimensional parameters among different liquid cooling plates are as consistent as possible. The basic dimensions for the three flow channels are listed in Table 3. The three liquid cooling plates have a uniform thickness of 4 mm. Additionally, the cross-sectional areas and volumes of the flow channels are almost the same, with the weight of the liquid cooling plates differing by less than 0.5%.

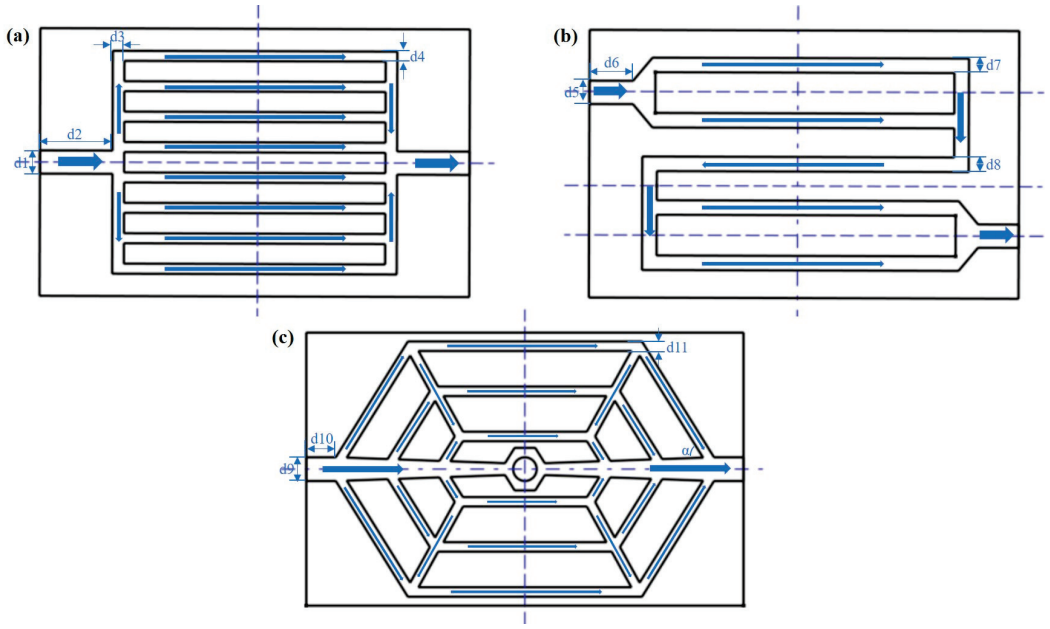

Figure 9. Types of channel structures: (**a**) Straight channel, (**b**) Serpentine channel, (**c**) Spider-web channel.

Table 3. Parameter settings of three channel structures.

Type of Channel	Geometric Parameter	Value/mm	The Cross-Sectional Area of the Channel/mm^2	Mass/g
Straight	d1, d2, d3, d4	8, 25, 4, 3.45	3496.8	129.07
Serpentine	d5, d6, d7, d8	8, 15, 5, 5.3	3490.7	129.11
Spider-web	d9, d10, d11, α	8, 10, 3.2, 60°	3493.6	129.09

The temperature contour plots of the batteries and pressure contour plots of three types of liquid cooling plates are shown in Figure 10. The corresponding data for the T_{max} and ΔP are listed in Table 4. It is evident that the T_{max} of the batteries is the highest in the straight flow channel, followed by the serpentine flow channel, and the lowest in the spider-web flow channel. As such, the cooling performance of the liquid cooling plate with the spider-web flow channel is better than the other two cases. In terms of ΔP, the advantage of the spider-web flow channel is more pronounced, with a significantly smaller ΔP compared to the other two flow channels. In contrast, the ΔP is highest for the serpentine flow channel structure, and the increased ΔP will result in higher power consumption of the pump. On the whole, the spider-web flow channel is superior to the other two flow channels in both cooling performance and power consumption. Hence, further optimization and research on the spider-web flow channel will be conducted in the following sections.

Table 4. The data for the T_{max} of the batteries and the ΔP.

Type of Channel	T_{max}/°C	ΔP/Pa
Straight	31.26	61.75
Serpentine	31.21	210.24
Spider-web	31.18	45.93

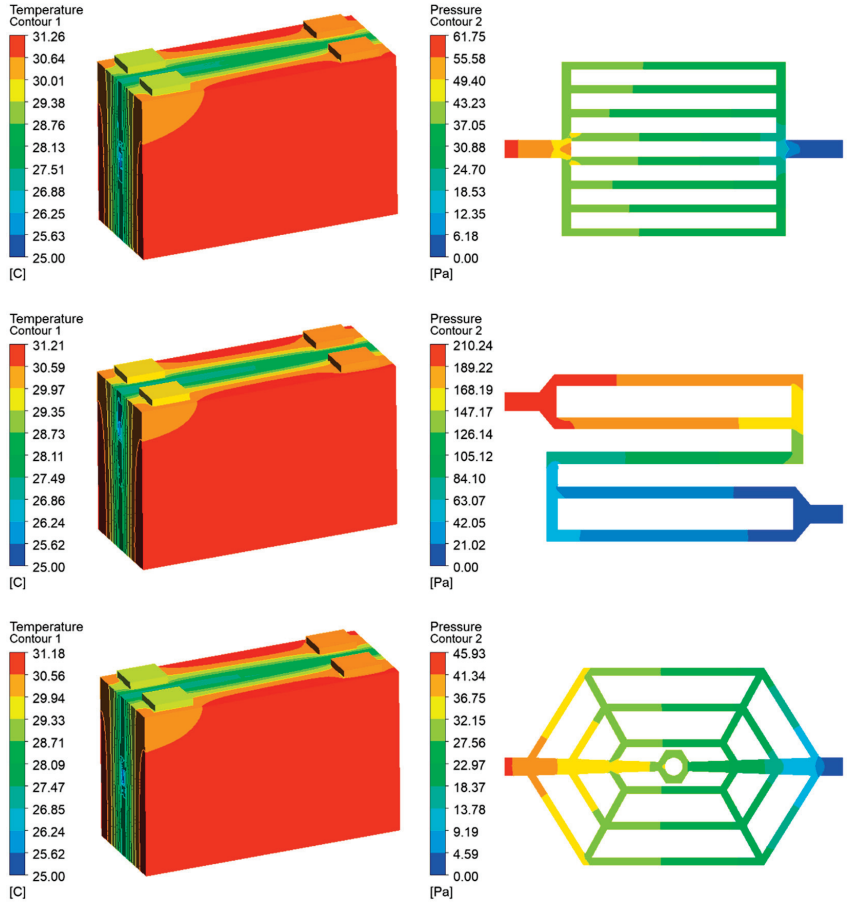

Figure 10. Temperature contour plots of the batteries and pressure contour plots of three types of liquid cooling plates.

4.2. Analysis of Different Influencing Factors

4.2.1. Influence of the Number of Branch Channels

The variation in performance is explored as the number of branch channels increases from 2 to 8, with an inlet velocity of 0.1 m·s^{-1}, a channel width of 3 mm, a channel depth of 2 mm, and a channel angle of 60°. The variation curves of the T_{max}, ΔT_{max}, and ΔP with the number of branch channels are shown in Figure 11. With the increase in the number of branch channels, the T_{max}, ΔT_{max}, and ΔP all decrease. When the number of branch channels is 2, the T_{max} is 31.49 °C, the ΔT_{max} is 4.74 °C, and the ΔP is 67.39 Pa. When the number of branch channels increases to 8, the T_{max} decreases to 31.08 °C, the ΔT_{max} decreases to 4.67 °C, and the ΔP decreases to 42.38 Pa. The main reason is that with the increase in the number of branch channels, the contact area between the fluid domain and the solid domain within the liquid cooling plate increases, resulting in enhanced thermal convection at the interface. At the same time, the increased cooling channel length effectively extends the heat exchange time between the coolant and the wall, thereby reducing the T_{max}. Furthermore, the increase in the number of branch channels reduces the

coolant flow velocity in each channel, which leads to a reduction in ΔP. Based on the above analysis, the liquid cooling plate with eight branch channels demonstrates better cooling performance and lower ΔP. As such, a liquid cooling plate with an eight-branch channel structure is selected for further research.

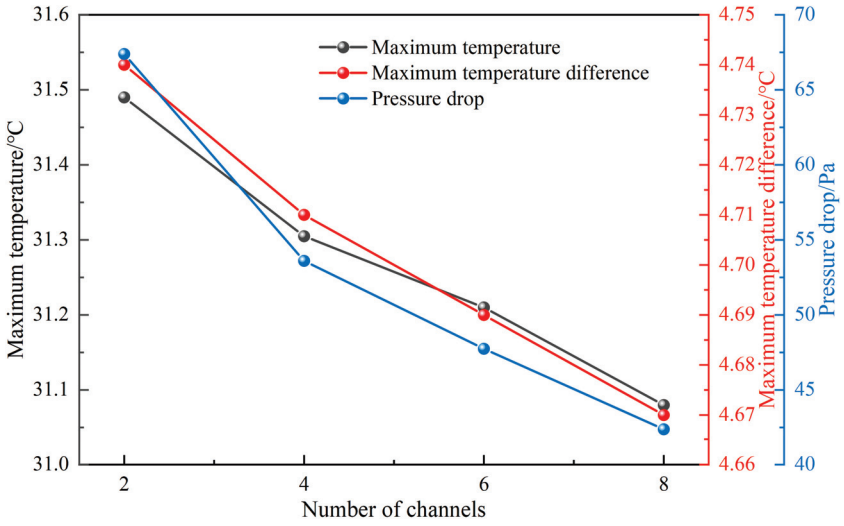

Figure 11. Influence of the number of branch channels on T_{max}, ΔT_{max}, and ΔP.

4.2.2. Influence of Different Inlet Velocity

The variation in performance is explored as inlet velocity increases from 0.05 m·s^{-1} to 0.45 m·s^{-1}, with eight branch channels, a channel width of 3 mm, a channel depth of 2 mm, and a channel angle of 60°. The variation curves of the T_{max}, ΔT_{max}, and ΔP with inlet velocity are shown in Figure 12. With the increase in inlet velocity, both the T_{max} and ΔT_{max} decrease significantly. As the inlet velocity increases from 0.05 m·s^{-1} to 0.45 m·s^{-1}, the T_{max} decreases from 32.31 °C to 30.02 °C, and the ΔT_{max} decreases from 4.94 °C to 4.48 °C. Moreover, the decreasing trend gradually slows down. The main reason is that as the inlet velocity continues to increase, the heat exchange between the coolant and battery gradually reaches a balance, so further increasing the inlet velocity no longer significantly improves the cooling performance of the liquid cooling plate. However, the ΔP increases continuously with the inlet velocity, rising from 18.14 Pa to 347.56 Pa. Although increasing the inlet velocity can lower the T_{max} and ΔT_{max}, it also increases the demands on pump power.

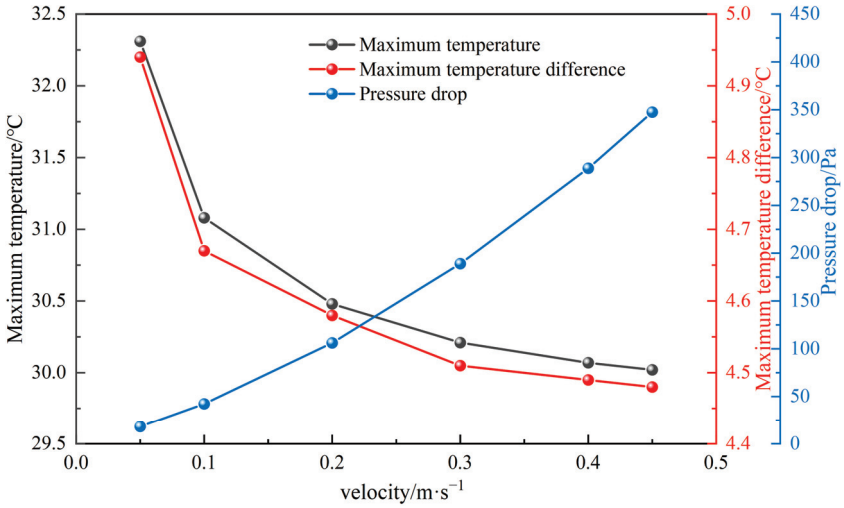

Figure 12. Influence of different inlet velocity on T_{max}, ΔT_{max}, and ΔP.

4.2.3. Influence of Different Channel Depths

The variation in performance is explored as the channel depth increases from 5 mm to 3.5 mm, with eight branch channels, an inlet velocity of 0.1 m·s^{-1}, a channel width of 3 mm, and a channel angle of 60°. The variation curves of the T_{max}, ΔT_{max}, and ΔP with the channel depth are shown in Figure 13. With the increase in channel depth, the T_{max}, ΔT_{max}, and ΔP all decrease, and the slopes of the corresponding curves decrease gradually. It is indicated that the cooling performance of the liquid cooling plate improves with increasing channel depth, but the improvement gradually flattens. The reason is that as the channel depth increases, the heat exchange area at the interface between the coolant fluid domain and the cooling plate solid domain increases, allowing the heat generated by the battery to be transferred to the coolant more promptly and effectively, thereby improving the overall heat dissipation performance.

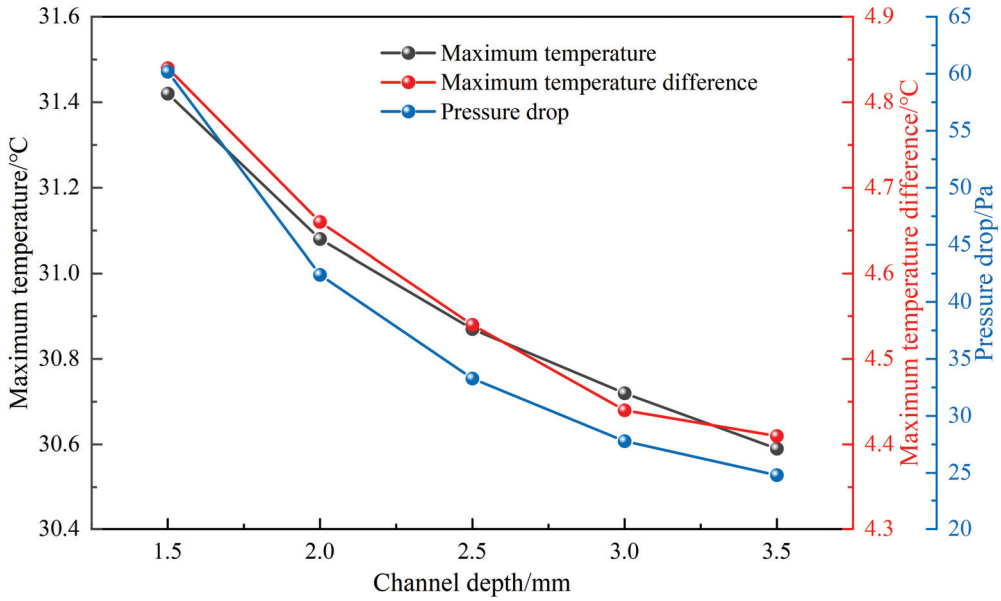

Figure 13. Influence of different channel depths on T_{max}, ΔT_{max}, and ΔP.

4.2.4. Influence of Different Channel Widths

The variation in performance is explored as the channel width increases from 2 mm to 6 mm, with eight branch channels, an inlet velocity of 0.1 m·s^{-1}, a channel depth of 2 mm, and a channel angle of 60°. The variation curves of the T_{max}, ΔT_{max}, and ΔP with the channel width are shown in Figure 14. As the channel width increases, both the T_{max} and ΔT_{max} decrease accordingly. When the channel width is 2 mm, the T_{max} is 31.18 °C and the ΔT_{max} is 4.7 °C. When the channel width is 6 mm, the T_{max} is 30.92 °C and the ΔT_{max} is 4.57 °C. The increased channel width enhances the heat exchange area between the coolant and the liquid cooling plate, thereby improving the cooling performance of the liquid cooling plate. The ΔP decreases from 54.7 Pa to 31.04 Pa, indicating that increasing the channel width helps reduce the ΔP and achieve lower power consumption.

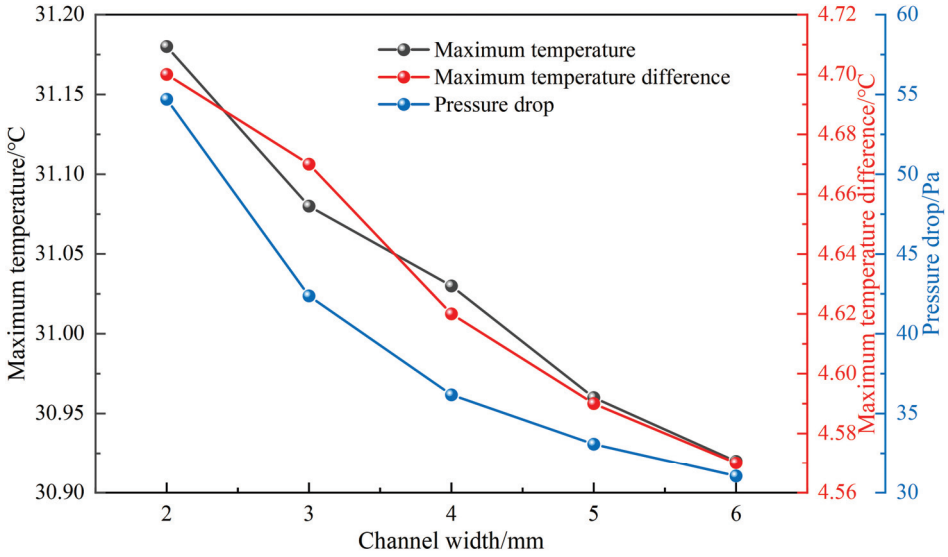

Figure 14. Influence of different channel widths on T_{max}, ΔT_{max}, and ΔP.

4.2.5. Influence of Different Channel Angles

The variation in performance is explored as the channel angle increases from 60° to 80°, with eight branch channels, an inlet velocity of 0.1 m·s^{-1}, a channel depth of 2 mm, and a channel width of 3 mm. The variation curves of the T_{max}, ΔT_{max}, and ΔP with the channel angle are shown in Figure 15. As the channel angle increases from 60° to 80°, there is a slight decrease in the T_{max} from 31.08 °C to 31.03 °C and a small reduction in the ΔT_{max} from 4.67 °C to 4.62 °C. This is attributed to the more uniform distribution of channels within the cooling plate, resulting in a slightly enhanced heat transfer efficiency for the cooling plate. Additionally, as the channel angle increases, the ΔP increases slightly from 42.38 Pa to 43.22 Pa.

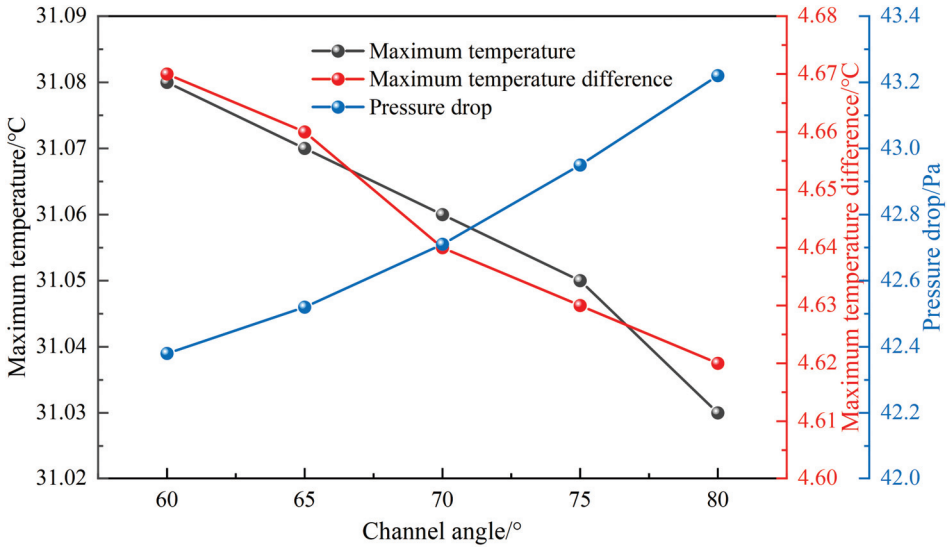

Figure 15. Influence of different channel angles on T_{max}, ΔT_{max}, and ΔP.

4.3. Sensitivity Analysis of Different Factors

The sensitivity analysis of diverse variables is conducted to identify those with significant influence. The formula for calculating the sensitivity factor SA_i is as follows [39].

$$SA_i = \frac{|(f_{\max}(x_i) - f_{\min}(x_i))|}{\sum_{j=1}^{n} |(f_{\max}(x_j) - f_{\min}(x_j)|} \times 100\% \quad (29)$$

where $f_{\max}(x_i)$ and $f_{\min}(x_i)$ are the maximum and minimum objective values.

The results of the sensitivity analysis are shown in Figure 16. It can be observed that the flow velocity has the greatest impact on the three objectives, particularly on the ΔP, with a sensitivity factor as high as 86.53%. This is primarily attributed to the fact that the pressure loss of coolant is directly proportional to the square of the flow velocity, so an increase in flow velocity significantly raises the ΔP. In contrast, the channel angle has the least impact on the three objectives, especially on the ΔP, with a sensitivity factor of only 0.22%. As such, changing the channel angle has a very limited influence on the three objectives. After comprehensive consideration, the channel depth, channel width, and flow velocity are selected as the input variables for multi-objective optimization.

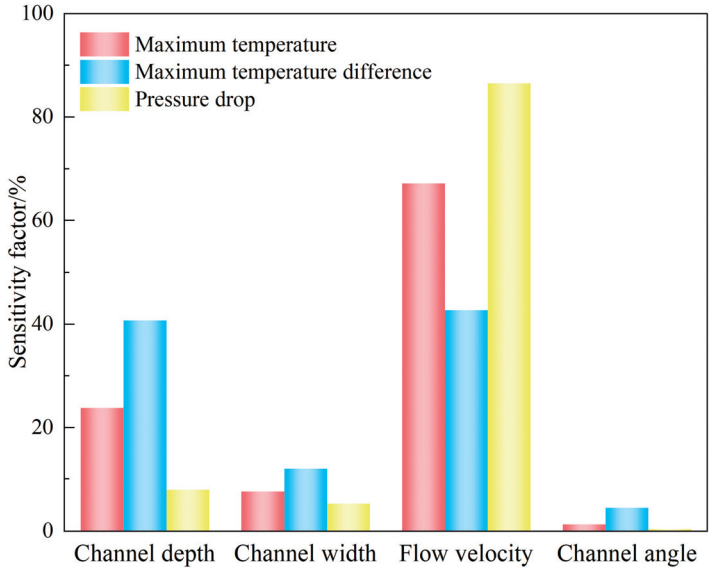

Figure 16. Sensitivity factors for the different variables.

4.4. Analysis of Prediction Results

4.4.1. Model Performance Evaluation

The prediction performance of the model is assessed using the correlation coefficient (R^2), mean absolute error (MAE), and root mean square error (RMSE). The corresponding equations are shown below:

$$R^2 = 1 - \frac{\sum_{i=1}^{n} (y_i - \hat{y}_i)^2}{\sum_{i=1}^{n} (y_i - \overline{y})^2} \quad (30)$$

$$MAE = \frac{1}{n} \sum_{i=1}^{n} |y_i - \hat{y}_i| \quad (31)$$

$$RMSE = \sqrt{\frac{1}{n} \sum_{i=1}^{n} (y_i - \hat{y}_i)^2} \quad (32)$$

where y_i is the simulated value, $\hat{y}_i$ is the predicted value, $\overline{y}$ is the average of the simulated values, and n is the number of test samples.

4.4.2. Analysis of Prediction Results on the Training Set

The optimal fitness variation curve of the PSO algorithm is depicted in Figure 17a. During the iterative process, the particle swarm gradually moves towards the optimal fitness value as a whole. In the first six iterations, the fitness value decreases significantly. After the sixth iterations, the fitness value changes little, with the optimization curve gradually converging. Once the preset 50 iterations are completed, the optimization process automatically terminates and outputs the optimal results. The optimal parameter combination obtained from the search is then substituted into the BPNN model for training to assess the prediction performance of the PSO-BPNN model on the previously designated 80% training set. Figure 17b–d shows the comparison between the predicted values and the true values for three objectives in the training set. It is clearly demonstrated by these figures that the prediction results for the training set are quite good, indicating that the PSO-BPNN model can effectively fit the training data. This further proves that the model possesses excellent multi-input and multi-output nonlinear fitting capabilities, thus qualifying it as a surrogate model for subsequent prediction validation on the test set.

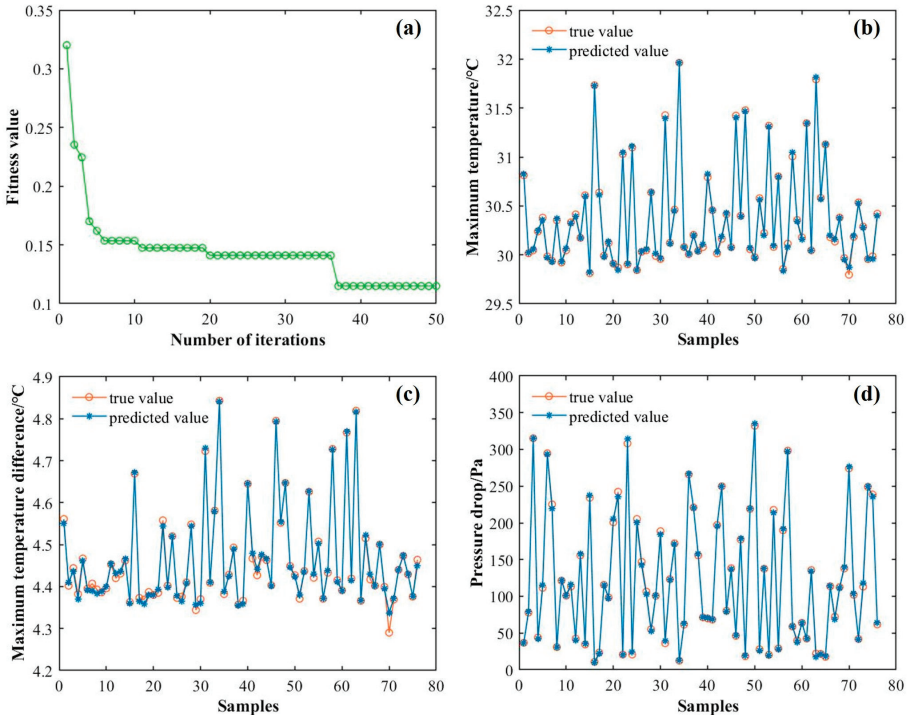

Figure 17. (**a**) Optimal fitness variation with iterations in the PSO algorithm, (**b**) T_{max} prediction curve, (**c**) ΔT_{max} prediction curve, and (**d**) ΔP prediction curve.

4.4.3. Analysis of Prediction Results on the Test Set

To confirm the efficiency of using the PSO algorithm, the prediction results on the test set are compared between the BPNN and the PSO-BPNN models. The comparison of the prediction results for the two models is shown in Figure 18, and the comparison of relevant evaluation metrics is presented in Table 5. Specifically, Figure 18a,c,e compares the true values with the predicted values for the PSO-BPNN model, while Figure 18b,d,f shows the same comparisons for the traditional BPNN model. As evident from the figure and table, the prediction results of the three objectives based on the PSO-BPNN model are closer to the true values compared to those of the traditional BPNN model. The errors of various evaluation metrics in the prediction results using the PSO-BPNN model are all smaller than those of the traditional BPNN model, while the R^2 values are higher. For the third

objective of ΔP, the RMSE and MAE are improved by 51.5% and 55.5%, respectively. This demonstrates that optimizing the number of hidden nodes, learning rate, initial weights, and initial thresholds of the BPNN using the PSO algorithm significantly enhances the prediction accuracy of the model, thus offering higher application value.

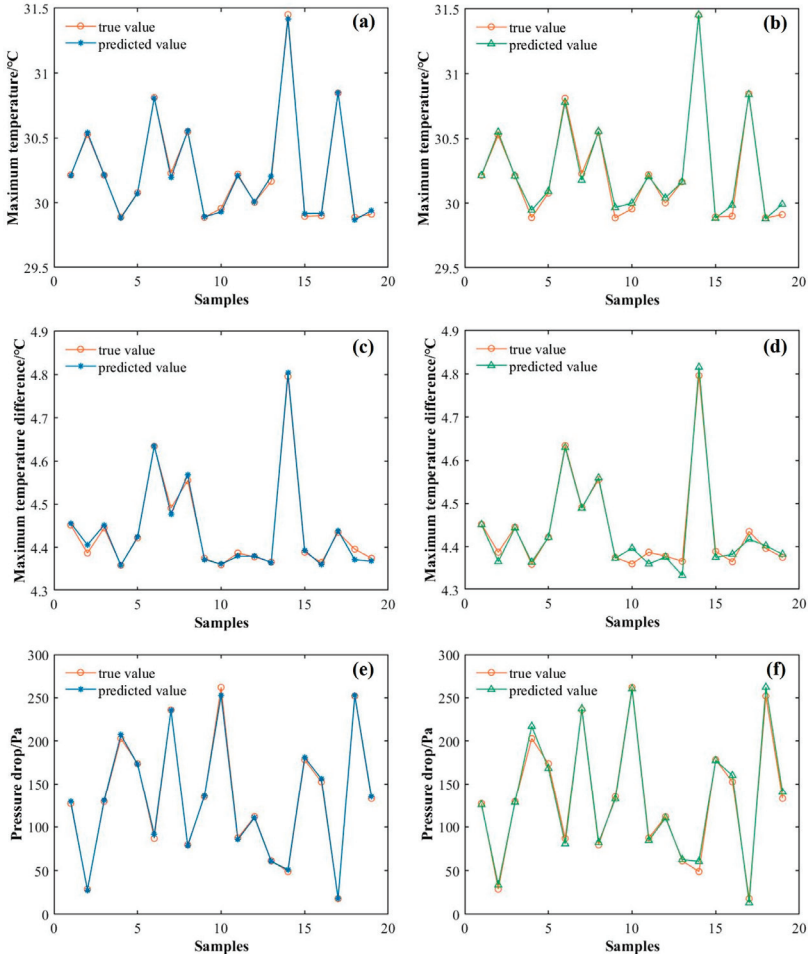

Figure 18. (**a**) T_{max} prediction curve in the PSO-BPNN, (**b**) T_{max} prediction curve in the BPNN, (**c**) ΔT_{max} prediction curve in the PSO-BPNN, (**d**) ΔT_{max} prediction curve in the BPNN, (**e**) ΔP prediction curve in the PSO-BPNN, (**f**) ΔP prediction curve in the BPNN.

Table 5. Comparison of the evaluation metrics between the two models.

	T_{max}/°C			ΔT_{max}/°C			ΔP/Pa		
Model	RMSE	MAE	R^2	RMSE	MAE	R^2	RMSE	MAE	R^2
BP	0.041	0.029	0.990	0.016	0.017	0.978	6.073	4.710	0.993
PSO-BP	0.019	0.015	0.998	0.009	0.007	0.993	2.944	2.096	0.998

4.5. Multi-Objective Optimization

The NSGA-II algorithm is employed with the following parameter settings: an initial population of 100 individuals, a total of 200 iterations, a crossover probability of 0.8, and a mutation probability of 0.1. After 200 generations of iterative calculations, a smooth curve composed of the Pareto solutions is finally obtained. As can be seen in Figure 19, the Pareto solutions are mutually restrictive, such that a decrease in the T_{max} and ΔT_{max} leads to an increase in ΔP. As such, these three objectives cannot be minimized simultaneously. The

Pareto front curve exhibits a convex trend towards the lower left corner, demonstrating good uniformity and distribution.

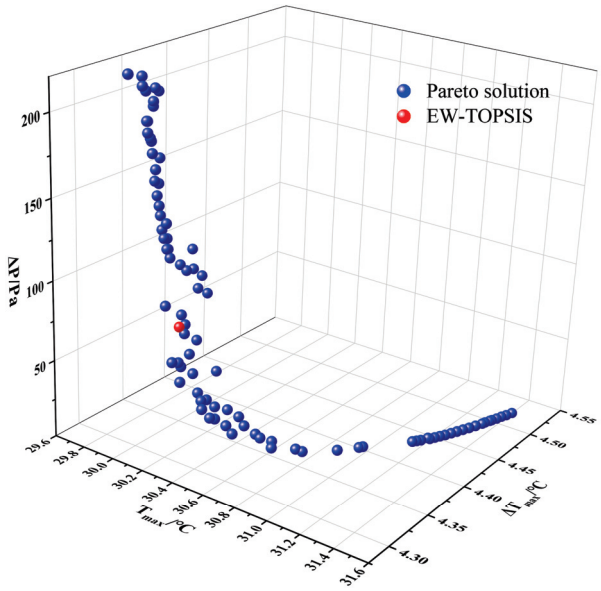

Figure 19. Pareto optimal solution set.

Each individual on the Pareto front is non-dominated, so it is necessary to comprehensively consider the three objectives to select an optimal solution from the Pareto front. In the actual selection process, decisions often rely on experience and personal preferences. Typically, the optimal solution is selected based on the Pareto front curve, with a tendency to choose points in the middle of the curve to balance the various optimization objectives. However, this approach is subjective and makes it difficult to ensure that the optimal solution is obtained. To address this issue, the entropy weight method is utilized to determine the weight of each objective, and then the TOPSIS method is used to objectively select the optimal solution.

4.6. Optimization Results of the Entropy Weight–TOPSIS Method

With the entropy weight results for the three objectives presented in Table 6, the weights for the T_{max}, ΔT_{max}, and ΔP are 0.498, 0.225, and 0.277, respectively. Among them, the objective of T_{max} holds the highest weight, while the objective of ΔT_{max} has the lowest weight. Based on the determined weights of the three objectives, the TOPSIS method is utilized to evaluate the performance of various combinations of variable parameters. When the channel width, channel depth, and inlet velocity are set to 6 mm, 3.4 mm, and 0.22 m·s^{-1}, respectively, the overall performance of the liquid cooling plate reaches its optimum. To verify the reliability of the multi-objective optimization results, simulations are conducted on the optimized flow channel, and the results are compared with those obtained from the optimization process. As shown in Table 7, the optimization values of the three objectives differ minimally from the simulation values, demonstrating that the multi-objective optimization results are reliable. Compared to the initial structure, although the ΔP in the optimized structure increases by 21.24 Pa, the T_{max} and ΔT_{max} are reduced by 1.09 °C and 0.41 °C, respectively. The temperature contour plots of the batteries in the initial and optimized structures are shown in Figure 20. It is evident that the T_{max} of the batteries decreases, along with a more uniform temperature distribution in the optimized structure. The thermal simulation results of the battery module incorporating the optimized structure

are supplied in Appendix A, showcasing the superior cooling performance in comparison with the straight and serpentine structures.

Table 6. Entropy weight results of the three objectives.

Objective	*S*	*G*	*w*
T_{max}/°C	0.9446	0.0554	0.498
ΔT_{max}/°C	0.9750	0.0250	0.225
ΔP/Pa	0.9692	0.0308	0.277

Table 7. Comparison of calculation results.

	T_{max}/°C	ΔT_{max}/°C	ΔP/Pa
NSGA-II	30.07	4.34	68.74
CFD	30.09	4.27	67.17
Relative error	0.07%	1.64%	2.34%

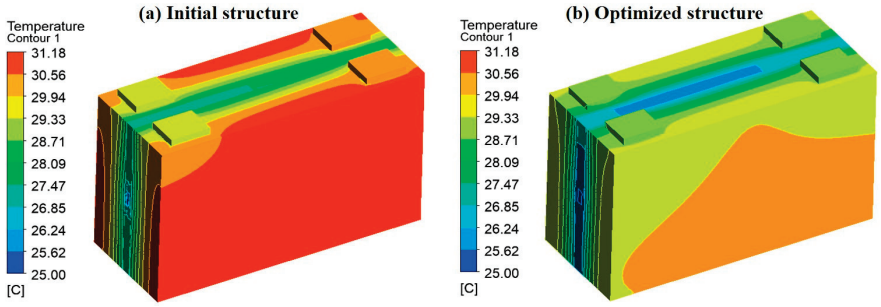

Figure 20. Temperature contour plots of the batteries: (**a**) the initial structure, (**b**) the optimized structure.

5. Conclusions

In this paper, a PSO-BPNN surrogate model is proposed to predict the cooling performance of the spider-web liquid cooling plate. The channel width, channel depth, and inlet velocity are selected as optimization variables, while the T_{max}, ΔT_{max}, and ΔP are the optimization objectives. Based on the surrogate model, the NSGA-II algorithm is employed to optimize the variables and obtain the Pareto solution set. The optimal solution is selected by the TOPSIS with entropy weight method. The major conclusions are summarized as follows:

(1) Compared to conventional straight and serpentine flow channels, the spider-web flow channel demonstrates superior cooling performance and has a smaller ΔP than the other two channel types. The channel depth and inlet velocity are the primary factors influencing the cooling performance of the spider-web flow channel, while the channel angle has a relatively minor impact.

(2) Based on the sample point data obtained through OLHS, a PSO-BPNN surrogate model is established to predict the cooling performance of the spider-web liquid cooling plate. The results indicate that the PSO-BPNN model exhibits superior performance in prediction accuracy, as evidenced by lower MAE and RMSE values and a higher R^2 value.

(3) By applying the entropy weight method, the weights for the T_{max}, ΔT_{max}, and ΔP are 0.498, 0.225, and 0.277, respectively. Based on these weights and the TOPSIS decision-making method, a good balance between cooling performance and energy consumption is achieved when the channel width, channel depth, and inlet velocity are 6 mm, 3.4 mm, and 0.22 m·s^{-1}, respectively. Compared to the initial structure, the T_{max} and ΔT_{max} are reduced by 1.09 °C and 0.41 °C in the optimized structure, respectively, with an increase in ΔP by 21.24 Pa.

Author Contributions: Investigation and writing—original draft, J.L.; methodology, J.L. and H.Z.; writing—review and editing, J.L., H.Z., W.Y. and Y.Z.; conceptualization, supervision, and funding acquisition, H.Z. All authors have read and agreed to the published version of the manuscript.

Funding: This research was funded by the National Natural Science Foundation of China (52476079).

Data Availability Statement: Data will be made available on request.

Conflicts of Interest: Author Yapeng Zhou was employed by the China Merchants Testing Vehicle Technology Research Institute Limited Company. The remaining authors declare that the research was conducted in the absence of any commercial or financial relationships that could be construed as a potential conflict of interest.

Nomenclature/Abbreviations

Nomenclature	
c	specific heat capacity/J·kg^{-1}·K^{-1}
D	hydraulic diameter/m
G	coefficient of variation
h	convective heat transfer coefficient/W·m^{-2}·K^{-1}
ΔP	pressure drop/Pa
q	volumetric heat generation rate/W·m^{-3}
S	entropy value
T	temperature/°C
$T_{\max}$	maximum temperature/°C
$\Delta T_{\max}$	maximum temperature difference/°C
v	velocity/m·s^{-1}
Greek letters	
ρ	density/kg·m^{-3}
λ	thermal conductivity/W·m^{-1}·K^{-1}
μ	dynamic viscosity/Pa·s
∇^2	laplacian operator
Subscripts	
a	ambient
bat	battery
f	fluid
lcp	liquid cooling plate
sur	surface
Abbreviations	
BPNN	back propagation neural network
BTMS	battery thermal management system
EW	entropy weight
MAE	mean absolute error
NSGA-II	non-dominated sorting genetic algorithm II
OLHS	optimal Latin hypercube sampling
PCM	phase change material
PSO	particle swarm optimization
R^2	correlation coefficient
RMSE	root mean square error
TOPSIS	technique for order preference by similarity to an ideal solution
UDF	user defined function

Appendix A

To demonstrate the cooling performance difference between the normal liquid cooling plates and the optimized spider-web liquid cooling plate. The temperature contour plots of the battery module are shown in Figure A1. The optimized spider-web liquid cooling plate has superior cooling performance, with the T_{max} of the battery module reaching 28.17 °C and the ΔT_{max} of 2.53 °C. Compared to the serpentine and straight liquid cooling plates, the T_{max} decreased by 0.69 °C (17.9%) and 0.54 °C (14.6%), respectively, while the ΔT_{max} decreased by 0.4 °C (13.7%) and 0.35 °C (12.2%). As such, the optimized spider-web liquid cooling plate is also applicable for module cooling.

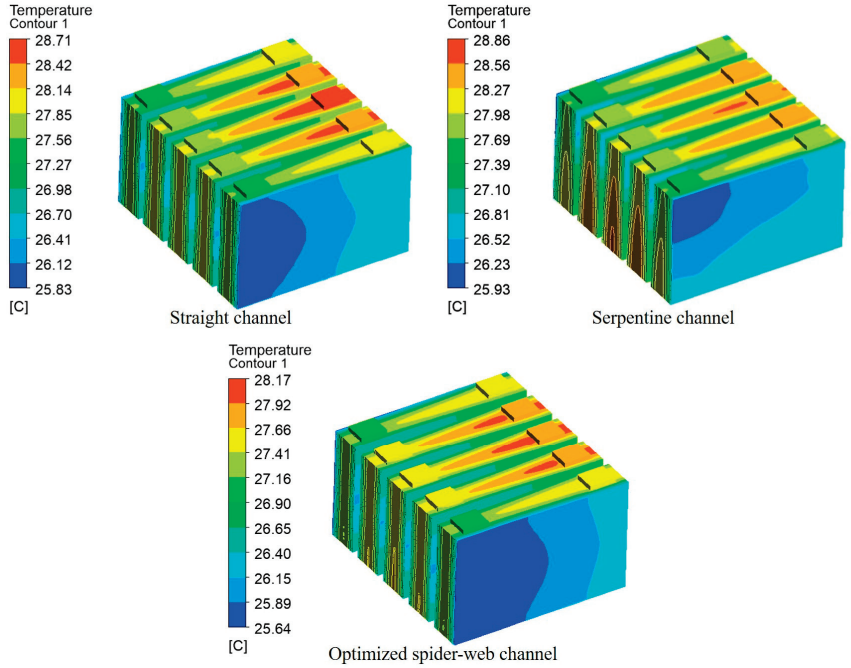

Figure A1. Temperature contour plots of the battery module.

References

1. Xiong, R.; Pan, Y.; Shen, W.; Li, H.; Sun, F. Lithium-ion battery aging mechanisms and diagnosis method for automotive applications: Recent advances and perspectives. *Renew. Sustain. Energy Rev.* **2020**, *131*, 110048. [CrossRef]
2. Zhang, X.; Li, Z.; Luo, L.; Fan, Y.; Du, Z. A review on thermal management of lithium-ion batteries for electric vehicles. *Energy* **2022**, *238*, 121652. [CrossRef]
3. Huang, Y.; Tang, Y.; Yuan, W.; Fang, G.; Yang, Y.; Zhang, X.; Wu, Y.; Yuan, Y.; Wang, C.; Li, J. Challenges and recent progress in thermal management with heat pipes for lithium-ion power batteries in electric vehicles. *Sci. China Technol. Sci.* **2021**, *64*, 919–956. [CrossRef]
4. Nazari, A.; Farhad, S. Heat generation in lithium-ion batteries with different nominal capacities and chemistries. *Appl. Therm. Eng.* **2017**, *125*, 1501–1517. [CrossRef]
5. Monika, K.; Datta, S. Comparative assessment among several channel designs with constant volume for cooling of pouch-type battery module. *Energy Convers. Manag.* **2022**, *251*, 114936. [CrossRef]
6. Khoshvaght-Aliabadi, M.; Abbaszadeh, A.; Salimi, A.; Salehi, N. Structural modifications of sinusoidal wavy minichannels cold plates applied in liquid cooling of lithium-ion batteries. *J. Energy Storage* **2023**, *57*, 106208. [CrossRef]
7. Zhang, Y.; Cheng, S.; Mei, W.; Jiang, L.; Jia, Z.; Cheng, Z.; Sun, J.; Wang, Q. Understanding of thermal runaway mechanism of $LiFePO_4$ battery in-depth by three-level analysis. *Appl. Energy* **2023**, *336*, 120695. [CrossRef]
8. Wang, C.; Xu, J.; Wang, M.; Xi, H. Experimental investigation on reciprocating air-cooling strategy of battery thermal management system. *J. Energy Storage* **2023**, *58*, 106406. [CrossRef]
9. Wang, M.; Teng, S.; Xi, H.; Li, Y. Cooling performance optimization of air-cooled battery thermal management system. *Appl. Therm. Eng.* **2021**, *195*, 117242. [CrossRef]

10. Wang, C.; Zhang, G.; Li, X.; Huang, J.; Wang, Z.; Lv, Y.; Meng, L.; Situ, W.; Rao, M. Experimental examination of large capacity $LiFePO_4$ battery pack at high temperature and rapid discharge using novel liquid cooling strategy. *Int. J. Energy Res.* **2018**, *42*, 1172–1182. [CrossRef]
11. Zhao, D.; Lei, Z.; An, C. Research on battery thermal management system based on liquid cooling plate with honeycomb-like flow channel. *Appl. Therm. Eng.* **2023**, *218*, 119324. [CrossRef]
12. Wang, X.; Xie, Y.; Day, R.; Wu, H.; Hu, Z.; Zhu, J.; Wen, D. Performance analysis of a novel thermal management system with composite phase change material for a lithium-ion battery pack. *Energy* **2018**, *156*, 154–168. [CrossRef]
13. Al-Abidi, A.; Mat, S.; Sopian, K.; Sulaiman, M.; Mohammad, A. Numerical study of PCM solidification in a triplex tube heat exchanger with internal and external fins. *Int. J. Heat Mass Transf.* **2013**, *61*, 684–695. [CrossRef]
14. Mbulu, H.; Laoonual, Y.; Wongwises, S. Experimental study on the thermal performance of a battery thermal management system using heat pipes. *Case Stud. Therm. Eng.* **2021**, *26*, 101029. [CrossRef]
15. Smith, J.; Singh, R.; Hinterberger, M.; Mochizuki, M. Battery thermal management system for electric vehicle using heat pipes. *Int. J. Therm. Sci.* **2018**, *134*, 517–529. [CrossRef]
16. Chen, K.; Wang, S.; Song, M.; Chen, L. Structure optimization of parallel air-cooled battery thermal management system. *Int. J. Heat Mass Transf.* **2017**, *111*, 943–952. [CrossRef]
17. Yan, J.; Wang, Q.; Li, K.; Sun, J. Numerical study on the thermal performance of a composite board in battery thermal management system. *Appl. Therm. Eng.* **2016**, *106*, 131–140. [CrossRef]
18. Li, W.; Qu, Z.; He, Y.; Tao, W. Experimental and numerical studies on melting phase change heat transfer in open-cell metallic foams filled with paraffin. *Appl. Therm. Eng.* **2012**, *37*, 1–9. [CrossRef]
19. Zhang, Z.; Wei, K. Experimental and numerical study of a passive thermal management system using flat heat pipes for lithium-ion batteries. *Appl. Therm. Eng.* **2020**, *166*, 114660. [CrossRef]
20. Xia, G.; Cao, L.; Bi, G. A review on battery thermal management in electric vehicle application. *J. Power Sources* **2017**, *367*, 90–105. [CrossRef]
21. Tan, X.; Lyu, P.; Fan, Y.; Rao, J.; Ouyang, K. Numerical investigation of the direct liquid cooling of a fast-charging lithium-ion battery pack in hydrofluoroether. *Appl. Therm. Eng.* **2021**, *196*, 117279. [CrossRef]
22. Wang, H.; Tao, T.; Xu, J.; Shi, H.; Mei, X.; Gou, P. Thermal performance of a liquid-immersed battery thermal management system for lithium-ion pouch batteries. *J. Energy Storage* **2022**, *46*, 103835. [CrossRef]
23. Li, X.; Zhao, J.; Duan, J.; Panchal, S.; Yuan, J.; Fraser, R.; Fowler, M.; Chen, M. Simulation of cooling plate effect on a battery module with different channel arrangement. *J. Energy Storage* **2022**, *49*, 104113. [CrossRef]
24. Sheng, L.; Su, L.; Zhang, H.; Li, K.; Fang, Y.; Ye, W.; Fang, Y. Numerical investigation on a lithium-ion battery thermal management utilizing a serpentine-channel liquid cooling plate exchanger. *Int. J. Heat Mass Transf.* **2019**, *41*, 658–668. [CrossRef]
25. Huang, Y.; Mei, P.; Lu, Y.; Huang, R.; Yu, X.; Chen, Z.; Roskilly, A. A novel approach for Lithium-ion battery thermal management with streamline shape mini channel cooling plates. *Appl. Therm. Eng.* **2019**, *157*, 113623. [CrossRef]
26. Wang, Y.; Xu, X.; Liu, Z.; Kong, J.; Zhai, Q.; Zakaria, H.; Wang, Q.; Zhou, F.; Wei, H. Optimization of liquid cooling for prismatic battery with novel cold plate based on butterfly-shaped channel. *J. Energy Storage* **2023**, *73*, 109161. [CrossRef]
27. Liu, F.; Chen, Y.; Qin, W.; Li, J. Optimal design of liquid cooling structure with bionic leaf vein branch channel for power battery. *Appl. Therm. Eng.* **2023**, *218*, 119283. [CrossRef]
28. Fan, X.; Meng, C.; Yang, Y.; Lin, J.; Li, W.; Zhao, Y.; Xie, S.; Jiang, C. Numerical optimization of the cooling effect of a bionic fishbone channel liquid cooling plate for a large prismatic lithium-ion battery pack with high discharge rate. *J. Energy Storage* **2023**, *72*, 108239. [CrossRef]
29. Li, A.; Yuen, A.; Wang, W.; Weng, J.; Yeoh, G. Numerical investigation on the thermal management of lithium-ion battery system and cooling effect optimization. *Appl. Therm. Eng.* **2022**, *215*, 118966. [CrossRef]
30. Chen, Y.; Li, D.; Feng, S.; Huang, Q.; Chen, Z.; Shu, D. Optimization and thermal-performance deep learning on carbon/epoxy composite panels with microchannel structure for battery cooling. *Appl. Therm. Eng.* **2022**, *217*, 119162. [CrossRef]
31. Ding, Y.; Ji, H.; Wei, M.; Liu, R. Effect of liquid cooling system structure on lithium-ion battery pack temperature fields. *Int. J. Heat Mass Transf.* **2022**, *183*, 122178. [CrossRef]
32. Shen, K.; Sun, J.; Zheng, Y.; Xu, C.; Wang, H.; Wang, S.; Chen, S.; Feng, X. A comprehensive analysis and experimental investigation for the thermal management of cell-to-pack battery system. *Appl. Therm. Eng.* **2022**, *211*, 118422. [CrossRef]
33. Monika, K.; Chakraborty, C.; Roy, S.; Dinda, S.; Singh, S.; Datta, S. An improved mini-channel based liquid cooling strategy of prismatic $LiFePO_4$ batteries for electric or hybrid vehicles. *J. Energy Storage* **2021**, *35*, 102301. [CrossRef]
34. Xin, Q.; Yang, T.; Zhang, H.; Yang, J.; Zeng, J.; Xiao, J. Experimental and numerical study of lithium-ion battery thermal management system using composite phase change material and liquid cooling. *J. Energy Storage* **2023**, *71*, 108003. [CrossRef]

35. Peng, Y.; Zhou, J.; Hou, L.; Wang, K.; Chen, C.; Zhang, H. A hybrid MCDM-based optimization method for cutting-type energy-absorbing structures of subway vehicles. *Struct. Multidisc. Optim.* **2022**, *65*, 228. [CrossRef]
36. Mason, K.; Duggan, J.; Howley, E. Multi-objective dynamic economic emission dispatch using particle swarm optimization variants. *Neurocomputing* **2017**, *270*, 188–197. [CrossRef]
37. He, Y.; Guo, H.; Jin, M.; Ren, P. A linguistic entropy weight method and its application in linguistic multi-attribute group decision making. *Nonlinear Dyn.* **2016**, *84*, 399–404. [CrossRef]
38. Li, Y.; Kong, B.; Qiu, C.; Li, Y.; Jiang, Y. Numerical study on air-cooled battery thermal management system considering the sheer altitude effect. *Appl. Therm. Eng.* **2025**, *258*, 124707. [CrossRef]
39. Chen, S.; Peng, X.; Bao, N.; Garg, A. A comprehensive analysis and optimization process for an integrated liquid cooling plate for a prismatic lithium-ion battery module. *Appl. Therm. Eng.* **2019**, *156*, 324–339. [CrossRef]

batteries

MDPI

Article

Investigating the Thermal Runaway Characteristics of the Prismatic Lithium Iron Phosphate Battery Under a Coupled Charge Rate and Ambient Temperature

Jikai Tian [1], Zhenxiong Wang [2], Lingrui Kong [1], Fengyang Xu [3], Xin Dong [2] and Jun Shen [2,4,*]

[1] Graduate Schools, Chinese People's Police University, Langfang 065000, China; 2023909038@cppu.edu.cn (J.T.); 2023909042@cppu.edu.cn (L.K.)
[2] School of Rescue and Command, Chinese People's Police University, Langfang 065000, China; wangzhenxiong@cppu.edu.cn (Z.W.); dongxin@cppu.edu.cn (X.D.)
[3] Graduate Schools, Monash University, Subang Jaya 47500, Selangor Darul Ehsan, Malaysia
[4] Emergency Rescue Technology Key Laboratory of Hebei Province, Langfang 065000, China
* Correspondence: shenjun@cppu.edu.cn; Tel.: +86-18810351618

Abstract: Optimizing the charging rate is crucial for enhancing lithium iron phosphate (LFP) battery performance. The substantial heat generation during high C-rate charging poses a significant risk of thermal runaway, necessitating advanced thermal management strategies. This study systematically investigates the coupling mechanism between charging rates and ambient temperatures in overcharge-induced thermal runaway, filling the knowledge gaps associated with multi-indicator thermal management approaches. Through experiments on prismatic LFP cells across five operational conditions (1C/35 °C, 1.5C/5 °C, 1.5C/15 °C, 1.5C/25 °C, and 1.5C/35 °C), synchronized infrared thermography and electrochemical monitoring quantitatively characterize the thermal–electric coupling dynamics throughout overcharge-to-runaway transitions. The experimental findings reveal three key observations: (1) Charge rate and temperature have synergistic amplification effects on triggering thermal runaway. (2) Contrary to intuition, while low-current/high-temperature charging enhances safety versus high-current/high-temperature conditions, low-temperature/high-current charging triggers thermal runaway faster than high-temperature/high-current scenarios. (3) Staged multi-indicator lithium battery thermal runaway warning signals would be more accurate (first peaks > 0.5 °C/s temperature rise rate + >10 V/s voltage drop rate). These findings collectively demonstrate the imperative for next-generation battery management systems integrating real-time ambient temperature compensation with adaptive C-rate control, fundamentally advancing beyond conventional single-variable thermal regulation strategies. Intelligent adaptation is critical for mitigating thermal runaway risks in LFP battery operations.

Keywords: lithium-ion batteries; lithium iron phosphate battery; thermal runaway; charging rate; ambient temperature; coupling mechanism

1. Introduction

The global push for clean energy and sustainable development has propelled electric vehicles (EVs) as a mainstream green transportation solution [1,2]. Lithium-ion batteries, particularly lithium iron phosphate (LFP) variants [3], have become the primary power source for EVs and energy storage systems due to their extended cycle life [4], high

energy density [5], and enhanced thermal stability [6]. However, persistent safety concerns regarding thermal runaway—triggered by mechanical impacts (e.g., crushing), thermal stress, or electrical faults (overcharging, short circuits)—continue to endanger lives and hinder widespread adoption of high-energy-density battery systems [7,8]. Understanding the fundamental mechanisms and critical influencing factors of thermal runaway remains essential for developing safe charging protocols, thereby preventing catastrophic failures like fires or explosions at their origin [9].

1.1. Related Work

Research into the thermal runaway characteristics of lithium-ion batteries began in the early 21st century. Early studies investigated short-circuit and overcharge behaviors in small-capacity $LiCoO_2$/graphite-based cells, revealing that extreme overcharging induces cell rupture and localized temperatures exceeding lithium's melting point, which triggers exothermic reactions and accelerates thermal runaway [10]. Concurrently, mechanical abuse conditions such as puncture-induced short circuits were identified to cause rapid localized heating, activating internal chemical reactions [4]. Calorimetric analyses further demonstrated a linear relationship between heat generation during overcharging and charging current, suggesting that effective heat dissipation through cooling systems could theoretically prevent thermal runaway under such conditions [11]. Subsequent reviews systematically summarized thermal runaway mechanisms under abuse scenarios, emphasizing chain reactions involving such mechanisms as material decomposition and internal short circuits, while proposing energy release diagrams to quantify reaction kinetics [9]. Comparative studies on lithium iron phosphate batteries revealed capacity-dependent thermal runaway behaviors [12]. And investigations explored low-temperature thermal runaway processes and internal exothermic reactions [13,14].

To enhance battery safety, research has focused on three main directions: mechanism elucidation [15,16], early-warning model development [17,18], and suppression strategies [19,20]. Electrochemical–thermal coupling models demonstrated that elevating electrolyte oxidation potentials and increasing thermal runaway initiation temperatures could improve overcharge tolerance [21]. Simultaneously, optimization of battery thermal management systems (BTMSs) was proposed to improve temperature uniformity in battery packs, thereby extending service life and mitigating thermal hazards. In suppression research, temperature control and voltage monitoring are prioritized. The core temperature control means to inhibit thermal runaway in lithium batteries include real-time monitoring of single cell temperature through the battery management system (BMS), setting the warning threshold (e.g., 50~60 °C), and triggering the current limitation protection [22]. Active/passive heat dissipation uses liquid cooling, air cooling, or high-thermal-conductivity materials (e.g., graphene), and rapid circuit cutoff at extreme high temperatures (e.g., 140 °C or above). Charging voltage control focuses on preventing overcharging: strictly limiting the charging cutoff voltage (e.g., LFP $\leq$ 3.65 V), and adopting CC-CV segmented charging algorithms to reduce the accumulation of polarization heat [23]. This involves dynamically adjusting the charging current and voltage thresholds in conjunction with the state of health of the battery (SOH), and realizing triple protection of voltage–temperature–capacity through the fuses, MOSFET hardware, and BMS software [24].

Current thermal runaway prevention systems for Li-ion batteries primarily emphasize single-factor regulation of intrinsic parameters (e.g., temperature, voltage) [25,26]. In temperature-dominant strategies, battery management systems (BMSs) monitor cell temperatures in real time while establishing graded response thresholds (e.g., 50 °C warning, 140 °C shutdown), supported by liquid/air cooling systems, for active thermal manage-

ment [27]. However, these strategies inadequately address dynamic thermal interactions between ambient temperature fluctuations and heat dissipation efficiency; for instance, elevated ambient temperatures may intensify thermal exchange loads in liquid cooling systems, amplifying localized overheating risks. For voltage-linearization control, CC-CV charging algorithms restrict cutoff voltages (NMC $\leq$ 4.2 V, LFP $\leq$ 3.65 V) with state-of-health (SOH)-based dynamic current adjustments [28]. Nevertheless, voltage protection mechanisms, designed under standardized laboratory conditions, neglect quantitative evaluation of ambient temperature-induced nonlinear polarization voltage distortions [29,30]. Notably, fixed current thresholds persist despite accelerated lithium deposition at low temperatures, potentially inducing dendrite penetration through separators [31]. Critical gaps persist in understanding thermal runaway evolution under ambient temperature-charging current coupling effects, necessitating urgent transition from single-parameter threshold frameworks to dual-factor coupled models (ambient temperature vs. charging current) to advance BMS algorithm development.

In this study, we conducted overload charging experiments at different charging rates on LFP batteries at different ambient temperatures. The temperature peak, voltage peak, temperature and voltage change trend, and mass loss, after the LFP battery thermal runaway occurred, were used to determine the severity of the thermal runaway. The main purpose is to explore factors that can reduce or delay the thermal runaway of LFP batteries. This study proposes a risk assessment method for LFP battery thermal runaway for the battery detection system, and is expected to avoid the occurrence of battery thermal runaway events.

1.2. Innovative Contributions

This study makes the following original contributions to the field of lithium-ion battery safety research:

(1) Multi-Stress Experimental Framework

A systematic overcharge protocol was established, combining extreme temperature gradients (5 °C to 35 °C) with varying charging rates (0.5–3C). This dual-stress methodology quantifies synergistic effects of thermal and electrochemical abuse conditions, revealing previously undocumented thresholds where capacity-dependent thermal stability variation exists [32].

(2) Predictive Severity Quantification

A four-dimensional thermal runaway severity index was developed, integrating peak temperature, critical voltage thresholds, dynamic response gradients, and post-event mass loss [33–35].

This multi-parameter risk metric bridges the critical gap between exploring the thermal runaway mitigation strategy and early warning for LFP batteries, providing actionable thresholds for battery safety management systems.

1.3. Organization

The structure of this paper is organized as follows. In Section 2, a theoretical analysis of overcharge-induced thermal runaway in LFP batteries is presented. Section 3 illustrates the experimental design for conducting overcharging thermal runaway. In Section 4, the experimental results are discussed and analyzed. Finally, in Section 5, the research conclusions and prospects are presented.

2. Theoretical Analysis of Overcharge-Induced Thermal Runaway in LFP Batteries

Under overcharge conditions, the progression severity of lithium battery thermal runaway exhibits cyclic dependence on thermal variations. Building upon a systematic

evaluation of existing thermal runaway mechanisms in lithium-ion systems, this study establishes a four-stage theoretical framework to elucidate the temperature-driven evolution of thermal runaway in LFP batteries [36]. The proposed analytical model delineates the phase-transition dynamics from initial thermal accumulation to final failure propagation, with the corresponding mechanistic interactions schematically illustrated in Figure 1. Due to the secrecy of the battery manufacturing technology of the battery manufacturer, it is considered in this section that the lithium salt component in the electrolyte is mainly lithium hexafluorophosphate (LiPF6), and the solvent is mainly ethylene carbonate (EC).

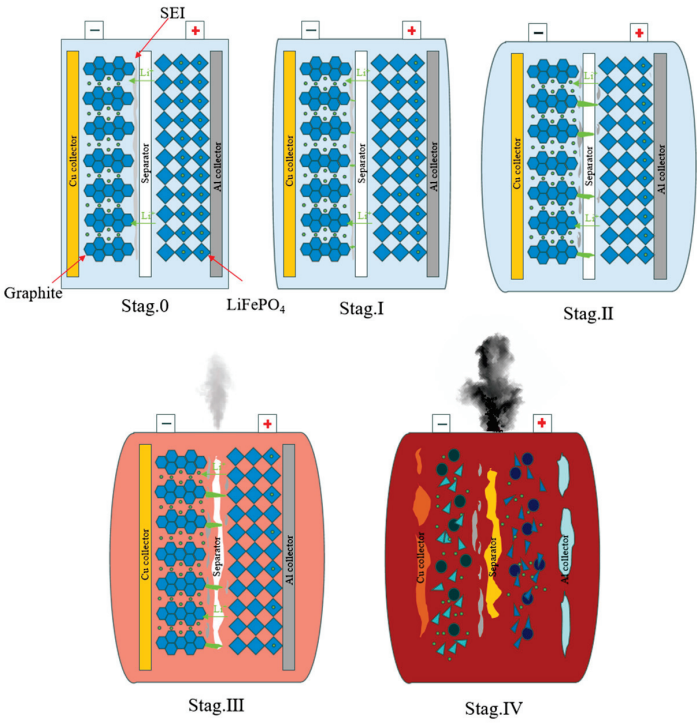

Figure 1. LFP battery thermal runaway stage division.

2.1. Stage I: Incipient Thermal Accumulation (Initially–80 °C)

Despite full state-of-charge conditions, residual electrochemical redundancy persists in electrodes. Overcharge beyond rated capacity initiates lithium dendrite nucleation at the graphite anode. Progressive temperature rise (0.2 °C /min) accompanies solid electrolyte interphase (SEI) film decomposition starting at 80 °C (Equation (1)) [37], primarily driven by ohmic heating from internal resistance.

$$ROCO_2Li \rightarrow Li_2CO_3 + CO_2 \uparrow + HC \uparrow \quad (1)$$

This phase manifests as (1) voltage plateau formation with <5% fluctuation; (2) initial gas generation (H_2, CH_4) [38] causing mild cell swelling [39].

2.2. Stage II: Electrochemical Interface Degradation (90–120 °C)

Continued decomposition of the solid electrolyte interphase (SEI) occurs on the graphite anode as temperatures escalate. This SEI breakdown exposes pristine graphite to direct electrolyte contact, simultaneously releasing organic byproducts and gaseous species (Equations (1)–(3)) that cause severe cell swelling.

$$LiPF_6 \rightarrow LiF + PF_5 \uparrow \quad (2)$$

$$PF_5 + H_2O \rightarrow 2HF \uparrow + POF_3 \quad (3)$$

This phase is characterized by the following: (1) voltage plateau stabilization ($\Delta V < 0.05$ V) signaling lithium over-deintercalation at the cathode; (2) dominant heat sources: ohmic losses (≈60%) + electrolyte decomposition. This indicates that the cathode and anode electrochemical reactions are extremely unbalanced, with a significant release of energy, which is one of the critical signs of thermal runaway.

2.3. Stage III: Thermal Escalation (120–150 °C)

Partial electrolyte solvents (ethylene carbonate) undergo exothermic decomposition (Equation (4)), releasing flammable gases such as C_2H_4. The internal pressure rises to approach the critical threshold of the pressure relief valve, initiating gas venting. Concurrently, accelerated temperature increase triggers separator melt shrinkage, potentially causing direct anode–cathode contact (short circuit) and sustained gas leakage through the valve (observed as white smoke emission) [40].

$$C_3H_4O_3(EC) \rightarrow CO_2 \uparrow + C_2H_4 \uparrow \quad (4)$$

This phase manifests as follows: (1) temperature ramp rate: 2–3 °C/s; (2) dominant gas species: C_2H_4 (>60% molar fraction).

2.4. Stage IV: Critical Thermal Runaway (150–300 °C)

Overcharging causes damage to the internal structure of the battery, and the battery enters a state of deep charging. At the same time, with a sharp rise in internal pressure, the voltage rapidly rises to a peak and then plummets. The heat after the short circuit causes the temperature to rise, triggering an autocatalytic chain reaction, inducing large-scale heat release through electrolyte decomposition, which further intensifies reaction kinetics. Specifically, at approximately 200 °C, the exothermic reaction between the negative electrode and the electrolyte generates substantial thermal energy, accelerating reaction rates under rising temperatures (Equation (5)). The system ultimately transitions into a complete thermal runaway state [41].

$$C + EC \rightarrow Li_xC + CO \uparrow + C_2H_4 \uparrow \quad (5)$$

This phase manifests as follows: (1) voltage spike–plummet cycle ($V_{max} > 4.8$ V → <2 V in 15 s); (2) thermal runaway propagation rate: 8–12 °C/s.

3. Experimental Design

3.1. Battery Sample Parameters

The experiment used Guoxuan 25 Ah prismatic lithium-ion cells, with lithium iron phosphate (LFP) as the cathode and graphite as the anode material. Key battery specifications are provided in Table 1. To ensure experimental stability and repeatability, all cells underwent three preconditioning charge–discharge cycles before testing. These cycles included constant current–constant voltage (CC-CV) charging and constant current (CC) discharging protocols. In CC mode, the cells were discharged to 2.3 V at 0.5C (12.5 A). Subsequently, a CC-CV protocol was applied with a voltage limit of 3.60 V and a 0.5C (12.5 A) current until the current decayed below 0.5 A, followed by a 30 s holding period.

Table 1. Sample parameter information of lithium-ion cells.

Name	Parameter
Positive electrode	Lithium iron phosphate ($LiFePO^4$)
Negative electrode	Graphite
Dimensions (length × width × height)	100 mm × 21 mm × 140 mm
Capacity	25 Ah
Mass	630 g
Nominal voltage	3.2 V
Operating voltage	2.3–3.65 V
Discharge temperature	−30–55 °C
AC impedance	0.6–1.5 mΩ
Specific heat capacity	830 J kg^{-1} K^{-1} [20]

3.2. Experimental Device

The experiment was conducted using the platform shown in Figure 2. A ZTE 2400 (ZXD2400-TFT32-Produced by ZTE Corporation in Foshan, China) programmable power supply provided constant current charging across multiple C-rates with a specified regulation accuracy of ±0.01 V (voltage) and ±0.01 A (current). Based on the unique properties of battery materials, testing was conducted within a temperature-controlled chamber (with a temperature regulation accuracy of ±1 °C) to maintain ambient temperature stability while minimizing the thermal gradient between the environment and the battery. For high-temperature test groups, heating pads (with a temperature regulation accuracy of ±0.1 °C) were affixed to the battery surfaces to reduce the temperature differential between the batteries and their surroundings. The temperature differential between the battery and its ambient environment was determined using integrated temperature sensors within the climate chamber and digital temperature readouts from the heating pads. Two 1 mm diameter K-type thermocouples were positioned at the pressure relief valve base and geometric center of the battery surface, with temperature data averaged accordingly. The thermocouple exhibits an operational temperature range from −200 °C to 1300 °C with a measurement accuracy of ±1 °C. Synchronized temperature and voltage signals were recorded at a 1 Hz sampling frequency using a Hongrun K728 (Produced by Hongrun Company in Fujian, China) data logger to ensure temporal alignment. The temperature and voltage signals acquired by the data logger were recorded with respective accuracies of ±1 °C and ±0.01 V. Visual documentation was captured with a 1920 × 1080/30 fps industrial camera, while a Hikvision P20MAX V2 (Produced by Hikvision in Shenzhen, China) infrared thermal imager recorded the evolution of the temperature field. Pre-/post-test mass measurements were performed with a 0.1 g precision balance (2 kg capacity).

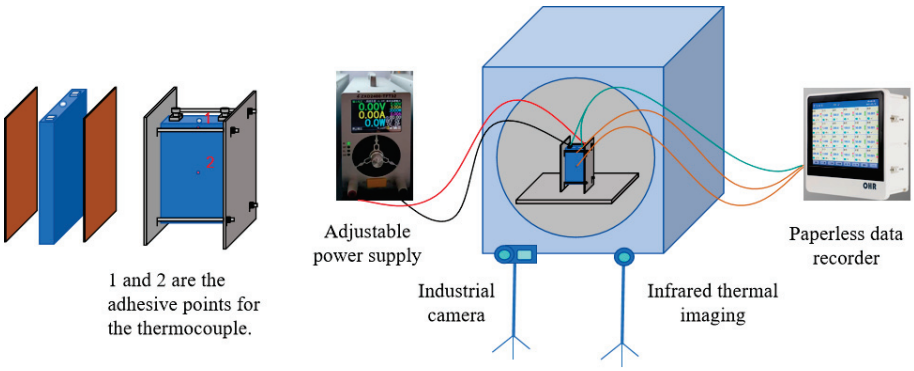

Figure 2. Experimental setup diagram.

3.3. Experimental Plan

To investigate the multifactorial influences on thermal runaway behavior and mechanisms in overcharged LFP batteries, five experimental matrices were designed. The configuration comprised four temperature gradients at a fixed charging rate and multiple charging rates at the peak temperature condition, as detailed in Table 2. Based on the experimental protocol, connect the battery to the data acquisition device first, then place it inside the constant-temperature chamber. For the high-temperature test group, heat the battery using a heating pad. One hour prior to the start of the experiment, activate the constant-temperature chamber and set its temperature; 30 min before the experiment starts, activate the heating pad and set its temperature. Configure the parameters of the overload charging power supply according to the requirements of each test group. Commence the experiment when the difference between the ambient temperature of the constant-temperature chamber and the battery temperature remains below 0.5 degrees Celsius for 30 consecutive seconds.

Table 2. Matrix contents.

Condition Abbreviation	C-Rate (C)	Ambient Temperature (°C)	Initial State of Charge (SOC)
100-1.0-35	1.0	35	100
100-1.5-05	1.5	05	100
100-1.5-15	1.5	15	100
100-1.5-25	1.5	25	100
100-1.5-35	1.5	35	100

4. Experimental Analysis and Discussion

4.1. Analysis of Battery State Changes

4.1.1. Changes in Shape and Surface

Key changing phenomena in shape and surface observed across five experimental groups are shown in Figure 3. Post-test analysis reveals that batteries in the 1C/35 °C and 1.5C/5 °C groups exhibited only mild bulging with limited gas venting through pressure relief valves, showing no severe thermal runaway. In contrast, the remaining three groups underwent significant morphological changes following intense thermal runaway. Comparative analysis demonstrates that the 1.5C/35 °C and 1.5C/15 °C groups experienced more extensive melting of surface polymer insulation under sustained high temperatures, exposing metallic casings. The 1.5C/25 °C battery catastrophically ruptured after valve activation due to excessive internal pressure from thermal runaway.

Temporal comparisons between the 1C/35 °C and 1.5C/35 °C groups reveal that identical ambient temperatures but differing C-rates produced similar deformation patterns at distinct onset times. Notably, all four 1.5C groups with varied ambient temperatures demonstrated comparable deformation timelines.

Based on the above analysis, the key observations that can be drawn mainly include the following:

1. Early-stage overcharging-induced deformation showed no ambient temperature dependence.
2. Higher C-rates accelerated deformation onset, though deformation alone did not necessarily trigger severe thermal runaway.
3. With the exception of Group 1.5C/5 °C (where thermal runaway may have been suppressed by low-temperature effects, as analyzed later), the severity of thermal runaway showed a positive correlation with ambient temperature across experimental groups.

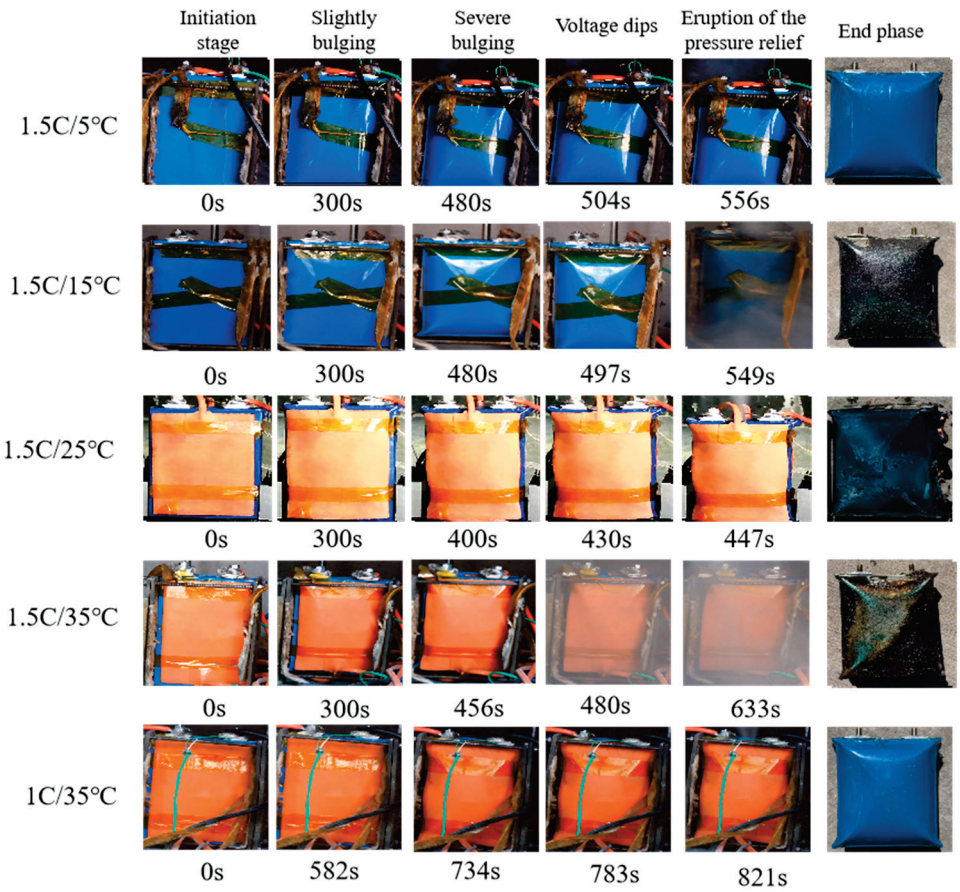

Figure 3. Key nodes in the test group.

4.1.2. Changes in Battery Mass

Pre- and post-test mass and thickness data for all five experimental groups are presented in Table 3. Notably, the 1.5C/25 °C group underwent catastrophic rupture, while the two severe thermal runaway groups exhibited minimal mass discrepancies (0.3 g) despite showing ~125 g reductions compared to initial values. Crucially, despite differing ambient temperatures, these thermal runaway groups demonstrated nearly identical mass losses, indicating that ambient conditions influence thermal runaway intensity but not the underlying chain reactions. These self-terminating reactions ceased upon reactant depletion, resulting in consistent final mass reductions. Non-thermal-runaway groups displayed ~50 g mass losses—70 g less than thermal runaway groups—confirming that overcharge-induced heating still triggered initial electrolyte vaporization and partial reactions without full runaway.

Table 3. Mass and thickness of batteries in each test group before and after the experiment.

	Initial	**1C/35 °C**	**1.5C/5 °C**	**1.5C/15 °C**	**1.5C/25 °C**	**1.5C/35 °C**
mass	630.0 g ± 5.0 g	574.3 g	580.8 g	506.1 g	404.2 g	506.4 g
thickness	21.0 mm	58.4 mm	54.7 mm	61.1 mm	Explosion	54.2 mm

Lithium battery mass analysis shows that the difference in energy release between complete thermal runaway and thermal runaway interruption is closely related to the mass, so it is necessary to carry out thermal runaway characterization of lithium batteries in stages. Combined with cross-condition mass/thickness correlations, this validates the

earlier conclusion from Section 4.1.1: Different ambient temperature changes will not affect the shape change of the lithium battery in the case of thermal runaway.

Given that the batteries were commercially sourced products, inherent manufacturing variations resulted in minor inter-cell mass differences within the experimental samples. The initial pre-experiment masses of battery specimens ranged from 625.0 g to 635.0 g (630.0 g ± 5.0 g), where the ±5.0 g deviation reflects intrinsic sample-to-sample variability—not measurement uncertainty of the weighing apparatus. The post-experiment masses presented in Table 3 represent the mean values derived from triplicate gravimetric measurements per individual battery unit.

4.1.3. Analysis of Battery Thermal Propagation

Since the test group with severe thermal runaway had similar states at different time points, infrared thermography in the 1.5C/15 °C group was selected for analysis in this section. The thermal propagation during complete thermal runaway (TR) in LFP batteries is illustrated in Figure 4. Figure 4a,b reveal Stage I (the initial overcharging phase), where proximity to the electrodes shows peak temperatures due to charging rate effects. Figure 4c,d demonstrate Stage II progression: rising SOC and temperature trigger $LiPF_6$ electrolyte decomposition, accompanied by heat accumulation zone relocation. Figure 4d,e document Stage III characteristics, showing bottom-to-top thermal propagation that correlates with observed cell expansion. Combined with morphological deformation patterns, Figure 4f captures diffuse venting from the upper region, confirming that Stage III temperature escalation accelerates electrolyte decomposition. This creates self-reinforcing expansion until internal gas pressure exceeds the relief valve's safety threshold. Figure 4g depicts Stage IV critical behavior marked by high-pressure jet emission from the safety valve. This final phase occurs when sustained chain reactions reach critical temperature thresholds, resulting in full valve rupture [42].

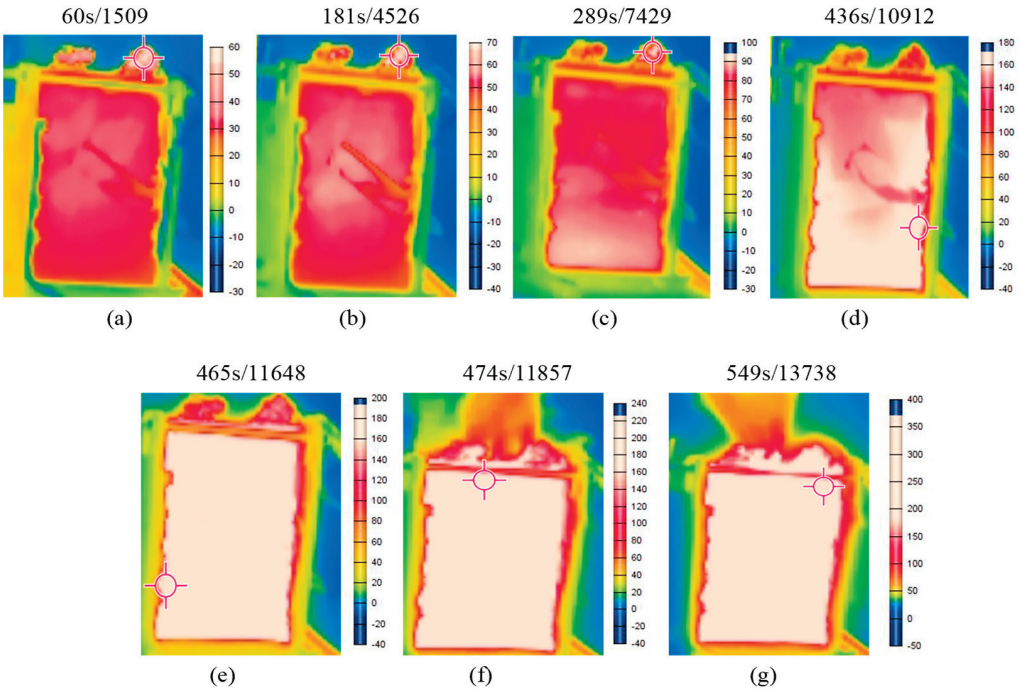

Figure 4. Infrared imaging of key nodes during thermal runaway. (**a**,**b**) The initial overcharging phase; (**c**–**e**) The emergence of hotspots and heat spread; (**f**) Gas overflow caused by excessive internal pressure; (**g**) A high-pressure gas jet occurs at the safety valve.

This thermal evolution analysis validates the proposed four-stage TR phase division in LFP batteries. The spatially resolved thermal profiling establishes a visual framework for subsequent stage-specific TR characteristic differentiation, ensuring analytical precision in mechanism studies.

4.2. Analysis of Temperature and Voltage

The voltage and temperature changes of LFP batteries during overcharge–thermal runaway at 1.5C and 1C at different ambient temperatures are shown in Figure 5. Figure 5a–e are the temperature and voltage change curves over time for 1C/35 °C, 1.5C/5 °C, 1.5C/15 °C, 1.5C/25 °C, and 1.5C/35 °C, respectively. Figure 5a,b did not experience severe thermal runaway, while Figure 5c–e all experienced severe thermal runaway at an overcharge current of 1.5C. Figure 5f shows the integral of temperature and time under five operating conditions.

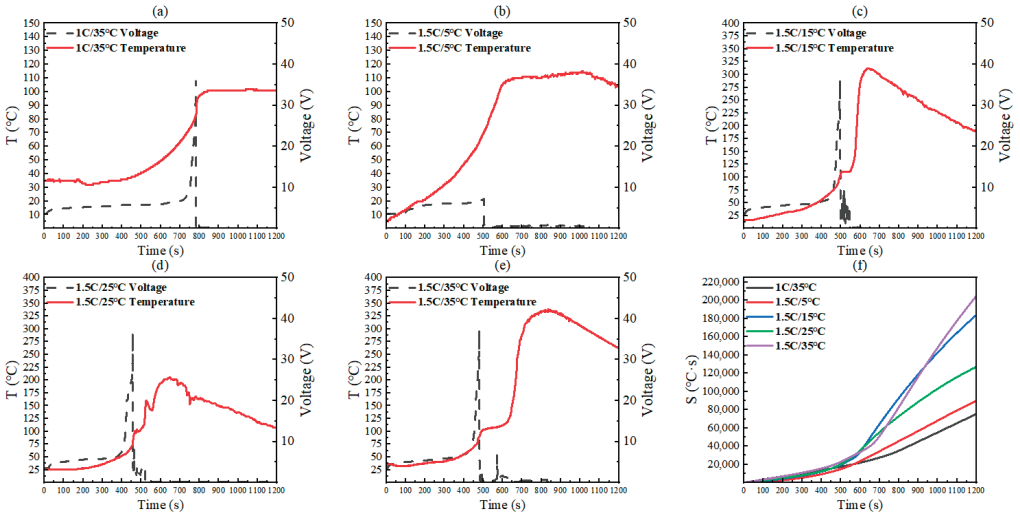

Figure 5. Curves of temperature and voltage changing with time under five working conditions. (**a**) 1C/35 °C; (**b**) 1.5C/5 °C; (**c**) 1.5C/15 °C; (**d**) 1.5C/25 °C; (**e**) 1.5C/35 °C; (**f**) Integral of temperature and time.

4.2.1. Changes in Complete Thermal Runaway Group

Temperature profiles of the 1.5C-rate test groups under varying ambient conditions are shown in Figure 5b–e. Comparative analysis of panels (c)–(e) reveals that higher ambient temperatures correlate with slower initial temperature progression during early-stage overcharging. This aligns with Stage I thermal runaway behavior, where reduced internal resistance at elevated temperatures diminishes Joule heating effects in high-ambient-temperature groups. Conversely, lower ambient temperatures intensify Joule heating (due to higher internal resistance), prioritizing thermal energy accumulation over electrochemical energy conversion. Notably, the 1.5C/35 °C group reached a peak temperature of 338 °C—26 °C higher than the 15 °C group.

All three severe thermal runaway groups exhibited post-voltage-plummet stabilization (0–10 V range) preceding abrupt temperature escalation. During this transitional phase, continuous energy input enabled decomposition-dominated heat generation. Subsequent separator melt/shrinkage triggered direct electrode contact, enabling rapid internal energy release that propelled the system into a catastrophic thermal runaway.

Peak temperature and voltage comparisons confirm ambient temperature's positive correlation with thermal runaway severity: higher initial ambient temperatures yield

greater peak temperatures and energy release magnitudes. This validates the critical role of ambient temperature in amplifying thermal runaway intensity during overcharge initiation.

4.2.2. Changes in Thermal Runaway Interruption Group

In Figure 5a, the 1C/35 °C group stabilized at 102 °C. A transient temperature surge (~780 s) with concurrent voltage spike indicated incipient Stage II transition. However, the low C-rate limited ohmic heating effects (primary early-stage mechanism), resulting in only 85 °C during voltage collapse. Though short-circuit-induced heating caused temporary temperature rise, insufficient energy accumulation prevented entry into Stage III, enabling eventual thermal equilibrium.

Figure 5b demonstrates that the 1.5C/5 °C group plateaued at 115 °C by 600 s without voltage surges. Cryogenic conditions increased electrolyte viscosity, inhibiting lithium dendrite growth while diverting overcharge energy to a gradual temperature increase. Low ambient temperature elevated internal resistance, further converting electrical energy to heat rather than sustaining chain reactions. Insufficient Joule heating from intermittent short circuits confined thermal runaway to Stage II.

Under identical durations, lithium batteries under 1C/35 °C conditions exhibit significantly lower thermal runaway energy than those under 1.5C/35 °C. Temperature integral calculations (Figure 5f) [27] comparing thermal energy accumulation are as follows:

$$k = \frac{Q_1}{Q_{1.5}} = \frac{\int_0^t T_1}{\int_0^t T_{1.5}} = \frac{70,000}{200,000} = 35\%$$

Thus, reducing the charging current by 0.5C suppresses approximately 65% of lithium battery thermal runaway energy.

The comparative analysis identifies two interruption mechanisms:

Insufficient peak temperatures from slow C-rates (gentle early-stage heating) or environmental heat dissipation prevent reaction sustainability.

Cryogenic effects increase electrolyte viscosity/internal resistance, redirecting energy to temperature rise rather than decomposition.

While the C-rate primarily governs thermal runaway initiation severity, ambient temperature critically modulates reaction sustainability. Both low C-rates and low temperatures inhibit thermal runaway through distinct mechanisms—by either limiting peak temperatures or disrupting reaction pathways—ultimately arresting chain reactions.

4.2.3. Change Rates of Temperature and Voltage

Temperature–time and voltage–time differential curves for all five test groups are presented in Figure 6a,b. Panel (a) reveals that severe thermal runaway groups exhibited heating rates exceeding 2 °C/s during runaway phases, while non-severe groups showed maximum rates below 1.5 °C/s. Consequently, a heating rate exceeding 2 °C/s can be established as the diagnostic threshold for severe thermal runaway (versus conventional thermal runaway), but it cannot serve as the initial warning trigger for lithium battery thermal runaway. To clarify the incipient warning signal, we theoretically analyzed charging rate effects on temperature rise kinetics. Incorporating C-rates into the dependent variable system acknowledges their critical impact on energy accumulation velocity and consequent thermal runaway initiation divergence. Among the five test groups, only Group 1 used 1C charging. Applying the energy formulation E = PT = V × I × T (with identical supply voltages), charging current emerged as the primary factor governing energy accumulation. Theoretical comparisons indicate 1C-charged batteries re-

quire 1.5 times longer energy accumulation duration than 1.5C-charged counterparts. Per the timing measurements in Figure 6, thermal runaway onset at 800 s for 1C charging corresponds to ~500 s for 1.5C charging—aligning with the first peak (not the second peak at ~700 s) in the purple curve. Hence, the initial temperature inflection peak provides superior warning accuracy. All five experiments distinctly exhibit first peaks (≈0.5 °C/s < L < 2 °C/s) and second peaks (≈L > 2 °C/s). Therefore, we designate the first peak (L > 0.5 °C/s) as the temperature-based early-warning indicator for incipient thermal runaway, and the second peak (≈L > 2 °C/s) as the diagnostic indicator for severe thermal runaway.

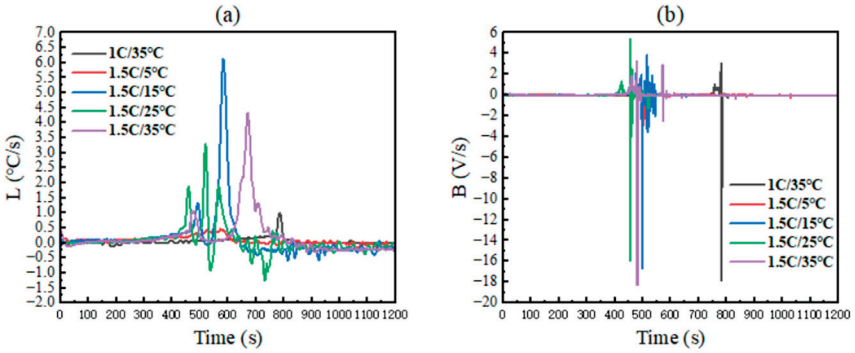

Figure 6. Temperature and voltage change rate curves. (**a**) Differential of temperature and time (**b**) Differentiation of voltage and time.

Notably, the duration of accelerated heating correlated positively with ambient temperature: the 1.5C/35 °C group displayed the longest heating window (600–770 s, Δt = 170 s), followed by the 25 °C and 15 °C groups. This confirms that under fixed ambient temperatures, higher C-rates intensify thermal accumulation and advance the onset of thermal runaway. Conversely, at fixed C-rates, elevated ambient temperatures also exacerbate thermal accumulation but paradoxically delay the timing of thermal runaway initiation. Experimental results confirm that high-temperature/low-current charging demonstrates greater safety compared to high-temperature/high-current conditions. However, contrary to conventional intuition, low-temperature/high-current charging accelerates thermal runaway progression more rapidly than high-temperature/high-current scenarios.

Panel (b) demonstrates that severe thermal runaway groups exhibited voltage collapse rates > 10 V/s, contrasting sharply with the 1.5C/5 °C group's maximum rate of 2.9 V/s. The 1C/35 °C group, despite experiencing thermal runaway interruption via environmental heat dissipation, still showed a >10 V/s voltage drop—distinct from the 1.5C/5 °C interruption mechanism.

Compared with the above analysis, the following can be found:

Contrary to intuition, while high-temperature/low-current charging enhances safety versus high-current/high-temperature conditions, low-temperature/high-current charging triggers thermal runaway faster than high-current/high-temperature scenarios.

Voltage drop rates >10 V/s alone cannot guarantee severe thermal runaway, which explains the pathway-dependent interruptions observed in Section 4.2.

Dual thresholds (>0.5 °C/s temperature rise rate + >10 V/s voltage drop rate) provide more reliable thermal runaway warnings than single-parameter criteria.

This analysis systematically links dynamic electrical–thermal behavior to ultimate thermal runaway severity, validating the necessity of multi-parameter monitoring for failure prediction.

5. Conclusions

This study systematically investigated the thermal runaway behavior of prismatic lithium iron phosphate (LFP) batteries under coupled C-rate and ambient temperature conditions. Through synchronized measurements of surface deformation, mass loss, temperature evolution, and voltage dynamics, a four-stage thermal runaway progression model was proposed and experimentally validated. Based on these findings, a multi-indicator thermal runaway warning system for LFP batteries was developed to quantitatively optimize the traditional single-factor thermal runaway warning strategy.

(1) Charge rate and ambient temperature exert synergistic amplification effects on triggering thermal runaway. The synergistic effect of high charging rate and high temperature significantly intensifies the severity of thermal runaway. Compared with the low-temperature high-rate group and the high-temperature low-multiplier group, the thermal runaway of the high-charge-multiplier high-temperature group reaches higher peak temperatures, resulting in greater mass loss. The coupling effect of temperature and charge rate on reaction kinetics is emphasized.

(2) Charge rate and ambient temperature influence thermal runaway via distinct mechanisms. The charge rate has a greater impact on the intensity of energy release during thermal runaway in LFP batteries, and experiments show that at a fixed ambient temperature, a higher charge rate will exacerbate the thermal accumulation in a short period of time, and trigger the thermal runaway in advance of the time. Ambient temperature has a more significant effect on the total energy release during thermal runaway in LFP batteries, and a low-temperature environment (e.g., 5 °C) significantly inhibits the thermal runaway process; the mechanism lies in the increase in electrolyte viscosity under low temperature to inhibit the rapid growth of lithium dendrites and the risk of diaphragm piercing, and at the same time reduces the kinetic rate of the SEI membrane decomposition and the reaction of the electrolyte.

(3) Stage-based multi-indicator warning signals improve LFP battery thermal runaway early-warning precision. Within the 80–120 °C range (Stage II), gas release and voltage fluctuations serve as precursors to interface degradation. In Stage III, a temperature ramp rate > 0.5 °C/s (first peaks) and a voltage drop > 10 mV/s jointly signal imminent thermal runaway. These features enable the development of multi-dimensional, real-time monitoring strategies.

The research results provide a theoretical basis for the optimization of electric vehicle battery management systems (BMSs). It is recommended to appropriately increase the charging rate in low-temperature environments and reduce the charging rate in high-temperature environments to balance efficiency and safety. Future battery management systems (BMSs) should integrate temperature gradient monitoring, gas evolution detection, and real-time TRSI calculation to achieve intelligent, multi-parameter thermal risk control.

Author Contributions: J.S.: conceptualization, methodology, writing—review and editing. J.T.: investigation, writing—original draft. L.K.: supervision. Z.W.: funding acquisition. F.X.: writing—review and editing. X.D.: formal analysis, writing—review and editing. All authors have read and agreed to the published version of the manuscript.

Funding: The authors gratefully acknowledge that this research was funded by the Science Research Project of Hebei Education Department (Grant No. QN2025154).

Data Availability Statement: The original contributions presented in the study are included in the article, further inquiries can be directed to the corresponding author.

Conflicts of Interest: The authors declare no conflict of interest.

References

1. Feng, X.; He, X.; Ouyang, M.; Wang, L.; Lu, L.; Ren, D.; Santhanagopalan, S. A Coupled Electrochemical-Thermal Failure Model for Predicting the Thermal Runaway Behavior of Lithium-Ion Batteries. *J. Electrochem. Soc.* **2018**, *165*, A3748. [CrossRef]
2. Wang, Q.; Jiang, B.; Li, B.; Yan, Y. A Critical Review of Thermal Management Models and Solutions of Lithium-Ion Batteries for the Development of Pure Electric Vehicles. *Renew. Sustain. Energy Rev.* **2016**, *64*, 106–128. [CrossRef]
3. Qasem, N.A.A.; Abdulrahman, G.A.Q. A Recent Comprehensive Review of Fuel Cells: History, Types, and Applications. *Int. J. Energy Res.* **2024**, *2024*, 7271748. [CrossRef]
4. Chen, Y.; Kang, Y.; Zhao, Y.; Wang, L.; Liu, J.; Li, Y.; Liang, Z.; He, X.; Li, X.; Tavajohi, N.; et al. A Review of Lithium-Ion Battery Safety Concerns: The Issues, Strategies, and Testing Standards. *J. Energy Chem.* **2021**, *59*, 83–99. [CrossRef]
5. Spotnitz, R.; Franklin, J. Abuse Behavior of High-Power, Lithium-Ion Cells. *J. Power Sources* **2003**, *113*, 81–100. [CrossRef]
6. Larsson, F.; Mellander, B.-E. Abuse by External Heating, Overcharge and Short Circuiting of Commercial Lithium-Ion Battery Cells. *J. Electrochem. Soc.* **2014**, *161*, A1611. [CrossRef]
7. Zhu, X.; Wang, Z.; Wang, Y.; Wang, H.; Wang, C.; Tong, L.; Yi, M. Overcharge Investigation of Large Format Lithium-Ion Pouch Cells with $Li(Ni_{0.6}Co_{0.2}Mn_{0.2})O_2$ Cathode for Electric Vehicles: Thermal Runaway Features and Safety Management Method. *Energy* **2019**, *169*, 868–880. [CrossRef]
8. Kumar, S.; Kim, H.-J. Recent Advances in Early Warning Methods and Prediction of Thermal Runaway Events in Li-Ion Batteries. *J. Ind. Eng. Chem.* **2025**, *145*, 63–74. [CrossRef]
9. Feng, X.; Ouyang, M.; Liu, X.; Lu, L.; Xia, Y.; He, X. Thermal Runaway Mechanism of Lithium Ion Battery for Electric Vehicles: A Review. *Energy Storage Mater.* **2018**, *10*, 246–267. [CrossRef]
10. Leising, R.A.; Palazzo, M.J.; Takeuchi, E.S.; Takeuchi, K.J. Abuse Testing of Lithium-Ion Batteries: Characterization of the Overcharge Reaction of $LiCoO_2$/Graphite Cells. *J. Electrochem. Soc.* **2001**, *148*, A838. [CrossRef]
11. Saito, Y.; Takano, K.; Negishi, A. Thermal Behaviors of Lithium-Ion Cells during Overcharge. *J. Power Sources* **2001**, *97–98*, 693–696. [CrossRef]
12. Kang, R.; Jia, C.; Zhao, J.; Zhao, L.; Zhang, J. Effects of Capacity on the Thermal Runaway and Gas Venting Behaviors of Large-Format Lithium Iron Phosphate Batteries Induced by Overcharge. *J. Energy Storage* **2024**, *87*, 111523. [CrossRef]
13. Meng, D.; Wang, X.; Chen, M.; Wang, J. Effects of Environmental Temperature on the Thermal Runaway of Lithium-Ion Batteries during Charging Process. *J. Loss Prev. Process Ind.* **2023**, *83*, 105084. [CrossRef]
14. An, C.; Zhai, J.; Luo, Z.; Lei, Z. Numerical Study on Thermal Runaway of LFP Batteries Triggered by Low Temperature Heating. *Fire Technol.* **2024**, *60*, 3927–3947. [CrossRef]
15. Santhanagopalan, S.; Ramadass, P.; Zhang, J. (Zhengming) Analysis of Internal Short-Circuit in a Lithium Ion Cell. *J. Power Sources* **2009**, *194*, 550–557. [CrossRef]
16. Ouyang, D.; Chung, Y.-H.; Liu, J.; Bai, J.; Zhou, Y.; Chen, S.; Wang, Z.; Shu, C.-M. Characteristics and Mechanisms of as Well as Evaluation Methods and Countermeasures for Thermal Runaway Propagation in Lithium-Ion Batteries. *Prog. Energy Combust. Sci.* **2025**, *108*, 101209. [CrossRef]
17. Ding, S.; Dong, C.; Zhao, T.; Koh, L.; Bai, X.; Luo, J. A Meta-Learning Based Multimodal Neural Network for Multistep Ahead Battery Thermal Runaway Forecasting. *IEEE Trans. Ind. Inform.* **2021**, *17*, 4503–4511. [CrossRef]
18. Feng, X.; Wong, S.K.; Chen, T.; Ouyang, M. An Automatic Identification Method of Thermal Physical Parameter for Lithium-Ion Batteries Suffering from Thermal Runaway. *J. Energy Storage* **2024**, *83*, 110358. [CrossRef]
19. Ren, D.; Liu, X.; Feng, X.; Lu, L.; Ouyang, M.; Li, J.; He, X. Model-Based Thermal Runaway Prediction of Lithium-Ion Batteries from Kinetics Analysis of Cell Components. *Appl. Energy* **2018**, *228*, 633–644. [CrossRef]
20. Tang, Z.; Ji, Y.; Yu, P.; Cheng, J. Investigation on the Thermal Management Performance of a Non-Contact Flow Boiling Cooling System for Prismatic Batteries. *J. Energy Storage* **2023**, *66*, 107499. [CrossRef]
21. Ren, D.; Feng, X.; Lu, L.; Ouyang, M.; Zheng, S.; Li, J.; He, X. An Electrochemical-Thermal Coupled Overcharge-to-Thermal-Runaway Model for Lithium Ion Battery. *J. Power Sources* **2017**, *364*, 328–340. [CrossRef]
22. Rao, H.; Huang, Z.; Zhang, H.; Xiao, S. Study of Fire Tests and Fire Safety Measures on Lithiumion Battery Used on Ships. In Proceedings of the 2015 International Conference on Transportation Information and Safety (ICTIS), Wuhan, China, 25–28 June 2015; pp. 865–870. [CrossRef]
23. Wang, Q.; Shao, G.; Duan, Q.; Chen, M.; Li, Y.; Wu, K.; Liu, B.; Peng, P.; Sun, J. The Efficiency of Heptafluoropropane Fire Extinguishing Agent on Suppressing the Lithium Titanate Battery Fire. *Fire Technol.* **2016**, *52*, 387–396. [CrossRef]
24. Liu, Y.; Duan, Q.; Xu, J.; Chen, H.; Lu, W.; Wang, Q. Experimental Study on the Efficiency of Dodecafluoro-2-Methylpentan-3-One on Suppressing Lithium-Ion Battery Fires. *RSC Adv.* **2018**, *8*, 42223–42232. [CrossRef] [PubMed]

25. Golubkov, A.W.; Scheikl, S.; Planteu, R.; Voitic, G.; Wiltsche, H.; Stangl, C.; Fauler, G.; Thaler, A.; Hacker, V. Thermal Runaway of Commercial 18650 Li-Ion Batteries with LFP and NCA Cathodes—Impact of State of Charge and Overcharge. *RSC Adv.* **2015**, *5*, 57171–57186. [CrossRef]
26. Mao, N.; Zhang, T.; Wang, Z.; Gadkari, S.; Wang, J.; He, T.; Gao, T.; Cai, Q. Revealing the Thermal Stability and Component Heat Contribution Ratio of Overcharged Lithium-Ion Batteries during Thermal Runaway. *Energy* **2023**, *263*, 125786. [CrossRef]
27. Jie, D.; Baohui, C.; Jiazheng, L.; Tiannian, Z.; Chuanping, W. Thermal Runaway and Combustion Characteristics, Risk and Hazard Evaluation of Lithium-iron Phosphate Battery under Different Thermal Runaway Triggering Modes. *Appl. Energy* **2024**, *368*, 123451. [CrossRef]
28. Cui, Y.; Shi, D.; Wang, Z.; Mou, L.; Ou, M.; Fan, T.; Bi, S.; Zhang, X.; Yu, Z.; Fang, Y. Thermal Runaway Early Warning and Risk Estimation Based on Gas Production Characteristics of Different Types of Lithium-Ion Batteries. *Batteries* **2023**, *9*, 438. [CrossRef]
29. Larsson, F.; Andersson, P.; Blomqvist, P.; Mellander, B.-E. Toxic Fluoride Gas Emissions from Lithium-Ion Battery Fires. *Sci. Rep.* **2017**, *7*, 10018. [CrossRef]
30. Wang, K.; Wu, D.; Chang, C.; Zhang, J.; Ouyang, D.; Qian, X. Charging Rate Effect on Overcharge-Induced Thermal Runaway Characteristics and Gas Venting Behaviors for Commercial Lithium Iron Phosphate Batteries. *J. Clean. Prod.* **2024**, *434*, 139992. [CrossRef]
31. Knott, L.M.; Long, E.; Garner, C.P.; Fly, A.; Reid, B.; Atkins, A. Insights Into Lithium-Ion Battery Cell Temperature and State of Charge Using Dynamic Electrochemical Impedance Spectroscopy. *Int. J. Energy Res.* **2024**, *2024*, 9657360. [CrossRef]
32. Wu, T.; Chen, H.; Wang, Q.; Sun, J. Comparison Analysis on the Thermal Runaway of Lithium-Ion Battery under Two Heating Modes. *J. Hazard. Mater.* **2018**, *344*, 733–741. [CrossRef] [PubMed]
33. Shah, K.; Chalise, D.; Jain, A. Experimental and Theoretical Analysis of a Method to Predict Thermal Runaway in Li-Ion Cells. *J. Power Sources* **2016**, *330*, 167–174. [CrossRef]
34. Li, H.; Duan, Q.; Zhao, C.; Huang, Z.; Wang, Q. Experimental Investigation on the Thermal Runaway and Its Propagation in the Large Format Battery Module with $Li(Ni_{1/3}Co_{1/3}Mn_{1/3})O_2$ as Cathode. *J. Hazard. Mater.* **2019**, *375*, 241–254. [CrossRef] [PubMed]
35. Yang, X.; Wang, H.; Li, M.; Li, Y.; Li, C.; Zhang, Y.; Chen, S.; Shen, H.; Qian, F.; Feng, X.; et al. Experimental Study on Thermal Runaway Behavior of Lithium-Ion Battery and Analysis of Combustible Limit of Gas Production. *Batteries* **2022**, *8*, 250. [CrossRef]
36. Liu, J.; Wang, Z.; Bai, J. Influences of Multi Factors on Thermal Runaway Induced by Overcharging of Lithium-Ion Battery. *J. Energy Chem.* **2022**, *70*, 531–541. [CrossRef]
37. Wang, D.; Peng, K.; Fu, Y.; Zhu, C.; Yang, Y. Kinetics of Lithium Dendrite Growth in Garnet-Type Solid Electrolyte. *J. Power Sources* **2021**, *487*, 229421. [CrossRef]
38. Li, S.; Zhou, S.; Zhao, S.; Jin, T.; Zhong, M.; Cen, Z.; Gao, P.; Yan, W.; Ling, M. Room Temperature Resistive Hydrogen Sensor for Early Safety Warning of Li-Ion Batteries. *Chemosensors* **2023**, *11*, 344. [CrossRef]
39. Jin, Y.; Zheng, Z.; Wei, D.; Jiang, X.; Lu, H.; Sun, L.; Tao, F.; Guo, D.; Liu, Y.; Gao, J.; et al. Detection of Micro-Scale Li Dendrite via H_2 Gas Capture for Early Safety Warning. *Joule* **2020**, *4*, 1714–1729. [CrossRef]
40. Zhang, Y.; Cheng, S.; Mei, W.; Jiang, L.; Jia, Z.; Cheng, Z.; Sun, J.; Wang, Q. Understanding of Thermal Runaway Mechanism of $LiFePO_4$ Battery In-Depth by Three-Level Analysis. *Appl. Energy* **2023**, *336*, 120695. [CrossRef]
41. Kim, H.; Jung, T.; Jung, J.; Noh, Y.; Lee, B. Accurate Prediction of Electrochemical Degradation Trajectory for Lithium-Ion Battery Using Self-Discharge. *Int. J. Energy Res.* **2024**, *2024*, 1758578. [CrossRef]
42. Chun, H.; Choi, H.; Jun, Y.; Lee, H. Comprehensive Study on Thermal Characteristics of Lithium-Ion Battery With Entropic Heat. *Int. J. Energy Res.* **2024**, *2024*, 8815580. [CrossRef]

batteries

MDPI

Article

Intrinsic Thermal Stability of Li-Rich Mn-Based Cathodes Enabling Safe High-Energy Lithium-Ion Batteries

Zhaoqiang Pei [1,2], Shaobo Feng [1,2], Zhibo Han [3], Zihua Wang [3], Chengshan Xu [1,2], Xiangming He [4], Li Wang [4,*], Yu Wang [1,2,5,*] and Xuning Feng [1,2]

[1] School of Vehicle and Mobility, Tsinghua University, Beijing 100084, China; zy2243502@buaa.edu.cn (Z.P.); fsb22@mails.tsinghua.edu.cn (S.F.); xcs_pcg@mail.tsinghua.edu.cn (C.X.); fxn17@tsinghua.edu.cn (X.F.)
[2] State Key Laboratory of Intelligent Green Vehicle and Mobility, Tsinghua University, Beijing 100084, China
[3] School of Material Science and Engineering, Beihang University, Xueyuan Road, Beijing 100191, China; 20375387@buaa.edu.cn (Z.H.); sy2343112@buaa.edu.cn (Z.W.)
[4] Institute of Nuclear and New Energy Technology, Tsinghua University, Beijing 100084, China; hexm@tsinghua.edu.cn
[5] Center for Combustion Energy, Tsinghua University, Beijing 100084, China
* Correspondence: wang-l@tsinghua.edu.cn (L.W.); lucywang@mail.tsinghua.edu.cn (Y.W.)

Abstract: Lithium-rich manganese-based oxides (LMR) are promising next-generation cathode materials due to their high capacity and low cost, but safety remains a critical bottleneck restricting the practical application of high-energy-density cathodes. However, the safety level of LMR batteries and the thermal failure mechanism of the cathode are still poorly understood, especially when compared with traditional high-energy nickel-rich (Ni-rich) cathodes. Here, we investigate the LMR cell's thermal runaway behavior and the thermal failure mechanism of the cathode. Compared to a Ni-rich cell, Accelerating Rate Calorimetry (ARC) shows the LMR pouch cell exhibits a 62.7 °C higher thermal runaway trigger temperature (T2) and 270.3 °C lower maximum temperature (T3). These results indicate that the cell utilizing a higher-energy-density LMR cathode presents significantly lower thermal runaway risks and hazards. The results of differential scanning calorimetry–thermogravimetry–mass spectrometry (DSC-TG-MS) and in situ heating X-ray diffraction (XRD) indicate that the LMR cathode has superior thermal stability compared with the Ni-rich cathode, with cathode oxygen released at higher temperatures and lower rates, which is beneficial for delaying and mitigating the exothermic reaction inside the battery. This study demonstrates that simultaneously enhancing cathode energy density and battery safety is achievable, and these findings provide theoretical guidance for the design of next-generation high-energy and high-safety battery systems.

Keywords: battery safety; thermal runaway; lithium-rich manganese-based oxides; NCM layered oxides; thermal stability; cathode oxygen release

1. Introduction

The growing demand for high-energy-density lithium-ion batteries (LIBs) in electric vehicles and grid-scale energy storage has driven the development of advanced cathode materials beyond conventional layered oxides [1–3]. Among these, lithium-rich mangsanese-based oxides (LMRs) deliver capacities exceeding 250 mAh g^{-1} through anion redox reactions, positioning them as one of the most promising next-generation cathode candidates [4,5]. However, as critical components of battery safety, the application

of high-energy-density cathodes may induce safety hazards typified by thermal runaway (TR), which constrains the further development and practical application of high-energy cathodes [6–10].

Conventional high-energy Ni-rich NCM layered oxides cathodes (Ni $\geq$ 80%) enhance energy density but suffer from intrinsic thermal instability and release of reactive oxygen species (O*, O_2 and so on), which exacerbate self-heating reactions under thermal abuse, ultimately triggering thermal runaway [11–14]. Further increasing Ni content to boost the energy density of NCM cathodes aggravates their thermal degradation, escalating thermal runaway risks [15–17]. Thus, employing Ni-rich cathodes often entails a trade-off between energy density and safety. But emerging LMR cathodes may overcome this trade-off.

Unlike NCM cathodes reliant on Ni-dominated cationic redox, LMR cathodes harness both transition-metal redox and anionic oxygen redox to achieve high specific capacity (>250 mAch g^{-1}) [18–20]. Moreover, LMR cathodes typically contain <50% Ni and form composite lattice frameworks (e.g., monoclinic C2/m layered phases integrated with Li_2MnO_3-like domains or spinel components), creating distinct oxygen sublattice configurations compared to NCM cathodes [21,22]. This suggests that LMR cathodes may deviate from the thermal stability trend observed in Ni-rich cathodes—their higher specific capacity and energy density do not necessarily compromise thermal stability or increase thermal runaway risk. However, the safety implications of LMR cathodes remain unclear, and differences in thermal stability and failure mechanisms—particularly phase-structure stability and cathode oxygen release behavior at elevated temperatures—between LMR and Ni-rich cathodes are poorly understood. This knowledge gap severely impedes the rational design of safe, high-energy cathodes.

Therefore, we first employed accelerating rate calorimetry (ARC) to compare the safety of fully charged 1Ah LMR | Graphite and NCM92 | graphite pouch cells, quantifying their thermal runaway risk and hazard. Complementary characterizations, including DSC-TG-MS, in-situ heating XRD, and HRTEM, were used to contrast the thermal stability, phase evolution, and cathode oxygen release behavior of fully charged LMR and NCM92 cathodes. Results demonstrate that cells equipped with higher-specific-capacity/energy LMR cathodes exhibit significantly reduced thermal runaway risks and severity (TR trigger temperature (T2) increased by 62.7 °C, TR maximum temperature (T3) decreased by 270.3 °C). Material-level analyses reveal that LMR cells' superior safety originates from enhanced thermal stability and suppressed cathode oxygen release rate. This allows sufficient oxygen reaction with inactive components, releasing CO_2 (rather than O_2) that migrates to the anode, thereby delaying and mitigating exothermic reactions. Thus, the total heat release of the LMR full cell DSC sample is 31% lower than that of the NCM92 sample. These findings demonstrate that it is possible to simultaneously apply high-energy cathodes and improve battery safety. While currently large-scale commercialized LFP batteries exhibit high safety owing to the excellent thermal stability of LFP cathodes, their low energy density restricts applications in specific scenarios. Our study demonstrates that LMR batteries, featuring both high energy density and high safety, precisely fill this unique market niche. The high thermal stability of the LMR cathode and the altered oxygen release behavior enable LMR batteries to exhibit enhanced safety, which provides a low-risk foundation for upgrading battery systems. This enables improvements in both the driving range of electric vehicles and the capacity of energy storage stations, while simultaneously reducing the burden on cooling systems of electric vehicle battery packs or enhancing the long-term safety of energy storage systems. This study provides new insights and material foundations for developing next-generation lithium-ion battery systems with both high energy density and high safety.

2. Materials and Methods

2.1. Experimental Materials and Battery Sample Preparation

The battery samples used in this study were 1 Ah NCM92|Gr pouch cells and 1 Ah LMR|Gr pouch cells. The dry cells were purchased from Hunan Li-Fun Technology Corporation Limited, Changsha, Hunan, China. The NCM92 cathode was loaded with 95.5% active material, the compaction density of the electrode was 3.3 g/cc, and the thickness of the current collector was 12 μm. The LMR cathode was loaded with 96% active material, the compaction density of the electrode was 3.3 g/cc, and the thickness of the current collector was 12 μm. The anode electrode was loaded with 95.7% graphite anode material, the compaction density was 1.5 g/cc, and the thickness of the current collector was 8 μm. The electrolyte used was a commercial EC-based electrolyte purchased from Suzhou Dodo Chemical Technology Corporation Limited, Suzhou, Jiangsu, China. The specific composition was 1 M LiPF6 in EC/DMC (volume ratio of 3/7). The electrolyte was injected into the dry cells (3.5 g/Ah) in a glove box. The cells were sealed and left for 48 h to allow the electrolyte to fully wet the cells. Then, the cells after electrolyte injection were formed by cycling with a current of 0.1 C. After the formation cycling, the cells were vacuum-sealed to obtain the finished cells. Before the cell disassembly and thermal safety performance tests, the cells were charged with constant-current and constant-voltage (CC-CV). They were charged to 100% SOC (NCM92 cell charging cut-off voltage is 4.2 V, LMR cell charging cut-off voltage is 4.8 V) with a current of 1/3 C and a cut-off current of 0.05 C. The difference in upper charge voltage limits stems from the operating mechanisms and voltage characteristics of the two cathode materials. The NCM92 cathode relies on Ni-dominated cationic redox reactions, reaching full capacity at ~4.2 V—a widely recognized upper limit in both commercial and academic research to avoid structural degradation. In contrast, the LMR cathode achieves its high specific capacity (>250 mAh g^{-1}) primarily through anionic redox reactions, which require a higher voltage (~4.8 V) to fully activate Li_2MnO_3-like domains and achieve complete delithiation. This voltage difference is not arbitrarily set but determined by the intrinsic electrochemical properties of each material: failing to charge LMR to 4.8 V would prevent capturing its actual full-capacity state, just as limiting NCM92 to a lower voltage would underestimate its true state of charge (SOC). This approach aligns with standard practices in comparative studies of cathode materials; for instance, when comparing Ni-rich NCM and LFP cathodes, LFP is typically charged to ~3.7 V (its intrinsic full-SOC voltage) rather than the ~4.2 V used for NCM [23].

2.2. Battery Safety Assessment-ARC Test

In the investigation of thermal failure characteristics in full cells, the Accelerating Rate Calorimeter (ARC) (Figure 1) is commonly employed for qualitative and quantitative analyses. Conducted under quasi-adiabatic conditions, ARC tests eliminate heat exchange between the battery and its surroundings, such that the temperature rise rate is solely determined by internal exothermic reactions and the battery's heat capacity. This allows ARC results to characterize the intrinsic safety of battery cells. Additionally, the adiabatic environment enhances the instrument's sensitivity in detecting self-heating induced by internal chemical reactions.

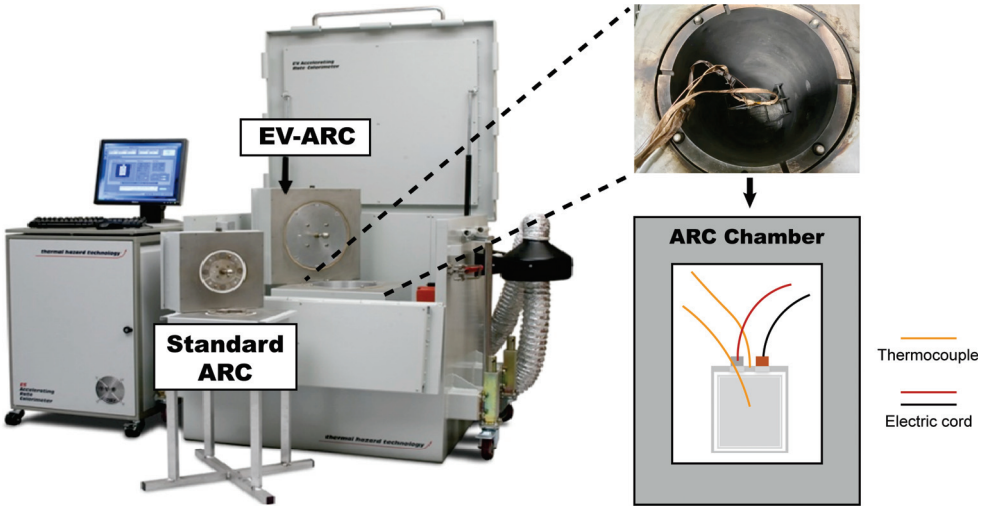

Figure 1. ARC equipment used to evaluate battery safety.

The ARC test in this study was carried out on the Extended Standard ARC (ES-ARC) of Thermal Hazard Technology (THT). Prior to the test, a K-type thermocouple was inserted into the central position inside the fully charged battery to obtain the accurate temperature changes in the battery during the test process. The pouch cells were tested using the Heat-Wait-Seek (HWS) program to acquire the characteristic temperatures that can characterize the battery safety as well as the self-heating rate. The temperature interval was set to 5–10 °C, and the waiting time was set to 20 min. When the battery exhibited self-heating, it entered the adiabatic state to determine the self-heating rate of the battery. If the battery did not experience continuous self-heating when heated to 250 °C, the test was terminated. As shown in Table 1, the temperature at which the battery's temperature rise rate was 0.02 °C/min was defined as the self-heating characteristic temperature T1, and the temperature at which the temperature rise rate was 1 °C/s was the thermal runaway triggering temperature T2 (which means the battery will undergo uncontrolled continuous heat release until it reaches the maximum temperature). The maximum temperature reached by the battery after thermal runaway was T3. These three characteristic temperatures are the key indicators for evaluating battery safety that need to be obtained by ARC test. Generally speaking, the higher the T1 and T2 of the battery in the ARC test, the lower the T3, the lower the risk and harm of thermal runaway of the battery, and the better the safety.

Table 1. Physical meaning and judgment criteria of characteristic temperature obtained by ARC test.

Characteristic Temperature	Physical Meaning	Criteria
T1	The starting temperature of the battery's continuous self-heating	dT/dt = 0.02 °C/min
T2	Battery thermal runaway trigger temperature	dT/dt = 1 °C/s
T3	Maximum temperature of battery thermal runaway	/

2.3. Material Level Thermal Failure Analysis Test—DSC-TG-MS

To analyze the thermal stability and exothermic behavior of fully charged electrode materials at the material level, 100% SOC pouch cells were disassembled to obtain electrode materials, with detailed procedures shown in Figure 2. First, the cells were charged to 100% SOC and then transferred into an inert gas-filled glove box (H_2O < 0.01 ppm, O_2 < 0.01 ppm). Under inert atmosphere protection, the aluminum–plastic film packaging of the cells was cut open using ceramic scissors. Anode/cathode electrodes and separators

were separated using ceramic tweezers. The electrodes were cut to appropriate sizes and soaked in excess DMC solvent for 1 h, respectively. After rinsing with DMC, the electrodes were soaked again in fresh DMC for another hour to thoroughly remove residual electrolyte and lithium salts. The washed electrodes were first dried in the glove box for 1 h, and then transferred to the glove box's transition chamber for vacuum drying. Subsequently, electrode material powders were gently scraped from the central area of the dried electrodes using a ceramic blade inside the glove box and stored in sealed tubes. This completed the disassembly of cells and preparation of fully charged electrode materials.

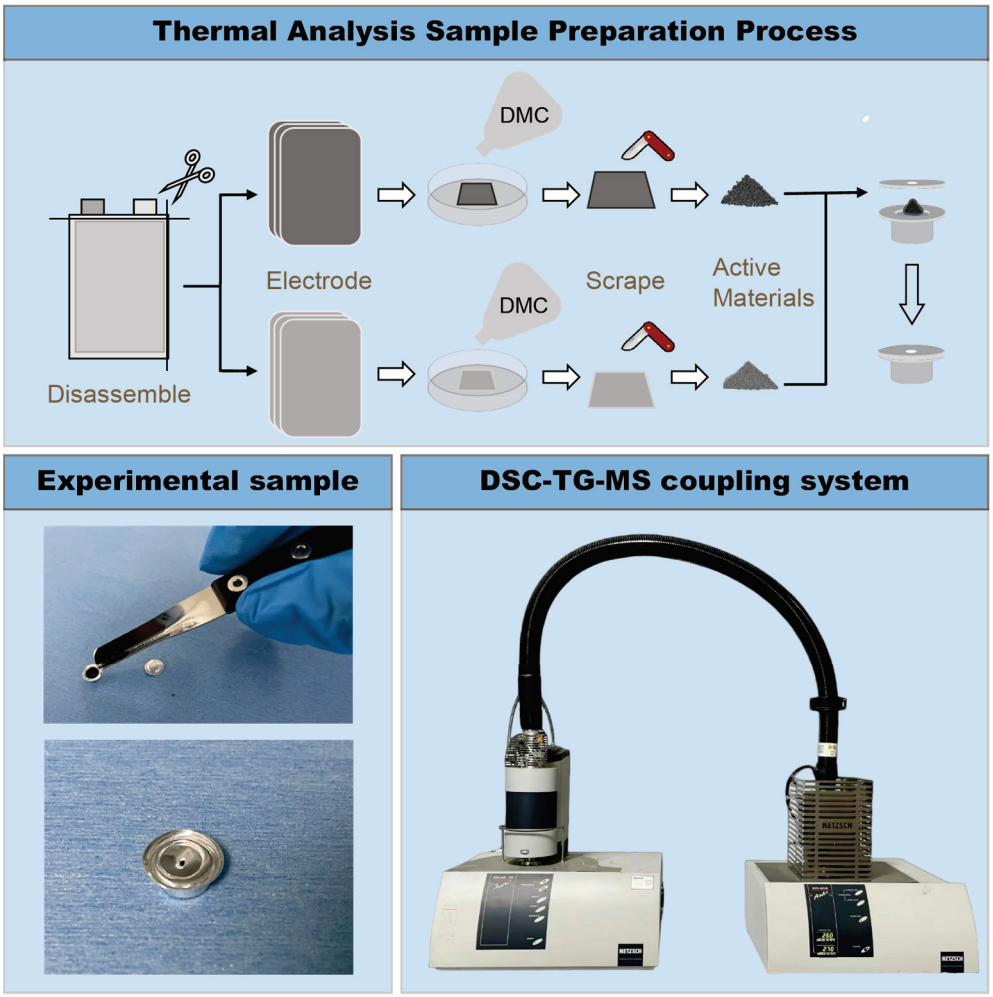

Figure 2. Process of disassembling batteries and obtaining charged samples for material thermal analysis.

Sample preparation for DSC-TG-MS tests was performed under inert atmosphere in the glove box. Single-component or mixed-component thermal analysis samples were prepared as needed, with mass ratios of cathode–anode–electrolyte consistent with those in the original cell. Electrode material powders, separators, and electrolyte were accurately weighed and loaded into standard aluminum crucibles (30 µL concave crucibles, NETZSCH-Gerätebau GmbH, Selb, Bavaria, Germany). The crucible lids were sealed using matching equipment (Figure 2). Immediately after sealing, the crucibles were quickly removed from the glove box, and a small hole was pierced at the center of the lid using a needle with diameter >0.7 mm. The crucibles were then rapidly placed into the sample cell of the DSC-TG-MS instrument (Figure 2). Finally, the required instrument parameters were set for testing. After completion, heat flow, mass loss, and gas evolution mass spectrometry

signals of the electrode materials or mixed samples as a function of temperature were obtained, enabling analysis of their thermal stability and thermal failure behavior.

2.4. Characterization

The fully charged pouch disassembled in an argon-filled glove box, and the electrodes were rinsed three times with DMC and dried to obtain the fully charged cathode electrodes. As shown in Figure 3, the fully charged cathode electrode was packaged in an aluminum plastic bag in an argon-filled glove box for subsequent in situ heating XRD testing. Meanwhile, such samples were also used to undergo heating abuse to obtain material samples after thermal failure. In situ heating XRD testing was performed from 40 °C to 240 °C with a temperature step of 20 °C. The fully charged cathode electrodes were packaged in aluminum–plastic bags and heated to 200 °C using a hot box, and then the heat-failed samples were disassembled in a glove box to obtain the heat-failed electrodes and material powder. For the SEM-EDS test of cathode materials, the cathode electrode was first processed with argon ion polisher (liquid nitrogen was used to maintain the temperature at −170 °C during the treatment), and then a scanning electron microscope (SEM) (ZEISS Merlin, Carl Zeiss AG, Oberkochen, Germany) was used to observe the cross-sectional morphology and element distribution of the cathode. X-ray powder diffraction patterns were collected using a Cu source Bruker D8 ADVANCE (Bruker Corporation, Billerica, MA, USA). High-resolution TEM (HRTEM) testing was conducted with a JEM2010F (JEOL Ltd., Tokyo, Japan) transmission electron microscope.

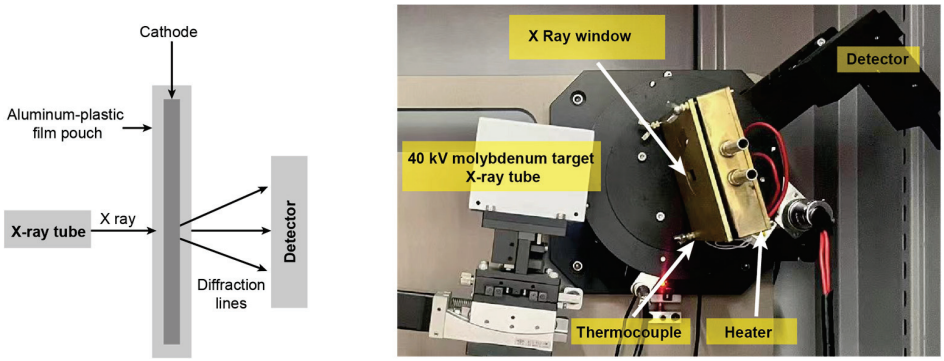

Figure 3. Schematic diagram and equipment picture of in situ heating XRD experiment.

3. Results and Discussion

3.1. Material Information and Electrochemical Performance

Lithium-rich manganese-based (LMR) cathodes ($Li_{1.2}Ni_{0.3}Mn_{0.5}O_2$) were paired with graphite anodes to assemble full cells, with detailed cell parameters provided in the Materials and Methods section. X-ray diffraction (XRD) was employed for preliminary structural characterization of the lithium-rich manganese-based cathode (Figure 4a). Rietveld refinement and crystal structure modeling revealed that the cathode consists of $LiTMO_2$ (TM = Ni, Mn) and Li_2MnO_3 phases. High-resolution transmission electron microscopy (HRTEM) images (Figure 4b) showed a distinct layered structure in the cathode, with an interplanar spacing of ~0.47 nm. Scanning electron microscopy-energy dispersive spectroscopy (SEM-EDS) was used to analyze the morphology and elemental distribution of the cathode: cross-sectional morphology indicated intact internal structures of initial particles without obvious defects or cracks (Figure 4c), while cross-sectional elemental mapping confirmed Ni and Mn as the transition metal elements in the cathode (Figure 4d). Meanwhile,

the internal structure of the NCM92 cathode remains intact, and it is primarily composed of $LiTMO_2$ (TM = Ni, Mn) phases (Figure S2).

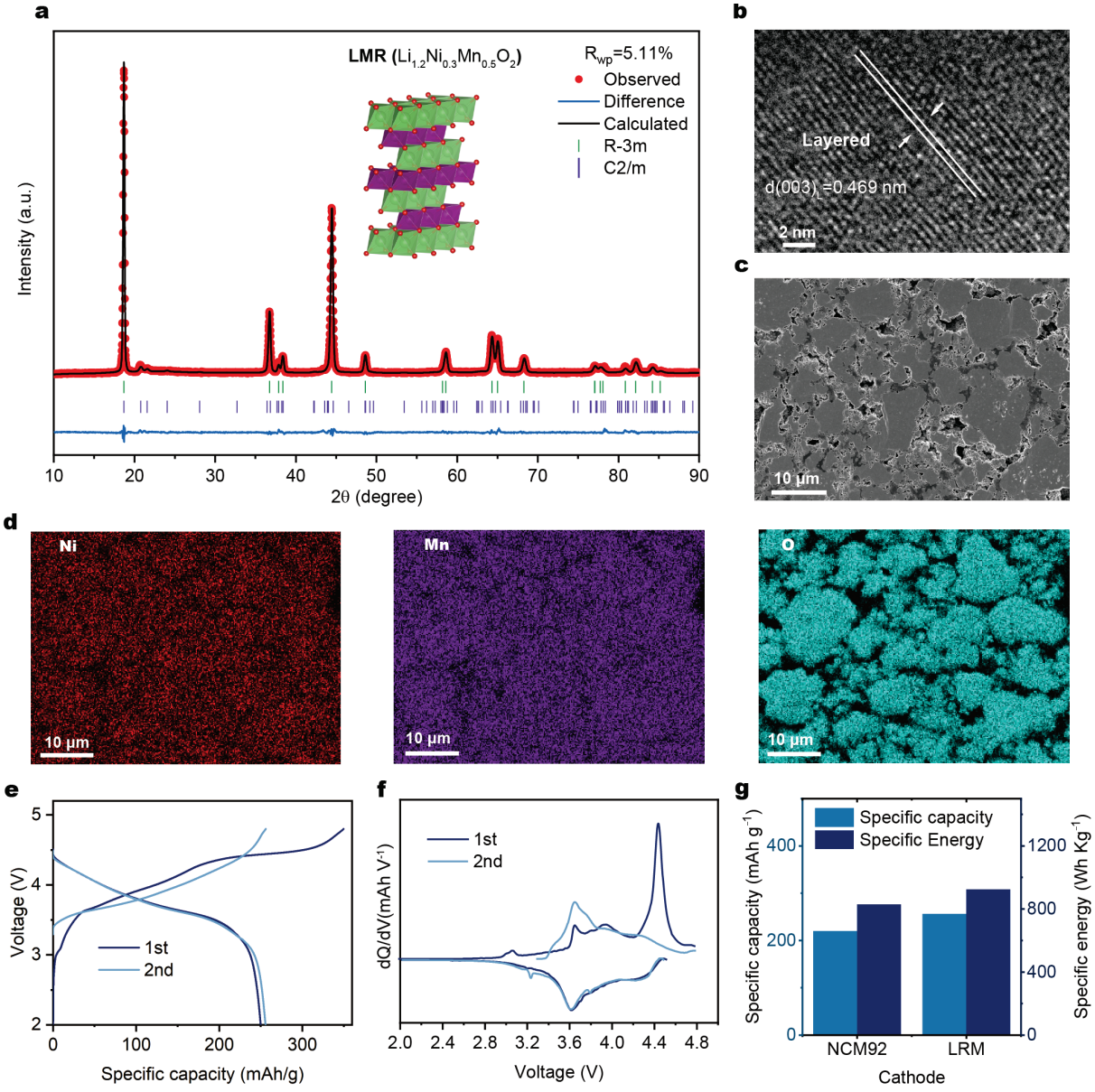

Figure 4. Lithium-rich manganese-based cathode material: (**a**) XRD pattern and Rietveld refinement results, (**b**) HRTEM image, (**c**) cross-sectional SEM image, and (**d**) elemental distribution; LMR battery: (**e**) first- and second-cycle voltage–capacity curves, (**f**) first- and second-cycle dQ/dV curves; (**g**) comparison of specific capacity and specific energy between LMR and NCM cathode materials.

Electrochemical tests were performed to evaluate the electrochemical performance of LMR cells. Figure 4e presents the specific capacity–voltage profiles of the first and second cycles. A prominent extended voltage plateau at ~4.5 V in the first charge profile corresponds to the activation of the lithium-rich Li_2MnO_3 phase. A sharp, intense oxidation peak near 4.5 V during the first charge cycle was also observed in the dQ/dV curve (Figure 4f), reflecting the Li_2MnO_3 activation reaction—a signature characteristic of lithium-rich cathodes. Additionally, the specific capacity and specific energy of the LMR cathode at 0.1 C were 256.0 mAh g^{-1} and 924.0 Wh Kg^{-1}, which were significantly higher than those of

the traditional high-energy nickel-rich NCM cathode (219.6 mAh g^{-1} and 829.0 Wh Kg^{-1}) (Figures 4g and S3).

3.2. Battery Safety Comparison

Accelerating rate calorimetry (ARC) tests were used to quantify battery safety. A fully charged 1 Ah LMR | Graphite cell was tested, with a fully charged 1 Ah NCM92 | Graphite cell as the control. This study focuses on the influence of material chemistry (e.g., crystal structure) on battery thermal runaway characteristics, rather than cycle-induced changes (e.g., CEI layer evolution or structural degradation); thus, the cells tested herein are fresh cells without long-term cycling. However, we recognize that long-term electrochemical cycling may alter thermal stability through surface or bulk structural changes, which constitutes a significant direction for future research. Results in Figure 5a show that compared to the LMR cell, the NCM92 cell underwent thermal runaway rapidly during testing, accompanied by a sharp temperature rise exceeding 700 °C. In contrast, despite using a higher-energy-density cathode, the LMR cell exhibited a lower temperature rise rate after the onset of self-heating and experienced thermal runaway only after a nearly three times longer duration of slow self-heating. The lower temperature rise rate and extended slow self-heating period facilitate the operation of thermal management systems and provide a time window for fire-fighting intervention, reflecting the intrinsic safety of the battery.

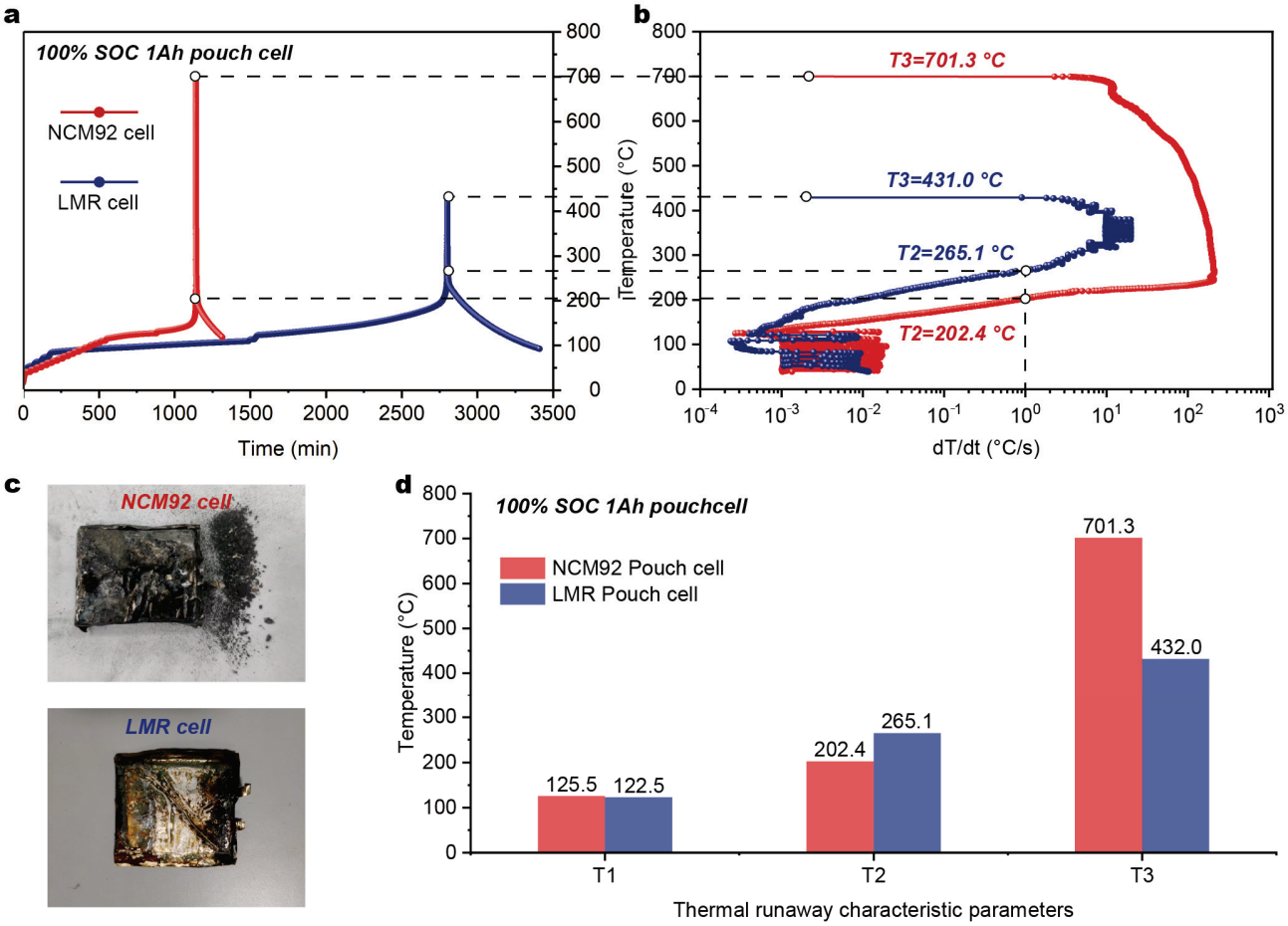

Figure 5. (**a**) Temperature–time curve in ARC test; (**b**) temperature rise rate–temperature curve in ARC test; (**c**) comparison of cell morphology after ARC test; (**d**) comparison of characteristic temperatures of two cells in ARC test.

Additionally, based on the physical significance of characteristic temperatures (Table 1), higher T1 and T2, combined with lower T3, indicate reduced thermal runaway risk and hazard, as well as higher intrinsic safety. Figure 5b shows that the LMR cell had a T2 of 256.1 °C, which is 62.7 °C higher than that of the NCM92 cell (202.4 °C), and a T3 of 431.0 °C, 270.3 °C lower than that of the NCM92 cell (701.3 °C). Images of cell residues in Figure 5c reveal severe bulging and structural damage in the NCM92 cell, indicating violent runaway and explosion during ARC testing, whereas LMR cell residues remained relatively intact with only slight bulging and no severe ejection of electrode materials—confirming their lower thermal runaway hazard.

Comparing the ARC characteristic temperatures of the two batteries: T1 values were comparable (T1 primarily depends on the thermal stability of the anode SEI), while the LMR cell showed a significantly higher T2 and a substantially lower T3 (Figure 5d). These results demonstrate that incorporating a higher-energy-density LMR cathode did not compromise the safety of lithium-ion batteries; instead, it significantly enhanced their intrinsic safety, challenging conventional understanding.

3.3. Thermal Stability of Cathode and Cathode Oxygen Release Behavior

Traditional high-energy-density Ni-rich batteries exhibit elevated thermal runaway risk due to poor cathode thermal stability and phase transitions accompanied by oxygen release at high temperatures. To address this, DSC-TG-MS was employed to analyze the thermal stability and gas release behavior of LMR cathodes. DSC results showed that the fully charged NCM92 cathode exhibits an exothermic peak at 236.8 °C with a rate of 0.96 W g^{-1}, whereas the fully charged LMR cathode shifts the exothermic peak to 290.8 °C with a reduced rate of 0.25 W g^{-1} (Figure 6a). TG results indicate that the fully charged NCM92 cathode reaches a maximum mass loss rate of 4.40% min^{-1} at 238.8 °C, while the fully charged LMR cathode showed a lower maximum mass loss rate of 1.10% min^{-1} at 322.6 °C (Figure 6b). Additionally, the total mass loss of the NCM92 cathode reaches 11.87% when heated to 350 °C, compared to only 4.85% for the LMR cathode. Comparative analysis of exothermic behavior and mass loss during thermal failure confirms the superior thermal stability of LMR cathode.

Mass spectrometry (MS) coupled with DSC-TG enables in situ monitoring of oxygen and other oxygen-containing gas release during high-temperature cathode failure. As shown in Figure 6c, the fully charged NCM92 cathode exhibits a distinct O_2 release peak (m/z = 32) at 252.6 °C, whereas no significant O_2 release peak is observed for the fully charged LMR cathode—consistent with the minimal mass loss in LMR's TG profile Under heating conditions, oxygen released from cathode materials may either be liberated as free O_2 or react with carbonaceous components in the cathode (e.g., conductive agents, binders, and other organic constituents) to form CO_2 [24]. Compared to the release of free O_2, the generation of CO_2 is more favorable for mitigating exothermic reactions within the battery [25]. As shown in Figure 6d, NCM92 cathode releases CO_2 (m/z = 44) at 243.5 °C, while LMR cathode exhibits an initial CO_2 peak at 199.6 °C (likely from CEI decomposition, as no significant mass loss occurs in LMR's TG curve at this stage). The main CO_2 release peak of LMR cathode appears at 297.5 °C, coinciding with its obvious mass loss. In summary, compared to NCM92, fully charged LMR cathodes not only possess better thermal stability but also release oxygen primarily as CO_2 rather than O_2, both of which help mitigate internal exothermic reactions and reduce thermal runaway risk and hazard.

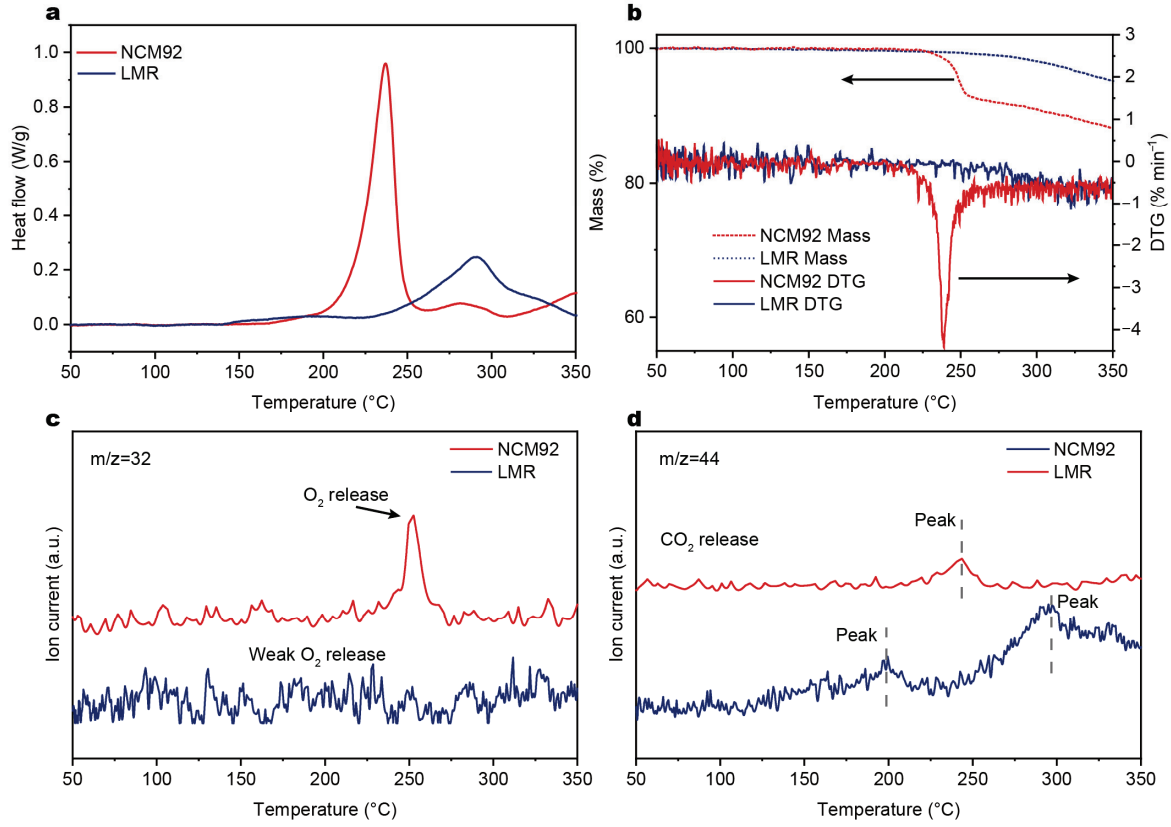

Figure 6. (**a**) DSC curves of the fully charged NCM92 cathode and the LMR cathode; (**b**) TG and DTG curves of the fully charged NCM92 cathode and the LMR cathode; MS signals of oxygen (m/z = 32) (**c**) and CO_2 (m/z = 44) (**d**) at the fully charged cathode during heating.

3.4. Structural Stability of Cathode During Heating

In situ heating XRD was employed to characterize the structural evolution of fully charged NCM92 and LMR cathodes under heating, aiming to compare the thermal stability of their crystal structures. By analyzing the diffraction peak of the layered phase-specific $(003)_L$ plane, it was observed that when heated from 40 °C to ~170 °C, the $(003)_L$ diffraction peak of the NCM92 cathode began to shift toward lower angles with a significant decrease in intensity—indicating the initiation of layered structure degradation (Figure 7a). In contrast, the $(003)_L$ peak of the fully charged LMR cathode showed an obvious shift to lower 2θ values only when heated to nearly 200 °C. At 200 °C, the $(003)_L$ peak intensity of the NCM92 cathode had weakened remarkably, while that of the LMR cathode decreased to a lesser extent, demonstrating slower degradation of the layered structure in the LMR cathode compared to NCM92 (Figure 7b).

The phase transition process was further clarified: the NCM92 cathode remained primarily in the layered phase below 172 °C, but started to transform into the spinel phase above 172 °C, forming a layered-spinel mixed phase, and completely converted to spinel phase at 207 °C (Figure 7a). For the fully charged LMR cathode, it maintained the layered phase as the dominant phase below 197 °C; the spinel phase began to emerge with further heating, but even at 240 °C, the transition to the spinel phase was incomplete (Figure 7b). Overall, in situ heating XRD results confirm that fully charged LMR cathodes exhibit higher structural thermal stability than NCM92 cathodes.

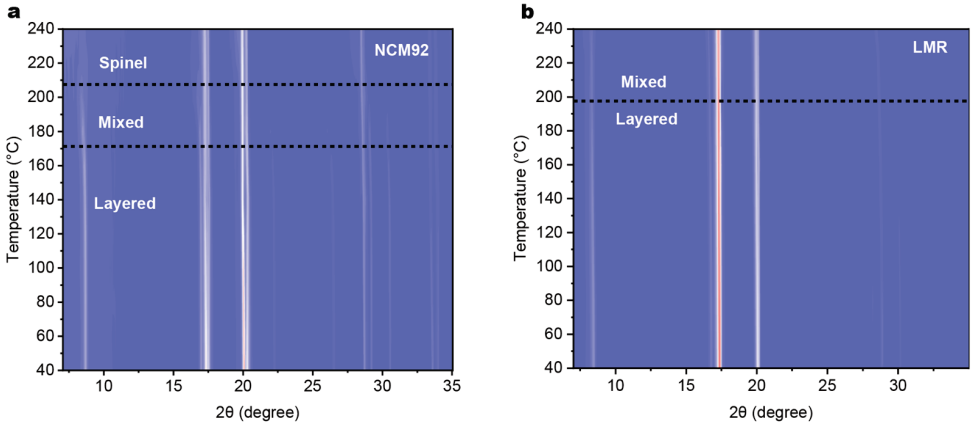

Figure 7. In situ heating XRD results of (**a**) fully charged NCM92 cathode and (**b**) fully charged LMR cathode.

3.5. Structural Degradation of Cathode After Thermal Abuse

To further verify the thermal stability of fully charged LMR cathodes, high-resolution transmission electron microscopy (HRTEM) was performed on fully charged NCM92 and LMR cathodes before and after 200 °C thermal abuse, aiming to analyze the degradation degree of their crystal structures after thermal failure. HRTEM images show that the fully charged NCM92 cathode primarily consists of a layered structure before thermal abuse (Figure 8a). After 200 °C thermal abuse, however, both the edge and bulk phases of the NCM92 cathode significantly degraded into spinel phase (Figure 8b), consistent with the in situ heating XRD results, confirming severe degradation of the layered structure in fully charged NCM92 cathode at 200 °C.

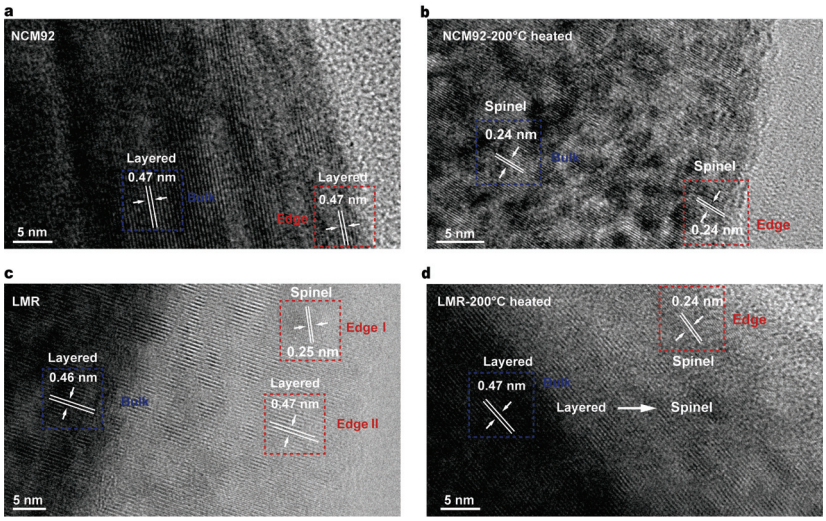

Figure 8. HRTEM images of the fully charged NCM92 cathode before thermal abuse (**a**) and after thermal abuse at 200 °C (**b**); HRTEM images of the fully charged LMR cathode before thermal abuse (**c**) and after thermal abuse at 200 °C (**d**).

In contrast, the fully charged LMR cathode mainly exhibits a layered structure before thermal abuse, with only a small amount of dispersed spinel phase at the material edge—likely representing surface degradation induced by high-voltage cycling (Figure 8c). After 200 °C thermal abuse, a continuous spinel phase forms at the edge of LMR cathode, accompanied by a layered-spinel mixed transition zone, while the bulk phase retains the

layered structure (Figure 8d). Collectively, these results confirm that fully charged LMR cathodes exhibit superior structural thermal stability compared to NCM92 cathodes.

3.6. Exothermic Behavior of Full-Cell Material-Level Reactions

To further analyze the influence of cathode materials on internal exothermic reactions in batteries, DSC was employed for material-level thermal testing of mixed samples (fully charged cathodes with electrolyte) and full-cell samples. DSC results showed that compared to the main exothermic reactions in the NCM92-cathode electrolyte sample, those in the LMR-cathode electrolyte sample occurred at higher temperature with a lower exothermic rate (Figure S1). DSC results for full-cell samples revealed that the full-cell sample with the NCM92 cathode exhibited the first exothermic peak at 190.1 °C with a rate of 0.86 W g^{-1}, whereas the full-cell sample with the LMR cathode showed its first exothermic peak at 207.0 °C, with a lower rate of 0.58 W g^{-1} (Figure 9).

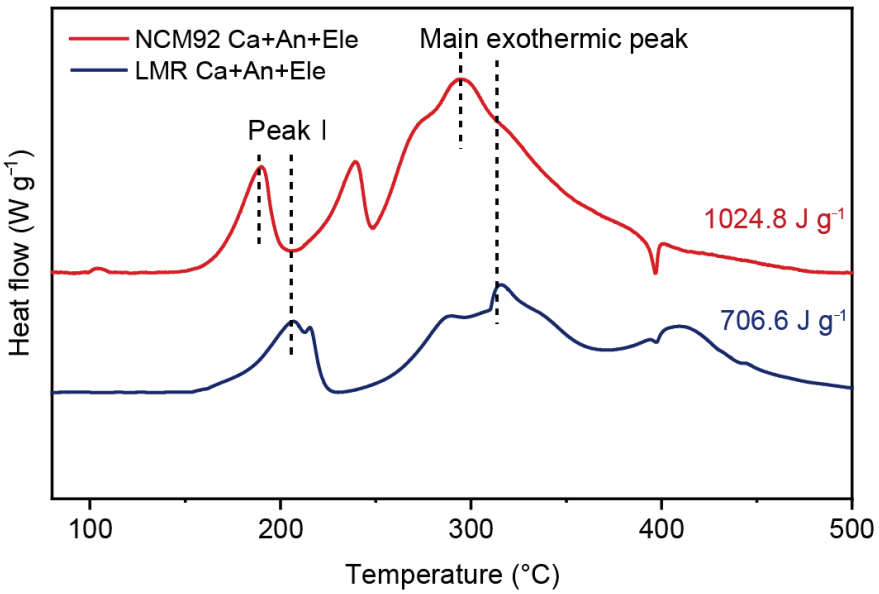

Figure 9. DSC curves of NCM92 and LMR full-cell DSC samples.

Additionally, the main exothermic reaction of the NCM92 full-cell sample occurred at 295.4 °C with a rate of 1.57 W g^{-1}, while the main exothermic peak of the LMR full-cell sample appeared at 316.3 °C with a rate of 0.87 W g^{-1} (Figure 9). Collectively, the temperature shift and attenuated heat flow at both reaction stages demonstrate that despite its higher specific capacity and energy density, the LMR cathode possesses superior thermal stability and lower reactivity than NCM92. This translates to a 31% reduction in total heat generation for the LMR full-cell sample (Figure 9), confirming its role in mitigating internal exothermic reactions.

4. Conclusions

In conclusion, systematic comparative analyses reveal that the application of higher-energy-density lithium-rich manganese-based (LMR) cathodes significantly reduces the thermal runaway risk and hazard of batteries, challenging the conventional notion that high-energy cathodes inevitably compromise battery safety. Material-level thermal analyses demonstrate that fully charged LMR cathodes exhibit superior thermal stability compared to NCM92 cathodes. Additionally, mass spectrometry results confirm that LMR cathodes release negligible O_2 during high-temperature failure, with oxygen primarily evolving as

CO_2. This difference in cathode oxygen release behavior helps mitigate internal exothermic reactions, reducing thermal runaway risks.

Furthermore, in situ heating XRD and HRTEM analyses clarify the high-temperature structural stability of fully charged cathodes: NCM92 cathodes begin transforming from layered to spinel phases at 172 °C, fully converting to spinel by 207 °C; in contrast, LMR cathodes only start forming spinel phases at 197 °C and remain incompletely transformed even at 240 °C. Microstructural observations after 200 °C thermal abuse further confirm that NCM92 cathodes almost fully convert to spinel, while LMR cathodes retain intact layered structures in their bulk phases—confirming superior high-temperature structural stability. This stability shifts the exothermic peaks of the LMR full-cell DSC sample to higher temperatures with lower rates, reducing the total exothermic heat by 31% and significantly enhancing intrinsic battery safety.

This study resolves the trade-off between high-energy cathode application and battery safety, highlights thermal stability and cathode oxygen release behavior as critical metrics for evaluating the safety of new cathodes, and provides guidance for developing high-energy cathodes. These findings enable the practical application of high-energy-density, high-safety batteries.

Supplementary Materials: The following supporting information can be downloaded at https://www.mdpi.com/article/10.3390/batteries11080311/s1, Figure S1: Heat flow curves of the reaction between the fully charged NCM cathode and the electrolyte and the LMR cathode and the electrolyte. Figure S2: NCM92 cathode material: (a) XRD pattern and Rietveld refinement results, (b) cross-sectional SEM image, (c) cross-sectional element distribution. Figure S3: LMR battery: (a) first and second cycle voltage-capacity curves, (b) first and second cycle dQ/dV curves.

Author Contributions: Conceptualization, Z.P. and X.F.; methodology, Y.W.; software, S.F.; validation, Z.P., Y.W. and S.F.; formal analysis, Z.H. and L.W.; investigation, Z.W.; resources, X.F., L.W. and X.H.; data curation, C.X.; writing—original draft preparation, Z.P.; writing—review and editing, L.W. and X.H.; visualization, Z.P. and C.X.; supervision, L.W. and X.H.; project administration, X.F. and Y.W.; funding acquisition, X.F. All authors have read and agreed to the published version of the manuscript.

Funding: This research was funded by the National Key R&D Program-Strategic Scientific and Technological Innovation Cooperation (Grant No. 2022YFE0207900); the National Key R&D Program-Strategic Scientific and Technological Innovation Cooperation (Grant No. 2022YFB2404400); the National Natural Science Foundation of China (Grant No. 51706117, Grant No. 52076121, Grant No. 52406256, Grant No. 22279070, Grant No. U21A20170, Grant No. 52422609 and Grant No. 52406256); and the Independent Research Project of the State Key Laboratory of Intelligent Green Vehicle and Mobility, Tsinghua University (Grant No. ZZ-PY-20250109).

Data Availability Statement: The data that support the findings of this study are available from the corresponding author upon reasonable request.

Acknowledgments: These authors contributed equally: Zhaoqiang Pei, Shaobo Feng. We would like to show gratitude to the Beijing Natural Science Foundation (L242005).

Conflicts of Interest: The authors declare no conflict of interest.

References

1. Tarascon, J.-M.; Armand, M. Issues and Challenges Facing Rechargeable Lithium Batteries. *Nature* **2001**, *414*, 359–367. [CrossRef]
2. Ji, H.; Wu, J.; Cai, Z.; Liu, J.; Kwon, D.-H.; Kim, H.; Urban, A.; Papp, J.K.; Foley, E.; Tian, Y.; et al. Ultrahigh Power and Energy Density in Partially Ordered Lithium-Ion Cathode Materials. *Nat. Energy* **2020**, *5*, 213–221. [CrossRef]
3. Lee, W.; Muhammad, S.; Sergey, C.; Lee, H.; Yoon, J.; Kang, Y.-M.; Yoon, W.-S. Advances in the Cathode Materials for Lithium Rechargeable Batteries. *Angew. Chem. Int. Ed.* **2020**, *59*, 2578–2605. [CrossRef]

4. Li, Q.; Zhou, D.; Chu, M.; Liu, Z.; Yang, L.; Wu, W.; Ning, D.; Li, W.; Liu, X.; Li, J.; et al. A Comprehensive Understanding on the Anionic Redox Chemistry of High-Voltage Cathode Materials for High-Energy-Density Lithium-Ion Batteries. *Chem. Soc. Rev.* **2025**, *54*, 3441–3474. [CrossRef] [PubMed]
5. Luo, D.; Zhu, H.; Xia, Y.; Yin, Z.; Qin, Y.; Li, T.; Zhang, Q.; Gu, L.; Peng, Y.; Zhang, J.; et al. A Li-Rich Layered Oxide Cathode with Negligible Voltage Decay. *Nat. Energy* **2023**, *8*, 1078–1087. [CrossRef]
6. Feng, X.; Ren, D.; He, X.; Ouyang, M. Mitigating Thermal Runaway of Lithium-Ion Batteries. *Joule* **2020**, *4*, 743–770. [CrossRef]
7. Deng, Z.; Liu, Y.; Wang, L.; Fu, N.; Li, Y.; Luo, Y.; Wang, J.; Xiao, X.; Wang, X.; Yang, X.; et al. Challenges of Thermal Stability of High-Energy Layered Oxide Cathode Materials for Lithium-Ion Batteries: A Review. *Mater. Today* **2023**, *69*, 236–261. [CrossRef]
8. Meng, J.; Qu, G.; Huang, Y. Stabilization Strategies for High-Capacity NCM Materials Targeting for Safety and Durability Improvements. *eTransportation* **2023**, *16*, 100233. [CrossRef]
9. Li, J.; Gao, P.; Tong, B.; Cheng, Z.; Cao, M.; Mei, W.; Wang, Q.; Sun, J.; Qin, P. Revealing the Mechanism of Pack Ceiling Failure Induced by Thermal Runaway in NCM Batteries: A Coupled Multiphase Fluid-Structure Interaction Model for Electric Vehicles. *eTransportation* **2024**, *20*, 100335. [CrossRef]
10. He, M.; Chartouni, D.; Landmann, D.; Colombi, S. Safety Aspects of Stationary Battery Energy Storage Systems. *Batteries* **2024**, *10*, 418. [CrossRef]
11. Liu, X.; Ren, D.; Hsu, H.; Feng, X.; Xu, G.-L.; Zhuang, M.; Gao, H.; Lu, L.; Han, X.; Chu, Z.; et al. Thermal Runaway of Lithium-Ion Batteries without Internal Short Circuit. *Joule* **2018**, *2*, 2047–2064. [CrossRef]
12. Wang, Y.; Feng, X.; Huang, W.; He, X.; Wang, L.; Ouyang, M. Challenges and Opportunities to Mitigate the Catastrophic Thermal Runaway of High-Energy Batteries. *Adv. Energy Mater.* **2023**, *13*, 2203841. [CrossRef]
13. Li, Y.; Liu, X.; Wang, L.; Feng, X.; Ren, D.; Wu, Y.; Xu, G.; Lu, L.; Hou, J.; Zhang, W.; et al. Thermal Runaway Mechanism of Lithium-Ion Battery with $LiNi_{0.8}Mn_{0.1}Co_{0.1}O_2$ Cathode Materials. *Nano Energy* **2021**, *85*, 105878. [CrossRef]
14. Shi, C.; Wang, H.; Shen, H.; Wang, J.; Li, C.; Li, Y.; Xu, W.; Li, M. Thermal Runaway Characteristics and Gas Analysis of $LiNi_{0.9}Co_{0.05}Mn_{0.05}O_2$ Batteries. *Batteries* **2024**, *10*, 84. [CrossRef]
15. Cui, Z.; Liu, C.; Wang, F.; Manthiram, A. Navigating Thermal Stability Intricacies of High-Nickel Cathodes for High-Energy Lithium Batteries. *Nat. Energy* **2025**, *10*, 490–501. [CrossRef]
16. Li, K.; Wang, L.; Wang, Y.; Feng, X.; Jiang, F.; Ouyang, M. Correlating Phase Transition with Heat Generation through Calorimetric Data. *eScience* **2024**, *4*, 100226. [CrossRef]
17. Sun, Y.; Ren, D.; Liu, G.; Mu, D.; Wang, L.; Wu, B.; Liu, J.; Wu, N.; He, X. Correlation between Thermal Stabilities of Nickel-Rich Cathode Materials and Battery Thermal Runaway. *Int. J. Energy Res.* **2021**, *45*, 20867–20877. [CrossRef]
18. Liu, T.; Liu, J.; Li, L.; Yu, L.; Diao, J.; Zhou, T.; Li, S.; Dai, A.; Zhao, W.; Xu, S.; et al. Origin of Structural Degradation in Li-Rich Layered Oxide Cathode. *Nature* **2022**, *606*, 305–312. [CrossRef]
19. Jin, Y.; Zhao, Z.; Ren, P.-G.; Zhang, B.; Chen, Z.; Guo, Z.; Ren, F.; Sun, Z.; Liu, S.; Song, P.; et al. Recent Advances in Oxygen Redox Activity of Lithium-Rich Manganese-Based Layered Oxides Cathode Materials: Mechanism, Challenges and Strategies (Adv. Energy Mater. 40/2024). *Adv. Energy Mater.* **2024**, *14*, 2470173. [CrossRef]
20. Zhang, X.; Wang, B.; Zhao, S.; Li, H.; Yu, H. Oxygen Anionic Redox Activated High-Energy Cathodes: Status and Prospects. *eTransportation* **2021**, *8*, 100118. [CrossRef]
21. Hua, W.; Wang, S.; Knapp, M.; Leake, S.J.; Senyshyn, A.; Richter, C.; Yavuz, M.; Binder, J.R.; Grey, C.P.; Ehrenberg, H.; et al. Structural Insights into the Formation and Voltage Degradation of Lithium- and Manganese-Rich Layered Oxides. *Nat. Commun.* **2019**, *10*, 5365. [CrossRef] [PubMed]
22. Shen, C.; Hu, L.; Duan, Q.; Liu, X.; Huang, S.; Jiang, Y.; Li, W.; Zhao, B.; Sun, X.; Zhang, J. Understanding Lattice Oxygen Redox Behavior in Lithium-Rich Manganese-Based Layered Oxides for Lithium-Ion and Lithium-Metal Batteries from Reaction Mechanisms to Regulation Strategies. *Adv. Energy Mater.* **2023**, *13*, 2302957. [CrossRef]
23. Ohneseit, S.; Finster, P.; Floras, C.; Lubenau, N.; Uhlmann, N.; Seifert, H.J.; Ziebert, C. Thermal and Mechanical Safety Assessment of Type 21700 Lithium-Ion Batteries with NMC, NCA and LFP Cathodes–Investigation of Cell Abuse by Means of Accelerating Rate Calorimetry (ARC). *Batteries* **2023**, *9*, 237. [CrossRef]
24. Xia, X.; Dahn, J.R. A Study of the Reactivity of De-Intercalated NaNi0.5Mn0.5O2 with Non-Aqueous Solvent and Electrolyte by Accelerating Rate Calorimetry. *J. Electrochem. Soc.* **2012**, *159*, A1048. [CrossRef]
25. Li, Q.; Li, Y.; Liu, M.; Li, Y.; Zhao, H.; Ren, H.; Zhao, Y.; Zhou, Q.; Feng, X.; Shi, J.; et al. Elucidating Thermal Decomposition Kinetic Mechanism of Charged Layered Oxide Cathode for Sodium-Ion Batteries. *Adv. Mater.* **2025**, *37*, 2415610. [CrossRef] [PubMed]

batteries

MDPI

Article

Multi-Objective Topology Optimization of the Cooling Plate for Battery Thermal Management

Tianshuo Yang [1,2], Huaqiang Liu [1,*], Wenjie Zhang [1], Aoshuang Ding [3] and Mengke Wu [4]

[1] Naval Architecture and Ocean Engineering College, Dalian Maritime University, Dalian 116026, China; yts3440926281@dlmu.edu.cn (T.Y.); zhangwenjie@dlmu.edu.cn (W.Z.)
[2] Houston International Institute, Dalian Maritime University, Dalian 116026, China
[3] CSSC Jiujiang Boiler Co., Ltd., Jiujiang 332000, China
[4] Locomotive Development Department, CRRC Dalian Locomotive and Rolling Stock Co., Ltd., Dalian 116022, China
* Correspondence: huaqiang.liu@dlmu.edu.cn

Abstract: The lifespan and performance of power batteries used in electric vehicles and ships are highly sensitive to the operating temperatures, demonstrating the indispensable role of an effective thermal management system. Topology optimization is a method that can achieve comprehensive optimization of thermal and flow performance. The inlet/outlet layout is an important parameter affecting the thermal management performance of topology-optimized channels. To optimize the inlet/outlet positions, this study establishes the relationship between inlet/outlet positions and evaluation indicators using the response surface method, and further obtains the optimal solution based on the NSGA II and TOPSIS algorithms. The results show that the topology-optimized liquid cooling plate with optimal inlet/outlet position (TOPO) presents a lower maximum temperature under different inlet velocities than the counterparts with the conventional inlet/outlet layout (0.13–0.22 K), straight channel with the optimal inlet/outlet position (0.89–1.03 K), and single inlet/outlet straight channel (1.8–2.6 K). Moreover, the comprehensive performance of the proposed TOPO is more pronounced at high inlet velocity conditions. When the inlet velocity is 0.13 m/s, compared with the other counterparts, the performance evaluation criterion of TOPO increases by 16.6%, 28.7%, and 79.4%, respectively.

Keywords: battery thermal management system; liquid cooling plate; topology optimization; inlet and outlet location; multi-objective optimization

1. Introduction

In recent years, more and more environmental problems have gradually emerged and gained attention [1]. Among them, as the number of traditional gasoline-powered vehicles continues to increase and as they are still being widely used, the problems of greenhouse gas emissions and the energy crisis have become increasingly serious [2]. Against this backdrop, promoting more environmentally friendly electric vehicles is regarded as the core solution [3]. Because of their high stability, low self-discharge rate, and high energy density, lithium-ion batteries are widely used as the power source for electric vehicles [4]. However, the safety and electrochemical performance of lithium-ion batteries are extremely sensitive to their operating temperature [5]. Studies have shown that the suitable operating temperature range for lithium-ion batteries is 15–35 °C, and the maximum temperature difference inside the battery cannot exceed 5 °C [6]. During operation, the internal resistance

and chemical reactions of the battery will continuously generate heat, which makes it impossible to control the temperature within the suitable range. This will damage the battery's lifespan and capacity. In severe cases, it may even lead to thermal runaway, resulting in fires, explosions, and other disasters [7]. Therefore, it is necessary to take appropriate intervention measures to prevent these dangers.

According to the cooling medium, battery thermal management systems (BTMSs) can be roughly classified into air cooling, liquid cooling, phase change material (PCM) cooling, and hybrid cooling [8]. The air-cooled BTMS achieves cooling by transferring the battery's heat to the air, and it has advantages such as low cost, simple structure, and no risk of leakage [9]. However, its poor heat transfer efficiency cannot meet the cooling requirements of batteries under high-rate discharge [10]. The BTMS based on PCM utilizes solid–liquid phase change to absorb heat and is considered a promising approach. However, the thermal conductivity of commonly used phase change materials is relatively low, and their cooling capacity is very limited after multiple charge–discharge cycles [11]. Meanwhile, due to the limitation of its phase change temperature range, it is difficult to be widely implemented in practical applications [12]. Liquid BTMS has been widely used by the electric vehicle market due to its high heat transfer coefficient and moderate manufacturing and maintenance costs [13]. In addition, the feasibility of hybrid BTMS designs, which could combine the advantages of different cooling methods [14,15], has been actively explored in recent years, such as liquid–PCM coupled BTMSs and liquid–heat pipe coupled BTMSs [16]. However, hybrid BTMSs are still under development and their feasibility remains to be proven [17]. Therefore, the BTMSs based on liquid coolants are still the prevalent option for practical application, especially in electric vehicles and ships.

The key to the performance of the liquid battery thermal management system lies in the channel structure of the liquid cooling plate [18]. In recent years, researchers have made many attempts to perfect the design of the channel structure of the liquid cooling plate. The most common channel structures are straight channels and serpentine channels. Many researchers have explored this. Liu et al. [19] introduced cross channels into the traditional serpentine channels and found that the V-shaped cross channels had the optimal structural parameters, achieving the best thermal performance: the number of crossings was seven, the width was 2.0 mm, and the angle was 45°. In addition, researchers were inspired by biological structures and proposed various biomimetic channel flow structure designs. Fan et al. [20], inspired by biomimetics, proposed a novel double-layer tree-shaped channel, and found that compared with the serpentine flow channel, its maximum temperature and standard deviation of surface temperature were reduced by 1.79% and 69.25%, respectively, and the pressure drop was reduced by 79.13%. Moreover, based on the traditional channel structure and biomimetic channel structure, researchers used optimization algorithms to optimize key parameters to improve performance. Xia et al. [21], based on the leaf vein biomimetic flow channel, used the NSGA-II algorithm to optimize four structural parameters: the distance from the outlet to the hexagon, the distance from the inlet to the hexagon, the spacing between adjacent hexagons, and the size of the hexagon. The results showed that the optimized liquid cooling plate had a pressure drop reduced by 14.2%, and a maximum temperature reduced by 0.7 °C. However, the structures of these liquid cooling plates are all proposed based on the researchers' experience. The optimization of structural parameters is also based on the fixed structures already proposed. This leads to very limited performance improvement brought on by the optimization.

The topology optimization method transforms the problem of optimizing the battery thermal management performance into a mathematical problem based on the actual geometric model and application scenarios. This approach significantly enhances the inno-

vation and design freedom of the liquid cooling plate structure design, and frees the design from the limitations of researchers' experience and ideas. In addition, multi-objective topology optimization enables the liquid cooling plate structure to achieve a balance between thermal performance and flow performance. With the development of additive manufacturing technology, the cost of manufacturing complex geometric components such as topology-optimized liquid cooling plates has been significantly reduced [22]. Therefore, the application of the topology optimization method to design liquid cooling plate structures is becoming increasingly widespread. Zhan et al. [23] explored the effects of inlet and outlet arrangement direction, quantity, channel depth, and total inlet mass flow rate on the performance of the liquid cooling plate. The results indicated that when adopting three inlets and three outlets in the width direction, with a channel depth of 3 mm and an inlet total mass flow rate of 15 g/s, the system heat dissipation and power consumption could achieve the best balance. Wang et al. [24] obtained two liquid cooling plate structures based on laminar and turbulent topology optimization. The results showed that the liquid cooling plate obtained through topology optimization under turbulent conditions achieved the best overall cooling effect. Zhan et al. [25] discussed the inlet and outlet positions of a single inlet and single outlet, and found that the parallel diagonal structure could minimize the pressure drop to the greatest extent, while the straight-in and straight-out structure performed best in terms of the highest temperature and temperature deviation. Lin et al. [26] established the relationship between Reynolds number, target function weight coefficients, and cooling performance through the response surface method (RSM), and further obtained the optimal design parameters using the NSGA-II algorithm.

Based on the above literature review, Zhan et al. [23] pointed out that the liquid cooling plate with three inlets and three outlets in the width direction has superior performance. However, at present, there is a lack of research on the optimal inlet and outlet locations for this situation. Wu et al. [27] adopted the layout where the two side inlets and outlets were placed at the outermost edges for the three-inlet and three-outlet configuration. Zhan et al. [25] discussed and analyzed representative examples of inlet and outlet positions with a single inlet and a single outlet. The results showed that there was a representative example for each in terms of thermal performance and flow performance. This method of listing and analyzing some of the inlet and outlet positions was not comprehensive and had difficulties identifying the optimal inlet and outlet positions that achieved the best overall thermal and flow performance. Lin et al. [26] established the relationship between design variables and the target function using the response surface method, providing a new approach. Based on the research gaps and current research status, the main work of this paper is as follows: 1. Based on the layout of three inlets and three outlets in the width direction, establish the relationship between the inlet/outlet position parameters and the key evaluation indicators of BTMS. 2. Use the NSGA-II algorithm to obtain the Pareto front and use TOPSIS to obtain the optimal solution for the inlet/outlet position parameters. 3. Conduct a comprehensive performance comparison between the topology-optimized liquid cooling plate with the optimal inlet/outlet positions, the topology-optimized liquid cooling plate with conventional inlet/outlet positions, and the straight channel. Furthermore, investigate the influence of inlet flow velocity on the observed performance differences.

2. Two-Dimensional Topology Optimization Design

Figure 1 presents the topology optimization concept design model of conjugate heat transfer applied to the thermal management system of liquid batteries. The design region is regarded as a porous medium, and the solid area and fluid area are distinguished by

introducing design variables γ. The design variables vary continuously from 0 to 1, where $\gamma = 1$ corresponds to the fluid region, and $\gamma = 0$ corresponds to the solid region.

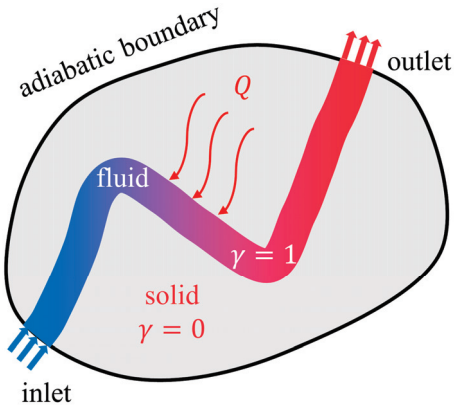

Figure 1. The conceptual model of topology optimization design.

2.1. Mathematical Model of Topology Optimization

2.1.1. Flow Equations

Assume that the fluid is incompressible, and the flow state within the channel is laminar, with the Reynolds number being less than 2300. Therefore, the continuity equation and the momentum equation can be expressed as follows:

$$\nabla \cdot u = 0 \tag{1}$$

$$\rho(u \cdot \nabla)u = -\nabla P + \mu \nabla^2 u + F \tag{2}$$

where ρ represents the density of the fluid, u represents the velocity of the fluid, P represents the pressure, μ represents the viscosity, and F represents the flow resistance. Under the assumption of porous media [28], the size of F is proportional to the speed of the fluid flow, which can be expressed as follows:

$$F = -\alpha u \tag{3}$$

where α represents the inverse permeability of the porous medium.

The inverse permeability is interpolated based on the design variables γ using the Darcy interpolation function, which is expressed as follows:

$$\alpha(\gamma) = \alpha_s + (\alpha_s - \alpha_f)\frac{q(1-\gamma)}{q+\gamma} \tag{4}$$

where q is the penalty factor, with a value of 0.01 in this paper. α_f is the inverse permeability of the fluid, which should be a very small value ($\approx$0). α_s is the inverse permeability of the solid, which is a function of the Reynolds number Re and the Darcy number Da, expressed as follows:

$$\alpha_s = \left(1 + \frac{1}{Re}\right)\frac{1}{Da} \tag{5}$$

2.1.2. Heat Transfer Equations

Assume that the heat transfer process is stable and the physical properties of each material do not change with temperature. During the heat transfer process, the heat transfer

modes in the fluid domain and the solid domain are different. The corresponding equations are as follows:

$$\rho C_{\mathrm{p}}(u \cdot \nabla)T = k_{\mathrm{f}}\nabla^2 T \text{ (in fluid)} \tag{6}$$

$$0 = k_{\mathrm{s}}\nabla^2 T + Q \text{ (in solid)} \tag{7}$$

where C_{p} is the specific heat capacity of the fluid, k_{f} is the thermal conductivity of the fluid, k_{s} is the thermal conductivity of the solid, and Q is the heat generation in the solid region.

By combining Equations (6) and (7) and introducing design variables γ, the following equation is obtained:

$$\gamma\rho C_{\mathrm{p}}(u \cdot \nabla)T = \Big[(1-\gamma)k_{\mathrm{s}} + \gamma k_{\mathrm{f}}\Big]\nabla^2 T + (1-\gamma)Q \tag{8}$$

where the heat source Q is proportional to the temperature difference, which can be expressed as follows:

$$Q = h(T_{\mathrm{Q}} - T) \tag{9}$$

where T_{Q} represents the reference temperature of the ideal heat source.

2.1.3. Dimensionless Processes

In order to save computing resources and improve the convergence of the calculation, the governing equations are subjected to dimensionless processing. The dimensionless gradient operator ∇^*, the dimensionless velocity u^*, the dimensionless pressure p^*, the dimensionless temperature T^*, the dimensionless heat generation coefficient h^*, the fluid's constant-pressure specific heat capacity C_{p}, and the Reynolds number Re are defined as follows:

$$\begin{aligned} &\nabla^* = L\nabla, u^* = \frac{u}{U}, p^* = \frac{p - p_0}{\rho U^2}, Re = \frac{\rho U L}{\mu} \\ &T^* = \frac{T - T_{\mathrm{in}}}{T_{\mathrm{r}} - T_{\mathrm{in}}}, h^* = \frac{hL^2}{k_{\mathrm{f}}}, C_p = Re \cdot Pr \end{aligned} \tag{10}$$

where L represents the characteristic length, U is the characteristic velocity, p_0 is the reference pressure, T_{in} is the inlet temperature, h^* is the dimensionless heat generation coefficient, Pr is the Prandtl number, and T_{r} is the reference temperature. The value of temperature T_{r} referred to in this article is the equivalent temperature T_{Q} of an ideal heat source. After performing dimensionless processing on the expressions Equations (1), (2), and (8), the following expressions can be obtained:

$$\nabla^* \cdot u^* = 0 \tag{11}$$

$$\rho(u^* \cdot \nabla^*)u^* = -\nabla^* p^* + \frac{1}{Re}\nabla^{*2}u^* - \left(1 + \frac{1}{Re}\right)\frac{1}{Da}\frac{q(1-\gamma)}{q+\gamma}u^* \tag{12}$$

$$\gamma RePr(u^* \cdot \nabla^*)T^* = [(1-\gamma)K + \gamma]\nabla^* T^* + (1-\gamma)h^*(1 - T^*) \tag{13}$$

2.2. Density Filter and Projection

The optimization results are prone to be affected by the grid-related factors, and usually exhibit a checkerboard pattern, thereby reducing the stability and reliability of the

optimization process. To address this issue, in the entire optimization process of this study, the Helmholtz density filter [29] was employed:

$$-{r_f}^2\nabla^2\gamma_n + \gamma_n = \gamma \tag{14}$$

where r_f is the filter radius and γ_n is the new design variable obtained after filtering.

The Helmholtz density filtering method often causes the boundaries between fluids and solids to become blurred, making it difficult to clearly define the boundaries for practical applications. In order to further reduce the gray area and make the fluid–solid boundary clearer, the hyperbolic tangent projection [30] is used throughout the entire topology optimization process:

$$\gamma_p = \frac{\tanh(\beta(\gamma_n - \gamma_\beta)) + \tanh(\beta\gamma_\beta)}{\tanh(\beta(1 - \gamma_\beta)) + \tanh(\beta\gamma_\beta)} \tag{15}$$

where β represents the projection slope, γ_β represents the projection point, and γ_p represents the new design variable after the hyperbolic tangent projection.

2.3. Optimization Objective Functions

This article optimizes the comprehensive performance of the liquid cooling plate from both thermal and flow performance perspectives. In terms of thermal performance, the focus was on minimizing the average temperature of the battery during high-rate discharge as well as achieving temperature uniformity. These two aspects are represented by minimizing the dimensionless average temperature (Objective 1) and minimizing the dimensionless temperature gradient (Objective 2), respectively. In addition, minimizing the pressure drop between the inlet and outlet (Objective 3) is attempted to achieve better flow performance. The three objective functions are, respectively, expressed as follows:

$$\begin{gathered} \phi_1 = \frac{\int T^* d\tau_q}{\int d\tau_q},\ \phi_2 = \frac{\int GradT^* d\tau_q}{\int d\tau_q},\ \phi_3 = p^*_{in} - p^*_{out} \\ GradT^* = \sqrt{(GradT^*_x)^2 + (GradT^*_y)^2},\ p^*_{in} = \frac{\int p^* d\Gamma_{in}}{\int d\Gamma_{in}}, p^*_{out} = \frac{\int p^* d\Gamma_{out}}{\int d\Gamma_{out}} \end{gathered} \tag{16}$$

Due to the significant differences in the value ranges of the three objective functions, a normalization coefficient is used to normalize each of the three objective functions separately:

$$\phi_1^N = \frac{\phi_1}{\phi_1^0},\ \phi_2^N = \frac{\phi_2}{\phi_2^0},\ \phi_3^N = \frac{\phi_3}{\phi_3^0} \tag{17}$$

where ϕ_1^0, ϕ_2^0, and ϕ_3^0 are the normalization coefficients of the three objective functions.

The weighting coefficients are used to combine the three objective functions into a total objective function:

$$\phi = w_1 \cdot \phi_1^N + w_2 \cdot \phi_2^N + (1 - w_1 - w_2) \cdot \phi_3^N \tag{18}$$

According to the research by Zhong et al. [12], the weights are set as $w_1 = 0.7, w_2 = 0.1$.

In order to obtain meaningful results, a limitation on the fluid volume fraction is imposed on the design domain:

$$\int_\Omega \gamma d\Omega \leqslant V_f \cdot V_\Omega \tag{19}$$

where V_Ω represents the volume of the design domain and V_f represents the maximum allowable volume fraction of the fluid domain.

After such processing, based on the actual application scenarios of battery thermal management and the desired performance improvements, this article transforms the optimization problem of this structure into a mathematical problem as follows:

$$\begin{cases} Find\ \gamma = (\gamma_1, \gamma_2, \ldots, \gamma_i), \gamma_i \in [0,1] \\ \text{Min}\ \phi = w_1 \cdot \phi_1^N + w_2 \cdot \phi_2^N + (1 - w_1 - w_2) \cdot \phi_3^N \\ \text{Subject to Eqs. (11)–(15)} \\ \int_\Omega \gamma d\Omega \leqslant V_f \cdot V_\Omega \end{cases} \tag{20}$$

2.4. Geometric Model and Boundary Conditions

The design area and corresponding boundary conditions for two-dimensional topology optimization are shown in Figure 2. Based on the actual dimensions of the rectangular lithium-ion battery (173 mm × 85 mm), the design domain for the two-dimensional topology optimization is regarded as 17 L × 8 L. The performance advantages brought about by the three inlets have been confirmed in previous studies. This article adopts a three-inlet and three-outlet layout for the inlets and outlets, and places particular emphasis on the discussion of the positions of the inlets and outlets.

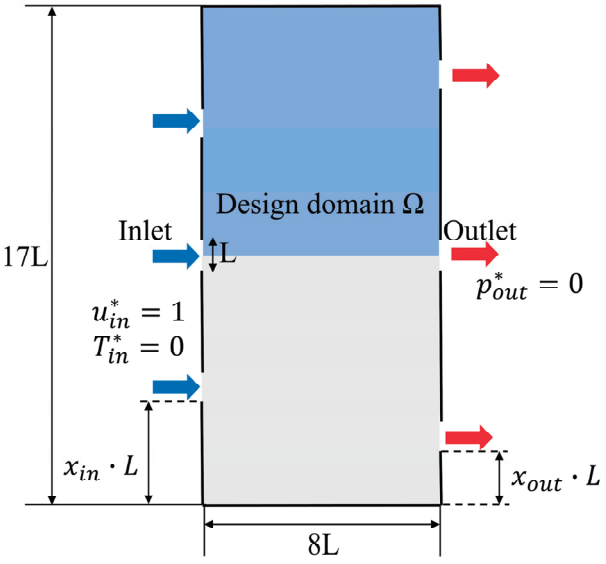

Figure 2. Two-dimensional geometric model and boundary conditions for topology optimization.

In order to save computing resources and improve efficiency, this paper only conducts the topology optimization design iteration process for half of the design domain based on the symmetry of the liquid cooling plate and its inlet and outlet arrangements. Based on previous studies [31], comparing the performance of different liquid cooling plates and ensuring that the inlet volumetric flow rate of the liquid is the same is fair. Therefore, for the inlet boundary conditions, this paper sets a constant inlet velocity and inlet temperature. For the outlet boundary conditions, this paper adopts a constant pressure boundary condition, which is consistent with the actual situation. Since this paper only considers the cooling performance of the liquid battery thermal management system, the natural convective heat transfer at the boundaries can be ignored. For the walls other than the inlet and outlet, an insulated boundary condition is set. The important parameters of the topology optimization design problem are shown in Table 1.

Table 1. Values of important parameters in the topology optimization design process.

Parameters	Values
Design domain size	17 L × 8 L
Reynolds number Re	150
Darcy number Da	10^{-4}
Prandtl number Pr	6.78
The ration of solid and fluid thermal conductivity K	1
Penalty parameter q	0.01
Dimensionless heat transfer coefficient h^*	100
Projection slope β	8
Projection point γ_p	0.5
Fluid volume fraction V_f	0.5

2.5. Topology Optimization Solving Procedure

This topology optimization design problem is solved using the multi-physics coupling software COMSOL Multiphysics 6.1. The sequential quadratic programming optimization algorithm (SNOPT) is employed to update the design variables, aiming to achieve an efficient and precise optimization process. Subsequently, the control equations are solved using the finite element method, and sensitivity analysis is conducted based on the adjoint method. If the difference between the two adjacent optimization results is less than 10^{-6}, the optimization iteration process is stopped and the results are output; otherwise, the same process is repeated.

In order to save computing time while maintaining the accuracy of the calculation, three objective functions were selected as indicators to conduct the grid independence test. Seven grid systems with the number of grids being 3132, 6800, 17,408, 24,939, 33,820, 42,600, and 48,792 were selected for evaluation. As shown in Figure 3, when the grid number is 33,820, the relative errors of the three objective functions are all less than 0.5%. Therefore, for the subsequent topology optimization, the grid density corresponding to the number of grids of 33,820 is selected.

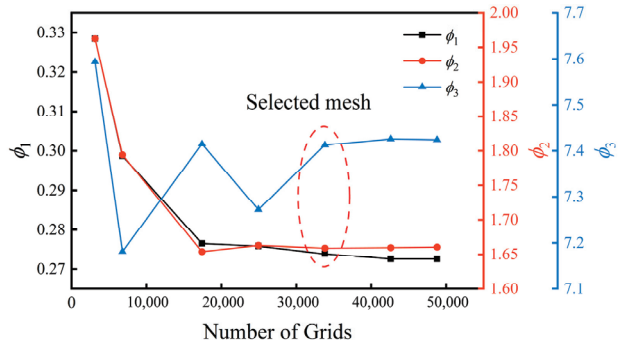

Figure 3. Grid independence test in the two-dimensional topology optimization process.

3. Three-Dimensional Numerical Simulation Model

3.1. Model Description

A single battery is unable to meet the actual working requirements of an electric vehicle, so multiple batteries are often combined to form a battery pack. As shown in Figure 4a, the battery and the liquid cooling plate are alternately combined to form a battery pack. Aluminum plates of 1 mm thickness are used on both the top and bottom of the flow channel to separate the coolant from the battery. Based on the actual size of the battery (173 mm × 85 mm), cold plates are expanded in the length and width directions

accordingly to prevent coolant leakage. The battery pack is symmetrical in the height direction. To save computing resources, the battery and half of the liquid cooling plates on both sides of it are selected as the simplified research objects, as shown in Figure 4b. The relevant size data are presented in Table 2.

Table 2. Physical dimensions of the battery thermal management system.

Parameter	Value (mm)	Parameter	Value (mm)
L	173	H_2	5
W	85	H_3	2.5
E_1	28	H_4	1.5
E_2	15	H_5	1
E_3	7	b_1	2.5
H_1	21	b_2	1.5

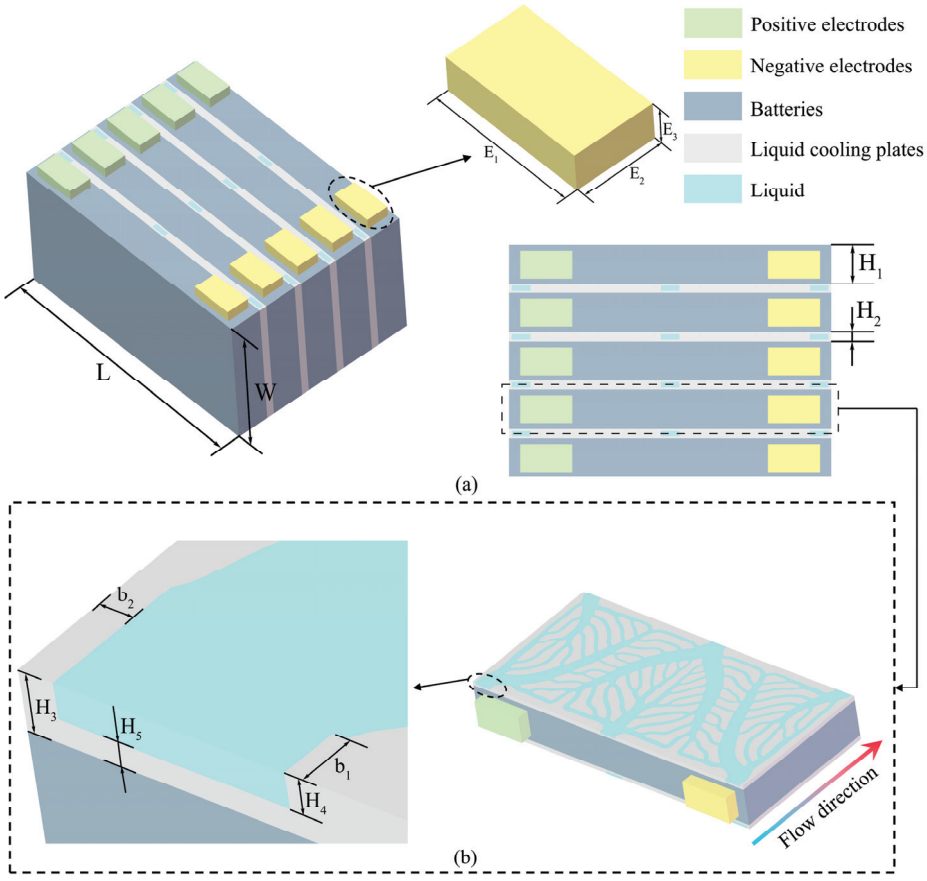

Figure 4. (**a**) Battery pack geometric model and dimensions. (**b**) Simplified model and dimensions.

3.2. Governing Equations for 3D Simulations

During the process of three-dimensional numerical simulation, some assumptions need to be made: the coolant is continuous and incompressible, and the physical parameters of lithium-ion batteries, coolant, and aluminum liquid cooling plates do not change with temperature. The continuity, momentum, and energy equations for the coolant are as follows:

$$\nabla \cdot u_f = 0 \tag{21}$$

$$\rho_f\left(\frac{\partial u_f}{\partial t} + u_f \cdot \nabla u_f\right) = -\nabla P_f + \mu_f \nabla^2 u_f \tag{22}$$

$$\rho_f C_{p,f}\left(\frac{\partial T_f}{\partial t} + u_f \cdot \nabla T_f\right) = \nabla \cdot (k_f \nabla T_f) \tag{23}$$

where u_f, P_f, and T_f, respectively, represent the speed, pressure, and temperature of the coolant. ρ_f, μ_f, $C_{p,f}$, and k_f, respectively, represent the density, viscosity, specific heat capacity, and thermal conductivity of the coolant. The energy equation of lithium-ion batteries is as follows:

$$\rho_b C_{p,b} \frac{\partial T_b}{\partial t} = \nabla \cdot (k_b \nabla T_b) + Q_b \tag{24}$$

where ρ_b, $C_{p,b}$, T_b, and k_b, respectively, represent the density, specific heat capacity, temperature, and thermal conductivity of the battery. According to the heat generation model established by Bernardi [32], the heat Q_b generated by the battery is as follows:

$$Q_b = -IT_b \frac{dE_{oc}}{dT_b} + I(E_{oc} - E) \tag{25}$$

where I, dE_{oc}/dT_b, E_{oc}, and E, respectively, represent the working current of the battery, the entropy coefficient related to density, charging status and temperature, the open-circuit voltage of the battery, and the working voltage of the battery. This study uses a second-order RC equivalent circuit model to establish the relationship of voltage changes during the battery discharge process. The relevant parameters in this model are obtained by fitting during the battery discharge experiment. After obtaining the relationship of voltage changes during the discharge process, it is substituted into the formula of the heat generation model to obtain the heat generation. The values of the physical parameters of the battery were measured through experiments. The values of the physical parameters of each material in the battery thermal management system are shown in Table 3.

Table 3. Physical parameters of the battery thermal management system.

Material	ρ ($\mathbf{kg \cdot m^{-3}}$)	C_p ($\mathbf{J \cdot kg^{-1} \cdot K^{-1}}$)	k ($\mathbf{W \cdot m^{-1} \cdot K^{-1}}$)	μ ($\mathbf{Pa \cdot s}$)
Solid/aluminum	2719	871	202.4	
Fluid/water	998.2	4182	0.6	0.001003
Positive tab	2719	871	202.4	
Negative tab	8978	381	387.6	
Battery	1986.2	853.6	19.61 (x), 19.61 (y), 7.78 (z)	

3.3. Boundary Conditions for Three-Dimensional Numerical Simulation

Set the constant inlet flow rate and inlet temperature boundary conditions as follows:

$$u = u_{in}, T = T_{in} \tag{26}$$

Set the constant pressure outlet boundary condition as follows:

$$P = P_{out} \tag{27}$$

Considering the natural convective heat transfer between the outer surface of the liquid battery thermal management system and the external environment,

$$Q_e = h_{ext} \cdot A_{out}(T_{bout} - T_{ext}) \tag{28}$$

The simplified model is derived based on the symmetry of the battery pack. Therefore, symmetric boundary conditions need to be applied to the upper surface of the upper half

of the liquid cooling plate and the lower surface of the lower half of the liquid cooling plate. Apply the no-slip condition at all the contact surfaces between fluids and solids. The capacity of this individual lithium-ion battery is 22.25 Ah. To investigate the battery's heat dissipation under high-rate discharge conditions, a discharge rate of 5C was adopted. This numerical simulation process was carried out in Ansys Fluent. Convergence requires that the residual of the continuity equation be less than 10^{-4}, the residual of the momentum equation be less than 10^{-6}, and the residual of the energy equation be lower than 10^{-6}. The specific values related to the boundary conditions are shown in Table 4.

Table 4. Specific parameters of boundary conditions.

Parameters	Values	Unit
Inlet temperature T_{in}	298.15	K
Natural convective heat transfer coefficient with respect to the external environment h_{ext}	5	$W \cdot m^{-2} \cdot K^{-1}$
External temperature T_{ext}	298.15	K
Outlet pressure P_{out}	0	atm
Inlet velocity u_{in}	0.03	$m \cdot s^{-1}$

3.4. Parameter Definitions

During the operation of the battery, the maximum temperature T_{max} and the average temperature T_{avg} of the battery can serve as indicators to reflect the cooling performance of the thermal management system of the liquid battery. The average temperature of the battery is defined as follows:

$$T_{avg} = \frac{\int_{V_b} T dV_b}{\int_{V_b} dV_b} \tag{29}$$

In addition, the ability of the liquid cooling plate to balance the temperature uniformity of the battery can be reflected by the standard deviation of the battery temperature T_σ:

$$T_\sigma = \sqrt{\frac{\int_{V_b} (T - T_{avg})^2 dV_b}{\int_{V_b} dV_b}} \tag{30}$$

The total heat removed by the coolant can be defined as follows:

$$Q_f = m_f C_{p,f} (T_{f,out} - T_{f,in}) \tag{31}$$

where m_f, $C_{p,f}$, $T_{f,out,}$ and $T_{f,in}$ are, respectively, defined as the inlet mass flow rate of the coolant, the specific heat capacity of the coolant, the average temperature of the coolant at the outlet, and the average temperature of the coolant at the inlet. The average heat transfer coefficient of a fluid h_{avg} is defined as follows:

$$h_{avg} = \frac{Q_f}{A_{sur} \Delta T_{s,f}} \tag{32}$$

$$\Delta T_{s,f} = T_{sur,avg} - T_{f,avg} \tag{33}$$

$$T_{f,avg} = \frac{T_{f,in} + T_{f,out}}{2} \tag{34}$$

where A_{sur}, $T_{sur,avg}$, and $T_{f,avg}$, respectively, represent the contact area between the coolant and the liquid cooling plate, the average temperature of the contact surface between the

coolant and the liquid cooling plate, and the average temperature of the coolant at the inlet and outlet.

The average Nusselt number Nu is defined as follows:

$$Nu = \frac{h_{avg} \cdot D_h}{k_f} \tag{35}$$

where D_h represents the hydraulic diameter, which can be defined as follows:

$$D_h = \frac{2 \cdot w \cdot h}{w + h} \tag{36}$$

where h and w represent the height and width of the channel.

The pumping power P_w is an important indicator reflecting the flow performance of the liquid cooling plate structure. Its definition is as follows:

$$P_w = \Delta P_{avg} \cdot A_{in} \cdot u_{in} \tag{37}$$

where ΔP_{avg}, A_{in}, and u_{in} represent the pressure drop from the outlet to the inlet, the inlet area, and the inlet flow velocity, respectively.

3.5. Verification of Grid Independence

Nusselt number and pressure drop were selected as the reference indicators for the grid independence test. The results of six grid numbers were compared: 1,679,121, 1,980,731, 2,197,103, 2,472,807, 2,725,435, and 3,125,763. When x_{in} = 0 and x_{out} = 0, the numerical simulation was conducted using the boundary conditions described in Table 4, and the results are shown in Figure 5a. For grid systems with a higher density than the one with 2,472,807 elements, the deviation of the two indicators remained below 0.2%. In order to strike a balance between calculation time and calculation accuracy, the grid system with a total of 2,472,807 elements was finally selected for the subsequent three-dimensional numerical simulation, the mesh details of which are also shown in Figure 5a. It can be seen that the grid density is higher at the solid-liquid interface, which is conducive to achieving a balance between accuracy and computation time.

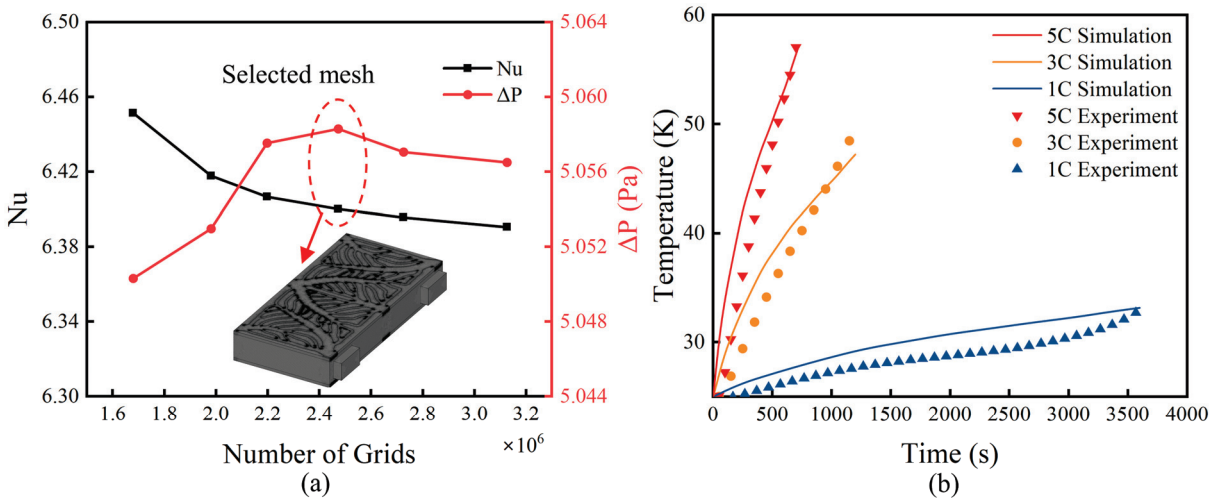

Figure 5. (**a**) Grid independence test for three-dimensional numerical simulation and (**b**) comparison with experimental data.

This paper conducted battery temperature rise tests under different discharge rates (1C, 3C, 5C) at an environmental temperature of 298.15 K. In the experiment, some thermocouples were used to measure the average temperature on the surface of the battery. These measurements were compared with the numerical simulation data under the corresponding conditions. The relevant data is shown in Figure 5b. It is obvious that the temperature changes obtained from numerical simulations and experiments under different discharge rates show good consistency. This further demonstrates the reliability and validity of the numerical simulation data.

4. Results and Discussion

Based on the situation of three inlets and outlets, this study focused on exploring the influence of the positions of the inlets and outlets on the performance of the liquid cooling plate. The values of variables x_{in} and x_{out} range from 0 to 7. In this study, the considered range is from 0 to 6. According to actual requirements, the highest temperature at the final discharge moment, the standard deviation of temperature, and the pressure drop are selected as evaluation indicators.

4.1. Single Factor Analysis

Set $x_{\text{out}} = 0$, and change the values of x_{in} from 0 to 6 with an interval of 1. The results of the two-dimensional topology optimization conducted at each inlet and outlet position are shown in Figure 6. As the value of x_{in} increases, the inlets on both sides move towards the center, and the main passage directly connecting the two inlets also shifts towards the center. At the same time, the main passageways that are directly connected to the two sides' outlets have become more prominent, and they gradually extend to both sides. This is due to the need to maintain the uniformity of the overall temperature and the heat exchange performance.

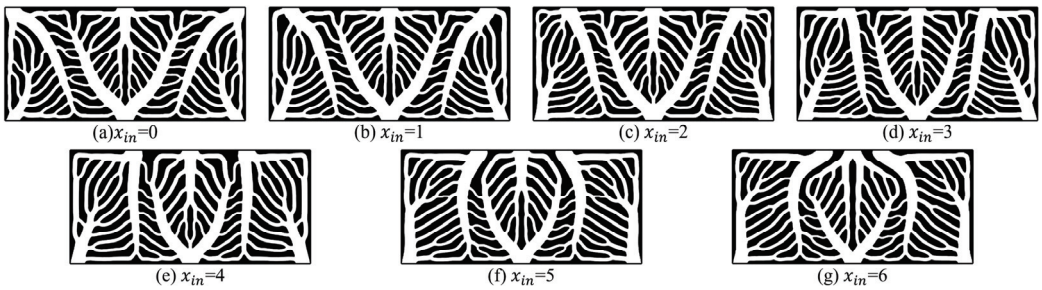

Figure 6. Two-dimensional topology optimization results for different inlet positions.

The three evaluation indicators obtained after conducting three-dimensional numerical simulations on the topology optimization results at different inlet positions are shown in Figure 7. It can be seen that all three indicators have become better within the range of x_{in} from 0 to 2. The maximum temperature shows a fluctuating trend as it increases from 2 to 6. The standard deviation of temperature has been increasing continuously as the value of x_{in} ranges from 2 to 6, and the situation has become even worse. The pressure drop decreases first and then increases as x_{in} rises from 2 to 6. The hot spot of the battery is prone to appear in the central area and the edge areas on both sides. As x_{in} increases from 0 to 6, the main channels at both sides of the inlet gradually change from inward to outward. What this process brings about is a certain change in the concentrated flow area. When $x_{\text{in}} = 2$, the main channels at both sides of the inlet slightly tilt inward. This allows the flow passing through the middle side of the outlet to increase appropriately while the flow to both sides is not too little, thereby better suppressing the generation of the hot spot, and

T_{max} reaches the lowest point. When x_{in} is further increased, the main channels at both sides of the inlet deviate outward, so the flow allocated to the middle area of the outlet is insufficient, and T_{max} increases. The change in T_σ is more directly related to the uniform distribution of the flow. When x_{in} = 2, that is, when the two inlets are, respectively, located in the middle of the outlet and the adjacent side outlet but appropriately deviated to both sides, T_σ reaches the lowest value. The size of ΔP is related to the bias of the main channel directly connected to the inlet and the length of the flow path. When x_{in} = 2–4, the flow paths of the coolant are not too long, so they are at a relatively low level. Since the coolant flows vertically into the flow channel and when the main channels directly connected to both inlet sides are parallel to the coolant's inlet flow direction (x_{in} = 4), the impact flow dissipation between the coolant and the solid structure constituting the main channel is the least. Therefore, in this case, the pressure drop is the lowest.

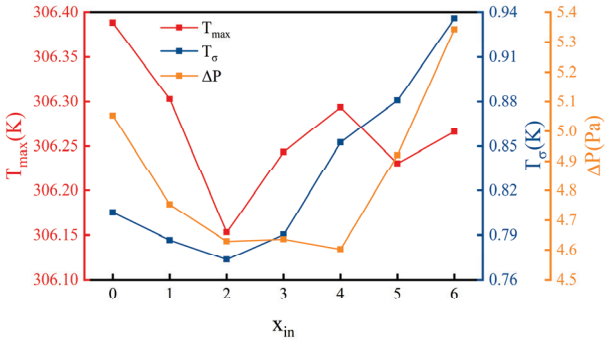

Figure 7. Evaluation indicators under different inlet positions.

Set x_{in} = 0. Then change the value of x_{out} from 0 to 6, with an interval of 1. The results of the two-dimensional topology optimization at each inlet and outlet position are shown in Figure 8. As x_{out} increases, the outlets on both sides move towards the center, and the main channel directly connected by the outlets on both sides also moves towards the center. At the same time, the main channel directly connected by the outlets on both sides becomes wider, and the main channel directly connected by the middle outlet gradually disappears.

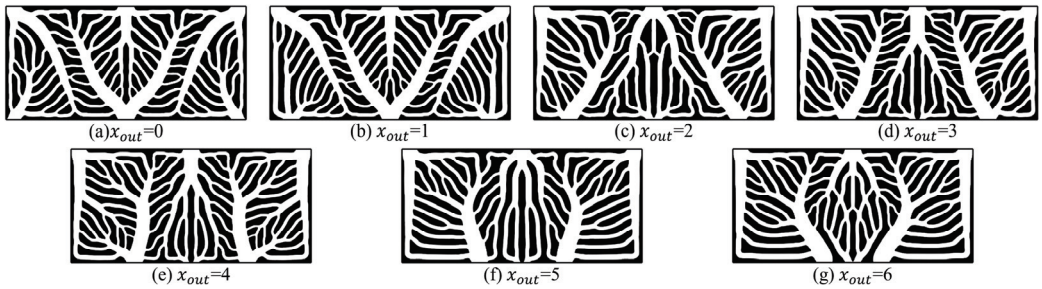

Figure 8. Two-dimensional topology optimization results for different outlet positions.

The three evaluation indicators obtained after conducting three-dimensional numerical simulations on the topology optimization results at different outlet positions are shown in Figure 9. It is obvious that the trends of the maximum temperature and the standard deviation of temperature are basically the same, both increasing first, then decreasing, and then increasing again. The reason for the increase in these two indicators first is that the outlet position moves inward, and the coolant entering from both sides flows out from the two outlet sides rapidly. This leads to an inappropriate distribution of flow and a weak effect in suppressing the high-temperature point in the middle of the outlet

side. The reason for the subsequent increase and decrease in these two indicators can also be explained by the rationality of the flow distribution. When the outlet positions are located at the middle of the inlets on both sides and slightly closer to the middle (x_{out} = 4), the flow distribution is conducive to the uniformity of the battery temperature and the reasonable suppression of the high-temperature point. The pressure drop shows a trend of first decreasing and then increasing, reaching its lowest value when x_{out} equals 2. This is related to the previously mentioned flow path length. Since the inlets on both sides are located at the edge, a reasonable outlet position on both sides is beneficial to reducing the flow dissipation during the flow process. In addition, the maximum temperature or the standard deviation of temperature is inversely related to the pressure drop. When x_{out} equals 2, the pressure drop reaches its optimal value, while the maximum temperature and the standard deviation of temperature reach their worst values.

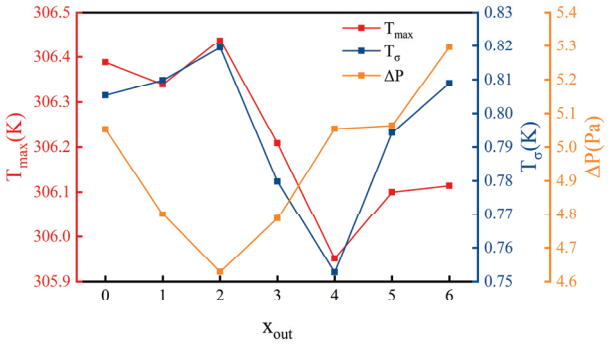

Figure 9. Evaluation indicators under different outlet positions.

4.2. Multi-Objective Optimization of Inlet and Outlet Locations

The single-factor analysis based on the control variable method in the previous section can to some extent reflect the relationship between the design factors and the objectives. However, based on the above analysis, it can be found that there are conflicts and complex relationships among the three objectives. By changing the position of the inlet and outlet, there is a complex relationship between reducing the maximum temperature of the battery, reducing the standard deviation of the battery temperature, and reducing the pressure drop of the liquid cooling plate. Due to the complex relationship between the design variables and the responses (evaluation indicators), a strategy is needed to achieve the global optimum. To obtain the optimal design parameters of the inlet and outlet position for topology optimization, this study obtained the set of Pareto front solutions based on the response surface method (RSM) and the non-dominated sorting genetic algorithm II (NSGA-II). Then, the optimal solution was selected from this solution set. As shown in Figure 10a, there is a nonlinear relationship between the position parameters of the inlet and outlet and the three evaluation indicators. This study used orthogonal experimental design to determine the experimental scheme. This way, more information can be obtained with fewer experimental trials. According to the previous section, the optimal values of the three evaluation indicators all fall within the range of 1–5, so the experimental design focuses on capturing the information within this range. Table 5 shows the design parameter levels used for the experimental design.

Subsequently, the response surface method was applied to the three evaluation indicators based on the designed scheme. The fitting degree of the evaluation indicators to the two input factors was evaluated through analysis of variance (ANOVA) [33], and the relevant results are shown in Table 6. The results show that for T_{max} and T_σ, the quadratic model demonstrates excellent statistical significance, while for ΔP, the modified cubic

model exhibits excellent statistical significance. The P-values of the three fitting models are all less than 0.0001, which proves this point. The R^2 values of the three fitting models are all very close to 1, indicating that the models have excellent predictive performance within the designed experimental scope. The difference between the adjusted R^2 and the predicted R^2 is all less than 0.1, indicating a strong correlation between the observed results and the predicted results. Adequate precision indicates the signal-to-noise ratio, and this value is much greater than 4, indicating that the model has sufficient stability [34]. Figure 10b compares the relationship between the actual evaluation indicators and the predicted evaluation indicators. It can be observed that the predicted values are in close agreement with the actual values, presenting a linear trend with a slope close to 1. This indicates that the established model can accurately and reliably predict the evaluation indicators, which is consistent with the results of the ANOVA analysis. As mentioned above, these three models can be used to establish the relationship between design variables and evaluation indicators, and the relevant expressions are as shown in Equations (38)–(40).

$$T_{\max} = 306.37669 - 0.239557 \cdot x_{\text{in}} - 0.054061 \cdot x_{\text{out}} + 0.069240 \cdot x_{\text{in}} \cdot x_{\text{out}} + 0.039378 \cdot x_{\text{in}}^2 - 0.005192 \cdot x_{out}^2 \quad (38)$$

$$T_{\sigma} = 0.867483 - 0.073874 \cdot x_{\text{in}} - 0.029033 \cdot x_{out} + 0.020088 \cdot x_{\text{in}} \cdot x_{out} + 0.013796 \cdot x_{\text{in}}^2 + 0.001551 \cdot x_{out}^2 \quad (39)$$

$$\Delta P = 5.37165 - 0.449289 \cdot x_{\text{in}} - 0.628297 \cdot x_{\text{out}} + 0.159161 \cdot x_{\text{in}} \cdot x_{\text{out}} + 0.066027 \cdot x_{\text{in}}^2 + 0.10066 \cdot x_{out}^2 - 0.015678 \cdot x_{\text{in}}^2 \cdot x_{\text{out}} - 0.010184 \cdot x_{\text{in}} \cdot x_{out}^2 \quad (40)$$

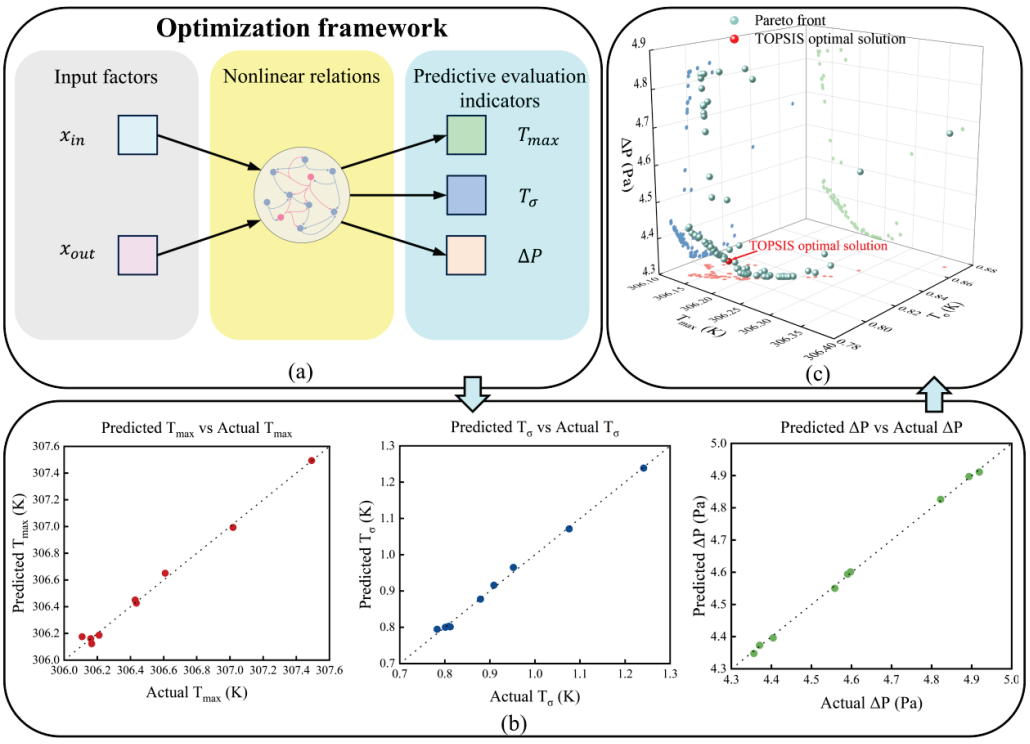

Figure 10. (**a**) Prediction framework between input factors and evaluation indicators; (**b**) the relationship between the predicted values and the actual values of the evaluation indicators; (**c**) the values of the evaluation indicators corresponding to the Pareto frontier and the optimal solution obtained using the TOPSIS decision-making strategy.

Table 5. Description of the level of design parameters.

Design Parameter	Coded Levels		
	1	**2**	**3**
x_{in}	1	3	5
x_{out}	1	3	5

Table 6. ANOVA analysis for three response targets.

Responses	T_{max}	T_σ	ΔP
Order	Quadratic	Quadratic	Modified cubic
R^2	0.9942	0.9972	0.9994
P-value	<0.0001	<0.0001	<0.0001
Adjusted R^2	0.9901	0.9952	0.9985
Predicted R^2	0.9460	0.9726	0.9258
Adequate precision	52.9757	74.6236	85.5677

Therefore, the optimal selection of the input port position can be obtained based on the fitted model derived from RMS. This multi-objective optimization problem is shown in Equation (41), aiming to reduce the maximum temperature of the battery, decrease the standard deviation of the battery temperature, and lower the pressure drop of the liquid cooling plate.

$$\begin{cases} \text{Find } x_{in},\ x_{out} \\ \text{Minimize } T_{max} = y_1(x_{in},\ x_{out}) \\ \text{Minimize } T_\sigma = y_2(x_{in},\ x_{out}) \\ \text{Minimize } \Delta P = y_3(x_{in},\ x_{out}) \\ x_{in} \in [1,5], x_{out} \in [1,5] \end{cases} \tag{41}$$

Based on the content of the previous section, it can be observed that there is a complex interplay of gains and losses among the three evaluation indicators in the optimization process. Use NSGA-II to obtain the Pareto front of the optimal solution. NSGA-II has been successfully applied to the optimization of battery thermal management systems. It features the elite non-dominated sorting method and significantly reduces the computational requirements through an efficient sorting algorithm. The important parameters set by NSGA-II are shown in Table 7. Figure 10c presents the Pareto front obtained by the NSGA-II algorithm. The figure shows the three evaluation indicators corresponding to each inlet/outlet position parameter under the solution. An appropriate decision-making scheme is of vital importance for identifying the optimal solution from the Pareto frontier solution set. This study employs TOPSIS to select the optimal solution from the Pareto frontier solution set. This method is based on ideal points and non-ideal points for calculation. To achieve the screening purpose, make the distance between the optimal solution and the non-ideal points the greatest, and the distance between the optimal solution and the ideal point the smallest:

$$d_{i+} = \sqrt{\sum_{j=1}^{m} \left(F_{ij} - F_j^{\text{ideal}} \right)^2} \tag{42}$$

$$d_{i-} = \sqrt{\sum_{j=1}^{m} \left(F_{ij} - F_j^{\text{non-ideal}} \right)^2} \tag{43}$$

$$i_{\text{final}} = i \in \max\left(\frac{d_{i-}}{d_{i+} + d_{i-}} \right) \tag{44}$$

where m represents the number of evaluation indicators, F_{ij} denotes the j-th evaluation indicator of the i-th Pareto front solution set, F_j^{ideal} is the ideal point of the j-th evaluation indicator, and $F_j^{\text{non-ideal}}$ is the non-ideal point of the j-th evaluation indicator. The final optimal solution obtained is $x_{\text{in}} = 2.132$, $x_{\text{out}} = 1.552$. In order to verify the accuracy of the model's predictions, a numerical model was developed for the topology optimization results under the given inlet and outlet parameters. Table 8 presents a comparison between the predicted results and the actual numerical simulation results. The results show that the error of the predicted values for all evaluation indicators is within 2%, indicating the reliability of the established prediction model and the reliability of the optimal solution obtained.

Table 7. Important parameter settings of NSGA-II.

Parameter	Value
Population size	100
Maximum number of iterations	2000
Mutation probability	0.1
Crossover probability	0.9

Table 8. Comparison between the predicted value and the simulated value of the optimal solution.

Evaluation Indicator	Predicted Value	Simulated Value	Error
$T_{\max}$ (K)	306.177641	306.0944013	0.027%
T_σ (K)	0.797838244	0.812113659	1.758%
ΔP (Pa)	4.344973923	4.318736201	0.608%

4.3. Performance Comparison of Liquid Cooling Plates with Different Structures

This section aims to verify the advantages of the topology-optimized liquid cooling plate structure after optimizing the inlet and outlet layout, and to reveal the reasons for its enhancement. As shown in Figure 11, the thermal management performance of batteries with four channel structures was compared under high-rate discharge (5C): the topology-optimized liquid cooling plate with the optimal inlet and outlet arrangement (TOPO), the topology-optimized liquid cooling plate with the conventional inlet and outlet arrangement (TOPC), the straight channel liquid cooling plate with the optimal inlet and outlet arrangement (SPO), and the single-inlet and single-outlet straight channel liquid cooling plate (SSSP). In addition, this section also discusses the influence of the inlet flow velocity on the thermal management performance of the battery.

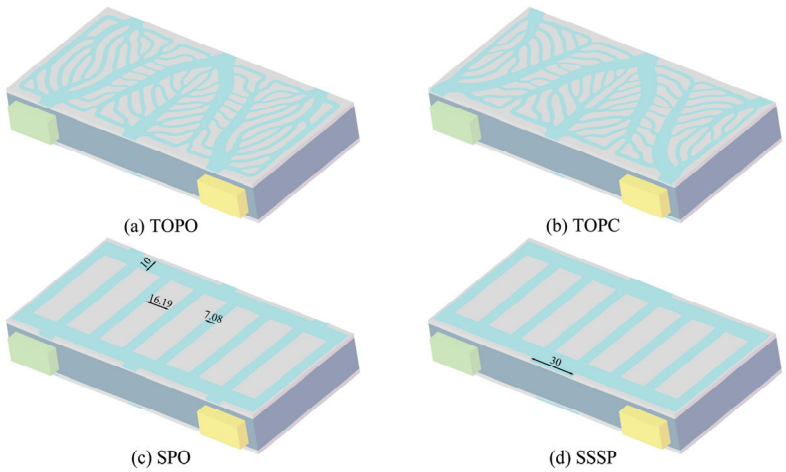

Figure 11. Different liquid cooling plate models and size specifications.

For the thermal management system of liquid batteries, it is crucial to simultaneously enhance both thermal performance and flow performance. Therefore, in addition to the evaluation indicators mentioned earlier, define the performance evaluation criterion (PEC) as a comprehensive indicator for evaluating the heat dissipation performance and flow performance. It is a commonly used indicator for assessing the overall performance of the liquid cooling plate. The calculation method of PEC is as follows [24]:

$$PEC = \frac{Nu/Nu_{SSSP}}{\left(\Delta P/\Delta P_{SSSP}\right)^{\frac{1}{3}}} \tag{45}$$

where Nu_{SSSP} and ΔP_{SSSP} represent the Nusselt number of SSSP and the pressure drop of SSSP, respectively.

Figure 12 shows the changes over time of the maximum and average temperatures of the battery during its operation (with the boundary conditions as described in Table 4), when the battery is cooled by using four different liquid cooling plates. This study presents corresponding images for representative lower inlet velocities (0.03 m/s) and higher velocities (0.13 m/s). All the curves exhibited the same trend: they rose rapidly at first, then fluctuated slowly upwards and reached the peak temperature at the final moment of discharge. It is obvious that after optimizing the layout of the inlets and outlets, T_{avg} and T_{max} of TOPO during operation are both lower than those of TOPC with the regular layout of inlets and outlets. Compared with the two straight current channels (SPO, SSSP), TOPO demonstrated a more significant advantage in terms of T_{avg} and T_{max} throughout the entire operation process. Among them, SPO, due to the use of optimized inlet and outlet layout, shows a significant trend in terms of T_{avg} and T_{max} compared to SSSP. In addition, at high inlet velocities, the advantage of using the TOPO in reducing temperature is more obvious. For example, in Figure 12a, the T_{max} of TOPO is higher than the T_{avg} of SPO, but in Figure 12b, the T_{max} of TOPO is lower than the T_{avg} of SPO. Based on this figure, the following conclusions can be drawn: 1. Compared with the conventional inlet and outlet layout, the topology-optimized liquid cooling plate, after optimizing the inlet and outlet layout, has to some extent reduced the average temperature and the maximum temperature of the battery during its entire operation process. 2. The optimized inlet and outlet layout applied to the straight channel results in a significant reduction in the average and maximum battery temperatures compared to the traditional single inlet and single outlet configuration. 3. At high inlet velocities, the advantage of temperature relief brought by the topology-optimized liquid cooling plate is more obvious compared to other liquid cooling plates.

Figure 13 shows the variations in the maximum temperature (T_{max}), average temperature (T_{avg}), temperature standard deviation (T_σ), and Nusselt number (Nu) of the battery with respect to the inlet flow velocity. As the inlet flow rate increases, the T_{max}, T_{avg}, and T_σ of the batteries using the four liquid cooling plates all show a downward trend, while the Nusselt number shows an upward trend. In addition, as the inlet flow rate increases, the extent of these indicators' changes gradually decreases. For different inlet flow rates, the superiority or inferiority of the performance indicators generally follows the following relationship: TOPO > TOPC > SPO > SSSP. Interestingly, as the inlet flow rate increases, TOPO shows a trend of further expanding its advantages compared to SPO, which only has a different flow channel structure. Compared with an inlet flow velocity of 0.03 m/s, when the inlet flow velocity is 0.13 m/s, the T_{max} and T_{avg} of TOPO decrease by 3.7 K and 3.16 K, respectively, while the T_{max} and T_{avg} of SPO decrease by 3.57 K and 3.15 K, respectively. This trend is more pronounced in terms of the uniformity of battery temperature. Compared with an inlet flow velocity of 0.03 m/s, when the inlet flow velocity is 0.13 m/s,

the T_σ of TOPO decreases by 35%, while the T_σ of SPO decreases by 28%. Compared with an inlet flow velocity of 0.03 m/s, when the inlet flow velocity was 0.13 m/s, the *Nu* of TOPO increased by 7.42 and that of SPO increased by 5.36. Under different inlet flow rates, compared with the other three liquid cooling plate structures, TOPO's Nu increases by 4.6–8.8%, 4.1–19.7%, and 33.3–42.2%, respectively. It is obvious that as the inlet flow rate increases, TOPO shows a trend of gradually expanding its advantages over SPO in various indicators. This demonstrates that the topology-optimized structure has a greater adaptability to different inlet flow rates in terms of thermal performance indicators. In addition, the topology-optimized liquid cooling plates have more fine and numerous branch flow channels and a larger heat exchange area ($A_{sur,TOPO}$ = 0.0250 m^2, $A_{sur,TOPC}$ = 0.0249 m^2, $A_{sur,SPO}$ = 0.0185 m^2, $A_{sur,SSSP}$ = 0.0185 m^2), which is also the key reason for its superior performance compared to the straight current channels.

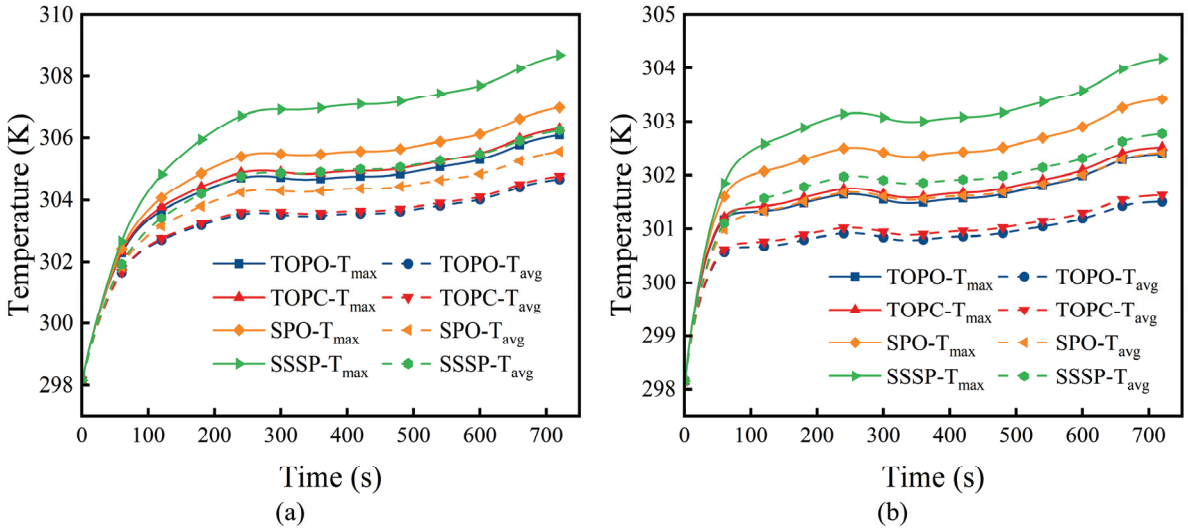

Figure 12. Comparisons of T_{max}, T_{avg} for different liquid cooling plates for (**a**) u_{in} = 0.03 m/s, (**b**) u_{in} = 0.13 m/s.

Figure 14a,b show the changes in pressure drop (ΔP) and performance evaluation criterion (PEC) with the variation in inlet flow velocity. For Figure 14a, as the inlet flow velocity increases, the pressure drop of all four liquid cooling plates shows an upward trend. Clearly, as the inlet flow velocity increases, the pressure drop of TOPO is further superior to that of SPO and TOPC. When the inlet flow velocity is 0.03 m/s, the pressure drops of TOPO, TOPC, and SPO are 4.32 Pa, 5.06 Pa, and 4.16 Pa, respectively. At this time, the pressure drop of TOPO is slightly higher than that of SPO because the topology optimization generates more complex channels and has a longer flow path. Therefore, during the flow process, more resistance is received, resulting in a higher pressure drop. When the inlet flow velocity is 0.13 m/s, the pressure drops of TOPO, TOPC, and SPO are 30.92 Pa, 38.06 Pa, and 38.44 Pa, respectively. At this time, the pressure drop of TOPO is significantly lower than that of TOPC and SPO. This indicates that the flow channels generated by topology optimization have a greater advantage at high inlet flow velocities. In addition, the optimized inlet and outlet arrangement can have better thermal performance at different inlet flow velocities while having lower pressure drop. For Figure 14b, as the inlet flow velocity increases, the PEC of TOPO and TOPC both increase, while the PEC of SPO decreases. This further indicates that the topology-optimized channel structure has stronger adaptability to high flow velocities, which is not possessed by traditional straight channels. In addition, as the inlet flow velocity increases, the increase

rate of TOPO's PEC is faster, and the comprehensive performance advantage of TOPO compared to other flow channel structures is further expanded. Compared with the inlet flow velocity of 0.03 m/s, when the inlet flow velocity is 0.13 m/s, the PEC of TOPO increases by 0.24, and the PEC of TOPC increases by 0.14. The increase rate of TOPO's PEC is 1.7 times that of TOPC, and the comprehensive performance advantage brought by the optimized inlet and outlet arrangement is considerable.

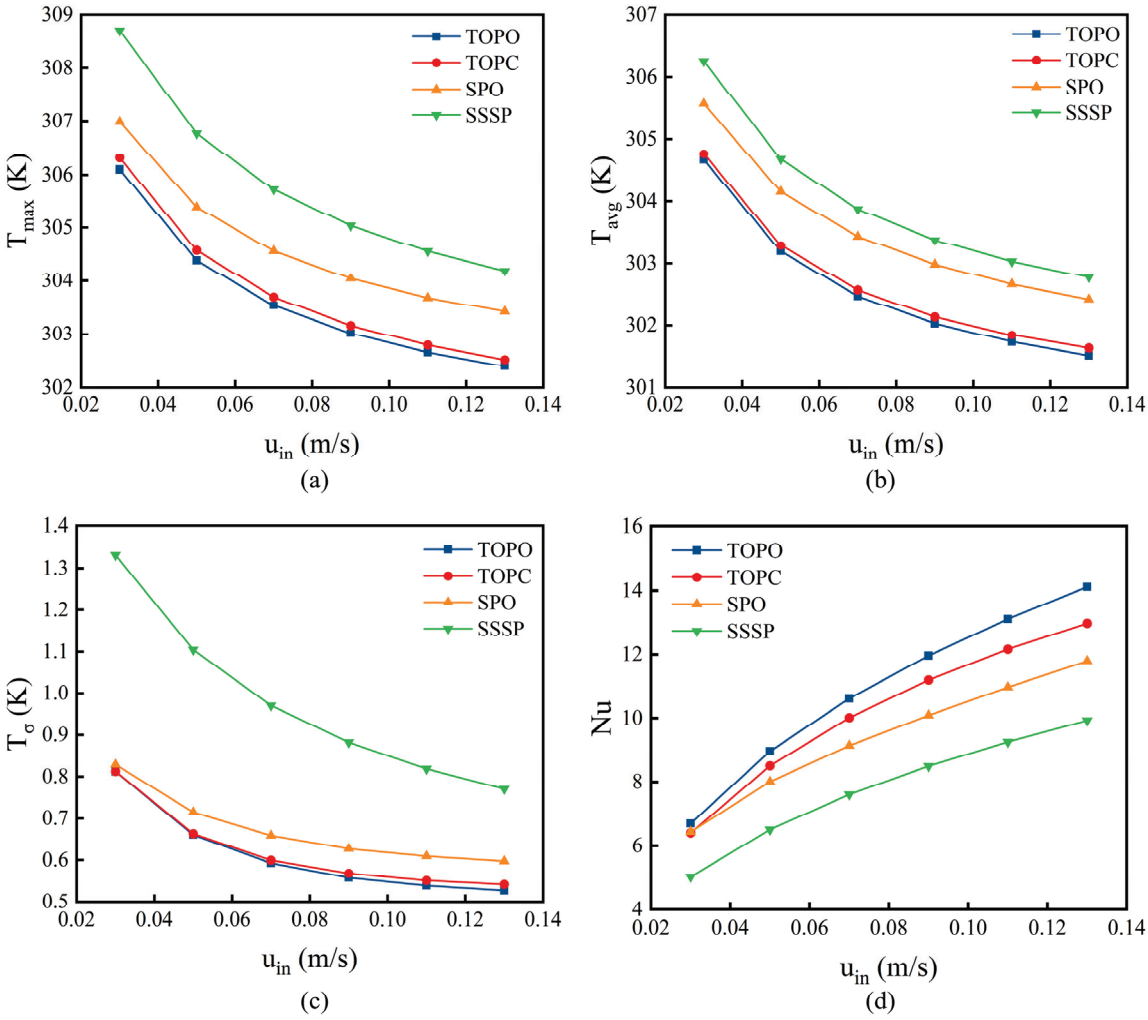

Figure 13. Under different inlet flow rates, the variations in the four liquid cooling plates in (**a**) the maximum temperature, (**b**) the average temperature, (**c**) the temperature standard deviation, and (**d**) the Nusselt number.

Figure 14c,d show the variations in the maximum temperature (T_{max}) and the standard deviation of the temperature (T_σ) under four different liquid cooling plates at different pumping powers. It is obvious that although the increase in pumping power is becoming increasingly significant, the improvements in the maximum battery temperature and the standard deviation of temperature are becoming smaller and smaller. Therefore, choosing the appropriate pumping power (that is, achieving a balance between pumping power and performance improvement) is of crucial importance in practical applications. For the four liquid cooling plate structures studied in this paper, TOPO can achieve better heat dissipation performance and temperature uniformity under the same pumping power, which is helpful in solving the energy issues in practical applications.

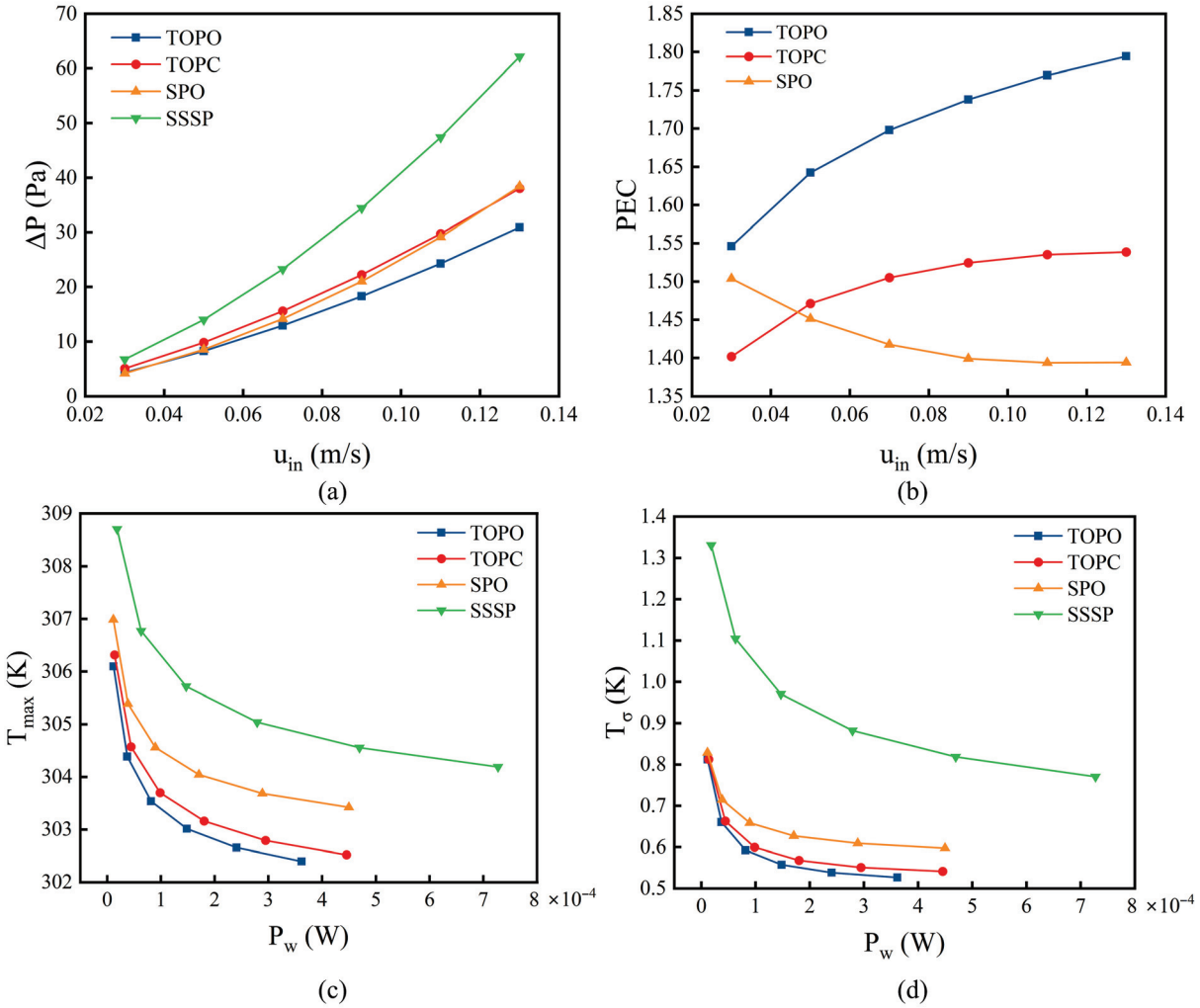

Figure 14. Under different inlet flow rates (or pumping powers), the variations in the four liquid cooling plates in (**a**) the pressure drop, (**b**) performance evaluation criterion, (**c**) maximum temperature, and (**d**) temperature standard deviation.

Figure 15 shows the various indicators of the three liquid cooling plates (TOPO, TOPC, SPO) under the conditions of inlet flow velocities of 0.03 m/s and 0.13 m/s. Except for PEC, where larger is better, all the other indicators are better when smaller. It is obvious that when the inlet flow rate is 0.03 m/s, TOPO is not the best among the three liquid cooling plates in terms of some indicators such as pressure drop. However, when the inlet flow rate was 0.13 m/s, TOPO achieved the best results in all five indicators and had a much greater advantage gap. Table 9 presents in greater detail the five evaluation indicators corresponding to the four liquid cooling plates when the inlet flow velocity is 0.03 m/s and 0.13 m/s. First, a comparison between TOPO and TOPC is conducted to analyze the effect of optimizing the layout of inlets and outlets. Within the range of inlet flow velocity from 0.03 to 0.13 m/s, compared with TOPC, TOPO's T_{max} decreased by 0.13–0.22 K, T_{avg} decreased by 0.096–0.121 K, T_{σ} decreased by 0.03–2.72%, pressure drop decreased by 14.62–18.75%, and PEC increased by 10.3–16.61%. Then there is a comparison with the traditional straight channels that are currently widely used. Within the range of inlet flow velocity from 0.03 to 0.13 m/s, compared with the two straight channels (SPO, SSSP), the T_{max} of TOPO decreased by 0.9–2.6 K, the T_{avg} decreased by 0.9–1.6 K, the T_{σ}

decreased by 2–40%, the pressure drop decreased by −3.93–50.25%, and the PEC increased by 2.82–79.43%.

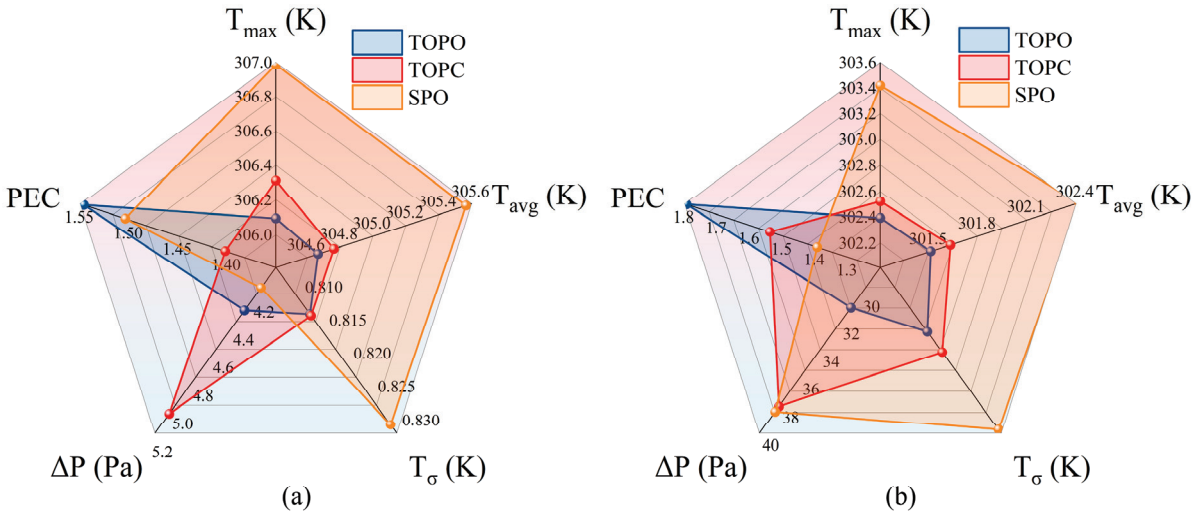

Figure 15. The comparison of various indicators when the inlet flow velocity is (**a**) 0.03 m/s and (**b**) 0.13 m/s.

Table 9. The various evaluation indicators of the four liquid cooling plates under low inlet flow rate (0.03 m/s) and high inlet flow rate (0.13 m/s).

Evaluation Indicators	u_{in} (m/s)	TOPO	TOPC	SPO	SSSP
T_{max} (K)	0.03	306.094	306.314	306.986	308.702
T_{max} (K)	0.13	302.394	302.519	303.420	304.189
T_{avg} (K)	0.03	304.667	304.763	305.566	306.251
T_{avg} (K)	0.13	301.511	301.631	302.420	302.771
T_{σ} (K)	0.03	0.812	0.812	0.829	1.331
T_{σ} (K)	0.13	0.527	0.542	0.597	0.770
ΔP (Pa)	0.03	4.319	5.058	4.156	6.742
ΔP (Pa)	0.13	30.921	38.058	38.435	62.156
PEC	0.03	1.546	1.402	1.504	1.000
PEC	0.13	1.794	1.539	1.394	1.000

Figure 16 shows the velocity distribution and flow lines within the flow channels of the four liquid cooling plates when the inlet flow velocity is 0.13 m/s. All four liquid cooling plates have a relatively high flow velocity at the inlet and outlet, but the two topology-optimized flow channels (TOPO, TOPC) have a more uniform velocity distribution. Since the layout of TOPO is more uniform, its uniformity of velocity distribution is better than that of TOPC. In contrast, both the straight channels have uneven flow distribution, and the coolant flows rapidly from the proximal straight channel to the outlet. SSSP, due to its single inlet, exhibits this phenomenon more significantly. This is the main reason for the poor cooling performance of the two straight channels, as the coolant does not adequately stay in the channels for heat exchange. The flow line analysis further explains the reasons for the differences in flow performance. Compared to the obvious vortices near the inlet of TOPC, the inlets on both sides of TOPO eliminate this phenomenon. This is because one of the objectives of optimizing the inlet and outlet layout is pressure drop, and reducing unnecessary vortices to lower the pressure drop is one of the objectives. And because the inlet coolant temperature is low, it can effectively carry away the heat generated by

the adjacent battery at the inlet. Therefore, the flow recirculation area near the inlet is unnecessary and is not conducive to the overall heat dissipation performance. In contrast, SPO and SSSP have very large ranges of vortices. However, the vortex distribution of SPO is more uniform, and the positions for enhancing local heat transfer are more uniform. This is one of the reasons why the thermal performance such as battery temperature uniformity is better with SPO than SSSP. The biomimetic structure similar to the root of a tree obtained through topology optimization design is conducive to making the coolant distribute more smoothly and uniformly in the flow channels. Such a flow channel structure can largely reduce flow loss and correspond to its advantages in flow performance.

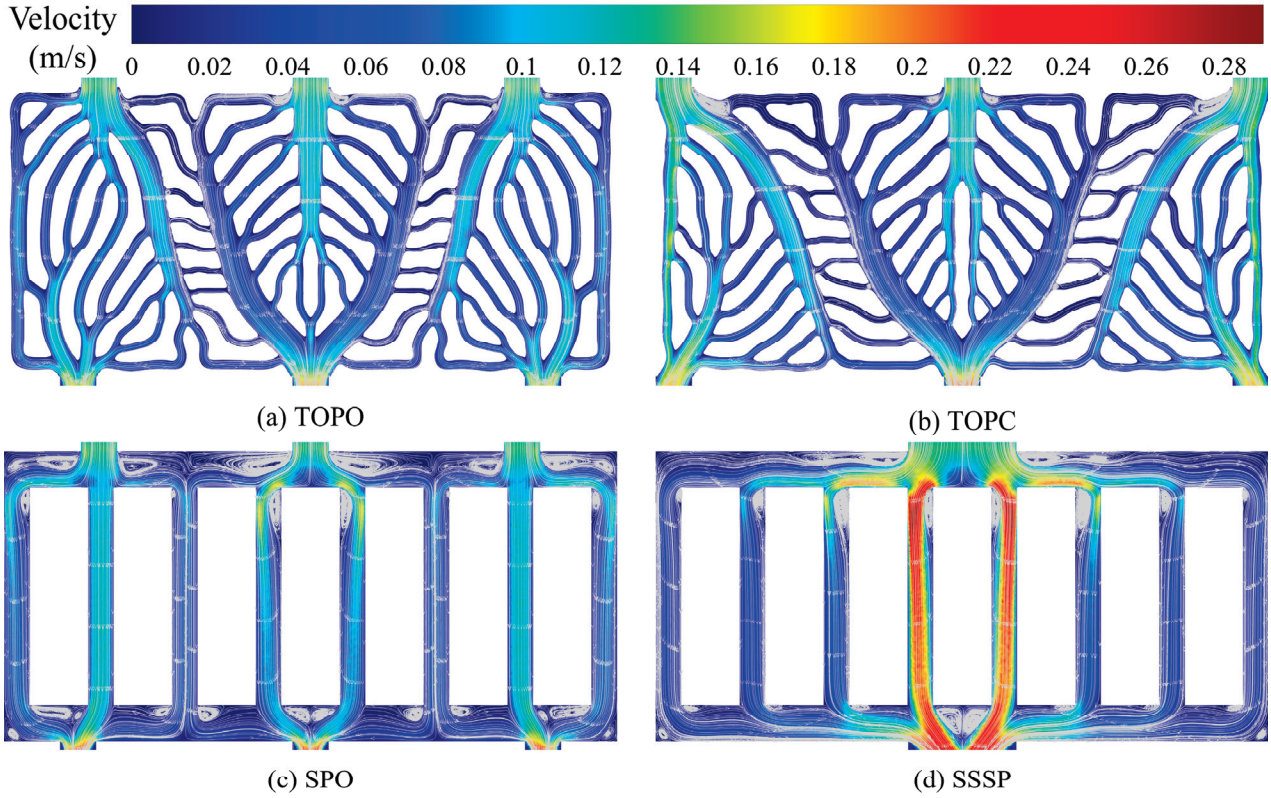

Figure 16. Velocity distributions and streamlines within flow channels of the four liquid cooling plate configurations when the inlet velocity is 0.13 m/s.

Figure 17 shows the temperature distribution diagrams of the battery discharge at the final moment when the inlet flow velocity is 0.13 m/s, under the application of four types of liquid cooling plates. The four figures show similar temperature distribution patterns. The battery temperature near the inlet is very low. This is because the coolant temperature at the inlet is low and the flow rate is high, which can effectively remove the heat from the battery. As the coolant moves away from the inlet, it continuously absorbs the heat from the battery, causing the temperature to gradually increase and the cooling effect to gradually weaken. Compared with the two straight channels (SPO, SSSP), the battery temperatures of the two topology optimization channel structures (TOPO, TOPC) are significantly lower, and the heat dissipation effect is better. According to Figure 16, TOPO has a more uniform velocity distribution. Compared with TOPC, TOPO has a more uniform temperature distribution and a wider cooling effect in the flow direction. Since the middle area and the two side areas on the outlet side are the areas where high-temperature points are likely to occur. The flow distribution of TOPO achieves a balance where the highest temperature in these areas with high-temperature points is the lowest.

This explains why the high-temperature area at the outlet surface under TOPO is smaller and the maximum temperature is lower.

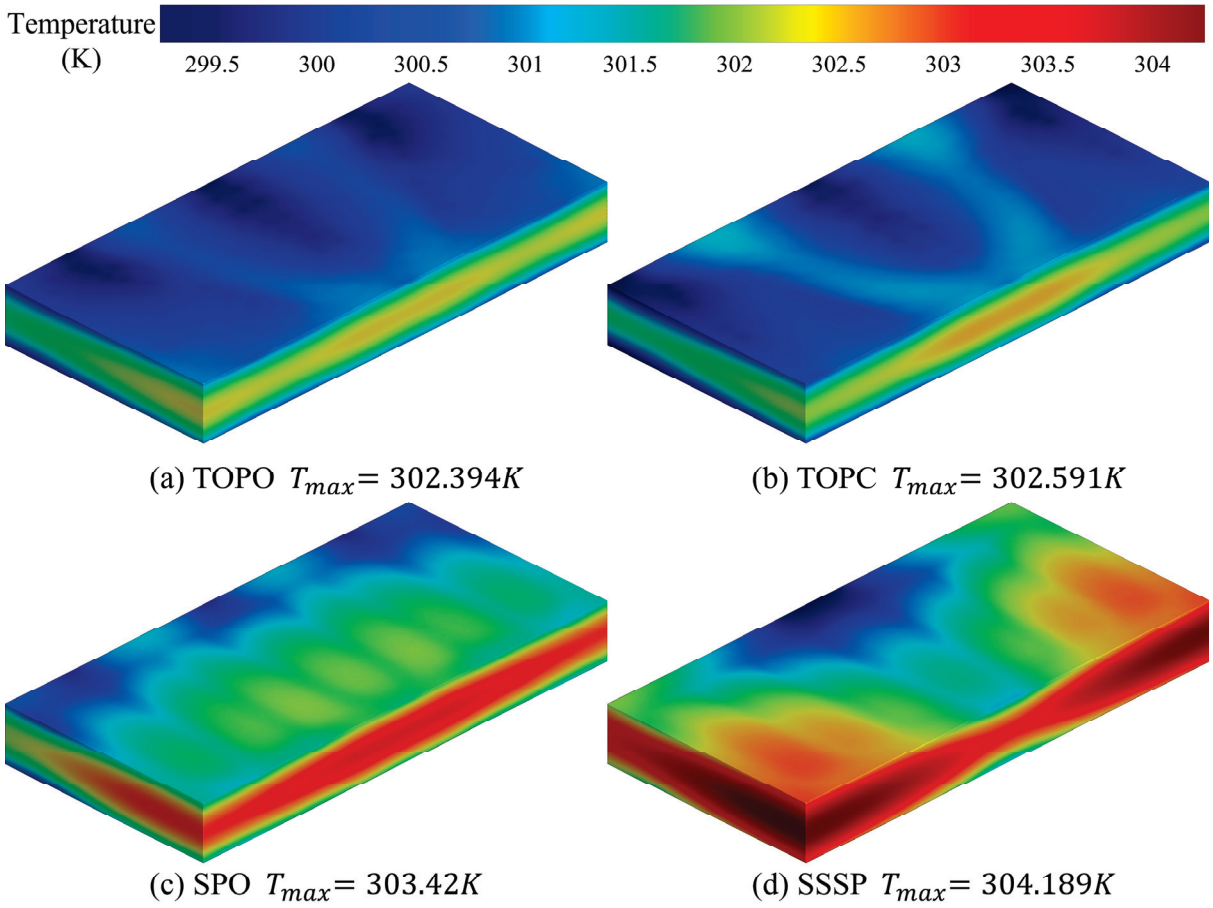

Figure 17. Temperature distributions for four liquid cooling plates when the inlet velocity is 0.13 m/s.

5. Conclusions

This study employed the topology optimization method to obtain the optimal liquid cooling plate structure for the liquid battery thermal management system (BTMS). Based on the situation of three inlets and three outlets in the width direction, a comprehensive discussion was conducted on the parameters of the inlet and outlet positions. The relationship between the design parameters (distances of side inlets/outlets from the edges) and the evaluation indicators (maximum battery temperature $T_{\max}$, temperature standard deviation T_{σ}, and pressure drop ΔP) was established using the response surface method (RSM). Subsequently, the Pareto front was obtained using the Non-dominated Sorting Genetic Algorithm II (NSGA-II), and the optimal solution was obtained using the TOPSIS strategy. Finally, a comprehensive comparison of the thermal management performance and flow performance was conducted between the topology-optimized liquid cooling plate with the optimal inlet and outlet arrangement (TOPO), the topology-optimized liquid cooling plate with the conventional inlet and outlet arrangement (TOPC), the straight channel liquid cooling plate with the optimal inlet and outlet arrangement (SPO), and the single-inlet and single-outlet straight channel liquid cooling plate (SSSP). The main conclusions are as follows:

1. When the outlet positions are fixed on both sides and the inlet positions are changed, the trends of the three evaluation indicators are relatively similar. When the inlet positions are fixed on both sides and the outlet positions are changed, the three evaluation indicators show a significant alternation phenomenon. In general, it is difficult to simultaneously achieve the optimization of all three indicators.

2. The expression of the design variables and the three evaluation indicators ($T_{\max}$, T_σ, ΔP) was constructed using the response surface method, with R^2 values of 0.9942, 0.9972, and 0.9994, respectively. According to the NSGA-II and TOPSIS decision methods, the optimal solution was $x_{\text{in}} = 2.132$, $x_{\text{out}} = 1.552$. The numerical verification indicates that the maximum relative error does not exceed 2%.

3. The BTMS using TOPO achieved better evaluation indicators ($T_{\max}$, T_{avg}, T_σ, ΔP, and performance evaluation criterion PEC) than using TOPC under different inlet flow rates. Among them, the advantage of PEC under different inlet flow rates was 10.3–16.61%.

4. TOPO has a more significant performance advantage for the other liquid cooling plates at high inlet flow rates (0.13 m/s) compared to low inlet flow rates (0.03 m/s).

5. At high inlet flow rates (0.13 m/s), compared with the traditional straight channel liquid cooling plate (SPO, SSSP), TOPO improved PEC by 28.7% and 79.4%, respectively.

The results of this study indicate that the liquid cooling plate structure obtained through topology optimization can improve the heat transfer efficiency while reducing the required power consumption simultaneously. In addition, by optimizing the positions of the inlets and outlets, the heat transfer efficiency can be further enhanced under a reduced power consumption. However, the flow channel structures obtained through topology optimization seem to be complex, which may impose challenge on the manufacturability and mass production. It is worth noting that with the rapid development of additive manufacturing technology, techniques such as selective laser melting provide promising solutions for mass production of cold plates. In addition, the mesh density of the topology optimization design can be limited to the accuracy required by traditional processing methods, in which way the liquid cooling plate structure obtained through topology optimization could meet the manufacturing accuracy requirements of large-scale production machine tools.

Author Contributions: T.Y.: writing—original draft, visualization, validation, methodology, investigation, formal analysis, data curation; H.L.: writing—review & editing, writing—original draft, supervision, resources, project administration, funding acquisition, conceptualization; W.Z.: writing—review & editing, validation, investigation, data curation; A.D.: writing—review & editing, project administration, funding acquisition; M.W.: writing—review & editing, project administration, funding acquisition. All authors have read and agreed to the published version of the manuscript.

Funding: This research was financially supported by National Key Research and Development Program of China (Grant No. 2023YFB4301703), National Natural Science Foundation of China (Grant No. 52306070), the Dalian High Level Talent Innovation Support Program (2024RQ009), Innovation Team Project of the Chinese Ministry of Education of China (8091B042204), Key Research and Development Program of Jiangxi Province (Grant No. 20244BBG73009), and the Fundamental Research Funds for the Central Universities (Grant No. 3132025124).

Data Availability Statement: The data presented in this study are available on request from the corresponding author. The data are not publicly available due to privacy.

Conflicts of Interest: Author Aoshuang Ding was employed by the company CSSC Jiujiang Boiler Co., Ltd; Author Mengke Wu was employed by the company Locomotive Development Department, CRRC Dalian Locomotive and Rolling Stock Co., Ltd.,. The remaining authors declare that the

research was conducted in the absence of any commercial or financial relationships that could be construed as a potential conflict of interest.

References

1. Liu, D.; Xu, L.; Sadia, U.H.; Wang, H. Evaluating the CO_2 emission reduction effect of China's battery electric vehicle promotion efforts. *Atmos. Pollut. Res.* **2021**, *12*, 101115. [CrossRef]
2. Ji, H.; Luo, T.; Dai, L.; He, Z.; Wang, Q. Topology design of cold plates for pouch battery thermal management considering heat distribution characteristics. *Appl. Therm. Eng.* **2023**, *224*, 119940. [CrossRef]
3. Zhang, X.; Li, Z.; Luo, L.; Fan, Y.; Du, Z. A review on thermal management of lithium-ion batteries for electric vehicles. *Energy* **2022**, *238*, 121652. [CrossRef]
4. Jouhara, H.; Khordehgah, N.; Serey, N.; Almahmoud, S.; Lester, S.P.; Machen, D.; Wrobel, L. Applications and thermal management of rechargeable batteries for industrial applications. *Energy* **2019**, *170*, 849–861. [CrossRef]
5. Liu, H.; Wei, Z.; He, W.; Zhao, J. Thermal issues about Li-ion batteries and recent progress in battery thermal management systems: A review. *Energy Convers. Manag.* **2017**, *150*, 304–330. [CrossRef]
6. Zhao, G.; Wang, X.; Negnevitsky, M.; Li, C. An up-to-date review on the design improvement and optimization of the liquid-cooling battery thermal management system for electric vehicles. *Appl. Therm. Eng.* **2023**, *219*, 119626. [CrossRef]
7. Khoshvaght-Aliabadi, M.; Abbaszadeh, A.; Salimi, A.; Salehi, N. Structural modifications of sinusoidal wavy minichannels cold plates applied in liquid cooling of lithium-ion batteries. *J. Energy Storage* **2023**, *57*, 106208. [CrossRef]
8. Shahjalal, M.; Shams, T.; Islam, M.E.; Alam, W.; Modak, M.; Hossain, S.B.; Ramadesigan, V.; Ahmed, M.R.; Ahmed, H.; Iqbal, A. A review of thermal management for Li-ion batteries: Prospects, challenges, and issues. *J. Energy Storage* **2021**, *39*, 102518. [CrossRef]
9. Chen, K.; Wu, W.; Yuan, F.; Chen, L.; Wang, S. Cooling efficiency improvement of air-cooled battery thermal management system through designing the flow pattern. *Energy* **2019**, *167*, 781–790. [CrossRef]
10. Akbarzadeh, M.; Kalogiannis, T.; Jaguemont, J.; Jin, L.; Behi, H.; Karimi, D.; Beheshti, H.; Van Mierlo, J.; Berecibar, M. A comparative study between air cooling and liquid cooling thermal management systems for a high-energy lithium-ion battery module. *Appl. Therm. Eng.* **2021**, *198*, 117503. [CrossRef]
11. Chen, Z.; Yang, S.; Pan, M.; Xu, J. Experimental investigation on thermal management of lithium-ion battery with roll bond liquid cooling plate. *Appl. Therm. Eng.* **2022**, *206*, 118106. [CrossRef]
12. Zhong, Q.; Chandra, P.K.; Li, W.; Gao, L.; Garg, A.; Lv, S.; Tai, K. A comprehensive numerical study based on topology optimization for cooling plates thermal design of battery packs. *Appl. Therm. Eng.* **2024**, *236*, 121918. [CrossRef]
13. Sheng, L.; Zhang, H.; Su, L.; Zhang, Z.; Zhang, H.; Li, K.; Fang, Y.; Ye, W. Effect analysis on thermal profile management of a cylindrical lithium-ion battery utilizing a cellular liquid cooling jacket. *Energy* **2021**, *220*, 119725. [CrossRef]
14. Zhang, F.; Gou, H.; Xie, C.; He, Y.; Zhu, Y.; Lu, F.; Liang, B.; Xiao, K. A new stepped-channel liquid cooling plate thermal management system combined with composite phase change materials. *Appl. Therm. Eng.* **2022**, *211*, 118439. [CrossRef]
15. Ge, X.; Li, X.; Jin, Y.; Zhang, G.; Deng, J.; Ge, J. Experimental investigation on thermal management system of composite phase change material coupled with serpentine tubes for battery module. *Appl. Therm. Eng.* **2023**, *219*, 119501. [CrossRef]
16. Zhao, Y.; Zhang, X.; Yang, B.; Cai, S. A review of battery thermal management systems using liquid cooling and PCM. *J. Energy Storage* **2024**, *76*, 109836. [CrossRef]
17. Jhariya, M.; Dewangan, A.K.; Moinuddin, S.Q.; Kumar, S.; Ahmad, A.; Yadav, A.K. Research progress on efficient battery thermal management system (BTMs) for electric vehicles using composite phase change materials with liquid cooling and nanoadditives. *J. Therm. Anal. Calorim.* **2024**, *149*, 13653–13680. [CrossRef]
18. Thakur, A.K.; Sathyamurthy, R.; Velraj, R.; Saidur, R.; Pandey, A.; Ma, Z.; Singh, P.; Hazra, S.K.; Sharshir, S.W.; Prabakaran, R. A state-of-the art review on advancing battery thermal management systems for fast-charging. *Appl. Therm. Eng.* **2023**, *226*, 120303. [CrossRef]
19. Liu, H.; Gao, X.; Zhao, J.; Yu, M.; Niu, D.; Ji, Y. Liquid-based battery thermal management system performance improvement with intersected serpentine channels. *Renew. Energy* **2022**, *199*, 640–652. [CrossRef]
20. Fan, Y.; Wang, Z.; Fu, T.; Wu, H. Numerical investigation on lithium-ion battery thermal management utilizing a novel tree-like channel liquid cooling plate exchanger. *Int. J. Heat Mass Transf.* **2022**, *183*, 122143. [CrossRef]
21. Xia, H.; Wang, J.; Shen, Y.; Fang, K. A liquid-cooled plate based on bionic flow channels evolved from the shape of leaf veins and tree roots. *Int. J. Therm. Sci.* **2025**, *208*, 109468. [CrossRef]
22. Zhong, Q.; Gao, L.; Li, W.; Zhao, J.; Garg, A.; Panda, B. A novel preheating systems for columnar lithium batteries for below zero degrees celsius environment based on topology optimization. *Int. Commun. Heat Mass Transf.* **2024**, *158*, 107789. [CrossRef]

23. Zhan, S.; Chen, Y.; Yin, Y.; Li, Z.; Yu, C. Examining the influence of number of inlets and outlets on the topology optimization design of battery liquid cooling plate. *Appl. Therm. Eng.* **2024**, *252*, 123691. [CrossRef]
24. Wang, Z.; Zou, Z.; Zhou, Y.; Geng, X.; Sun, Y.; Huang, X.; Hao, M. Performance comparison of battery cold plates designed using topology optimization across laminar and turbulent flow regime. *Int. J. Heat Mass Transf.* **2025**, *238*, 126450. [CrossRef]
25. Zhan, S.; Cheng, Z.; Yin, Y.; Yu, C.; Zhao, C. Effect of inlet and outlet positions on heat dissipation performance of lithium-ion battery cold plates: An analysis based on topology optimization. *Int. J. Heat Mass Transf.* **2023**, *215*, 124436. [CrossRef]
26. Lin, X.-W.; Shi, M.-Y.; Zhou, Z.-F.; Chen, B.; Lu, Y.-J.; Jing, D.-W. Multi-objective topology optimization design of liquid-based cooling plate for 280 Ah prismatic energy storage battery thermal management. *Energy Convers. Manag.* **2025**, *325*, 119440. [CrossRef]
27. Wu, J.P.; Liu, H.L.; Li, C.C.; Li, C.H.; Xie, G. Topological optimization and thermal performance of cold plates for lithium-ion battery with non-uniform heat sources. *Appl. Therm. Eng.* **2024**, *254*, 123922. [CrossRef]
28. Qian, S.; Lou, S.; Ge, C.; Wang, W.; Tian, X.; Cai, Y. The influence of temperature dependent fluid properties on topology optimization of conjugate heat transfer. *Int. J. Therm. Sci.* **2022**, *173*, 107424. [CrossRef]
29. Wu, Y.; Li, Z.; Zhi, C.; Li, Z.; Shi, C.; Tan, G.; Ming, T. Pseudo three-dimensional topology optimization of cold plates for electric vehicle power packs. *Int. J. Heat Mass Transf.* **2024**, *232*, 125966. [CrossRef]
30. Zhang, K.; Li, Y.; Chang, S.-M.; Hu, L.; Wang, X.; Yu, M. Hydraulic and thermal performance enhancement for the cold plate using topology optimization. *Appl. Therm. Eng.* **2024**, *236*, 121829. [CrossRef]
31. Xia, Y.; Chen, L.; Luo, J.; Tao, W. Numerical investigation of microchannel heat sinks with different inlets and outlets based on topology optimization. *Appl. Energy* **2023**, *330*, 120335. [CrossRef]
32. Wang, J.; Shao, Z.; Du, J.; Chen, F.; Song, Z. Effects of inlet and outlet configurations on the topological optimization design of cooling plates for lithium-ion batteries. *J. Energy Storage* **2024**, *79*, 110124. [CrossRef]
33. Sui, Z.; Lin, H.; Sun, Q.; Dong, K.; Wu, W. Multi-objective optimization of efficient liquid cooling-based battery thermal management system using hybrid manifold channels. *Appl. Energy* **2024**, *371*, 123766. [CrossRef]
34. Yan, W.; Meng, X.; Cui, X.; Liu, Y.; Chen, Q.; Jin, L. Evaporative cooling performance prediction and multi-objective optimization for hollow fiber membrane module using response surface methodology. *Appl. Energy* **2022**, *325*, 119855. [CrossRef]

batteries

MDPI

Article

Water-Immersion Cooling for Lithium-Ion Battery Thermal Management: A Systematic Experimental and Numerical Study

Xiahua Zuo [1,2,3,†], Peng Peng [1,2,3,†], Yiwei Wang [1,2,3], Wenling Li [1,2,3], Wanyi Wu [1,2,3,4], Yishu Qiu [1,2,3,*] and Fangming Jiang [1,2,3,4,*]

[1] Laboratory of Advanced Energy Systems, Guangzhou Institute of Energy Conversion, Chinese Academy of Sciences (CAS), Guangzhou 510640, China
[2] CAS Key Laboratory of Renewable Energy, Guangzhou 510640, China
[3] Guangdong Provincial Key Laboratory of Renewable Energy, Guangzhou 510640, China
[4] School of Energy Science and Engineering, University of Science and Technology of China, Guangzhou 510640, China
* Correspondence: qiuys@ms.giec.ac.cn (Y.Q.); jiangfm@ms.giec.ac.cn (F.J.)
† These authors contributed equally to this work.

Abstract: In recent years, immersion cooling has gained wide interest for thermal management of lithium-ion batteries. Usually, dielectric oils or fluorinated liquid are used as immersion coolants to avert short circuits, but they have low thermal conductivity and high cost. Although water offers superior heat-transfer performance, its poor dielectric property means it cannot be used directly as an immersion coolant. Near full-depth partial immersion (NFDPI) was proposed as a viable alternative, in which water does not contact the tabs of batteries. In this study, an NFDPI experimental system is set up, and the effects of coolant flow rate, discharge rate, and inlet–outlet configuration on thermal management performance are investigated. Since direct observation of the immersion tank's internal flow is challenging, numerical simulations are conducted to resolve the flow field under various operating conditions. The experimental and simulated results reveal that NFDPI cooling effectively limits the module's maximum temperature, and the module's maximum temperature spread is mainly attributed to the cell's vertical temperature gradient. These findings offer guidance for the practical deployment of water-based NFDPI lithium-ion battery energy storage systems.

Keywords: lithium-ion battery energy storage; immersion cooling; thermal management; water cooling; near full depth partial immersion

1. Introduction

The lithium-ion battery (LIB) is gradually growing to be a primary energy storage technology due to its high energy density, long service life, low memory effect, etc. [1]. In China, by the end of 2023, electrochemical energy storage had achieved a cumulative installed capacity of 31.39 GW/66.87 GWh for operational new energy storage projects. Among these, lithium-ion battery storage overwhelmingly dominates, accounting for 97.4% of the total capacity.

The performance and safety of LIBs are significantly influenced by temperature, making thermal management a critical factor in ensuring battery safety [2–4]. The ideal operating temperature range for LIBs is typically 25–40 °C. Within this window, LIB's

electrothermal performance, cycle life, and safety are optimized, ensuring the entire system operates both safely and efficiently. Without effective thermal management, the heat generated within the cell cannot be dissipated promptly. The ensuing temperature rise accelerates degradation and thickening of the SEI layer, elevates internal resistance, intensifies polarization, and promotes lithium dendrite formation and parasitic reactions, thereby reducing energy-conversion efficiency. In severe cases, these processes can precipitate thermal runaway.

Common thermal management methods for LIBs include air cooling [5,6], liquid cooling [7–11], phase change material (PCM) cooling [12–16], and heat pipe cooling [17–20]. Air cooling is categorized into natural convection cooling and forced convection cooling, while liquid cooling is divided into indirect cooling and immersion cooling. Forced air cooling effectively lowers the battery module's temperature. Its overall performance is governed by multiple factors, including the length and cross-sectional area of the airflow path, the cooling air temperature, and the airflow velocity [21]. The indirect liquid cooling system has already been integrated into commercial electric vehicles and energy storage systems owing to its superior heat-transfer efficiency and compact design. The thermal performance can be optimized via liquid channel configuration design and/or tailoring the heat-transfer fluid's properties [22]. PCM-based battery thermal management systems, as a passive cooling strategy, feature low operating costs and commendable temperature uniformity. The primary approach to enhance the heat-transfer performance of PCM is to add high thermal conductivity metals, metal oxides, and expanded graphite [23]. Heat pipe cooling is receiving increasing attention in battery thermal management owing to its superconductive heat-transfer capacity, robustness, minimal maintenance, and longevity. However, most current studies focus on cell- and module-level, whereas large-scale heat pipe thermal management receives far less attention [17].

Immersion cooling has recently emerged as a novel technique for thermal management of LIBs [24–27]. Depending on whether the coolant undergoes a phase change, it can be classified as single-phase or two-phase. In single-phase systems, the heat generated by the battery is primarily dissipated through convective heat transfer between the coolant and the battery surface. In two-phase systems, enhanced cooling performance derives from the latent heat of evaporation during liquid–vapor phase transitions, coupled with the subsequent two-phase turbulent flow. Due to the phase change, two-phase systems present additional system complexity. The heat removal capabilities of single-phase immersion cooling can be up to two orders of magnitude greater than air cooling, while two-phase immersion cooling has the potential to achieve three orders of magnitude higher efficiency [28].

Some researchers have investigated methods to enhance immersion cooling performance. Shi et al. [29] put forward a single-phase spray-enhanced immersion cooling method to optimize the flow field and enhance thermal characteristics in BTMS, substantially improving the thermal uniformity and cooling efficiency of battery modules by optimizing spray parameters (nozzle diameter and angle). Bao et al. [30] proposed a multi-mode composite immersion cooling method that combines static and dynamic immersion cooling. Compared to static and dynamic immersion cooling, this composite method significantly reduces both the maximum temperature and the maximum temperature difference of the battery module, while its cooling performance is less influenced by the coolant flow rate. Zhong et al. [31] proposed an innovative guided sequential immersion cooling (GSIC) system, which improves the overall temperature uniformity of the battery module by prioritizing cooling in high thermal risk areas, such as the battery tab region, through controlled coolant flow sequencing. Wei et al. [32] designed an immersion cooling scheme where

cylindrical batteries mimic cells, and cooling channels resemble blood vessels, inspired by the bionic concept of cell cooling in biological tissues. They investigated the effects of inlet diameter, branch angles, flow rate, and spiral baffles on coolant flow uniformity and temperature distribution within the battery pack.

Under single-phase immersion cooling conditions, the maximum temperature and maximum temperature difference of battery modules are negatively correlated with the coolant's thermal conductivity and positively correlated with its viscosity [29]. Consequently, to achieve optimal temperature control, a coolant with higher thermal conductivity and lower viscosity should be selected. In full-depth immersion cooling, a dielectric coolant is essential to prevent short circuits. Currently, commonly used dielectric fluids for lithium-ion battery immersion cooling include fluorinated liquids, esters, mineral oil, silicone oil, etc. The key properties of fluorinated liquids are incombustibility, chemical inertness, and electrical insulation properties, which makes them promising for thermal management in LIBs. Nevertheless, the high cost and volatility restrict the large-scale application of fluorinated liquids as immersion coolants. Esters, mineral oil, and silicone oil are widely employed in electrical applications (such as transformers) for effective heat dissipation. They exhibit higher thermal conductivity than fluorinated liquids but also possess a markedly higher viscosity. At the same time, esters and oils are flammable, and in the event of thermal runaway, they can further propagate fires, leading to greater hazards.

Given the limitations of fluorinated liquids, esters, and oil-based coolants, alternative liquids can be considered. Water, the most common liquid, is typically excluded as an immersion coolant for LIBs due to its lack of dielectric properties. However, compared to traditional immersion coolants, water offers higher thermal conductivity, greater specific heat capacity, and lower viscosity. From a purely thermophysical perspective, water exhibits superior coolant properties. Partially immersing the battery in water while preventing direct contact between water and the battery's conductive components is an effective measure to avoid short circuits.

In this study, thermal management of LIB modules is achieved using a water-based NFDPI strategy. In NFDPI cooling, the liquid level (immersion depth) is controlled to prevent the coolant from contacting the battery tabs. To elucidate how hydraulic and structural parameters influence NFDPI thermal performance, an NFDPI experimental system is constructed. Experiments systematically examine the effects of coolant volumetric flow rate, module discharge rate, and inlet–outlet configuration on the module's maximum temperature and maximum temperature difference. Complementary numerical simulations are performed to resolve the coolant flow fields. This work provides new design insights and optimization pathways for employing water as a partial immersion coolant in the thermal management of LIB energy storage systems.

2. Experiment Investigation

2.1. Experimental System

Figure 1a illustrates the NFDPI thermal-management experimental diagram, which uses water as the immersion coolant. The experiment system comprises an immersion tank, a battery module, and thermocouples, and it is externally connected to data acquisition devices and LIB charge–discharge instruments. The battery module consists of five 24 Ah prismatic batteries connected in series (5s1p).

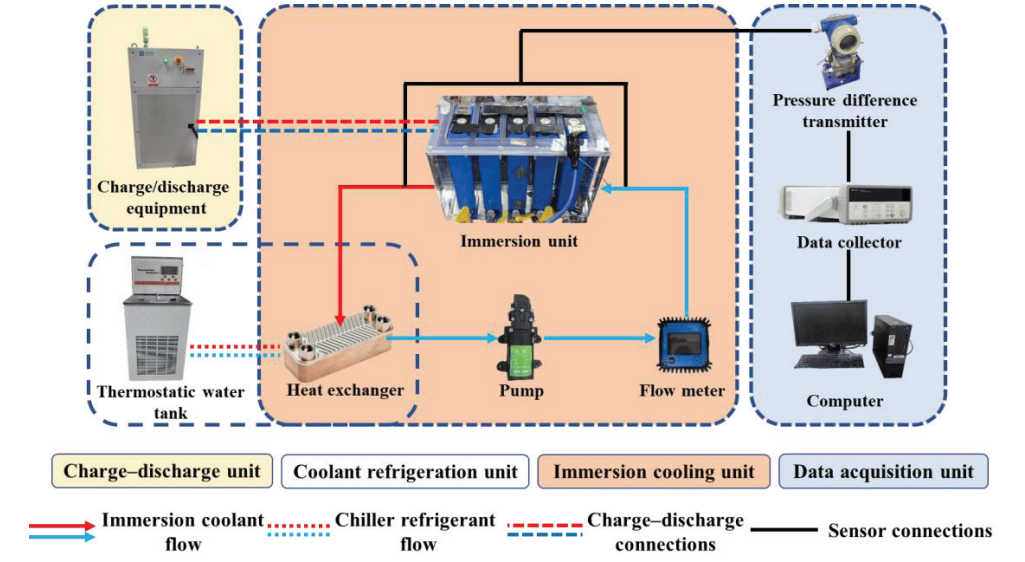

(**a**)

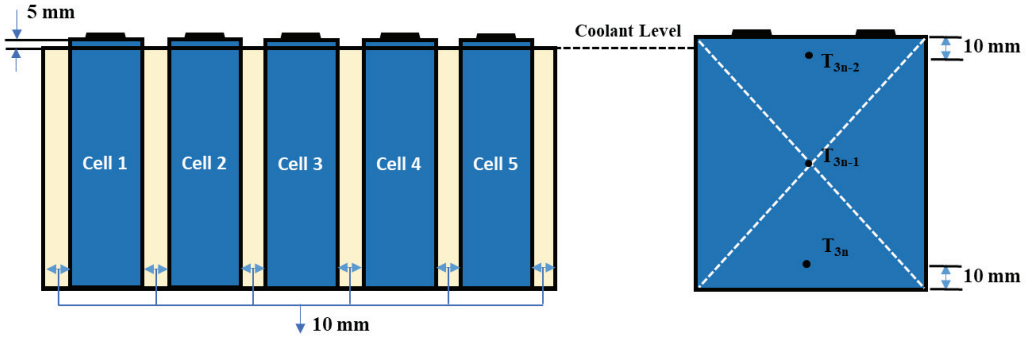

(**b**)

Figure 1. Experimental system of NFDPI cooling: (**a**) experimental diagram, (**b**) the coolant immersion depth, inter-cell intervals, and temperature testing point distribution.

The immersion tank is fabricated from polymethyl methacrylate (PMMA) with 10 mm wall thickness. Its internal dimensions are 195 × 90 × 128.5 mm. The tank is fitted with a 5 mm thick lid whose surface contains five rectangular apertures sized to the cell cross-sections, which position and constrain the battery module. The front and rear faces each incorporate five M10 threaded ports that function as coolant inlets and outlets. The ports are aligned with the cell centerlines. Figure 1b illustrates the coolant immersion depth, inter-cell intervals, and temperature testing point distribution of the immersion cooling unit. The five batteries are arranged at equal intervals with a spacing of 10 mm. In this experiment, the coolant circulates within a sealed immersion cooling loop and contacts air only at the top of the tank. By Bernoulli's principle, the coolant liquid level can be maintained flush with the upper edges of the inlet and outlet ports above the tank, since all other flow passages remain sealed. On this basis, the coolant level was stably maintained 5 mm below the cells' upper edge.

A variable-speed brushless DC pump (HY-521, Huyue Technologies Co., Ltd., Linyi, China) is employed to drive the coolant flow. An electronic turbine flow meter (K24, AWT Technologies Co., Ltd.) is installed near the inlet of the immersion tank to measure the coolant's inlet flow rate. A differential pressure transmitter (DP1300-DP4E22M4B1, Guangzhou Senex Instrument Ltd., Guangzhou, China) is used to measure the pressure

difference between the inlet and outlet of the immersion tank, serving as an indicator of the coolant's flow resistance.

2.2. Battery and Coolant

In the experiment, 24 Ah prismatic batteries (LP2770134, Lishen Ltd., Tianjin, China) were selected as the research subjects, with their specifications listed in Table 1. The battery has a nominal voltage of 3.2 V, an operating voltage range of 2.5 V to 3.65 V, a maximum continuous charging current of 24 A, and a maximum continuous discharging current of 48 A. Prior to the experiment, single batteries were screened using the Hybrid Pulse Power Characterization (HPPC) method [33] to ensure similar internal resistance values among the selected batteries. The battery parameters are listed in Table 1.

Table 1. Specification of prismatic batteries.

Specifications	Parameter
Anode/cathode	$LiFePO_4$/Graphite
Nominal capacity	24 Ah (Minimum 23.5 Ah)
Nominal voltage	3.2 V
Operating voltage range	2.5 V–3.65 V
Maximum charge/discharge rate	1 C/2 C (continuous)
Internal resistance	$\leq$6 mΩ
Dimensions	70 mm $\times$ 27 mm $\times$ 133.5 mm
Weight	513 $\pm$ 8 g

The deionized water (DI water) produced by an ultrapure-water system (CJ-CS-K03, Dongguan Sibaikang Environmental Protection Technology Co., Ltd., Dongguan, China) was used as the immersion coolant. The relevant thermophysical properties and price of DI water at normal temperature (25 °C) are listed in Table 2.

Table 2. The thermophysical parameters (at 25 °C) of deionized water.

Specifications	Parameter
Density (kg/m^3)	997
Conductivity (W/m·K)	0.609
Specific heat (J/kg·K)	4179
Viscosity(m^2/s)	9.1×10^{-7}
Boiling point (°C)	100
Price (CNY/kg)	1.5

2.3. Experimental Procedure

A constant current–constant voltage (CC-CV) charging procedure was employed for the battery module. The charging rate is 0.5 C. The cutoff voltage of charging is 18 V for the 5s1p module, with a cutoff current of 2.4 A (0.1 C). Discharging was conducted under a constant current (CC) protocol, with discharge rate settings at 0.5 C, 1 C, 1.5 C, and 2 C. The cutoff voltage of discharging is 12.5 V for the 5s1p module. Between charge–discharge cycles, the module rested for 1 h to return to its initial temperature and allow electrochemical stabilization. Because heat generation during charging is lower than during discharging, this study focuses on thermal-management performance during discharge. The charge–discharge curves at various C-rates are shown in Figure 2. In all experiments, both the initial cell temperature and the ambient temperature were set to 25 °C.

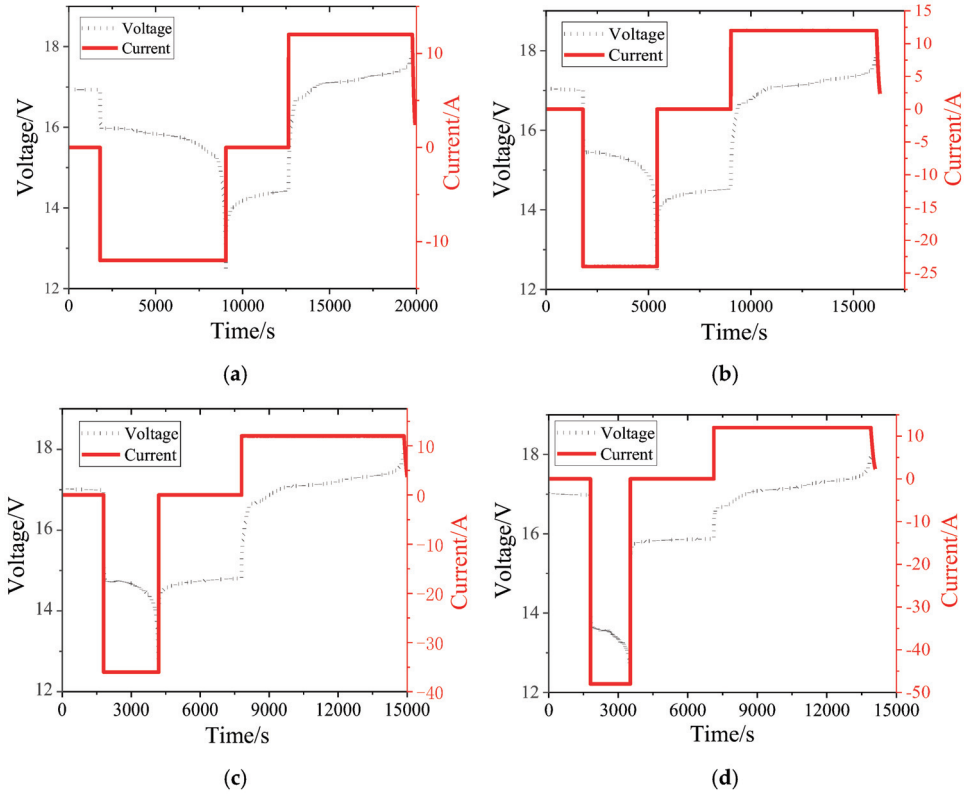

Figure 2. The charge–discharge curves at various C-rates: (**a**) 0.5 C discharge and 0.5 C charge, (**b**) 1 C discharge and 0.5 C charge, (**c**) 1.5 C discharge and 0.5 C charge, and (**d**) 2 C discharge and 0.5 C charge.

2.4. Uncertainty Analysis

Type A uncertainty (u_A) can be measured repeatedly [34]. The u_A was calculated by Equation (1). Here, n is the number of repeated measurements, and x_i and $\overline{x}$ are the individual and mean measured values. Type B uncertainty (u_B) is used to assess parameters based on the inherent data uncertainty of the experimental instruments, typically derived from specifications provided in the instrument's manual [35], which can be calculated by Equation (2). And α is the measurement error of the equipment. Type C uncertainty (u_C) is obtained by combining the Type A and Type B uncertainties, which can be calculated according to Equation (3).

$$u_A = \sqrt{\frac{1}{n(n-1)}\sum_{i=1}^{n}(x_i - \overline{x})^2} \tag{1}$$

$$u_B = \frac{\alpha}{\sqrt{3}} \tag{2}$$

$$u_C = \sqrt[2]{u_A^2 + u_B^2} \tag{3}$$

The primary measured parameters in this experiment include temperature, volumetric flow rate, current, and voltage. Temperature is measured using K-type thermocouples, volumetric flow rate is measured with a flowmeter, and current and voltage are recorded by the battery measurement system of the charge/discharge equipment. The uncertainties associated with these parameters are listed in Table 3.

Table 3. Equipment uncertainty and accuracy of the parameters.

Parameters	u_A	u_B	u_C
Temperature	0.089 °C	0.168 °C	0.190 °C
Volumetric flow rate	-	0.5%	0.5%
Current	-	0.05%	0.05%
Voltage	-	0.05%	0.05%

3. Numerical Model

Direct observation of immersion coolant flow within the immersion tank is challenging. Accordingly, numerical simulations were performed to resolve the flow field under the tested conditions, and the results were integrated with experiments to analyze the thermal-management performance of NFDPI.

3.1. Description of the Module

Figure 3 shows the physical model of the immersion unit. The physical model matches the dimensions of the NFDPI cooling unit used in the experiments. The model includes both the fluid domain (coolant) and the solid domain (battery).

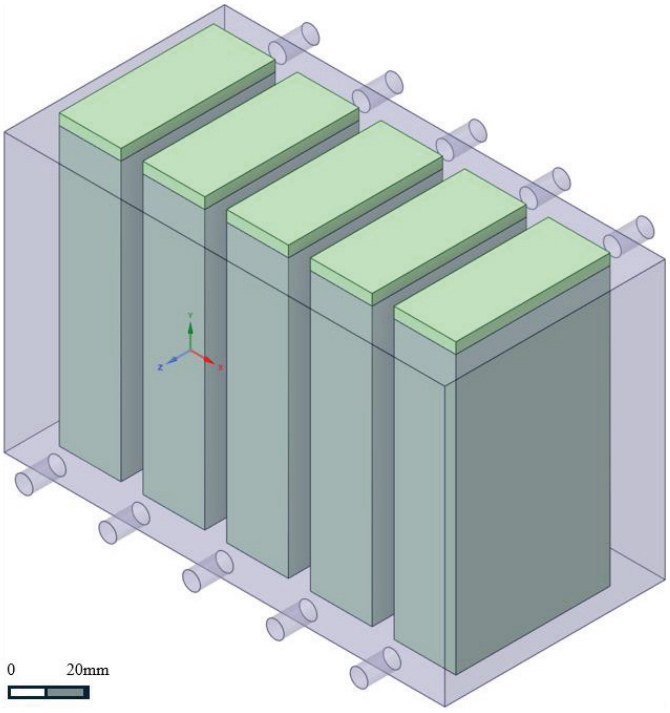

Figure 3. Physical model of the immersion unit.

3.2. Governing Equations

The fluid enters the cooling system through the inlet and subsequently flows through the established fluid channel. The governing equations, including the continuity equation (Equation (4)) and the momentum conservation equation (Equation (5)) to determine the flow field of the cooling fluid, are presented as follows [36]:

Continuity equation:

$$\nabla \cdot \left(\vec{u} \right) = 0 \tag{4}$$

Momentum conservation equation:

$$\frac{\partial}{\partial t}\left(\rho_c \vec{u}\right) + \nabla\left(\rho_c \vec{u}\right)\vec{u} = -\nabla p + \mu_c \nabla^2 \vec{u} \tag{5}$$

where ρ_c, μ_c, and $\vec{u}$ are the density, viscosity, and velocity of the coolant, respectively.

The Reynolds number is a dimensionless quantity that describes the ratio of inertial forces to viscous forces within a fluid and is estimated by Equation (6):

$$Re = \frac{VL}{\mu} \tag{6}$$

Here, V is the volumetric flow rate of coolant; L denotes the characteristic length of the coolant flow channel, which is regarded as the liquid level; and μ represents the dynamic viscosity of the coolant. The Reynolds number under the investigated conditions ranges from 73.77 to 442.64. Accordingly, a laminar-flow model was employed for the numerical simulations.

3.3. Boundary Conditions and Initial Conditions

All inlets were assigned a specified velocity boundary condition, with the velocity vector oriented normal to the boundary surface. Under different operating conditions, the volume flow rates of the immersion coolant at the inlets were set to 250 mL/min, 500 mL/min, 1000 mL/min, and 1500 mL/min, respectively, with equal mass flow rates distributed among all inlets. At the outlets, a pressure boundary condition was applied, with the gauge pressure set to 0 Pa.

3.4. Numerical Strategy

The numerical model for the immersion cooling system was developed within the framework of the commercial Computational Fluid Dynamics (CFD) solver, Fluent® (Ansys Ltd., Canonsburg, PA, USA). This solver utilizes the finite volume method for spatial discretization. For the advective terms, a second-order upwind differencing scheme was employed.

Figure 4 shows the computational mesh of the model. The computational mesh is composed of hexahedral elements. To ensure sufficient resolution, local mesh refinement was applied in regions near walls and at the inlet/outlet boundaries. A grid independence study was conducted to assess the sensitivity of the simulation results to the mesh density. The verification process is illustrated using an example with a flow rate of 1500 mL/min. This example employs a top-in/bottom-out configuration, featuring a single, centrally located inlet and outlet. Four different meshes are applied to discretize the model, and the cross-sectional average velocities of the fluid are presented in Table 4. The results indicate that a grid size of 4.5×10^5 is appropriate, as further increases in grid size result in negligible improvements in the results.

Table 4. Grid independence verification.

Case	Number of Grids (Million)	Cross-Sectional Average Velocity (m/s)
1	0.3	2.60×10^{-3}
2	0.4	2.66×10^{-3}
3	0.45	2.69×10^{-3}
4	0.55	2.70×10^{-3}

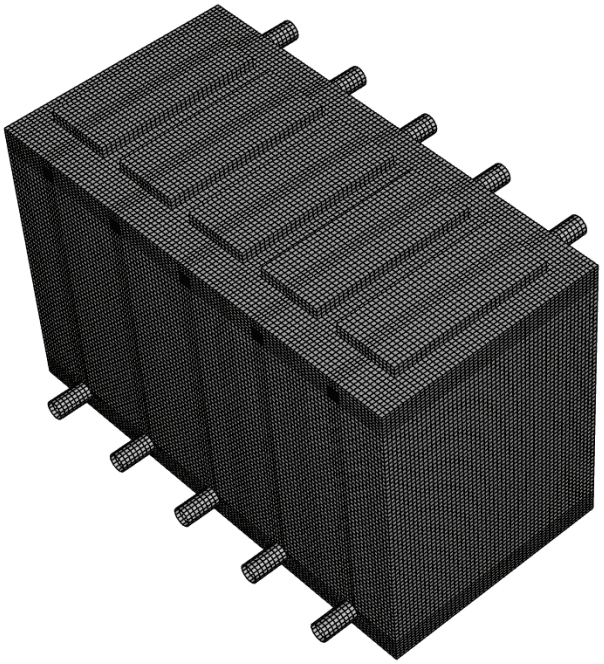

Figure 4. Computational mesh of the model.

4. Results and Discussion

The experimental and numerical results of the battery module's thermal management performance are discussed in this section. The module's maximum temperature ($T_{\max}$) and the maximum temperature difference within the module ($\Delta T_{\max}$) are defined as follows:

$$T_{max} = \max\{T_{1-15}\} \tag{7}$$

$$\Delta T_{max} = \max\{T_{1-15}\} - \min\{T_{1-15}\} \tag{8}$$

Under NFDPI immersion cooling, intra-cell temperature nonuniformity must be considered. Because the cell's upper region carries a higher current density and is partially immersed, its temperature exceeds that of the lower region. The maximum vertical temperature difference within a single cell is calculated as follows:

$$\Delta T_{v-max} = \max\{T_{3n-2} - T_{3n}\} \tag{9}$$

where n is the cell number (n = 1, 2, 3, 4, 5).

4.1. Air Natural Convection Cooling

Air natural convection was first evaluated as the baseline condition. The 5s1p battery module was placed in an empty immersion tank without liquid coolant, relying solely on ambient air for heat removal. Under 1 C discharge, Figure 5a shows the evolution of each cell's surface temperature, and Figure 5b shows the module's $T_{\max}$ and $\Delta T_{\max}$.

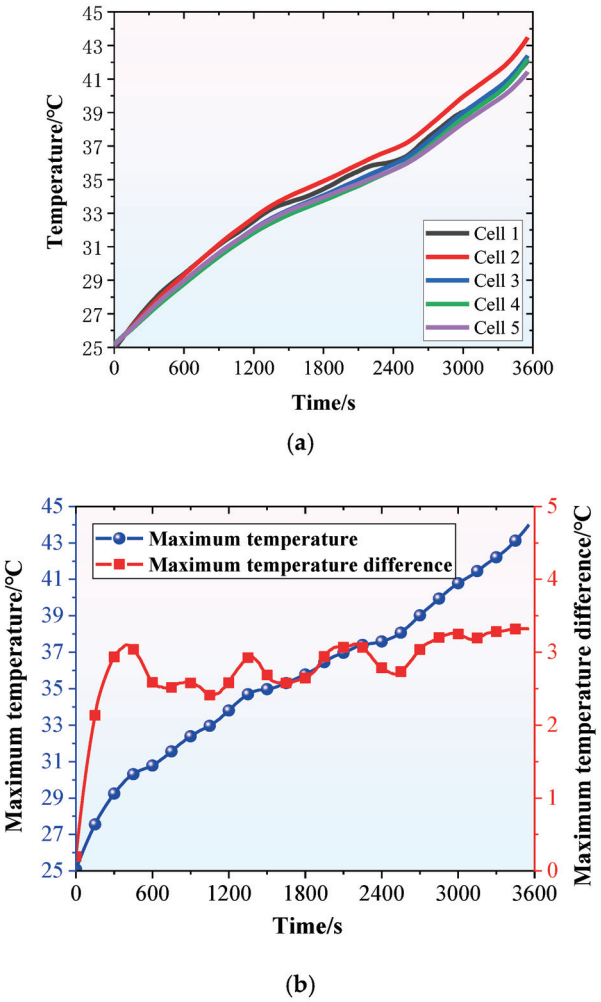

Figure 5. Thermal management performance under natural convection cooling: (**a**) the temperature variation of the cells; (**b**) T_{max} and ΔT_{max}.

During discharge, the average maximum temperature across the five cells reaches 42.33 °C, an increase of 17.16 °C from the initial state. As shown in Figure 5b, the module's T_{max} is 43.97 °C, and ΔT_{max} is 3.43 °C. Because air natural convection provides limited cooling capacity, each cell's T_{max} exceeds 40 °C, surpassing commonly recommended limits for long-term LIB operation. The module's ΔT_{max} rises rapidly after the onset of discharge and then fluctuates around a steady value. The temperature nonuniformity arises primarily from (i) intrinsic cell-to-cell variations and (ii) nonuniform heat-dissipation conditions. Therefore, air natural convection alone is inadequate for thermal management at high discharge rates and cannot ensure module safety or reliability.

4.2. Static Partial Immersion Cooling

For comparison, a static immersion cooling test was performed as an additional baseline. Under static immersion (no forced flow), Figure 6a shows the cell-level temperature variation, and Figure 6b shows the module's T_{max} and ΔT_{max}. During discharge, the average maximum temperature across the five cells reaches 32.17 °C, an increase of 7.16 °C from the initial state. As shown in Figure 5a, the module's T_{max} is 33.07 °C, and ΔT_{max} is 2.10 °C. Relative to natural convection, both the peak temperature and intra-module temperature nonuniformity are markedly lower.

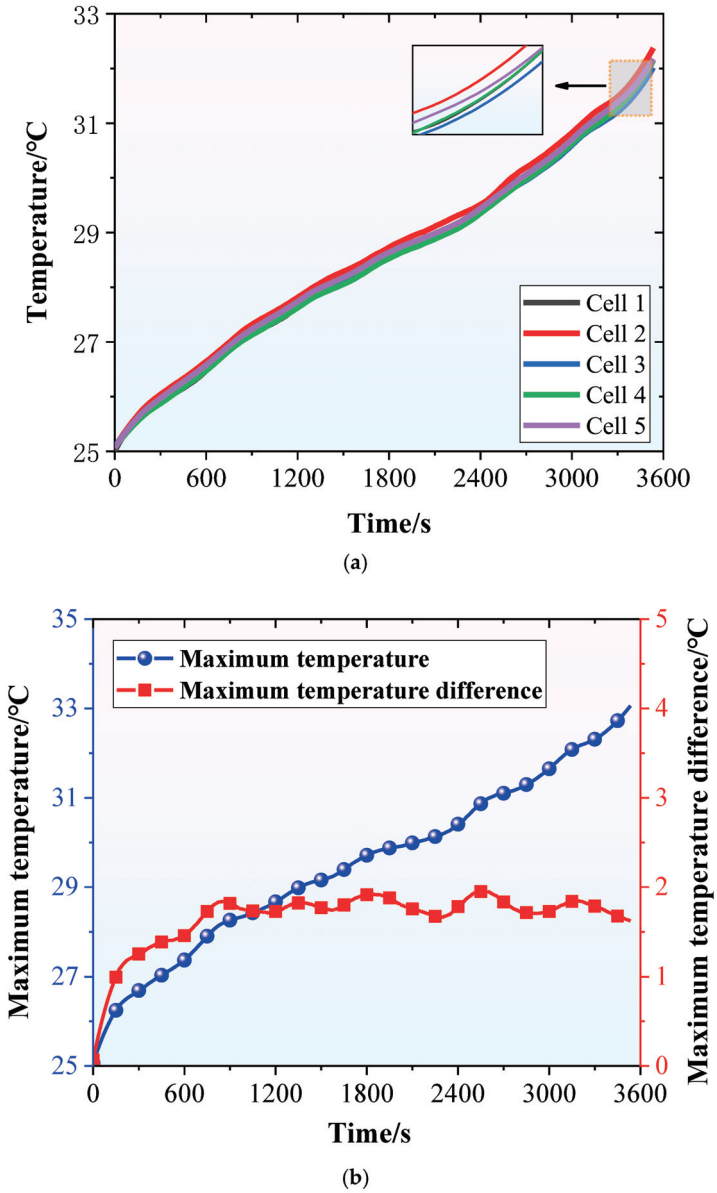

Figure 6. Thermal management performance under static immersion cooling: (**a**) the temperature variation of the cells; (**b**) T_{max} and ΔT_{max}.

Because static immersion cooling relies primarily on thermal conduction and natural convection, the temporal evolution of the cell temperature under static immersion closely resembles that under air natural convection. The key difference is the presence of a liquid coolant that wets most of the cell—only a small, unsubmerged region remains air-cooled—while the liquid's higher thermal conductivity and heat capacity markedly reduce overall temperatures. Direct liquid–solid contact also promotes more uniform heat transfer to the surrounding fluid, mitigating local hot spots. Overall, static immersion cooling outperforms natural air convection by lowering the average temperature and improving module-level thermal uniformity.

4.3. Effect of the Coolant Flow Rate

In LIBs' immersion cooling systems, the coolant flow rate is a primary determinant of heat-transfer performance. It controls the cell-surface convective heat-transfer coefficient and overall cooling capacity, but it also dictates the circulation loop's energy consumption.

A systematic investigation of flow-rate effects, therefore, can clarify the thermal response across cooling and support selection of an operating condition that balances thermal performance and energy efficiency.

In this subsection, flow rates of 250, 500, 1000, and 1500 mL/min were tested under a top-in/bottom-out configuration with a single, centrally located inlet and outlet. The initial temperatures of both the cells and the coolant were maintained at 25.0 ± 0.2 °C. The chiller setpoint supplying the coolant was held constant across tests.

Figure 7 presents the 1 C discharge response at 250 mL·min^{-1}. The five cell temperatures exhibit a rapid–gradual–slight re-acceleration rising pattern. Early in the discharge, temperature climbs quickly because ohmic heating dominates while the coolant–cell temperature difference is small, limiting convection. During the mid-stage, the fluid convection is strong, and the temperature rise moderates. Near end-of-discharge, as the open-circuit voltage falls and internal resistance increases, polarization losses raise heat generation, producing a renewed temperature upturn. At cutoff, the average peak cell temperature is 28.08 °C; the module T_{max} is 29.35 °C, and the ΔT_{max} is 2.35 °C. Compared with natural convection and static immersion, the lower T_{max} reflects the enhanced cooling capacity of pump-driven forced convection. The temperature nonuniformity is smaller than under natural convection but larger than under static immersion, attributable to flow maldistribution around individual cells. During discharge, the coolant inlet temperature remains essentially constant, whereas the outlet temperature rises in step with the cell temperatures. The outlet temperature reaches a maximum of 26.53 °C.

Subsequently, higher flow rates were tested to assess the NFDPI system's cooling performance. Figures 8–10 show the module temperature evolution during 1 C discharge at 500, 1000, and 1500 mL/min, respectively. Meanwhile, the T_{max} and ΔT_{max} of the battery module during the whole discharge across flow rates are listed in Table 5. Increasing flow slightly reduces the module-average temperature and the T_{max} due to enhancing the cell-coolant convective heat transfer. In addition, because water has a high heat capacity, its temperature rise is limited; for similar inlet temperatures, a higher flow shortens the residence time in the immersion tank and further reduces the outlet temperature.

The module's ΔT_{max} decreases with increasing flow rate, which is contrary to the common expectation. Usually, for a fixed-geometry battery module, increasing the coolant flow rate exacerbates flow maldistribution around the cells and, as a result, increases the ΔT_{max}. In water-based NFDPI cooling, however, ΔT_{max} arises from multiple sources: (i) intrinsic cell-to-cell variation, (ii) flow maldistribution, and (iii) vertical temperature gradients within individual cells caused by height-dependent heat removal. As the cells were pre-screened for comparable internal resistance, intrinsic variation is unlikely to be the dominant contributor.

Because direct visualization of the in-tank flow field is challenging, numerical simulations were conducted across the tested flow rates; the resulting flow fields are shown in Figure 11. The coolant enters through the inlet and impinges directly on Cell 3, then splits laterally. Peak velocities occur near the lower outer regions of Cells 1 and 5, whereas the channels adjacent to Cell 2 and between Cells 3 and 4 exhibit weaker throughflow. Both side channels next to Cell 3 carry throughflow, but their fractional share of the total flow decreases slightly as the bulk flow rate increases. Overall, increasing the flow rate does not substantially alter the in-tank flow topology or the degree of inter-cell flow maldistribution.

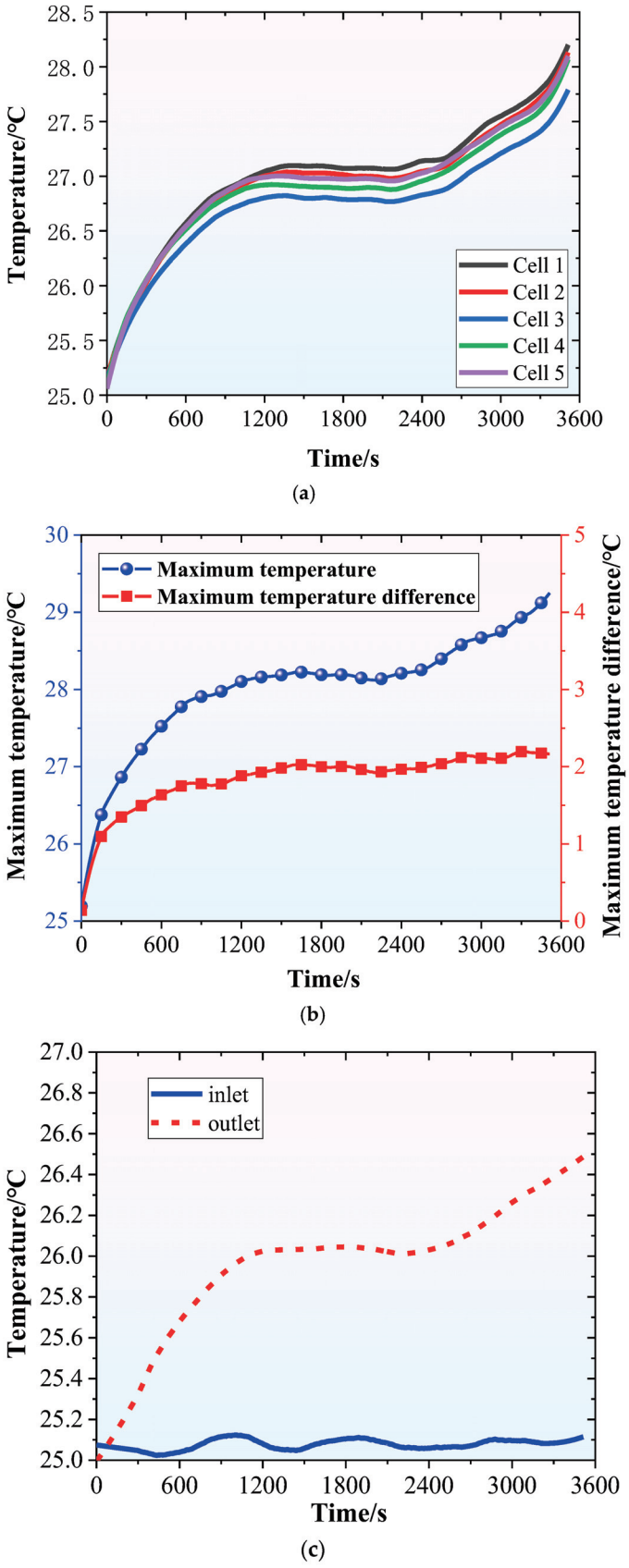

Figure 7. Thermal management performance at 250 mL/min flow rate: (**a**) the temperature variation of the cells; (**b**) T_{max} and ΔT_{max}; (**c**) inlet and outlet temperature.

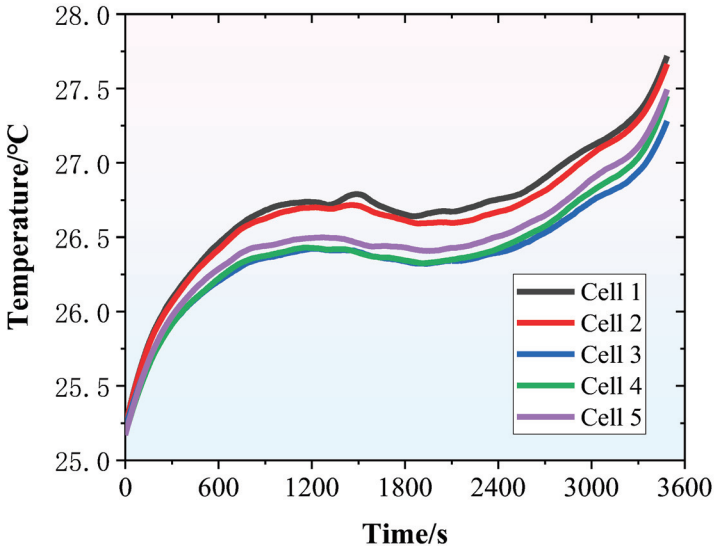

(**a**)

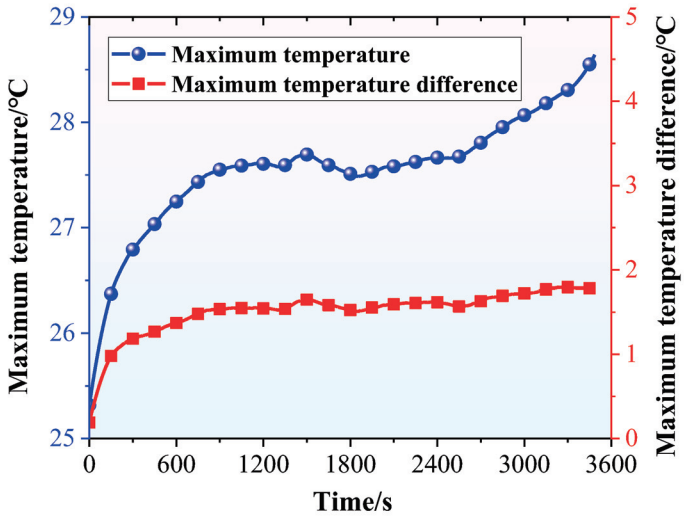

(**b**)

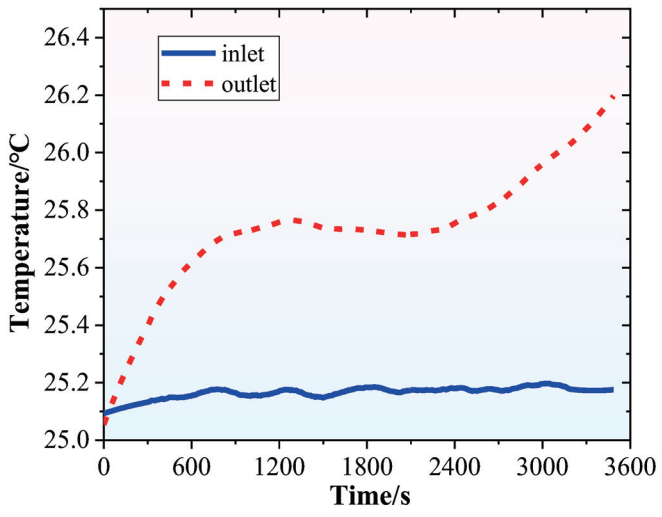

(**c**)

Figure 8. Thermal management performance at 500 mL/min flow rate: (**a**) the temperature variation of the cells; (**b**) T_{max} and ΔT_{max}; (**c**) inlet and outlet temperature.

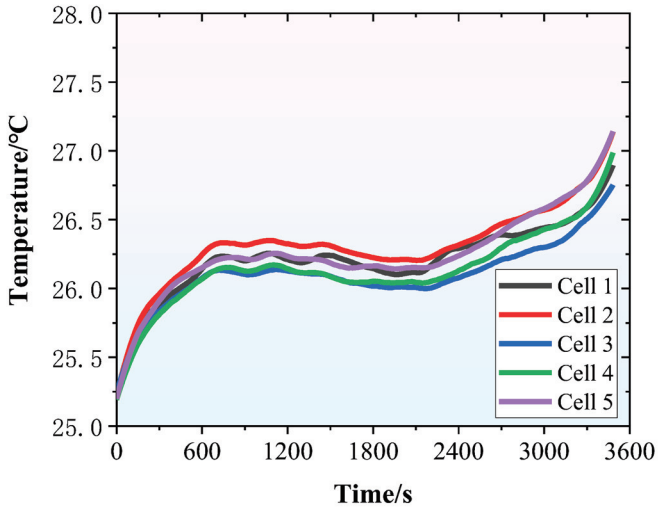

(**a**)

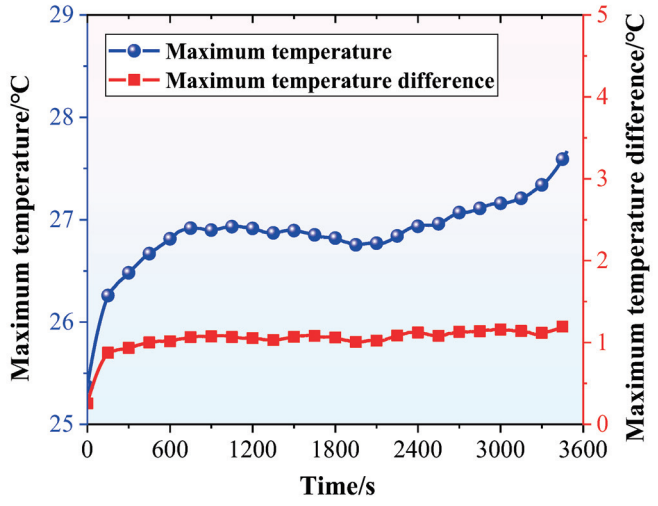

(**b**)

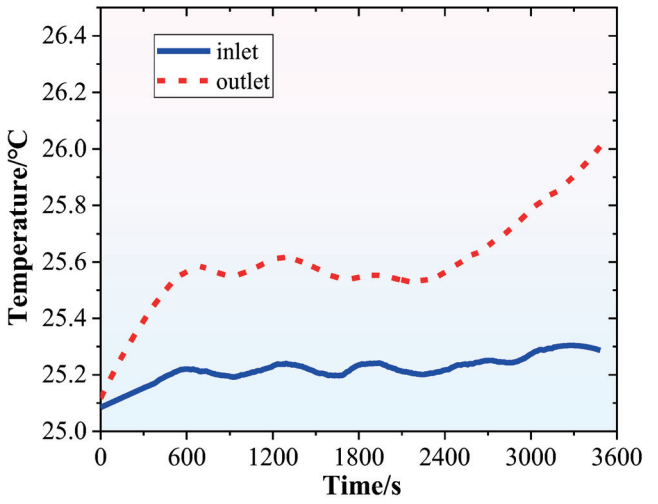

(**c**)

Figure 9. The thermal management performance at 1000 mL/min flow rate: (**a**) the temperature variation of the cells; (**b**) T_{max} and ΔT_{max}; (**c**) inlet and outlet temperature.

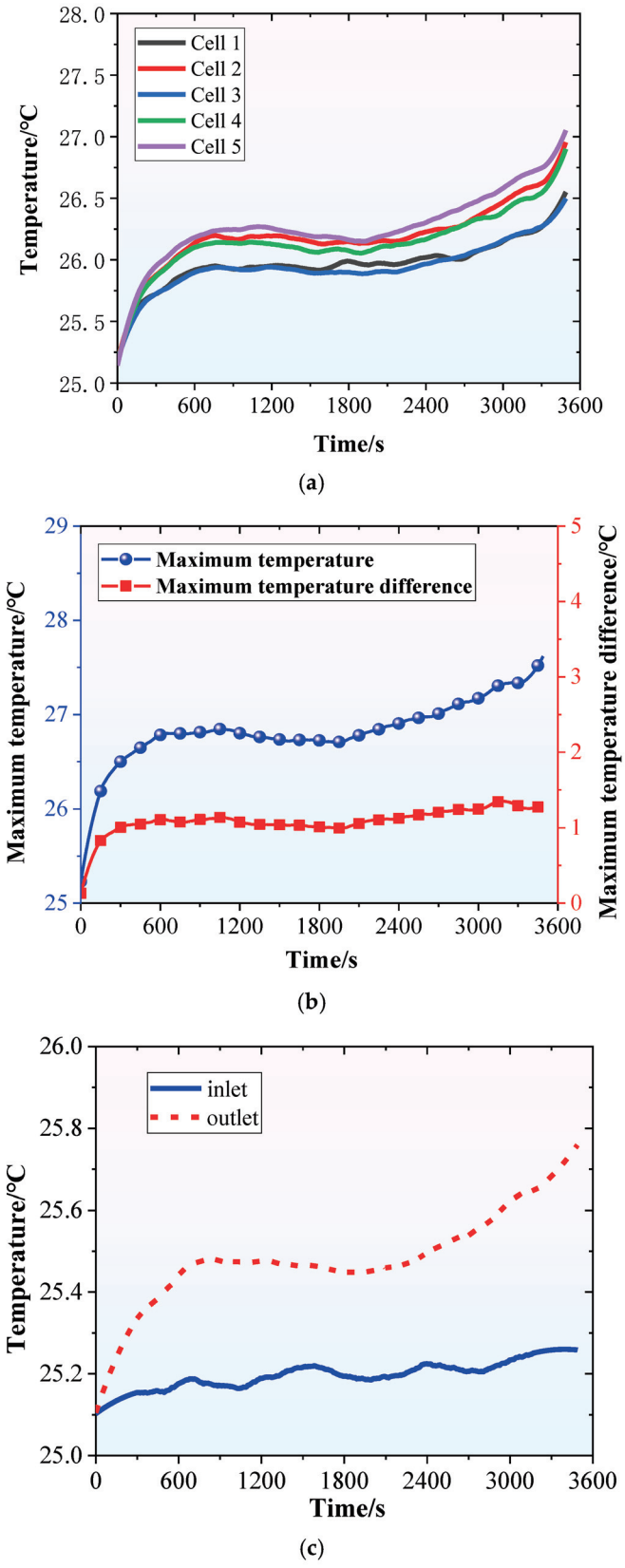

Figure 10. Thermal management performance at 1500 mL/min flow rate: (**a**) the temperature variation of the cells; (**b**) T_{max} and ΔT_{max}; (**c**) inlet and outlet temperature.

Table 5. Overall T_{max}, ΔT_{max}, and $\Delta T_{v\text{-}max}$ across flow rates.

Flow Rate (mL/min)	T_{max} (°C)	ΔT_{max} (°C)	$\Delta T_{v\text{-}max}$ (°C)
250	29.35	2.35	2.13
500	28.73	1.91	1.86
1000	27.70	1.46	1.17
1500	27.67	1.34	1.11

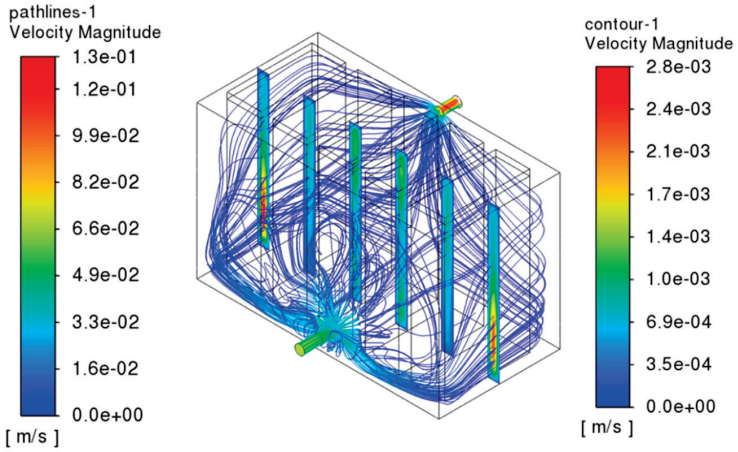

(**a**)

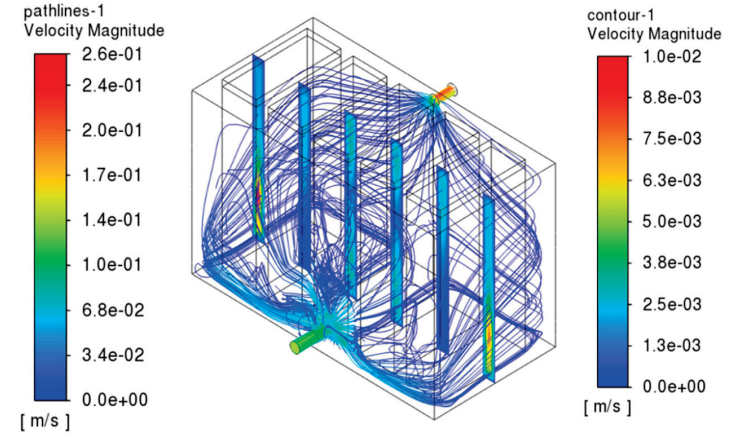

(**b**)

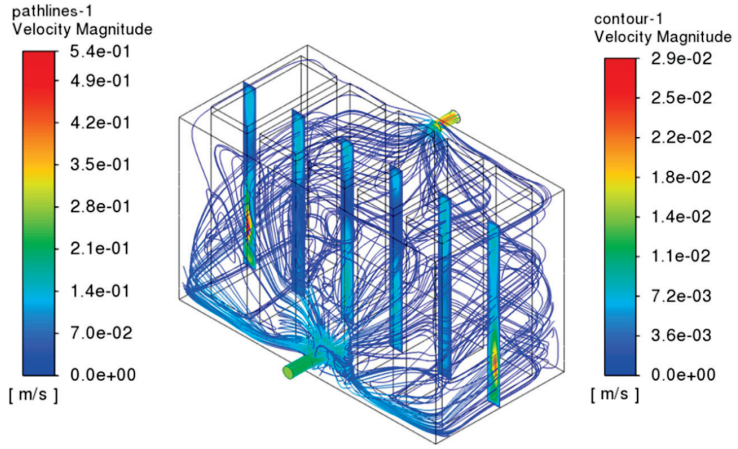

(**c**)

Figure 11. *Cont.*

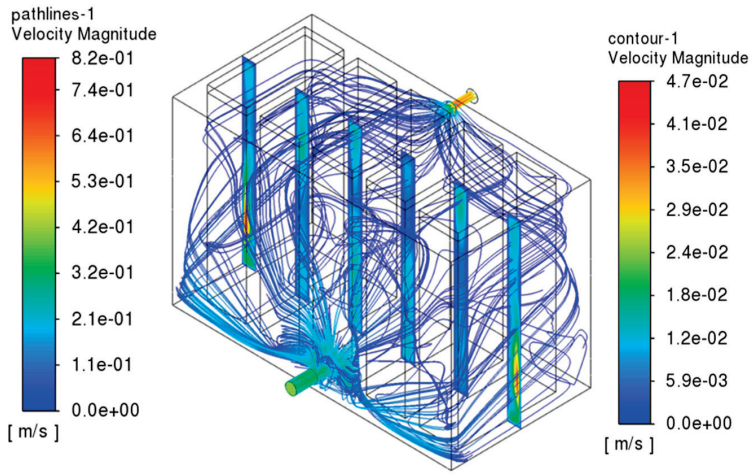

(**d**)

Figure 11. Flow distribution in the immersion tank at different coolant flow rates: (**a**) 250 mL/min, (**b**) 500 mL/min, (**c**) 1000 mL/min, and (**d**) 1500 mL/min.

Under NFDPI immersion cooling, heat is removed from each cell by two mechanisms: natural convection over the unsubmerged region and forced convection between the liquid coolant and the immersed surfaces, the latter being markedly more effective. Because current density is nonuniform—especially near the tabs—the upper half experiences greater ohmic/polarization heating than the lower half, producing a hotter top and cooler bottom during discharge. Table 5 also summarizes the maximum vertical intra-cell temperature difference ($\Delta T_{\text{v-max}}$) and the module-level $\Delta T_{\max}$ for each flow rate. Across flow rates, the vertical $\Delta T_{\text{v-max}}$ is only slightly smaller than $\Delta T_{\max}$, indicating that intra-cell vertical gradients dominate the module's temperature nonuniformity. As the flow rate increases, stronger forced convection—particularly on the inlet side—reduces the temperature of the cell's upper region, thereby decreasing the $\Delta T_{\max}$ and $\Delta T_{\text{v-max}}$.

A differential-pressure transmitter measured the pressure drop across the system (between the main inlet and outlet) at each flow rate; the results are summarized in Table 6. Because pressure drop—and thus pump power consumption—increases markedly with flow rate, the selected flow should balance thermal performance against system-level energy consumption.

Table 6. Pressure drop between the main inlet and outlet at different flow rates.

Flow Rate (mL/min)	Pressure Drop (Pa)
250	15.8
500	289.0
1000	831.8
1500	1499.3

4.4. Effect of the Discharge Rate

Under NFDPI immersion cooling, higher discharge rates increase heat generation and exacerbate intra-cell vertical temperature gradients, thereby increasing the module-level $\Delta T_{\max}$. Assessing NFDPI across discharge rates therefore delineates suitable operating conditions and optimization. Discharge rates of 0.5, 1.0, 1.5, and 2.0 C were examined under identical hydraulic conditions (500 mL/min; top-central inlet, bottom-central outlet) to quantify variations in cooling effectiveness.

Figure 12 presents the temperature evolution under NFDPI cooling at 0.5 C discharge. The mean cell temperature increases only gradually during discharge; at cutoff, it is 26.07 °C, while the module's peak temperature and maximum spread are 26.35 °C and 0.56 °C, respectively. Hence, at 0.5 C, NFDPI provides strong thermal control, maintaining both the T_{max} and ΔT_{max} at low levels.

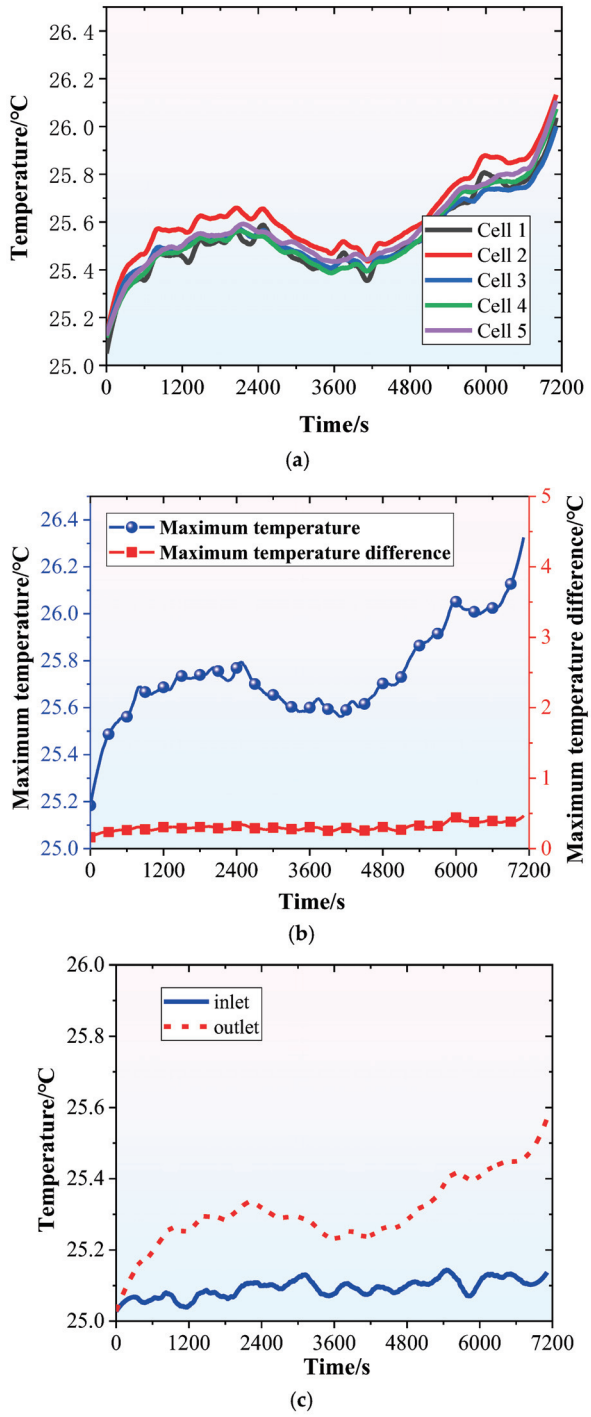

Figure 12. Thermal management performance at 0.5 C discharge rate: (**a**) the temperature variation of the cells; (**b**) T_{max} and ΔT_{max}; (**c**) inlet and outlet temperature.

Figure 12 presents the temperature evolution under NFDPI immersion cooling during 0.5 C discharge. The surface cell temperature rose gradually; at cutoff, it is 26.07 °C,

whereas the module's T_{max} and ΔT_{max} are 26.35 °C and 0.56 °C, respectively. NFDPI cooling provides effective thermal control, maintaining low T_{max} and ΔT_{max} at 0.5 C.

Figure 13 presents the temperature evolution under NFDPI immersion cooling during 1.5 C discharge. At the end of discharge, the average cell temperature is 29.50 °C; the module's T_{max} is 31.94 °C, and the ΔT_{max} is 4.06 °C. Thus, at 1.5 C, NFDPI maintains effective temperature control; however, both ΔT_{max} and the cell-level peak temperature increase markedly relative to 0.5 and 1.0 C.

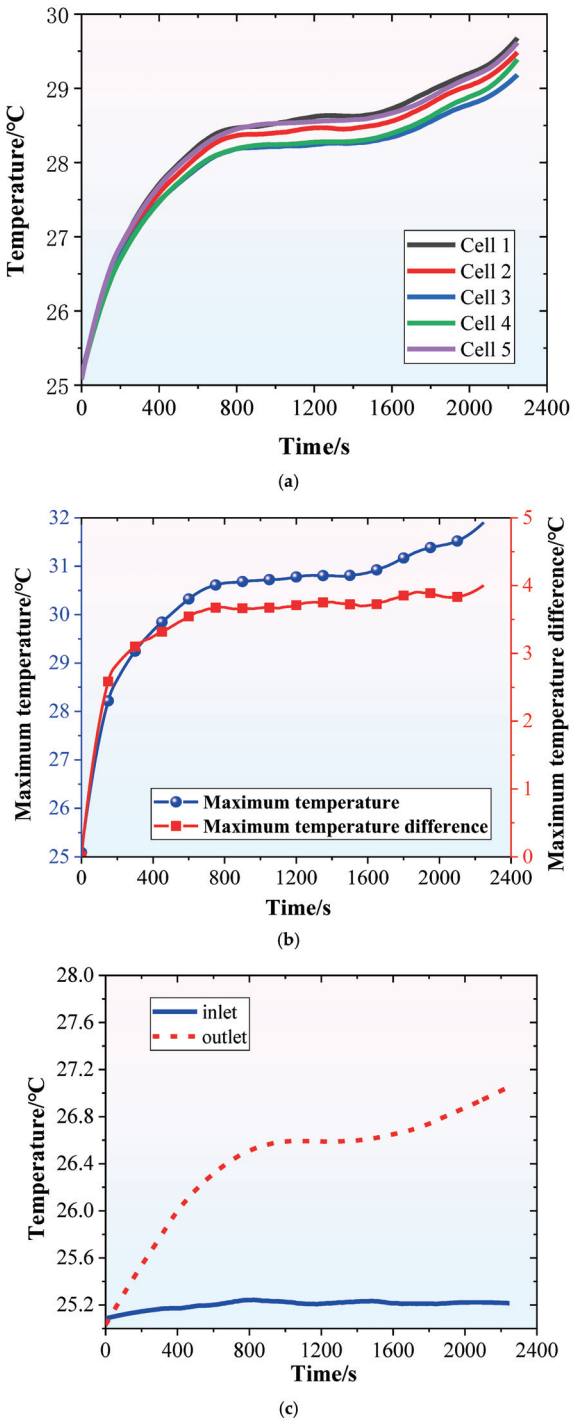

Figure 13. Thermal management performance at 1.5 C discharge rate: (**a**) the temperature variation of the cells; (**b**) T_{max} and ΔT_{max}; (**c**) inlet and outlet temperature.

Figure 14 presents the temperature evolution under NFDPI immersion cooling during 2.0 C discharge. At cutoff, the average cell temperature is 31.68 °C; the module's T_{max} is 36.75 °C, and the ΔT_{max} is 8.01 °C. Although absolute temperatures remain moderate, ΔT_{max} exceeds 5 °C, indicating that this NFDPI configuration does not meet thermal-management requirements at 2.0 C. Table 7 presents the module's T_{max}, ΔT_{max}, and $\Delta T_{v\text{-}max}$ across different discharge rates. With increasing discharge rate, T_{max}, ΔT_{max}, and $\Delta T_{v\text{-}max}$ rise markedly, though T_{max} remains below 40 °C. When the discharge rate is no more than 1.5 C, ΔT_{max} stays within 5 °C, meeting LIBs' thermal-management requirements. When the discharge is up to 2 C, both ΔT_{max} and $\Delta T_{v\text{-}max}$ exceed acceptable limits. Sustaining NFDPI at higher discharge rates would require further optimization of the flow configuration to reduce the temperature of the cell's upper region.

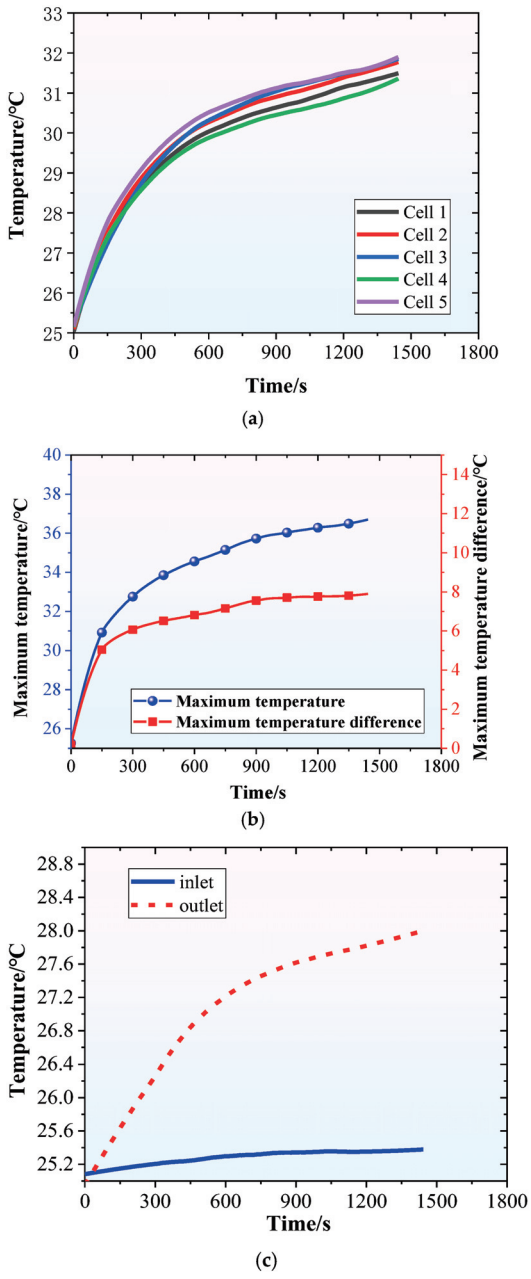

Figure 14. Thermal management performance at 2 C discharge rate: (**a**) the temperature variation of the cells; (**b**) T_{max} and ΔT_{max}; (**c**) inlet and outlet temperature.

Table 7. Overall T_{max}, ΔT_{max}, and $\Delta T_{v\text{-}max}$ across discharge rates.

Discharge Rate	T_{max} (°C)	ΔT_{max} (°C)	$\Delta T_{v\text{-}max}$ (°C)
0.5	26.35	0.56	0.44
1	28.73	1.91	1.86
1.5	31.94	4.06	3.82
2	36.75	8.01	7.97

Under typical operating conditions, heat generation in an LIB arises mainly from two contributions: (i) irreversible (ohmic/Joule) heating associated with internal resistance and (ii) reversible entropic heat from electrochemical reactions. Assuming spatially uniform volumetric heat generation, Bernardi et al. [37] analyzed these mechanisms and derived a theoretical expression for the cell heat-generation rate:

$$Q_{cell} = -IT\frac{dU}{dT} + I(OCV - U) \tag{10}$$

Here, $-IT(\mathrm{d}U/\mathrm{d}T)$ represents the reversible heat associated with the entropy change of the electrochemical reaction, while $I(OCV-U)$ denotes the irreversible heat arising from ohmic and polarization losses. I is the current (positive for charging, negative for discharging); OCV is the open-circuit voltage; T is the absolute temperature; U is the operating voltage; and $\mathrm{d}U/\mathrm{d}T$ is the entropy coefficient.

According to the Bernardi energy-balance relation, increasing the discharge rate raises irreversible (ohmic/polarization) heating rapidly, thereby increasing the cell-surface heat flux q. Under the present conditions, the flow in the immersion tank remains largely laminar, so the local convective heat-transfer coefficient h increases only modestly. Thus, characteristic temperature gradients scale approximately with q/h. Moreover, the NFDPI configuration is vertically asymmetric: the immersed lower region experiences liquid–solid forced convection, whereas the unsubmerged upper region relies solely on natural air convection. At higher discharge rates, the upper region cannot reject the additional heat promptly, amplifying the cell's longitudinal temperature gradient. Meanwhile, Joule heating near the tabs is often above the liquid surface, which means this part of heat is less effectively removed by air natural convection. Consequently, in water-based NFDPI, absolute temperatures remain moderate at elevated discharge rates, but the module ΔT_{max} increases substantially relative to lower discharge rates.

4.5. Effect of the Inlet and Outlet Configuration

In water-based NFDPI cooling, the inlet–outlet configuration affects the coolant flow and heat transfer within the immersion unit, thereby governing both the T_{max} and the ΔT_{max}. Only a single-inlet/single-outlet, top-in/bottom-out configuration was considered in the preceding analysis. This subsection evaluates alternative inlet–outlet configurations.

4.5.1. Effect of the Position of Inlet and Outlet

Figure 15 presents the temperature evolution and flow-field distribution for the bottom-in/top-out configuration. Compared with the top-in/bottom-out arrangement, the mean cell temperature and the module's ΔT_{max} are lower—27.33 °C and 28.58 °C, respectively—while the ΔT_{max} is higher at 2.19 °C. Zhong et al. [31] observed that natural convection should not be ignored, even with pump-driven forced convection, especially at low flow rates. Under the present conditions, dimensionless numbers can be used to judge whether buoyancy effects may be neglected.

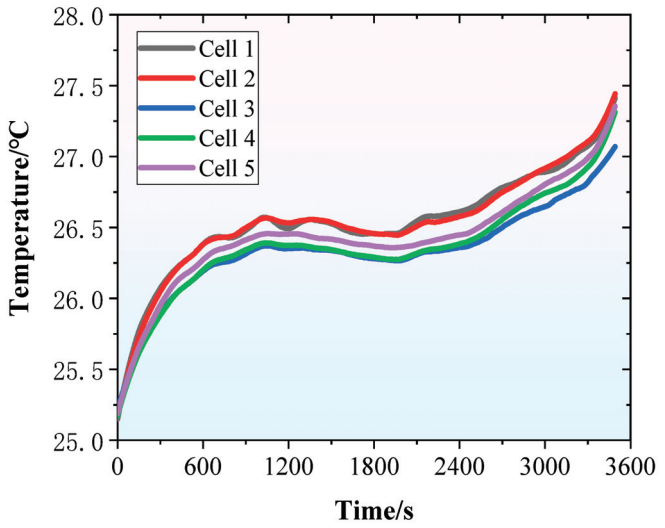

(**a**)

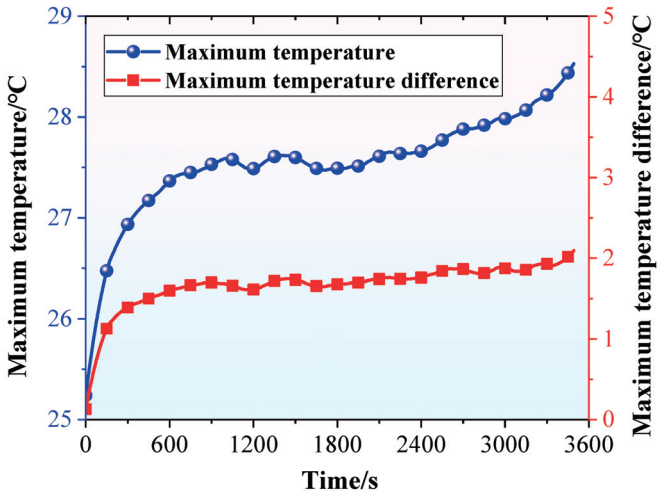

(**b**)

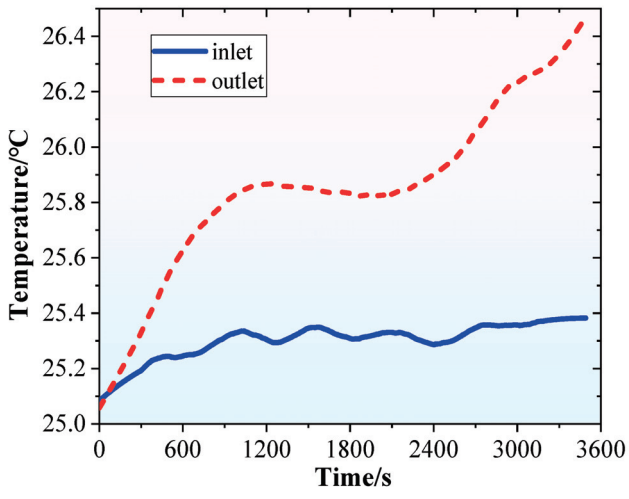

(**c**)

Figure 15. *Cont.*

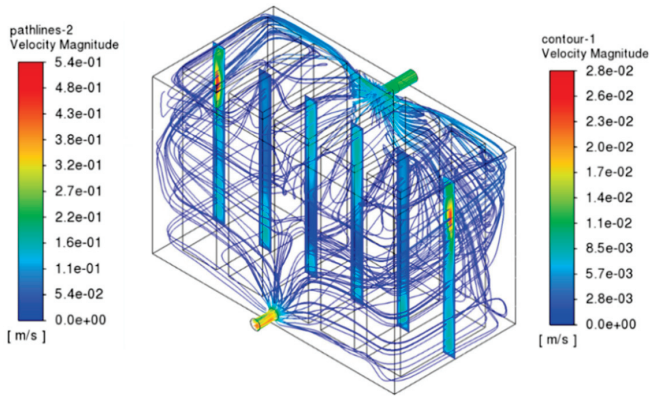

(**d**)

Figure 15. Thermal management performance with a bottom-in/top-out configuration: (**a**) the temperature variation of the cells; (**b**) T_{max} and ΔT_{max}; (**c**) inlet and outlet temperature; (**d**) flow-field distribution.

Figure 15 presents the temperature evolution and the flow field for the bottom-in/top-out configuration. At the end of discharge, the average cell temperature and the module's T_{max} are 27.33 °C and 28.58 °C, respectively, which are lower than those of the top-in/bottom-out arrangement. The ΔT_{max} is 2.19 °C, which is higher than that of the top-in/bottom-out arrangement. Zhong et al. [31] observed that natural convection remains non-negligible, even with pump-driven forced convection, particularly at low flow rates.

To quantify the relative strength of buoyancy and viscous resistance in a fluid, the Grashof number (Gr) is a dimensionless number in fluid dynamics and heat transfer, representing the ratio of buoyancy forces to viscous forces in a fluid. It is used to quantify the intensity of natural convection and is calculated by Equation (11):

$$Gr = \frac{g\beta\left(T_{battery} - T_{water}\right)l^3}{v^2} \tag{11}$$

where g is the represents the acceleration of gravity, 9.8 m/s^2; β is the thermal expansion coefficient of the coolant; $T_{battery}$ is the average temperature of the battery module; T_{water} is the temperature of coolant; v is the kinematic viscosity of the coolant; and l is the characteristic length, which is regarded as the coolant's immersion depth.

To characterize the relative strength of buoyancy and inertial forces in mixed convection, the Archimedes number (Ar) can evaluate the characteristics of mixed convection. The Ar is calculated by Equation (12):

$$Ar = \frac{Gr}{Re^2} \tag{12}$$

When $Ar < 0.01$, the influence of natural convection can be neglected; when $0.01 < Ar < 0.1$, the influence of natural convection is weak; when $0.1 < Ar < 10$, natural convection and forced convection act together [38]. Based on the calculations, the stabilized Archimedes number (Ar) falls between 0.14 and 0.24, indicating mixed convection in which forced and natural convection coexist. With the bottom-in/top-out layout, the lower region remains cooler while the upper region becomes warmer along the flow path. Buoyancy therefore reinforces the pump-driven upward flow, enhancing heat transfer and yielding lower module-average and peak temperatures than the top-in/bottom-out scheme. However, the cells are cooler at the bottom and hotter at the top, and the coolant

exhibits the same vertical stratification. Consequently, the intra-cell vertical temperature gradient steepens, increasing the ΔT_{max}. The increase in ΔT_{max} is driven predominantly by the strengthened vertical gradient in the unsubmerged upper region, compounded by inter-cell flow maldistribution.

Figure 16 presents the temperature evolution and flow field for the upper-right inlet/lower-left outlet configuration. Under this arrangement, at the end of discharging, the average cell temperature and the module's T_{max} are 27.60 °C and 28.98 °C, respectively, while the ΔT_{max} is 2.10 °C. Relative to the top-in/bottom-out layout, the hydraulic path is longer, and in addition to the primary downward stream, a right-to-left crossflow develops. The simulated flow field exhibits stagnation zones. The right-to-left crossflow traps heat in that direction, leading to lateral accumulation. Consequently, ΔT_{max} remains comparatively large. The extended hydraulic path also increases the pressure drop. Simulations further reveal that under this inlet–outlet configuration, flow is highly maldistributed across the module. Coolant circulation is markedly weaker around cells farther from the inlet.

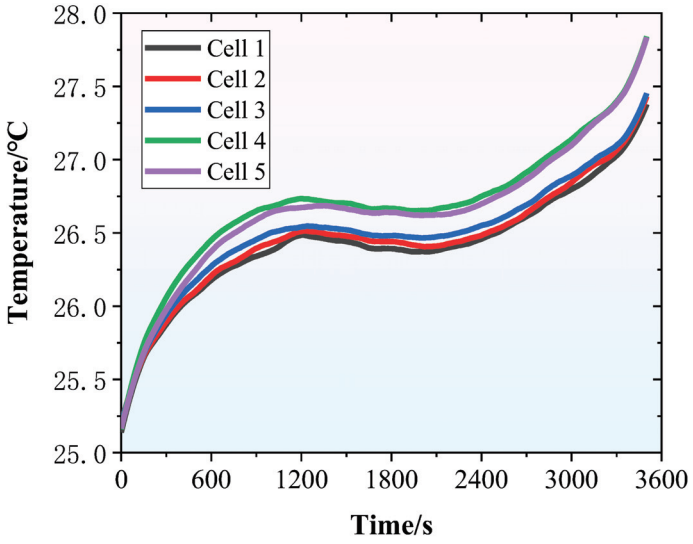

(a)

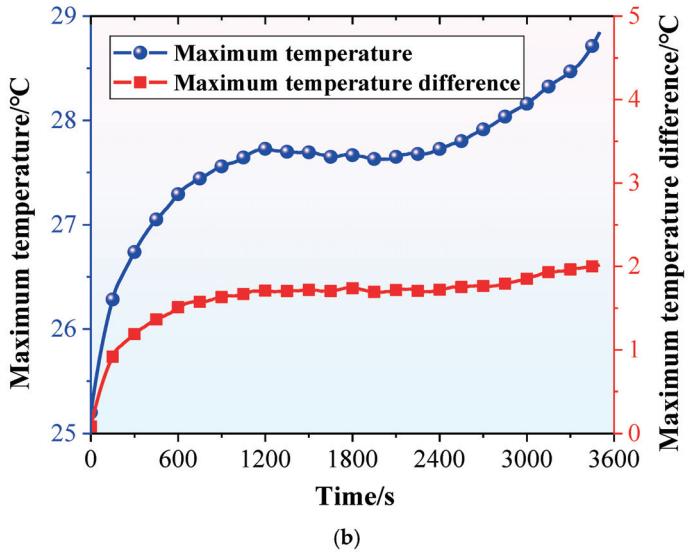

(b)

Figure 16. *Cont.*

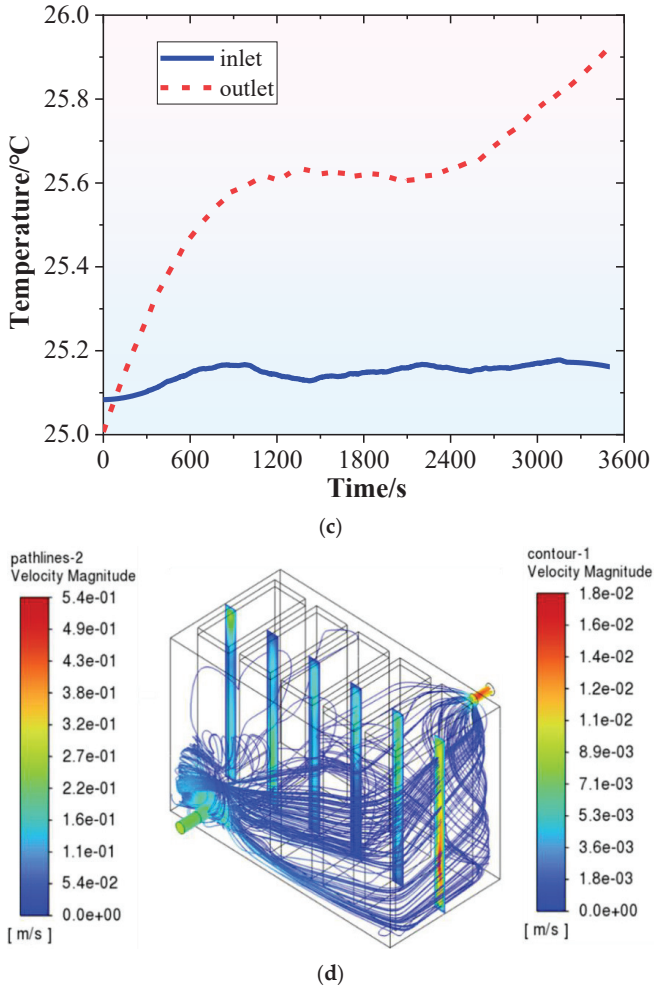

Figure 16. Thermal management performance with a top-right-in/bottom-left-out configuration: (**a**) the temperature variation of the cells; (**b**) T_{max} and ΔT_{max}; (**c**) inlet and outlet temperature; (**d**) flow-field distribution.

4.5.2. Effect of the Number of Inlets

The effect of increasing the number of inlets on NFDPI immersion cooling was examined, considering three and five inlets (Figures 17 and 18). With three inlets, the module's T_{max} is 29.34 °C, and the ΔT_{max} is 2.48 °C; with five inlets, the corresponding values are 29.22 °C and 2.39 °C. Table 8 lists T_{max}, ΔT_{max}, and $\Delta T_{v\text{-}max}$ across the inlet number. Compared with the single-inlet case, dividing the total flow among multiple inlets slightly increases both the T_{max} and ΔT_{max}. Table 8 also shows that a larger vertical temperature gradient coincides with a higher ΔT_{max}. In simulations under identical total flow rate, inlet temperature, and operating conditions, increasing the number of top inlets from three to five improves flow-distribution uniformity. Distributing the injected momentum among more entry points produces multi-point feeding at the top, which breaks the primary circulation into several smaller eddies and reduces low-velocity and recirculation zones. Increasing the number of inlets improves coolant circulation around the cell upper regions, with the effect most pronounced in the three central cells. However, dividing the fixed total volumetric flow among additional inlets reduces the per-inlet flow rate and jet momentum, so the overall cooling performance shows only marginal improvement over the three-inlet configuration.

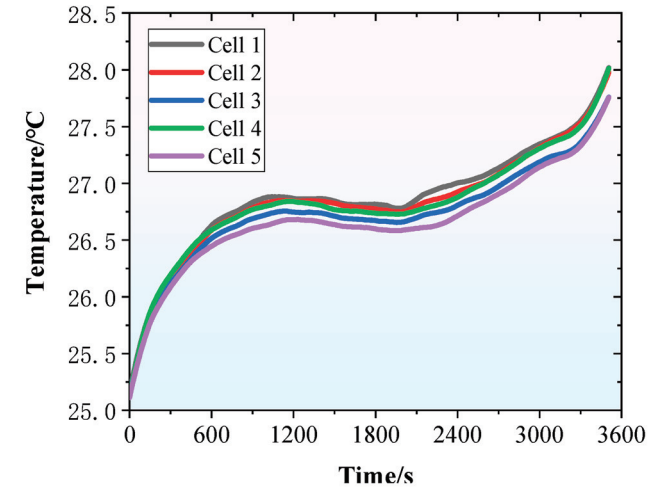

(a)

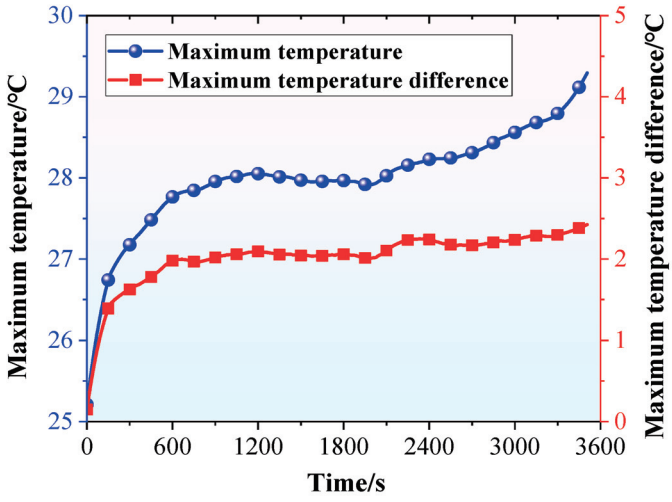

(b)

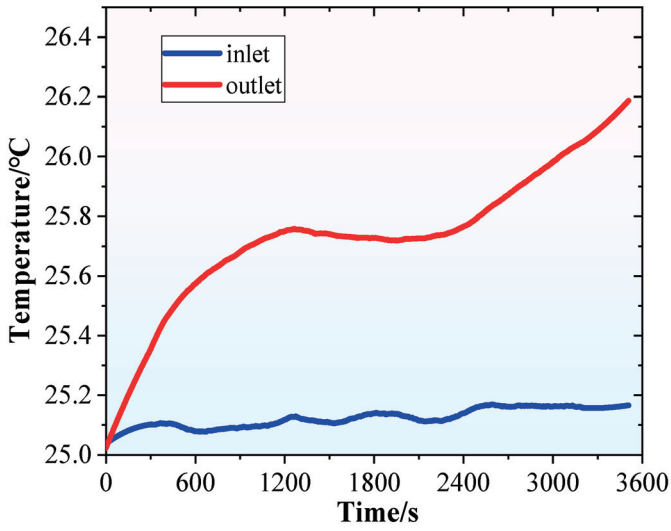

(c)

Figure 17. *Cont.*

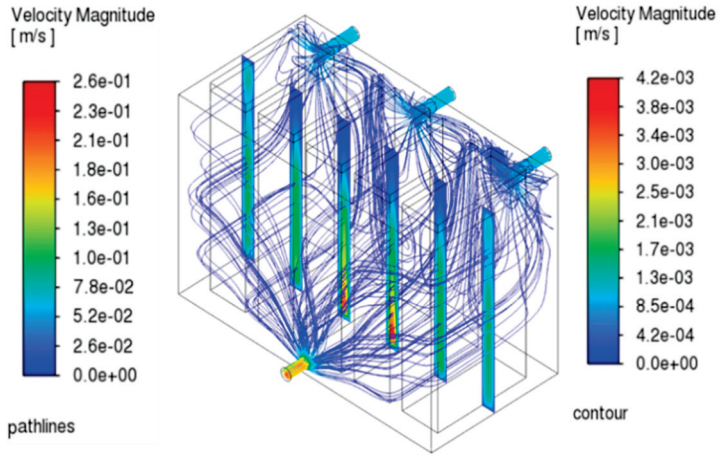

(**d**)

Figure 17. Thermal management performance with inlet number 3: (**a**) the temperature variation of the cells; (**b**) T_{max} and ΔT_{max}; (**c**) inlet and outlet temperature; (**d**) flow-field distribution.

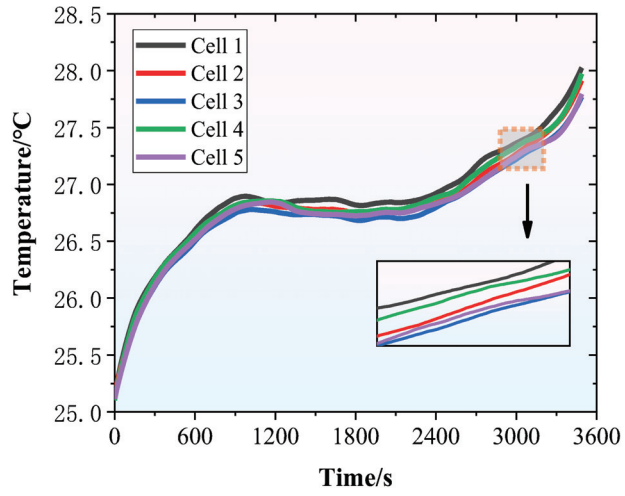

(**a**)

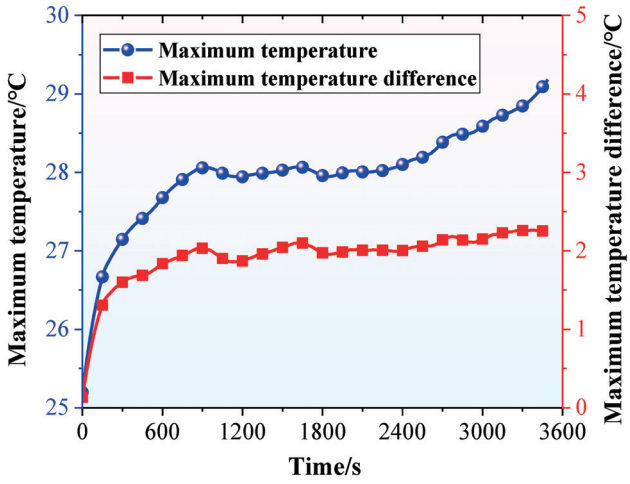

(**b**)

Figure 18. *Cont.*

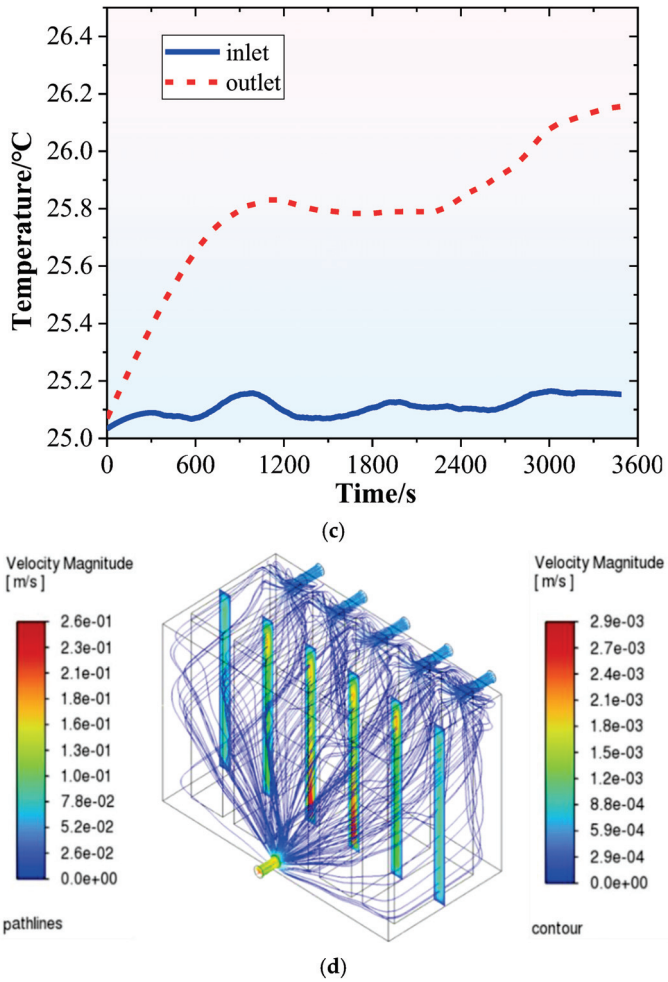

Figure 18. Thermal management performance with inlet number 5: (**a**) the temperature variation of the cells; (**b**) T_{max} and ΔT_{max}; (**c**) inlet and outlet temperature; (**d**) flow-field distribution.

Table 8. Overall T_{max}, ΔT_{max}, and $\Delta T_{v\text{-}max}$ across inlet number.

Inlet Number	T_{max} (°C)	ΔT_{max} (°C)	$\Delta T_{v\text{-}max}$ (°C)
1	28.73	1.91	1.86
3	29.34	2.48	2.24
5	29.22	2.39	2.31

Flow resistance depends on the inlet–outlet configuration. Table 9 summarizes the total pressure drop between the main inlet and outlet for each configuration. The bottom-in/top-out layout yields a higher pressure drop than the top-in/bottom-out layout because the flow ascends against gravity. Increasing the number of inlets increases the effective flow area, reduces the mean velocity, and lowers the pressure drop.

Table 9. Pressure drop between the main inlet and outlet at different inlet and outlet configurations.

Inlet and Outlet Configurations	Pressure Drop (Pa)
Bottom-in/top-out configuration	394.0
Top-right-in/bottom-left-out configuration	453.6
Inlet number is 3	185.3
Inlet number is 5	170.6

4.6. FMEA of the NFDPI System

To comprehensively assess the reliability and safety of the proposed NFDPI cooling system, a simplified Failure Modes and Effects Analysis (FMEA) was conducted. The analysis identifies potential failure modes, causes, effects, and mitigation strategies across key components of the system, including the battery module, DI water immersion coolant, and pump/flow circuit.

Table 10 summarizes the major failure modes and their associated Risk Priority Numbers (RPNs). The RPN can be calculated by Equation (13):

$$RPN = S \times \mathrm{O} \times \mathrm{D} \tag{13}$$

where the S (Severity) is the failure consequence level; the O (Occurrence) is the possibility of occurrence; and the D (Detection) denotes how easily a failure can be detected through design or control measures before it occurs or leads to severe consequences. These three parameters are rated on a 1–10 scale according to severity. The FMEA results indicate that the most critical risks originate from battery failure and seal degradation, which exhibit relatively high RPN values.

Table 10. Simplified FMEA for the NFDPI cooling system.

Component	Failure Mode	Possible Cause	RPN = S × O × D
Battery	Thermal runaway	Ageing or short circuit	81 = 9 × 3 × 3
Immersion coolant	Contamination	Impurities	40 = 5 × 4 × 2
Pump and pipeline	Pump failure or blockage	Motor burnout, debris	48 = 8 × 3 × 2
Sealing system	Seal degradation	Seal wear, improper assembly	72 = 9 × 4 × 2

4.7. Comparison with Alternative Cooling Technologies

To further highlight the advantages of the proposed NFDPI cooling method, a qualitative comparison with several representative thermal management approaches for LIB energy storage systems is presented. Table 11 summarizes five common methods: forced air cooling, cold-plate liquid cooling, full immersion (oil-based) cooling, full immersion (fluorinated liquid) cooling, and the current NFDPI (water-based) cooling. Key evaluation criteria include system complexity, thermal-management performance, energy consumption, estimated cost, and so on.

From the table, it can be seen that while forced air cooling offers the lowest cost and simplest system, its thermal-management performance is limited. Cold-plate liquid cooling improves performance but at increased complexity and cost. Full immersion using dielectric oils or fluorinated liquids provides excellent thermal uniformity and low temperature rise, yet suffers from high cost, potential flammability (for oils), and system complexity. In contrast, the water-based NFDPI cooling system achieves a favorable performance, which offers high cooling performance and temperature uniformity and lower cost and energy penalty while maintaining moderate system complexity and cost.

Table 11. Comparison with alternative LIB thermal management technologies.

Method	Coolant	System Complexity	Thermal Management Performance	Energy Consumption	Estimated Cost
Forced Air Cooling	Air	Low	Low	Low	Low
Cold-Plate Liquid Cooling	Water/Glycol	Moderate	Moderate–high	Moderate	Moderate
Full Immersion (Oil-based)	Dielectric oil	Moderate–High	High	High	Moderate-high
Full Immersion (Fluorinated liquid)	Fluorinated liquid	High	High	Moderate	High
NFDPI (Water-based, this study)	DI Water	Moderate	Very high	Moderate	Moderate

This comparative analysis demonstrates that the proposed NFDPI cooling holds significant promise for large-scale LIB energy storage applications, offering a highly competitive option in terms of both performance and practical deployment.

5. Conclusions

This study experimentally evaluated the thermal-management performance of NFDPI immersion cooling, quantifying the effects of coolant flow rate, battery discharge rate, and inlet–outlet configuration to inform practical implementation. The main findings are summarized below.

(1) Water-based NFDPI immersion cooling outperforms both natural convection and static immersion (no flow), yielding a lower module maximum temperature (T_{max}) and a smaller maximum temperature difference (ΔT_{max}).

(2) At 1 C, increasing the flow rate strengthens convection and reduces the module-average temperature and the T_{max} at end-of-discharge. As the vertical temperature gradient weakens with increasing flow and then saturates, the ΔT_{max} decreases initially and then approaches a plateau. The vertical temperature difference with a single cell is a primary contributor to ΔT_{max}.

(3) As the C-rate increased, NFDPI maintained effective temperature control up to 2.0 C. At 2.0 C, the module T_{max} was 36.75 °C, but the module-level ΔT_{max} reached 8.01 °C, exceeding safe-operating limits. NFDPI exhibited robust thermal management performance at and below 1.5 C.

(4) Inlet–outlet layout strongly shapes performance. Bottom-in/top-out yields a lower peak temperature than top-in/bottom-out, but with a larger ΔT_{max} and higher inlet–outlet pressure drops. Diagonal inlet–outlet arrangements increase both T_{max} and ΔT_{max} and further raise the pressure drop. Increasing the number of inlets slightly elevates peak and average temperatures while significantly reducing pressure drop.

These findings lay a foundation for designing safer, more efficient NFDPI immersion cooling strategies for LIBs.

Author Contributions: Conceptualization, X.Z., Y.Q. and F.J.; Methodology, X.Z., P.P., Y.W., W.L., W.W., Y.Q. and F.J.; Software, F.J.; Validation, X.Z., P.P., Y.W., W.L., W.W. and Y.Q.; Formal analysis, X.Z., P.P., Y.W., W.L., W.W. and Y.Q.; Investigation, X.Z., P.P., Y.W., W.L., W.W., Y.Q. and F.J.; Resources, F.J.; Data curation, X.Z., P.P., Y.W., W.L., W.W. and Y.Q.; Writing—original draft, X.Z. and P.P.; Writing—review & editing, F.J.; Visualization, X.Z., P.P., W.L. and Y.Q.; Supervision, Y.Q. and F.J.; Project administration, F.J.; Funding acquisition, F.J. All authors have read and agreed to the published version of the manuscript.

Funding: The Postdoctoral Fellowship Program of China Postdoctoral Science Foundation funded project (Grant Number GZC20232687) and the State Grid Zhejiang Electric Power Co., Ltd. Science and Technology Research Program (Grant Number B311DS24000H) supported this work.

Data Availability Statement: The original contributions presented in this study are included in the article. Further inquiries can be directed to the corresponding authors.

Conflicts of Interest: The authors declare no conflict of interest. The authors declare that this study received funding from the State Grid Zhejiang Electric Power Co., Ltd. The funder was not involved in the study design, collection, analysis, interpretation of data, the writing of this article or the decision to submit it for publication.

References

1. Kim, T.; Song, W.; Son, D.-Y.; Ono, L.K.; Qi, Y. Lithium-ion batteries: Outlook on present, future, and hybridized technologies. *J. Mater. Chem. A* **2019**, *7*, 2942–2964. [CrossRef]
2. Feng, Y.; Zhou, L.; Ma, H.; Wu, Z.; Zhao, Q.; Li, H.; Zhang, K.; Chen, J. Challenges and advances in wide-temperature rechargeable lithium batteries. *Energy Environ. Sci.* **2022**, *15*, 1711–1759. [CrossRef]
3. Hasib, S.A.; Islam, S.; Chakrabortty, R.K.; Ryan, M.J.; Saha, D.K.; Ahamed, M.H.; Moyeen, S.I.; Das, S.K.; Ali, M.F.; Islam, M.R.; et al. A Comprehensive Review of Available Battery Datasets, RUL Prediction Approaches, and Advanced Battery Management. *IEEE Access* **2021**, *9*, 86166–86193. [CrossRef]
4. Qiu, Y.; Jiang, F. A review on passive and active strategies of enhancing the safety of lithium-ion batteries. *Int. J. Heat Mass Transf.* **2022**, *184*, 122288. [CrossRef]
5. Sabbah, R.; Kizilel, R.; Selman, J.R.; Al-Hallaj, S. Active (air-cooled) vs. passive (phase change material) thermal management of high power lithium-ion packs: Limitation of temperature rise and uniformity of temperature distribution. *J. Power Sources* **2008**, *182*, 630–638. [CrossRef]
6. Ling, Z.; Wang, F.; Fang, X.; Gao, X.; Zhang, Z. A hybrid thermal management system for lithium ion batteries combining phase change materials with forced-air cooling. *Appl. Energy* **2015**, *148*, 403–409. [CrossRef]
7. Tousi, M.; Sarchami, A.; Kiani, M.; Najafi, M.; Houshfar, E. Numerical study of novel liquid-cooled thermal management system for cylindrical Li-ion battery packs under high discharge rate based on AgO nanofluid and copper sheath. *J. Energy Storage* **2021**, *41*, 102910. [CrossRef]
8. Ling, Z.; Cao, J.; Zhang, W.; Zhang, Z.; Fang, X.; Gao, X. Compact liquid cooling strategy with phase change materials for Li-ion batteries optimized using response surface methodology. *Appl. Energy* **2018**, *228*, 777–788. [CrossRef]
9. Jang, D.S.; Yun, S.; Hong, S.H.; Cho, W.; Kim, Y. Performance characteristics of a novel heat pipe-assisted liquid cooling system for the thermal management of lithium-ion batteries. *Energy Convers. Manag.* **2022**, *251*, 115001. [CrossRef]
10. Cao, J.; Luo, M.; Fang, X.; Ling, Z.; Zhang, Z. Liquid cooling with phase change materials for cylindrical Li-ion batteries: An experimental and numerical study. *Energy* **2020**, *191*, 116565. [CrossRef]
11. Cao, J.; Ling, Z.; Fang, X.; Zhang, Z. Delayed liquid cooling strategy with phase change material to achieve high temperature uniformity of Li-ion battery under high-rate discharge. *J. Power Sources* **2020**, *450*, 227673. [CrossRef]
12. Wang, K.; Cai, N.; Yu, F.; Wang, M. Bead-like PCM composite network with reinforced heat storage performance for highly efficient battery cooling. *J. Energy Storage* **2022**, *54*, 105335. [CrossRef]
13. Mousavi, S.; Siavashi, M.; Zadehkabir, A. A new design for hybrid cooling of Li-ion battery pack utilizing PCM and mini channel cold plates. *Appl. Therm. Eng.* **2021**, *197*, 117398. [CrossRef]
14. Liu, X.; Yao, L.-C.; Su, C.-Q.; Xiong, X.; Wang, Y.-P. A hybrid battery thermal management system coupling with PCM and optimized thermoelectric cooling for high-rate discharge condition. *Case Stud. Therm. Eng.* **2023**, *49*, 103269. [CrossRef]
15. Isfahani, M.S.; Gharehghani, A.; Saeedipour, S.; Rabiei, M. PCM/metal foam and microchannels hybrid thermal management system for cooling of Li-ion battery. *J. Energy Storage* **2023**, *72*, 108789. [CrossRef]
16. Bondareva, N.S.; Sheremet, M.A. Conjugate heat transfer in the PCM-based heat storage system with finned copper profile: Application in electronics cooling. *Int. J. Heat Mass Transf.* **2018**, *124*, 1275–1284. [CrossRef]
17. Weragoda, D.M.; Tian, G.; Burkitbayev, A.; Lo, K.-H.; Zhang, T. A comprehensive review on heat pipe based battery thermal management systems. *Appl. Therm. Eng.* **2023**, *224*, 120070. [CrossRef]
18. Wang, J.; Gan, Y.; Liang, J.; Tan, M.; Li, Y. Sensitivity analysis of factors influencing a heat pipe-based thermal management system for a battery module with cylindrical cells. *Appl. Therm. Eng.* **2019**, *151*, 475–485. [CrossRef]
19. Behi, H.; Karimi, D.; Behi, M.; Jaguemont, J.; Ghanbarpour, M.; Behnia, M.; Berecibar, M.; Van Mierlo, J. Thermal management analysis using heat pipe in the high current discharging of lithium-ion battery in electric vehicles. *J. Energy Storage* **2020**, *32*, 101893. [CrossRef]
20. Behi, H.; Karimi, D.; Behi, M.; Ghanbarpour, M.; Jaguemont, J.; Sokkeh, M.A.; Gandoman, F.H.; Berecibar, M.; Van Mierlo, J. A new concept of thermal management system in Li-ion battery using air cooling and heat pipe for electric vehicles. *Appl. Therm. Eng.* **2020**, *174*, 115280. [CrossRef]
21. Wang, T.; Tseng, K.J.; Zhao, J.; Wei, Z. Thermal investigation of lithium-ion battery module with different cell arrangement structures and forced air-cooling strategies. *Appl. Energy* **2014**, *134*, 229–238. [CrossRef]
22. Wu, W.; Wang, S.; Wu, W.; Chen, K.; Hong, S.; Lai, Y. A critical review of battery thermal performance and liquid based battery thermal management. *Energy Convers. Manag.* **2019**, *182*, 262–281. [CrossRef]
23. Luo, J.; Zou, D.; Wang, Y.; Wang, S.; Huang, L. Battery thermal management systems (BTMs) based on phase change material (PCM): A comprehensive review. *Chem. Eng. J.* **2022**, *430*, 132741. [CrossRef]

24. Wang, Y.; Li, C.; Wen, X.; Cai, W.; Jiang, Y.; Wen, C.; Wang, Y.; Hu, L.; Yu, H.; Zhu, H.; et al. Experimental studies on two-phase immersion liquid cooling for Li-ion battery thermal management. *J. Energy Storage* **2023**, *72*, 108748. [CrossRef]
25. Trimbake, A.; Singh, C.P.; Krishnan, S. Mineral Oil Immersion Cooling of Lithium-Ion Batteries: An Experimental Investigation. *J. Electrochem. Energy Convers. Storage* **2022**, *19*, 021007. [CrossRef]
26. Patil, M.S.; Seo, J.-H.; Lee, M.-Y. A novel dielectric fluid immersion cooling technology for Li-ion battery thermal management. *Energy Convers. Manag.* **2021**, *229*, 113715. [CrossRef]
27. Liu, Y.; Aldan, G.; Huang, X.; Hao, M. Single-phase static immersion cooling for cylindrical lithium-ion battery module. *Appl. Therm. Eng.* **2023**, *233*, 121184. [CrossRef]
28. Roe, C.; Feng, X.; White, G.; Li, R.; Wang, H.; Rui, X.; Li, C.; Zhang, F.; Null, V.; Parkes, M.; et al. Immersion cooling for lithium-ion batteries—A review. *J. Power Sources* **2022**, *525*, 231094. [CrossRef]
29. Shi, H.; Zeng, Z.; Kong, B.; Yuan, N. Enhancing high-density battery performance through innovative single-phase spray technology in immersion cooling systems. *J. Power Sources* **2025**, *626*, 235770. [CrossRef]
30. Bao, R.; Wang, Z.; Yang, H.; Zhang, B.; Gao, Q.; Chen, S. Comparison analysis of thermal behavior of Lithium-ion batteries based on a novel multi-modal composite immersion liquid cooling system coupled with fin/micro-heat pipe array. *J. Energy Storage* **2024**, *104*, 114379. [CrossRef]
31. Zhong, K.; Wang, C.; Luo, Q.; Zhang, Z.; Zheng, J. Experimental study of a novel guided sequential immersion cooling system for battery thermal management. *Appl. Therm. Eng.* **2024**, *257*, 124337. [CrossRef]
32. Wei, Y.; Zeng, Z.; Du, R.; Baig, A.; Farooq, M.S.; Liu, S. Design of alveolar biomimetic enhanced heat transfer structure for cylindrical lithium battery pack. *J. Energy Storage* **2024**, *101*, 113721. [CrossRef]
33. Wang, Y.; Hu, F.; Wang, Y.; Guo, J.; Yang, Z.; Jiang, F. Revolutionizing the Afterlife of EV Batteries: A Comprehensive Guide to Echelon Utilization Technologies. *ChemElectroChem* **2023**, *11*, e202300666. [CrossRef]
34. Lazar, N.A. Statistics of Extremes: Theory and Applications:Statistics of Extremes: Theory and Applications. *Technometrics* **2005**, *47*, 376–377. [CrossRef]
35. Bell, S. A Beginner's Guide to Uncertainty of Measurement. 1999. Available online: https://www.esscolab.com/uploads/files/measurement-guide.pdf (accessed on 5 November 2025).
36. Zhu, H.; Ma, Y.; Jiaqiang, E.; Wei, S. Channel structure design and optimization for immersion cooling system of lithium-ion batteries. *J. Energy Storage* **2024**, *77*, 109930. [CrossRef]
37. Bernardi, D.; Pawlikowski, E.; Newman, J. A general energy balance for battery systems. *J. Electrochem. Soc.* **1985**, *132*, 5. [CrossRef]
38. Aydm, O. Aiding and opposing mechanisms of mixed convection in a shear- and buoyancy-driven cavity. *Int. Commun. Heat Mass Transf.* **1999**, *26*, 1019–1028. [CrossRef]

batteries

MDPI

Article

Thermal System Simulation of Heating Strategies for 21700 Lithium-Ion Battery Modules Under Cold-Start Conditions

Grace Parra-Panchi [1,2], Hanieh Nasrollahzadeh [1,2], Xiao-Yu Wu [1,3,*], Michael Fowler [2,3,*] and Yverick Rangom [2,*]

[1] Greener Production Group, University of Waterloo, 200 University Avenue West, Waterloo, ON N2L 3G1, Canada; gparrapanchi@uwaterloo.ca (G.P.-P.); hnasrollahzadeh@uwaterloo.ca (H.N.)
[2] Department of Chemical Engineering, University of Waterloo, 200 University Avenue West, Waterloo, ON N2L 3G1, Canada
[3] Department of Mechanical and Mechatronics Engineering, University of Waterloo, 200 University Avenue West, Waterloo, ON N2L 3G1, Canada
* Correspondence: xiaoyu.wu@uwaterloo.ca (X.-Y.W.); mfowler@uwaterloo.ca (M.F.); yrangom@uwaterloo.ca (Y.R.)

Abstract: Rapid heating strategies are essential for the cold-start of lithium-ion batteries at subzero temperatures to avoid severe performance losses. This study explores different external and battery-powered heating strategies and evaluates the time required for 21700 lithium-ion battery modules to reach the minimum safe-operating temperature. Three heating strategies were simulated: battery discharge, external heating, and combined configurations at ambient temperatures of −20 to 0 °C with initial state of charges (SOCs) of 20–80%. Results show that with discharge-only heating, the module heated up slowly and was unable to completely discharge at −20 °C and 20% SOC. Yet when the external surface-heating strategy was applied, the module was heated up 75–86% faster to reach the safe-operating temperature, which allowed the module to discharge completely under all conditions. Furthermore, in a combined configuration strategy where the external surface-heating is applied while the module discharges, the module achieved an additional 7–21% faster temperature rise. Lastly, at −20 °C and 20% SOC, external heater energy exceeded the module's usable output, while at 0 °C and moderate SOC, heater demand was only 2–3% of available battery capacity. Overall, findings show combining external heating discharge enables a reliable cold-start for the battery modules studied.

Keywords: heat strategies; subzero operation; cold start; external heating; battery-powered heating; thermal management

1. Introduction

Lithium-ion batteries (LIBs) are widely used in electric vehicles and extensively studied in research [1]. However, they still face one of their most recognized challenges: reduced performance at sub-zero temperatures [2], which may continue to limit broader electric vehicle (EV) adoption in cold regions. Due to the electrochemical nature of lithium-ion batteries, many of the operating mechanisms are temperature dependent [2]. The internal resistance of the battery is affected by temperature, which in turn directly affects the power output and heat generation of the battery during operation [2]. These effects ultimately might compromise the driving performance of EVs under cold conditions [3]. In extreme cases, cold conditions may even prevent vehicle start-up due to the rise in internal resistance, which severely limits power sourcing [4]. In response to these challenges,

Xu et al. [5] conclude that proper operation of battery modules and a flexible thermal management system (TMS) are required to provide heating in cold conditions and cooling in high temperatures.

Several strategies have been explored to address the challenge of heating lithium-ion batteries under low-temperature conditions. Previous reviews [6,7] have categorized heating strategies as either internal or external to the battery. Internal methods include self-heating, which utilizes the cell's own resistance during charge or discharge to generate heat [8], and pulse heating [7]. On the other hand, external heating approaches can be classified into air heating, liquid heating, phase changing material (PCM) heating, and external device heating [7]. Examples of external heating devices include Peltier effect and burner heating, electrical films, heat pipes, and heating plates [7]. Overall, the study [7] has concluded that while heating is essential to restore available capacity by mitigating impedance growth and support high-rate operation in cold environments, no existing method fully satisfies the combined demands of efficiency, safety, cost, and uniformity.

Previous studies also compare the internal and external heating approaches, each with distinct advantages and limitations for battery thermal management. Internal methods generate heat through the battery's own resistance and can provide better temperature control, but they remain challenging to implement being still under fundamental study [7]. By contrast, external heating strategies are simple to apply and continue to dominate in practice, [7] even though they require significant energy input and often suffer from inefficient heat transfer [9,10]. The prevalence of external heating methods in both research and practical applications underscores their role as a primary focus in supporting battery TMS.

Currently, air- and liquid-based heating methods are the most widely adopted in commercial EVs [7,9,10]. External heating is particularly common in recent models equipped with NCM batteries [11], which are widely used for their high energy density [12]. For example, several EV models released between 2020 and 2023 employed external heating strategies that utilize liquid coolant to manage battery temperature [11].

Air heating functions by warming the air first and then channeling it across the battery surface to facilitate heat transfer [13]. This approach has the lowest heating effectiveness among external heating systems [14], but it is inexpensive [4], requires little equipment, is dependable, and is quite safe [15,16]. On the other hand, liquid heating takes advantage of its high thermal conductivity and high specific heat capacity of coolant, providing more effective heating compared to air heating [17]. Liquid-based cooling could be classified as direct or indirect depending on whether the coolant contacts the battery [18]. Direct-contact systems immerse the battery in a dielectric fluid, while indirect-contact systems use intermediate heat-conducting components such as cold plates [18]. Therefore, it is slightly more complicated than air heating, and to avoid short circuits, equipment must be properly sealed [4].

PCMs also offer a promising solution for passive thermal management in battery systems because of their efficient temperature control, straightforward structure, and avoidance of auxiliary components such as pumps and fans that require additional energy [19,20]. They have high latent heat, suitable working temperatures, recyclable nature, and the capacity to maintain almost constant temperatures across phase transitions [21]. Furthermore, research has explored the use of PCMs for their potential to enable rapid preheating through the Joule heating effect, although these systems often depend on an external electrical source to generate the required heat, which may limit their practicality [9].

Another common method for achieving an efficient battery TMS is the combination of fluid cooling and PCM. One example is the integrated system that incorporated forced air cooling and a serpentine PCM plate was proposed by [22]. In terms of thermal control

performance, the battery module with this hybrid TMS performed better than the air cooling TMS, enabling the maximum temperature and temperature differential to be restricted below 51.9 and 0.8 °C, respectively. A hybrid system combining PCM and liquid pipes was proposed in [23], which also quantitatively examined the system's power consumption and heat removal effect while considering non-uniform battery heat generation. The hybrid system limited the maximum temperature to 47.6 °C at 3C discharge with the aid of liquid cooling [23].

Lastly, external heating devices are also used. For example, some EVs illustrate the use of electrothermal plates and films for preheating its 24 kWh battery, which has about 100 km of range when operated at speeds of 90 km/h or lower [14,24].

Hybrid heating systems, which combine both external and internal methods, have also been introduced. In a recent study [25], the long period needed for external preheating can be efficiently shortened by combining direct-current (DC) discharge heating and external heating, which decreases the preheating time by about 50% as compared to using external heating alone [25].

In practice, major EV manufacturers implement these heating strategies through distinct approaches to manage cold-start conditions. According to [26,27], some EV manufacturers utilize an integrated waste-heat recovery architecture together with an advanced heat-pump and a multi-mode coolant-routing valve ("octovalve") to route thermal energy from the drivetrain, cabin, and battery as required, enabling fast pre-conditioning and improved seasonal efficiency.

Refs. [28,29] summarized that predictive pre-conditioning strategies integrating navigation data and scheduled charging are used to pre-heat both the battery and cabin while the vehicle is plugged in. These approaches rely on vehicle control systems and BMS logic to improve low-temperature charge acceptance without drawing traction energy during trips.

In addition, several Chinese manufacturers favor modular dual-loop liquid-cooling architectures with externally actuated coolant pre-heaters to rapidly warm modules and maintain thermal uniformity [29,30].

A more conventional strategy is also adopted by some manufacturers: targeted resistive (high-voltage) heaters and simpler coolant routing or small heat-pump integration strike a balance between cost and performance. Peer-reviewed analyses indicate that while these systems provide reliable preheating, they incur larger energy draw from the traction system if used while unplugged [31,32].

Since existing heating strategies provide a solid foundation on heating at cell level, the present work focuses on integrating them into a 21700 LIB (SAMSUNG SDI Co., Ltd., Yongin, Republic of Korea) module and evaluates how different strategies perform through thermal system simulations under realistic boundary conditions and operating scenarios. By replicating cold-start environments, the analysis explores how heater configurations influence thermal response. The objective is to identify the configuration that improves cold-start performance with rapid heating while minimizing overall energy consumption. The results of this research contribute knowledge to the field of battery thermal management by integrating module parameters with dynamic heating simulations showing how a simulation-led approach, grounded in practical design considerations, can guide early-stage heating strategy development.

2. Materials and Methods

The thermal system simulation model was developed in AVL CRUISE^{TM} M 2024 R1 (AVL List GmbH, Graz, Austria) based on a battery module designed for a cargo van. The

module uses 21700 lithium-ion cells arranged in a 26p10s configuration. The electrothermal properties of the cells were implemented in the simulation using a Batemo cell model (BATEMO GmbH, Karlsruhe, Germany) of the Samsung INR21700-50G lithium-ion cell (SAMSUNG SDI Co., Ltd., Yongin, Republic of Korea) integrated within AVL CRUISE^{TM} M. While this model provides a representation of cell behavior, its applicability should be interpreted within the context of the model itself. This consideration is supported by findings in the literature showing that manufacturer data and in-house measurements often differ, as performance depends on application-specific conditions and testing environments [33]. Therefore, the results presented in this study should be interpreted as a best-case scenario assuming ideal cell behavior. The module was composed of four side walls, a bottom plate, and a top cover. The top cover had two layers: an exterior enclosure layer and an interior aluminum layer representing the busbars. All enclosure components were intended to be made from a thermoplastic characterized by low thermal conductivity (~0.2 $Wm^{-1}K^{-1}$ [34]) and electrical insulation; therefore, polypropylene was selected as the representative material.

Non-critical features such as fasteners, detailed busbar geometry, and cell spacers were neglected in the simulation as this study focuses on the dominant thermal interactions between the cells and surrounding structure. With this simplification, the model disregards the specific thermal conduction path provided by the busbars, which has been shown to depend on their thickness and material [35]. It also omits the insulating effect the cell spacers provide [36]. Although the geometric spacing is preserved, their absence simplifies the heat-transfer pathway. Thus, the model may represent an idealized scenario with a more uniform heat distribution than would occur in a real battery module.

Two system simulation layouts were developed to evaluate the thermal behavior of the battery module under cold-start conditions, i.e., with and without an external heater, as shown in Figure 1. Although both share the similar layouts, each is adapted to capture distinct thermal responses. In both cases, the module is modeled in AVL CRUISE^{TM} M using the Battery Module Cylindrical model, which is solved as a coupled electrothermal system. Within this setup, the governing equations combine the electrical relations that describe the discharge behavior of the interconnected cells with the thermal energy balance, which includes the heat generated within the cells, provided by the Batemo cell model, and its transfer through conduction and convection depending on the layout.

The first layout in Figure 1a presents the module operating without an external heater. The interface conditions include convection on the side walls and conduction through the bottom surface to the cold plate. All boundary condition details used in the simulations and their parameters are defined in Appendix A. Building on this layout and boundary condition framework, the second layout in Figure 1b has only one modification: the top cover is now connected to an external heating element for active cold-start heating.

The external heater was modeled as a continuous surface layer (i.e., heating strips) placed on top of the battery module, covering the same area as the top cover of the module to ensure uniform heat distribution. No thermal contact resistance between the heater and the module cover was considered. The specification of the heating input: the lowest available power density (1.55 W/cm^2) was selected, resulting in a total constant heating power of 2683 W. This level was chosen to minimize energy consumption while still providing sufficient thermal support under cold ambient conditions. From a practical standpoint, using constant-power heating elements during continuous cold operation could lead to a longer stabilization time at the target temperature, as the system relies on an on–off mechanism. Conversely, a feedback-regulated configuration might allow for smaller temperature deviations and, therefore, lower energy consumption by continuously

adjusting the power input. Nevertheless, implementing such an advanced control strategy would likely require careful tuning to ensure robust and reliable operation [37].

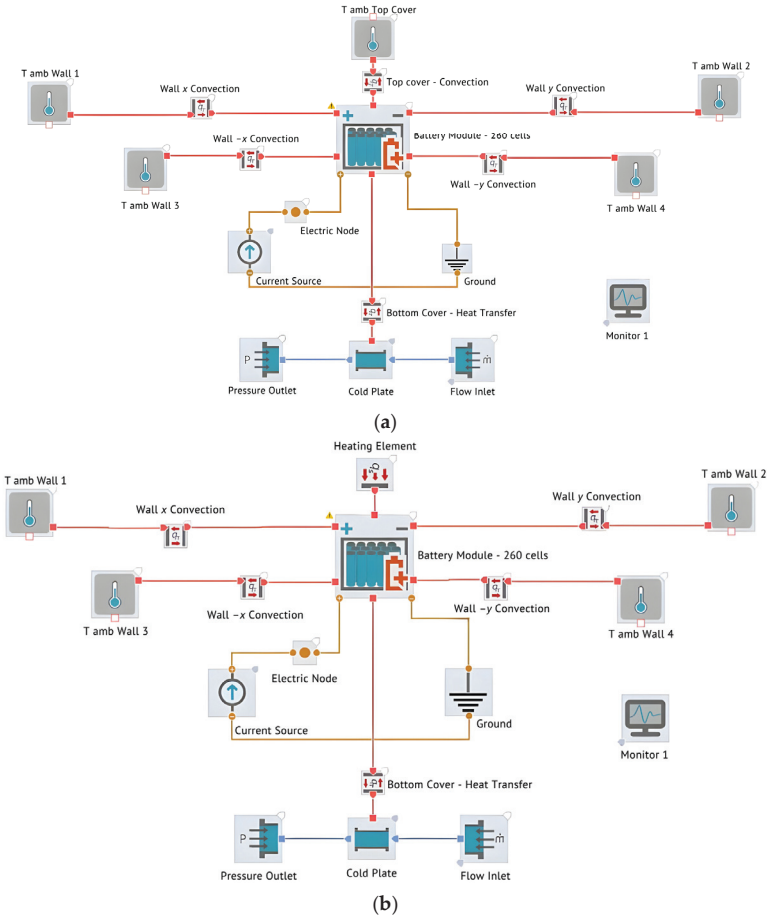

Figure 1. Simulation model configuration showing boundary conditions and component interactions for: (**a**) unheated cold-start scenario and (**b**) heated cold-start scenario.

Three heating strategies were studied on different conditions to evaluate their performances, which are shown as three cases in Table 1, i.e., battery discharge at 1C, external surface-heating element, and a combined battery discharge and externally heating. Each case varies in terms of heating configuration, power source, and whether the battery is actively discharging at 1C.

Table 1. The three cases of different strategies applied to the battery module in cold start.

Case	Heating Strategy	Heating Power Source	Battery Operation (1C Discharge)	Description
A	Battery discharge only	NA	On	Baseline configuration. No external heating is applied. The battery operates.
B	Surface-heating element	External	Off	Heating elements are externally powered. The battery does not operate while the heater is on.
C	Surface-heating element	External	On	Heating elements are externally powered. The battery operates at the same time.

The cold-start conditions evaluated vary at ambient temperatures and initial state of charges (SOCs). Three below zero temperatures were considered: −20 °C, −10 °C and 0 °C. These levels were selected to reflect typical winter startup conditions in cold climates while considering the operating range restricted by the cell manufacturer [38]. And the initial SOCs were evaluated at 80%, 50% and 20%. These levels capture the typical upper and lower bounds of recommended battery usage, including a mid-range value for comparison. To assess the impact of these factors on cold-start performance, two key outcomes were monitored for the module to reach 10 °C: the time required and the final SOC. Note that the module discharge is limited to 25 V, as recommended by the cell manufacturer's lower voltage threshold [38].

Lastly, we compared the usable energy in the battery module and the energy required for the external heating system under different cold-start conditions. Case A showed the total energy E_{usable} that the battery module could deliver from the initial SOC to full discharge (i.e., SOC = 0%) under cold conditions without external heating. Meanwhile, in Case C, the energy that is required by the external heating system to bring the module to target temperature, i.e., 10 °C while it is discharging can be calculated as:

$$E_{heater} = P_{heater} \times t_C \quad (1)$$

where P_{heater} is the constant heating power of the external heater, and t_C is the time required to achieve the target temperature.

The thermal system simulation model in this study was idealized to focus on the impacts of the heating strategies. All 21700 battery cells were assumed to be identical, balanced, and free from significant manufacturing or aging-related variations, with uniform internal heat generation. It is worth noting that as the battery ages, it tends to generate more heat under identical operating conditions, and because it functions year-round rather than solely at low temperatures, continuous operation accelerates component degradation, resulting in a significant increase in the rate of temperature rise [39]. Therefore, the time required to heat up the module may decrease as the battery ages. However, capacity losses of around 20–28%, as reported for aged lithium-ion cells [40], indicate that low-temperature operation would likely result in reduced available energy. This effect could be explored in future work to account for changes in heater operation time and energy availability as the battery module ages.

In addition, a liquid-cooled cold plate is introduced beneath the module solely to support temperature uniformity across it [25]. The inlet flow rate and temperature are defined as fixed inputs. The outlet is treated as a pressure outlet, assuming steady-state turbulent flow and outlet temperature profiles [41]. Other assumptions were adopted from [41], including negligible thermal radiation effects, and constant thermophysical properties for both the battery materials and surrounding air. Lastly, during battery discharging, a constant current of 1C is drawn through the module using a current source, and no variable load profiles or state-based electrical control logic is applied. All the inputs and assumptions can be found in Table A1.

3. Results and Discussion

The cold-start effectiveness of heating strategies could be revealed through a direct comparison of their thermal and energy performance. Case A and Case B were first compared to isolate the individual heating effects of cold discharge and external heating. Then, Case B was contrasted with Case C to determine the additional contribution of heat generated by battery discharge. Case A was further analyzed against Case C to evaluate

energy consumption, expressed as SOC reduction during cold discharge. Broader insights were drawn from the overall temperature evolution and heating trends observed across the cases. Finally, the energy consumed by the heating elements, E_{heater} was compared against the usable energy available from the battery module, E_{usable}.

3.1. Thermal Response Under Discharge Only and Heating Only Conditions

The time required for the module to reach 10 °C in Case A (Battery discharge at 1C only) and Case B (External heating only) is presented in Figure 2. It can be seen that it took longer times to reach 10 °C in Case A, because the heat generation rate by battery discharge only was slower than that from the external heating elements. The use of heating elements significantly reduced heating time by about 80%, highlighting the importance of employing an external heater. At a low SOC of 20% and cold ambient temperatures of −20 and −10 °C, the battery discharge alone could not provide sufficient heat to reach the operational temperature of 10 °C before the minimum operating voltage was reached. Under such conditions, the external heating became critical, as the external heating preconditioning allowed the battery to reach 10 °C in a short duration, consistent with previous findings: [10,42], that emphasized the need for plug-in preconditioning at low SOCs under cold ambient temperatures.

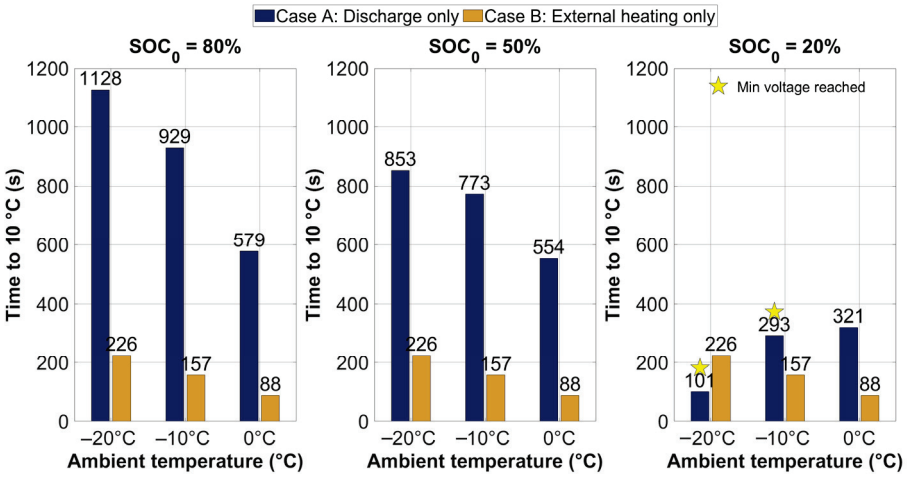

Figure 2. Time required for the module to reach 10 °C under cold-start conditions for Case A (Battery discharge at 1C only) and Case B (External heating only) at different initial SOC levels of 80%, 50%, and 20% and ambient temperatures of −20 °C, −10 °C, and 0 °C. The stars show the cases where the battery module reached minimum operating voltage and stopped discharging before reaching 10 °C.

In Case A, lowering the initial SOC from 80% to 50% speeds up heating by increasing heat generation, most notably at the lowest temperature due to higher internal resistance at low SOC. However, this benefit was limited, as the battery could quickly reach its minimum allowable voltage, making operation infeasible, which is observed at 20% SOC under −20 °C and −10 °C conditions.

In Case B, the heating time decreased at higher ambient temperatures. Since no discharge occurred in this case, SOC has no effect on the results, and the temperature rise was governed by the interaction between the applied constant heating power and the heat losses to the environment and the heat capacity of the battery.

3.2. Heating Behavior with and Without Battery Discharge

Cases B and C were contrasted to evaluate how battery discharge influences the heating behavior when external surface heating is applied. Both cases use external heating,

but only Case C includes battery discharge to study the thermal contribution of the battery under load versus idle conditions. The time taken for the battery module to reach 10 °C under each condition is shown in Figure 3.

Across all ambient temperatures, Case C consistently shows faster heating because battery discharge contributes additional thermal energy that enhances the overall heating rate. Yet the time reduction depends on the temperature and SOC. This difference is most significant at −20 °C and 20% initial SOC, where the battery's internal resistance is highest, resulting in greater Joule heating in discharging. At this condition, the heating time is reduced by 21% due to battery discharge.

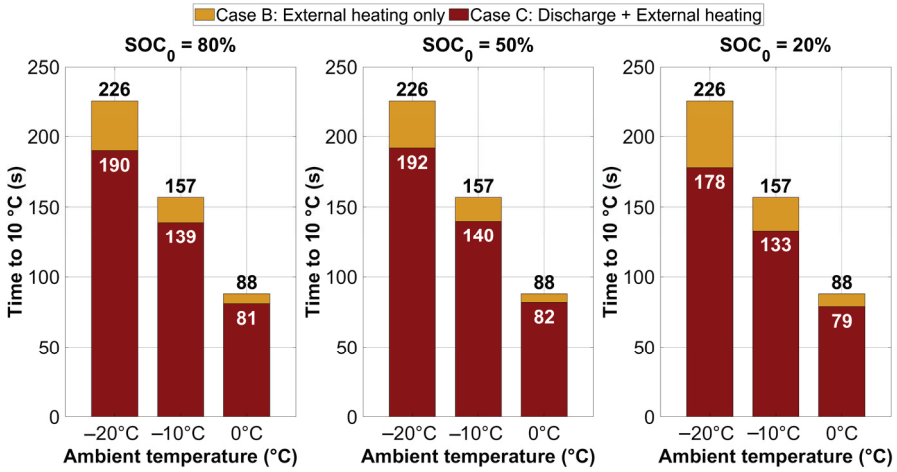

Figure 3. Time required for the module to reach 10 °C under cold-start conditions for Case B (external heating only) and Case C (Discharge + External heating) at initial SOC levels of 80%, 50%, and 20%, across ambient temperatures of −20 °C, −10 °C, and 0 °C.

In addition, the results also emphasize the influence of initial SOC at low temperatures, even when external heating is applied. At −20 °C, the reduction in heating time in Case C is more significant at 20% SOC than at 50% and 80% SOCs where time reduction is 15% and 16%, respectively. This suggests that low SOC amplifies the overall cell heat generation, likely due to stronger electrochemical polarization effects [43,44]. Nevertheless, the presence of external heating prevented complete energy depletion and avoided the battery reaching its minimum voltage limit before reaching 10 °C. Lastly, as the ambient temperature rises, the gap between Cases B and C narrows, indicating that the relative contribution of internal heat decreases under milder temperature conditions.

The absolute reduction in heating time ranges from 6 to nearly 48 s in all the cases studied, which shows improvements in EV applications with less delays during cold start-tups. Both external heating and battery discharge offer valuable contributions, especially in the most challenging thermal conditions.

3.3. Cold Discharge with and Without External Heating

Besides warm-up time, the final SOC was evaluated across different initial SOC levels to assess energy retention during cold discharge. Figure 4 presents the decrease in SOC during cold-start operation, comparing Case A and Case C across different initial SOCs and ambient temperatures.

Figure 4 demonstrates how the initial SOC influences the discharge performance of the battery module during cold start. In Case A, due to the lack of external heating, the battery consistently experiences greater SOC reduction than that in Case C. In some conditions, the module under Case A also drops to the minimum voltage before reaching

10 °C, which highlights the vulnerability of low-SOC operation under cold conditions. In contrast, Case C, with externally powered heating, shows a significantly smaller SOC decrease across all conditions, even at 20% initial SOC. In these scenarios, the battery avoids premature voltage cut-off and retains 15–17% final SOC, indicating a more stable and complete discharge. This improvement suggests that external heating helps preserve usable charge by maintaining internal conditions that prevent rapid voltage drop, which is especially critical when operating near the lower SOC limit.

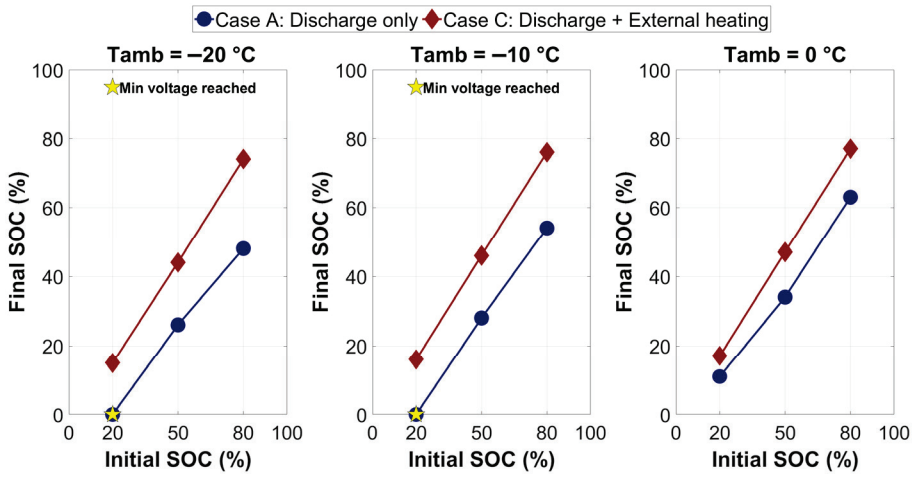

Figure 4. Final SOCs, measured when the module reached 10 °C during discharge, are shown as a function of initial SOC for Case A (discharge only) and Case C (discharge + external heating) under cold-start conditions. Results are presented for initial SOCs of 80%, 50%, and 20% at ambient temperatures of −20 °C, −10 °C, and 0 °C. Stars show the conditions when the module dropped to the minimum voltage before reaching 10 °C.

An interesting observation in Case C is that the SOC decrease remains nearly constant across all initial SOC levels for a given temperature. For instance, at −20 °C, the SOC decrease is consistently around 5 to 6% no matter if the battery starts at 80%, 50%, or 20% SOC. This suggests that the external heating strategy provides sufficient thermal support to stabilize the battery's internal resistance and voltage response, regardless of SOCs. This behavior reflects a uniform improvement in electrochemical accessibility enabled by external heating, making the discharge process more predictable.

Furthermore, as seen in the previous comparisons, at lower initial SOC levels, the battery exhibits a quicker rise in temperature. As a result, under low SOCs, the module reaches the 10 °C threshold faster than that with high SOCs. In contrast, higher initial SOC levels result in slower temperature rise. This highlights a trade-off where low SOC enables faster initial warming, while high SOC might support more extended heating.

Overall, the results confirm that low initial SOC conditions significantly limit discharge capability during cold starts, primarily due to early voltage cut-off. External heating mitigates this limitation by enabling better access to the remaining charge, making it particularly valuable when the module requires a cold start at reduced SOC levels.

3.4. Overall Comparison

The resulting temperature distributions in the module (at 3 different times) for Cases A, B and C under the condition of 50% initial SOC and −20 °C are shown in Figure 5. These visualizations provide a general overview of how the surface temperature evolves during the heating process and support the trends discussed in the previous sections.

At 50% initial SOC, the simulation results illustrate the module's thermal behavior under the three strategies. In Case A (Figure 5a), where no external heating is applied, the cells warm only through internal losses, and their temperature remains below 0 °C even after 192 s. In Case B (Figure 5b), with surface heating alone, the module cover reaches the highest temperature, while the cells remain cooler and appear at a lower temperature than in Case C at 120 s. In Case C (Figure 5c), surface heating is combined with internal heat generation, allowing the top surface to reach the highest temperature and enabling the cells to reach 10 °C within 192 s, demonstrating the effectiveness of this approach. Despite the temperature rise, the heating pattern of Case C remains like Case B.

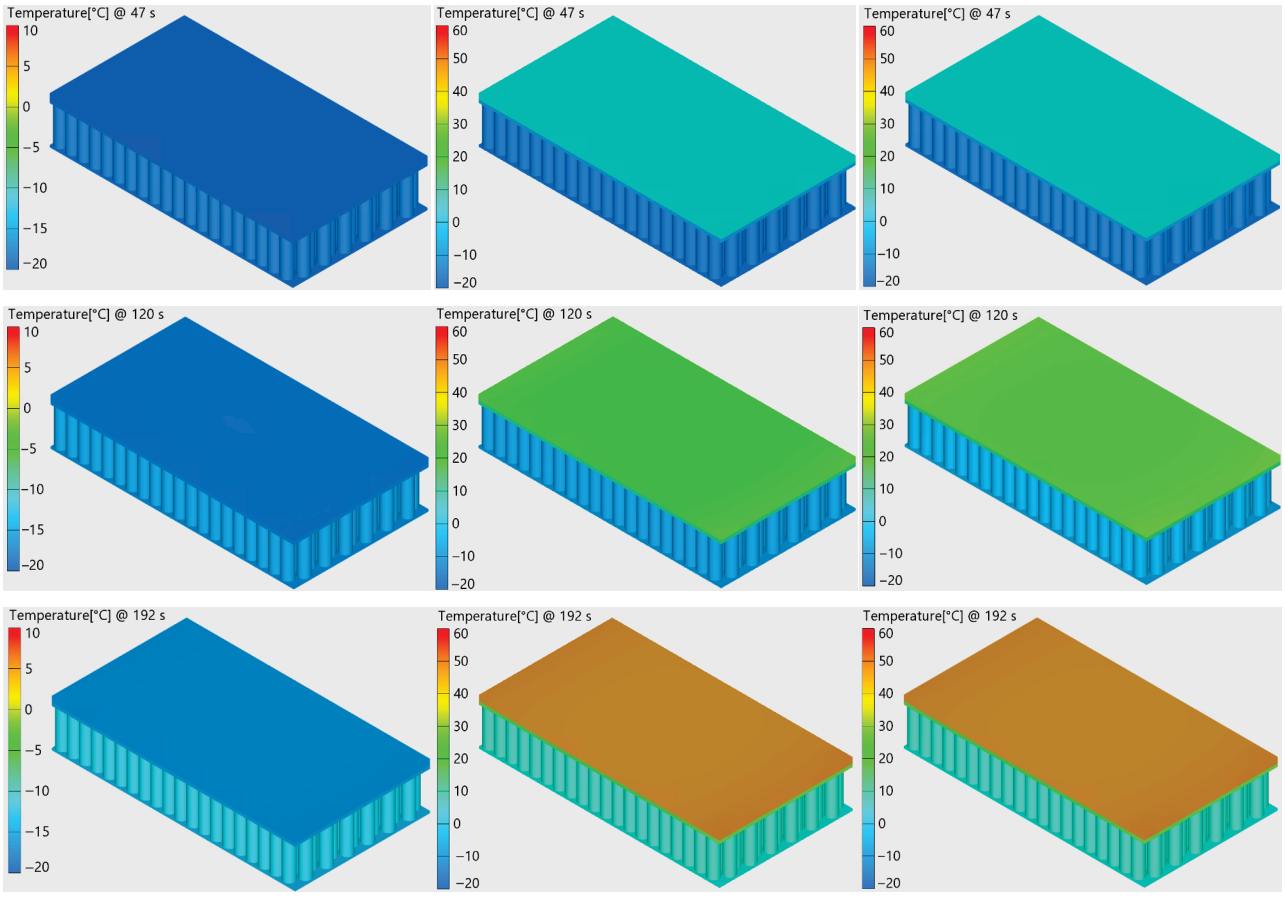

Figure 5. Evolution of temperature distributions over time at −20 °C and 50% initial SOC for (**a**) Case A, (**b**) Case B and (**c**) Case C. The side walls are hidden to visualize the effect on the 21700 cells block.

The sensitivity analysis was conducted for the battery-on cases at −20 °C, as these represent the most thermally demanding conditions. The heat transfer coefficient (h) was varied within the natural convection range (10 and 25 W/m^{2}K) [45], using 20 W/m^{2}K as the baseline in previous simulations. The results show that heating time is only marginally affected by variations in h: Case A at 80% SOC exhibited moderate sensitivity (up to 8%), while Case A at 20% SOC and both Case C conditions showed negligible changes ($\leq$0.3%). This demonstrates that small parameter variations produce minimal impact on the results, confirming the robustness of the model under low-temperature conditions.

Following the quantitative results presented previously, these observations provide further insight into the thermal behavior of the module. However, it is important to note that these results are based on a simplified representation, and the temperature distributions

reflect overall trends rather than precise spatial variations. To better understand the detailed temperature distribution, heat transfer pathways, and potential hotspots within the module, further analysis using 3D simulations is recommended which is not within the scope of this work.

3.5. Battery Usable Energy vs. External Heating Energy

Table 2 shows the results of the energy comparison between the heating demand of the external heater, E_{heater}, and the usable battery energy, E_{usable}, under different ambient temperatures and initial SOC levels.

Table 2. Comparison of required energy to power the heating elements, E_{heater}, and usable battery energy, E_{usable}, at different ambient temperatures and initial SOC levels.

Initial SOC (%)	Ambient Temperature (°C)	Required Energy Heater, E_{heater} (kJ)	Usable Battery Energy, E_{usable} (kJ)	Heating Energy Ratio E_{heater}/E_{usable} (%)
80	−20	509.8	11,529.5	4
	−10	372.9	11,804.8	3
	0	217.3	12,016.9	2
50	−20	515.1	6196.59	8
	−10	375.6	6520.59	5
	0	220.0	6862.73	3
20	−20	477.6	346.43	N/A [1]
	−10	356.8	1025.71	35
	0	212.0	1497.09	14

[1] $E_{usable} < E_{heater}$.

The results highlight the energy consumption by the external heater, which depends strongly on both ambient temperature and initial SOC. At higher initial SOC levels (80% and 50%), the battery has far more usable energy than the amount required by the heating system. For example, at −20 °C and 80% initial SOC, the external heating energy demand is 509.8 kJ, which is around 4% of the energy that the battery can supply, i.e., 11,529.50 kJ. Even at −20 °C and 50% initial SOC, the battery module still contains much more energy than that required by the external heater, corresponding to only 8% of the battery energy. This indicates that at medium to high SOC levels, the energy required by the external heaters is manageable.

However, at 20% SOC, the heating energy ratio becomes more significant, especially under severe cold conditions. At −20 °C, the battery can only deliver 346.43 kJ usable energy, which is less than the required 477.6 kJ for external heating. At −10 °C and 0 °C, the heating energy is still quite high compared to the usable energy of the module, i.e., heating energy ratios as 35% and 14%, respectively. These high ratios suggest that at 20% initial SOC, the external heater would require energy source outside the battery module. Specifically, under −20 °C and 20% SOC conditions, it would be essential to rely on an external power supply, such as plug-in conditioning, to provide the energy required by the heating elements, as demonstrated in previous studies highlighting the effectiveness of this approach [10,42].

Overall, the findings indicate that the external heating energy requirement is small compared to battery module's usable energy at moderate to high initial SOC levels across all tested temperatures, but it becomes more significant compared to battery modules at low SOCs, especially under severe cold. This again highlights the importance of employing external powered heating strategies when expecting cold-start operation at low SOC levels.

Although this work evaluates heating strategies for 21700 lithium-ion modules, the qualitative conclusions are broadly transferable to other formats. The relative performance of external surface heating, discharge-assisted heating, and combined strategies is not lim-

ited to this specific cell size [46]. However, the exact heating time to reach safe temperature and the energy required will vary with cell chemistry and whether the design prioritizes power or energy [46]. While self-heating and external heater approaches can provide rapid warm-up even at low ambient temperatures, the heat generation rate and usable discharge energy differ by chemistry and cell design, so the heater energy fraction and warm-up rate may change for chemistries such as NMC, NCA, LFP, and LTO [46].

This behavior can be further understood by considering the broader distinction between high-power and high-energy cells, which show different heating behaviors under similar conditions. High-power cells typically have lower internal resistance and therefore generate more instantaneous heat during discharge-assisted heating [47,48]. This enables faster initial warm-up but increases the risk of local hotspots that require tighter thermal control [47,48]. High-energy cells, such as the INR21700-50G (SAMSUNG SDI Co., Ltd., Yongin, Republic of Korea) used in this study, provide higher capacity and store more total thermal energy [47–49]. They create less heat per ampere but are more sensitive to heat accumulation over longer heating periods [47,48]. Consequently, the results presented in this study appear to be applicable mainly to cold-start conditions rather than extended operation and it is recommended that the heating duration be carefully controlled.

In brief, thermal diffusivity and heat-generation characteristics vary significantly across chemistries in low-temperature operation [50]. These variations alter the time needed to reach safe-operation temperature and change the external heater power demand even under similar SOC and ambient conditions [50]. Multiple studies consistently show the same ranking for heating approaches, with external heating being fastest and combined mode faster than either approach alone [51]. Therefore, the control strategy framework developed in this work is broadly applicable; however, chemistry-specific validation may still be required to extrapolate these results.

Future work will focus on expanding and validating the present study's findings through targeted experimental testing. Although the current model is simulation-based, its reliability is supported by peer-reviewed and industry-verified assumptions, providing a solid foundation for subsequent experimental validation. This study is limited by the exclusion of certain structural components and by the idealized thermal contact conditions assumed in the simulations. Nevertheless, these simplifications allow for a clear evaluation of the proposed heating system's intrinsic performance, offering valuable insights into its potential efficiency under controlled conditions.

4. Conclusions

This study explored different heating strategies for the cold-start of a 21700 cylindrical lithium-ion based battery module using thermal system simulation. Various initial SOCs and ambient temperatures were simulated. The main conclusions are:

- The battery module requires over 1100 s of self-heating through discharge alone to reach 10 °C in extreme cold conditions.
- External heating alone enables rapid battery recovery, reaching the target temperature in less than 300 s without consuming battery energy.
- Adding discharge during external heating further reduces heating times by about 21% compared with external heating alone.
- The most effective strategy was identified as external heating during discharge, which shortened warm-up times by up to 86% and prevented premature voltage cut-offs at −20 °C and 20% initial SOC.
- In cases where external heating operated alongside discharge at −20 °C, the SOC dropped by only 5 to 6% regardless of starting SOC (80%, 50%, or 20%), suggest-

ing that the heating system provides sufficient thermal support to stabilize the battery's performance.

- For cases above 50% initial SOC, external heater consumes less than 10% of the usable energy in the battery module. But at −20 °C and 20% initial SOC, the external heater's energy demand exceeds the battery module's usable energy.

These findings confirmed that external heating strategies are not only more effective but also critical for maintaining operational readiness for cold start in sub-zero conditions. This work also highlights the need for integrated, application-specific thermal solutions and lays the foundation for future optimization of heating control and module architecture.

Author Contributions: Conceptualization, X.-Y.W. and Y.R.; methodology, G.P.-P.; software, G.P.-P.; validation, X.-Y.W. and Y.R.; formal analysis, G.P.-P.; investigation, G.P.-P. and H.N.; resources, Y.R.; data curation, G.P.-P.; writing—original draft preparation, G.P.-P.; writing—review and editing, G.P.-P., H.N., X.-Y.W. and Y.R.; visualization, X.-Y.W. and G.P.-P.; supervision, X.-Y.W. and Y.R.; project administration, Y.R. and M.F.; funding acquisition, Y.R. All authors have read and agreed to the published version of the manuscript.

Funding: This work was supported by the Departments of Chemical Engineering, Mechanical and Mechatronics Engineering at the University of Waterloo, and the Natural Sciences and Engineering Research Council of Canada (NSERC) Discovery Grants Program (RGPIN-2021–02453 and RGPIN-2025-04807).

Data Availability Statement: The original contributions presented in this study are included in the article. Further inquiries can be directed to the corresponding authors.

Acknowledgments: Acknowledgment is extended to AVL for providing access to the simulation tool AVL CRUISE^{TM} M and to Batemo GmbH for granting access to the Batemo cell model.

Conflicts of Interest: The authors declare no conflicts of interest.

Abbreviations

The following abbreviations are used in the manuscript:

A	Area (cm^2)
E_{usable}	Usable energy (kJ)
EV	Electric vehicle
E_{heater}	Heater energy (kJ)
h	Heat transfer coefficient (W/m^2 K)
I	Current (A)
LFP	Lithium Iron Phosphate
LTO	Lithium Titanate Oxide
$\dot{m}$	Mass flow rate (kg/s)
NA	Not applicable
N/A	Not available
NCA	Lithium Nickel Cobalt Aluminum Oxide
NMC	Lithium Nickel Manganese Cobalt Oxide
P_{heater}	Heater power (W)
P_0	Inlet pressure (bar)
P_f	Outlet pressure (bar)
PCM	Phase changing material
SOC	State of charge
T_{amb}	Ambient temperature (°C)
t_C	Time to achieve the target temperature (s)
TMS	Thermal management system

Appendix A

Table A1 presents the parameters used for simulation setups presented in Figure 1.

Table A1. Simulation components, descriptions and assigned parameter values for the unheated cold-start scenario.

Component	Description	Simulation Parameters and Values
Battery module—260 cells	Thermal and electrical body under analysis	Electrically connected 26p10s Physical layout = 13x 20y
Top Cover–Convection	Convection to ambient through the top surface	A_z = 1730.78 cm^2 h = 20 W/m^2 K
Wall x Convection	Convection boundaries on both lateral sides of the module	A_x = 345.30 cm^2 h = 20 W/m^2 K
Wall −x Convection	Convection boundaries on both lateral sides of the module	A_x = 345.30 cm^2 h = 20 W/m^2 K
Wall y Convection	Convection boundaries on front and back sides of the module	A_y = 180.30 cm^2 h = 20 W/m^2 K
Wall −y Convection	Convection boundaries on front and back sides of the module	A_y = 180.30 cm^2 h = 20 W/m^2 K
T_{amb} Wall 1	Ambient conditions	$T_{amb} = -20$ °C
T_{amb} Wall 2	Ambient conditions	$T_{amb} = -20$ °C
T_{amb} Wall 3	Ambient conditions	$T_{amb} = -20$ °C
T_{amb} Wall 4	Ambient conditions	$T_{amb} = -20$ °C
Electric Node	Distributes current input	NA
Current Source	Simulates discharge	I = 127.4 A per module (1C)
Ground	Electrical ground reference	NA
Bottom Cover–Heat Transfer	Heat transfer via cold plate	A_{-z} = 546 cm^2 h = 20 W/m^2 K
Cold Plate	Cooling interface connected to the module bottom surface	Geometry = Rectangular Width = 59 cm Depth = 0.4 cm Length = 84.6 cm Propylene glycol/Water 50/50 [52] Friction coefficient = 0.06
Flow Inlet	Defines coolant flow into cold plate	P_0 = 1 bar $T_{amb} = -20$ °C $\dot{m} = 0.267 \frac{kg}{s}$
Pressure Outlet		P_f = 1 bar $T_{amb} = -20$ °C
Monitor	Records data outputs	NA

References

1. Cicconi, P.; Kumar, P. Design approaches for Li-ion battery packs: A review. *J. Energy Storage* **2023**, *73*, 109197. [CrossRef]
2. Tete, P.R.; Gupta, M.M.; Joshi, S.S. Developments in battery thermal management systems for electric vehicles: A technical review. *J. Energy Storage* **2021**, *35*, 102255. [CrossRef]
3. Seo, J.; Vijayagopal, R.; Kim, N.; Rousseau, A.; Stutenberg, K. Effects of ambient temperature on electric vehicle range considering battery Performance, powertrain Efficiency, and HVAC load. *Energy Convers. Manag.* **2025**, *326*, 119493. [CrossRef]
4. Hu, X.; Zheng, Y.; Howey, D.A.; Perez, H.; Foley, A.; Pecht, M. Battery warm-up methodologies at subzero temperatures for automotive applications: Recent advances and perspectives. *Prog. Energy Combust. Sci.* **2020**, *77*, 100806. [CrossRef]

5. Xu, X.; Zhu, J.; Zhang, H.; Yi, Z.; Wang, X.; Zhao, G. Low cost energy-efficient preheating of battery module integrated with air cooling based on a heat spreader plate. *Appl. Therm. Eng.* **2023**, *232*, 121024. [CrossRef]
6. Bibin, C.; Vijayaram, M.; Suriya, V.; Ganesh, R.S.; Soundarraj, S. A review on thermal issues in Li-ion battery and recent advancements in battery thermal management system. *Mater. Today Proc.* **2020**, *33*, 116–128. [CrossRef]
7. Shao, D.; Hu, L.; Zhang, J.; Hu, R.; Zhang, G.; Jiang, L.; Wang, X.; Wen, Y. Advanced low-temperature preheating strategies for power lithium-ion batteries applied in electric vehicles: A review. *Int. J. Electrochem. Sci.* **2024**, *19*, 100817. [CrossRef]
8. Wang, Y.; Zhang, X.; Chen, Z. Low temperature preheating techniques for Lithium-ion batteries: Recent advances and future challenges. *Appl. Energy* **2022**, *313*, 118832. [CrossRef]
9. Li, W.; Klemeš, J.J.; Wang, Q.; Zeng, M. Efficient thermal management strategy of Li-ion battery pack based on sorption heat storage. *Energy Convers. Manag.* **2022**, *256*, 115383. [CrossRef]
10. Ye, Z.; Fu, X.; Zhou, S. Research on control strategy of rapid preheating for power battery in electric vehicle at low temperatures. *Appl. Therm. Eng.* **2024**, *245*, 122770. [CrossRef]
11. Wang, Y.; Liu, Q.; Hao, S.; Cheng, L.; Zhang, W.; Han, K.; Wang, E.; Ouyang, M.; Lu, L.; Li, X. Low temperature heating methods for lithium-ion batteries: A state-of-art review based on knowledge graph. *Renew. Sustain. Energy Rev.* **2025**, *213*, 115389. [CrossRef]
12. Assi, M.; Amer, M. A Comparative Analysis of Lithium-Ion Batteries Using a Proposed Electrothermal Model Based on Numerical Simulation. *World Electr. Veh. J.* **2025**, *16*, 60. [CrossRef]
13. Yang, Y.; Wang, R.; Shen, Z.; Yu, Q.; Xiong, R.; Shen, W. Towards a safer lithium-ion batteries: A critical review on cause, characteristics, warning and disposal strategy for thermal runaway. *Adv. Appl. Energy* **2023**, *11*, 100146. [CrossRef]
14. Laurikko, J.; Granstrom, R.; Haakana, A. Realistic estimates of EV range based on extensive laboratory and field tests in Nordic climate conditions. In Proceedings of the 2013 World Electric Vehicle Symposium and Exhibition (EVS27), Barcelona, Spain, 17–20 November 2013; pp. 1–12. [CrossRef]
15. Budt, M.; Wolf, D.; Span, R.; Yan, J. A review on compressed air energy storage: Basic principles, past milestones and recent developments. *Appl. Energy* **2016**, *170*, 250–268. [CrossRef]
16. Wang, T.; Tseng, K.; Zhao, J. Development of efficient air-cooling strategies for lithium-ion battery module based on empirical heat source model. *Appl. Therm. Eng.* **2015**, *90*, 521–529. [CrossRef]
17. Liu, Z.; Liu, X.; Meng, H.; Guo, L.; Zhang, Z. Numerical analysis of the thermal performance of a liquid cooling battery module based on the gradient ratio flow velocity and gradient increment tube diameter. *Int. J. Heat Mass Transf.* **2021**, *175*, 121338. [CrossRef]
18. Liu, H.; Shi, C.; Liu, C.; Chang, W. A Review of Lithium-Ion Battery Thermal Management Based on Liquid Cooling and Its Evaluation Method. *Energies* **2025**, *18*, 4569. [CrossRef]
19. Liu, Q.; Deng, Q.; Zhao, R.; Cheng, W.-L.; Wang, Y.-D. A novel flexible flame-retardant phase change materials with battery thermal management test. *J. Energy Storage* **2023**, *70*, 108077. [CrossRef]
20. Fan, Y.; Wang, Z.; Xiong, X.; Zhu, J.; Gao, Q.; Wang, H.; Wu, H. Novel concept design of low energy hybrid battery thermal management system using PCM and multistage Tesla valve liquid cooling. *Appl. Therm. Eng.* **2023**, *220*, 119680. [CrossRef]
21. Okogeri, O.; Stathopoulos, V.N. What about greener phase change materials? A review on biobased phase change materials for thermal energy storage applications. *Int. J. Thermofluids* **2021**, *10*, 100081. [CrossRef]
22. Lv, Y.; Liu, G.; Zhang, G.; Yang, X. A novel thermal management structure using serpentine phase change material coupled with forced air convection for cylindrical battery modules. *J. Power Sources* **2020**, *468*, 228398. [CrossRef]
23. Ping, P.; Zhang, Y.; Kong, D.; Du, J. Investigation on battery thermal management system combining phase changed material and liquid cooling considering non-uniform heat generation of battery. *J. Energy Storage* **2021**, *36*, 102448. [CrossRef]
24. Wu, S.; Xiong, R.; Li, H.; Nian, V.; Ma, S. The state of the art on preheating lithium-ion batteries in cold weather. *J. Energy Storage* **2020**, *27*, 101059. [CrossRef]
25. Wu, X.; Wei, Z.; Sun, Y.; Sun, J.; Du, J. Integrated All-Climate Heating/Cooling System Design and Preheating Strategy for Lithium-Ion Battery Pack. *Batteries* **2022**, *8*, 179. [CrossRef]
26. Wray, A.; Ebrahimi, K. Octovalve Thermal Management Control for Electric Vehicle. *Energies* **2022**, *15*, 6118. [CrossRef]
27. Bae, J.; Yun, J.; Han, J. Performance and Efficiency Evaluation of a Secondary Loop Integrated Thermal Management System with a Multi-Port Valve for Electric Vehicles. *Energies* **2024**, *17*, 5729. [CrossRef]
28. Sørensen, Å.L.; Ludvigsen, B.; Andresen, I. Grid-connected cabin preheating of Electric Vehicles in cold climates—A non-flexible share of the EV energy use. *Appl. Energy* **2023**, *341*, 121054. [CrossRef]
29. Rahmani, A.; Dibaj, M.; Akrami, M. Recent Advancements in Battery Thermal Management Systems for Enhanced Performance of Li-Ion Batteries: A Comprehensive Review. *Batteries* **2024**, *10*, 265. [CrossRef]

30. Luo, Y.; Zhou, D.; Zou, Z.; Bi, C.; Yang, X.; Li, X.; Yang, X. A Battery Thermal Management System Integrating Immersion Preheating and Immersion Cooling. *ACS Omega* **2024**, *9*, 43523–43533. [CrossRef]
31. Maiorino, A.; Cilenti, C.; Petruzziello, F.; Aprea, C. A review on thermal management of battery packs for electric vehicles. *Appl. Therm. Eng.* **2024**, *238*, 122035. [CrossRef]
32. Murphy, M.; Akrami, M. Advanced Thermal Management of Cylindrical Lithium-Ion Battery Packs in Electric Vehicles: A Comparative CFD Study of Vertical, Horizontal, and Optimised Liquid Cooling Designs. *Batteries* **2024**, *10*, 264. [CrossRef]
33. Marzook, M.W.; Eaton, J.; Samieian, M.A.; Patel, Y.; Offer, G.; Marinescu, M. Performance Benchmarking of Lithium-Ion Batteries: The Effect of Test Conditions on the Down-Selection of Cylindrical Cells. *SSRN* **2023**, 4620843. [CrossRef]
34. C-Therm Technologies Ltd. The Thermal Conductivity of Unfilled Plastics. Available online: https://ctherm.com/resources/newsroom/blog/the-thermal-conductivity-of-unfilled-plastics/ (accessed on 9 September 2025).
35. Chen, H.; Zhang, T.; Hua, Y.; Gao, Q.; Han, Z.; Yang, K.; Xu, Y.; Liu, X.; Xu, X.; Wang, S. Simulation study on the interaction between the battery module and busbar under typical driving conditions of electric vehicles. *Case Stud. Therm. Eng.* **2023**, *45*, 103006. [CrossRef]
36. Madaoui, S.; Guzowski, B.; Gozdur, R.; Dimitrova, Z.; Audiot, N.; Sabatier, J.; Vinassa, J.-M.; Guillemard, F. Assessment of a Top and Bottom Cooling Strategy for Prismatic Lithium-Ion Cells Intended for Automotive Use. *Batteries* **2024**, *10*, 403. [CrossRef]
37. Shang, Y.; Chen, G.; Peng, Q.; Zhu, T.; Liu, K. An Intelligent Preheating Approach Based on High-Gain Control for Lithium-Ion Batteries in Extremely Cold Environment. *IEEE Trans. Ind. Electron.* **2024**, *71*, 4697–4706. [CrossRef]
38. Samsung SDI Co., Ltd. *Samsung INR21700-50G (Data Sheet)*; Samsung SDI Co., Ltd.: Yongin-si, Republic of Korea, 2024.
39. Shen, W.; Wang, N.; Zhang, J.; Wang, F.; Zhang, G. Heat Generation and Degradation Mechanism of Lithium-Ion Batteries during High-Temperature Aging. *ACS Omega* **2022**, *7*, 44733–44742. [CrossRef] [PubMed]
40. Rafik, O.; Capitaine, A.; Briat, O.; Vinassa, J.-M. Performance characterization of lithium-ion battery and aging under constant stress conditions at low temperature. *Microelectron. Reliab.* **2025**, *171*, 115785. [CrossRef]
41. Yang, T.-F.; Yan, W.-M.; Lin, P.-Y.; Lin, C.-Y.; Yang, C.-C.; Sajjad, U. Thermal management of 21700 Li-ion battery packs: Experimental and numerical investigations. *Appl. Therm. Eng.* **2024**, *236*, 121518. [CrossRef]
42. Gamra, K.A.; Zähringer, M.; Ladner, A.; Allgäuer, C.; Lienkamp, M. Examining Model-Based Fast-Charging and Preconditioning on a Vehicle Level. *World Electr. Veh. J.* **2024**, *15*, 377. [CrossRef]
43. Li, Q.; Yi, D.; Dang, G.; Zhao, H.; Lu, T.; Wang, Q.; Lai, C.; Xie, J. Electrochemical Impedance Spectrum (EIS) Variation of Lithium-Ion Batteries Due to Resting Times in the Charging Processes. *World Electr. Veh. J.* **2023**, *14*, 321. [CrossRef]
44. Guo, J.; Guo, Q.; Liu, J.; Wang, H. The Polarization and Heat Generation Characteristics of Lithium-Ion Battery with Electric–Thermal Coupled Modeling. *Batteries* **2023**, *9*, 529. [CrossRef]
45. Wu, H.-W.; Ciou, Y.-C.; Wu, J.-K.; Huang, D.-A. Study of Natural Convection of Lithium-Ion Battery Module Employing Phase Change Material. *Processes* **2021**, *9*, 2023. [CrossRef]
46. Shahjalal, M.; Shams, T.; Islam, E.; Alam, W.; Modak, M.; Bin Hossain, S.; Ramadesigan, V.; Ahmed, R.; Ahmed, H.; Iqbal, A. A review of thermal management for Li-ion batteries: Prospects, challenges, and issues. *J. Energy Storage* **2021**, *39*, 102518. [CrossRef]
47. Huang, H.; Tang, X.; Zhou, Y. A Review of Battery Thermal Management System for New Energy Vehicles at Subzero Temperatures. In Proceedings of the WCX SAE World Congress Experience, SAE International, Detroit, MI, USA, 16–18 April 2024. [CrossRef]
48. Madani, S.S.; Hajihosseini, M.; Ziebert, C. A brief survey on heat generation in lithium-ion battery technology. *Renew. Energy Environ. Sustain.* **2024**, *9*, 9. [CrossRef]
49. Guo, B.; He, R.; Li, Y.; Zhou, S.; Zhang, L.; Liu, X.; Yang, S. Aging mechanisms of cylindrical NCA/Si-graphite battery with high specific energy under dynamic driving cycles. *J. Energy Storage* **2024**, *103*, 114287. [CrossRef]
50. Ahmadian-Elmi, M.; Zhao, P. Review of Thermal Management Strategies for Cylindrical Lithium-Ion Battery Packs. *Batteries* **2024**, *10*, 50. [CrossRef]
51. Ruan, H.; Barreras, J.V.; Steinhardt, M.; Jossen, A.; Offer, G.J.; Wu, B. The heating triangle: A quantitative review of self-heating methods for lithium-ion batteries at low temperatures. *J. Power Sources* **2023**, *581*, 233484. [CrossRef]
52. Broatch, A.; Pla, B.; Bares, P.; Agizza, L. Single value decomposition for sparse temperature sensing and state observation in multicell battery packs. *J. Energy Storage* **2024**, *97*, 112888. [CrossRef]

batteries

MDPI

Article

Polymer-BN Composites as Thermal Interface Materials for Lithium-Ion Battery Modules: Experimental and Simulation Insights

Sajib Kumar Mohonta [1], Shinto Mundackal Francis [1], Andrew Ferebee [1], Gajendra Bohara [1], Pooja Puneet [1], Yi Ding [2] and Ramakrishna Podila [1,*]

[1] Laboratory of Nano-Biophysics, Department of Physics and Astronomy, Clemson University, Clemson, SC 29634, USA; smohont@g.clemson.edu (S.K.M.); shintof@g.clemson.edu (S.M.F.); aferebe@clemson.edu (A.F.); gbohara@clemson.edu (G.B.); ppuneet@g.clemson.edu (P.P.)

[2] U.S. Army DEVCOM-Ground Vehicle Systems Center (GVSC), Warren, MI 48397, USA; yi.ding8.civ@army.mil

* Correspondence: rpodila@g.clemson.edu

Abstract: Efficient thermal management is critical for the safety and performance of lithium-ion battery (LIB) systems, particularly under high C-rate charge–discharge cycling. Here, we investigate two classes of polymer composite thermal interface materials (TIMs): graphene-PLA (GPLA) fabricated via 3D printing and boron nitride nanoplatelets (BN)-loaded thermoplastic polyurethane (TPU) composites with 20 and 40 wt.% BN content. To understand cooling dynamics, we developed a simple analytical model based on Newtonian heat conduction, predicting an inverse relationship between the cooling rate and the TIM thermal diffusivity. We validated this model experimentally using a six-cell LIB module equipped with active liquid cooling, and complemented it with finite-element simulations in COMSOL Multiphysics incorporating experimentally derived parameters. Across all approaches, analytical, numerical, and experimental, we observed excellent agreement in predicting the temperature decay profiles and inter-cell temperature differentials (ΔT). Charge–discharge cycling studies at varying C-rates demonstrated that high-diffusivity TIMs enable faster cooling but require careful design to minimize lateral thermal gradients. Our results establish that an ideal TIM must simultaneously support rapid vertical heat sinking and effective lateral thermal diffusion to ensure thermal uniformity. Among the studied materials, the 40% BN–60% TPU composite achieved the best overall performance, highlighting the potential of BN filler-engineered polymer composites for scalable thermal management in next-generation battery systems.

Keywords: thermal interface materials; graphene composites; boron nitride; lithium-ion batteries; thermal diffusivity; COMSOL simulation; 3D printing; battery thermal management

1. Introduction

As lithium-ion batteries (LIBs) become increasingly indispensable in electric vehicles (EVs), portable electronics, and stationary energy storage systems, their thermal management has emerged as a central engineering challenge [1–8]. Battery operation generates substantial heat, particularly under fast-charging or high-discharge conditions, leading to temperature gradients, accelerated degradation, and, in severe cases, thermal runaway [9,10]. Even a small ($\leq$1 °C) but persistent gradient between cells can induce cell-to-cell capacity drift and uneven state-of-charge evolution ultimately affecting pack

balancing. Thus, maintaining thermal uniformity and dissipating heat efficiently are critical for battery performance, safety, and lifespan.

In typical battery modules, heat is dissipated through passive and active cooling strategies, including airflow, liquid cooling manifolds, and heat pipes [2–5,11–13]. However, a significant thermal bottleneck persists at the interface between battery cells and their surrounding cooling infrastructure. Imperfect contact, surface roughness, and the low thermal conductivity of adhesives or structural materials contribute to significant thermal contact resistance [9,11,14–18]. This makes developing effective thermal interface materials (TIMs) crucial to advancing battery thermal management systems (BTMS).

TIMs are designed to bridge the thermal resistance gap between solid interfaces, such as battery casings and heat sinks. Polymer-based TIMs are often favored due to their mechanical flexibility, electrical insulation, and ease of processing [9,11,15,16,18,19]. Yet, the low intrinsic cross-plane thermal conductivity of most polymers (typically $< 0.5\ \mathrm{W\,m^{-1}\ K^{-1}}$) severely limits their ability to conduct heat. To overcome this, high-conductivity fillers such as graphite, metal oxides, and carbon nanostructures like graphene are incorporated into the polymer matrix to form thermally conductive composites [20–22] .

Graphene, with its exceptional in-plane thermal conductivity (up to $5000\ \mathrm{W\,m^{-1}\,K^{-1}}$), high aspect ratio, and tunable surface chemistry, has emerged as one of the most promising TIM fillers [18,23–27]. Its incorporation into polymer matrices can dramatically enhance thermal performance, particularly when oriented or networked to form continuous heat conduction paths [15,28–33]. However, graphene composites are also electrically conducting, which is a disadvantage in preventing undesired short circuits within the battery module.

Hexagonal boron nitride (h-BN), often dubbed "white graphene," offers similarly high thermal conductivity along with electrical insulation, making it attractive for TIM applications where dielectric performance is important [17]. BN-polymer composites have demonstrated thermal conductivities up to $10\ \mathrm{W\,m^{-1}\,K^{-1}}$ depending on filler loading, morphology, and processing method [16,18,34–37]. A table summarizing prior results of thermal conductivity for various TIMs is presented in Table S1 [38–55]. Recent advances in filler surface functionalization, hybrid filler strategies, and anisotropic alignment have further improved the thermal transport efficiency of such composites .

While the thermal performance of individual materials is important, their integration into real-world systems poses additional design constraints. For example, TIMs must conform to irregular geometries, maintain thermal performance under cyclic loading, and avoid adding excessive mass or volume to the battery pack [11]. A comprehensive evaluation of TIMs requires multiscale assessment from intrinsic thermal properties such as thermal diffusivity to system-level metrics like inter-cell temperature gradients and transient cooling behavior [9]. Finite-element simulations, particularly those implemented in platforms such as COMSOL Multiphysics 6.2, have become essential in linking material properties with thermal field evolution in complex battery assemblies [35,56].

In this study, we investigated the fabrication and thermal performance of two classes of polymer composite TIMs: graphene–PLA (GPLA) fabricated by 3D printing, and boron nitride (BN)–loaded thermoplastic polyurethane (TPU) composites containing 20 and 40 wt.% BN. Building on prior reports of enhanced thermal conductivity in such systems [11,15,17,18,28,35,56], we conducted both experiments and simulations using two complementary setups designed to evaluate TIM performance under distinct thermal conditions. In the first configuration, individual cylindrical cells were coupled to an external heat source to quantify heat dissipation through each TIM. In the second, the TIMs were implemented in a compact 3s2p battery module, where the cells were

charged and discharged at controlled C-rates. All experiments were performed with an active liquid-cooling manifold and external forced convection. For both setups, finite-element simulations were performed in COMSOL under identical boundary conditions to the experiments.

The electro-thermal model in COMSOL employed the standard $LiMn_2O_4$–graphite chemistry available in the built-in `Lithium-Ion Battery Module` to represent heat generation, while the electrochemical kinetics were not modeled explicitly. Instead, the heat source term was normalized for the capacity and *C*-rate of the NCA-based experimental cells, ensuring consistency of the total Joule-heating magnitude. The focus of the simulations was therefore comparative: to evaluate how temperature evolves with different TIMs rather than to reproduce charge–discharge voltage behavior. The cell and TIM material properties were assigned from experimentally measured or literature-reported values, and the analysis centered on the relative change in temperature for low- and high-diffusivity TIMs (PLA and 40 wt.% BN-TPU, respectively). The simulations closely reproduced the experimental temperature evolution, yielding excellent correlation for both the relative temperature difference ΔT between TIMs and the cooling time constant τ extracted from the decay curves. The strong agreement between experiment and simulation confirms that the adopted comparative, heat-transfer-focused framework reliably captures the influence of TIM thermal diffusivity on module-level temperature uniformity.

While the comparative analysis highlights the consistency between experiment and simulation, it also reveals an intrinsic design trade-off in thermal interface engineering. A material with lower thermal diffusivity acts as a transient heat reservoir, storing heat and moderating short-term temperature spikes but offering slower lateral equilibration. Conversely, a high-diffusivity TIM rapidly spreads and dissipates heat, minimizing local hot spots yet transferring energy more quickly to the cooling infrastructure. In the present study, the GPLA system exemplifies the heat-storage regime, whereas the 40 wt.% BN–TPU composite represents the heat-dissipation regime with superior thermal uniformity across cells. This balance between transient thermal buffering and efficient dissipation defines the optimal operating window for polymer–composite TIMs in battery enclosures.

2. Materials and Methods

2.1. Materials

Polylactic acid or PLA filament was purchased from Hacthbox (Rowland Heights, CA, USA) while graphene-loaded PLA or GPLA filament was purchased from Blackmagic3D.com (Ronkonkoma, NY, USA). Thermoplastic polyurethane or TPU filament and TPU pellets were purchased from TCPoly (Pineville, NC, USA). Hexagonal boron nitride (h-BN) micropowder and N, N-dimethylformamide (DMF) were purchased from Sigma Aldrich (St. Louis, MO, USA).

2.2. Fabrication of Thermal Interface Materials

For preparing thermoplastic polyurethane or TPU-BN composites, TPU pellets were dried in a vacuum oven at 100 °C for 4 h. Exfoliated micro h-BN micropowder was dispersed in N, N-dimethylformamide (DMF) using a tip sonicator at 10 watts for 30 min. After sonication, the mixture was placed on a hot plate at 80 °C and magnetically stirred at 150 rpm. Dried TPU pellets were added to the mixture slowly. Subsequently, the mixture was stirred at 80 °C and 150 rpm for 4 h. Finally, the viscous mixture was cast onto a thin kitchen aluminum foil using an MTI doctor blade casting system to maintain a uniform thickness of 1.4 mm. The films were dried overnight at room temperature inside a chemical

hood (120 cfm airflow) to remove the solvent slowly. Once dried, the TIMs were peeled from the foil and cut into 70 × 30 × 1.4 mm slabs.

We prepared multiple controls such as neat TPU, polylactic acid (PLA) and graphene-loaded PLA (GPLA) through 3D printing to validate trends against BN–TPU composites. The GPLA composites included as a reference material to benchmark the effect of a thermally conductive and electrically active filler against the insulating BN–polymer systems. Although not intended for direct battery use, GPLA provides a useful control for isolating filler-type effects on heat transport and interfacial coupling. For 3D printing, a 70 × 30 × 1.4 mm slab was designed using the geometry module of COMSOL Multiphysics 6.2. Upon finalizing the geometry, the design was exported and sliced in PrusaSlicer 2.9.4 software to generate the code for 3D printing. The exported code was then printed using a Prusa i3 MKS3+ 3D printer (Prusa by Josef Prusa, Prague, Czech Republic).

2.3. Characterization Techniques

All TIMs were characterized using thermogravimetric (TGA) analysis (TA instrument SDT Q600, New Castle, DE, USA) under nitrogen gas flow at 100 mL/min from room temperature to 600 °C with a ramp of 20 °C/min (Figure 1). Cross-plane thermal diffusivity was measured using the laser flash technique (Linseis LZT meter, Selb, Germany). Before diffusivity measurements, all samples were coated with graphite 33 spray to ensure uniform contact for heat flow.

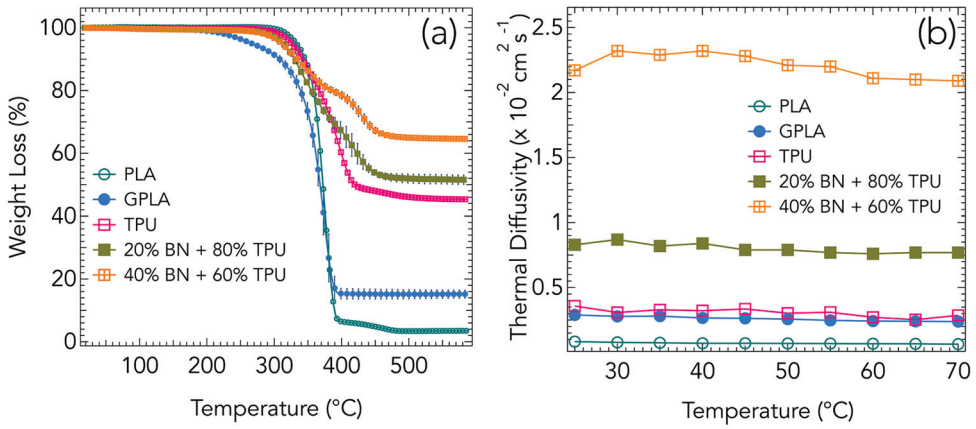

Figure 1. (**a**) Thermogravimetric analysis (TGA) showing the weight loss (%) as a function of temperature for different polymer composites: neat PLA, graphene-PLA (GPLA), neat TPU, 20 wt.% BN + 80 wt.% TPU, and 40 wt.% BN + 60 wt.% TPU. All measurements on composite samples represent the average of three measurements presented along with corresponding error bars. PLA and GPLA exhibit sharp degradation around 350–400 °C, while TPU and BN-TPU composites show enhanced thermal stability, with the 40 wt.% BN composite exhibiting the highest residue at 600 °C. (**b**) Thermal diffusivity as a function of temperature from 25 °C to 70 °C for the same samples. The addition of BN significantly enhances thermal diffusivity, with 40 wt.% BN + 60 wt.% TPU reaching values around 2.32 × 10^{-2} cm^2/s at temperature 30 °C, much higher than neat PLA and GPLA, indicating the effectiveness of BN as a thermally conductive filler.

To evaluate the performance of the TIMs, two complementary experimental setups were implemented using identical cooling and measurement configurations. In the first setup, six 18650-type cells (Panasonic NCR18650GA, 3300 mAh) were mounted in a custom aluminum manifold with internal coolant tubes (Figure 2a) similar in design to the liquid-cooling plates employed in commercial EV battery packs (e.g., Tesla Model 3). The liquid coolant (deionized water) was circulated through the manifold at a flow rate of 40 mL min^{-1}

using an electric pump. As shown in Figure 2, TIMs were placed between the cooling tubes and the battery surfaces on both sides of the module to ensure uniform thermal contact. Six *K*-type thermocouples were inserted to monitor the temperature of each cell, and data were recorded using the PICOLOG 6 software. In addition, an infrared camera (FLIR E60, Wilsonville, OR, USA) was used to capture thermal images at different stages of the heating and cooling process. The battery module was heated externally using a hot plate to approximately 45 °C and subsequently cooled inside a hood with controlled airflow at 120 cfm. All measurements were performed in triplicate ($n = 3$) to ensure statistical reproducibility.

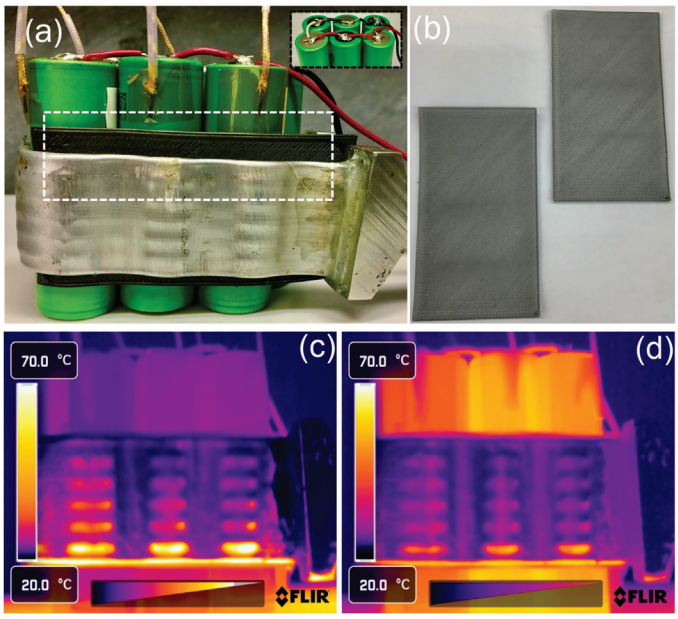

Figure 2. (**a**) A 6-cell (3s2p) cylindrical Li-ion battery module integrated with thermal interface materials (TIMs) and an aluminum cooling plate for thermal performance evaluation. The inset shows the electrical wiring of the battery pack. (**b**) A representative photograph of PLA and TPU polymer composites used as TIMs. (**c**) Infrared (IR) thermal image of the battery module with TIMs under operation, showing thermal gradients with initial heat concentrated at the bottom of the cells. (**d**) IR thermal image of the battery module after 30 min showing heat distributed across the entire body of 18650 cells. Thermal imaging was conducted using a FLIR camera, with the temperature range set from 20 °C to 70 °C.

In the second setup, the TIMs were tested under active electro-thermal cycling in a prototype battery pack configured as 3s2p using six Panasonic NCR18650GA cells. The pack was enclosed in an environmental chamber (Neware) and fitted with the same aluminum coolant manifold, thermocouple placement, and coolant flow conditions as in the external-heating setup. The pack was charged and discharged continuously at different C-rates using a Neware CE6000 (20 A/60 V) testing system (Shenzhen, China) while monitoring the surface temperatures of each cell. The water coolant was circulated continuously during operation (40 mL min^{-1}), and the chamber was sealed to maintain consistent ambient conditions. Tests were repeated for both TIM configurations (PLA and 40 wt.% BN–60 wt.% TPU) following the same experimental protocol. This dual approach enabled the evaluation of TIM performance under both externally induced thermal loading and realistic charge–discharge cycling conditions, providing a comprehensive assessment of thermal dissipation and uniformity.

Scanning electron microscope images, presented in Figures S1 and S2 of the supporting information, were obtained using a Hitachi 6600 SEM (Schaumburg, IL, USA). High resolution X-ray diffraction (HR-XRD) is performed using a RIGAKU Ultima IV diffractometer (Tokyo, Japan) employing Cu Kα radiation, on powder samples that were held by a standard Al sample holder. Quantitative analysis using Rietveld refinement is performed on the XRD peaks using PDXL 2 software. Atomic force microscopy (AFM) measurements were performed in a non-contact mode using AIST-NT SPM Smart system (HORIBA, Kyoto, Japan) and cantilevers (HQ: NSC14/Al BS-50) from Micromasch. AIST-NT image analysis and processing (Version 3.2.14) software was used for AFM image analysis. Malvern Zetasizer 90 (Westborough, MA, USA) was used for dynamic light scattering measurements. Based on the DLS measurements, the average lateral size of BN particles is 745 ± 92 nm, which is consistent with the average size deduced from AFM measurements that showed an average lateral size of 600–800 nm with a thickness of 70–100 nm (see Figure S3 in the supporting information). Differential scanning calorimetry was performed to extract the specific heat values (Figure S4) using TA instruments Discovery DSC (New Castle, DE, USA) from 25 to 600 °C.

2.4. COMSOL Modeling

The computational modeling of heat-transfer behavior was carried out using COMSOL MULTIPHYSICS 6.2 employing the finite-element method (FEM). The goal of the simulations was not to model electrochemical reactions or voltage behavior, but rather to evaluate the thermal efficiency of different TIMs under controlled and comparable boundary conditions. Accordingly, the built-in electro-thermal *Li-ion Battery Module* (`liion`) was used with the standard $LiMn_2O_4$ (LMO)–graphite chemistry available in the COMSOL materials library [57–59]. This configuration provides a well-validated electro-thermal coupling framework for heat generation without explicitly solving the full electrochemistry. To represent the NCA-based Panasonic NCR18650GA cells used experimentally, the model was normalized to their nominal capacity and *C*-rate (3.7 V, 3300 mAh, 1C = 3.3 A) so that the total heat generation corresponded to the actual operating conditions of the commercial cells. Because all TIMs and boundary conditions were held identical across simulations, this normalization allows for a direct comparative assessment of thermal performance without affecting the relative temperature trends.

Two simulation configurations were developed, mirroring the experimental setups described earlier. In the first configuration, six cylindrical 18650 cells were modeled within an aluminum cooling manifold subjected to an external heat flux to replicate the controlled-heating experiments. The coolant flow and convective boundary conditions were identical to those in the laboratory tests. Additionally, individual-cell simulations were performed to study the effect of *C*-rate on temperature evolution by charging single cells independently at different C-rates. In the second configuration, a 3s2p battery module was modeled, with all six cells electrically connected in series–parallel and operated under a continuous charge–discharge protocol. This setup replicates the electro-thermal-cycling experiments performed in the environmental chamber.

The electro-thermal model was coupled to the Heat Transfer in Solids and Fluids (`ht`) module using the spatially averaged heat-generation rate $Q_{h(\mathrm{avg})}$ and temperature T_{avg} from the `liion` module. The coolant flow through the aluminum manifold was implemented using the *Laminar Flow* (`spf`) module with a non-slip boundary condition and a volumetric flow rate of matching the experimental value of 40 mL min^{-1}. The heat-transfer and flow physics were coupled through the *Non-Isothermal Flow* (`nitf`) interface to capture the conjugate heat exchange between the cells, TIMs, and coolant. For the second

configuration, *battery pack* (bp) interface was used instead, with *electrochemical heating* (ech) as the multiphysics to account for the.

The geometric dimensions and material properties of the TIMs ($70 \times 30 \times 1.4$ mm) matched those used experimentally. Anisotropic thermal conductivities were assigned to the cylindrical cells in a local coordinate system to approximate the spiral-wound electrode geometry. Normal meshing (maximum element size 11.4 mm) was applied to the solid domains, and finer meshing (maximum element size 5.3 mm) was used along the coolant tube surfaces to resolve temperature gradients accurately. The simulations yielded transient temperature profiles for all cells and TIM configurations, which were then analyzed to extract the cooling time constant τ, the inter-cell temperature differential ΔT, and relative temperature differences with different TIMs.

3. Results

Figure 1a presents the TGA curves for five materials: neat PLA, GPLA, neat TPU, and TPU loaded with 20 wt.% and 40 wt.% BN. All samples were heated under nitrogen atmosphere up to 600 °C, and weight loss was monitored to evaluate thermal degradation behavior and filler content. Neat PLA and GPLA both exhibit a sharp one-step degradation between 300 °C and 400 °C, consistent with known depolymerization and chain scission mechanisms of PLA [11]. However, the GPLA sample demonstrates a slightly earlier onset of decomposition and retains significantly more mass at high temperature due to the presence of graphene fillers. Specifically, at 450 °C, PLA retains less than 2% of its initial mass, whereas GPLA retains approximately 15%. This difference indicates that there is ∼15 wt.% of graphene incorporated into GPLA. Neat TPU shows a broader and more gradual weight loss profile with a single step beginning near 300 °C, and a residual mass of around 45% at 450 °C. Such a single-step decomposition process is characteristic of the breakdown of both hard and soft segments in the polymer matrix. The addition of BN significantly alters this behavior. The 20%BN–80%TPU composite exhibits a two-step decomposition with a second decomposition onset at 400 °C and retains approximately 52% of its initial mass at 450 °C. The 40%BN–60%TPU sample demonstrates the highest thermal stability among all samples, retaining nearly 70% of its mass at the same temperature. The two-step decomposition is more evident in 40%BN–60%TPU sample. The progressive increase in residue with h-BN loading is indicative of the high thermal stability of h-BN, which acts as an inert filler resisting oxidative or thermal degradation [16]. The emergence of a second decomposition step in BN–TPU composites at 400 °C can be attributed to interfacial interactions between the BN fillers and the TPU chains. The high thermal stability and inertness of BN not only provide a thermal shielding effect but also restrict the mobility of TPU chains through non-covalent interactions such as van der Waals forces or hydrogen bonding (e.g., N–H$\cdots$BN). These interfacial effects delay the decomposition of segments closely associated with BN surfaces, resulting in the observed higher-temperature degradation step. Therefore, the two-step decomposition is indicative of filler-mediated stabilization and heterogeneous breakdown of the polymer matrix in the presence of thermally robust BN domains.

Figure 1b shows the thermal diffusivity of the same five samples as a function of temperature up to 70 °C. The diffusivity data reveals a clear hierarchy in thermal transport performance, strongly dependent on the type and concentration of thermally conductive fillers. The highest thermal diffusivity is observed in the 40%BN–60%TPU composite, with value 2.32×10^{-2} cm^2 s^{-1} at a temperature of 30 °C. This value is more than an order of magnitude higher than that of the base TPU, which maintains a diffusivity near 3.5×10^{-3} cm^2 s^{-1}. The 20%BN–80%TPU composite shows intermediate performance, with

a diffusivity of approximately 8.5×10^{-3} cm^2 s^{-1}. This behavior is consistent with general percolation theory for platelet-based composites, where continuous thermally conductive pathways typically emerge near one-third filler loading (30–35 wt.%), as reported for polymer systems with platelet shaped fillers such as h-BN and graphene [18,31]. Below this threshold (as in the 20%BN–80%TPU composite), filler particles are isolated and heat transfer remains matrix-dominated. Above the threshold (as in the 40%BN–60%TPU composite), an interconnected BN network enhances phonon transport and suppresses interfacial resistance. The GPLA sample exhibits only a marginal improvement over neat PLA, with diffusivity values of about 3.0×10^{-3} cm^2 s^{-1} compared to 2.1×10^{-3} cm^2 s^{-1} for PLA. This modest increase suggests graphene in PLA matrix (15 wt.% based on TGA in Figure 1a) is suboptimal for effective thermal transport. The enhancement of thermal diffusivity in TIMs after incorporation of BN filler into the neat polymer matrix is also observable in TIM IR images different temperatures (see supporting information Figure S6).

TIM expeimental characterization using the first setup with an external heat source: As mentioned in Section 2, two complementary experimental setups were implemented using identical cooling and measurement configurations. Below, we discuss the results from the first setup where a module comprising six cylindrical Li-ion cells was assembled with the TIM inserted between the cells and the liquid cooling manifold (Figure 2a,b). The module was subjected to controlled external heating inside a forced-air convection hood with an airflow rate of 120 cfm. Heating was continued until the average temperature of the battery module reached approximately 45 °C, at which point the heat source was turned off, initiating the cooling phase. Each cell was attached with an independent thermocouple to monitor transient temperature profiles throughout the heating and cooling cycles. The aqueous liquid coolant was pumped through the Al manifold throughout the heating and cooling cycles. Typical IR images of the cells at different stages of heating are shown in Figure 2c,d.

Figure 3a shows the representative thermal response for all six cells when PLA was used as the TIM. Although all cells were exposed to the same environmental conditions, the temperature evolution was non-uniform, with distinct differences in heating rates and peak temperatures. Notably, Battery-1 reached the highest temperature while Battery-6 remained significantly cooler, exhibiting a temperature difference of nearly 4 °C at the peak. These differences reflect the anisotropic thermal conductance within the module and asymmetries in cell-to-manifold contact. Figure 3b shows the average temperature ($\bar{T}$) of the entire module, obtained from the temperature readings from all six thermocouples. The average curve shows a smooth and symmetric profile with a clear demarcation between the heating and cooling phases. To evaluate thermal uniformity within the module, the temperature difference $\Delta T_i(t) = |T_i(t) - \bar{T}(t)|$ was computed for each cell i with respect to the instantaneous average temperature $\bar{T}(t)$. The results are plotted in Figure 3c. The ΔT curves show that thermal nonuniformity peaks near the end of the heating phase, where some cells lag in temperature rise compared to others. During the cooling phase, ΔT gradually decreases as heat is more uniformly extracted via the manifold, but notable differences persist over the full transient period.

The transient cooling behavior of the battery module, following the removal of the external heat source, was analyzed using the following thermal conduction model. TIM serves as the dominant path for heat dissipation from the battery cells to the cooling manifold. Assuming negligible heat generation during the cooling phase and lumped thermal capacity of the cells, the rate of temperature decay can be modeled by equating the rate of internal energy loss to the conductive heat flux through the TIM. The rate of heat loss from the battery can be expressed as

$$-\dot{Q} = C_{p,\text{dev}} M_{\text{dev}} \frac{dT}{dt} \tag{1}$$

where $C_{p,\text{dev}}$ is the specific heat capacity and M_{dev} is the effective thermal mass of the battery module. In the absence of a cooling liquid, the heat flux through the TIM is modeled as

$$\dot{Q} = \frac{\kappa A_{\text{TIM}}}{d_{\text{TIM}}} (T - T_\infty) \tag{2}$$

where κ is the thermal conductivity of the TIM, A_{TIM} is the contact area, d_{TIM} is the TIM thickness, T is the instantaneous temperature of the battery, and T_∞ is the steady-state temperature.

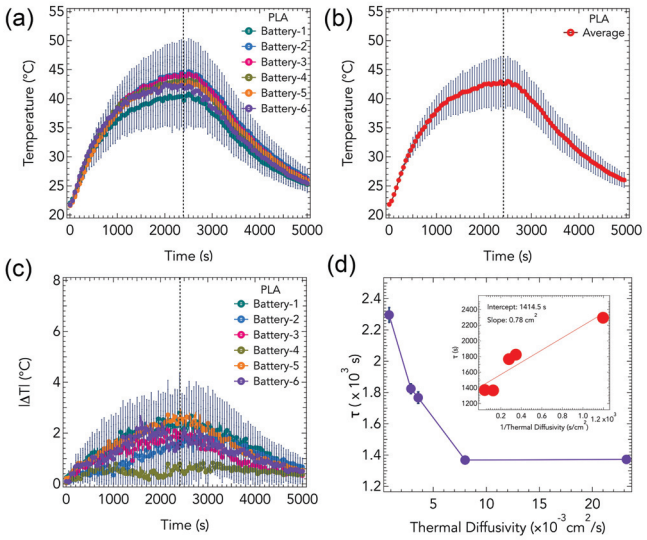

Figure 3. (**a**) Temperature profiles of six individual battery cells within a module equipped with a PLA thermal pad during a heating-cooling cycle. All cells show consistent temperature rise and fall, with slight variations among them. (**b**) Average temperature profile of the battery module with clear distinction between heating and cooling phases, with the switching point around 2200 s. (**c**) Temperature deviation (ΔT) from the average for individual batteries over time, indicating thermal non-uniformity within the module during operation. (**d**) Correlation between thermal time constant τ and thermal diffusivity of different TIM materials. The inset shows a linear fit of τ versus inverse thermal diffusivity, confirming expected thermal transport behavior. Higher diffusivity materials lead to faster heat dissipation and lower τ values.

Equating these expressions yields the governing differential equation for temperature decay:

$$C_{p,\text{dev}} M_{\text{dev}} \frac{dT}{dt} = -\frac{\kappa A_{\text{TIM}}}{d_{\text{TIM}}} (T - T_\infty) \tag{3}$$

which simplifies to

$$\frac{dT}{dt} = -\frac{\kappa A_{\text{TIM}}}{C_{p,\text{dev}} M_{\text{dev}} d_{\text{TIM}}} (T - T_\infty) \tag{4}$$

Introducing the thermal diffusivity $\alpha = \kappa / (\rho C_{p,TIM})$, the time constant τ governing exponential decay is given by

$$\tau = \frac{C_{p,\text{dev}} M_{\text{dev}} d_{\text{TIM}}}{\rho_{\text{TIM}} C_{p,\text{TIM}} \alpha_{\text{TIM}} A_{\text{TIM}}} \tag{5}$$

showing that τ is inversely proportional to the thermal diffusivity α_{TIM} of the interface material. Thus, the solution to the temperature decay equation is an exponential approach to T_∞:

$$T(t) = T_\infty + (T_0 - T_\infty)e^{-t/\tau} \tag{6}$$

where T_0 is the initial temperature at the start of the cooling phase. Equation (6) was used to fit the experimental cooling data for each TIM configuration. The extracted decay constant τ provides a quantitative measure of the rate at which the battery module sheds heat. All the fit values are provided in Table S2 in the supporting information. Lower values of τ correspond to faster cooling and more thermally effective TIMs. The fitted results were subsequently compared across different TIM materials and correlated with their independently measured thermal diffusivities to verify the predicted inverse relationship $\tau \propto 1/\alpha_{\mathrm{TIM}}$. A representative plot (see Figure 3d) confirms this trend.

It is important to note that the analytical model presented above isolates the dominant contribution of heat conduction through the TIM, while assuming other paths and contact resistances to be constant. In the actual experimental configuration, heat is dissipated simultaneously through (i) the liquid coolant flowing in the Al manifold and (ii) external forced convection at an airflow rate of 120 cfm. The complete heat-transfer network therefore consists of the TIM conduction resistance in series with contact, aluminum, and coolant-side resistances, acting in parallel with the external convective branch. To account for these effects, Equation (3) can be generalized as

$$\dot{Q}_{\mathrm{tot}} = (T - T_\infty)\left[\frac{1}{\frac{d_{\mathrm{TIM}}}{k_{\mathrm{TIM}}A_{\mathrm{TIM}}} + R_{c,\mathrm{cell|TIM}} + R_{c,\mathrm{TIM|manifold}} + R_{\mathrm{Al}} + \frac{1}{h_{\mathrm{liq}}A_{\mathrm{liq}}}} + h_{\mathrm{ext}}A_{\mathrm{ext}}\right], \tag{7}$$

where $R_{c,\mathrm{cell|TIM}}$ and $R_{c,\mathrm{TIM|manifold}}$ denote the contact resistances at the respective interfaces, R_{Al} is the conduction resistance of the Al manifold, and $h_{\mathrm{liq}}A_{\mathrm{liq}}$ and $h_{\mathrm{ext}}A_{\mathrm{ext}}$ represent the convective heat-transfer coefficients and effective areas for the liquid and air cooling paths, respectively. The corresponding cooling time constant can then be expressed as

$$\tau = \frac{C_{p,\mathrm{dev}}M_{\mathrm{dev}}}{G_{\parallel}} = \frac{C_{p,\mathrm{dev}}M_{\mathrm{dev}}}{\frac{1}{R_{\mathrm{series}}} + h_{\mathrm{ext}}A_{\mathrm{ext}}}, \tag{8}$$

where $R_{\mathrm{series}} = \frac{d_{\mathrm{TIM}}}{k_{\mathrm{TIM}}A_{\mathrm{TIM}}} + R_{c,\mathrm{cell|TIM}} + R_{c,\mathrm{TIM|manifold}} + R_{\mathrm{Al}} + \frac{1}{h_{\mathrm{liq}}A_{\mathrm{liq}}}$ and $G_{\parallel}$ is the total parallel conductance. Under identical cooling conditions across all experiments, the comparative dependence of τ on $1/\alpha_{\mathrm{TIM}}$ remains valid, with the slope determined by the TIM properties and the intercept representing the cumulative parasitic resistances (see the inset in Figure 3d).

Figure 4 presents the time-resolved temperature deviations $\Delta T_i(t) = |T_i(t) - \bar{T}(t)|$ for each of the six cells in the attery module using five different TIMs: (a) PLA, (b) GPLA, (c) TPU, (d) 20%BN–80%TPU, and (e) 40%BN–60%TPU. The metric ΔT quantifies the deviation of each cell's temperature from the instantaneous module average $\bar{T}(t)$, providing a dynamic measure of inter-cell thermal uniformity. Interestingly, the PLA TIM—despite having the lowest thermal diffusivity among the tested materials—exhibits the narrowest spread in ΔT, with all six cells maintaining relatively close thermal trajectories. The peak ΔT remains below 3 °C throughout the thermal cycle. This result appears counterintuitive given PLA's poor thermal conductivity. However, it can be rationalized by considering the relatively uniform thermal impedance across all cell–manifold interfaces: in the absence of

a highly conductive path, each cell dissipates heat at a similar, albeit slow, rate (as indicated by a high τ for PLA in Figure 3d). The system behaves almost adiabatically on short time scales, and thermal gradients develop primarily due to intrinsic differences in cell positioning or contact pressure rather than material-mediated heat spreading.

In contrast, the introduction of higher-diffusivity TIMs such as GPLA and TPU increases the magnitude and spread of ΔT. Notably, the GPLA TIM (Figure 4b) exhibits the largest inter-cell thermal heterogeneity, with Battery-6 showing a pronounced deviation exceeding 5 °C. This suggests that while the thermal conductivity of GPLA is higher than PLA, it remains insufficient to rapidly redistribute heat, and may accentuate local differences arising from subtle variations in thermal contact resistance. Similarly, the TPU-only TIM (Figure 4c) produces a broader ΔT spread than PLA, albeit less pronounced than GPLA. These observations underscore the sensitivity of thermal equilibration to both filler dispersion and the quality of interface coupling between cells and the cooling manifold. For the 20%BN–80%TPU system (Figure 4d), peak ΔT values slightly increased, with Battery-1 deviating significantly from the average. In the 40%BN–60%TPU composite (Figure 4e), the inter-cell temperature differences become markedly lower, and the spread among all six cells narrows considerably. This suggests that only beyond a critical threshold of thermal diffusivity does the TIM effectively serve its homogenizing function, enabling lateral heat spreading across the module to suppress local temperature peaks.

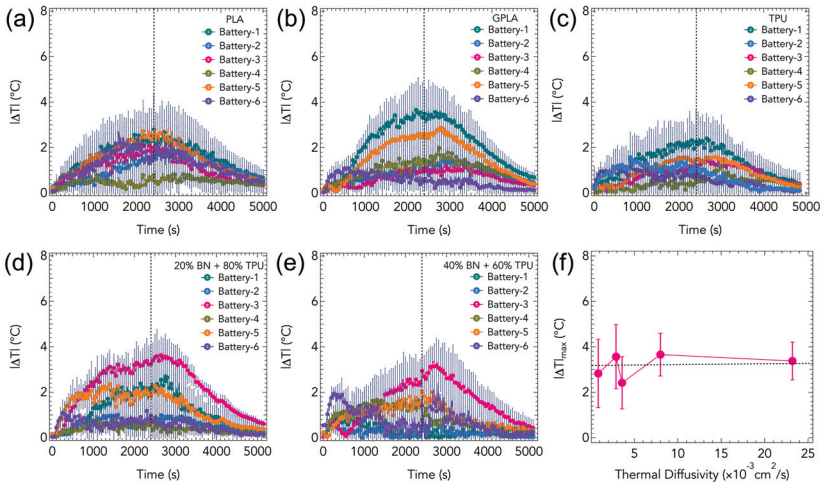

Figure 4. Inter-cell temperature deviation $\Delta T_i(t) = |T_i(t) - \bar{T}(t)|$ as a function of time for six battery cells using different thermal interface materials (TIMs): (**a**) PLA, (**b**) graphene–PLA, (**c**) TPU, (**d**) 20%BN–80%TPU, and (**e**) 40%BN–60%TPU. Each curve represents the temperature deviation of an individual cell relative to the instantaneous module-average temperature during a controlled heating–cooling cycle. The temporal evolution and spread of ΔT reveal the extent of lateral thermal nonuniformity. Panel (**f**) shows the peak ΔT, averaged across all six cells, plotted against the corresponding thermal diffusivity of each TIM. Error bars denote standard deviation from multiple trials. A downward trend is observed, with a marked reduction in ΔT at higher thermal diffusivities ($>10^{-2}$ cm^2/s), suggesting a threshold for effective lateral heat spreading.

It should be noted that an ideal TIM should simultaneously exhibit both a high rate of cooling (see Figure 3d) and a low spread of ΔT, which is achieved in our case through 40%BN–60%TPU composites. The physical mechanism underlying these trends can be understood in terms of the competition between two thermal processes: (1) vertical heat sinking into the cooling manifold, and (2) lateral thermal diffusion across adjacent cell interfaces via the TIM. At low diffusivity (e.g., PLA), both mechanisms are weak,

resulting in symmetric but slow heat loss across the module. As diffusivity increases without reaching the percolation threshold (e.g., GPLA, 20%BN–TPU), lateral diffusion becomes anisotropic and non-uniform, which can amplify local hotspots, especially near the geometric or thermal boundaries of the module. Once the TIM achieves sufficiently high diffusivity (e.g., 40%BN–TPU), lateral heat transfer dominates, allowing efficient redistribution of thermal energy from warmer to cooler regions and thus reducing ΔT. Edge effects are also evident in these data due to the finite size of the battery module and the small number of monitored cells (N = 6). Cells located at the periphery (e.g., Battery-1 or Battery-6) often show the largest deviation from the average temperature. This behavior is consistent with the expectation that edge cells experience asymmetric thermal environments—differing airflow exposure, partial insulation, or varying proximity to the cooling manifold boundaries. To further elucidate the relationship between TIM thermal properties and inter-cell thermal uniformity, we extracted the peak values of ΔT for each configuration and plotted them against the measured thermal diffusivity of the corresponding materials, as shown in Figure 4f. Error bars represent the standard deviation of the peak ΔT values across three replicates for each TIM. In summary, the performance of a TIM involves a fundamental trade-off between heat storage and heat dissipation. Materials with low thermal diffusivity can buffer transient heat and delay propagation, whereas those with higher diffusivity promote rapid heat spreading and minimize local temperature gradients. In the present study, GPLA represents a heat-storage-dominated regime, while BN–TPU (particularly 40 wt.%) exemplifies a high-diffusivity, heat-dissipating regime that enhances thermal uniformity across cells.

COMSOL simulation of TIM performance using the first setup with an external heat source: To evaluate the dynamic thermal response of the battery module under practical operating conditions, COMSOL Multiphysics simulations were conducted across a range of charge–discharge (CD) rates (1C, 2C, 4C, and 8C) [2,60–65]. A six-cell Li-ion battery module was subjected to 10 continuous charge–discharge cycles at varying C-rates (1C, 2C, 4C, and 8C), followed by a 2.5-h cooling period with various TIMs placed between the cells, as shown in Figure 5. Figure 5a presents a representative image of the temperature profile at the end of the first cycle using PLA as the TIM. The thermal distribution among the cells is relatively symmetric. However, we notice an increase in the cell temperature, as evidenced by different colors of the liquid-cooling manifold (hot pink) compared to the cells (golden yellow). Figure 5b–f depict the temperature profiles at the end of the tenth cycle for the different TIMs. For PLA (Figure 5b), a significant temperature increase is evident, with pronounced hotspots in TIM toward the left edge of the cell. The GPLA and TPU TIMs (Figure 5c,d) demonstrate improved thermal performance relative to PLA, but still exhibit notably asymmetry as noticed from different colors for the liquid-cooling manifold (purple) and the cells (orange for GPLA and hot pink for TPU). These results are consistent with their moderate thermal diffusivities, which enable some degree of vertical heat sinking but are insufficient for complete lateral thermal equilibration. The 20% BN–TPU composite (Figure 5e) provides a further reduction in maximum temperature and a modest improvement in uniformity. The most striking improvement is observed with the 40% BN–TPU composite (Figure 5f), where the temperature field is both lower in magnitude and more homogeneous with the liquid-cooling manifold and the cells both showing similar color.

To analyze more quantitatively, we present the average temperature profiles in Figure 6. Each subplot compares the temperature rise for different TIM configurations: PLA, GPLA, TPU, 20% BN–TPU, and 40% BN–TPU. Across all conditions, a clear and systematic increase in temperature with increasing C-rate is observed, consistent with the enhanced internal heat generation governed by the relation $Q \propto I^2R$, where I is the current and R is the internal resistance of the cell. At low C-rates (e.g., 1C in Figure 6a), the thermal load is moderate leading

to maximum temperature $\leq 22\,^{\circ}C$. At 1C, all TIMs appear reasonably effective in preventing excessive temperature rise, although subtle differences in performance are already discernible with 40% BN–TPU showing the best performance, as expected. As the C-rate increases (particularly at 4C and 8C) in Figure 6b–d, the distinctions among TIMs become significantly more pronounced. Notably, the PLA TIM, which exhibits the lowest thermal diffusivity among the tested materials, results in the highest average temperatures at every C-rate. In contrast, the 40% BN–TPU composite consistently demonstrates the lowest temperature profiles across all C-rates, highlighting the role of enhanced thermal diffusivity in facilitating vertical heat sinking and efficient thermal management. Furthermore, all materials exhibit a thermal staircase in peak temperature with increasing C-rate, indicating cumulative heating effects due to incomplete thermal recovery between successive cycles.

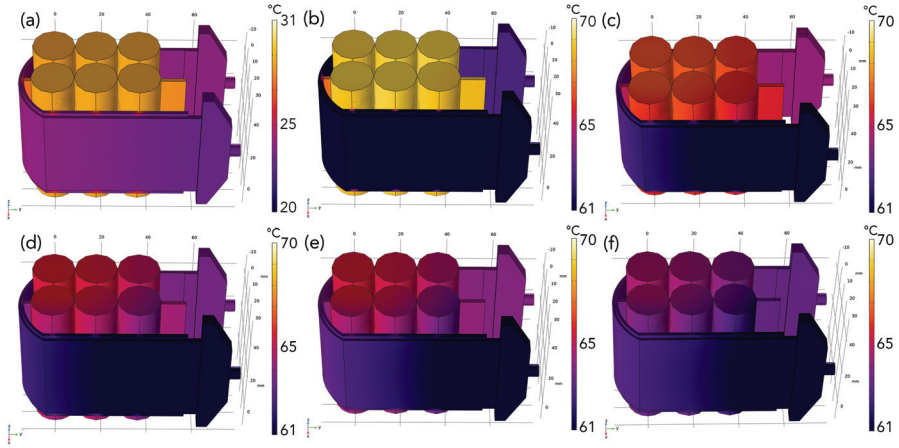

Figure 5. 3D temperature mapping on the 6 cell module captured at (**a**) 900 s (i.e., the end of the first charge discharge) evaluated at 8C with PLA as the TIM material. The temperature profiles at the end of 10th cycle for different TIM materials, (**b**) PLA, (**c**) GPLA, (**d**) TPU (**e**) 20% BN-TPU and (**f**) 40% BN-TPU.

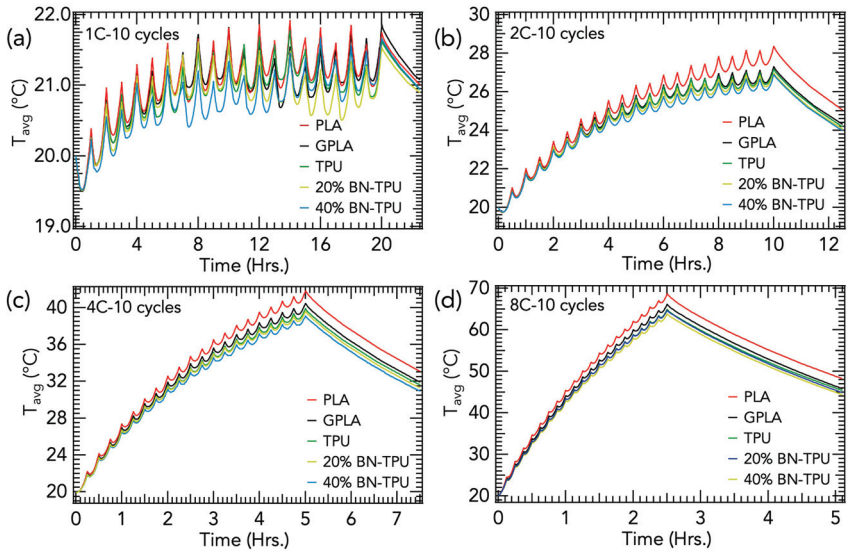

Figure 6. The average temperature profile measured across six individual battery cells within a module equipped with different TIM materials during charge–discharge cycles at (**a**) 1C, (**b**) 2C (**c**) 4C and (**d**) 8C rates. PLA, GPLA, TPU, 20% BN-TPU and 40% BN-TPU were used as different TIM while TPU was employed to isolate batteries in between. All models were solved for 10 continuous cycles (individual charge–discharge), followed by a 2.5-h cooling period. PLA (40% BN-TPU) showed the maximum (minimum) T, with all materials exhibiting a thermal staircase rise in dT with increasing C-rate.

At the highest C-rate of 8C, PLA exhibited the largest T_{avg}, reaching slightly above 50 °C over the course of the cycles (Figure 7a). In contrast, the 40%BN–TPU TIM, which demonstrated the highest experimental thermal diffusivity, limited the thermal rise to below 50 °C, despite identical electrochemical and convective boundary conditions. Figure 7b–e present the average inter-cell temperature deviation, calculated as $\delta\bar{T}_{CD}$=$\Sigma(T_i - T_{avg})/6; (i = 1, .., 6)$, for each TIM configuration across charge–discharge cycles at different C-rates. Across all C-rates, a clear hierarchy in $\delta\bar{T}_{CD}$ emerges. Low-diffusivity TIMs such as PLA and GPLA exhibit the lowest inter-cell deviations in contrast to high-diffusivity TIMs (similar to results discussed in Figure 4). As discussed earlier, this can be rationalized in terms of the balance between vertical heat transfer to the manifold vs. the lateral heat spreading. While high diffusivity TIMs enable faster heat decay through vertical heat transfer (cf. Figure 3d), there is asymmetric lateral heat diffusion resulting in higher inter-cell deviations.

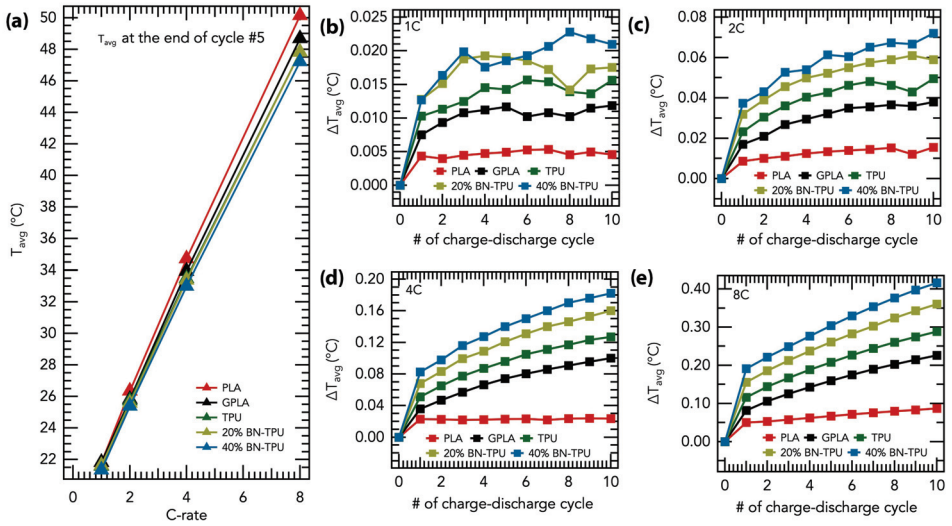

Figure 7. (**a**) The average temperature (T_{avg}) as a function of the C-rate for different TIM materials. The average temperature deviation, $\delta\bar{T}_{CD}$ across the batteries within the module during charge–discharge cycles when operated at (**b**) 1C, (**c**) 2C, (**d**) 4C and (**e**) 8C. A clear non-uniformity in the temeprature distribution was observed at all C-rates with significant dependence on the TIM material used.

TIM performance using the second setup with a 3s2p module: To gain a deeper understanding of the effect of TIMs on battery pack thermal management and compare with COMSOL simulation, we designed a 3s2p battery pack with an aluminum coolant tube and TIMs (PLA and 40% BN + 60% TPU) configuration in COMSOL Multiphysics. The simulation was run at different charge–discharge rates. The respective 3D temperature mappings are shown in Figure 8. A significant decline in the average surface temperature was observed when 40%BN+TPU was used as the TIM material (Figure 8c,d) compared to PLA (Figure 8b,e).

Figure 9a shows the COMSOL simulated results for the average temperature of the battery pack at 1.4 C-rate. Clearly, the average temperature decreases when using BN-filled TPU TIM compared to PLA. To compare with experimental results, we measured temperature of six 18650 Li-ion batteries configured in 3s2p (along with a coolant tube and TIMs) similar to the simulation design. Each battery in the pack was connected with a thermocouple to record the temperature. The experiment was run at a continuous constant current charge–discharge rate of 1.4 C for 10 cycles. In Figure 9b, the average temperature

of the battery pack is plotted after 10 cycles with neat PLA and 40% BN + 60% TPU TIMs. The results show that the average battery pack temperature reaches approximately 43 °C with PLA. In contrast, with BN-filled TPU TIM, the average pack temperature is recorded at approximately 38 °C. The percent difference between 40% BN + 60% TPU and PLA, observed in both experiment and simulations, are shown in Figure 9c. The observed trend reveals a remarkably strong relationship between the experimental and simulated results with a Pearson correlation coefficient of 0.9775. This indicates excellent linear agreement in their trends, where 97.75% of the variance in one series is explained by the other, demonstrating that the sequences evolve in near-perfect lockstep. Furthermore, the normalized correlation (using z-scores to focus solely on scale-invariant shape and pattern) mirrors this value at 0.9775, underscoring the simulation's fidelity in capturing the temporal dynamics of the experimental data [66,67].

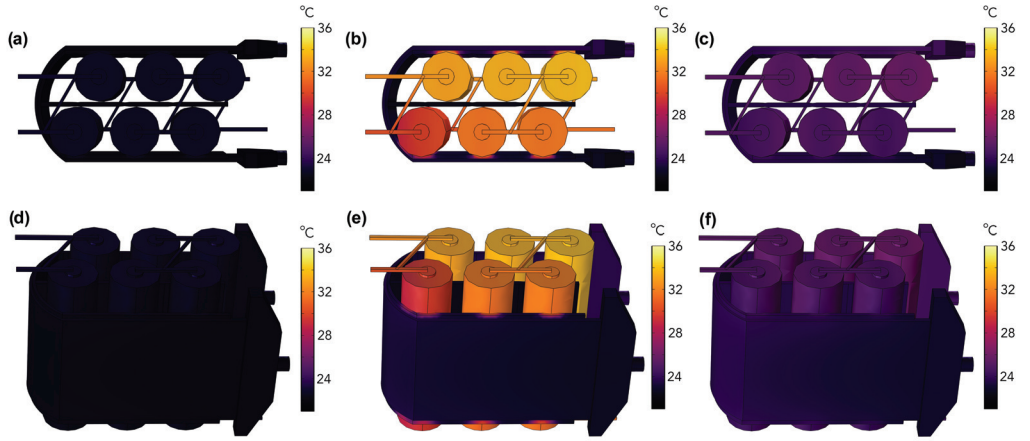

Figure 8. 3D temperature mapping on the battery module arranged in 3s2p configuration with different TIM materials. All connections were made with aluminum strips with external temperature set to 22 °C. Module was simulated at 1C rate for 10 cycles with coolant flow through the aluminum tubes maintained at 40 mL/min. Top view of the module (**a**) at the beginning of the change discharge cycles, at the end of 10th cycle with (**b**) PLA and (**c**) 40%BN+TPU as the TIM material. Corresponding side views of the same are show in (**d**–**f**). Color bars indicate the maximum surface temperature. A 6 °C decline in the heat distribution is observed on the system with 40%BN+TPU as the TIM material when compared to PLA at the end of 10th cycle.

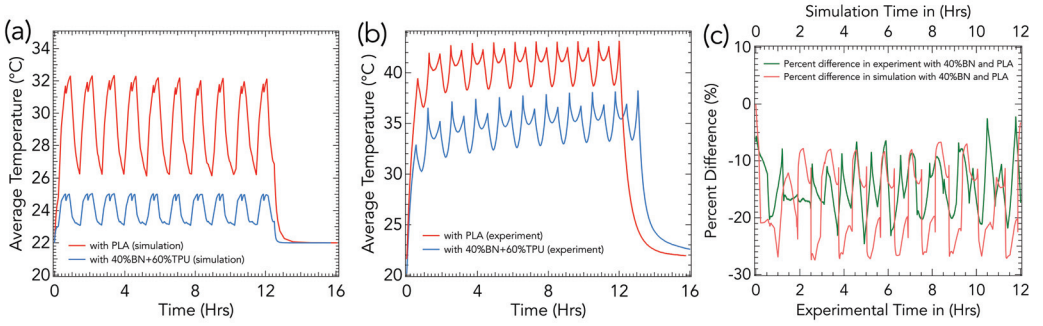

Figure 9. Average temperature profiles of the 3s2p 18650 battery pack with different TIMs (PLA and 40% BN + 60% TPU) at charge–discharge rate 1.4 C after 10 cycles (**a**) Simulation (**b**) Experiment. The use of BN-filled TPU TIM significantly reduced the average temperature of the battery pack compared to PLA, demonstrating its good thermal conductivity and heat dissipation capability. (**c**) A comparison of the percent difference (T_{BN}-T_{PLA}) in average temperature between PLA and 40% BN + 60% TPU, shown for both experimental results and simulations, as a function of cycle number. Negative percent difference indicates that the average temperature with BN TIM is lower than PLA.

Figure 10 compares the experimental and simulated thermal responses of the 3s2p battery module under continuous charge–discharge cycling at different C-rates. Panels (a)–(c) present the percent temperature difference between the high-diffusivity (40 wt.% BN–TPU) and low-diffusivity (PLA) TIMs at 1.35C, 2C, and 2.7C, respectively. In both experiment and simulation, the BN–TPU composite consistently exhibits lower average cell temperatures throughout the cycling process, with the difference becoming more pronounced at higher current loads. The time-dependent profiles show strong overlap between the simulated and measured percent differences, confirming that the COMSOL model accurately captures the transient thermal behavior of the module. As the C-rate increases, the average temperature of the cells rises due to enhanced Joule heating, whereas the relative temperature reduction provided by the BN–TPU TIM ($T_{\mathrm{BN-TPU}} - T_{\mathrm{PLA}}$) remains consistently negative, indicating superior heat dissipation (Figure 10d,e). The excellent agreement between experiment and simulation, within ±10% for the relative temperature difference, demonstrates the validity of the capacity- and C-rate-normalized electro-thermal model. Together, these results confirm that the high-diffusivity BN–TPU composite provides more effective heat removal and temperature uniformity across the module at all tested operating conditions.

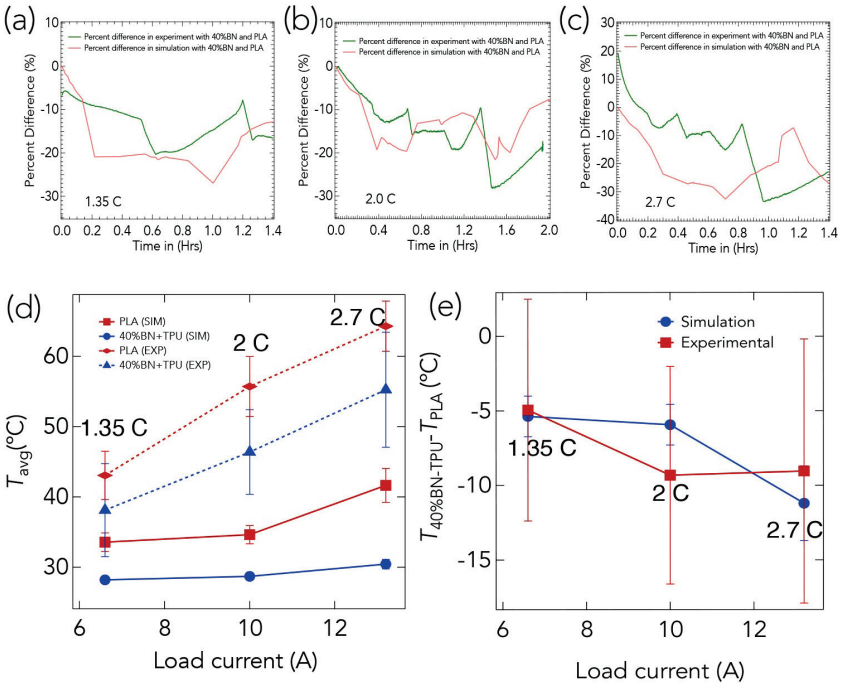

Figure 10. Comparison between experimental and simulated thermal responses of the 3s2p battery module with different TIMs (PLA and 40 wt.% BN–TPU) under various C-rates. (**a**–**c**) Percent temperature difference between BN–TPU and PLA as a function of time during cycling at 1.35C, 2C, and 2.7C, respectively. (**d**) Average cell temperature (T_{avg}) as a function of load current for both TIMs in experiment and simulation. (**e**) Difference in average temperature between BN–TPU and PLA ($T_{\mathrm{BN-TPU}} - T_{\mathrm{PLA}}$) as a function of load current, showing consistent temperature reduction with the high-diffusivity TIM. Error bars denote standard deviation across three independent measurements ($n = 3$). The close match between experiment and simulation confirms the robustness of the normalized electro-thermal model and the superior cooling efficiency of the BN–TPU TIM.

4. Conclusions

We systematically evaluated the thermal performance of graphene-PLA (GPLA) and boron nitride (BN)-loaded TPU composites as thermal interface materials (TIMs) for lithium-ion battery modules. Material characterization confirmed that the incorporation of high

thermal conductivity fillers significantly enhanced both thermal stability and thermal diffusivity. Through a combination of analytical modeling, finite-element simulations in COMSOL Multiphysics, and experimental thermal cycling studies, we established a direct inverse relationship between the TIM thermal diffusivity and the heat decay rate of the battery module. Our analysis further revealed that optimal TIMs must balance vertical heat sinking into the cooling infrastructure with lateral thermal diffusion across adjacent cells to minimize inter-cell temperature gradients. Among the materials studied, the 40%BN–60%TPU composite demonstrated superior performance, achieving both rapid cooling and thermal uniformity. These findings underscore the potential of filler-engineered, additive-manufactured polymer composites for scalable, efficient thermal management in high-power lithium-ion battery applications.

Supplementary Materials: The following supporting information can be downloaded at: https://www.mdpi.com/article/10.3390/batteries11120431/s1, Figure S1: Scanning Electron Microscopy (SEM) images of thermal interface material composites at different magnifications: (a–c) neat TPU, (d–f) 20% BN + 80% TPU, and (g–i) 40% BN + 60% TPU. Each set shows increasing magnification from left to right. The micrographs reveal the evolution of filler dispersion and network formation with increasing BN content. The 40% BN composite (g–i) exhibits denser and more continuous BN particle networks, indicating improved percolation and thermal transport pathways compared to the less aggregated structures in neat TPU (a–c) and 20% BN composites (d–f). Figure S2: (a) Raman spectrum of graphene-loaded polylactic acid (GPLA) showing characteristic D, G, and 2D bands of graphene at ∼1350, ∼1580, and ∼2700 cm^{-1}, respectively. The symmetric stretching mode of the PLA's CH_3 group appears near 2950 cm^{-1}. (b,c) Scanning Electron Microscopy (SEM) images of the fractured surface of 3D printed GPLA composite at different magnifications. The microstructure reveals a dense polymer matrix with embedded graphene nanoplatelets and voids, which may serve as thermal conduction pathways or stress points depending on filler dispersion. Figure S3: (a) X-ray diffraction (XRD) pattern of exfoliated BN micro powder deposited on an aluminum sample holder. The characteristic peaks at approximately 26°, 42°, 50°, and 55° correspond to the (002), (100), (102), and (004) planes of h-BN, while peaks at 38° and 44° originate from the aluminum holder. A lattice constant of 3.29 Å was calculated from the XRD data. (b) Raman spectrum of pristine BNNPs using 532 nm laser excitation, showing the E_{2g} phonon mode centered at 1366 cm^{-1} with a full width at half maximum (FWHM) of 11 cm^{-1}. (c) Atomic force microscopy (AFM) image of exfoliated BN micro powder deposited on SiO_2/Si substrate, revealing platelet-like morphology with lateral dimensions on the order of hundreds of nanometers. (d) Height profile line scans corresponding to two representative BNNPs shown in (c), confirming thicknesses and lateral sizes consistent with DLS measurements. The average lateral size was determined to be 745 ± 92 nm with a thickness of 80 ± 20 nm. Figure S4: Differential Scanning Calorimetry (DSC) curves for PLA, GPLA, TPU, 20%BN–80%TPU, and 40%BN–60%TPU composites. PLA exhibits a two-step degradation process with significant exothermic peaks between 350–450 °C, while GPLA shows slightly earlier onset due to graphene incorporation. Neat TPU and BN–TPU composites demonstrate enhanced thermal stability, with increasing BN content shifting the onset of degradation to higher temperatures and reducing the overall heat flow, indicating improved thermal resistance. The 40%BN–60%TPU composite exhibits the most thermally stable profile among all samples. Figure S5: (a) Specific heat capacity (Cp) and (b) Thermal conductivity (k) as a function of temperature for pristine polymers (PLA, GPLA, and TPU) and BN-loaded TPU composites (20%BN-80%TPU and 40%BN-60%TPU). PLA and GPLA exhibit pronounced Cp transitions near their glass transition temperatures, while TPU and BN composites gradually increase with temperature. The thermal conductivity significantly increases with BN loading, which indicates its effectiveness as a thermal conductive filler for thermal interface materials. Figure S6: Infrared images (IR) of different thermal interface materials (TIMs) — GPLA, PLA, TPU, and 40%BN–60%TPU composites at (a) low-temperature and (b) high-temperature conditions. The color scale represents the surface temperature distribution ranging from 20–70 °C.

Enhanced heat distribution is observed in the 40%BN–60%TPU composite, indicating improved thermal conductivity compared to the neat polymer. Table S1: Comparison of cross-plane thermal conductivity of this work with other BN-Polymer composites. Table S2: Fit coefficients (a, b) with uncertainties for various TIM materials.

Author Contributions: R.P. and P.P. instigated and conceptualized the study. S.K.M. and G.B. prepared the thermal composites with assistance from R.P. and conducted all characterization and experimental measurements. A.F. and S.M.F. performed COMSOL simulations and data visualization under R.P.'s supervision. Y.D. provided design inputs and assisted with data analysis. All authors participated in data analysis, data visualization, and drafting the results. All authors have read and agreed to the published version of the manuscript.

Funding: This work was supported by Clemson University's Virtual Prototyping of Autonomy Enabled Ground Systems (VIPR-GS), under Cooperative Agreement W56HZV-21-2-0001 with the US Army DEVCOM Ground Vehicle Systems Center (GVSC). The sub-project number is 2.23.11 2016337 (PI: Podila). DISTRIBUTION STATEMENT A. Approved for public release; distribution is unlimited (OPSEC 9863).

Data Availability Statement: The raw data supporting the conclusions of this article and Supplementary Materials will be made available by the authors on request.

Acknowledgments: SKM and RP gratefully acknowledge Sriparna Bhattacharya at the Clemson Nanomaterials Institute (CNI) for assistance with the Linseis thermal diffusivity instrument and Rakesh Sachdeva from the Department of Chemistry at Clemson University for support with thermogravimetric analysis (TGA) measurements.

Conflicts of Interest: The authors declare no conflicts of interest.

Abbreviations

The following abbreviations are used in this manuscript:

LIB	Lithium-ion battery
TIMs	Thermal interface materials
PLA	Polylactic acid PLA
GPLA	Graphene-PLA
BN	Boron nitride
TPU	Thermoplastic polyurethane
EVs	Electric vehicles
BTMS	Battery thermal management systems
h-BN	Hexagonal boron nitride
TGA	Thermogravimetric analysis
DMF	N, N-dimethylformamide
XRD	X-ray diffraction
AFM	Atomic force microscopy
DSC	Differential scanning calorimetry
FEM	Finite element method

References

1. Kermani, J.R.; Taheri, M.M.; Pakzad, H.; Minaei, M.; Bijarchi, M.A.; Moosavi, A.; Shafii, M.B. Hybrid battery thermal management systems based on phase transition processes: A comprehensive review. *J. Energy Storage* **2024**, *86*, 111227. [CrossRef]
2. Zhao, Y.; Zhang, X.; Yang, B.; Cai, S. A review of battery thermal management systems using liquid cooling and PCM. *J. Energy Storage* **2024**, *76*, 109836. [CrossRef]
3. Vikram, S.; Vashisht, S.; Rakshit, D.; Wan, M.P. Recent advancements and performance implications of hybrid battery thermal management systems for Electric Vehicles. *J. Energy Storage* **2024**, *90*, 111814. [CrossRef]

4. Liu, J.; Yadav, S.; Salman, M.; Chavan, S.; Kim, S.C. Review of thermal coupled battery models and parameter identification for lithium-ion battery heat generation in EV battery thermal management system. *Int. J. Heat Mass Transf.* **2024**, *218*, 124748. [CrossRef]
5. Hwang, F.S.; Confrey, T.; Reidy, C.; Picovici, D.; Callaghan, D.; Culliton, D.; Nolan, C. Review of battery thermal management systems in electric vehicles. *Renew. Sustain. Energy Rev.* **2024**, *192*, 114171. [CrossRef]
6. Olabi, A.; Maghrabie, H.M.; Adhari, O.H.K.; Sayed, E.T.; Yousef, B.A.; Salameh, T.; Kamil, M.; Abdelkareem, M.A. Battery thermal management systems: Recent progress and challenges. *Int. J. Thermofluids* **2022**, *15*, 100171. [CrossRef]
7. Lin, J.; Liu, X.; Li, S.; Zhang, C.; Yang, S. A review on recent progress, challenges and perspective of battery thermal management system. *Int. J. Heat Mass Transf.* **2021**, *167*, 120834. [CrossRef]
8. Ghalkhani, M.; Habibi, S. Review of the Li-ion battery, thermal management, and AI-based battery management system for EV application. *Energies* **2022**, *16*, 185. [CrossRef]
9. Longchamps, R.S.; Yang, X.G.; Wang, C.Y. Fundamental insights into battery thermal management and safety. *ACS Energy Lett.* **2022**, *7*, 1103–1111. [CrossRef]
10. Li, H.; Wang, H.; Xu, Z.; Wang, K.; Ge, M.; Gan, L.; Zhang, Y.; Tang, Y.; Chen, S. Thermal-responsive and fire-resistant materials for high-safety lithium-ion batteries. *Small* **2021**, *17*, 2103679. [CrossRef]
11. Wang, Z.; Wu, Z.; Weng, L.; Ge, S.; Jiang, D.; Huang, M.; Mulvihill, D.M.; Chen, Q.; Guo, Z.; Jazzar, A.; et al. A roadmap review of thermally conductive polymer composites: Critical factors, progress, and prospects. *Adv. Funct. Mater.* **2023**, *33*, 2301549. [CrossRef]
12. Chen, K.; Zhang, Z.; Wu, B.; Song, M.; Wu, X. An air-cooled system with a control strategy for efficient battery thermal management. *Appl. Therm. Eng.* **2024**, *236*, 121578. [CrossRef]
13. Kalaf, O.; Solyali, D.; Asmael, M.; Zeeshan, Q.; Safaei, B.; Askir, A. Experimental and simulation study of liquid coolant battery thermal management system for electric vehicles: A review. *Int. J. Energy Res.* **2021**, *45*, 6495–6517. [CrossRef]
14. Yu, W.; Liu, C.; Qiu, L.; Zhang, P.; Ma, W.; Yue, Y.; Xie, H.; Larkin, L.S. Advanced thermal interface materials for thermal management. *Eng. Sci.* **2018**, *2*, 1–3. [CrossRef]
15. Guo, H.; Zhao, H.; Niu, H.; Ren, Y.; Fang, H.; Fang, X.; Lv, R.; Maqbool, M.; Bai, S. Highly thermally conductive 3D printed graphene filled polymer composites for scalable thermal management applications. *Acs Nano* **2021**, *15*, 6917–6928. [CrossRef]
16. Ma, H.; Gao, B.; Wang, M.; Yuan, Z.; Shen, J.; Zhao, J.; Feng, Y. Strategies for enhancing thermal conductivity of polymer-based thermal interface materials: A review. *J. Mater. Sci.* **2021**, *56*, 1064–1086. [CrossRef]
17. Lin, Y.; Li, P.; Liu, W.; Chen, J.; Liu, X.; Jiang, P.; Huang, X. Application-driven high-thermal-conductivity polymer nanocomposites. *ACS Nano* **2024**, *18*, 3851–3870. [CrossRef]
18. Lewis, J.S.; Perrier, T.; Barani, Z.; Kargar, F.; Balandin, A.A. Thermal interface materials with graphene fillers: Review of the state of the art and outlook for future applications. *Nanotechnology* **2021**, *32*, 142003. [CrossRef] [PubMed]
19. Akula, R.; Balaji, C. Thermal management of 18650 Li-ion battery using novel fins–PCM–EG composite heat sinks. *Appl. Energy* **2022**, *316*, 119048. [CrossRef]
20. Yuan, Z.; Ma, H.; Hussien, M.A.; Feng, Y. Development and challenges of thermal interface materials: A review. *Macromol. Mater. Eng.* **2021**, *306*, 2100428. [CrossRef]
21. Chen, J.; Xu, X.; Zhou, J.; Li, B. Interfacial thermal resistance: Past, present, and future. *Rev. Mod. Phys.* **2022**, *94*, 025002. [CrossRef]
22. Zhang, Y.; Ma, J.; Wei, N.; Yang, J.; Pei, Q.X. Recent progress in the development of thermal interface materials: A review. *Phys. Chem. Chem. Phys.* **2021**, *23*, 753–776. [CrossRef]
23. Shahil, K.M.; Balandin, A.A. Graphene–multilayer graphene nanocomposites as highly efficient thermal interface materials. *Nano Lett.* **2012**, *12*, 861–867. [CrossRef] [PubMed]
24. Naghibi, S.; Kargar, F.; Wright, D.; Huang, C.Y.T.; Mohammadzadeh, A.; Barani, Z.; Salgado, R.; Balandin, A.A. Noncuring graphene thermal interface materials for advanced electronics. *Adv. Electron. Mater.* **2020**, *6*, 1901303. [CrossRef]
25. Zhang, Y.F.; Han, D.; Zhao, Y.H.; Bai, S.L. High-performance thermal interface materials consisting of vertically aligned graphene film and polymer. *Carbon* **2016**, *109*, 552–557. [CrossRef]
26. Yun, J.; Lee, J.; Kim, J.; Lee, J.; Choi, W. Hexagonal boron nitride nanosheets/graphene nanoplatelets/cellulose nanofibers-based multifunctional thermal interface materials enabling electromagnetic interference shielding and electrical insulation. *Carbon* **2024**, *228*, 119397. [CrossRef]
27. Chung, D. Performance of thermal interface materials. *Small* **2022**, *18*, 2200693. [CrossRef] [PubMed]
28. Luo, T.; Lloyd, J.R. Enhancement of thermal energy transport across graphene/graphite and polymer interfaces: A molecular dynamics study. *Adv. Funct. Mater.* **2012**, *22*, 2495–2502. [CrossRef]

29. Huang, J.; Zhu, Y.; Xu, L.; Chen, J.; Jiang, W.; Nie, X. Massive enhancement in the thermal conductivity of polymer composites by trapping graphene at the interface of a polymer blend. *Compos. Sci. Technol.* **2016**, *129*, 160–165. [CrossRef]
30. Li, A.; Zhang, C.; Zhang, Y.F. Thermal conductivity of graphene-polymer composites: Mechanisms, properties, and applications. *Polymers* **2017**, *9*, 437. [CrossRef]
31. Zhang, P.; Zeng, J.; Zhai, S.; Xian, Y.; Yang, D.; Li, Q. Thermal properties of graphene filled polymer composite thermal interface materials. *Macromol. Mater. Eng.* **2017**, *302*, 1700068. [CrossRef]
32. Lu, X.H.; Liu, J.; Shu, C.; Zhang, S.C.; Zhao, H.Y.; Zhang, Y.; Wang, Q.; Yu, Z.Z.; Li, X. Densifying conduction networks of vertically aligned carbon fiber arrays with secondary graphene networks for highly thermally conductive polymer composites. *Adv. Funct. Mater.* **2025**, *35*, 2417324. [CrossRef]
33. Dai, W.; Wang, Y.; Li, M.; Chen, L.; Yan, Q.; Yu, J.; Jiang, N.; Lin, C.T. 2D materials-based thermal Interface materials: Structure, properties, and applications. *Adv. Mater.* **2024**, *36*, 2311335. [CrossRef] [PubMed]
34. Li, M.; Han, S.; Dan, C.; Wu, T.; You, F.; Jiang, X.; Wu, Y.; Dang, Z.M. Boron Nitride-Polymer Composites with High Thermal Conductivity: Preparation, Functionalization Strategy and Innovative Structural Regulation. *Small* **2025**, *21*, 2412447. [CrossRef] [PubMed]
35. Jia, P.; An, L.; Yu, L.; Pan, Y.; Fan, H.; Qin, L. Strategies for optimizing interfacial thermal resistance of thermally conductive hexagonal boron nitride/polymer composites: A review. *Polym. Compos.* **2024**, *45*, 10587–10618. [CrossRef]
36. Hu, J.; Huang, Y.; Yao, Y.; Pan, G.; Sun, J.; Zeng, X.; Sun, R.; Xu, J.B.; Song, B.; Wong, C.P. Polymer composite with improved thermal conductivity by constructing a hierarchically ordered three-dimensional interconnected network of BN. *ACS Appl. Mater. Interfaces* **2017**, *9*, 13544–13553. [CrossRef]
37. Ravichandran, V.; Varrla, E. Sustainable high-yield h-BN nanosheet production by liquid exfoliation for thermal interface materials. *RSC Appl. Interfaces* **2025**, *2*, 534–549. [CrossRef]
38. Xu, L.; Zhan, K.; Ding, S.; Zhu, J.; Liu, M.; Fan, W.; Duan, P.; Luo, K.; Ding, B.; Liu, B.; et al. A Malleable Composite Dough with Well-Dispersed and High-Content Boron Nitride Nanosheets. *ACS Nano* **2023**, *17*, 4886–4895. [CrossRef]
39. Liang, Z.; Pei, Y.; Chen, C.; Jiang, B.; Yao, Y.; Xie, H.; Jiao, M.; Chen, G.; Li, T.; Yang, B.; et al. General, Vertical, Three-Dimensional Printing of Two-Dimensional Materials with Multiscale Alignment. *ACS Nano* **2019**, *13*, 12653–12661. [CrossRef]
40. Liu, G.; Ding, A.; Xu, P.; Zhu, M.; Zhang, H.; Zheng, Y.; Luo, Y.; Zhang, L.; Zhang, P.; Chen, A.; et al. Thermal conductivity of epoxy composites containing 3D honeycomb boron nitride filler. *Chem. Eng. J.* **2024**, *489*, 151170. [CrossRef]
41. Chen, J.; Huang, X.; Sun, B.; Wang, Y.; Zhu, Y.; Jiang, P. Vertically Aligned and Interconnected Boron Nitride Nanosheets for Advanced Flexible Nanocomposite Thermal Interface Materials. *ACS Appl. Mater. Interfaces* **2017**, *9*, 30909–30917. [CrossRef]
42. Hong, H.; Jung, Y.H.; Lee, J.S.; Jeong, C.; Kim, J.U.; Lee, S.; Ryu, H.; Kim, H.; Ma, Z.; Kim, T. Anisotropic Thermal Conductive Composite by the Guided Assembly of Boron Nitride Nanosheets for Flexible and Stretchable Electronics. *Adv. Funct. Mater.* **2019**, *29*, 1902575. [CrossRef]
43. Song, Q.; Zhu, W.; Deng, Y.; Hai, F.; Wang, Y.; Guo, Z. Enhanced through-plane thermal conductivity and high electrical insulation of flexible composite films with aligned boron nitride for thermal interface material. *Compos. Part A Appl. Sci. Manuf.* **2019**, *127*, 105654. [CrossRef]
44. Gao, C.; Zhu, Z.; Shen, Y.; Wang, T.; Xiang, D. Efficient construction of boron nitride network in epoxy composites combining reaction-induced phase separation and three-roll milling. *Compos. Part B Eng.* **2020**, *198*, 108232. [CrossRef]
45. Yuan, W.; Li, W.; Zhu, S.; Chu, Z.; Gan, W. 3D-network of hybrid epoxy-boron nitride microspheres leading to epoxy composites of high thermal conductivity. *J. Mater. Sci.* **2022**, *57*, 11698–11713. [CrossRef]
46. Wang, Z.; Wang, X.; Zhang, Z.; Liang, L.; Zhao, Z.; Shi, J. Preparation of a 3D BN network structure by a salt template assisted method filled with epoxy resin to obtain high thermal conductivity nanocomposites. *Polym. Compos.* **2023**, *44*, 3610–3621. [CrossRef]
47. Leng, X.; Xiao, C.; Chen, L.; Su, Z.; Zheng, K.; Zhang, X.; Tian, X. An efficient approach for constructing 3-D boron nitride networks with epoxy composites to form materials with enhanced thermal, dielectric, and mechanical properties. *High Perform. Polym.* **2019**, *31*, 350–358. [CrossRef]
48. Jung, D.W.; Kim, J.M.; Yoon, H.W.; Nam, K.M.; Kwon, Y.E.; Jeong, S.; Baek, Y.H.; Choi, Y.S.; Chang, S.J.; Yi, G.R.; et al. Solution-processable thermally conductive polymer composite adhesives of benzyl-alcohol-modified boron nitride two-dimensional nanoplates. *Chem. Eng. J.* **2019**, *361*, 783–791. [CrossRef]
49. Xu, Q.; Chen, Z.; Li, X.; Hu, J.; Liao, Y.; Liu, Y.; Li, L.; Wei, S.; Li, Z. Improved out-of-plane thermal conductivity of boron nitride nanosheet-filled polyamide 6/polyethylene terephthalate composites by a rapid solidification method. *Mater. Adv.* **2023**, *4*, 1490–1501. [CrossRef]
50. Zhao, N.; Li, J.; Wang, W.; Gao, W.; Bai, H. Isotropically Ultrahigh Thermal Conductive Polymer Composites by Assembling Anisotropic Boron Nitride Nanosheets into a Biaxially Oriented Network. *ACS Nano* **2022**, *16*, 18959–18967. [CrossRef]

51. Zhan, K.; Chen, Y.; Xiong, Z.; et al. Low thermal contact resistance boron nitride nanosheets composites enabled by interfacial arc-like phonon bridge. *Nat. Commun.* **2024**, *15*, 2905. [CrossRef]
52. Chen, X.; Lim, J.; Yan, W.; Guo, F.; Liang, Y.; Chen, H.; Lambourne, A.; Hu, X. Salt template assisted BN scaffold fabrication toward highly thermally conductive epoxy composites. *ACS Appl. Mater. Interfaces* **2020**, *12*, 16987–16996. [CrossRef]
53. Pan, D.; Li, Q.; Zhang, W.; Dong, J.; Su, F.; Murugadoss, V.; Liu, Y.; Liu, C.; Naik, N.; Guo, Z. Highly thermal conductive epoxy nanocomposites filled with 3D BN/C spatial network prepared by salt template assisted method. *Compos. Part B Eng.* **2021**, *209*, 108609. [CrossRef]
54. Zhou, Y.; Wang, Y.; Li, M.; et al. Ultra-high thermal conductivity multifunctional composites with uniaxially oriented boron nitride sheets for future wireless charging technology. *Adv. Compos. Hybrid Mater.* **2025**, *8*, 237. [CrossRef]
55. Yu, C.; Gong, W.; Tian, W.; Zhang, Q.; Xu, Y.; Lin, Z.; Hu, M.; Fan, X.; Yao, Y. Hot-pressing induced alignment of boron nitride in polyurethane for composite films with thermal conductivity over 50 W/mK. *Compos. Sci. Technol.* **2018**, *160*, 199–207. [CrossRef]
56. Ravichandran, V.; Chandrashekar, A.; Prabhu, T.N.; Varrla, E. SPI-modified h-BN nanosheets-based thermal interface materials for thermal management applications. *ACS Appl. Mater. Interfaces* **2024**, *16*, 34367–34376. [CrossRef] [PubMed]
57. Arora, P.; Doyle, M.; Gozdz, A.S.; White, R.E.; Newman, J. Comparison between computer simulations and experimental data for high-rate discharges of plastic lithium-ion batteries. *J. Power Sources* **2000**, *88*, 219–231. [CrossRef]
58. Ekström, H.; Fridholm, B.; Lindbergh, G. Comparison of lumped diffusion models for voltage prediction of a lithium-ion battery cell during dynamic loads. *J. Power Sources* **2018**, *402*, 296–300. [CrossRef]
59. Doyle, M.; Newman, J.; Gozdz, A.S.; Schmutz, C.N.; Tarascon, J. Comparison of Modeling Predictions with Experimental Data from Plastic Lithium Ion Cells. *J. Electrochem. Soc.* **1996**, *143*, 1890. [CrossRef]
60. Liu, Z.; Wang, B.; Chen, S.; Li, P. Lithium-ion battery pack thermal management under high ambient temperature and cyclic charging-discharging strategy design. *J. Energy Storage* **2024**, *80*, 110391. [CrossRef]
61. Mahmood, A.; Cockerill, T.; de Boer, G.; Voss, J.; Thompson, H. Heat Transfer Modeling and Optimal Thermal Management of Electric Vehicle Battery Systems. *Energies* **2024**, *17*, 4575. [CrossRef]
62. Smith, K.; Wang, C.Y. Power and thermal characterization of a lithium-ion battery pack for hybrid-electric vehicles. *J. Power Sources* **2006**, *160*, 662–673. [CrossRef]
63. Cai, L.; White, R.E. Mathematical modeling of a lithium ion battery with thermal effects in COMSOL Inc. Multiphysics (MP) software. *J. Power Sources* **2011**, *196*, 5985–5989. [CrossRef]
64. Srinivasan, V.; Wang, C.Y. Analysis of electrochemical and thermal behavior of Li-ion cells. *J. Electrochem. Soc.* **2002**, *150*, A98. [CrossRef]
65. Weragoda, D.M.; Tian, G.; Burkitbayev, A.; Lo, K.H.; Zhang, T. A comprehensive review on heat pipe based battery thermal management systems. *Appl. Therm. Eng.* **2023**, *224*, 120070. [CrossRef]
66. Dubarry, M.; Vuillaume, N.; Liaw, B.Y. Origins and accommodation of cell variations in Li-ion battery pack modelling. *Int. J. Energy Res.* **2010**, *34*, 216–231. [CrossRef]
67. Beck, D.D.P.; Junker, M.; Sauer, D.U.; Dubarry, M. Inhomogeneities and cell-to-cell variations in lithium-ion batteries: A review. *Energies* **2021**, *14*, 3276. [CrossRef]

batteries

MDPI

Article

A Study on Thermal Performance Enhancement of Mini-Channel Cooling Plates with an Interconnected Design for Li-Ion Battery Cooling

Armanto P. Simanjuntak, Joohan Bae, Benrico Fredi Simamora and Jae Young Lee *

Department of Mechanical and Control Engineering, Handong Global University, Pohang 37554, Republic of Korea; armant.ost@gmail.com (A.P.S.); joohanbae@handong.edu (J.B.); benricosimamora@gmail.com (B.F.S.)
* Correspondence: jylee7@handong.edu; Tel.: +82-54260-1392

Abstract: The increasing adoption of lithium-ion (Li-ion) batteries in electric vehicles (EVs) and renewable energy systems has heightened the demand for efficient Battery Thermal Management Systems (BTMS). Effective thermal regulation is critical to prevent performance degradation, extend battery lifespan, and mitigate safety risks such as thermal runaway. Liquid cooling has become the dominant strategy in commercial EVs due to its superior thermal performance over air cooling. However, optimizing liquid cooling systems remains challenging due to the trade-off between heat transfer efficiency and pressure drop. Recent studies have explored various coolant selection, nanofluid enhancements, and complex channel geometries, an ideal balance remains difficult to achieve. While advanced methods such as topology optimization offer promising performance gains, they often introduce significant modeling and manufacturing complexity. In this study, we propose a practical alternative: an interconnected straight-channel cooling plate that introduces lateral passages to disrupt the thermal boundary layer and enhance mixing. Comparative analysis shows that the design improves temperature uniformity and reduces peak battery temperature, all while maintaining a moderate pressure drop. The proposed configuration offers a scalable and effective solution for next-generation BTMS, particularly in EV applications where thermal performance and manufacturability are both critical.

Keywords: battery thermal management; interconnected; lithium-ion; heat transfer; pressure drop; electric vehicles

1. Introduction

The urgency to mitigate global warming and reduce greenhouse gas emissions has driven extensive research into renewable energy generation and storage technologies [1]. Among these, batteries play a central role in improving the reliability of renewable systems, especially in off-grid applications with intermittent energy supply. In addition to stationary applications, batteries are also essential components in modern transportation systems [2–4]. Electric vehicles (EVs) are increasingly recognized as a cleaner transportation option capable of lowering emissions in urban environments [4,5]. However, the broader deployment of EVs still relies on ongoing improvements in battery performance, including reductions in cost and enhancements in safety, efficiency, and durability [4]. Lithium-ion (Li-ion) batteries have become the preferred technology due to their high energy density, long cycle life, and suitability for both mobile and stationary applications [5,6]. Despite these strengths, Li-ion batteries still face critical challenges, especially in thermal management [7–9]. Performance

degrades at low temperatures, while high temperatures accelerate aging and, in severe cases, may lead to thermal runaway and fire hazards [7,10–12].

Over the past decade, extensive research on Battery Thermal Management Systems (BTMS) has explored a wide range of cooling strategies for lithium-ion batteries [13–17]. Commonly reported approaches include air cooling [13,14], liquid cooling using various coolants such as water, ethylene glycol, mineral oils, and dielectric fluids [15–17], phase change material (PCM)-based cooling [18], and heat pipe-assisted systems [19]. Among these, air- and water-based liquid cooling have been most widely adopted in commercial electric vehicles (EVs) due to their favorable trade-off between performance, complexity, and cost [14,20]. In contrast, PCM and heat pipe cooling remain largely limited to experimental or niche applications. Several recent studies have also proposed hybrid strategies—such as combining direct liquid cooling with forced air [21] or integrating PCM with liquid cooling and pulsed operation [22]—to overcome the limitations of single-mode systems. Other passive enhancements like PCM-metal foam-fin composites have also been explored to reduce hotspots and improve energy buffering [23]. While these hybrid or passive designs show promise, they often involve added complexity or limited scalability. Comparative studies such as Akbarzadeh et al. [24] have confirmed that liquid cooling—particularly direct-contact or immersion types—offers superior thermal performance and uniformity over air cooling, which is critical for improving cell balancing, extending battery lifespan, and reducing safety risks like thermal runaway.

Despite the demonstrated superiority of liquid cooling compared to other methods, optimization through various approaches is still being actively reported. These efforts can be broadly categorized into two directions: coolant-based improvements and geometry-based modifications. On the coolant side, several studies explore the use of different liquids to enhance thermal performance. Liu et al. [15] evaluated various cooling media including water, ethylene glycol, engine oil, and their mixtures with 5% alumina nanofluids. Water was found to outperform ethylene glycol and engine oil in cooling efficiency, and the addition of nanoparticles further reduced the maximum temperature rise by 1.2 °C. However, this enhancement came with nearly a 50% increase in pressure drop. Similarly, Trimbake et al. [25] reported that using mineral oil in a submerged jet and jet impingement configuration resulted in a highly uniform surface temperature distribution, with deviations kept under 1 °C. Chen et al. [26] compared direct and indirect liquid cooling using water, mineral oil, and water-glycol mixtures, confirming water's superior thermal performance but also noting limitations in specific configurations.

On the geometry side, researchers have proposed numerous flow channel layouts to improve thermal distribution and reduce hot spots. Tao Deng et al. [9] investigated various serpentine-shaped channel configurations and flow directions to optimize heat transfer across the cooling plate. Panchal et al. [27] conducted both experimental and numerical studies on mini-channel cold plates operated at different coolant temperatures and discharge rates, providing insights into real-world battery cycling scenarios. Amalesh et al. [28], using Liu et al. [15] as a baseline, introduced multiple redesigned channel geometries that achieved up to a 13 °C reduction in peak battery temperature at a 3C discharge rate. However, this thermal gain incurred a 250% increase in pressure drop. Another approach was presented by Zekung Jiang et al. [29] proposing an immersion technique which utilized gravity to increase the liquid flow, and by this the optimization of temperature difference and pressure drop were reported to be 79% and 13%, respectively. However, this attempt is still dependent on special dielectric liquid with low viscosity. Beyond the traditional approach of changing liquid and geometry, recent studies using topology optimization were also reported. Yasong Sun et al. [30] applied topology optimization using porous

medium domains and compared the results to serpentine and rectangular designs. At equal pressure drop (~55 Pa), their topological design reduced the maximum temperature by approximately 10 °C when compared to serpentine and by 8 °C when compared to rectangular layouts. Sen Zhan et al. [31] introduced a bionic leaf-vein cooling structure via NSGA-II and density-based topology optimization, reporting substantial reductions in temperature standard deviation (40.79%) and pressure drop (71.25%) over baseline designs. Chaofeng Pan et al. [32] also proposed a dual-outlet, topology-optimized plate, showing a 0.5% reduction in temperature and a 24% lower pressure drop compared to traditional straight channel. This suggests that despite the complexity, the topology optimizations show a promising potential for resolving thermal efficiency and pressure drop.

While topology optimization has demonstrated its potential to push the limits of structural performance, as emphasized in the review by Jihong [33], its practical application still demands advanced modeling, multi-axis manufacturing capabilities, and careful handling of thermal-process effects. Therefore, a more straightforward and practical approach is needed to achieve an efficient balance between thermal management and hydraulic performance in battery cooling systems. In this study the authors propose an interconnected straight-channel design, introducing a mixing zone that disrupts the thermal boundary layer, thereby enhancing heat transfer. The proposed interconnected channel differs fundamentally from the porous-fin and bionic flow-path concepts reported by Zhan et al. [31] and Sun et al. [13]. While those designs rely on complex porous or biomimetic structures that distribute coolant through tortuous micro-paths or fractal branches, the present design preserves a conventional mini-channel layout but introduces periodic open bridges that enable controlled lateral coolant exchange between adjacent channels. This approach generates beneficial secondary flow and mixing similar to bionic designs but maintains lower pressure drop, simpler geometry, and straightforward manufacturability using standard milling or stamping methods. This approach not only improves temperature uniformity and lowers the maximum battery temperature but does so with a pressure drop increase significantly lower than that reported in some earlier studies. By leveraging a simpler yet highly effective modification, our design provides a practical and scalable solution for battery thermal management.

2. Numerical Method

2.1. Governing Equations

The fluid flow and heat transfer within the cooling system are numerically analyzed using the Eulerian approach, where it is analyzed within a fixed control volume. A set of governing equations—conservation of mass, momentum, and energy equations—are solved at each control volume to accurately capture the heat transfer and fluid flow behavior within the cooling system. These equations, expressed in Cartesian tensor form, are presented in Equation (1), Equation (2), and Equation (3), respectively.

$$\nabla \cdot \vec{v} = 0 \tag{1}$$

Momentum equation of laminar flow,

$$\rho_f \left[\frac{\partial \vec{v}}{\partial t} + \left(\vec{v} \cdot \nabla \right) \vec{v} \right] = -\nabla P + \mu \nabla^2 \vec{v} \tag{2}$$

and for energy equation,

$$\rho_f Cp_f \frac{\partial T_f}{\partial t} + \nabla \cdot \left(\rho_f Cp_f \vec{v} T_f \right) = \nabla \cdot \left(k_f \nabla T_f \right) \tag{3}$$

In the solid domain of the cooling plate, conduction serves as the primary mode of heat transfer. The governing energy equation for heat conduction in the cooling plate is given by Equation (4):

$$\rho_b Cp_b \frac{\partial T_b}{\partial t} = \frac{\partial}{\partial x}\left(k_{bx} \frac{\partial T_b}{\partial x} \right) + \frac{\partial}{\partial y}\left(k_{by} \frac{\partial T_b}{\partial y} \right) + \frac{\partial}{\partial z}\left(k_{bz} \frac{\partial T_b}{\partial z} \right) \tag{4}$$

To establish thermal continuity between the solid and fluid domains, boundary conditions ensuring temperature continuity and heat flux balance at the solid–fluid interface will be applied, which will be explained in the coming section. Additionally, to replicate the heat generation process within the battery, a heat source term is incorporated into the solid volume, representing internal losses from electrochemical reactions and ohmic heating. This modifies the energy equation in the battery domain to Equation (5).

$$\rho_b Cp_b \frac{\partial T_b}{\partial t} = \frac{\partial}{\partial x}\left(k_{bx} \frac{\partial T_b}{\partial x} \right) + \frac{\partial}{\partial y}\left(k_{by} \frac{\partial T_b}{\partial y} \right) + \frac{\partial}{\partial z}\left(k_{bz} \frac{\partial T_b}{\partial z} \right) + \dot{Q}_{gen} \tag{5}$$

All governing equations for solid and liquid are solved using commercial CFD software ANSYS Fluent 2025 R1 [34], which employs finite volume as the method for discretization. Assumptions are applied for more simplified computation such as incompressible flow and isotropic material properties. Contact resistance is considered negligible, allowing direct heat transfer between the batteries and cooling plate. This simplification was also considered by two previous studies, by Liu et al. [15] and Amalesh et al. [28]. Besides that, Lai et al. [35] and Wang et al. [36] also considered the same simplification for different battery geometry. Finally, adiabatic conditions are imposed on remaining external walls, assuming no heat loss to the surroundings.

The internal heat generation of the battery per unit volume is represented by the source term $\dot{Q_{gen}}$. The amount of heat generated not only depends on the rate of discharge (1C, 2C, or 3C) but also on the state of discharge (SOD). Therefore, a transient calorimetric measurements of Li-ion battery heat reported by Liu et al. [15] will be used in this model. The equation is approximated using a polynomial function of time t as follows:

$$\dot{Q}_{gen} = A_1 t^6 + A_2 t^5 + A_3 t^4 + A_4 t^3 + A_5 t^2 + A_6 t + A_7 \tag{6}$$

where A1 through A7 are the polynomial coefficients [13] corresponding to the three distinct discharge rates (1C–3C) shown in Table 1. This polynomial formulation is later implemented into the solver software using a User-Defined Function (UDF), allowing the heat generation term to be dynamically computed at each time step for 1C, 2C, and 3C discharge rates during the simulation.

Table 1. Polynomial coefficients of heat generation at different battery discharging rates.

Discharge Rate	A1	A2	A3	A4	A5	A6	A7
1C	4.9132×10^{-16}	-3.7742×10^{-12}	1.0679×10^{-8}	-1.3417×10^{-5}	0.0076	−2.2208	17,151.7482
2C	1.2578×10^{-13}	-4.8310×10^{-10}	6.8347×10^{-7}	-4.2934×10^{-4}	0.12160	−17.763	66,623.3365
3C	3.2235×10^{-12}	-8.2542×10^{-5}	7.7851×10^{-6}	-3.2303×10^{-3}	0.61570	−59.961	148,414

2.2. Boundary Conditions

The following boundary conditions are applied to represent battery heat generation and cooling plate operating conditions. At initial time (t = 0), the entire domain including fluid, cooling plate, and battery are assumed to be at uniform initial temperature of 25 °C.

At the inlet of the cooling plate, a uniform velocity profile is imposed along the y-axis (see Figure 1) and is expressed by Equation (7). At the outlet, the pressure condition is applied as expressed in Equation (8).

$$u = 0\ m/s;\ v = 0.08\ \sim\ 0.16\ m/s;\ w = 0\ m/s \tag{7}$$

$$P_{out} = 0\ Pa \tag{8}$$

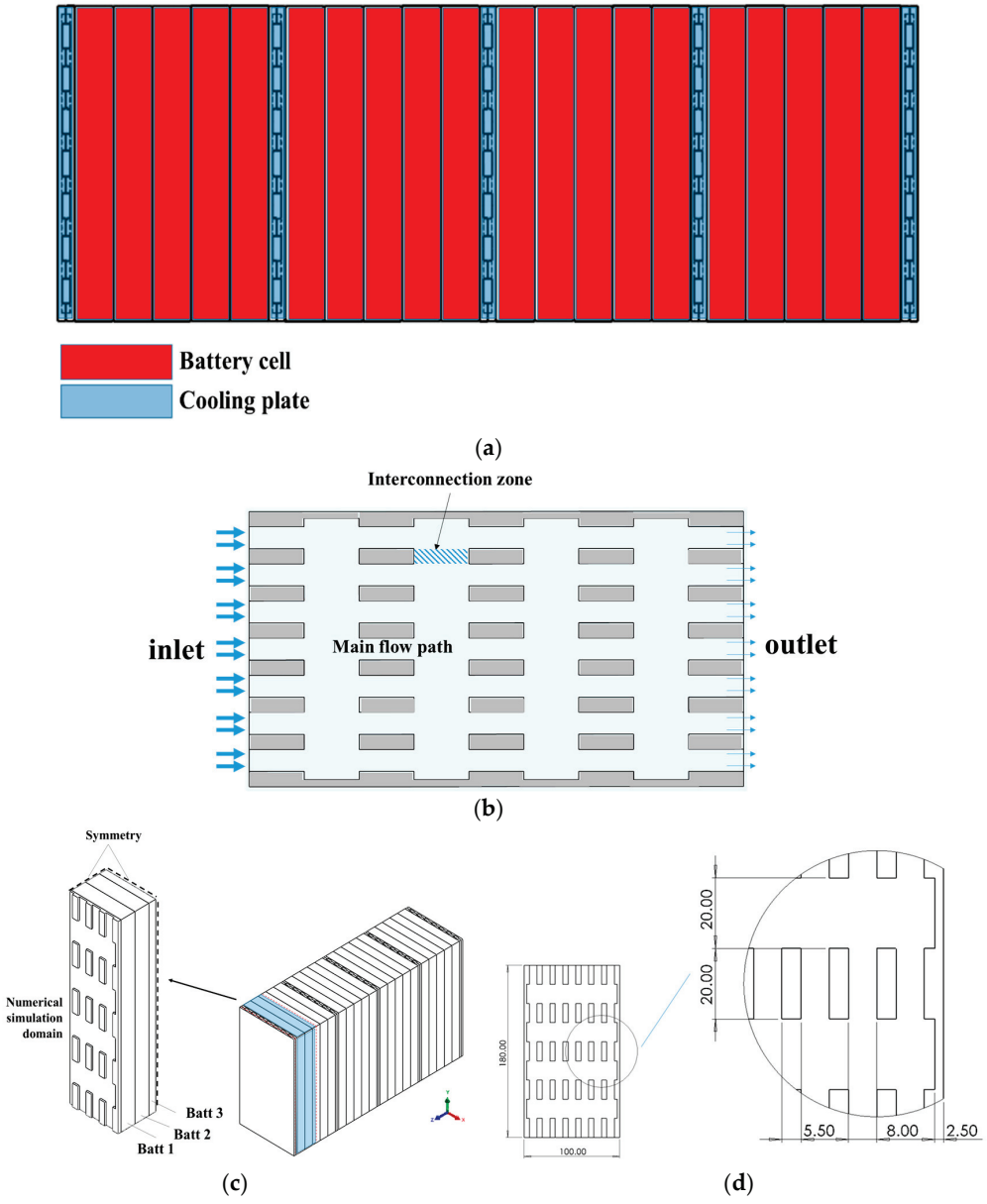

Figure 1. (**a**) Schematic of the battery module. (**b**) Flow arrangement of interconnected design. (**c**) Symmetrical assumption. (**d**) Interconnected design.

A no-slip boundary condition was applied at the inner walls of the fluid domain, which is expressed in the following equation.

$$u_w = v_w = w_w = 0\ m/s \tag{9}$$

Thermal boundary conditions are given as follows: At the inlet of the liquid flow channel, fluid temperature is set at a constant value, T_{in} = 25 °C. At the interface between the battery (solid) and the liquid coolant (fluid), a coupled boundary condition is applied to allow heat transfer between the two domains, ensuring continuity of temperature and heat flux across the interface. The coupling is expressed by the following equation.

$$k_b \frac{\partial T_b}{\partial n} = k_f \frac{\partial T_f}{\partial n} \tag{10}$$

Subscript b and f refer to battery and fluid, respectively, while n refers to the normal direction to the interface between solid and fluid domains.

To reduce computational cost, a symmetry boundary condition is applied at the center of the half cooling plate and battery 3 (see Figure 1b). Under this assumption, no heat or mass flux occurs across the symmetry boundary ($\partial T = 0$).

At the remaining surfaces of battery domain, adiabatic boundary conditions are applied, which is expressed by this following equation.

$$q'' = k_d \frac{\partial T_d}{\partial x} = k_d \frac{\partial T_d}{\partial y} = k_d \frac{\partial T_d}{\partial z} = 0 \tag{11}$$

The simulation conditions used in this study are summarized in Table 2.

Table 2. Summary for computational settings.

Category	Location	Condition Type	Specification/Value
Initial Condition	Entire Domain	Temperature	25 °C
Flow Condition	Inlet	Velocity	Uniform velocity at *y*-axis (0.08; 0.10; 0.12; 0.14; 0.16 m/s)
	Outlet	Pressure	0 Pa
	Fluid–solid walls	No-slip condition	-
Thermal Conditions	Inlet	Temperature	25 °C
	Battery–coolant interface	Coupled condition	-
	Symmetry plane	Symmetry condition	-
	External battery surface	Adiabatic wall	Zero heat flux (Equation (11))

2.3. Cooling Plate and Benchmark Design

A typical Li-ion battery pack consists of multiple battery modules arranged in a particular pattern. Each module has several batteries connected in series/parallel combinations depending on the design requirements. The number of batteries in an EV ranges from a few hundred to several thousand as per the size/weight of the batteries and their overall capacity to match the vehicle's power requirements.

Figure 1a illustrates the rectangular Li-ion battery pack and module analyzed in this study. The battery pack consists of several prismatic Li-ion battery modules, with each module containing five Li-ion batteries (180 mm × 100 mm × 14 mm, 45 Ah capacity), cooled by two aluminum cooling plates on either side. The coolant employed is water entering at a constant temperature of 25 °C.

The straight-channel cooling plate design consists of seven rectangular channels, each 8 mm wide, 3 mm high, with a 5.5 mm spacing between channels. The module design and geometry, as shown in Figure 1a, is identical to the study by Liu et al. [15] and serves as the baseline for validating the present model and comparing the seven proposed designs. The interconnected modification being proposed in this study is explained diagrammatically and shown in Figure 1d.

Figure 1b shows the flow arrangement of cooling fluid inside the plate. Fluid flows entering the inlet of the cooling plate and passing through the main flow path. Between two main flow paths, an additional interconnection zone were introduced to increase the surface area and periodically disrupt the thermal boundary layer.

Figure 1c illustrates the concept of symmetrical analysis, applied due to the geometric arrangement of the battery module. This approach significantly reduces computational time while preserving accuracy.

The important parameters both for benchmarking and evaluating the results are temperature rise (ΔT_{max}) temperature difference within the battery (ΔT_{diff}). These parameters are calculated from the numerical solution using these following equations.

$$\Delta T_{max}(t) = \max T(x, y, z) - T_{t=0\mathrm{s}} \tag{12}$$

$$\Delta T_{diff}(t) = \max T(x, y, z) - \min T(x, y, z) \tag{13}$$

2.4. Mesh Generation and Grid Sensitivity

In this study, the accuracy of the numerical model is influenced by the quality of generated mesh and time-step size. To ensure that the solution is independent of these factors, seven trials with different mesh and time-step parameters were conducted.

Figure 2 presents the grid independence test for the interconnected channel cold plate design with a constant inlet velocity of $v_{in} = 0.1\ m/s$. The number of mesh elements varies between 800,000 and 4,000,000 with equal time step of 1 s. Figure 2a shows that the predicted maximum battery temperature rise (ΔT_{max}) remains nearly unchanged beyond the mesh size of 2,000,000. Similarly, in Figure 2b the effect of time-step sizes was studied, varying between 0.1 s and 5 s. Four cases have been conducted at time steps of 0.1 s, 0.5 s, 1 s, and 5 s. In this trial, the predicted (ΔT_{max}) is not significantly influenced for the time step of 1 s and above. Hence, in this study, the total number of mesh elements for the interconnected design was set to 2,000,000, with a time step of 1 s.

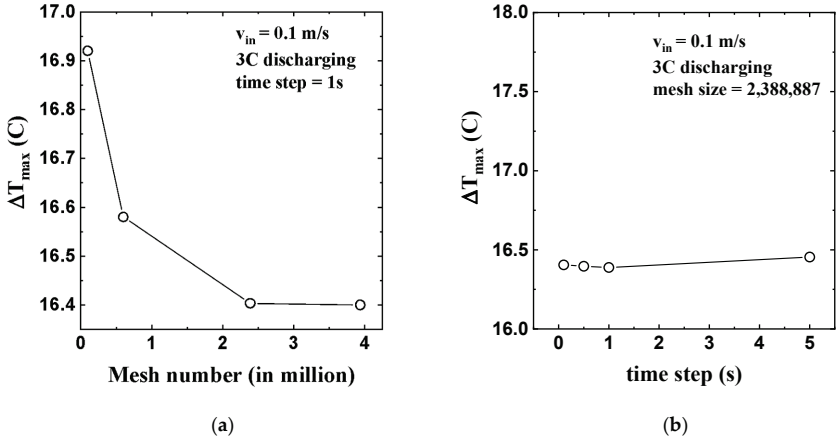

Figure 2. Grid independence study of the interconnected cooling plate design, showing the maximum temperature rise as a function of mesh number (**a**) and time step (**b**).

3. Results and Discussion

3.1. Numerical Model Validation

In this study, the validity of the numerical solutions is verified by numerical grid convergence study as described in Section 2.4, and further verified against the baseline reported by Liu et al. [15] and Amalesh et al. [28]. These studies were selected due to their alignment with the current research objective. This comparison provides a benchmark for evaluating the accuracy and reliability of the proposed numerical model, ensuring that the predicted thermal and hydraulic performance aligns with established findings.

In this study, a 45 Ah Li-ion battery discharging at 1C, 2C, and 3C rates was simulated and compared with the reported results of Liu et al. [15] and Amalesh et al. [28]. Figure 3a shows the temperature trend of the battery running at different discharging rates under adiabatic conditions (no cooling plate installed). It can be seen that the present model closely agrees with the benchmark studies of Liu et al. [15] and Amalesh et al. [28] Similarly, Figure 3b compares the cooling performance of the cooling plate for the battery module using a straight rectangular channel. The performance of the cooling plate predicted by the proposed model agrees with the results of Liu et al. [15] and Amalesh et al. [28] under all three discharge rates. These results provide evidence that the numerical model applied in this study is reliable. As the next step, an optimization approach was carried out by applying an interconnected path along the straight channel.

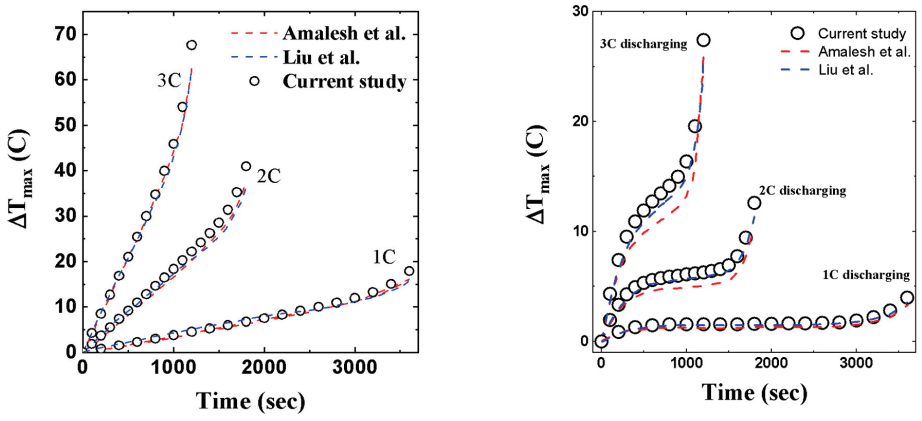

Figure 3. Maximum temperature rises ΔT_{max} under: (**a**) adiabatic condition; and (**b**) after installing cooling plate at 0.1 m/s inlet velocity [15,28].

Under the proposed design, several parameters, including temperature rise (ΔT_{max}), temperature difference within the battery (ΔT_{diff}), pressure drop of the coolant, and velocity contour, were analyzed. The results will be discussed in detail in the following sections.

3.2. Thermal Performance

Figure 3a shows the transient maximum temperature rise in the battery module at different discharge rates (1C, 2C, and 3C) under adiabatic conditions. Consistent with the findings of Liu et al. [15], the results indicate that temperature increases with the increase in discharge rate. At a discharge rate of 3C, the maximum temperature rise is around 62 °C, whereas for 1C and 2C discharge rates, the observed maximum temperature rise was 36 °C and 16 °C, respectively. At a 3C discharge rate, the temperature increases linearly for the first 1000 s and then rises sharply afterward. A similar trend is also observed at discharge rates of 2C and 1C, where the temperature rise remains linear up to 1500 s and 3200 s,

respectively. Figure 3a shows a sharp turning point when the battery is near the stage of EOD (end of discharge) as the internal resistance of the battery increases.

Figure 3b shows how the presence of the cooling plate can limit the temperature rise in the battery. Under the baseline design, featuring a straight rectangular channel, the results indicate that the temperature remains below 27 °C for the 3C discharge rate. For 2C and 1C discharge rates, the temperature rise is 12.6 °C and 3.9 °C, respectively.

The temperature difference within the battery (ΔT_{diff}) indicates its temperature uniformity. Figure 3b shows the battery temperature difference in the baseline design at an inlet velocity of 0.1 m/s under 1C, 2C, and 3C discharging rates. At a 3C discharge rate, the maximum temperature difference is 15.9 °C, while under 2C and 1C discharge rates, the maximum temperature difference is 7.4 °C and 2.4 °C, respectively. This result is in good agreement with the results of Liu et al. [15]. Hence, the temperature difference in the current model is successfully validated.

3.3. Effect of Additional Inter-Connected Passage

An interconnecting passage is hypothesized to enhance heat transfer by increasing the heat transfer area and disrupting the thermal boundary layer. The interaction of thermal and hydraulic boundary layers through secondary flow can enhance heat transfer. In this study, the effect of an interconnecting passage is investigated to evaluate its impact on battery temperature regulation, thermal uniformity, and flow characteristics.

Figure 4 presents the streamwise variation in the local Nusselt number (Nu_x) for the baseline straight-channel and interconnected (ID) designs, along with the analytical correlation of Shah and London [37] for fully developed laminar flow in rectangular ducts. The baseline profile shows excellent agreement with the Shah and London prediction, validating the numerical accuracy of the present model. Both designs display a sharp Nu_x peak near the inlet due to strong entrance effects, followed by a decline as the thermal boundary layer develops downstream. The ID design maintains substantially higher Nu_x values—approximately 2–2.5 times greater than the baseline in the fully developed region ($x/L > 0.3$)—confirming that the interconnections effectively disturb and re-energize the boundary layer. Minor oscillations in the ID curve correspond to local recirculation and mixing near each interconnection bridge, while the baseline trend converges smoothly toward the theoretical fully developed value predicted by Shah and London.

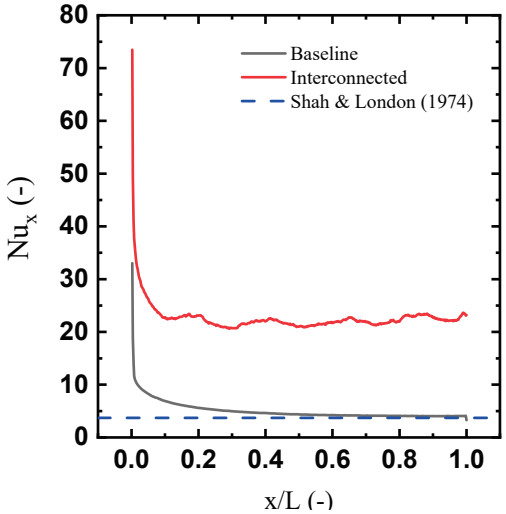

Figure 4. Streamwise variation in local Nusselt number for both baseline design and interconnected design compared with Shah and London [37].

The thermal performance of the baseline and interconnected designs was evaluated by analyzing maximum temperature rise and temperature difference using Equation (12) and Equation (13), respectively. The evaluation results are shown in Figure 5. For maximum temperature rise (Figure 5a-left), the baseline and interconnected designs start to show a noticeable difference at 100 s. At this point, the interconnected design is preferable, with a temperature 0.5 °C lower than the baseline. At the end of discharge, the interconnected design achieved a maximum temperature 8 °C lower than the baseline design. This achievement is important, considering that the aging rate of Li-ion batteries increases when operating at higher temperatures [26]. For temperature uniformity (Figure 5a-right), the difference between the two designs starts to appear beyond 200 s. The effect of the optimized interconnected design becomes stronger as discharge time exceeds 200 s. By the end of the 3C discharge cycle, the interconnected design improves temperature uniformity by approximately 3.5 °C.

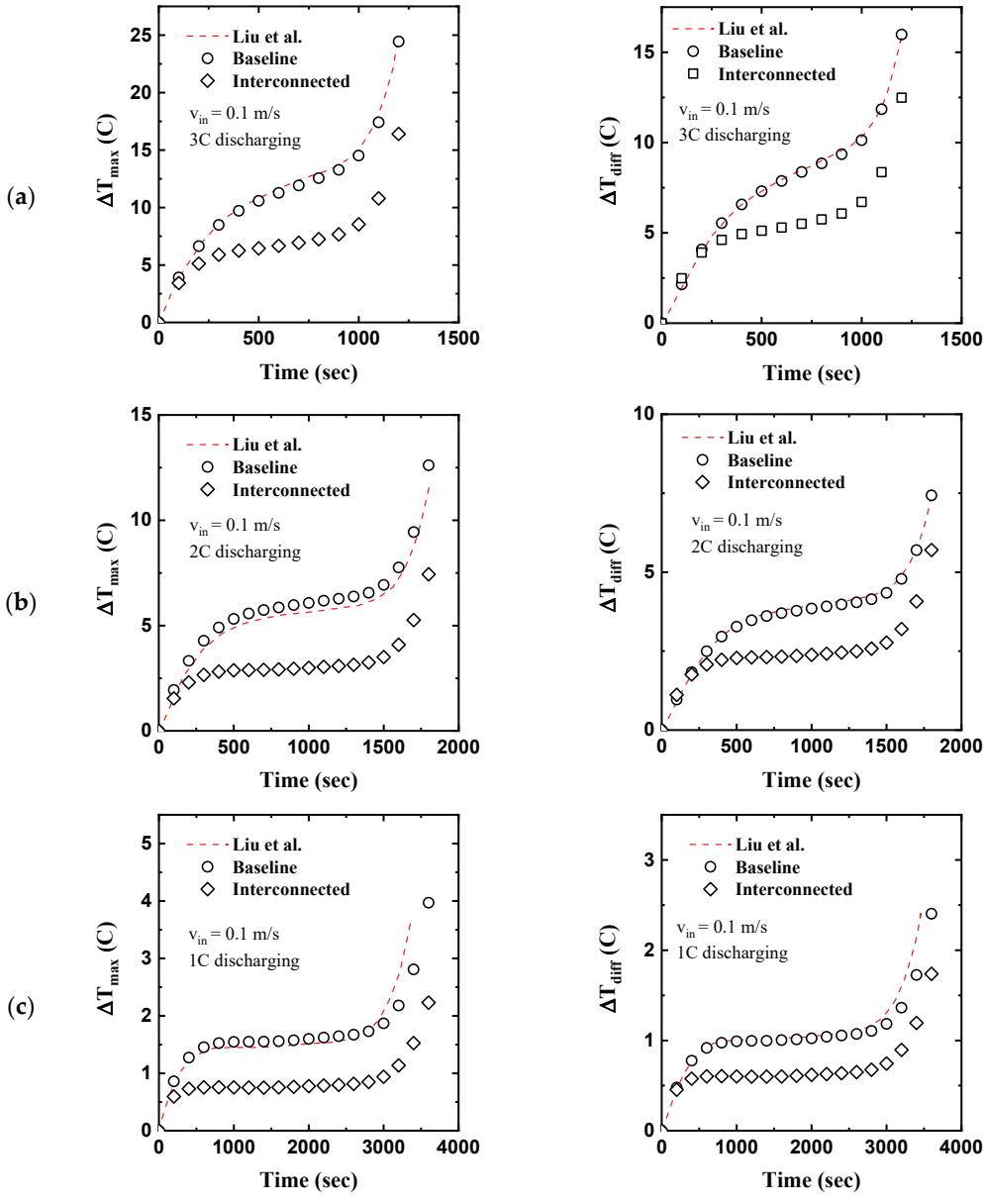

Figure 5. Maximum temperature rises ΔT_{max} (**left**) and temperature difference ΔT_{diff} (**right**) of both baseline and proposed design under different discharge rate and 0.1 m/s inlet velocity (**a**) 3C, (**b**) 2C, (**c**) 1C [15].

A similar trend can be observed in the performance evaluation at 2C, as shown in Figure 5b. In the case of 2C, the maximum temperature rise starts to differ by 0.5 °C at around 100 s. By the end of discharge, the Interconnected design shows a 5.2 °C lower maximum temperature rise (Figure 5b-left). Regarding temperature uniformity, a noticeable difference of 0.5 °C appears only after 300 s. This is longer than 3C; this is because it is more affected by heat generation of the battery rather than the cooling plate heat transfer coefficient. By the end of the discharge cycle, the interconnected design improves temperature uniformity by 1.7 °C.

Figure 5c shows the thermal evaluation at the 1C discharge rate. Due to the lower heat generated by the battery, the temperature difference is not as significant as in the 2C and 3C cases.

However, the trend illustrates that the interconnected design is still preferable in terms of cooling performance. For maximum temperature rise, the interconnected design shows a 0.1 °C lower temperature at 100 s. By the end of discharge, the interconnected design shows a maximum temperature that is 1.7 °C lower than that of the baseline design (Figure 5c-left). For temperature uniformity, Figure 5c-right shows that the interconnected design achieves slightly better uniformity than the baseline design, with a 0.6 °C improvement by the end of discharge.

3.4. Effect of Inlet Velocity

The inlet velocity of the coolant plays a crucial role in determining the overall thermal performance of the cooling plate. Higher inlet velocities enhance convective heat transfer by increasing the heat transfer coefficient. This section describes how the effect of velocity changes the maximum temperature at both baseline design and interconnected design.

Figure 6a-left presents the maximum temperature of an individual battery at a 3C discharge rate under different coolant inlet velocities for the Baseline design. Different flow velocities ranging from 0.08 m/s to 0.16 m/s are investigated, with Battery 1 positioned closest to the cooling plate. The velocity 0.08 m/s to 0.16 m/s corresponds to Reynolds number Re = 347–Re = 695. This value corresponds to 1.5 L/min–4.6 L/min for each module which is a typical EV coolant loop range, which is around 1–5 L/min per module. Besides that, this is also to be consistent with Liu [15] and Amalesh [28] who studied a similar coolant velocity value. The graph indicates that ΔT_{max} decreases with increasing inlet velocity, aligning with the principles of convective heat transfer. Figure 6a-right presents the maximum temperature of an individual battery at a 3C discharge rate under different coolant inlet velocities for the interconnected design. The temperature trends in the interconnected design follow a similar pattern to the baseline design, where the maximum temperature decreases as the inlet velocity increases. This also confirms the superior thermal performance of the Interconnected design. Both graphs also show that the highest ΔT_{max} occurs at Battery 3, which is the farthest from the cooling plate. This is due to the thermal resistance of the battery material.

In addition to the maximum temperature rise (ΔT_{max}), variations in ΔT_{diff} for each battery under different velocities are evaluated and shown in Figure 6b. The evaluation of temperature uniformity of different batteries is also important to evaluate since it affects efficiency and lifespan [25]. Consistent with previous findings, Figure 6b-right shows the ΔT_{diff} of interconnected design has lower ΔT_{diff} compared to baseline design in Figure 6b-left. This implies that proposed design also improves the uniformity of the battery to the level of each individual battery.

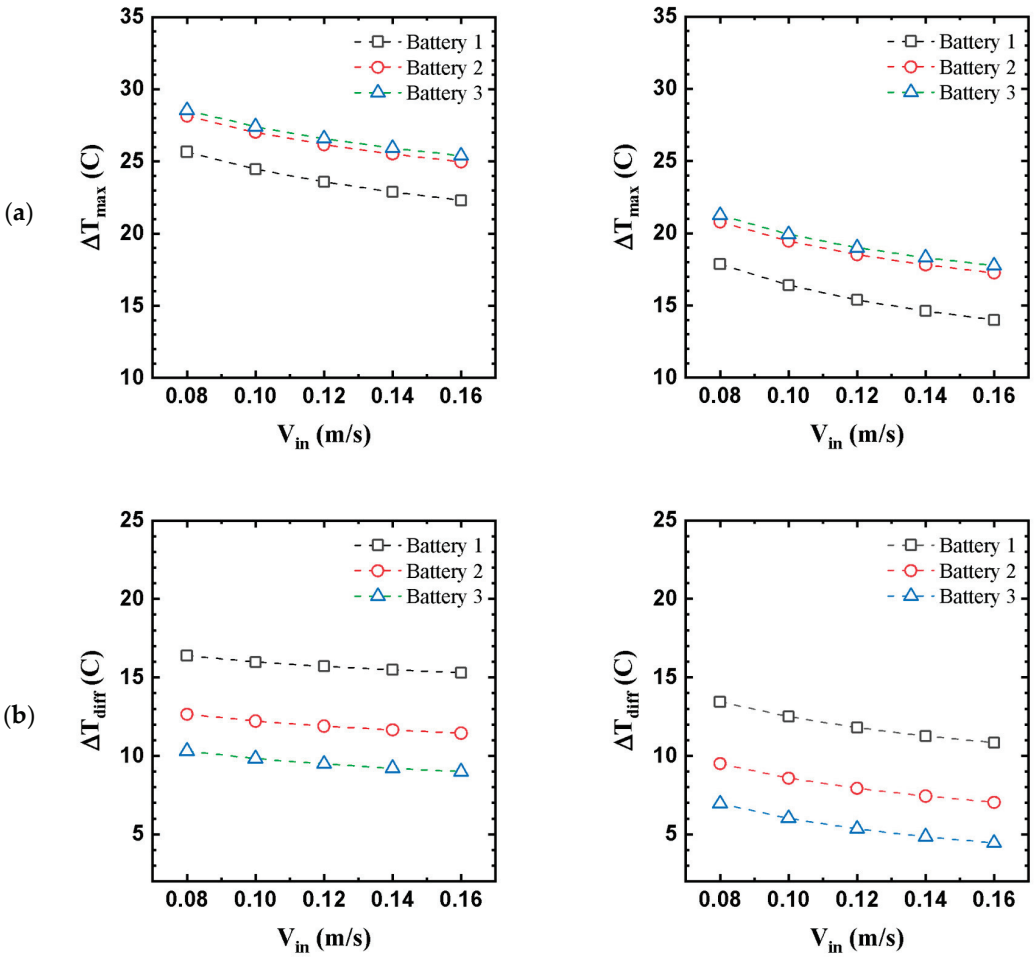

Figure 6. Variation in the effect of velocities on the maximum temperature (**a**) and temperature difference (**b**) comparing the case for baseline (**left**) and interconnected (**right**).

Figure 7 shows the variation in the average heat-transfer coefficient (HTC) with coolant velocity for the proposed interconnected (ID) plate and the baseline design of Liu et al. [15]. As the inlet velocity increases from 0.08 to 0.16 m·s^{-1}, both designs exhibit a monotonic rise in *HTC*, reflecting the expected convective enhancement with thinner boundary layers at higher flow rates. The ID plate achieves an overall ≈ 17% higher *HTC* than the baseline, confirming that the introduced interconnections promote additional lateral mixing and local turbulence. However, the relative improvement becomes slightly smaller at higher velocities, suggesting that the advantage of the interconnection structure is more pronounced under low-flow conditions, where it effectively compensates for weaker natural convection and limited axial mixing.

However, while a higher inlet velocity enhances *HTC* by strengthening forced convection, it is crucial to consider the associated trade-offs. Increased velocity leads to a higher pressure drop, which in turn raises the pumping power requirements. Excessive pressure drop can reduce overall energy efficiency and limit the practical application of the cooling system in battery thermal management. Therefore, achieving an optimal balance between heat transfer enhancement and hydraulic efficiency is essential. The impact of pressure drop will be discussed in detail in the following section.

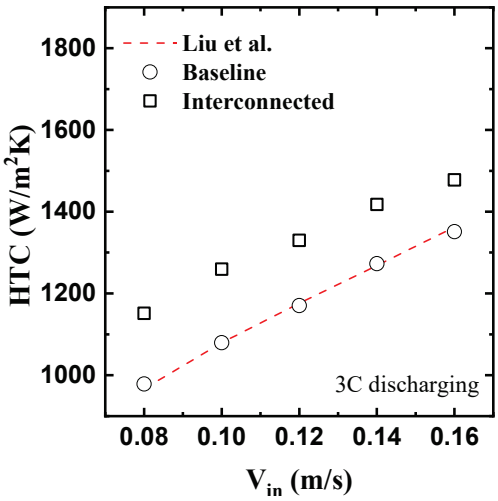

Figure 7. Comprehensive comparison on baseline and interconnected design, depicted through heat transfer coefficient [15].

3.5. Pressure Drop Consideration

Pressure drop is a critical factor in cooling plate design, as it directly influences system efficiency, energy consumption, and operational cost. A higher pressure drop indicates greater resistance to coolant flow, requiring more pumping power to maintain circulation. This increased power demand raises energy consumption, reducing system cost-effectiveness. However, minimizing the pressure drop comes with the risk of poor thermal performance, potentially causing the battery to operate at elevated temperatures, which increases the likelihood of thermal runaway or, at the very least, shortens its life-cycle. An optimal cooling plate design must balance heat dissipation and hydraulic resistance, maintaining effective thermal regulation without excessive energy consumption or inefficiencies.

Figure 8 compares the maximum temperature (ΔT_{max}) and pressure drop (ΔP) of the proposed interconnected (ID) plate with seven benchmark configurations (D1–D7) from Amalesh et al. [28] and the baseline design of Liu et al. [15]. The D-series represents major liquid-cooling concepts: D1—straight parallel channels, D2—serpentine path, D3—pin-fin structure, D4—wavy/sinusoidal channel, D5—triangular manifold, D6—hybrid manifold-pin design, and D7—cross-linked multi-branch layout.

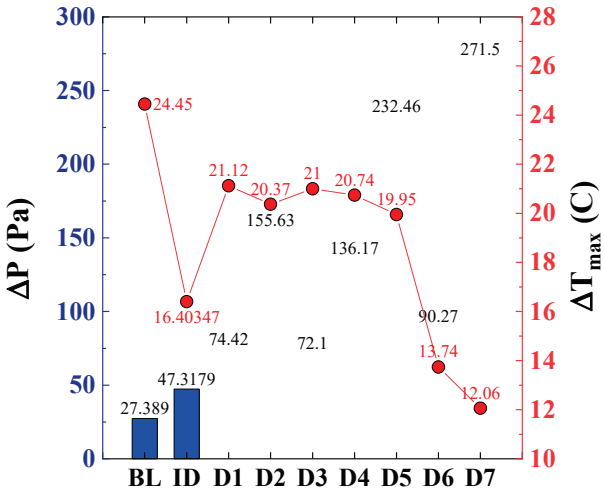

Figure 8. Comprehensive comparison on baseline, interconnected design, and several benchmark studies depicted through pressure drop to ΔT_{max} Relation.

From the figure, an improvement in thermal efficiency is shown by the maximum temperature drop of 8 °C with a considerable increase in pressure drop. Despite showing an increase in pressure drop of almost 75%, the design improvement is still necessary due to that at 3C charging rate, the baseline condition shows a temperature rise approaching 25 °C. Such temperature is far beyond the optimal working temperature of lithium-ion batteries, which is in the range of 15–35 °C [38]. At such high temperature, prioritizing hydraulic performance over thermal performance will risk the safety of the battery's lifespan.

The graph demonstrates that compared to previously proposed model, the interconnected design shows a relatively low maximum temperature rise, indicating enhanced thermal performance, while maintaining a moderate pressure drop. Compared to the D1–D7 series, it generally provides better heat dissipation, except for D4 and D6, which achieve lower temperatures but at the cost of higher pressure drops. Conversely, the D1 and D7 designs exhibit lower pressure drops but at the cost of a higher temperature rise, suggesting that their flow distribution is less effective in dissipating heat efficiently. These findings highlight the importance of optimizing cooling plate design to achieve effective heat dissipation while maintaining a balanced pressure drop, ensuring efficient battery thermal management with minimal energy consumption and performance trade-offs.

Figure 9a presents the velocity contour for the interconnected design, illustrating the flow behavior within the interconnecting zone. In the straight-channel configuration, where no interconnecting zone is present, the coolant flows independently along separate channels. This limits fluid mixing and prevents the formation of secondary flows. In contrast, in the cooling plate with an interconnection zone, the low-pressure region across the interconnection area induces stationary circulation zones, leading to the formation of secondary flows as shown in Figure 9b. This additional flow pathway increases the heat transfer area between the heating surface and the coolant, thereby enhancing convective heat transfer. Additionally, this geometry enhances turbulence by inducing fluid mixing and disrupting the thermal boundary layer. As a result, the boundary layer thickness is reduced, leading to a higher heat transfer coefficient (*HTC*) and improved convective cooling performance. In terms of temperature distribution, the thermal boundary condition is continuously developing from inlet to downstream. The higher temperature appears at the channel downstream due to the higher thermal boundary layer. Due to the presence of the interconnection area, a small transverse flow through the interconnection zone occurs. It raises the temperature at the area compared to the main stream path as shown in Figure 9c.

Figure 9d illustrates the temperature contour along the flow channel in the interconnected cooling plate design (left), along with the temperature contour on the battery solid body (right). The visualization reveals that temperature is lower near the inlet, where the coolant enters the system at a lower temperature and absorbs heat through convective heat transfer. As the coolant moves downstream, it carries the absorbed heat, resulting in an elevated temperature at the outlet due to sensible heat transfer. Additionally, the figure highlights temperature variations across the battery arrangement. Batteries positioned farther from the cooling plate experience less effective cooling, leading to higher localized temperatures. Figure 10 presents how this value changes overtime, for 3C discharge rate at 0.1 m/s for interconnected design. As time progresses, all three cells exhibit a controlled temperature rise, with the interconnected design ensuring that thermal gradients remain minimal. This highlights the success of the proposed cooling strategy in maintaining temperature uniformity and preventing excessive heating, even under high discharge conditions.

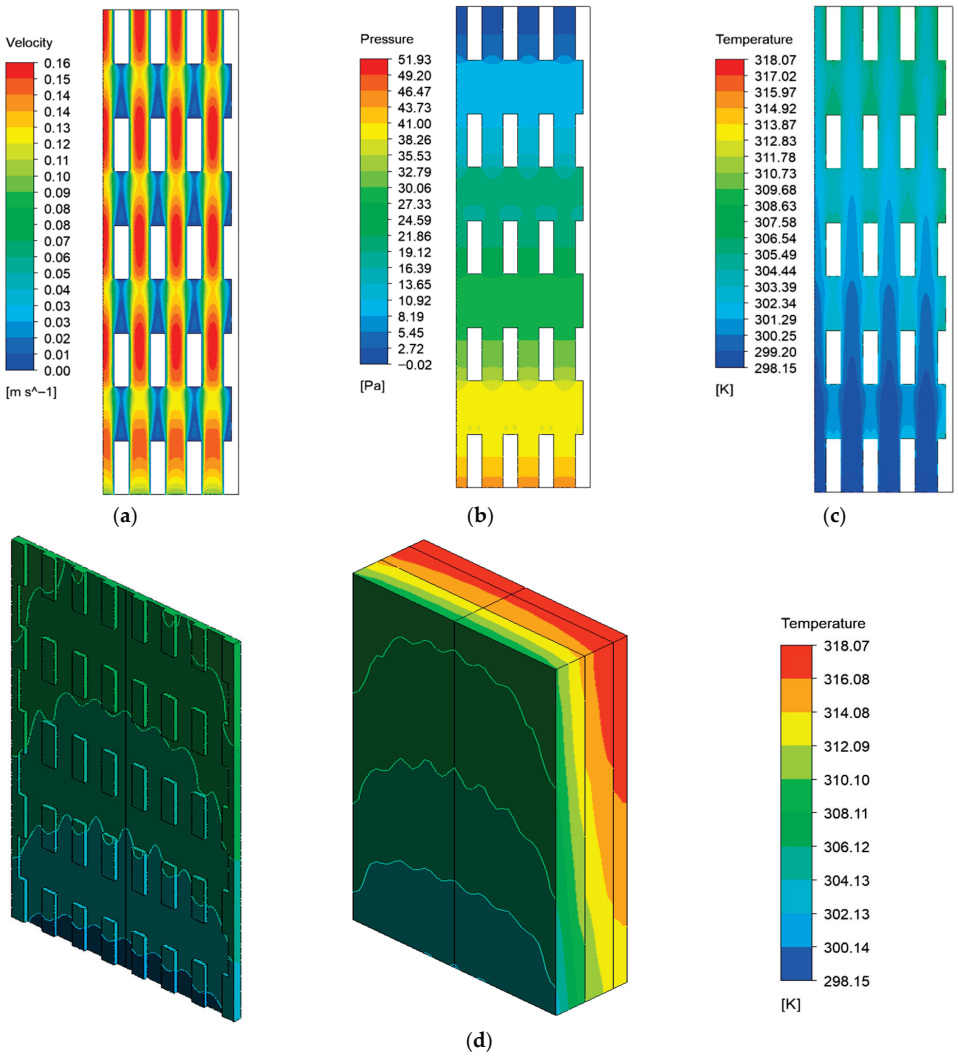

Figure 9. Velocity (**a**), pressure (**b**) and temperature contour along channel (**c**) and temperature contour on the battery body (**d**) under interconnected design.

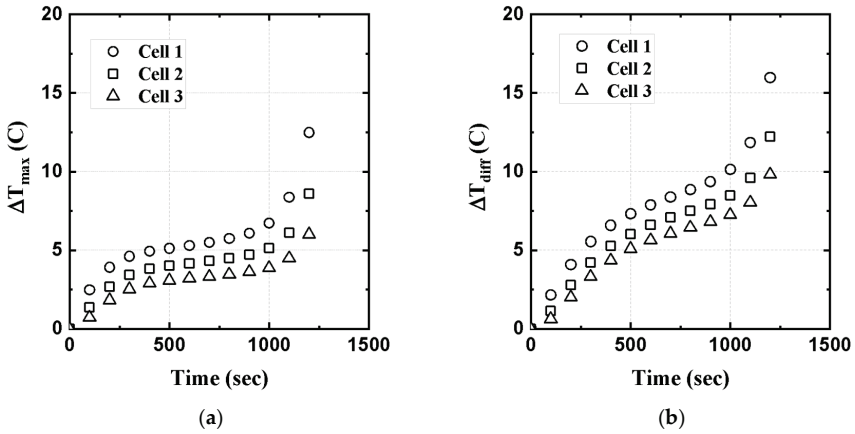

Figure 10. Maximum temperature rise (**a**) and temperature difference ΔTdiff (**b**) of proposed design under 3C discharge rate and 0.1 m/s inlet velocity on specified single battery cell.

4. Conclusions

This study provides an in-depth analysis of cooling plate design and its impact on battery thermal performance, specifically focusing on maximum temperature rise and

pressure drop. The comparative assessment of the baseline (BL), interconnected (ID), and D-series (D1–D7) cooling plate designs has yielded significant insights into the trade-offs between cooling efficiency and hydraulic resistance. The key conclusions drawn from this study are as follows:

- The interconnected (ID) design effectively reduces maximum temperature rise, demonstrating superior thermal performance compared to the baseline (BL) design and achieving comparable cooling efficiency to the best-performing D-series designs.
- The ID design improves temperature uniformity, enhancing thermal safety by reducing the risk of thermal runaway, minimizing localized hotspots, and contributing to a longer battery lifespan through more uniform heat dissipation.
- While certain D-series designs (D4 and D6) demonstrate excellent cooling performance, they experience high pressure drops, resulting in greater energy consumption and increased pumping power requirements.
- The interconnected design achieves a well-balanced compromise, providing enhanced cooling performance while maintaining moderate flow resistance, making it a practical and efficient solution for battery thermal management systems.

Author Contributions: Conceptualization, A.P.S. and J.B.; methodology, A.P.S. and J.B.; software, A.P.S.; validation, A.P.S.; formal analysis, A.P.S.; investigation, A.P.S.; resources, J.B. and J.Y.L.; data curation, A.P.S. and B.F.S.; writing—original draft preparation, A.P.S. and B.F.S.; writing—review and editing, A.P.S. and B.F.S.; visualization, A.P.S.; supervision, J.Y.L.; project administration, J.B.; funding acquisition, J.Y.L. All authors have read and agreed to the published version of the manuscript.

Funding: The authors would like to acknowledge The Korea Institute of Energy Technology Evaluation and Planning (KETEP) and the Ministry of Climate, Energy & Environment (MCEE) of the Republic of Korea (No. RS-2024-00398425) and partially was supported by Korea Hydro & Nuclear Power Co and Local Government (Pohang) (2025).

Data Availability Statement: The data presented in this study are available on request from the corresponding author.

Conflicts of Interest: The authors declare no conflicts of interest.

Nomenclature

v	Velocity (m/s)	***Greek symbol***	
T	Temperature (°C)	ρ	Density kg/m^3
P	Pressure (Pa)	μ	Viscosity (Pa.s)
k	Thermal conductivity (W/mK)		
Q	Power (W)	***Subscript***	
q	Heatflux (W/m^2)	f	Fluid
u	Velocity component in the x-dir. (m/s)	b	Battery-body
v	Velocity component in the y-dir. (m/s)	max	Maximum temperature at time
w	Velocity component in the z-dir. (m/s)	diff	Maximum-minimum temperature
Cp	Sensible heat capacity (J/Kg °C)	w	wall
t	Time (s)		

References

1. Peng, J.; Meng, J.; Chen, D.; Liu, H.; Hao, S.; Sui, X.; Du, X. A review of lithium-ion battery capacity estimation methods for onboard battery management systems: Recent progress and perspectives. *Batteries* **2022**, *8*, 229. [CrossRef]
2. Cao, K.L.A.; Ogi, T. Advanced carbon sphere-based hybrid materials produced by innovative aerosol process for high-efficiency rechargeable batteries. *Energy Storage Mater.* **2025**, *74*, 103901. [CrossRef]

3. Hannan, M.A.; Wali, S.; Ker, P.; Rahman, M.A.; Mansor, M.; Ramachandaramurthy, V.; Muttaqi, K.; Mahlia, T.; Dong, Z. Battery energy-storage system: A review of technologies, optimization objectives, constraints, approaches, and outstanding issues. *J. Energy Storage* **2021**, *42*, 103023. [CrossRef]
4. Wolfram, P.; Lutsey, N. *Electric Vehicles: Literature Review of Technology Costs and Carbon Emissions*; ICCT: Washington, DC, USA, 2016.
5. Ahmad, F.; Khalid, M.; Panigrahi, B.K. Development in energy storage system for electric transportation: A comprehensive review. *J. Energy Storage* **2021**, *43*, 103153. [CrossRef]
6. Broussely, M.; Nazri, G.; Pistoia, G. Lithium-Ion batteries for EV, HEV and other applications. In *Lithium Batteries*; Kluwer Publishers: New York, NY, USA, 2004; Chapter 21.
7. Bandhauer, T.M.; Garimella, S.; Fuller, T.F. A critical review of thermal issues in lithium-ion batteries. *J. Electrochem. Soc.* **2011**, *158*, R1. [CrossRef]
8. Liu, H.; Wei, Z.; He, W.; Zhao, J. Thermal issues about Li-ion batteries and recent progress in battery thermal management systems: A review. *Energy Convers. Manag.* **2017**, *150*, 304–330. [CrossRef]
9. Deng, T.; Zhang, G.; Ran, Y.; Liu, P. Thermal performance of lithium ion battery pack by using cold plate. *Appl. Therm. Eng.* **2019**, *160*, 114088. [CrossRef]
10. Zhang, T.; Gao, C.; Gao, Q.; Wang, G.; Liu, M.; Guo, Y.; Xiao, C.; Yan, Y. Status and development of electric vehicle integrated thermal management from BTM to HVAC. *Appl. Therm. Eng.* **2015**, *88*, 398–409. [CrossRef]
11. Leng, F.; Tan, C.M.; Pecht, M. Effect of temperature on the aging rate of Li ion battery operating above room temperature. *Sci. Rep.* **2015**, *5*, 12967. [CrossRef] [PubMed]
12. Song, W.; Chen, M.; Bai, F.; Lin, S.; Chen, Y.; Feng, Z. Non-uniform effect on the thermal/aging performance of Lithium-ion pouch battery. *Appl. Therm. Eng.* **2018**, *128*, 1165–1174. [CrossRef]
13. Sun, H.; Dixon, R. Development of cooling strategy for an air cooled lithium-ion battery pack. *J. Power Sources* **2014**, *272*, 404–414. [CrossRef]
14. Zhao, G.; Wang, X.; Negnevitsky, M.; Zhang, H. A review of air-cooling battery thermal management systems for electric and hybrid electric vehicles. *J. Power Sources* **2021**, *501*, 230001. [CrossRef]
15. Liu, H.; Chika, E.; Zhao, J. Investigation into the effectiveness of nanofluids on the mini-channel thermal management for high power lithium ion battery. *Appl. Therm. Eng.* **2018**, *142*, 511–523. [CrossRef]
16. Mondal, B.; Lopez, C.F.; Mukherjee, P.P. Exploring the efficacy of nanofluids for lithium-ion battery thermal management. *Int. J. Heat Mass Transf.* **2017**, *112*, 779–794. [CrossRef]
17. Adhikari, N.; Bhandari, R.; Joshi, P. Thermal analysis of lithium-ion battery of electric vehicle using different cooling medium. *Appl. Energy* **2024**, *360*, 122781. [CrossRef]
18. Farzaneh, F.; Zhang, Q.; Jung, S. Enhancing electric vehicle battery safety and performance: Aluminum tubes filled with PCM. *J. Energy Storage* **2024**, *97*, 112922. [CrossRef]
19. Abdelkareem, M.A.; Maghrabie, H.M.; Abo-Khalil, A.G.; Adhari, O.H.K.; Sayed, E.T.; Radwan, A.; Rezk, H.; Jouhara, H.; Olabi, A. Thermal management systems based on heat pipes for batteries in EVs/HEVs. *J. Energy Storage* **2022**, *51*, 104384. [CrossRef]
20. Wang, Y.; Gao, Q.; Wang, G.; Lu, P.; Zhao, M.; Bao, W. A review on research status and key technologies of battery thermal management and its enhanced safety. *Int. J. Energy Res.* **2018**, *42*, 4008–4033. [CrossRef]
21. Zhao, L.; Li, W.; Wang, G.; Cheng, W.; Chen, M. A novel thermal management system for lithium-ion battery modules combining direct liquid-cooling with forced air-cooling. *Appl. Therm. Eng.* **2023**, *232*, 120992. [CrossRef]
22. Wu, T.; Zhang, Z.; Xie, Y.; Wang, C.; Hu, Y.; Liu, J.; Cai, S. Integrated pulsed cooling with non-uniform channel liquid plate and phase change material for high-energy-density battery thermal management. *Int. J. Heat Mass Transf.* **2025**, *247*, 127191. [CrossRef]
23. Khaboshan, H.N.; Jaliliantabar, F.; Abdullah, A.A.; Panchal, S. Improving the cooling performance of cylindrical lithium-ion battery using three passive methods in a battery thermal management system. *Appl. Therm. Eng.* **2023**, *227*, 120320. [CrossRef]
24. Akbarzadeh, M.; Kalogiannis, T.; Jaguemont, J.; Jin, L.; Karimi, D.; Beheshti, H.; Van Mierlo, J.; Berecibar, M. A comparative study between air cooling and liquid cooling thermal management systems for a high-energy lithium-ion battery module. *Appl. Therm. Eng.* **2021**, *198*, 117503. [CrossRef]
25. Trimbake, A.; Singh, C.P.; Krishnan, S. Mineral oil immersion cooling of lithium-ion batteries: An experimental investigation. *J. Electrochem. Energy Convers. Storage* **2022**, *19*, 021007. [CrossRef]
26. Chen, D.; Jiang, J.; Kim, G.-H.; Yang, C.; Pesaran, A. Comparison of different cooling methods for lithium ion battery cells. *Appl. Therm. Eng.* **2016**, *94*, 846–854. [CrossRef]
27. Panchal, S.; Khasow, R.; Dincer, I.; Agelin-Chaab, M.; Fraser, R.; Fowler, M. Thermal design and simulation of mini-channel cold plate for water cooled large sized prismatic lithium-ion battery. *Appl. Therm. Eng.* **2017**, *122*, 80–90. [CrossRef]

28. Amalesh, T.; Narasimhan, N.L. Introducing new designs of minichannel cold plates for the cooling of Lithium-ion batteries. *J. Power Sources* **2020**, *479*, 228775. [CrossRef]
29. Jiang, Z.; Xuan, W.; Ma, R.; Xu, C.; Yu, B.; Wang, D.; Shi, J.; Chen, J. A high-efficiency immersion cooling system with integrated flow distribution plates for vehicle-scale high-energy-density battery modules. *Energy* **2025**, *330*, 136885. [CrossRef]
30. Sun, Y.; Bai, R.; Ma, J. Design and thermal analysis of a new topological cooling plate for prismatic lithium battery thermal management. *Appl. Therm. Eng.* **2023**, *219*, 119547. [CrossRef]
31. Zhan, S.; Liang, L.; Li, Z.; Yu, C.; Wang, F. Topology optimization of liquid cooling plate for lithium battery heat dissipation based on a bionic leaf-vein structure. *Int. J. Heat Mass Transf.* **2024**, *231*, 125898. [CrossRef]
32. Pan, C.; Wu, J.; Wang, J.; Wang, L.; Liu, L. Topology optimization-based design and performance analysis of liquid cooling plates for lithium-ion batteries. *J. Energy Storage* **2025**, *124*, 116842. [CrossRef]
33. Zhu, J.; Zhou, H.; Wang, C.; Zhou, L.; Yuan, S.; Zhang, W. A review of topology optimization for additive manufacturing: Status and challenges. *Chin. J. Aeronaut.* **2021**, *34*, 91–110. [CrossRef]
34. ANSYS. *ANSYS Fluent 18.1 Theory Guide*; Ansys Inc.: Canonsburg, PA, USA, 2017.
35. Lai, Y.; Ding, J.; Liu, L. Numerical investigation on the cooling performance of lithium-ion battery using liquid cooled-plate with integrated grooves and secondary microchannel structures. *Int. J. Therm. Sci.* **2025**, *217*, 110094. [CrossRef]
36. Wang, T.; Wang, Y.; Hu, H. Topological approach for optimization of liquid cooled plate with different inlet/outlet parameters. *Case Stud. Therm. Eng.* **2025**, *71*, 106201. [CrossRef]
37. Shah, R.K.; London, A.L. Thermal boundary conditions and some solutions for laminar duct flow forced convection. *J. Heat Transf.* **1974**, *96*, 159–165. [CrossRef]
38. Ma, S.; Jiang, M.; Tao, P.; Song, C.; Wu, J.; Wang, J.; Deng, T.; Shang, W. Temperature effect and thermal impact in lithium-ion batteries: A review. *Prog. Nat. Sci. Mater. Int.* **2018**, *28*, 653–666. [CrossRef]

batteries

MDPI

Article

Comparative Evaluation of Power Management Strategies in Multi-Stack Fuel Cell-Battery Hybrid Truck via TOPSIS

Sanghyun Yun [1] and Jaeyoung Han [1,2,3,*]

[1] Department of Mechanical Engineering, Kongju National University, 1223-24 Cheonan-daero, Cheonan-si 31080, Republic of Korea; sanghyun9543@smail.kongju.ac.kr
[2] Department of Future Automotive Engineering, Kongju National University, 1223-24 Cheonan-daero, Cheonan-si 31080, Republic of Korea
[3] Institute of Intelligent Vehicle, Kongju National University, 1223-24 Cheonan-daero, Cheonan-si 31080, Republic of Korea
* Correspondence: hjyt11@kongju.ac.kr; Tel.: +82-41-521-9272; Fax: +82-41-555-9123

Abstract

Multi-stack Polymer electrolyte Membrane Fuel Cell (PEMFC) systems are increasingly adopted in heavy-duty mobility to overcome the power limitations and thermal instability of single-stack configurations. However, the overall energy efficiency, hydrogen utilization, and thermal behavior of multi-stack fuel cell trucks are highly dependent on the applied Power Management System (PMS). In this study, high-fidelity, system-level dynamic model of multi-stack fuel cell truck was developed using Matlab/Simscape^{TM}, and three PMS approaches (rule-based control, state-machine control, and fuzzy logic control) were comparatively evaluated. The analysis includes coolant temperature regulation, hydrogen consumption, battery State of Charge (SoC) dynamics, and the parasitic power demand of Balance of Plant (BoP) components. Results show that the fuzzy logic PMS provides the most balanced operating profile by smoothing transient fuel cell loading and actively leveraging the battery during high-demand periods. In the thermal domain, the fuzzy logic PMS reduced temperature overshoot by up to 61.20%, demonstrating the most stable thermal control among the three strategies. Hydrogen consumption decreased by 3.08% and 0.89% compared with the rule-based and state-machine PMS, respectively, while parasitic power consumption decreased by 7.12% and 3.32%, confirming improvements in overall energy efficiency. TOPSIS-based multi-criteria decision analysis further showed that the fuzzy logic PMS achieved the highest closeness coefficient (0.9112), indicating superior system-level performance. These findings highlight the importance of PMS design for achieving energy-optimal and thermally stable operation of multi-stack PEMFC trucks and provide practical guidance for future control strategies, heavy-duty mobility applications, and next-generation hydrogen powertrain optimization.

Keywords: configuration; cooling uniformity; dual-stack; fuzzy logic control; hotspot; polymer electrolyte membrane fuel cell; power management system; technique for order of preference by similarity to ideal solution; thermal management system

1. Introduction

1.1. Research Background

Internal combustion engine (ICE) vehicles still dominate the global automotive market, accounting for nearly 75% of total sales, while battery electric vehicles (BEVs) represent around 16.2%, plug-in hybrid electric vehicles (PHEVs) about 8.7%, and hydrogen-powered

vehicles less than 0.1% [1–3]. However, the continued reliance on fossil-fuel-based transportation has intensified environmental challenges such as greenhouse gas emissions and urban air pollution, leading governments worldwide to impose increasingly stringent emission regulations [4]. This shift has accelerated the transition toward eco-friendly mobility technologies, including BEVs and hydrogen electric vehicles (HEVs).

Despite the rapid progress of battery technology, heavy-duty applications, such as long-haul trucks, pose unique challenges. They require extended driving ranges and high payload capacities, which in turn demand substantial onboard energy storage. This often results in a significant increase in battery weight, thereby compromising payload capacity and vehicle efficiency [5,6]. In such cases, hydrogen-powered fuel cell vehicles present a more practical solution due to their higher energy density and shorter refueling time.

PEMFC is particularly attractive for heavy-duty transport, offering advantages such as high efficiency, rapid start-up, low acoustic noise, and zero tailpipe emissions [7,8]. Additionally, they are well suited to applications with high power demand and frequent load fluctuations, conditions commonly encountered in commercial freight operations [9,10]. However, despite these advantages, fuel cell technologies still face several challenges in commercial applications. In particular, during long-term operation, fuel cells experience gradual performance degradation caused by a combination of electrode material degradation, catalyst loss, mechanical damage to the membrane electrode assembly (MEA), and variations in operating conditions. Such degradation not only reduces efficiency and power output but also shortens system lifetime and increases maintenance and replacement costs [11]. These issues become more pronounced in heavy-duty freight applications, where high loads and frequent load transients are unavoidable. To mitigate these limitations, multi-stack (multi-reactor) fuel cell architectures have recently attracted growing attention. By distributing power demand across multiple stacks, multi-stack configurations can alleviate localized thermal and electrical stresses, thereby improving system reliability and extending operational lifetime. This scalability makes PEMFC systems suitable for high-power applications ranging from compact single-stack systems to large-scale multi-stack configurations [12–14]. Nevertheless, single-stack systems often fall short of meeting the stringent power requirements of heavy-duty vehicles [15,16].

To overcome these limitations, multi-stack fuel cell systems have been introduced to enhance power output, durability, efficiency, and overall system reliability [17–19]. In particular, they provide significant thermal management advantages over single-stack systems, which typically suffer from limited natural convection cooling capacity and require additional energy for heat removal. Effective thermal control strategies are therefore crucial to maintaining optimal operating conditions and minimizing auxiliary power consumption. Furthermore, to address the inherently slow dynamic response of fuel cells, hybrid architectures combining PEMFC with auxiliary battery system is widely adopted. Such configurations improve system responsiveness, support rapid load transitions, and extend fuel cell lifetime. Consequently, an advanced Power Management System (PMS) is essential to dynamically allocate power between the fuel cell and battery with load demand and operating conditions. Thie need for intelligent hybrid power management becomes even more critical in emerging PEMFC with limited thermal margins. In addition to water-cooled PMEFC system widely adopted in heavy-duty truck, air-cooled PEMFC has recently attracted significant attention in lightweight and compact mobility applications due to their simplified balance of plant structure and high power density. However, air-cooled system inherently exhibits narrower thermal margins and stronger coupling between stack temperature, auxiliary power consumption, and dynamic load variations. Therefore, advanced hybrid power management strategies that jointly consider energy efficiency and

https://doi.org/10.3390/batteries12020065

thermal stability are essential not only for heavy-duty water-cooled system but also for emerging air-cooled PMEFC system.

1.2. Research Survey

Extensive research has been conducted to overcome the inherent limitations of single-stack fuel cell systems by adopting multi-stack configurations. These efforts have focused on improving system efficiency, reliability, and power distribution under varying load conditions. For instance, Han et al. [20] demonstrated through optimized power simulations that activating auxiliary sub-stacks beyond a specific load threshold can significantly enhance overall system efficiency. Similarly, Dépature et al. [21] developed a simulation-based control design framework and confirmed that multi-stack systems outperform single-stack architectures in terms of integration, reliability, and performance. Zhou et al. [22] explored power allocation strategies that account for both efficiency and stack lifetime, while Marx et al. [23] proposed a rule-based energy management framework incorporating a combined index to balance efficiency with long-term durability. In addition to fuel cell–centric studies, parallel research efforts have also focused on energy management strategies for other electrochemical energy storage systems employed in hybrid powertrains.

In parallel with fuel cell–based hybrid powertrains, energy management strategies for other electrochemical energy storage systems, such as lithium-ion batteries and supercapacitors, have also been widely investigated. Battery management systems (BMS) focus on state estimation, charge–discharge control, and lifetime management, with model-based approaches such as extended Kalman filtering and equivalent circuit modeling being commonly adopted for real-time applications [24,25]. Comprehensive surveys further indicate that battery management requirements depend strongly on the assigned role of the battery and system-level integration within the powertrain [26]. Beyond batteries, supercapacitors have attracted attention as auxiliary energy storage devices due to their high power density and fast dynamic response, and hybrid battery–supercapacitor energy management strategies, including model predictive control approaches, have been proposed to mitigate transient load fluctuations and improve overall system performance [27,28].

Thermal management has also been a key research focus, given its critical role in ensuring stack performance, efficiency, and lifespan. Qiu et al. [29] compared series and parallel cooling architectures for multi-stack systems under various load conditions, identifying their respective operational advantages. Shen et al. [30] further highlighted that series configurations provide superior temperature uniformity under steady-state loads, whereas parallel layouts offer improved thermal control during transient operations. Fault detection and control approaches have also been proposed, including Su et al.'s [31] Unscented Kalman Filter-based method for sensor fault diagnosis and Saygili et al.'s [32] ITAE-based controller optimization to minimize parasitic power losses. Additionally, Hu et al. [33] introduced a robust incremental fuzzy control method for cooling components such as pumps and bypass valves, improving system resilience to parameter variations and disturbances.

Parallel to thermal studies, power management strategy (PMS) research for fuel cell electric vehicles (FCEVs) has evolved to address the dual-source power distribution challenge between the fuel cell and battery. Existing PMS approaches can be broadly classified into rule-based control, state-machine-based control, and fuzzy-logic-based control strategies. Rule-based PMS methods have been widely adopted due to their simplicity, transparency, and ease of implementation, and have been shown to provide robust performance under predefined operating conditions [34–36]. State-machine-based approaches extend rule-based strategies by introducing explicit operating modes and state transition logic, enabling improved adaptability to varying load and operating conditions [37,38].

https://doi.org/10.3390/batteries12020065

More recently, fuzzy-logic-based PMS methods have attracted increasing attention due to their ability to handle nonlinear system behavior and uncertainties without requiring precise mathematical models, offering enhanced performance in terms of energy efficiency and thermal stability [39,40]. In addition to these heuristic-based strategies, optimization-oriented PMS approaches, such as dynamic programming and predictive control, have also been investigated to further improve system-level performance [41,42]. However, these methods often involve higher computational complexity, which may limit their real-time applicability in large-scale vehicle systems.

Despite these advances, most previous studies have concentrated on subsystem-level optimization, such as air supply, hydrogen flow, or thermal regulation, or have evaluated PMS strategies primarily based on state of charge and hydrogen consumption. However, comprehensive vehicle-level evaluations that simultaneously consider multi-stack architecture, thermal management, and power control remain limited. To address this gap, the present study develops a full-vehicle physical model of a hydrogen-powered truck using MATLAB/Simscape™ based on the Hyundai Xcient. The model integrates electrochemical, thermal-fluid, and mechanical domains and implements three distinct power management approaches, rule-based control, state machine control, and fuzzy logic control, which are comparatively evaluated using the TOPSIS method. Furthermore, this comparative evaluation approach may serve as a conceptual basis for future studies on air-cooled PEMFC-based hybrid systems, provided that appropriate system models and parameters are established.

2. System Configuration

A dynamic model of the hydrogen-powered electric truck was constructed based on the specifications of Hyundai's Xcient heavy-duty truck. The overall system architecture and key parameters are summarized in Figure 1 and Table 1. The vehicle powertrain was structured into three primary subsystems:

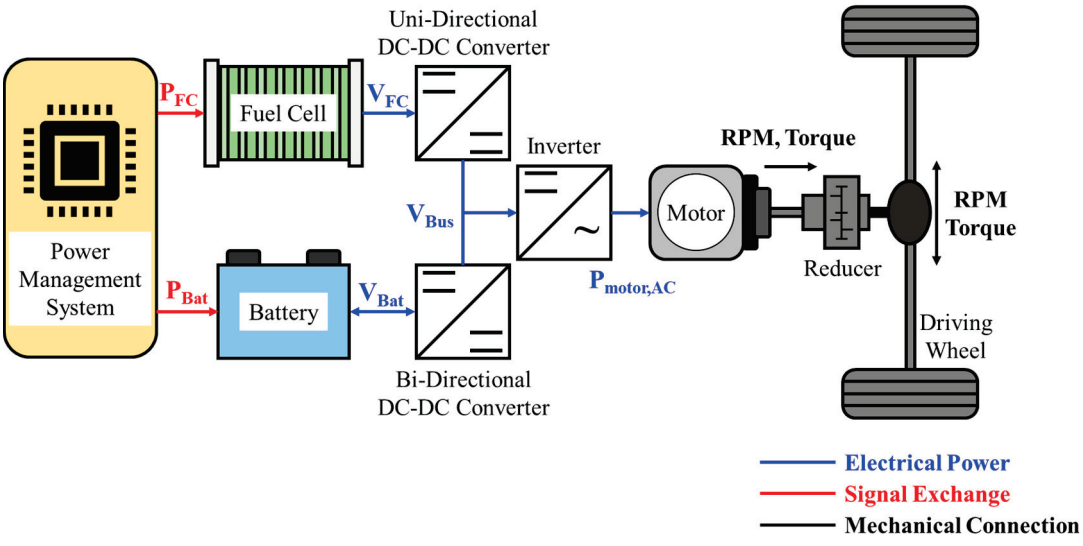

Figure 1. Hydrogen electric truck system model schematic.

(1) Power Source Module: comprising dual PEM fuel cell stacks and high-voltage battery pack, which jointly supply the electrical energy required for propulsion
(2) Power Conversion Module: including DC-DC converter and inverter that regulate voltage levels and enable efficient energy transfer to the traction motor

https://doi.org/10.3390/batteries12020065

(3) Drivetrain Module: consisting of an electric traction motor coupled with a reduction gear to convert electrical energy into mechanical motion and deliver the required torque to the wheels

Table 1. Fuel cell system specifications.

System	Components	Parameters	Unit
Power Supply System	Number of Stack	2	-
	Power of Stack	90	kW
	Number of Battery	3	ea
	Power of Battery	24	kWh
Driving System	Power of Motor	350	kW
	Torque of Motor	2237	Nm

Furthermore, a power management system was integrated into the model to coordinate energy distribution between the fuel cell and battery in real time, ensuring stable operation and optimal performance under varying load conditions.

2.1. Fuel Cell System

To meet the high power requirements of heavy-duty applications, the vehicle integrates two PEMFC stacks, each rated at 90 kW, forming a combined primary power source for the propulsion system. To maintain reliable operation, the fuel cell subsystem incorporates a comprehensive Balance of Plant (BoP), which includes hydrogen delivery, air supply, and thermal regulation units. These subsystems ensure stable reactant supply, appropriate humidity control, and precise temperature regulation under dynamic load conditions.

The dynamic fuel cell model developed in this study was constructed under several simplifying assumptions to facilitate system-level simulation and reduce computational complexity:

- Hydrogen and air flows are modeled as ideal gases with fixed stoichiometric ratios and constant relative humidity.
- The electrochemical reaction is considered spatially uniform, and concentration gradients within the electrodes are neglected.
- The temperature field inside the stack is represented using a lumped parameter approach, assuming homogeneous temperature distribution throughout the cell layers.

2.1.1. Fuel Processing System

The vehicle incorporates seven onboard high-pressure hydrogen storage tanks, each capable of storing compressed hydrogen gas at 700 bar. To deliver hydrogen safely to the fuel cell stacks, a two-stage pressure regulation mechanism is implemented [43]. Specifically, the hydrogen supply pressure is reduced in two sequential stages. In the first stage, the pressure is decreased from the storage level of 700 bar to an intermediate pressure of approximately 10 bar, which ensures safe downstream handling and protects system components from excessive mechanical stress. In the second stage, the hydrogen pressure is further regulated from this intermediate level to the operating pressure required at the fuel cell stack inlet, enabling stable and reliable hydrogen supply under varying load conditions. This multi-step pressure reduction process plays a critical role in maintaining system safety and performance, as directly supplying high-pressure hydrogen could lead to mechanical stress, component damage, or rapid degradation of electrochemical performance [44–48]. By stabilizing the supply pressure, the system ensures consistent and efficient fuel cell operation across a wide range of load conditions.

https://doi.org/10.3390/batteries12020065

The hydrogen flow rate required for stack operation is primarily governed by the load current. Based on the consumption rate, the remaining hydrogen mass in the storage tanks can be estimated using the following relationship:

$$\dot{m}_{H_2} = \frac{i}{nF} \times A \times n_{cell} \times stoi \tag{1}$$

$$m_{H_2,remain} = m_{H_2,tank} \times n_{tank} - \int \dot{m}_{H_2} \tag{2}$$

Here, $\dot{m}_{H_2}$ represents the molar flow rate of hydrogen, F represents the Faraday constant, i is the current density, A is the active area, and $stoi$ denotes the stoichiometric ratio. In addition, n represents the number of electrons involved in the electrochemical reaction, and n_{cell} denotes the number of cells in the fuel cell stack. Where the hydrogen consumption is obtained by time integration of the hydrogen molar flow rate over time t.

2.1.2. Air Processing System

Air supply systems for PEMFC stacks can be broadly divided into atmospheric and pressurized types, depending on the required performance characteristics and system design constraints [49–51]. In this study, a pressurized supply configuration was selected, employing a centrifugal compressor to provide sufficient oxidant flow for the dual 90 kW-class fuel cell stacks. The adoption of a pressurized air system enables rapid transient response and enhances overall stack efficiency under dynamic load conditions.

Similar to the hydrogen subsystem, the required air flow rate is governed by the load current, ensuring proper stoichiometric balance during operation. The compressor discharge pressure is determined as a function of system efficiency and the specific heat ratio, as expressed by the following relationship:

$$\dot{m}_{Air} = \frac{i}{nF} \times A \times n_{cell} \times stoi \tag{3}$$

$$P = \left(1 + \frac{\eta(\dot{m},\ U)}{T_{atm} C_P}\right)^{\frac{\gamma}{(\gamma-1)}} \times P_{atm} \tag{4}$$

Here, $\dot{m}_{Air}$ represents the molar flow rate of air, η is the compressor efficiency, γ is the specific heat ratio, and C_P is the specific heat at constant pressure.

2.1.3. Stack

The output voltage of a fuel cell stack is influenced by several electrochemical and transport-related phenomena. The theoretical reversible potential, often referred to as the Open Circuit Voltage (OCV), is reduced in practical operation due to multiple overvoltage losses. These include activation overvoltage associated with charge transfer kinetics, concentration overvoltage caused by mass transport limitations of the reactants, and ohmic overvoltage resulting from resistance to electron and ion conduction within the cell components. The overall cell voltage can therefore be expressed as follows:

$$V_{cell} = E - V_{act} - V_{con} - V_{ohm} \tag{5}$$

$$E = -\frac{\Delta g_f}{nF} = -\frac{\Delta g_f^0}{nF} + \frac{RT}{nF} ln\left(\frac{p_{H_2} p_{O_2}^{0.5}}{p_{H_2O}}\right) \tag{6}$$

https://doi.org/10.3390/batteries12020065

$$V_{act} = \frac{RT}{n\alpha F} ln\left(\frac{i}{i_0}\right) \tag{7}$$

$$V_{conc} = \frac{RT}{nF} ln\left(1 - \frac{i}{i_L}\right) \tag{8}$$

$$V_{ohm} = I \times R_{ohm} \tag{9}$$

Here, n is the number of electrons involved in the electrochemical reaction, p denotes the partial pressure of each reactant, and α is the charge transfer coefficient. In addition, E represents the reversible open-circuit voltage, V_{act}, V_{conc}, and V_{ohm} denote the activation, concentration and ohmic overvoltages, respectively, and i_L denotes the limiting current density constrained by mass transport limitations.

The fuel cell stack model developed in this study was validated against experimental data reported in previous single-cell studies, as illustrated in Figure 2 [52]. In that study, the PEMFC polarization characteristics were measured under steady-state operating conditions at a cell temperature of 65 °C using a three-cell PEMFC stack with an effective active area of 25 cm^2 per cell. Humidified hydrogen and air were supplied to the anode and cathode, respectively, and the polarization curve was obtained over a current density range of 0–1.6 A/cm^2. The stack's overall performance characteristics were extrapolated from single-cell results by proportionally scaling the specifications with the total number of unit cells. To ensure reliable operation under high-load conditions and to prevent issues such as increased membrane resistance, water and thermal management instability, and the rise of concentration and activation overpotentials, the maximum operating current density was constrained to below 0.8 A/cm^2 [53–58].

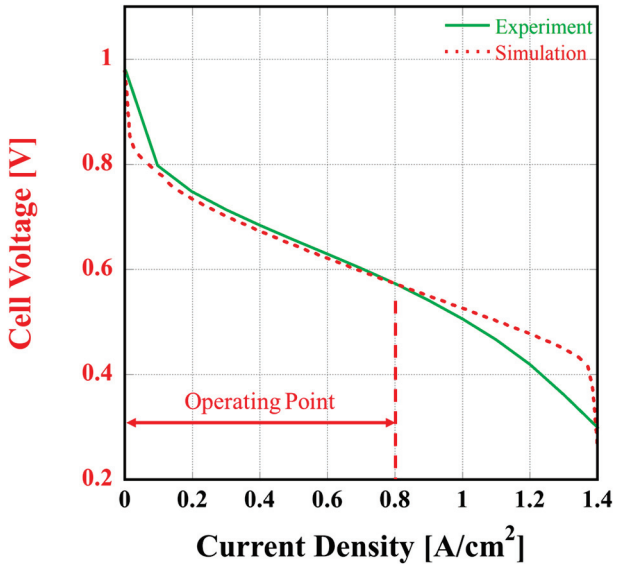

Figure 2. Polarization curve characteristic of fuel cell.

2.1.4. Thermal Management System

The thermal management architecture developed for the hydrogen-powered truck is composed of distribution valve, three-way valve, coolant circulation pump, radiator, and cooling fan, as shown in Figure 3. The specifications and configurations of these components were derived from a validated reference model, whose performance had been experimentally verified in a hydrogen fuel cell truck application [59]. Based on this design reference, the same component parameters were adopted in the present system model to ensure realistic thermal behavior and system performance.

https://doi.org/10.3390/batteries12020065

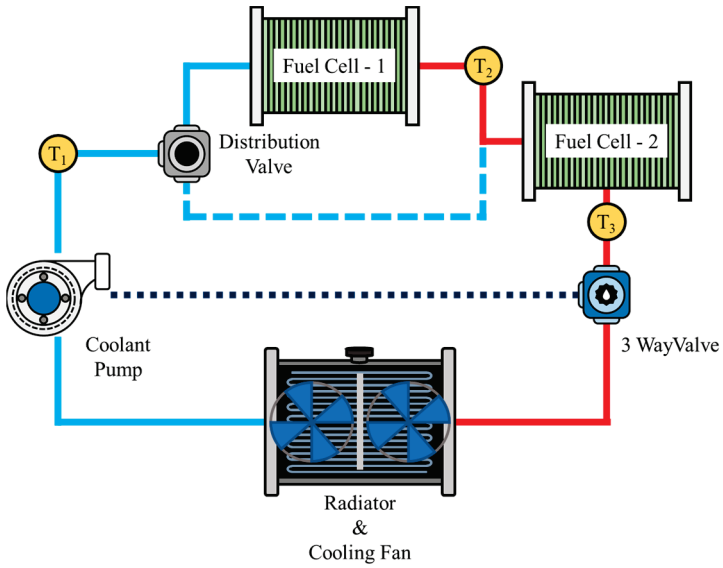

Figure 3. Hydrogen electric truck thermal management system structure.

Maintaining the fuel cell stacks within an optimal thermal operating range is essential for maximizing electrochemical efficiency and ensuring long-term durability. In particular, stable operation of both Stack 1 and Stack 2 at approximately 343.15 K enhances reaction kinetics, thereby improving overall system performance and extending component lifetime [60–62]. To achieve precise thermal regulation under varying load conditions, Proportional Integral (PI) controllers were implemented across multiple subsystems. The cooling fan was controlled to maintain the coolant temperature at point T1 around 333.15 K, while additional PI controllers regulated the distribution valve (T2) and coolant pump (T3) to sustain their respective setpoints near 343.15 K.

The radiator employed in the thermal management system is configured as a louver-fin type heat exchanger. During operation, the coolant absorbs heat generated within the fuel cell stack and is subsequently cooled as thermal energy is transferred to the ambient airflow, which is supplied either by the vehicle's forward motion (ram air) or by the operation of the cooling fan. The heat exchanger's thermal performance is quantitatively assessed based on its effectiveness (ε) and Number of Transfer Units (NTU), which are defined as follows:

$$\varepsilon = \frac{1 - exp[-NTU(1-c)]}{1 - C\,exp[-NTU(1-c)]} \tag{10}$$

$$\mathrm{NTU} = \frac{1}{c_{min} \times R} \tag{11}$$

Here, c_{min} represents the minimum heat capacity rate, and R denotes the thermal resistance component. The heat transfer rate is calculated based on the effectiveness as shown below, while the maximum heat transfer rate is determined by the minimum heat capacity rate and the temperatures of the coolant and air entering the heat exchanger.

$$\dot{Q} = \varepsilon \times \dot{Q}_{max} \tag{12}$$

$$\dot{Q}_{max} = \frac{c_{min}}{(T_{coolant,in} - T_{air,in})} \tag{13}$$

https://doi.org/10.3390/batteries12020065

Through this heat transfer process, the outlet temperatures of the coolant and air can be calculated as follows:

$$T_{coolant,out} = T_{coolant,in} - \frac{\dot{Q}}{c_{coolant}} \quad (14)$$

$$T_{air,out} = \frac{\dot{Q}}{c_{air}} + T_{air,in} \quad (15)$$

Although temperature regulation is applied across all sections of the cooling loop, the concurrent operation of multiple controllers at the same control point can result in interaction effects, potentially degrading system stability and control performance [63–65]. To mitigate this issue, a simplified rule-based control strategy was implemented for the three way valve in place of a more complex control algorithm. In this scheme, the valve opening ratio is modulated with the fuel cell stack load, thereby enabling stable and responsive thermal control.

2.2. Battery

The battery system in the hydrogen-powered truck functions as a supplementary energy source, playing a crucial role in compensating for the inherently slow dynamic response of the fuel cell system during transient load changes [66–68]. In this study, the battery was configured based on the specifications of Hyundai's Xcient as a high-voltage lithium-ion pack with a total capacity of 72 kWh, comprising three modules of 24 kWh each. The nominal system voltage is 630 V. Operating in a hybrid configuration alongside the fuel cell stacks, the battery ensures continuous and reliable power delivery under varying load conditions, thereby enhancing vehicle responsiveness and overall energy management performance.

2.3. DC-DC Converter

To match the distinct voltage levels of the fuel cell and battery with the requirements of the traction motor, DC–DC power converters were integrated into the system architecture [69,70]. Because the battery undergoes both charging and discharging processes depending on its SoC during vehicle operation, a bidirectional converter is necessary to enable power flow in both directions. Accordingly, a unidirectional converter was assigned to the fuel cell subsystem to step up its output voltage, while a bidirectional converter was incorporated into the battery subsystem to manage bidirectional energy exchange, ensuring proper voltage conversion and seamless hybrid power operation.

2.4. Powertrain System

The powertrain subsystem converts the electrical energy generated by the fuel cell and battery into mechanical power via the traction motor, enabling the vehicle's propulsion. It delivers the tractive force necessary to counteract various resistive loads that occur during driving, such as gravitational forces from vehicle mass, road incline resistance, and aerodynamic drag. These resistive components are calculated using the following equations, with detailed system parameters summarized in Table 2. Furthermore, because the traction motor inherently operates with low torque and high rotational speed, a reduction gear is integrated into the drivetrain to increase output torque and satisfy the propulsion requirements of the vehicle [71–73].

$$\sum F_{vehicle} = F_{drive} - F_{brake} - F_{resist} \quad (16)$$

$$F_{drive} = \frac{\tau_{axle}}{r_{tire}} \quad (17)$$

https://doi.org/10.3390/batteries12020065

$$F_{brake} = F_B tanh\left(\frac{\omega_{axle}}{\omega_1}\right) \quad (18)$$

$$F_{resist} = (F_{tire}cos\theta + F_{air})tanh\left(\frac{v_x}{v_1}\right) + mgsin\theta \quad (19)$$

Table 2. Xcient vehicle specification [9].

System	Components	Parameters	Unit
Vehicle Specification	Vehicle Mass	28,000	kg
	Tire Rolling Radius	0.286	m
	Tire Rolling Coefficient	0.008	-
	Air Drag Coefficient	1.15	-
	Vehicle Front Area	2.54 × 3.73	m^2
	Reduction Gear Ratio	8	-
	Gravitational Acceleration	9.81	m/s^2

Here, F_{drive} denotes the traction force generated by the motor, which is driven by the power supplied from the hydrogen fuel cell and battery, and is calculated through torque and wheel radius. F_{brake} represents the braking force generated for vehicle deceleration. In addition, F_{resist} represents the total resistive force, which includes rolling resistance caused by tire-road contact, aerodynamic drag caused by air during vehicle motion, and gravitational resistance due to road slope.

2.5. Power Management System

To ensure a fair comparison among the three power management strategies, all PMSs were designed to determine the fuel cell output power based on the same input information, namely the traction load power and battery SoC. The PMSs differ only in the complexity and adaptability of their control logic and are classified into rule-based control, state machine control, and fuzzy logic control strategies. The hydrogen electric truck operates under a hybrid powertrain architecture that integrates hydrogen fuel cell system with a high-voltage battery. Effective coordination between these two energy sources requires well-designed PMS capable of dynamically allocating power with the vehicle's traction demand. The PMS plays a crucial role in optimizing overall system efficiency while distributing power within the physical and operational constraints of both subsystems [74,75]. In this study, three different PMS strategies—rule-based control, state machine control, and fuzzy logic control—were developed and evaluated.

The rule-based control approach is widely adopted due to its simplicity and ease of implementation, as control decisions are derived from predefined logic rules. However, the static nature of these rules often limits adaptability, making it challenging to maintain optimal performance under rapidly changing or unpredictable operating conditions. State machine control, on the other hand, models system behavior using discrete operational states and transition conditions, providing a structured and easily interpretable control. Yet, as system complexity increases, the number of states can grow significantly, complicating controller design and increasing maintenance efforts. Finally, fuzzy logic control offers high flexibility in managing nonlinear and uncertain environments by using linguistic variables and membership functions. Despite its robustness, the computational cost associated with processing many fuzzy rules can become a limiting factor in real-time applications [76–81].

https://doi.org/10.3390/batteries12020065

2.5.1. Rule-Based Control PMS

Rule-based control is widely recognized for its simplicity and rapid implementation, as control decisions are derived directly from predefined logical rules [82]. In this study, a rule-based PMS was developed using a conditional if–then structure, with SoC and power demand serving as the primary control variables. SoC thresholds were set at 0.4 and 0.6 to define the system's operating regions. Based on these thresholds, the control strategy was divided into three distinct operating modes: battery-dominant drive, hybrid drive, and fuel-cell-dominant drive, as illustrated in Figure 4.

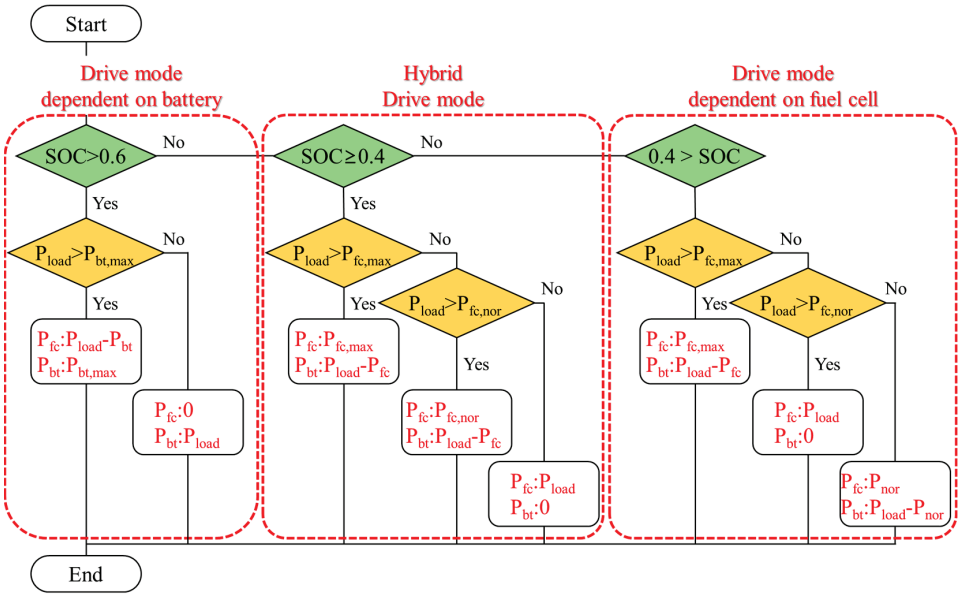

Figure 4. Flow cart of rule-based control PMS.

In the battery-dominant drive mode, which is activated when the SoC exceeds 0.6, the traction power is supplied primarily by the battery, utilizing its maximum power capability. When the SoC is within the intermediate range (0.4–0.6), the system transitions into the hybrid drive mode, in which both the fuel cell and battery contribute to power delivery. In this mode, the fuel cell stack operates near its rated power to supply the base load, while additional power requirements are met by the battery. Finally, when the SoC drops below 0.4, the system enters the fuel-cell-dominant mode, where the fuel cell becomes the primary power source. Under light-load conditions in this mode, the fuel cell not only supports propulsion but also charges the battery to restore its SoC. In this study, the rule-based control logic was explicitly implemented using a conditional if–then structure to ensure transparency and reproducibility.

(1) When the battery SoC exceeds 0.6, the fuel cell output power is restricted to its minimum operating level, and the traction power demand is mainly supplied by the battery.
(2) For intermediate SoC values ($0.4 \leq SoC \leq 0.6$), the fuel cell operates at a predefined base power level to cover the nominal load, while additional power demand is supplemented by the battery, resulting in hybrid operation.
(3) When the SoC falls below 0.4, battery discharge is limited and the fuel cell is assigned as the primary power source to meet the traction demand; under low-load conditions, surplus fuel cell power is utilized to recharge the battery.

These control rules were consistently applied throughout all simulations, ensuring deterministic behavior and reproducibility of the rule-based PMS.

https://doi.org/10.3390/batteries12020065

2.5.2. State Machine Control PMS

State machine control is a supervisory control approach that governs system operation by defining discrete operating states and the conditions under which transitions between them occur. The framework typically consists of four key elements: state, event, transition, and action. Here, a state represents a specific operating condition of the system, while an event acts as a trigger that may initiate a state change. A transition occurs when predefined logical conditions are satisfied in response to an event, leading to an action, which refers to the control operation executed after entering the new state.

In this study, the battery's SoC was divided into three operating states: Low, Medium, and High. Simultaneously, the traction power demand was segmented into five discrete levels, from $P_{\mathrm{Load},1}$ to $P_{\mathrm{Load},5}$. Based on the combination of these state definitions, the output power of the fuel cell stack was determined with the control logic summarized in Table 3. When the system operates in the Low-SoC state, the controller increases fuel cell power output relative to the load level to compensate for insufficient battery contribution and to initiate recharging. In contrast, during the High-SoC state, the fuel cell output is deliberately reduced, shifting a larger share of the power supply responsibility to the battery and thereby minimizing fuel cell operation. The Medium-SoC state serves as an intermediate condition, where power distribution is dynamically adjusted with real-time load demand and system operating conditions. In the implemented state machine control PMS, the operating logic was explicitly defined by the combination of discrete battery SoC states and load power levels. The battery SoC was classified into three states (Low, Medium, and High), while the traction load power was discretized into five predefined levels. Each unique combination of SoC state and load level corresponds to a specific operating state, in which the fuel cell output power is deterministically assigned according to the predefined state table. State transitions occur when either the SoC crosses its threshold values or the load power moves between adjacent load regions, ensuring predictable and structured control behavior. Through this formulation, the state machine controller provides transparent control logic and guarantees reproducible power allocation across all simulation scenarios.

Table 3. State machine control state.

State	SoC [-]	Load Power [kW]	Fuel Cell Power [kW]
1	Low	$P_{load} > P_{Load,1}$	$P_{load} + P_8$
2	Low	$P_{load} > P_{Load,2}$	$P_{load} + P_6$
3	Low	$P_{load} > P_{Load,3}$	P_{load}
4	Low	$P_{load} > P_{Load,4}$	$P_{load} - P_1$
5	Low	$P_{load} > P_{Load,5}$	$P_{load} - P_2$
6	Medium	$P_{load} > P_{Load,1}$	P_{load}
7	Medium	$P_{load} > P_{Load,2}$	P_{load}
8	Medium	$P_{load} > P_{Load,3}$	$P_{load} - P_6$
9	Medium	$P_{load} > P_{Load,4}$	$P_{load} - P_7$
10	Medium	$P_{load} > P_{Load,5}$	$P_{load} - P_8$
11	High	$P_{load} > P_{Load,1}$	P_{load}
12	High	$P_{load} > P_{Load,2}$	P_{load}
13	High	$P_{load} > P_{Load,3}$	$P_{load} - P_8$
14	High	$P_{load} > P_{Load,4}$	$P_{load} - P_9$
15	High	$P_{load} > P_{Load,5}$	$P_{load} - P_{10}$

https://doi.org/10.3390/batteries12020065

2.5.3. Fuzzy Logic Control PMS

Fuzzy logic control (FLC) is an intelligent control technique that utilizes fuzzy set theory to provide flexible and robust control, enabling various implementation approaches such as manual tuning, self-learning, and adaptive fuzzy schemes. In this study, the Mamdani-type fuzzy inference model was selected due to its intuitive rule-based structure, simplicity, and broad applicability in complex dynamic systems [83–85]. The FLC design consists of three main stages. In the fuzzification stage, crisp input variables are transformed into fuzzy sets through membership function evaluation. The inference stage then applies a series of fuzzy rules to derive control decisions based on predefined linguistic conditions. Finally, the defuzzification stage converts the fuzzy outputs into a precise control signal suitable for system actuation.

As shown in Figure 5, the controller was implemented with two input variables, battery SoC and system load power, and one output variable: the fuel cell stack power. Figure 5a–c illustrate the membership functions for SoC, load power, and fuel cell power output, respectively, while Figure 5d presents the resulting fuzzy rule surface. The SoC variable was divided into five linguistic categories: VL (Very Low), L (Low), M (Medium), H (High), and VH (Very High). System load power was described using seven categories: Off, VS (Very Small), S (Small), M (Medium), L (Large), VL (Very Large), and Max. The fuel cell output was further segmented into nine membership levels, ranging from idle operation to full power.

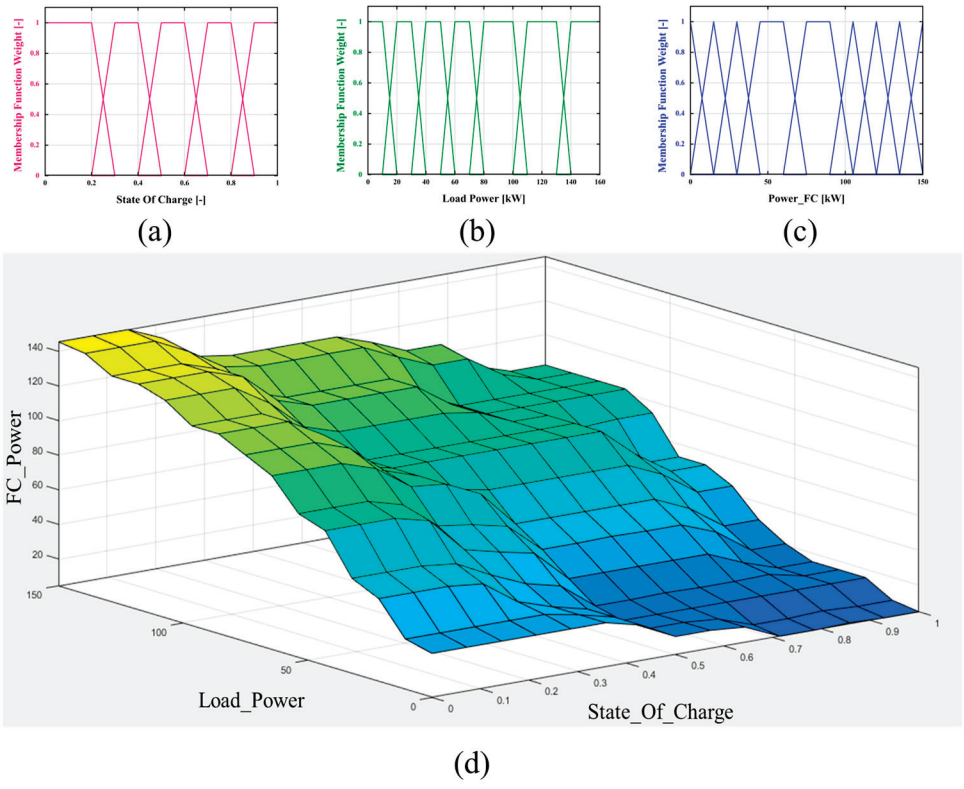

Figure 5. Fuzzy logic control. (**a**) membership function of SoC; (**b**) membership function of load power; (**c**) membership function of fuel cell power; (**d**) 3d graph of fuzzy logic control.

Because the durability and lifetime of fuel cells are highly sensitive to operational dynamics, particularly frequent start-stop cycles, rapid power fluctuations, and extended high-power operation, the membership functions for fuel cell power were carefully designed to ensure smooth power transitions. To further clarify the implementation of the fuzzy logic controller, representative fuzzy rules are summarized as follows. When the battery SoC is Very Low (VL) and the load power is Large or Very Large, the fuel cell output

https://doi.org/10.3390/batteries12020065

is set to a High or Very High level to ensure sufficient traction power while preventing excessive battery discharge. When the SoC is Medium and the load power is Medium, the fuel cell operates at a Medium power level, resulting in balanced hybrid operation between the fuel cell and battery. In contrast, when the SoC is High or Very High and the load power is Small, the fuel cell output is reduced to a Low level, allowing the battery to supply a larger portion of the traction demand. These fuzzy rules collectively enable continuous and nonlinear power allocation, avoiding abrupt switching behavior and ensuring smooth fuel cell power trajectories across varying load and SoC conditions. By preventing abrupt output changes, the fuzzy controller minimizes degradation mechanisms and significantly improves the long-term stability of the fuel cell system [86].

3. Results and Discussion

The performance of the proposed hydrogen electric truck model was assessed using an identical driving cycle designed to reflect representative Korean road gradients and real-world driving patterns. For each power management strategy, power distribution between the fuel cell and battery was determined with the corresponding control logic. The resulting system behavior was then comparatively evaluated across key performance indicators, including battery SoC variation, hydrogen consumption, temperature overshoot characteristics, and parasitic energy demand.

3.1. Simulation Scenario

To evaluate the performance of the proposed PMS strategies, a representative driving cycle was designed based on road gradient data from previous studies conducted in Korea, as shown in Figure 6 [87,88]. The vehicle's speed profile spans a range of 0–80 km/h, incorporating an acceleration period of approximately 1600 s followed by a deceleration phase lasting 900 s. Throughout the driving cycle, the vehicle maintains an average velocity of about 58.7 km/h. Additionally, a steady-speed segment was included between 6800 and 8200 s, during which the vehicle operates at a constant 70 km/h. This portion of the test cycle was specifically designed to investigate the influence of road gradients on traction power demand. Incline variations of −3°, 0°, and +3° were introduced to examine power fluctuation and system response under different slope conditions.

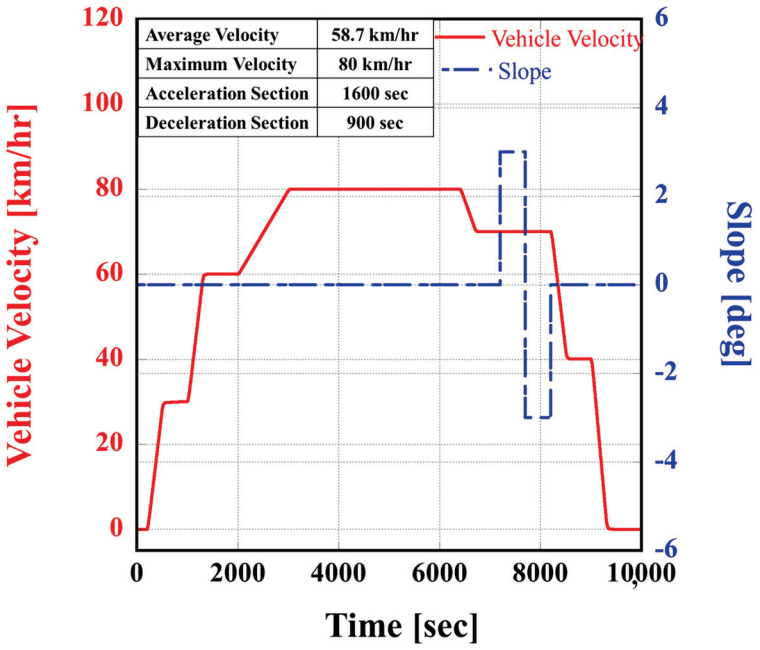

Figure 6. Korean road driving cycle of a truck.

https://doi.org/10.3390/batteries12020065

3.2. Vehicle Performance

The dynamic performance of the hydrogen electric truck under the designed Korean driving cycle is presented in Figure 7. As illustrated, the vehicle closely follows the prescribed speed and road gradient profiles, demonstrating reliable speed-tracking capability throughout the simulation. Minor deviations occur during transitions in the target velocity profile, with the maximum speed error of approximately 0.3 km/h observed near 200 s in the initial acceleration phase. This deviation results from the rapid increase in motor and gearbox torque required to overcome the vehicle's inertial resistance when accelerating from rest.

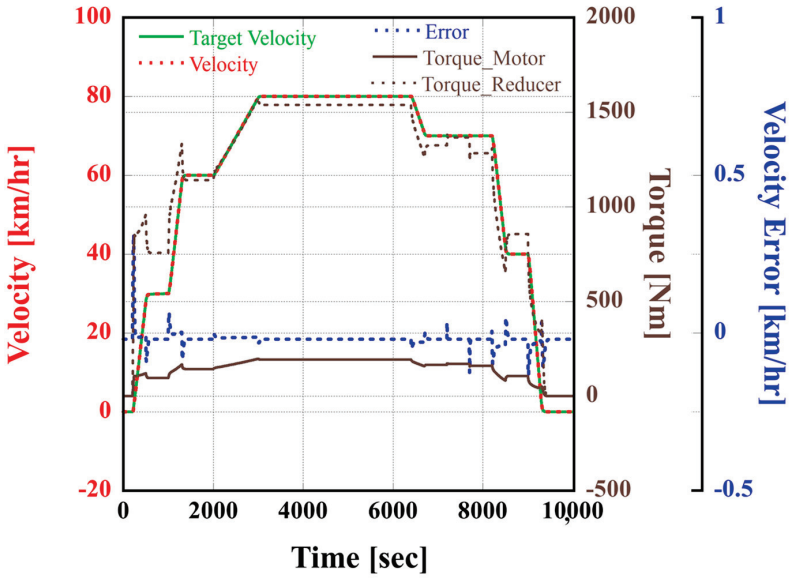

Figure 7. Vehicle velocity data with target velocity & error, torque data of motor & reducer.

During both the start-up phase and subsequent speed transitions, the control system actively modulates torque to minimize tracking error. Once steady-state operation is achieved, torque demand stabilizes under constant-speed conditions. Notably, within the 6800–8200 s interval, which corresponds to sustained operation at 70 km/h, a noticeable rise in torque demand occurs between 7200 and 7700 s due to the uphill segment. Conversely, as the vehicle transitions to a downhill slope from 7700 to 8200 s, the required torque decreases because the gravitational component assists vehicle propulsion.

Vehicle transitions to a downhill slope from 7700 to 8200 s, the required torque decreases because the gravitational component assists vehicle propulsion.

3.3. Power Management System Comparison

The PMS plays a crucial role in determining both the energy efficiency and operational stability of a hydrogen electric truck. Therefore, this study performed a comparative evaluation of system performance under identical initial SoC and driving conditions, with a particular emphasis on assessing the influence of different PMS approaches.

3.3.1. Result of Rule-Based Control PMS

Figure 8 presents the power distribution profile and the evolution of battery SoC under the rule-based control PMS strategy. At the beginning of the driving cycle, the vehicle operates exclusively on battery power since the traction demand is relatively low, and the fuel cell remains inactive. As the load gradually increases, the fuel cell is activated at around 500 s and assumes the role of the primary power source, while the battery supplements the system by compensating for transient power deficits, enabling hybrid operation. Once the

https://doi.org/10.3390/batteries12020065

SoC falls below 0.4 at approximately 5700 s, the battery ceases to discharge, and the fuel cell becomes the sole source of traction power under high-load conditions. As the power demand decreases later in the cycle, the fuel cell not only continues to meet a portion of the propulsion requirements but also contributes to recharging the battery. Over time, the SoC recovers to a stable level, and the system reaches a steady operating state. The simulation results demonstrate that the rule-based control PMS maintains a relatively stable power-sharing behavior by adjusting the power contribution from the fuel cell and battery with predefined control logic. However, fluctuations in load demand and SoC occasionally led to abrupt variations in the power output of both energy sources, highlighting a limitation of the rule-based control approach.

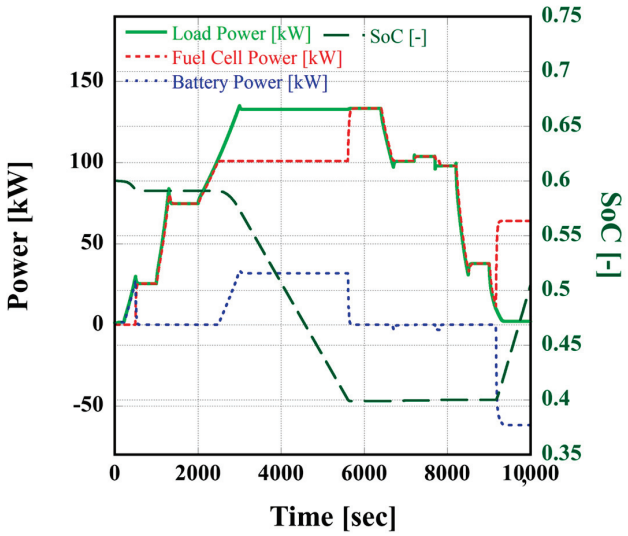

Figure 8. Power distribution with rule-based control PMS.

3.3.2. Result of State Machine Control PMS

Figure 9 illustrates the operational characteristics of the power management system governed by state machine control, where operating modes are determined by the combination of battery SoC and load power conditions. During the initial 1000 s of the driving cycle, the SoC remains within the medium range and the power demand is relatively low, resulting in fuel cell–only operation (State 5). As the load gradually increases, the control logic transitions the system into hybrid operation modes (States 8 and 9), where both the fuel cell and battery contribute to power delivery.

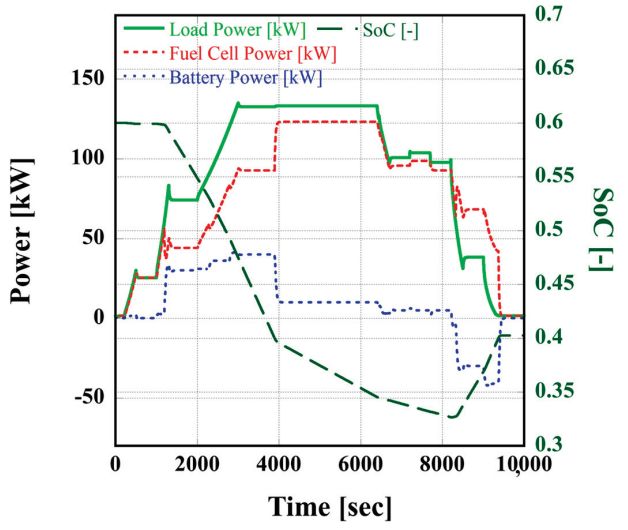

Figure 9. Power distribution with state machine control PMS.

https://doi.org/10.3390/batteries12020065

Beyond approximately 4000 s, the battery SoC drops below 0.4, limiting the battery's contribution and causing the fuel cell to supply most of the propulsion power under high-demand conditions (State 4). After 8200 s, during the reduced-load phase, the fuel cell continues to operate at elevated output levels to facilitate battery recharging (States 1 and 2). Because the state machine framework operates according to explicitly defined conditions and state transitions, it offers predictable and structured system behavior. However, one drawback of this approach is the occurrence of sudden power fluctuations during state changes, which can reduce control flexibility when responding to rapidly varying load conditions.

3.3.3. Result of Fuzzy Logic Control PMS

Figure 10 shows the power management behavior of the FLC strategy, where fuel cell output is determined through fuzzy inference using the membership functions of battery SoC and load power. At the beginning of the driving cycle, when the SoC is around 0.6, the system primarily falls within the Medium and Low membership regions. During this stage, the fuel cell operates under low-load conditions to support battery charging. As the load demand increases and the SoC gradually decreases between 3000 and 6500 s, the control system transitions into the Medium operating region, resulting in hybrid operation with both the fuel cell and battery supplying power. Under conditions classified as Very Large load, the battery delivers a greater share of the total power demand to support peak loads. After 8000 s, as the load decreases while the SoC remains low, the fuel cell once again ramps up its power output to recharge the battery. The fuzzy logic control PMS exhibits nonlinear and continuous control characteristics, allowing adaptive adjustment of fuel cell output in response to dynamic changes in SoC and load. This continuous control behavior reduces abrupt load fluctuations on the fuel cell, thereby minimizing parasitic energy losses and mitigating transient response effects across the system.

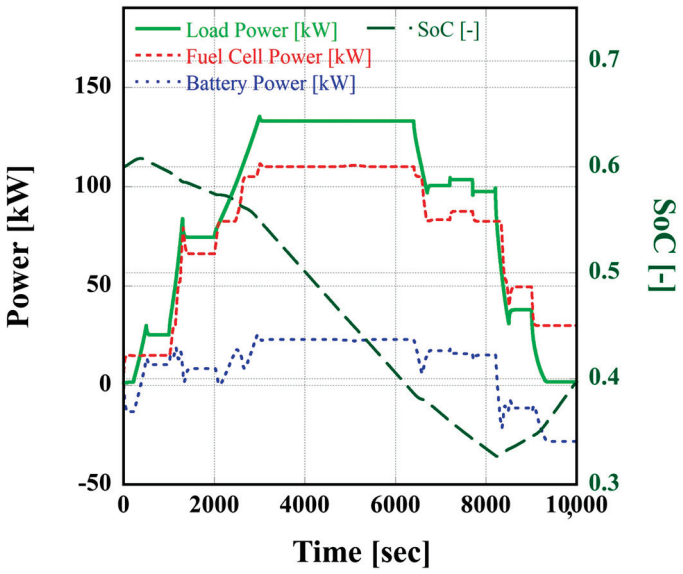

Figure 10. Power distribution with fuzzy logic control PMS.

3.4. Thermal Management System Comparison

Depending on the power required from the fuel cell, the corresponding heat generation varies depending on the applied PMS of the hydrogen electric truck. However, to prevent performance degradation, such as material damage, electrolyte dehydration, and thermal deformation, the operating temperature of the fuel cell stack is typically maintained within the range of 333.15 K to 353.15 K [89–92]. Accordingly, in this study, the inlet and outlet

https://doi.org/10.3390/batteries12020065

temperatures of the fuel cell coolant were controlled to 333.15 K and 343.15 K, respectively. The resulting temperature profiles under each PMS are shown in Figure 11. In the rule-based control and state machine control cases, the fuel cell experienced abrupt high-power operation at approximately 5800 s and 4000 s, respectively. In contrast, the fuzzy logic control strategy mitigated such high load operation by effectively utilizing the battery as an auxiliary power source during the 3000–6400 s interval, thereby distributing the fuel cell load and preventing thermal stress on the stack.

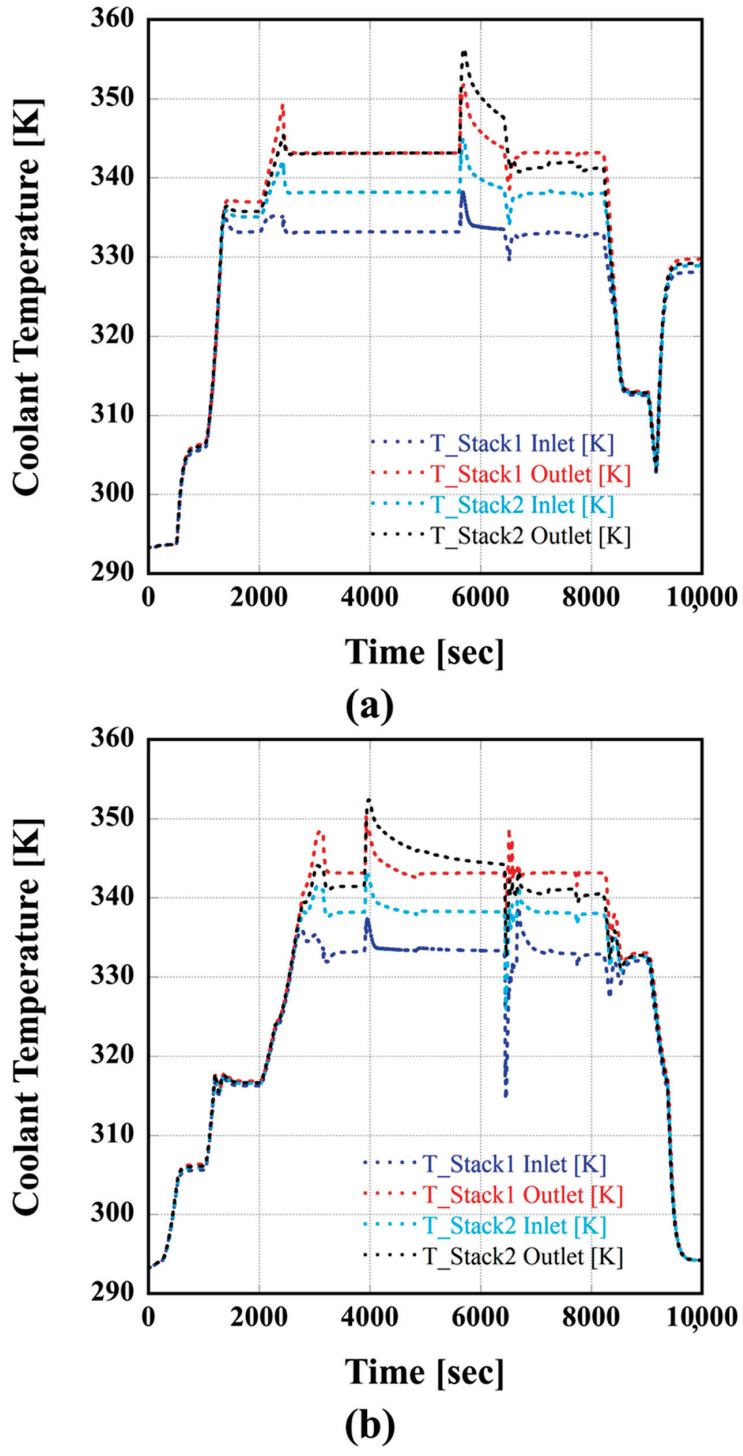

Figure 11. *Cont.*

https://doi.org/10.3390/batteries12020065

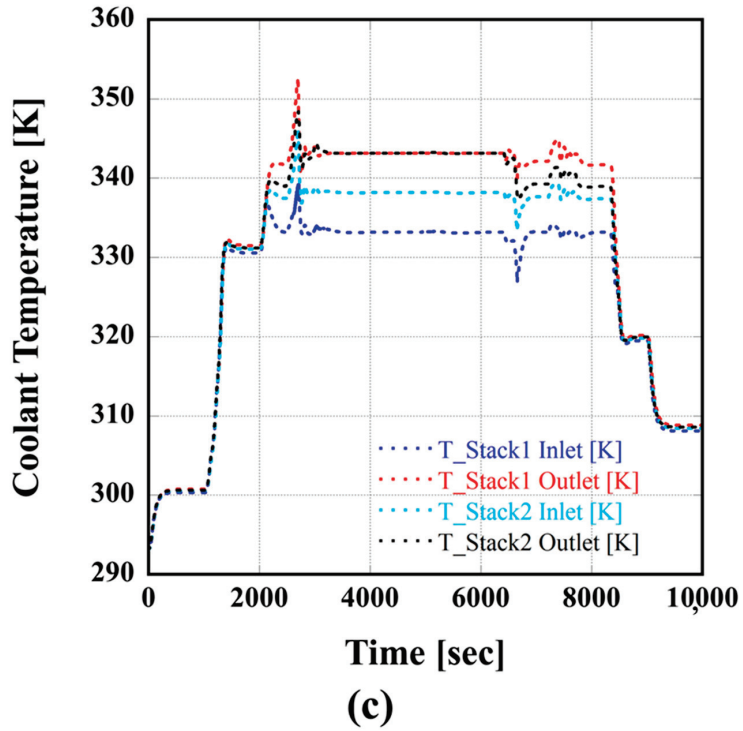

Figure 11. Result of coolant temperature. (**a**) rule-based control PMS, (**b**) state machine control PMS, (**c**) fuzzy logic control PMS.

To quantitatively evaluate temperature regulation performance across different PMS strategies, temperature overshoot was calculated as defined in Equation (20).

$$Overshoot = \left(\frac{T_{Max} - T_{Target}}{T_{Target}} \right) \times 100 \quad (20)$$

The calculated temperature overshoot at the inlet of Stack 1 was 1.51% under the rule-based control PMS, 1.71% under state machine control, and 1.22% when using fuzzy logic control. At the outlet of Stack 2, the corresponding overshoot values were 3.84%, 2.69%, and 1.49%, respectively. These results demonstrate that the fuzzy logic control significantly reduced temperature fluctuations compared with the other control methods, achieving up to 28.65% lower overshoot at the Stack 1 inlet and as much as 61.20% reduction at the Stack 2 outlet. The superior thermal management performance of the fuzzy logic–based PMS is primarily attributed to its ability to mitigate rapid variations in fuel cell load, thereby suppressing abrupt changes in heat generation. Since the heat generation of the fuel cell stack is directly coupled with variations in output power and current, stepwise changes in fuel cell output—such as those observed in the rule-based and state machine–based PMSs—can lead to pronounced temperature overshoot due to the inherent response delay of the cooling system. In contrast, the fuzzy logic–based PMS processes the battery SoC and traction load power as continuous fuzzy sets, enabling gradual and nonlinear modulation of the fuel cell output power. This allows the battery to be actively utilized as an auxiliary power source under high-load conditions, limiting sudden increases in fuel cell output and maintaining the cooling system within a more stable operating range. As a result, the temperature overshoot is effectively reduced. Such improvements in temperature stability can mitigate the occurrence of local hotspots and repetitive thermal stress, which are known to accelerate catalyst degradation, membrane–electrode assembly (MEA) damage, and long-term performance degradation of fuel cell stacks. From this perspective, the enhanced thermal stability achieved by the fuzzy logic–based PMS suggests a positive potential

https://doi.org/10.3390/batteries12020065

impact not only on short-term thermal management performance but also on the long-term reliability and durability of the fuel cell system [93]. The enhanced thermal performance is primarily due to the fuzzy controller's capability to smooth out rapid load transitions through gradual and adaptive power allocation. This mitigates sudden temperature spikes within the stack, thereby improving thermal stability and overall system reliability. Beyond short-term thermal stability, temperature regulation is closely related to the long-term durability of PEMFC stacks. Previous experimental studies have demonstrated that temperature fluctuations and local thermal non-uniformity accelerate catalyst degradation, membrane mechanical stress, and overall performance decay [94]. From this perspective, the reduced temperature overshoot and enhanced thermal stability achieved by the fuzzy-logic-based PMS in this study are expected to mitigate thermally induced degradation mechanisms. Although the present model assumes a spatially uniform stack temperature, the observed improvement in thermal stability indicates a favorable operating condition for long-term fuel cell reliability.

3.5. Hydrogen Consumption

The hydrogen consumption of a PEMFC system is directly related to the load current supplied to the stack, and its relationship can be described by the current-based formulation shown below.

$$Consumption_{H_2} = \int \frac{i}{nF} \times stoi \times n_{cell} \times M \tag{21}$$

where the hydrogen consumption is obtained by time integration of the hydrogen molar flow rate over time t. In addition, $Consumption_{H_2}$ represents the total hydrogen consumption, n_{cell} is the number of fuel cell in the stack, and M is the molar mass of hydrogen. The calculation results are presented in Table 4. Consequently, the higher power demand supplied by the fuel cell under the rule-based and state machine strategies led to increased hydrogen consumption relative to the fuzzy logic approach. The fuzzy logic controller achieved reductions of approximately 3.08% and 0.89% in hydrogen usage compared with the rule-based and state machine controls, respectively. This enhanced performance is mainly due to the optimized fuzzification process, which enables smoother power regulation and minimizes high-load operation and rapid power fluctuations in the fuel cell stack.

Table 4. Hydrogen consumption with PMS.

	Rule-Based Control PMS	State Machine Control PMS	Fuzzy Logic Control PMS
Hydrogen Consumption [kg]	17.1689	16.7903	16.6408

3.6. Parasitic Power

Stable power generation in a fuel cell system requires the reliable operation of BoP components, including the air compressor for oxidant supply as well as the coolant pump and cooling fan for thermal regulation. However, a portion of the power produced by the fuel cell is inevitably consumed by these auxiliary devices, known as parasitic power, which reduces the net output available for propulsion and external loads. Thus, minimizing BoP-related power consumption is a key consideration for enhancing overall system efficiency.

In this study, the parasitic power consumption of BoP components—namely the air compressor, coolant pump, and cooling fan—was quantitatively compared over time under three different power management strategies, and the results are summarized in Table 5 As shown in the table, the air compressor accountss for the largest share of total parasitic power consumption under all operating conditions, followed by the coolant pump and

https://doi.org/10.3390/batteries12020065

the cooling fan. For the rule-based control PMS, the parasitic power consumption of the air compressor and coolant pump increases steadily with operating time. This behavior is mainly attributed to the stepwise variations in fuel cell load, which induce abrupt changes in the required air flow rate and coolant flow rate. In particular, as the system enters high-load operating regions, the compressor power consumption increases significantly and becomes the dominant contributor to the overall parasitic power. In the state machine–based PMS, the increase in parasitic power is partially mitigated during certain operating intervals; however, relatively high power consumption of the air compressor and coolant pump is still observed due to output variations associated with state transitions. In contrast, the fuzzy logic–based PMS maintains the lowest power consumption of the air compressor and coolant pump under identical operating conditions, while variations in cooling fan power remain comparatively limited. These results indicate that the fuzzy logic–based PMS effectively reduces parasitic power consumption of key BoP components, particularly the air compressor and coolant pump. As a result, the total parasitic power consumption is reduced by 7.12% compared with the rule-based PMS and by 3.32% relative to the state machine–based PMS.

Table 5. Parasitic energy consumption of BoP components under different power management system.

Time [sec]	Rule-Based Control PMS			State Machine Control PMS			Fuzzy Logic Control PMS		
	Cooling Fan [kJ]	Coolant Pump [kJ]	Compressor [kJ]	Cooling Fan [kJ]	Coolant Pump [kJ]	Compressor [kJ]	Cooling Fan [kJ]	Coolant Pump [kJ]	Compressor [kJ]
2000	3.12	5.35	1333.50	2.79	5.45	949.83	2.79	5.43	1179.37
4000	7.61	11.17	4402.93	5.53	11.08	3464.57	7.46	15.27	4358.94
6000	12.96	19.00	7809.13	13.65	47.56	7473.48	14.24	34.89	7876.31
8000	20.84	51.39	11,337.96	102.36	86.68	10,757.89	19.20	47.18	10,754.21
10,000	25.26	59.10	13,042.95	106.86	94.16	12,409.59	23.17	52.53	12,116.30

3.7. Discussion

Although the performance of each PMS was individually assessed in terms of SoC regulation, thermal management effectiveness, hydrogen consumption, and parasitic power losses, such an approach is insufficient to determine the most suitable strategy from a holistic perspective. To address this limitation, the TOPSIS method, which is widely used in multi-criteria decision making, was employed. The method ranks each alternative based on its closeness to the Positive Ideal Solution (PIS), which represents the best achievable performance for each criterion, and its distance from the Negative Ideal Solution (NIS), which corresponds to the worst performance.

(1) Decision Matrix Construction: A decision matrix is formulated by compiling performance data for each power management strategy based on the selected evaluation criteria.

(2) Normalization: Each element of the matrix is normalized by dividing it by the vector norm of its respective column to eliminate the influence of units and ensure comparability across criteria.

$$r_{ij} = \frac{x_{ij}}{\sqrt{\sum_{i=1}^{m} x_{ij}^2}} \tag{22}$$

(3) Weight Assignment: The weights of the evaluation criteria were objectively determined using a standard deviation–based weighting method, assuming that criteria with larger variability among PMS strategies have greater influence on the decision-making process.

https://doi.org/10.3390/batteries12020065

(4) PIS/NIS Determination: For each performance indicator, the Positive Ideal Solution (PIS) and Negative Ideal Solution (NIS) are identified, corresponding to the best and worst attainable values, respectively.
(5) Distance and Closeness Coefficient Calculation: The Euclidean distances between each alternative and the PIS/NIS are computed, and the closeness coefficient is derived to rank the alternatives based on their overall performance.

$$S_i^+ = \sqrt{\sum_{j=1}^{n} \left(v_{ij} - v_j^+ \right)^2} \tag{23}$$

$$S_i^- = \sqrt{\sum_{j=1}^{n} \left(v_{ij} - v_j^- \right)^2} \tag{24}$$

$$C_i = \frac{S_i^-}{S_i^+ - S_i^-} \tag{25}$$

In the first step of the analysis, a decision matrix was formulated using multiple performance indicators, such as SoC, thermal regulation effectiveness, hydrogen consumption, and parasitic power usage, as shown below.

$$X = \begin{bmatrix} 0.5 & 1.51 & 3.84 & 17.17 & 13,127.31 \\ 0.4 & 1.71 & 2.69 & 16.79 & 12,610.61 \\ 0.4 & 1.22 & 1.49 & 16.64 & 12,192.01 \end{bmatrix} \tag{26}$$

In the next step, the decision matrix was transformed into a normalized form with Equation (26) to eliminate the influence of differing units among the criteria and enable direct comparison across all performance indicators.

$$R = \begin{bmatrix} 0.6657 & 0.5837 & 0.7806 & 0.5876 & 0.5992 \\ 0.5309 & 0.6610 & 0.5468 & 0.5747 & 0.5756 \\ 0.5244 & 0.4716 & 0.3029 & 0.5696 & 0.5565 \end{bmatrix} \tag{27}$$

The weighting factors for the normalized matrix were assigned by considering the variability of each criterion, under the assumption that indicators exhibiting larger fluctuations exert a greater influence on the decision-making process. Consequently, the weights were derived from the standard deviation values of the evaluation criteria. This method assigns higher weights to criteria exhibiting larger performance variations among the PMS strategies, thereby reflecting their greater discriminatory power in the multi-criteria decision-making process. By avoiding subjective judgment or expert scoring, the adopted weighting approach enhances the transparency, objectivity, and reproducibility of the TOPSIS analysis.

$$\omega = [0.1794 \quad 0.2142 \quad 0.5373 \quad 0.0210 \quad 0.0481] \tag{28}$$

By applying the calculated weights to the normalized matrix, the Euclidean distances to both the PIS and NIS were derived, and the corresponding closeness coefficients were obtained, as summarized in Table 6. The analysis revealed that the fuzzy logic control strategy achieved the highest closeness coefficient, indicating superior overall performance. The state machine control and rule-based control strategies followed, ranking second and third, respectively.

https://doi.org/10.3390/batteries12020065

Table 6. Closeness coefficient of PMS with TOPSIS analysis.

	Rule-Based Control PMS	**State Machine Control PMS**	**Fuzzy Logic Control PMS**
Distance to Ideal Solution (S^+)	0.2578	0.1393	0.0253
Distance to Negative Ideal Solution (S^-)	0.0303	0.1256	0.2599
Closeness Coefficient (C)	0.1051	0.4741	0.9112

4. Conclusions

In this study, a hydrogen electric truck equipped with a multi-stack fuel cell system was modeled and analyzed under different power management strategies. Three types of PMS approaches—rule-based control, state machine control, and fuzzy logic control—were developed and evaluated with respect to vehicle dynamics and driving conditions, including road gradient variations. The key findings can be summarized as follows:

(1) A dual 90 kW fuel cell configuration was implemented alongside essential BoP subsystems, including hydrogen and air supply units, a thermal management circuit, and auxiliary components such as a high-voltage battery, DC/DC converter, and drive motor model.

(2) For thermal regulation, a series-parallel cooling architecture integrating a distribution valve, coolant pump, three-way valve, radiator, and cooling fan was designed. PI controllers were applied to maintain target temperatures at each critical location.

(3) To manage power flow in the hybrid fuel cell–battery system, three PMS strategies were implemented: a rule-based method based on load demand and SoC, a state machine controller with discretized operational modes, and a fuzzy logic controller capable of adaptive load distribution via membership functions.

(4) The fuzzy logic PMS demonstrated the most effective load balancing by utilizing the battery as an auxiliary source during high-power demand periods, thereby alleviating sudden load transients on the fuel cell. As a result, hydrogen consumption decreased by 3.08% and 0.89% compared to rule-based and state machine control, respectively. Parasitic power consumption was reduced by 7.12% and 3.32%, and temperature overshoot was minimized by up to 61.20%.

(5) Finally, multi-criteria decision analysis using the TOPSIS method confirmed that the fuzzy logic strategy achieved the highest closeness coefficient (0.9112), demonstrating superior overall performance in terms of energy efficiency, thermal stability, and hydrogen utilization. The proposed PMS comparison and TOPSIS-based decision methodology provides a system-level evaluation method that may be extended to other PEMFC architectures, such as air-cooled systems, in future work, subject to dedicated modeling and experimental validation.

(6) In addition to improving instantaneous thermal performance, the enhanced temperature stability achieved by the fuzzy-logic-based PMS is expected to contribute positively to the long-term durability of PEMFC stacks by mitigating thermally induced degradation mechanisms, highlighting the importance of durability-aware thermal and power management strategies for next-generation hydrogen power systems.

https://doi.org/10.3390/batteries12020065

Author Contributions: S.Y.: Model design, Methodology, Software, Writing-original draft. J.H.: Supervision, Writing—review & editing. All authors have read and agreed to the published version of the manuscript.

Funding: This work was supported by the research grant of Kongju National University in 2025. And This work was supported by the Korea Institute of Energy Technology Evaluation and Planning (KETEP) and the Ministry of Trade, Industry & Energy (MOTIE) of the Republic of Korea (No. RS-2024-00394769).

Data Availability Statement: Dataset available on request from the authors.

Conflicts of Interest: The authors declared that there is no conflict of interest.

Nomenclature

A	Active area [cm^2]
F	Faraday constant [C/mol]
F	Force [N]
g_{ratio}	Gear Ratio [-]
I	Current [A]
m	Mass [kg]
n_{cell}	Number of cells [ea]
P	Power [kW]
p	Pressure [Pa]
Q	Heat Transfer [kW]
R	Ideal Gas Constant [J/K·mol]
r	Radius [m]
T	Temperature [K]
V	Voltage [V]

Subscripts and superscripts

act	Activation
con	Concentration
FC	Fuel cell
H_2	Hydrogen
H_2O	Water
O_2	Oxygen
ohmic	Ohmic

References

1. Available online: https://www.visualcapitalist.com/combustion-vehicle-sales-peak/ (accessed on 31 January 2026).
2. Available online: https://www.spglobal.com/mobility/en/research-analysis/2024-ev-forecast-the-supply-chain-charging-network-and-battery.html (accessed on 31 January 2026).
3. Available online: https://www.mckinsey.com/industries/automotive-and-assembly/our-insights/hydrogen-the-next-wave-for-electric-vehicles (accessed on 31 January 2026).
4. Yang, Q.; Zeng, T.; Zhang, C.; Zhou, W.; Xu, L.; Zhou, J.; Jiang, P.; Jiang, S. Modeling and simulation of vehicle integrated thermal management system for a fuel cell hybrid vehicle. *Energy Convers. Manag.* **2023**, *278*, 116745. [CrossRef]
5. de las Nieves Camacho, M.; Jurburg, D.; Tanco, M. Hydrogen fuel cell heavy-duty trucks: Review of main research topics. *Int. J. Hydrogen Energy* **2022**, *47*, 29505–29525. [CrossRef]
6. Bethoux, O. Hydrogen fuel cell road vehicles: State of the art and perspectives. *Energies* **2020**, *13*, 5843. [CrossRef]
7. Simmons, K.; Guezennec, Y.; Onori, S. Modeling and energy management control design for a fuel cell hybrid passenger bus. *J. Power Sources* **2014**, *246*, 736–746. [CrossRef]
8. Morrison, G.; Stevens, J.; Joseck, F. Relative economic competitiveness of light-duty battery electric and fuel cell electric vehicles. *Transp. Res. Part C Emerg. Technol.* **2018**, *87*, 183–196. [CrossRef]
9. Yun, S.; Yun, J.; Han, J. Development of a 470-Horsepower Fuel Cell–Battery Hybrid Xcient Dynamic Model Using Simscape™. *Energies* **2023**, *16*, 8092. [CrossRef]

https://doi.org/10.3390/batteries12020065

10. Xu, J.; Zhang, C.; Wan, Z.; Chen, X.; Chan, S.H.; Tu, Z. Progress and perspectives of integrated thermal management systems in PEM fuel cell vehicles: A review. *Renew. Sustain. Energy Rev.* **2022**, *155*, 111908. [CrossRef]
11. Meng, X.; Mei, J.; Tang, X.; Jiang, J.; Sun, C.; Song, K. The degradation prediction of proton exchange membrane fuel cell performance based on a transformer model. *Energies* **2024**, *17*, 3050. [CrossRef]
12. Wang, Y.; Chen, W.; Li, Q.; Han, Y.; Guo, A.; Wang, T. Coordinated optimal power distribution strategy based on maximum efficiency range of multi-stack fuel cell system for high altitude. *Int. J. Hydrogen Energy* **2024**, *50*, 374–387. [CrossRef]
13. Zhou, S.; Fan, L.; Zhang, G.; Gao, J.; Lu, Y.; Zhao, P.; Wen, C.; Shi, L.; Hu, Z. A review on proton exchange membrane multi-stack fuel cell systems: Architecture, performance, and power management. *Appl. Energy* **2022**, *310*, 118555. [CrossRef]
14. Ren, P.; Pei, P.; Fu, X.; Li, Y.; Chen, D.; Meng, Y.; Zhu, Z.; Song, X.; Zhang, L.; Wang, M. Diagnosis and mechanism analysis of startup-shutdown-induced fuel cell degradation in stack-level. *Energy Convers. Manag.* **2022**, *269*, 116140. [CrossRef]
15. Wu, P.; Partridge, J.; Bucknall, R. Cost-effective reinforcement learning energy management for plug-in hybrid fuel cell and battery ships. *Appl. Energy* **2020**, *275*, 115258. [CrossRef]
16. De-Troya, J.J.; Álvarez, C.; Fernández-Garrido, C.; Carral, L. Analysing the possibilities of using fuel cells in ships. *Int. J. Hydrogen Energy* **2016**, *41*, 2853–2866. [CrossRef]
17. Zhang, G.; Zhou, S.; Gao, J.; Fan, L.; Lu, Y. Stacks multi-objective allocation optimization for multi-stack fuel cell systems. *Appl. Energy* **2023**, *331*, 120370. [CrossRef]
18. Zhang, C.; Zeng, T.; Wu, Q.; Deng, C.; Chan, S.H.; Liu, Z. Improved efficiency maximization strategy for vehicular dual-stack fuel cell system considering load state of sub-stacks through predictive soft-loading. *Renew. Energy* **2021**, *179*, 929–944. [CrossRef]
19. Abuzant, S.; Jemei, S.; Hissel, D.; Boulon, L.; Agbossou, K.; Gustin, F. A review of multi-stack PEM fuel cell systems: Advantages, challenges and on-going applications in the industrial market. In *Proceedings of the 2017 IEEE Vehicle Power and Propulsion Conference (VPPC), Belfort, France, 11–14 December 2017*; IEEE: New York, NY, USA, 2017; pp. 1–6.
20. Han, X.; Li, F.; Zhang, T.; Zhang, T.; Song, K. Economic energy management strategy design and simulation for a dual-stack fuel cell electric vehicle. *Int. J. Hydrogen Energy* **2017**, *42*, 11584–11595. [CrossRef]
21. Dépature, C.; Boulon, L.; Sicard, P.; Fournier, M. Simulation model of a multi-stack fuel cell system. In *Proceedings of the 2013 15th European Conference on Power Electronics and Applications (EPE), Lille, France, 2–6 September 2013*; IEEE: New York, NY, USA, 2013; pp. 1–10.
22. Zhou, S.; Zhang, G.; Fan, L.; Gao, J.; Pei, F. Scenario-oriented stacks allocation optimization for multi-stack fuel cell systems. *Appl. Energy* **2022**, *308*, 118328. [CrossRef]
23. Marx, N.; Hissel, D.; Gustin, F.; Boulon, L.; Agbossou, K. On the sizing and energy management of an hybrid multistack fuel cell–Battery system for automotive applications. *Int. J. Hydrogen Energy* **2017**, *42*, 1518–1526. [CrossRef]
24. Plett, G.L. Extended Kalman filtering for battery management systems of LiPB-based HEV battery packs: Part 3. State and parameter estimation. *J. Power Sources* **2004**, *134*, 277–292. [CrossRef]
25. Hu, X.; Li, S.; Peng, H. A comparative study of equivalent circuit models for Li-ion batteries. *J. Power Sources* **2012**, *198*, 359–367. [CrossRef]
26. Hu, X.; Zou, C.; Zhang, C.; Li, Y. Technological developments in batteries: A survey of principal roles, types, and management needs. *IEEE Power Energy Mag.* **2017**, *15*, 20–31. [CrossRef]
27. Burke, A. Ultracapacitors: Why, how, and where is the technology. *J. Power Sources* **2000**, *91*, 37–50. [CrossRef]
28. Zhang, S.; Xiong, R.; Sun, F. Model predictive control for power management in a plug-in hybrid electric vehicle with a hybrid energy storage system. *Appl. Energy* **2017**, *185*, 1654–1662. [CrossRef]
29. Qiu, Y.; Zeng, T.; Zhang, C.; Wang, G.; Wang, Y.; Hu, Z.; Yan, M.; Wei, Z. Progress and challenges in multi-stack fuel cell system for high power applications: Architecture and energy management. *Green Energy Intell. Transp.* **2023**, *2*, 100068. [CrossRef]
30. Shen, W.; Fan, L.; Pan, Z.; Chen, C.; Wang, N.; Zhou, S. Comparison of different topologies of thermal management subsystems in multi-stack fuel cell systems. *Energies* **2022**, *15*, 5030. [CrossRef]
31. Gao, J.; Jiang, Y.; Zhou, S. Fault Diagnosis of Sensors for Multi-stack Fuel Cell Thermal Management Subsystem Based on UKF. *J. Electrotechnol. Electr. Eng. Manag.* **2024**, *7*, 33–41. [CrossRef]
32. Saygili, Y.; Eroglu, I.; Kincal, S. Model based temperature controller development for water cooled PEM fuel cell systems. *Int. J. Hydrogen Energy* **2015**, *40*, 615–622. [CrossRef]
33. Hu, P.; Cao, G.Y.; Zhu, X.J.; Hu, M. Coolant circuit modeling and temperature fuzzy control of proton exchange membrane fuel cells. *Int. J. Hydrogen Energy* **2010**, *35*, 9110–9123. [CrossRef]
34. Farhadi Gharibeh, H.; Farrokhifar, M. Online multi-level energy management strategy based on rule-based and optimization-based approaches for fuel cell hybrid electric vehicles. *Appl. Sci.* **2021**, *11*, 3849. [CrossRef]
35. Peng, H.; Li, J.; Thul, A.; Deng, K.; Ünlübayir, C.; Löwenstein, L.; Hameyer, K. A scalable, causal, adaptive rule-based energy management for fuel cell hybrid railway vehicles learned from results of dynamic programming. *Etransportation* **2020**, *4*, 100057. [CrossRef]

https://doi.org/10.3390/batteries12020065

36. Yuan, H.B.; Zou, W.J.; Jung, S.; Kim, Y.B. A real-time rule-based energy management strategy with multi-objective optimization for a fuel cell hybrid electric vehicle. *IEEE Access* **2022**, *10*, 102618–102628. [CrossRef]
37. Wang, Y.; Sun, Z.; Chen, Z. Energy management strategy for battery/supercapacitor/fuel cell hybrid source vehicles based on finite state machine. *Appl. Energy* **2019**, *254*, 113707.
38. Li, Q.; Yang, H.; Han, Y.; Li, M.; Chen, W. A state machine strategy based on droop control for an energy management system of PEMFC-battery-supercapacitor hybrid tramway. *Int. J. Hydrogen Energy* **2016**, *41*, 16148–16159.
39. Nivolianiti, E.; Karnavas, Y.L.; Charpentier, J.F. Fuzzy logic-based energy management strategy for hybrid fuel cell electric ship power and propulsion system. *J. Mar. Sci. Eng.* **2024**, *12*, 1813. [CrossRef]
40. Zhang, D.; Zhou, Y.; Liu, K.P.; Chen, Q.Q. A study on fuzzy control of energy management system in hybrid electric vehicle. In Proceedings of the 2009 Asia-Pacific Power and Energy Engineering Conference, Wuhan, China, 28–31 March 2009; pp. 1–4.
41. Sciarretta, A.; Back, M.; Guzzella, L. Optimal control of parallel hybrid electric vehicles. *IEEE Trans. Control. Syst. Technol.* **2004**, *12*, 352–363. [CrossRef]
42. Kirschbaum, F.; Back, M.; Hart, M. Determination of the fuel-optimal trajectory for a vehicle along a known route. *IFAC Proc.* **2002**, *35*, 235–239. [CrossRef]
43. Available online: https://ecv.hyundai.com/global/en/products/xcient-fuel-cell-truck-fcev (accessed on 31 May 2024).
44. Chen, F.Q.; Ren, X.D.; Hu, B.; Li, X.S.; Gu, C.W.; Jin, Z.J. Parametric analysis on multi-stage high pressure reducing valve for hydrogen decompression. *Int. J. Hydrogen Energy* **2019**, *44*, 31263–31274. [CrossRef]
45. Ye, X.; Zhang, T.; Chen, H.; Cao, J.; Chen, J. Fuzzy control of hydrogen pressure in fuel cell system. *Int. J. Hydrogen Energy* **2019**, *44*, 8460–8466. [CrossRef]
46. Yu, S.P.; Lai, M.W.; Chu, C.Y.; Huang, C.L.; Lin, C.Y.; Borzenko, V.I.; Dunikov, D.O.; Kazakov, A.N. Integration of low-pressure hydrogen storage cylinder and automatic controller for carbon deposit removal in car engine. *Int. J. Hydrogen Energy* **2016**, *41*, 21795–21801. [CrossRef]
47. Chen, F.Q.; Zhang, M.; Qian, J.Y.; Fei, Y.; Chen, L.L.; Jin, Z.J. Thermo-mechanical stress and fatigue damage analysis on multi-stage high pressure reducing valve. *Ann. Nucl. Energy* **2017**, *110*, 753–767.
48. Chen, F.Q.; Qian, J.Y.; Chen, M.R.; Zhang, M.; Chen, L.L.; Jin, Z.J. Turbulent compressible flow analysis on multi-stage high pressure reducing valve. *Flow Meas. Instrum.* **2018**, *61*, 26–37. [CrossRef]
49. Lee, Y.B.; Kim, C.H.; Ahn, S.Y.; Choi, Y.M.; Ahn, B.K.; Oh, J. Turbo Blower for 80 kW Proton Exchange Membrane Fuel Cell Vehicle. In Proceedings of the 5th WSEAS International Conference on Power Systems and Electromagnetic Compatibility, Corfu, Greece, 23–25 August 2005; p. 498-271.
50. Han, J.; Yu, S.; Sun, Y. Oxygen excess ratio control for proton exchange membrane fuel cell using model reference adaptive control. *Int. J. Hydrogen Energy* **2019**, *44*, 18425–18437. [CrossRef]
51. Gelfi, S.; Stefanopoulou, A.G.; Pukrushpan, J.T.; Peng, H. Dynamics of low-pressure and high-pressure fuel cell air supply systems. In *Proceedings of the 2003 American Control Conference, Denver, CO, USA, 4–6 June 2003*; IEEE: New York, NY, USA, 2003; Volume 3, pp. 2049–2054.
52. Han, J.; Han, J.; Yu, S. Investigation of FCVs durability under driving cycles using a model-based approach. *J. Energy Storage* **2020**, *27*, 101169. [CrossRef]
53. Fletcher, T.; Thring, R.; Watkinson, M. An Energy Management Strategy to concurrently optimise fuel consumption & PEM fuel cell lifetime in a hybrid vehicle. *Int. J. Hydrogen Energy* **2016**, *41*, 21503–21515. [CrossRef]
54. Bezmalinovic, D.; Simic, B.; Frano Barbir, F. Characterization of PEM fuel cell degradation by polarization change curves. *J. Power Sources* **2015**, *294*, 82–87. [CrossRef]
55. Chang, Y.; Liu, J.; Li, R.; Zhao, J.; Qin, Y.; Zhang, J.; Yin, Y.; Li, X. Effect of humidity and thermal cycling on the catalyst layer structural changes in polymer electrolyte membrane fuel cells. *Energy Convers. Manag.* **2019**, *189*, 24–32. [CrossRef]
56. Petrone, R.; Yeetsorn, R.; Harel, F.; Hissel, D.; Pera, M.C.; Breaz, E.; Giurgea, S. Accelerated stress tests oriented load profile for PEM Fuel Cells durability in automotive applications. In *Proceedings of the 2017 IEEE Vehicle Power and Propulsion Conference (VPPC), Belfort, France, 11–14 December 2017*; IEEE: New York, NY, USA, 2017; pp. 1–5.
57. Chen, H.; Song, Z.; Zhao, X.; Zhang, T.; Pei, P.; Liang, C. A review of durability test protocols of the proton exchange membrane fuel cells for vehicle. *Appl. Energy* **2018**, *224*, 289–299. [CrossRef]
58. Thiele, P.; Yang, Y.; Dirkes, S.; Wick, M.; Pischinger, S. Realistic accelerated stress tests for PEM fuel cells: Test procedure development based on standardized automotive driving cycles. *Int. J. Hydrogen Energy* **2024**, *52*, 1065–1080. [CrossRef]
59. Han, J.; Yu, S. Ram air compensation analysis of fuel cell vehicle cooling system under driving modes. *Appl. Therm. Eng.* **2018**, *142*, 530–542. [CrossRef]
60. Riascos, L.A.M.; Pereira, D.D. Controlling operating temperature in PEM fuel cells. In *Proceedings of the ABCM Symposium Series in Mechatronics, Gramado, RS, Brazil, 15–20 November 2009*; ABCM: Rio de Janeiro, Brazil; Volume 4, pp. 137–146.
61. Tawalbeh, M.; Alarab, S.; Al-Othman, A.; Javed, R.M.N. The operating parameters, structural composition, and fuel sustainability aspects of PEM fuel cells: A mini review. *Fuels* **2022**, *3*, 449–474. [CrossRef]

https://doi.org/10.3390/batteries12020065

62. Soupremanien, U.; Le Person, S.; Favre-Marinet, M.; Bultel, Y. Tools for designing the cooling system of a proton exchange membrane fuel cell. *Appl. Therm. Eng.* **2012**, *40*, 161–173. [CrossRef]
63. Sun, Z.; Chen, Z.; Wang, Y.; Yuan, H. PEM fuel cell thermal management strategy based on multi-model predictive control. In *Proceedings of the 2022 IEEE/IAS Industrial and Commercial Power System Asia (I&CPS Asia), Shanghai, China, 8–11 July 2022*; IEEE: New York, NY, USA, 2022; pp. 625–630.
64. Deng, B.; Zhang, X.; Yin, C.; Luo, Y.; Tang, H. Improving a fuel cell system's thermal management by optimizing thermal control with the particle swarm optimization algorithm and an artificial neural network. *Appl. Sci.* **2023**, *13*, 12895. [CrossRef]
65. Zhao, R.; Qin, D.; Chen, B.; Wang, T.; Wu, H. Thermal management of fuel cells based on diploid genetic algorithm and fuzzy PID. *Appl. Sci.* **2022**, *13*, 520. [CrossRef]
66. Sulaiman, N.; Hannan, M.A.; Mohamed, A.; Majlan, E.H.; Daud, W.W. A review on energy management system for fuel cell hybrid electric vehicle: Issues and challenges. *Renew. Sustain. Energy Rev.* **2015**, *52*, 802–814. [CrossRef]
67. Li, X.; Xu, L.; Hua, J.; Lin, X.; Li, J.; Ouyang, M. Power management strategy for vehicular-applied hybrid fuel cell/battery power system. *J. Power Sources* **2009**, *191*, 542–549. [CrossRef]
68. Li, C.-Y.; Liu, G.-P. Optimal fuzzy power control and management of fuel cell/battery hybrid vehicles. *J. Power Sources* **2009**, *192*, 525–533. [CrossRef]
69. Cai, J.; Zhong, Q.C.; Stone, D. A compact power converter for hybrid energy systems. In *Proceedings of the IECON 2014—40th Annual Conference of the IEEE Industrial Electronics Society, Dallas, TX, USA, 29 October–1 November 2014*; IEEE: New York, NY, USA, 2014; pp. 995–1000.
70. Reddy, K.J.; Natarajan, S. Energy sources and multi-input DC-DC converters used in hybrid electric vehicle applications—A review. *Int. J. Hydrogen Energy* **2018**, *43*, 17387–17408. [CrossRef]
71. Spanoudakis, P.; Moschopoulos, G.; Stefanoulis, T.; Sarantinoudis, N.; Papadokokolakis, E.; Ioannou, I.; Piperidis, S.; Doitsidis, L.; Tsourveloudis, N.C. Efficient gear ratio selection of a single-speed drivetrain for improved electric vehicle energy consumption. *Sustainability* **2020**, *12*, 9254. [CrossRef]
72. Peng, M.; Lin, J.; Liu, X. Optimizing design of powertrain transmission ratio of heavy duty truck. *IFAC-PapersOnLine* **2018**, *51*, 892–897. [CrossRef]
73. Fayaz, H.; Saidur, R.; Razali, N.; Anuar, F.S.; Saleman, A.R.; Islam, M.R. An overview of hydrogen as a vehicle fuel. *Renew. Sustain. Energy Rev.* **2012**, *16*, 5511–5528. [CrossRef]
74. Teng, T.; Zhang, X.; Dong, H.; Xue, Q. A comprehensive review of energy management optimization strategies for fuel cell passenger vehicle. *Int. J. Hydrogen Energy* **2020**, *45*, 20293–20303. [CrossRef]
75. Yue, M.; Jemei, S.; Gouriveau, R.; Zerhouni, N. Review on health-conscious energy management strategies for fuel cell hybrid electric vehicles: Degradation models and strategies. *Int. J. Hydrogen Energy* **2019**, *44*, 6844–6861. [CrossRef]
76. Lei, T.; Wang, Y.; Jin, X.; Min, Z.; Zhang, X.; Zhang, X. An optimal fuzzy logic-based energy management strategy for a fuel cell/battery hybrid power unmanned aerial vehicle. *Aerospace* **2022**, *9*, 115. [CrossRef]
77. Du, J.; Zhao, X.; Liu, X.; Liu, G.; Xiong, Y. A Fuzzy Logic Control-Based Approach for Real-Time Energy Management of the Fuel Cell Electrical Bus Considering the Durability of the Fuel Cell System. *World Electr. Veh. J.* **2024**, *15*, 92. [CrossRef]
78. Vivas, F.J.; Segura, F.; Andújar, J.M.; Palacio, A.; Saenz, J.L.; Isorna, F.; López, E. Multi-objective fuzzy logic-based energy management system for microgrids with battery and hydrogen energy storage system. *Electronics* **2020**, *9*, 1074.
79. Gao, D.; Jin, Z.; Lu, Q. Energy management strategy based on fuzzy logic for a fuel cell hybrid bus. *J. Power Sources* **2008**, *185*, 311–317. [CrossRef]
80. Liu, X.; Guo, H.; Du, J.; Zhao, X. A modified model-free-adaptive-control-based real-time energy management strategy for plug-in hybrid electric vehicle. *Energy Sci. Eng.* **2022**, *10*, 4007–4024. [CrossRef]
81. Wirasingha, S.G.; Emadi, A. Classification and review of control strategies for plug-in hybrid electric vehicles. *IEEE Trans. Veh. Technol.* **2010**, *60*, 111–122. [CrossRef]
82. Du, C.; Huang, S.; Jiang, Y.; Wu, D.; Li, Y. Optimization of energy management strategy for fuel cell hybrid electric vehicles based on dynamic programming. *Energies* **2022**, *15*, 4325. [CrossRef]
83. Lee, C.-C. Fuzzy logic in control systems: Fuzzy logic controller. I. *IEEE Trans. Syst. Man Cybern.* **1990**, *20*, 404–418.
84. Cordón, O. A historical review of evolutionary learning methods for Mamdani-type fuzzy rule-based systems: Designing interpretable genetic fuzzy systems. *Int. J. Approx. Reason.* **2011**, *52*, 894–913.
85. Sugeno, M.; Yasukawa, T. A fuzzy-logic-based approach to qualitative modeling. *IEEE Trans. Fuzzy Syst.* **1993**, *1*, 7. [CrossRef]
86. Ragab, A.; Marei, M.I.; Mokhtar, M. Comprehensive Study of Fuel Cell Hybrid Electric Vehicles: Classification, Topologies, and Control System Comparisons. *Appl. Sci.* **2023**, *13*, 13057. [CrossRef]
87. An, Y.; Lee, N.; Park, J.; Lee, J.; Kim, W.; Woo, N. Comparative analysis of road gradient measurement method. In Proceedings of the Korea Automotive Engineering Society Spring Conference, Gunsan, Republic of Korea, 12–14 August 2016.

https://doi.org/10.3390/batteries12020065

88. Kim, M.; Lee, J.; Lee, H. Development of Model Predictive Controller for Electrified Vehicles through System Identification Considering Road Slope. In Proceedings of the Korea Automotive Engineering Society Spring Conference, Busan, Republic of Korea, 2–4 June 2022.
89. Huang, Y.; Xiao, X.; Kang, H.; Lv, J.; Zeng, R.; Shen, J. Thermal management of polymer electrolyte membrane fuel cells: A critical review of heat transfer mechanisms, cooling approaches, and advanced cooling techniques analysis. *Energy Convers. Manag.* **2022**, *254*, 115221. [CrossRef]
90. Zhang, G.; Jiao, K. Multi-phase models for water and thermal management of proton exchange membrane fuel cell: A review. *J. Power Sources* **2018**, *391*, 120–133. [CrossRef]
91. Yan, Q.; Toghiani, H.; Causey, H. Steady state and dynamic performance of proton exchange membrane fuel cells (PEMFCs) under various operating conditions and load changes. *J. Power Sources* **2006**, *161*, 492–502. [CrossRef]
92. Bvumbe, T.J.; Bujlo, P.; Tolj, I.; Mouton, K.; Swart, G.; Pasupathi, S.; Pollet, B.G. Review on management, mechanisms and modelling of thermal processes in PEMFC. *Hydrog. Fuel Cells* **2016**, *1*, 1–20.
93. Song, K.; Hou, T.; Jiang, J.; Grigoriev, S.A.; Fan, F.; Qin, J.; Sun, C. Thermal management of liquid-cooled proton exchange membrane fuel cell: A review. *J. Power Sources* **2025**, *648*, 237227. [CrossRef]
94. Tang, X.; Yang, M.; Shi, L.; Hou, Z.; Xu, S.; Sun, C. Adaptive state-of-health temperature sensitivity characteristics for durability improvement of PEM fuel cells. *Chem. Eng. J.* **2024**, *491*, 151951. [CrossRef]

https://doi.org/10.3390/batteries12020065

batteries

MDPI

Article

Multi-Objective Optimization of CPCM–Liquid Cooling Hybrid Thermal Management Systems for Lithium-Ion Batteries via NSGA-II Optimized Artificial Neural Networks

Qianqian Xin [1,†], Xu Zhang [2,†], Tianqi Yang [3,*], Hengyun Zhang [4,*] and Jinsheng Xiao [3]

[1] School of Mechanical Engineering, Wuhan Vocational College of Software and Engineering, Wuhan 430205, China; qianqianxin@whvcse.edu.cn
[2] National Automobile Quality Supervision and Test Center, Xiangyang 441004, China; zhangxu@nast.com.cn
[3] State Key Laboratory of Light Superalloys, Wuhan University of Technology, Wuhan 430070, China; jinsheng.xiao@whut.edu.cn
[4] School of Mechanical and Automotive Engineering, Shanghai University of Engineering Science, Shanghai 201620, China
* Correspondence: tqyang@whut.edu.cn (T.Y.); zhanghengyun@sues.edu.cn (H.Z.)
† These authors contributed equally to this work.

Abstract

Considering the synergistic optimization design of battery thermal safety and system economy in extreme environments, a hybrid lithium-ion battery thermal management system (BTMS) employing composite phase change material (CPCM) with liquid cooling is proposed by comparing four BTMSs of pure air cooling, pure CPCM, pure liquid cooling, and the hybrid cooling using CPCM and liquid cooling. The proposed hybrid cooling system demonstrates the capability to maintain the maximum battery temperature at 45.27 °C under extreme operating conditions, including elevated ambient temperatures of 40 °C combined with 5C discharge rate. Notably, this thermal regulation performance is achieved without requiring additional power input, highlighting the energy-efficient design of the system. Further, to address the critical challenge of thermal runaway prevention under summer extreme temperature up to 50 °C, an artificial neural network (ANN) model is established for the hybrid cooling, integrated with the non-dominated sorting genetic algorithm II (NSGA-II) algorithm, leading to the maximum temperature controlled at 48.68 °C and minimum system power consumption of 158 W, achieving a 12.1% reduction in thermal fluctuation amplitude and a 5.9% reduction in power consumption compared to initial design and optimal solutions, respectively. The proposed BTMS introduces the NSGA-II-ANN model for multi-objective collaborative optimization to solve the contradiction between thermal safety and energy consumption under extreme working conditions, enhancing the safety measures of power batteries and economic viability for electric vehicles.

Keywords: lithium-ion battery; composite phase change material; liquid cooling; NSGA-II-ANN; thermal safety; energy consumption

1. Introduction

1.1. State-of-the-Art

Lithium-ion power batteries have emerged as the optimal choice for electric vehicle power sources due to their exceptional attributes, including high voltage, high energy density, long lifespan, low self-discharge rate, no memory effect, and green environmental

protection. However, the performance, lifespan, and safety of the batteries are sensitive to temperature during operation. The development of high-performance BTMS constitutes a critical technological imperative for ensuring operational stability and safety in lithium-ion battery applications. With the increasing complexity in driving conditions and growing demand for extended driving mileage in electric vehicles, achieving thermal management with reduced energy consumption and enhanced energy efficiency has become increasingly significant [1].

The cooling methods utilized in electric vehicles encompass active techniques: air cooling [2] and liquid cooling [3], as well as passive approaches: phase change materials (PCMs) [4] and heat pipes (HPs) [5], or a combination of multiple methods [6–9]. Air cooling is suitable for lower ambient temperatures and discharge rates, but unsuitable for high-temperature environments and conditions with high discharge rates [10–12]. Liquid cooling has been widely employed in the field of battery thermal management for electric vehicles. However, liquid cooling still encounters challenges such as temperature non-uniformity for extreme conditions like super-fast charging conditions with increased pump power, and the large number of mini-channels and their intricate dimension and distribution [13–15]. To address these aforementioned issues, PCM has emerged as one of the most promising solutions due to its simplistic structure, cost-effectiveness, exceptional cooling performance, and high latent heat capacity, which facilitates the absorption of a substantial amount of heat during the phase transition process, thereby maintaining the battery temperature in close proximity to the phase change temperature for an extended duration [4]. However, the low thermal conductivity of PCM poses a significant technical challenge, as it hampers the heat transfer rate within PCMs and diminishes their cooling capacity. When the PCM is fully melted, efficient dissipation of the absorbed heat to the surroundings becomes crucial, underscoring the imperative to enhance PCM thermal conductivity [16]. In addition, heat pipes (HPs) have also been considered in battery thermal management due to their excellent heat-transfer capabilities. However, there is still limited research on integrating HPs with liquid- or air-cooling systems specifically for cylindrical battery modules operating under extreme working conditions. Therefore, hybrid cooling systems combining active methods such as liquid cooling with passive methods like PCM are regarded as highly promising technologies for precise temperature control.

The hybrid thermal management system integrating PCM with liquid cooling has emerged as the most technically viable solution for lithium-ion battery modules, demonstrating superior temperature regulation capabilities compared to conventional single-mode cooling approaches. Current research directions focus on developing self-sealing PCM composites with shape-stabilized additives and modularized quick-connect interfaces to address the challenges related to PCM maintenance and battery replacement. In general, the hybrid cooling performance, achieved through CPCM with liquid cooling, is influenced by numerous factors related to both the thermophysical properties of PCM and the parameters of liquid cooling. However, a comprehensive analysis is lacking. Therefore, selecting an appropriate optimization method, qualitatively analyzing influencing factors, and designing an optimal structure are crucial for improving the lightweight design, economy, and safety of BTMS. As a multi-objective optimization technique inspired by biological evolutionary mechanisms, the non-dominated sorting genetic algorithm II (NSGA-II) demonstrates superior convergence efficiency and generates well-distributed Pareto-optimal solutions. This computational approach has proven particularly effective in addressing complex BTMS requiring simultaneous optimization of competing objectives. Jin et al. [17] employed a combined approach of an artificial neural network (ANN) surrogate model and non-dominated sorting genetic algorithm II (NSGA-II) for multi-objective optimization, aiming to achieve the optimal thermal performance of the battery model

https://doi.org/10.3390/batteries12030078

by considering structural parameters and inlet wind speed as variables. The optimized solution resulted in a reduction of 1.97 °C, 6.32 °C, and 2.82 Pa in maximum temperature, temperature difference, and pressure loss, respectively. Zuo et al. [18] proposed a multi-objective optimization approach for enhancing the heat transfer coefficient and reducing energy consumption of multi-channel cold plates under intermittent pulsating conditions by integrating response surface methodology (RSM) with NSGA-II. The amplitude and frequency of steady flow velocity pulsation were considered as independent variables, and the optimal parameter values were determined based on the Pareto optimal solution.

1.2. Novelty of the Present Work

Despite extensive research efforts on the BTMS under low-temperature conditions and moderate discharge regimes (typically below 3C), a critical knowledge gap persists in systematically evaluating multiphysics-coupled performance. Current investigations predominantly emphasize singular thermal metrics, while insufficient attention has been directed toward establishing multi-criteria evaluation frameworks that concurrently address the thermal equilibrium maintenance under extreme operating conditions (>5C discharge rate). This knowledge gap may impede the sustainable development of electric vehicles. In addition, numerous studies have confirmed the effective utilization of ANN for predicting the relationship between battery modules and various structural parameters.

Therefore, this study proposes a hybrid BTMS integrating CPCM and liquid cooling, designed to address the dual challenges of thermal safety and economic viability under extreme operating conditions. A comprehensive evaluation framework was implemented to analyze four distinct thermal management configurations: air-cooled system, CPCM module, liquid-cooled pipe system, and hybrid CPCM–liquid cooling integration under extreme temperature and different discharge rate conditions. Furthermore, to address the critical challenge of thermal runaway prevention under summer extreme temperature of 50 °C and maximum discharge rate of 5C, we establish an ANN prediction model coupled with the NSGA-II algorithm. This integrated approach enables simultaneous optimization of three key parameters, such as the mass fraction of EG in CPCM, coolant velocity, and coolant temperature, while targeting maximum temperature and system power consumption as outputs. The work provides a solution for electric vehicles by resolving the inherent conflict between thermal safety and energy efficiency through material–structure–algorithm co-optimization. The ANN-NSGA-II integration establishes a methodological framework for intelligent thermal management in next-generation battery systems.

The work incorporates a multi-objective optimization framework that integrates CPCM with liquid cooling, which is less explored in the context of lithium-ion batteries under extreme operational conditions (up to 50 °C ambient temperature with a 5C discharge rate). It systematically examines a wide range of parameters, including coolant velocity, coolant temperature, and EG mass fraction in CPCM, while considering extreme temperatures and discharge rates, which are often not addressed comprehensively in existing literature. In addition, the NSGA-II algorithm is used in combination with an ANN surrogate model for efficient multi-objective optimization, ensuring optimal trade-offs between temperature minimization and energy consumption. This hybrid approach significantly enhances the overall thermal safety and efficiency of the system. The work provides a solution for electric vehicles by resolving the inherent conflict between thermal safety and energy efficiency through material–structure–algorithm co-optimization. The ANN-NSGA-II integration establishes a methodological framework for intelligent thermal management in next-generation battery systems.

https://doi.org/10.3390/batteries12030078

2. Physical and Mathematical Models

2.1. Physical Models

A battery module comprises a linear arrangement of 5 × 5 26650 lithium-ion batteries. The distance between two adjacent batteries is maintained at 37 mm for both parallel and series connections. A comparative evaluation framework was established to assess thermal management efficacy across four distinct cooling strategies under varying operational loads (1C, 3C, 5C discharge rates) and high environmental conditions of 40 °C. As illustrated in Figure 1, the systematically designed thermal architectures comprise an air-cooled BTMS where all batteries are housed within an aluminum (AL) frame measuring 188 mm × 188 mm × 65 mm, as the baseline case (Case 1); Case 2, which represents a BTMS with a 4 mm thick CPCMs (paraffin wax blended with EG; melting temperature range of 41~43 °C); Case 3, a liquid-cooled thermal management architecture comprising 16 discrete 3 mm internal diameter conduits arranged in bifurcated flow configuration (the inlet parts are depicted in blue color while the outlet parts are depicted in red color in Figure 1); and Case 4, a hybrid thermal regulation strategy synergistically integrating CPCM modules with active liquid cooling infrastructure, establishing a dual-mode heat dissipation mechanism.

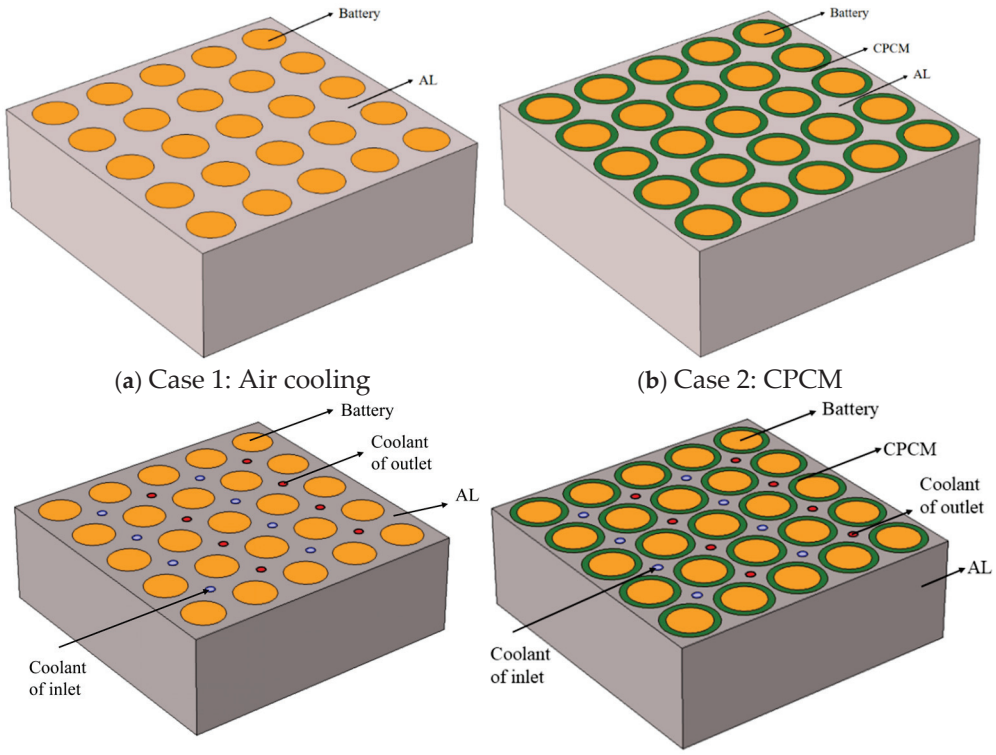

(**a**) Case 1: Air cooling (**b**) Case 2: CPCM

(**c**) Case 3: Liquid cooling (**d**) Case 4: CPCM + liquid cooling

Figure 1. Physical models of four cases for BTMSs: (**a**) air cooling of Case 1; (**b**) CPCM of Case 2; (**c**) liquid cooling of Case 3; (**d**) CPCM with liquid cooling of Case 4.

Additionally, the influence of electrical connection bars is not explicitly modeled in this study. As shown in reference [19], connection bars can affect the temperature distribution due to Joule heating and heat conduction effects. In the present study, to balance the computational efficiency required for the massive data generation (96 sets) for the ANN training and NSGA-II optimization, the geometric model is simplified by focusing on the thermal interaction between the battery cells and the hybrid cooling system (CPCM/liquid). Consequently, the specific geometry of the connection bars is not modeled, and the battery

https://doi.org/10.3390/batteries12030078

terminals are assumed to be adiabatic boundaries. The model verification of a single battery and a single battery with PCM will be verified for accuracy in Section 3.1.

The primary goal of this paper is to propose a relatively simple and engineering-friendly hybrid thermal management solution under extreme conditions, aiming to verify the feasibility and optimization potential of the collaboration between CPCM and liquid cooling. Additionally, the PCM used in this study is not the traditional low-conductivity PCM but rather a CPCM enhanced with expanded graphite (EG). The heat is primarily transferred rapidly through conduction to the surrounding aluminum frame and cooling pipe walls, significantly reducing its equivalent thermal resistance. In future work, fins or porous structures may be introduced on the existing CPCM–liquid cooling framework, and their geometric parameters could be incorporated into multi-objective optimization variables to further enhance the system's transient response and thermal safety under extreme conditions.

The material selection criteria and thermophysical characterization of critical BTMS components are systematically summarized in Table 1. Comparative analysis in Table 2 subsequently provides structural parametrization of cooling modules alongside thermal performance metrics in Section 3.2.

Table 1. Material selection criteria and thermophysical characterization of critical components [8].

Materials	Density ($kg \cdot m^{-3}$)	Specific Heat Capacity ($J \cdot kg^{-1} \cdot K^{-1}$)	Thermal Conductivity ($W \cdot m^{-1} \cdot K^{-1}$)
Battery	2059	1375	0.98
Aluminum	2719	871	202.4
CPCM	897	1852	5.74
Water	998.2	4128	0.635

Table 2. Applicability of four cases under high temperature of 40 °C.

Cases	Cooling Method	Applicability of Working Conditions		
		1C + 40 °C	3C + 40 °C	5C + 40 °C
Case 1	Air cooling	√	×	×
Case 2	CPCM	√	√	×
Case 3	Liquid cooling	√	√	×
Case 4	CPCM + liquid cooling	√	√	√

2.2. Mathematical Equations for Battery Module

The established lithium-ion battery model incorporates three fundamental assumptions: (1) electrode assemblies maintain isotropic material distribution with invariant bulk density during electrochemical cycling; (2) thermal transport mechanisms are restricted to conductive pathways, with convective and radiative heat transfer modes excluded under quasi-static electrolyte conditions; (3) thermodynamic parameters including specific heat capacity and effective thermal conductivity remain invariant with state-of-charge variations.

The heat generation of the battery is commonly described using the model proposed by Bernardi et al. [20], which decomposes the total heat generation into Joule heat and reversible reaction heat to characterize the thermal behavior during the discharge process of lithium-ion batteries. To describe the thermal effects of the lithium-ion battery discharge process, the formula for the heat effect can be expressed as follows:

$$q = \frac{I}{V}\left[(E_{OC} - E) + T\frac{dE_{OC}}{dT}\right] = \frac{1}{V}\left[I^2R - IT\frac{dE_{OC}}{dT}\right] \quad (1)$$

https://doi.org/10.3390/batteries12030078

where I, E_{oc}, E, V, and R represent the battery current, open circuit voltage, battery voltage, battery volume, and battery internal resistance, respectively, and q is the heat production per unit volume. The first term represents Joule heat induced by the internal resistance of the battery, which is irreversible in nature and constitutes the dominant source of heat generation. The second term corresponds to the reversible reaction heat arising from electrochemical reactions. Compared with the irreversible Joule heat, the contribution of reversible reaction heat is relatively minor under high-discharge-rate conditions. Therefore, in this study, the reversible reaction heat is neglected during the battery discharge process to simplify the thermal analysis without compromising accuracy. The formula for the heat effect can be expressed as follows:

$$\rho_b C_{p,b} \frac{\partial T}{\partial t} = \nabla \cdot (k_b \nabla T) + q \tag{2}$$

The CPCM mathematical model incorporates three fundamental thermodynamic postulates: (1) phase-specific physical parameters (including density, specific heat capacity, and dynamic viscosity) maintain phase-wise invariance during phase transition processes; (2) liquid-phase CPCM exhibits incompressible Newtonian fluid characteristics governed by the Navier–Stokes equations; (3) material homogeneity ensures isotropic thermal conductivity within the computational domain. Furthermore, for battery modules with externally configured PCM, the Rayleigh number is significantly lower than the typical critical value of 1000, which is commonly used to characterize natural convection phenomena. Additionally, since the radial direction of heat flow is perpendicular to gravity, it is reasonable to simplify the model by neglecting natural convection within the PCM [21].

The modified apparent heat capacity method [22] is implemented to characterize the phase-transition dynamics, a well-established numerical approach extensively validated in PCM thermal simulations. This computational framework enables robust phase-change modeling through commercial multiphysics platforms, with COMSOL Multiphysics 6.2 being strategically selected for its enhanced convergence algorithms in handling nonlinear thermal coupling. The enhanced apparent heat capacity formulation introduces three key methodological innovations: (1) dynamic thermal parameterization reconstructs the effective heat capacity as a temperature-dependent piecewise function spanning solid, mushy, and liquid phases, where latent heat is mathematically transformed into equivalent sensible heat through Gaussian distribution integration over the phase-change temperature band; (2) conservation law unification maintains baseline values in pure phases within phase transition zone, preserving identical energy conservation equation forms across material states through enthalpy–temperature coupling; (3) thermal inertia characterization reveals transient peaks during solid–liquid transition, thereby establishing an intrinsic thermal buffering mechanism that effectively mitigates thermal shock in Li-ion battery modules through delayed phase-front propagation.

The energy conservation equation for the PCM is summarized as follows:

$$\rho_{\mathrm{PCM}} c_{p,eff} \frac{\partial T}{\partial t} = \nabla \cdot (k_{\mathrm{PCM}} \nabla T) \tag{3}$$

$$C_{p,eff} = \begin{cases} C_{p,s} & T \le T_s \\ (1-\beta) C_{p,s} + \beta C_{p,l} \dfrac{L_{\mathrm{PCM}}}{(T_l - T_{\mathrm{s}})} & T_s < T < T_l \\ C_{p,l} & T \ge T_l \end{cases} \tag{4}$$

$$\beta = \begin{cases} 0 & T \le T_s \\ \frac{T_{\mathrm{PCM}} - T_{\mathrm{s}}}{T_l - T_{\mathrm{s}}} & T_s < T < T_l \\ 1 & T \ge T_l \end{cases} \tag{5}$$

https://doi.org/10.3390/batteries12030078

The computational fluid dynamics (CFD) model employs deionized water as the working fluid, governed by the incompressible Newtonian formulation with temperature-dependent properties modeled using piecewise polynomial functions. Flow regime control is achieved through systematic velocity modulation, where the maximum inlet velocity (0.2 m/s) corresponds to Reynolds numbers (Re = $\rho vD/\mu$) that remain below 2300 across all simulation conditions. This deliberate parameter selection ensures laminar flow dominance while maintaining computational stability through velocity–pressure coupling verification.

The energy conservation equation, mass equation, and momentum equation for the coolant are summarized as follows:

$$\frac{\partial}{\partial t}\left(\rho_w C_{p,w} T_w\right) + \nabla \cdot \left(\rho_w C_{p,w} \vec{v} T_w\right) = \nabla \cdot \left(k_w \nabla T_w\right) \tag{6}$$

$$\frac{\partial \rho_w}{\partial t} + \nabla \cdot \left(\rho_w \vec{v}\right) = 0 \tag{7}$$

$$\frac{\partial}{\partial t}\left(\rho_w \vec{v}\right) + \nabla \cdot \left(\rho_w \vec{v}\vec{v}\right) = -\nabla p + \nabla \cdot \left(\mu \nabla \vec{v}\right) \tag{8}$$

where ρ_b, k_b, and C_p are the density, thermal conductivity, and specific heat capacity of the battery, respectively. ρ_{PCM}, $C_{\mathrm{p,eff}}$, k_{PCM} and L_{PCM} are the density, equivalent specific heat capacity, thermal conductivity, and latent heat of PCM, respectively. The subscripts of s and l are the solid state and liquid state of PCM, respectively. ρ_w is the density of water, $\vec{v}$ is the velocity vector of water, $C_{p,w}$, k_{w} and p denote the specific heat capacity, thermal conductivity, and static pressure of the cooling fluid, respectively.

It is important to highlight that, to streamline the computational process and ensure stable convergence, several modeling assumptions have been made. Given the operating temperature of the battery, thermal radiation, governed by the Stefan–Boltzmann law, is considered negligible in comparison to conductive and convective heat transfer. These simplifications are aimed at balancing simulation accuracy and efficiency [23,24]. Additionally, the thermophysical properties of the phase change material (PCM), including density, thermal conductivity, and specific heat capacity, are assumed to remain constant across solid, liquid, and molten states. Latent heat is treated as uniform, and volume changes due to phase transitions are neglected. While these assumptions facilitate the analysis, they may introduce deviations in energy storage calculations under transient thermal conditions. Therefore, the temperature comparison between experiment results and simulation results of a single battery temperature with different discharge rates at the room temperature will be discussed below, demonstrating excellent agreement between experiment and simulation results, validating the accuracy of the model, and providing essential theoretical support for simulating battery modules in subsequent work.

2.3. Boundary and Initial Conditions

The boundary and interfacial conditions are set in COMSOL Multiphysics, which are established as follows:

$$-k_b \frac{\partial T_b}{\partial n_b} = -k_{\mathrm{PCM}} \frac{\partial T_{\mathrm{PCM}}}{\partial n_{\mathrm{PCM}}} \tag{9}$$

$$-k_b \frac{\partial T_b}{\partial n_b} = -k_{\mathrm{AL}} \frac{\partial T_{\mathrm{AL}}}{\partial n_{\mathrm{AL}}} \tag{10}$$

$$-k_{\mathrm{PCM}} \frac{\partial T_{\mathrm{PCM}}}{\partial n_{\mathrm{PCM}}} = -k_{\mathrm{AL}} \frac{\partial T_{\mathrm{AL}}}{\partial n_{\mathrm{AL}}} \tag{11}$$

https://doi.org/10.3390/batteries12030078

$$-k_{\mathrm{AL}}\frac{\partial T_{\mathrm{AL}}}{\partial n_{\mathrm{AL}}} = -k_{\mathrm{pipe}}\frac{\partial T_{\mathrm{pipe}}}{\partial n_{\mathrm{pipe}}} \tag{12}$$

where n represents the direction along the normal of the outer surface of each component, and $\partial T/\partial n$ represents the temperature gradient of each component. k_b, k_{PCM}, k_{FHP}, k_{AL} and k_{pipe} represent the thermal conductivity of the battery, PCM, FHP, AL plate, and cooling pipe, respectively.

The numerical initialization protocol establishes two baseline field parameters: (1) thermal field homogeneity with $T = T_0$ corresponding to ISO standard ambient conditions; and the steady-state hydrodynamic initialization at $v = v_0$ to ensure smooth flow development. The hydrodynamic boundary configuration implements three distinct regimes: (2) cooling pipe inlet enforces a fully developed velocity profile with laminar flow specification; (3) outlet boundary adopts static pressure outlet relative to standard atmosphere; (4) all solid–fluid interfaces impose no-slip boundary conditions through enhanced wall treatment coupled with standard wall functions.

3. Model Verification and Numerical Results

3.1. Model Verification and Grid Independence

Model verification of a single battery and the grid independence of the battery module play a crucial role in achieving optimal thermal performance for battery thermal management. Figure 2a illustrates the temperature comparison between experimental results [25] and simulated results of a single battery temperature with different discharge rates at the ambient temperature of 25 °C. The experimental value is higher than the simulated value during the initial discharge. The main reason is that the simulation model ignores the contact thermal resistance of the battery during the simulation process and does not consider the reaction heat. In the later stage of the discharge, the heat generation rate of the battery module caused by internal resistance is quite high due to the high discharge rate. The experimental value and the simulated one are almost the same in the end. The results demonstrate excellent agreement between experiment and simulation results, with the maximum temperature difference not exceeding 1 °C, validating the accuracy of the model and providing essential theoretical support for simulating battery modules in subsequent work.

Additionally, the previous research [8] on comparison between the simulated and experimental [26,27] temperatures of the battery module based on a battery and CPCM at the ambient temperature of 28 °C has verified the feasibility of the battery module with CPCM, as the temperature of the simulation accords well with the experimental one. Moreover, according to references [26,27], to reduce the thermal resistance between the battery and the PCM cylinder, a layer of conductive silicone grease is applied to the surface of the battery, and the accuracy of the model is also verified. The methods based on single-battery verification and single-battery module verification have been widely applied in battery thermal management simulations, and the subsequent work can be carried out by modifying the boundary conditions to be applicable to different battery modules. COMSOL Multiphysics is employed to partition the model into grids, with six different numbers of grids (63,710, 177,301, 513,618, 830,023, 1,965,110, and 4,487,930) examined for Case 4 to assess the impact on independence as shown in Figure 2b. It can be observed that increasing the number of grids leads to a decrease in maximum battery module temperature. However, once the number of grids reaches 830,023, the battery temperature stabilizes. Therefore, to enhance computational efficiency while ensuring accurate model calculations during subsequent simulations, we select a grid size of 830,023.

https://doi.org/10.3390/batteries12030078

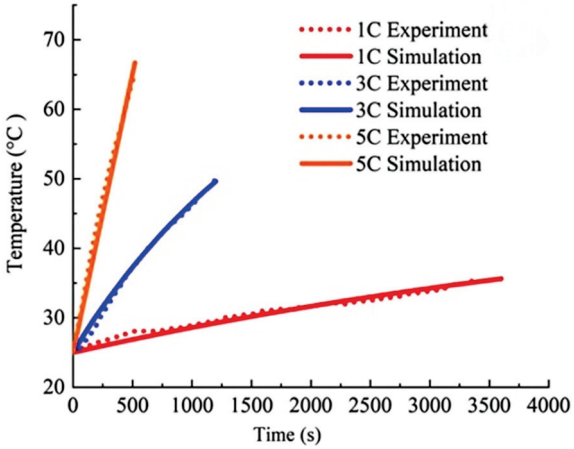

(**a**)

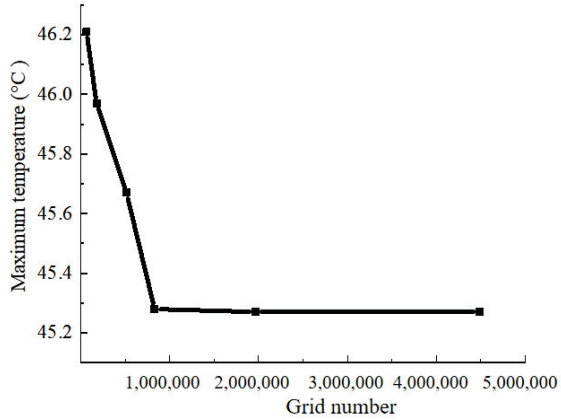

(**b**)

Figure 2. Comparison between experiment results [25] and simulation results for a single battery temperature at different discharge rates under an ambient temperature of 25 °C (**a**). Grid independence of Case 4 under an ambient temperature of 40 °C and a discharge rate of 5C (**b**).

3.2. Numerical Results and Discussion for Battery Modules

The thermal performance of the four cases under a high-temperature condition of 40 °C and discharge rates of 1C, 3C, and 5C is presented in Figure 3. It is shown that all cases effectively control the maximum temperatures of no more than 50 °C under a 1C discharge rate. Notably, Case 1 with air cooling proves to be effective in reducing the maximum temperature of the battery module at lower discharge rates; however, it is not suitable for higher discharge rates. Case 1 experiences an increase in its maximum temperature to 53.31 °C under a discharge rate of 3C, while it reaches up to 65.21 °C under a discharge rate of 5C, both surpassing the normal operating temperature range for batteries. Moreover, in Case 2, due to the thermal storage effect provided by CPCM, the maximum temperature of the battery module remains close to the phase transition temperature of CPCM during a discharge rate of 1C and 3C; however, under high-discharge conditions such as with a rate of 5C, the maximum temperature of the battery exceeds 50 °C, as does the temperature difference. The thermal performance achieved by Case 3 using liquid cooling alone demonstrates better results at lower discharge rates but proves unsuitable for high-discharge rates. Case 4 (CPCM–liquid hybrid system) demonstrates high-rate thermal stabilization, which maintains battery maximum temperature at 45.27 °C under a 5C discharge rate.

https://doi.org/10.3390/batteries12030078

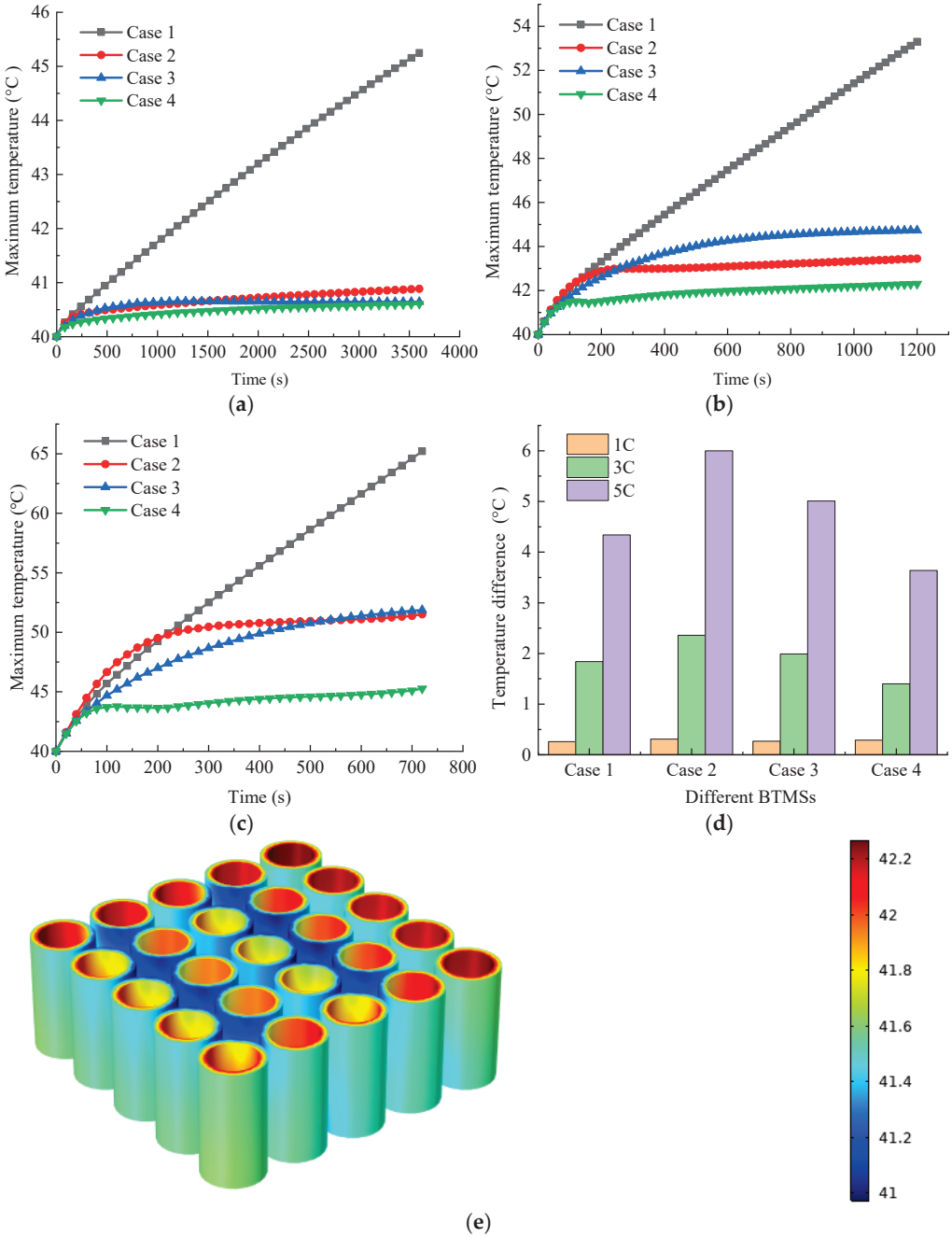

Figure 3. Maximum temperature of four cases under high temperature of 40 °C and different discharge rates: (**a**) 1C; (**b**) 3C; (**c**) 5C. (**d**) Temperature differences in four cases. (**e**) Temperature cloud chart of CPCM in Case 4.

It is noted that for Case 2 with pure CPCM, the cooling relies primarily on the passive thermal storage of the CPCM. As the battery temperature rises above the melting point (41 °C), the CPCM undergoes a phase change, absorbing a significant amount of latent heat. The temperature stabilization around 50 °C under a high discharge rate of 5C indicates that the system is reaching a thermal equilibrium where heat generation is balanced by the sensible and latent heat absorption of the CPCM. On the other hand, Case 4 is employed with CPCM and liquid cooling; in this hybrid system, the active liquid cooling works synergistically with the CPCM. The coolant fluid continuously extracts heat from the module, significantly enhancing the heat-rejection rate. This active heat removal prevents the CPCM from reaching higher temperatures, allowing the system to reach a steady-state

https://doi.org/10.3390/batteries12030078

condition at a lower temperature compared to the pure CPCM case, demonstrating the best thermal performance.

Moreover, Figure 3e shows the temperature cloud chart of CPCM in Case 4. The maximum temperature of CPCM is 42.2 °C (the melting temperature of CPCM is 41~43 °C), which indicates that the amount of CPCM is sufficient to fully absorb the heat released by the battery while maintaining a small change in its own temperature. The optimized performance is designed to be sustainable rather than purely transient. The active liquid cooling works synergistically with the CPCM in the hybrid system. While the CPCM provides passive thermal storage and high latent heat capacity to absorb initial heat, the continuous flow of coolant extracts heat from the module and dissipates it to the surroundings. This active heat removal ensures the system reaches a steady-state thermal equilibrium where heat generation is balanced by liquid cooling, preventing the CPCM from reaching a fully melted state indefinitely. This indicates that the latent heat capacity of the CPCM is utilized to buffer peak loads, while the liquid cooling ensures the system does not "saturate" or experience thermal runaway during prolonged operation.

In summary, the CPCM–liquid cooling architecture is chosen because it provides an optimized, cost-effective, and easy-to-manufacture solution that resolves the inherent conflict between thermal safety and energy efficiency under extreme working conditions (a high temperature of 40 °C and a high discharge rate of 5C). Therefore, Case 4 will be studied as the base case for multi-objective optimization to further enhance the thermal safety of the battery in high-temperature environments and under high discharge rates in the subsequent work.

The operational envelope analysis in Table 2 reveals that all configurations demonstrate sufficient thermal buffering capacity for 1C discharge; conventional PCM (Case 2) and liquid-cooled (Case 3) systems exhibit viable 3C operation but suffer from respective limitations; and the hybrid CPCM–liquid system (Case 4) uniquely maintains thermal stability under extreme 5C/40 °C conditions through synergistic phase change enthalpy utilization and adaptive liquid flow modulation.

3.3. Single Factor Analysis of Case 4

The optimization process commences with a single-factor analysis, where a single input parameter of the baseline case (Case 4) is varied. The impacts of different system parameters on the optimization objectives are examined through the single-factor test, as illustrated in Table 3 and Figures 4–7. The study focuses on the thermal performance analysis of battery modules under extreme operating conditions, such as a high-temperature environment of 40 °C and a high discharge rate of 5C. The input parameters selected for the single-factor analysis, namely, the mass fraction of EG, coolant velocity, and coolant temperature, are chosen because they represent the most critical controllable factors influencing the trade-off between thermal safety and system economy.

Table 3. Different simulation cases of sensitivity analysis using a single-factor test.

	Description	Mass Fraction of EG (%)	v (m/s)	T_w (°C)
Case 4	Hybrid CPCM with liquid cooling	12	0.01	40
Case 4-1	Varying mass fraction of EG	0–30	0.01	40
Case 4-2	Varying coolant velocity	12	0.01–0.2	40
Case 4-3	Varying coolant temperature	12	0.01	25–40

https://doi.org/10.3390/batteries12030078

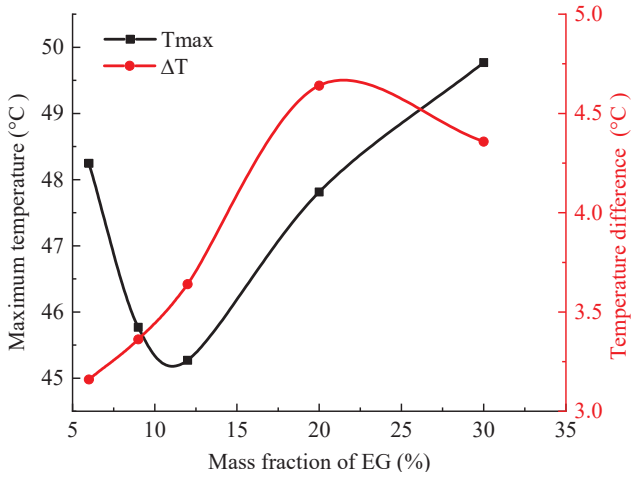

Figure 4. Maximum temperature and temperature difference in the battery module under different mass fractions of EG.

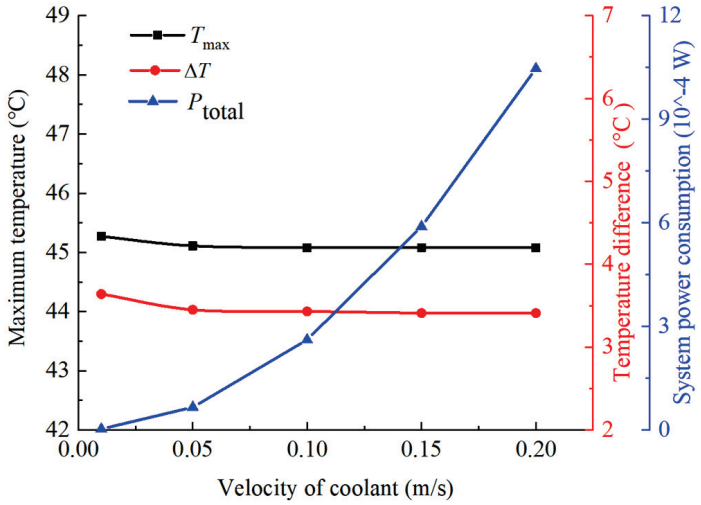

Figure 5. Maximum temperature and temperature difference in the battery module under different coolant velocities.

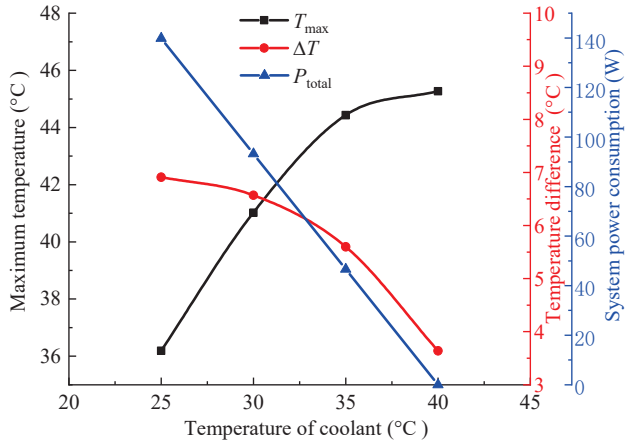

Figure 6. Maximum temperature and temperature difference in the battery module under different coolant temperatures.

https://doi.org/10.3390/batteries12030078

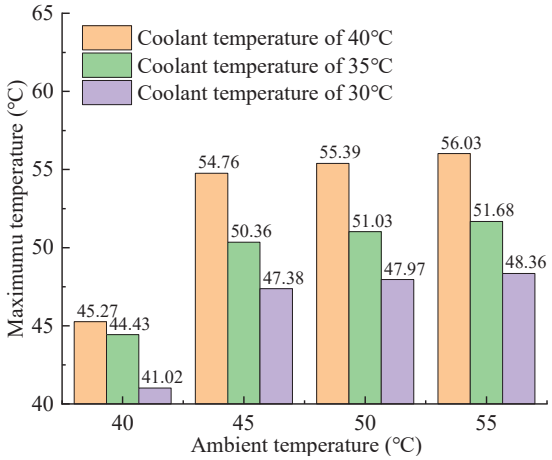

Figure 7. Maximum temperature of the battery module at different ambient temperatures as a function of coolant temperature.

To ensure battery safety and optimal performance, it is critical to maintain the operating temperature below 50 °C, as exceeding this limit may lead to accelerated capacity decay or thermal hazards. For effective thermal regulation, the PCM should be selected with a phase transition temperature range of 40~50 °C, slightly below the upper safety threshold. This allows the PCM to absorb heat during battery operation before temperatures approach critical levels. A phase transition temperature that is too low fails to function effectively at high temperatures, while a phase transition temperature that is excessively high hampers the temperature control of the battery. Consequently, this study selects CPCM with a phase transition temperature of 41~43 °C for investigation. Furthermore, following the methodologies reported in [26,27], EG powder is initially dried in a vacuum oven at 60 °C for 24 h, followed by a rapid expansion in a muffle furnace at 800 °C for 60 s. Due to the preserved in-plane lattice structure, the thermal conductivity of the resulting EG remains comparable to that of pristine graphite. To prepare the CPCMs, liquid paraffin (RT44HC) is infused into the EG matrices at various mass fractions (3%, 6%, 9%, 12%, 16%, 20%, and 30%) via capillary action and surface tension. Finally, the composite powders are compressed into cylindrical samples under a pressure of 4 MPa for application in Li-ion battery thermal management. As discussed in the reference [8], increasing the mass fraction of EG in CPCM enhances heat transfer performance; however, it concurrently reduces the available latent heat for battery thermal management. Consequently, an optimal EG content in CPCM exists, with a corresponding optimal thermal conductivity coefficient of CPCM.

Moreover, the coolant velocity is varied because it directly affects heat transfer performance. An increased flow rate enhances heat conduction but also increases system power consumption due to higher pumping requirements. By analyzing this parameter, an optimal flow rate is aimed to identify that minimizes the maximum battery temperature while considering the system energy consumption.

The coolant temperature is chosen for variation to evaluate its influence on the thermal performance of the system. Lower coolant temperatures can reduce the maximum temperature of the battery module but may also lead to increased thermal stress and greater power consumption for the coolant system. A balance is identified where the coolant temperature minimizes temperature fluctuations without excessively increasing system power requirements.

As shown in Table 3, Case 4-1 involves adjustments to the mass fraction of EG in CPCM based on Case 4; Case 4-2 explores different coolant flow rates while maintaining the conditions of Case 4; and Case 4-3 designs various coolant temperatures within the

https://doi.org/10.3390/batteries12030078

framework of Case 4. Each single-factor test encompasses five levels within the designated design space.

Figure 4 demonstrates the variation tendency of optimization objectives by changing the mass fraction of EG (wt.%) in CPCM. It is evident that increasing the mass fraction of EG effectively reduces the maximum temperature until 12 wt.%, but it increases with further increase in the mass fraction of EG. Conversely, the temperature difference shows an opposite trend. This can be attributed to the fact that as the mass fraction of EG increases, the thermal conductivity of CPCM increases while latent heat decreases. Experimental studies have demonstrated an optimal range for the mass fraction of EG in CPCM to achieve balanced thermal management performance.

Figure 5 illustrates the thermal performance of Case 4 under different coolant velocities. As the coolant flow rate increases, the maximum temperature shows a downward trend and stabilizes. However, the system's pump power consumption increases exponentially. This is because a higher flow rate enhances the heat conductivity and system pressure drop. The higher the heat conductivity is, the faster the battery module cools down, and the system temperature decreases. The system pressure drop increases, thus requiring more power consumption from the system pumps. The system power consumption is a key index for evaluating the economic viability of the BTMS. The total system power consumption P_{total} is defined as the sum of the pumping power P (as shown in Equation (13)) and the cooling power P_c (as shown in Equation (15)). Therefore, choosing the appropriate coolant temperature while meeting the temperature requirements is of great significance for improving the economy of the system. Hence, it is not blindly pursuing a higher coolant velocity. On the premise of meeting temperature requirements, using a lower coolant velocity as much as possible is beneficial to the economy of the system. When the flow velocity is stable, the energy consumption of the coolant can be determined using the following equation [28]:

$$P = n\Delta p v_c A \tag{13}$$

where n is the number of liquid cooling pipes. Δp is the inlet and outlet pressure difference in the coolant. v_c is the coolant velocity. A is the cross-sectional area of the liquid cooling pipe.

As shown in Figure 5, the ambient and coolant temperatures are both set to 40 °C without additional cooling power. Therefore, $P_c = 0$, $P_{\text{total}} = P$. In addition, to account for the three-dimensional pressure variations mentioned, the pressure drop Δp is obtained through area-averaging in the COMSOL Multiphysics environment. Δp is computed as the difference between the area-averaged static pressure at the entire inlet section and the area-averaged static pressure at the outlet section. The pressure distribution within the conduits is solved using the incompressible Navier–Stokes equations. This numerical approach naturally integrates the three-dimensional variations (including two-dimensional variations at the cross-sections) into a macroscopic pressure drop value used for power calculation. The Reynolds number is maintained below 2300 to ensure laminar flow conditions, and the boundary conditions are set with a fully developed velocity profile at the inlet and static pressure at the outlet.

Moreover, the impact of coolant temperatures is depicted in Figure 6. The parametric analysis reveals a critical thermal management trade-off, where the coolant inlet temperature is reduced from 40 °C to 20 °C under 5C discharge conditions, achieves 21.0% reduction in maximum battery temperature (from 45.27 °C to 35.83 °C), but simultaneously increases temperature inhomogeneity (from 3.64 °C to 8.02 °C) due to enhanced thermal stress concentration at current collector interfaces. Hence, there exists an optimal value for coolant temperature that balances both maximum temperature and temperature uniformity. In addition, as the coolant temperature decreases, the required system power increases

https://doi.org/10.3390/batteries12030078

significantly, which greatly increases the cooling cost of the system. When the steady state is reached, the cooling power could be obtained conservatively based on the outlet/inlet temperature difference under the following liquid cooling condition [29,30]:

$$Q_{\mathrm{c}} = n\dot{m}c_p\Delta T \tag{14}$$

$$P_{\mathrm{c}} = Q_{\mathrm{c}}/\mathrm{COP} \tag{15}$$

where Q_c is the heat removal rate, n is the number of liquid cooling pipes, $\dot{m}$ is the mass flow rate, ΔT is the outlet/inlet temperature difference, and COP is the coefficient of performance.

The cooling power is derived from Q_c and COP. Q_c is calculated based on the mass flow rate and the temperature difference between the inlet and outlet. The parameter COP is used to characterize the energy efficiency of the external active cooling source (such as a chiller or the vehicle's air-conditioning system) required to maintain the coolant at a specific inlet temperature. As investigated in the study, when the ambient temperature reaches extreme levels (up to 50 °C), the system requires active refrigeration to pre-cool the coolant before it enters the battery module. In the subsequent work, the total system power consumption P_{total} (the pumping power P and the cooling power P_c) calculated for multi-objective optimization is presented in the Appendix A.

As shown in Figure 7, the maximum temperature changes in the battery module are studied with different high-temperature extreme conditions under the temperatures of the coolant. Under the working conditions of an environmental temperature of 40 °C, the system does not need to pre-cool the coolant. By maintaining the same temperature as the environment, the battery thermal management temperature requirements can be met. However, when the ambient temperature exceeds 40 °C, the system must pre-cool the coolant. As can be seen from the figure, the coolant temperature is pre-cooled between 30 and 35 °C, and there is an optimal temperature value that ensures the system temperature does not exceed 50 °C and also results in the lowest system power consumption. Therefore, further optimization of the parameters is necessary to ensure that the thermal management requirements of the system are met while also considering the economic aspects.

Based on the above analysis, the hybrid CPCM–liquid cooling strategy (Case 4) demonstrates exceptional thermal regulation capability under extreme operational stress, maintaining the maximum temperature at 45.27 °C under concurrent 40 °C ambient and 5C discharge conditions without pre-cooling intervention. However, considering the mid-latitude region in summer, according to the report from the World Meteorological Organization [31], over the past year, widespread, intense, and prolonged heat waves have hit all continents. Daily temperatures exceeded 50 °C in multiple locations in at least ten countries. The BTMS should incorporate a pre-cooling mechanism for the coolant to maintain precise control over the maximum temperature and ensure uniform thermal distribution. This approach effectively mitigates thermal runaway risks while enhancing the operational safety of electric vehicles. The following research will carry out multi-objective optimization of various parameters of the system under the condition of extreme high temperature environment of 50 °C to improve the economy of the system while ensuring system safety.

https://doi.org/10.3390/batteries12030078

4. ANN Models and NSGA-II Algorithm Optimization for Case 4 Under Extreme Condition

4.1. Artificial Neural Network (ANN) Model

4.1.1. Design of ANN Model

In recent years, artificial neural networks (ANN) have gained widespread application in various fields, including optimization problem-solving [32]. ANNs possess the ability to learn based on the interconnectedness of neurons in the human brain, exhibiting a high degree of automation and proven effectiveness in predicting target–variable relationships [33]. The back propagation (BP) neural network (BPNN) is a multi-layer feedforward neural network trained according to the error backpropagation algorithm [34], typically consisting of an input layer, a hidden layer, and an output layer [35]. The structure of ANNs has been simplified compared with human brains; multiple hidden layers are more accurate and complex, but only one hidden layer is used in many cases, particularly for cases with small sample sizes. The accuracy of an ANN can be improved by adjusting the number of neurons in the hidden layer.

Figure 8 displays the ANN structure diagram for BTMS. Three parameters, namely mass fraction of EG, coolant velocity, and coolant temperature, are set as inputs for the ANN. A single hidden layer is employed within this neural network configuration. In addition, maximum temperature and system power consumption are selected as evaluation indicators for the thermal safety of the BTMS under extreme conditions of 50 °C ambient temperature and 5C discharge rate. The objective of maximum temperature is selected as the absolute primary indicator for thermal safety. Maintaining the operating temperature below 50 °C is critical, as exceeding this limit leads to accelerated capacity decay or severe thermal hazards. Controlling T_{max} prevents thermal runaway under extreme conditions, such as a 5C discharge rate at a 50 °C ambient temperature. Moreover, power consumption is selected as the other objective because it is a key index for evaluating the economic viability of the BTMS. While active cooling effectively lowers temperatures, it introduces a severe energy penalty due to intensified pumping work and auxiliary cooling demands. Optimizing P_{total} directly addresses the inherent conflict between thermal safety and energy efficiency, then serves as outputs to construct the ANN.

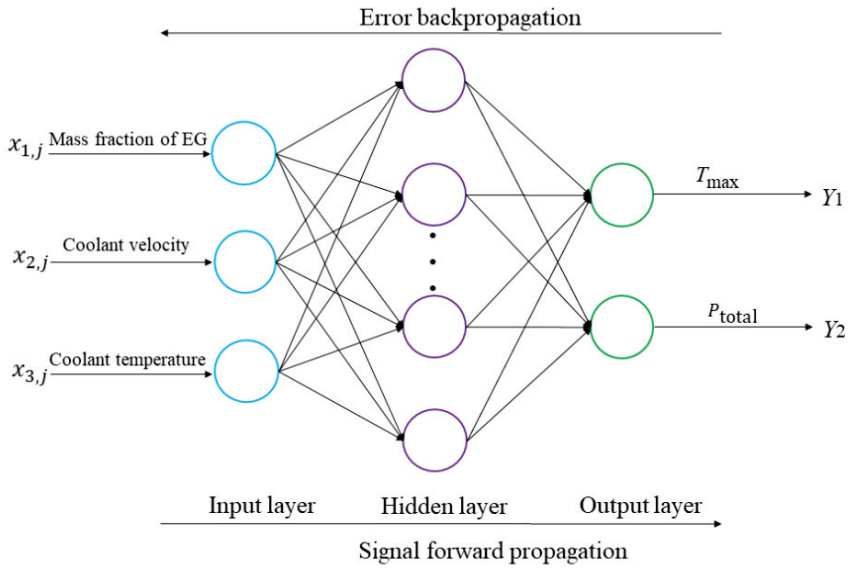

Figure 8. ANN structure diagram of battery thermal management system.

The mass fraction of EG in CPCM, coolant velocity, and coolant temperature are selected as the input values of the ANN, corresponding to the input state vector of X_i,

https://doi.org/10.3390/batteries12030078

$X_i = \{x_{ij} | i = 1, 2, 3\}$, representing different design parameters within the feasible region; the lower and upper bounds of input values are listed in Table 4. The physical properties of CPCMs are shown in Table 5. The output state vector of Y_i, $Y_i = \{x_{ij} | i = 1, 2\}$, which corresponded to the maximum temperature and system power consumption of the battery module. For the prediction model established before, the NSGA-II algorithm is used to solve the multi-objective problem, which is transformed into the mathematical model of Equation (16). Based on the results of the single-factor analysis, the output variables are utilized as constraint functions to minimize two competing objective functions simultaneously by adjusting a three-dimensional design vector within a defined feasible region. The problem is formulated to find the minimum of the following vector function.

$$\begin{cases} T_{\max} = f_1(X_1, X_2, X_3) \\ P_{\text{total}} = f_2(X_1, X_2, X_3) \\ mixF(X) = [f_1(X),\ f_2(X)]^T = [T_{max}(X),\ P_{\text{total}}(X)]^T \end{cases} \quad (16)$$

where f_1(X) is the maximum battery temperature (T_{max}) and f_2(X) is the total system power consumption (P_{total}).

Table 4. Lower and upper bounds of the ANN input of BTMS.

Bounds	Mass Fraction of EG (%)	Coolant Velocity (m/s)	Coolant Temperature (°C)
ub	30	0.15	35
lb	3	0.01	32

Table 5. Physical properties of composite phase change materials [26].

Mass Fraction of EG (%)	Specific Heat Capacity ($J \cdot kg^{-1} \cdot K^{-1}$)	Thermal Conductivity ($W \cdot m^{-1} \cdot K^{-1}$)	Latent Heat ($kJ \cdot kg^{-1}$)
3	1963	0.58	266.8
6	1926	1.23	258.3
9	1889	3.50	250.3
12	1852	5.74	242
20	1754	10.60	220
30	1631	13.85	192.5

4.1.2. Training of ANN Model

Considering the safety and feasibility of thermal design for lithium-ion battery modules, the mass fraction of EG is set to seven levels, [3, 6, 9, 12, 20, 30], the coolant velocity has five levels, [0.01, 0.05, 0.1, 0.15], and the coolant temperature has four levels [32, 33, 34, 35]. The ANN development protocol implements a three-stage quality assurance framework for training data acquisition and model validation. Stratified sampling architecture employs optimized latin hypercube sampling (LHS) with an enhanced stochastic evolutionary algorithm, and it has been widely used in the training data of ANN, which means that a small number of samples can represent the entire sample space and ensure that each sample is represented in a fully hierarchical manner. The predictive fidelity of trained neural networks requires comprehensive evaluation through a dual-metric validation framework combining the mean squared error (MSE) and the correlation coefficient (R) [36]. Minimizing the root-mean-square error serves as a constraint to prevent the model from converging

https://doi.org/10.3390/batteries12030078

to local optima and overfitting during training, thereby reducing the discrepancy between the desired and predicted outputs. A comprehensive dataset comprising 96 simulation instances was generated through COMSOL Multiphysics. The LHS is employed to generate the sample points shown in Table A1 in the Appendix A under the upper and lower boundaries. These sample sets are generally divided into three parts: training set, validation set, and testing set, with a ratio of 70:15:15. The dataset of ANN is normalized to make the input and output values between [0, 1] according to the following equation [37]:

$$x_i^{\text{norm}} = \frac{x_i - x_{\min}}{x_{\max} - x_{\min}} \tag{17}$$

where x_i is the target value of the simulation results, $x_{\min}$ is the minimum value, $x_{\max}$ is the maximum value, x_i^{norm} is the normalized value of x_i.

During the training process, the mean squared error (MSE) is selected as the loss function in the ANN. The formula for the mean squared error is shown as follows:

$$\text{MSE}(X) = \frac{1}{n}\sum_1^n (y_i - f(x_i))^2 \tag{18}$$

where n is the sample number, y_i is the real value, $f(x_i)$ is the predicted value.

Based on this approach, unifying the dimensions of each parameter can solve the problem of poor convergence during the learning process, and the inverse normalization method is employed to continue recovering the sample data after the optimization is completed. In this work, the generalization ability of GA and individual fitness are mainly described through testing errors. In cases where the testing error is low, it corresponds to higher fitness, representing higher individual quality.

4.2. NSGA-II Algorithm Optimized ANN Model

4.2.1. NSGA-II Algorithm Model

The genetic algorithm (GA) is a typical evolutionary algorithm widely employed for solving nonlinear problems, offering the following advantages. NSGA-II has emerged as one of the most practical multi-objective evolutionary algorithms for energy system optimization, particularly excelling in scenarios requiring concurrent optimization of conflicting objectives like cost minimization, emission reduction, and reliability maximization. It employs fast non-dominated sorting to reduce computational complexity, and the elitist preservation strategy to maintain Pareto-optimal solutions across generations through parent–offspring co-evolution, which is widely favored for its robustness and efficient crowd distance estimation, making it particularly valuable in addressing complex multi-objective optimization problems in energy systems [38].

In this work, the combination of ANN and NSGA-II is studied to form the NSGA-ANN model. Figure 9 inhibits the NSGA-II optimization workflow for optimizing the ANN. The left part represents the ANN workflow. Following this, training and testing of the ANN are conducted using a previously constructed database. The model utilized in this study belongs to a multi-objective optimization model with three inputs and two outputs. The right part depicts the NSGA-II workflow. The NSGA-II algorithm screens individuals through selection, crossover, and mutation. During the continuous evolutionary iterations, elite individuals are preferentially selected to achieve the optimal solution on the Pareto front that meets the specified conditions. Consequently, combining these two methods can fully leverage their respective strengths while mitigating individual method shortcomings when tackling multi-objective optimization problems, thereby optimizing the BTMs.

https://doi.org/10.3390/batteries12030078

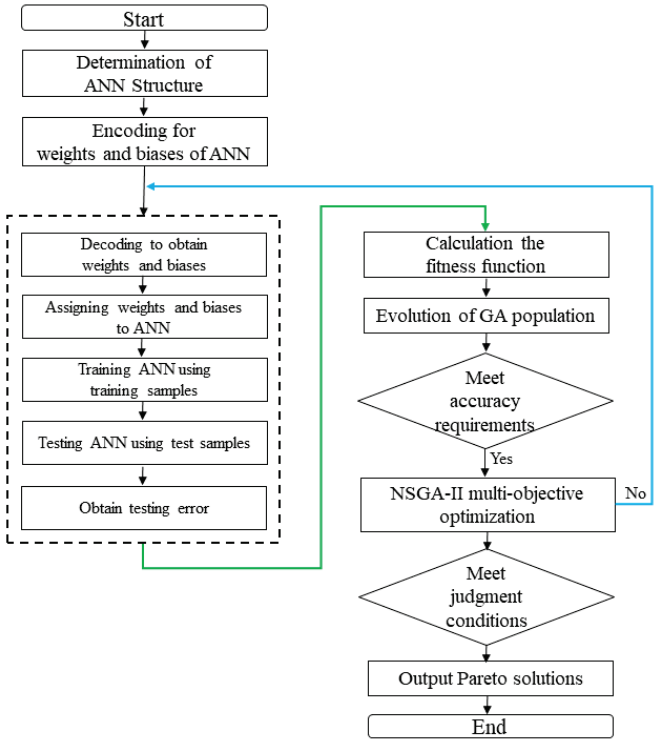

Figure 9. NSGA-II optimization workflow for optimizing ANN.

4.2.2. NSGA-II Optimized ANN Model

In the three-layer ANN structure, the number of neurons at each level is appropriately determined. The input layer and hidden layer have specific neuron counts, and there exists a relationship between them. In the parameters of the BTMS, the optimal number of hidden layer nodes obtained through the ANN setting is 13. Based on the previous parameters, weights and biases are assigned with respective numbers of 42 and 10, leading to a total of 52 parameters that require optimization. Therefore, the total number of parameters that need to be optimized is 52. Consequently, when employing the NSGA-II algorithm, initialization of the entire population becomes necessary along with binary encoding [0, 1] for weight and bias values in each layer. Subsequently, the encoding length of each value can be calculated based on the number of weights and biases present. The specific NSGA parameter settings are presented in Table 6. By using GA for iterative optimization of ANN models, it becomes feasible to rapidly identify precise parameter combinations meeting requirements, which can then be employed within the COMSOL Multiphysics simulation platform for verification.

Table 6. Parameter settings for the genetic algorithm.

Name	Parameter Setting
Iterations	210
Population size	40
Generation gap	0.95
Crossover probability	0.7
Mutation probability	0.01

This section establishes the training and prediction of various parameter data that influence the BTMS based on the ANN, as well as the training and prediction of these parameters using an ANN structure optimized by GA. Through this method, the test and training sample errors of the two optimized structures can be obtained, and the error

https://doi.org/10.3390/batteries12030078

size can be judged to clarify the application effect of the model. Finally, the optimized parameter combination is substituted into the simulation model for comparison to verify the accuracy of optimization and ensure that the battery thermal management system has the best heat-dissipation performance.

5. Results and Discussion on Multi-Objective Optimization

5.1. Verify the Accuracy of the ANN Model

The corresponding MSE values for the training process are presented in Figure 10a. It shows that the training, validation, and test sets exhibit similar performance without overfitting. Notably, the model achieves its optimal performance at the 18th epoch. The comparison between the actual and predicted values of the maximum temperature and temperature difference is shown in Figure 10b, demonstrating a good fit.

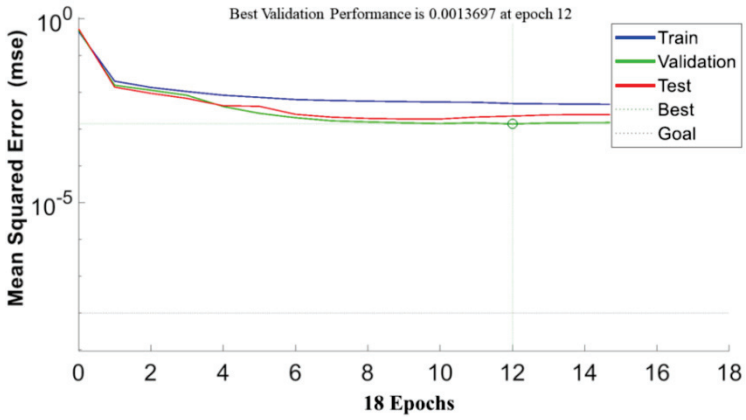

(**a**)

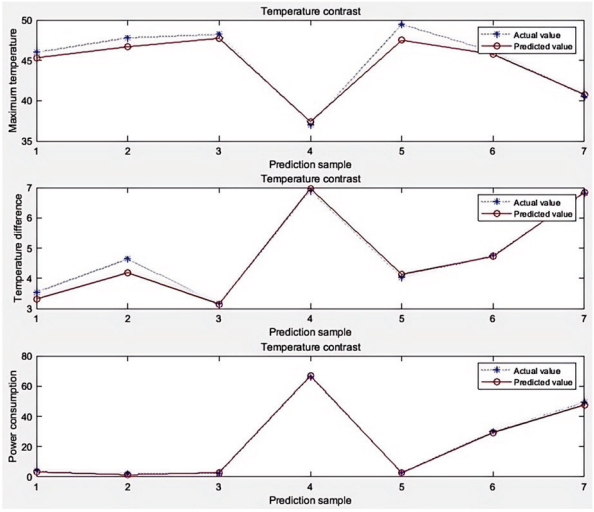

(**b**)

Figure 10. ANN training: (**a**) MSE of training set, validation set, and test set; (**b**) comparison between actual and predicted values.

5.2. Results of Multi-Objective Optimization by NSGA-II Algorithm

Figure 11a illustrates the correlation coefficient between the COMSOL detailed model target and ANN prediction output, with a resulting regression coefficient (R) approaching one and evenly distributed data points along the diagonal line. Consequently, it can be concluded that the ANN model exhibits high accuracy and can effectively predict BTMS parameters. Moreover, the prediction results optimized by the NSGA-II algorithm and the COMSOL Multiphysics model are presented in Figure 11b, with a correlation coefficient R

https://doi.org/10.3390/batteries12030078

of 0.9999 (higher than that in Figure 11a), which verifies that the ANN optimized by NSGA-II has higher prediction accuracy for the optimization of the comprehensive optimization of BTMS parameters.

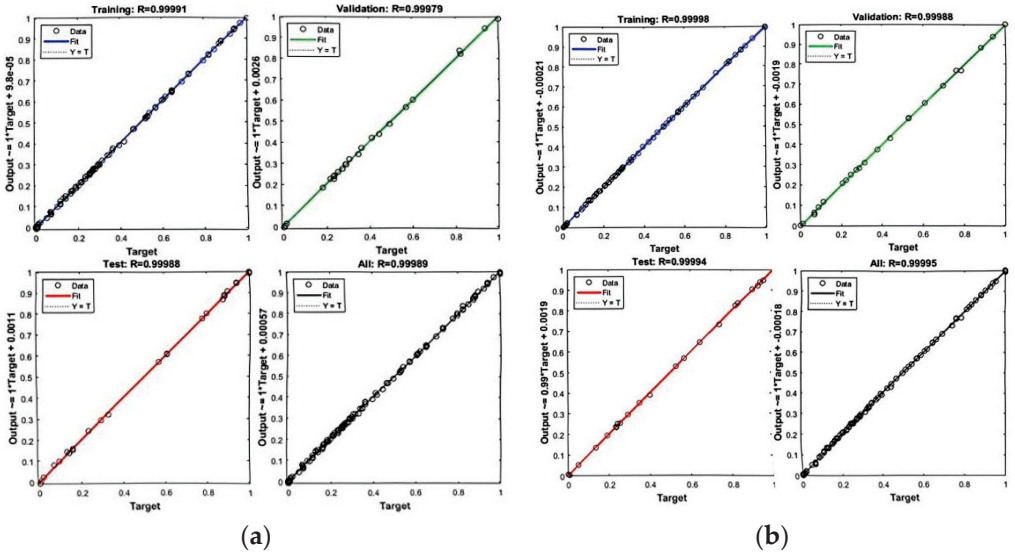

Figure 11. (**a**) Regression analysis of the ANN model; (**b**) regression analysis of the NSGA-ANN model.

It needs to be emphasized that to determine the optimal architecture, the model performance is evaluated by systematically adjusting the number of neurons in the hidden layer. Through this optimization process, 13 neurons in the hidden layer yielded the optimal performance, which provided the best balance between computational efficiency and prediction accuracy, minimizing the MSE without overfitting. Figure 12 is the simulation errors of the testing and training samples in the ANN model and the ANN optimized by NSGA-II after 210 iterations of genetic evolution. As detailed in Figure 12, the optimized NSGA-ANN model significantly reduced simulation errors, from 0.1192 to 0.0127 and from 1.2471 to 0.7318, respectively, indicating the NSGA-II algorithm effectively improved the reliability and accuracy of the ANN model. The model demonstrates a high degree of agreement between predicted values and actual numerical simulation results, possessing excellent stability and generalization ability for predicting the thermal behavior of the battery system.

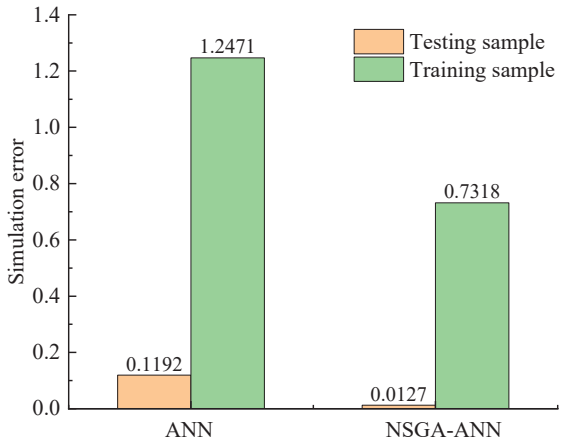

Figure 12. Comparison of simulation errors between test samples and training samples in ANN and NSGA-ANN.

https://doi.org/10.3390/batteries12030078

The solutions located along the Pareto-optimal frontier exhibit inherent trade-offs between conflicting objectives. Specifically, points "A" and "C" represent extreme cases where one objective is minimized/maximized through a complete sacrifice of the other, forming the endpoints of the Pareto front. Meanwhile, points "B" and "D" correspond to solutions closest to the hypothetical ideal point (simultaneous optimization of all objectives) and nadir point (simultaneous worst-case values of all objectives), respectively. In this selection process, the Technique for Order Preference by Similarity to Ideal Solution (TOPSIS) was employed. This is a traditional multi-criteria decision-making (MCDM) method originally proposed by Hwang and Yoon [39]. It provides a robust framework for comparative performance analysis in complex decision environments. The NSGA-ANN model has accurately predicted the thermal performance of the BTMS. The optimal results are calculated through the f_{mincon} function using MATLAB R2025b tools, and the corresponding optimization scenarios are depicted in Figure 13.

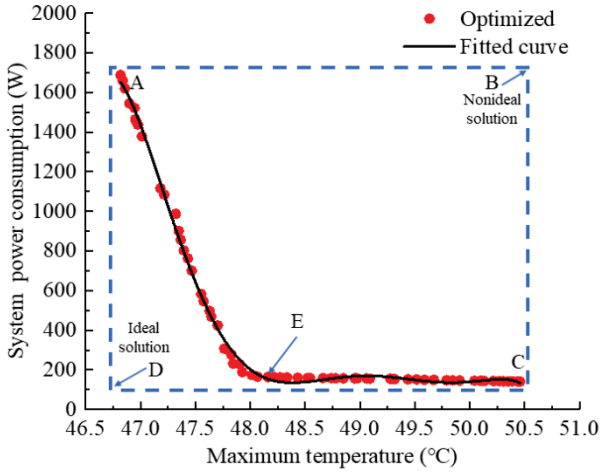

Figure 13. Pareto-optimal frontier of T_{max} and P_{total}.

As shown in Figure 13, T_{max} is correlated with P_{total} negatively, which implies that it is impossible to achieve the optimal solution for both simultaneously. The decrease in maximum temperature of the battery module is primarily due to a decrease in temperature and velocity of the coolant, leading to greater system power consumption. In practical engineering applications, a more reasonable analysis must be performed based on the actual situation context, rather than on numerical data. Therefore, if two objective functions are equally important, such as the maximum temperature and power consumption in this work, the point E can be selected as the optimal point for multi-objective optimization because it is closest to the ideal point [40,41]. The thermal equilibrium analysis reveals a critical trade-off between cooling efficacy and energy penalty. While the maximum temperature is suppressed through enhanced active cooling mechanisms, the concomitant system power consumption exhibits a surge due to intensified pumping work and auxiliary thermal regulation demands. Then, after point E, a lower system power consumption can be employed to ensure that the maximum temperature of the battery module is not higher than 50 °C within the operating temperature requirements.

It is worth noting that the NSGA-ANN is utilized as a fast-running surrogate model to address the prohibitive computational burden of direct CFD optimization, which would require approximately 8400 evaluations (based on the NSGA-II configuration of 210 iterations and a population size of 40) for a high-fidelity model featuring 830,023 grid elements. Direct simulations under extreme conditions (5C discharge and 50 °C ambient temperature) consume significant CPU time and require thousands of hours in total, making them unfeasible for engineering design cycles. ANN is strategically trained on a manageable dataset

https://doi.org/10.3390/batteries12030078

of only 96 CFD simulation sets generated via LHS. The resulting NSGA-II-ANN framework achieves millisecond-level prediction speeds, exceptional accuracy with a regression coefficient R of 0.99995, and verification errors between ANN predictions and subsequent COMSOL simulations below 0.33%. This approach enables a comprehensive search of the continuous design space while utilizing only approximately 1.1% of the computational effort required by a traditional direct optimization approach.

Table 7 shows the Pareto-optimal solutions after the NSGA-II algorithm optimized the ANN model. X_j represents the optimized parameter combination, Y_j represents the prediction results of the NSGA-ANN model, and Z_j represents the simulation results obtained by inputting X_j based on the COMSOL Multiphysics. It can be seen that the optimized parameters can control the maximum temperature to 48.52 °C with the lowest system power consumption of 158 W, achieving a 12.1% reduction in thermal fluctuation amplitude compared to initial Case 4; it reduced energy consumption by 5.9% while ensuring minimal temperature increase compared to Case 4-1. The output results obtained by the NSGA-ANN model with the simulation results of COMSOL Multiphysics are compared in Table 7. The error percentages of the results are all less than 0.33%, indicating that parameter optimization using the NSGA-II algorithm can effectively address issues related to temperature rise and system power in battery modules through an ANN proxy prediction model construction approach with strong generalization ability suitable for battery temperature control applications during the BTMS design.

Table 7. Initial values and optimized values of the NSGA-II algorithm with different constraints.

Type	X_j (EG%, T_w, v)	NSGA-ANN of Y_j	COMSOL Model of Z_j
Initial Case 4	[12; 40.00; 0.01]	—	[55.39; 93]
Case 4-1	[26; 32.06; 0.01]	[48.06; 168]	[48.01; 168]
Case 4-2	[26; 32.66; 0.01]	[48.33; 161]	[48.43; 161]
Case 4-3	[26; 32.96; 0.01]	[48.52; 158]	[48.68; 158]

In addition, the temperature cloud slices of the middle five batteries are selected for a more intuitive comparison between the original model of Case 4 and the optimized model by NSGA-ANN of Case 4-3, as displayed in Figure 14. It can be seen that the optimized parameters of Case 4-3 can control the maximum temperature to 48.68 °C with the lowest system power consumption of 158 W, achieving a 12.1% reduction in thermal fluctuation amplitude compared to initial Case 4, and it reduced energy consumption by 5.9% while ensuring minimal temperature increase compared to Case 4-1. Other Pareto solutions are also viable options. The selection among these solutions can be determined by the decision maker based on specific requirements. For instance, it can be achieved by decreasing the coolant temperature for higher cooling efficiency. Under extremely high-temperature conditions, Case 4-1, Case 4-2, and Case 4-3 need to pre-cool the coolant, resulting in an increase in system power consumption compared to the initial Case 4. However, all cases can control the maximum temperature of the battery module to not exceed 50 °C, greatly improving the system safety under an extreme ambient temperature of 50 °C and a high discharge rate of 5C.

https://doi.org/10.3390/batteries12030078

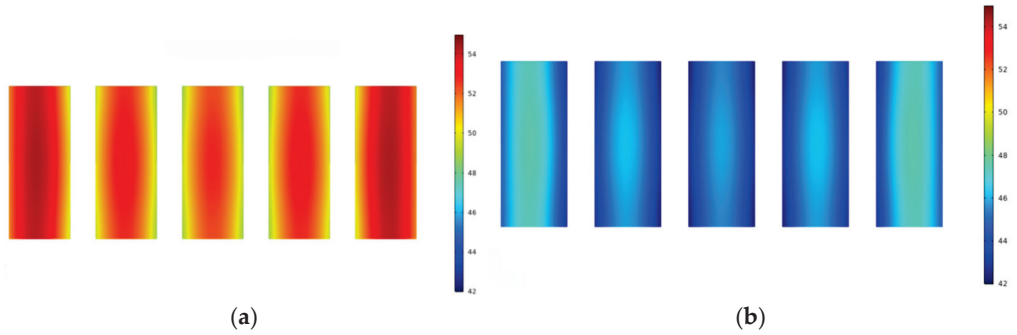

(**a**) (**b**)

Figure 14. Comparison between the original model of Case 4 and the optimized model of Case 4-3 for the temperature cloud slices of the middle five batteries: (**a**) original model; (**b**) optimized model using NSGA-ANN.

5.3. Engineering Relevance

In addition to the methodological contributions, this work provides clear engineering relevance for thermal management design of lithium-ion battery modules under extreme operating conditions. A power consumption of 158 W is a negligible fraction of a typical auxiliary load, ensuring it does not penalize the driving range. Moreover, based on the Arrhenius-type temperature–lifetime relationship [42] commonly adopted in battery engineering, a 10 °C reduction in operating temperature approximately doubles battery lifetime. In the present study, the NSGA-ANN optimized design reduces the maximum battery temperature from 55.39 °C to 48.68 °C under extreme conditions, corresponding to a temperature reduction of 6.71 °C, nearly a 59% increase in battery lifetime compared with the baseline case. The proposed NSGA-ANN optimization framework offers practical guidance for selecting key design parameters, enabling engineers to achieve reduced peak battery temperature while minimizing auxiliary power consumption.

The optimized hybrid BTMS combining CPCM and liquid cooling demonstrates an effective balance between thermal safety and energy efficiency, particularly in high-rate discharge scenarios (up to 5C) and elevated ambient temperatures (up to 50 °C). Therefore, the findings of this study are not only academically meaningful but also valuable for the development of next-generation BTMS solutions with improved reliability, durability, and applicability in realistic engineering conditions.

6. Conclusions

This study conducts a systematic evaluation of four BTMSs configurations under extreme operational conditions, specifically examining their thermal performance under 40 °C ambient temperature across varying discharge intensities (1C, 3C, and 5C). To address multi-objective optimization challenges, a hybrid artificial intelligence framework integrating an ANN with the NSGA-II algorithm was proposed. This computational model successfully identifies Pareto-optimal parameter sets that simultaneously enhance operational safety and energy efficiency for electric vehicles under strenuous working conditions. The conclusions are as follows:

(1) The comparative analysis reveals distinct thermal mitigation characteristics: Case 1 (pure air cooling) demonstrates limitations in maintaining thermal equilibrium beyond 2C operation; Case 2 (pure CPCM) and Case 3 (pure liquid cooling) exhibit superior thermal management capabilities under normal ambient temperature and 3C discharge conditions; Case 4, which utilizes a hybrid BTMS integrating CPCM and liquid cooling, successfully maintains battery surface temperature at 45.27 °C under extreme conditions (40 °C ambient temperature + 5C discharge rate), achieving 13.5% and 15.01% reduction, respectively, in temperature fluctuation amplitude compared to Case 2 and Case 3.

https://doi.org/10.3390/batteries12030078

(2) The proposed multi-objective optimization framework employs NSGA-II to systematically refine the ANN hyperparameters through non-dominated sorting of synaptic weights and bias thresholds. This evolutionary–ANN hybrid architecture achieves remarkable prediction fidelity, with a coefficient of determination (R^2) improving from 0.874 to 0.983 during cross-validation. Crucially, the optimized BTMS parameter constellation reduces mean absolute percentage error (MAPE) by 89.3% (from 0.1192 to 0.0127) in extreme-conditions simulations while maintaining Pareto optimality in energy-safety trade-offs.

(3) The Pareto-optimal solutions demonstrate robust multi-objective coordination. The extremities of the Pareto front offer singular benefits, minimizing temperature to 47 °C at the cost of significant power consumption (more than 1600 W) at one end (point A), or minimizing power to 150 W at the risk of breaching the 50 °C safety threshold at the other (point C). The optimized design focuses on the utopia point (point E). This balance point effectively regulates the peak battery temperature at 48.68 °C under concurrent harsh conditions (50 °C ambient temperature and 5C discharge rate). This achieves a 12.1% reduction in thermal fluctuation amplitude compared to the initial design and, through CPCM-assisted pre-cooling, maintains a low energy consumption of 158 W (5.9% reduction compared to other optimal solutions). This confirms that the utopia point provides the most effective compromise between preventing thermal runaway and ensuring economic viability.

Author Contributions: Methodology, Q.X., X.Z. and H.Z.; software, Q.X.; validation, Q.X.; formal analysis, Q.X., X.Z., T.Y. and H.Z.; investigation, Q.X. and X.Z.; data curation, X.Z.; writing—original draft, Q.X.; writing—review and editing, Q.X., T.Y., H.Z. and J.X.; visualization, J.X.; supervision, T.Y.; project administration, T.Y.; funding acquisition, Q.X. and H.Z. All authors have read and agreed to the published version of the manuscript.

Funding: This research was funded by the Joint Fund Project of Natural Science Foundation of Hubei Province, China, grant number 2025AFD087, and the National Natural Science Foundation of China, grant number 52476079. And The APC was funded by the Joint Fund Project of Natural Science Foundation of Hubei Province.

Data Availability Statement: The original contributions presented in this study are included in the article. Further inquiries can be directed to the corresponding author.

Acknowledgments: This research is funded by the Joint Fund Project of Natural Science Foundation of Hubei Province, China (2025AFD087), and the National Natural Science Foundation of China (52476079).

Conflicts of Interest: The authors declare no conflict of interest.

Nomenclature

C_p	specific heat capacity (J/kg·K)
k	thermal conductivity (W/m·K)
q	heat generation rate (W/m^3)
t	time (s)
T	temperature (K)
$\vec{v}$	velocity vector (m/s)
v	velocity (m/s)
Δp	pressure differential (Pa)
Subscripts	
b	battery
w	water
Greek symbols	
ρ	density (kg/m^3)
μ	dynamic viscosity (Pa·s)

https://doi.org/10.3390/batteries12030078

Acronyms

AL	aluminum
ANN	artificial neural network
BTMS	battery thermal management system
COP	coefficient of performance
CPCM	composite phase change material
EG	expanded graphite
GA	genetic algorithm
HP	heat pipe
LHS	Latin hypercube sampling
MSE	mean squared error
NSGA	on-dominated sorting genetic algorithm
PCM	phase change material
RSM	response surface methodology
TE	total expenditure

Appendix A

Table A1. A total of 96 sets of simulation sample data generated by COMSOL Multiphysics.

Number	EG (%)	T_w (°C)	v (m/s)	T_{max} (°C)	P_{total} (W)
1	3	32	0.01	55.58	167.77
2	3	32	0.05	55.08	838.87
3	3	32	0.1	54.56	1677.74
4	3	32	0.15	54.56	2516.62
5	3	33	0.01	56.38	158.44
6	3	33	0.05	55.88	792.2
7	3	33	0.1	55.3	1584.4
8	3	33	0.15	55.3	2376.77
9	3	34	0.01	57.18	149.12
10	3	34	0.05	56.68	745.6
11	3	34	0.1	56.13	1491.2
12	3	34	0.15	56.13	2236.96
13	3	35	0.01	57.98	139.8
14	3	35	0.05	57.48	699
15	3	35	0.1	56.9	1398
16	3	35	0.15	56.9	2097.15
17	6	32	0.01	51.74	167.77
18	6	32	0.05	51.27	838.87
19	6	32	0.1	50.69	1677.74
20	6	32	0.15	50.69	2516.62
21	6	33	0.01	52.55	158.44
22	6	33	0.05	52.05	792.2
23	6	33	0.1	51.55	1584.4
24	6	33	0.15	51.55	2376.77
25	6	34	0.01	53.37	149.12
26	6	34	0.05	52.87	745.6
27	6	34	0.1	52.37	1491.2
28	6	34	0.15	52.37	2236.96
29	6	35	0.01	54.21	139.8
30	6	35	0.05	53.71	699
31	6	35	0.1	53.2	1398
32	6	35	0.15	53.2	2097.15

https://doi.org/10.3390/batteries12030078

Table A1. *Cont.*

Number	EG (%)	T_w (°C)	v (m/s)	T_{max} (°C)	P_{total} (W)
33	9	32	0.01	49.28	167.77
34	9	32	0.05	48.74	838.87
35	9	32	0.1	48.2	1677.74
36	9	32	0.15	48.2	2516.62
37	9	33	0.01	50.08	158.44
38	9	33	0.05	49.58	792.2
39	9	33	0.1	49.04	1584.4
40	9	33	0.15	49.04	2376.77
41	9	34	0.01	50.93	149.12
42	9	34	0.05	50.43	745.6
43	9	34	0.1	49.9	1491.2
44	9	34	0.15	49.9	2236.96
45	9	35	0.01	51.79	139.8
46	9	35	0.05	51.2	699
47	9	35	0.1	50.7	1398
48	9	35	0.15	50.7	2097.15
49	12	32	0.01	48.54	167.77
50	12	32	0.05	48.04	838.87
51	12	32	0.1	47.54	1677.74
52	12	32	0.15	47.54	2516.62
53	12	33	0.01	49.32	158.44
54	12	33	0.05	48.82	792.2
55	12	33	0.1	48.3	1584.4
56	12	33	0.15	48.3	2376.77
57	12	34	0.01	50.16	149.12
58	12	34	0.05	49.66	745.6
59	12	34	0.1	49.1	1491.2
60	12	34	0.15	49.1	2236.96
61	12	35	0.01	51.03	139.8
62	12	35	0.05	50.53	699
63	12	35	0.1	50.03	1398
64	12	35	0.15	50.03	2097.15
65	20	32	0.01	48.04	167.77
66	20	32	0.05	47.54	838.87
67	20	32	0.1	47.01	1677.74
68	20	32	0.15	47.01	2516.62
69	20	33	0.01	48.78	158.44
70	20	33	0.05	48.28	792.2
71	20	33	0.1	47.78	1584.4
72	20	33	0.15	47.78	2376.77
73	20	34	0.01	49.64	149.12
74	20	34	0.05	49.12	745.6
75	20	34	0.1	48.62	1491.2
76	20	34	0.15	48.62	2236.96
77	20	35	0.01	50.52	139.8
78	20	35	0.05	50.02	699
79	20	35	0.1	49.52	1398
80	20	35	0.15	49.52	2097.15
81	30	32	0.01	47.86	167.77
82	30	32	0.05	47.34	838.87

https://doi.org/10.3390/batteries12030078

Table A1. *Cont.*

Number	EG (%)	T_w (°C)	v (m/s)	T_{max} (°C)	P_{total} (W)
83	30	32	0.1	46.79	1677.74
84	30	32	0.15	46.79	2516.62
85	30	33	0.01	48.58	158.44
86	30	33	0.05	48.03	792.2
87	30	33	0.1	47.53	1584.4
88	30	33	0.15	47.53	2376.77
89	30	34	0.01	49.44	149.12
90	30	34	0.05	48.94	745.6
91	30	34	0.1	48.5	1491.2
92	30	34	0.15	48.5	2236.96
93	30	35	0.01	50.32	139.8
94	30	35	0.05	49.82	699
95	30	35	0.1	49.3	1398
96	30	35	0.15	49.3	2097.15

References

1. Zhao, Y.; Zhang, X.; Yang, B.; Cai, S. A review of battery thermal management systems using liquid cooling and PCM. *J. Energy Storage* **2024**, *76*, 109836. [CrossRef]
2. Wang, C.; Xu, J.; Wang, M.; Xi, H. Experimental investigation on reciprocating air-cooling strategy of battery thermal management system. *J. Energy Storage* **2023**, *58*, 106406. [CrossRef]
3. Xie, J.; Liu, X.; Zhang, G.; Yang, X. A novel strategy to optimize the liquid cooling plates for battery thermal management by precisely tailoring the internal structure of the flow channels. *Int. J. Therm. Sci.* **2023**, *184*, 107877. [CrossRef]
4. Zare, P.; Perera, N.; Lahr, J.; Hasan, R. A novel thermal management system for cylindrical lithium-ion batteries using internal-external fin-enhanced phase change material. *Appl. Therm. Eng.* **2024**, *238*, 121985. [CrossRef]
5. Chung, W.S.; Lee, J.S.; Rhi, S.H. Thermal management system using pulsating heat pipe of cylindrical battery cell. *J. Mech. Sci. Technol.* **2023**, *37*, 6711–6725. [CrossRef]
6. Yang, T.; Su, S.; Xin, Q.; Zeng, J.; Zhang, H.; Zeng, X.; Xiao, J. Thermal Management of Lithium-Ion Batteries Based on Honeycomb-Structured Liquid Cooling and Phase Change Materials. *Batteries* **2023**, *9*, 287. [CrossRef]
7. Xin, Q.; Yang, T.; Zhang, H.; Zeng, J.; Xiao, J. Simulation and Optimization of Lithium-Ion Battery Thermal Management System Integrating Composite Phase Change Material, Flat Heat Pipe and Liquid Cooling. *Batteries* **2023**, *9*, 334. [CrossRef]
8. Xin, Q.; Xiao, J.; Yang, T.; Zhang, H.; Long, X. Thermal management of lithium-ion batteries under high ambient temperature and rapid discharging using composite PCM and liquid cooling. *Appl. Therm. Eng.* **2022**, *210*, 118230. [CrossRef]
9. Xin, Q.; Yang, T.; Zhang, H.; Yang, J.; Zeng, J.; Xiao, J. Experimental and numerical study of lithium-ion battery thermal management system using composite phase change material and liquid cooling. *J. Energy Storage* **2023**, *71*, 108003. [CrossRef]
10. Lyu, C.; Song, Y.; Yang, D.; Wang, W.; Zhu, S.; Ge, Y.; Wang, L. Surrogate model of liquid cooling system for lithium-ion battery using extreme gradient boosting. *Appl. Therm. Eng.* **2022**, *213*, 118675. [CrossRef]
11. Liu, Y.; Zhang, J. Design a J-type air-based battery thermal management system through surrogate-based optimization. *Appl. Energy* **2019**, *252*, 113426. [CrossRef]
12. Ma, K.; Wang, J.; Wang, Q.; Mao, Q. Numerical simulation of battery thermal management based on ring microchannel cold plate. *Int. J. Therm. Sci.* **2025**, *210*, 109563. [CrossRef]
13. Xu, X.; Su, Y.; Kong, J.; Chen, X.; Wang, X.; Zhang, H.; Zhou, F. Performance analysis of thermal management systems for prismatic battery module with modularized liquid-cooling plate and PCM-negative Poisson's ratio structural laminboard. *Energy* **2024**, *286*, 129620. [CrossRef]
14. Liu, Z.; Huadan, C.; Wang, B.; Li, P. Coupling optimization of protruding fin and PCM in hybrid cooling system and cycle strategy matching for lithium-ion battery thermal management. *Int. J. Therm. Sci.* **2025**, *207*, 109372. [CrossRef]
15. Lian, Y.; Ling, H.; Song, G.; Gong, K.; Fan, C.; Wang, F.; He, B. Optimization and thermal performance analysis of direct cooling plates with multi-splitting-merging channels for electric-vehicle battery thermal management. *Int. J. Therm. Sci.* **2025**, *214*, 109900. [CrossRef]
16. Sun, Z.; Fan, R.; Yan, F.; Zhou, T.; Zheng, N. Thermal management of the lithium-ion battery by the composite PCM-Fin structures. *Int. J. Heat Mass Transf.* **2019**, *145*, 118739. [CrossRef]

https://doi.org/10.3390/batteries12030078

17. Jin, L.; Xi, H. Multi-objective parameter optimization of the Z-type air-cooling system based on artificial neural network. *J. Energy Storage* **2024**, *86*, 111284. [CrossRef]
18. Zuo, W.; Li, D.; Li, Q.; Cheng, Q.; Zhou, K.; Jiaqiang, E. Multi-objective optimization of multi-channel cold plate under intermittent pulsating flow by RSM and NSGA-II for thermal management of electric vehicle lithium-ion battery pack. *Energy* **2023**, *283*, 129085. [CrossRef]
19. Bianco, N.; Somma, M.; Iasiello, M.; Menale, C.; Piccirillo, F.; Vellucci, F. Experimental and numerical electro-thermal analysis of a pouch cell battery accounting for connection bar effects via equivalent boundary conditions on tabs. *J. Energy Storage* **2026**, *147*, 119641. [CrossRef]
20. Bernardi, D.; Pawlikowski, E.; Newman, J. A general energy balance for battery systems. *J. Electrochem. Soc.* **1985**, *132*, 5–12. [CrossRef]
21. Piccirillo, F.; Iasiello, M.; Bianco, N. Thermal management of cylindrical lithium-ion batteries using internal and external phase change material placement. *Int. J. Numer. Methods Heat Fluid Flow* **2025**, 1–33. [CrossRef]
22. Alawadhi, E.M.; Amon, C.H. PCM thermal control unit for portable electronic devices: Experimental and numerical studies. *IEEE Trans. Compon. Packag. Technol.* **2003**, *26*, 116–125. [CrossRef]
23. Li, J.; Yang, J.; Sun, Y.; Ren, X. Performance analysis of battery thermal management system composed of copper foam/paraffin and wavy liquid cooling microchannels. *Renew. Energy* **2026**, *256*, 123928. [CrossRef]
24. Wang, Y.; Wang, Y.; He, T.; Mao, N. A numerical study on a hybrid battery thermal management system based on PCM and wavy microchannel liquid cooling. *Renew. Energy* **2024**, *235*, 121273. [CrossRef]
25. Jiang, G. *Study on Preparation of Composite Phase Change Material with High Thermal Conductivity and Its Application in Power Battery Thermal Management*; Nanchang University: Nanchang, China, 2017.
26. Jiang, G.; Huang, J.; Fu, Y.; Cao, M.; Liu, M. Thermal optimization of composite phase change material/expanded graphite for li-ion battery thermal management. *Appl. Therm. Eng.* **2016**, *108*, 1119–1125. [CrossRef]
27. Jiang, G.; Huang, J.; Liu, M.; Cao, M. Experiment and simulation of thermal management for a tube-shell li-ion battery pack with composite phase change material. *Appl. Therm. Eng.* **2017**, *120*, 1–9. [CrossRef]
28. Wang, J.; Yu, Y.; Song, L.; Yue, Y.; Zeng, W.; Mei, W.; Wang, Q. Thermal management performance and optimization of a novel system combining heat pipe and composite fin for prismatic lithium-ion batteries. *Energy Convers. Manag.* **2024**, *302*, 118106. [CrossRef]
29. Jiang, L.; Zhang, H.; Li, J.; Xia, P. Thermal performance of a cylindrical battery module impregnated9with PCM composite based on thermoelectric cooling. *Energy* **2019**, *188*, 116048. [CrossRef]
30. An, Z.; Liu, H.; Gao, W.; Gao, Z. Cooling and preheating performance of dual-active lithium-ion battery thermal management system under harsh conditions. *Appl. Therm. Eng.* **2024**, *242*, 122421. [CrossRef]
31. Available online: https://news.un.org/zh/story/2024/08/1130481 (accessed on 11 August 2024).
32. Xu, A.; Chang, H.; Xu, Y.; Li, R.; Li, X.; Zhao, Y. Applying artificial neural networks (ANNs) to solve solid waste-related issues: A critical review. *Waste Manag.* **2021**, *124*, 385–402. [CrossRef]
33. Li, A.; Yuen, A.C.Y.; Wang, W.; Weng, J.; Yeoh, G.H. Numerical investigation on the thermal management of lithium-ion battery system and cooling effect optimization. *Appl. Therm. Eng.* **2022**, *215*, 118966. [CrossRef]
34. Zhang, H.; Tian, Z. Failure analysis of corroded high-strength pipeline subject to hydrogen damage based on FEM and GA-BP neural network. *Int. J. Hydrogen Energy* **2022**, *47*, 4741–4758. [CrossRef]
35. Weigert, T.; Tian, Q.; Lian, K. State-of-charge prediction of batteries and battery–supercapacitor hybrids using artificial neural networks. *J. Power Sources* **2011**, *196*, 4061–4066. [CrossRef]
36. Ye, L.; Li, C.; Wang, C.; Zheng, J.; Zhong, K.; Wu, T. A multi-objective optimization approach for battery thermal management system based on the combination of BP neural network prediction and NSGA-II algorithm. *J. Energy Storage* **2024**, *99*, 113212. [CrossRef]
37. Deng, Z.; Hu, X.; Lin, X.; Che, Y.; Xu, L.; Guo, W. Data-driven state of charge estimation for lithium-ion battery packs based on Gaussian process regression. *Energy* **2020**, *205*, 118000. [CrossRef]
38. Liang, K.; Zhang, Y.; Wang, W.; Gao, C.; Chen, H.; Li, K.; Zhou, X.; Chen, B.; Cao, Y.; Wang, W.; et al. Performance analysis and multi-objective optimization of refrigerant-based integrated thermal management system for electric vehicles. *Appl. Therm. Eng.* **2024**, *244*, 122707. [CrossRef]
39. Liu, G.; Pu, L.; Zhao, H.; Chen, Z.; Li, G. Multi-objective optimization of CO_2 ejector by combined significant variables recognition, ANN surrogate model and multi-objective genetic algorithm. *Energy* **2024**, *295*, 131010. [CrossRef]
40. Luo, H.; Xiao, J.; Bénard, P.; Chahine, R.; Yang, T. Multi-objective optimization of cascade storage system in hydrogen refuelling station for minimum cooling energy and maximum state of charge. *Int. J. Hydrogen Energy* **2022**, *47*, 10963–10975. [CrossRef]

https://doi.org/10.3390/batteries12030078

41. Farsi, A.; Dincer, I.; Naterer, G.F. Multi-objective optimization of an experimental integrated thermochemical cycle of hydrogen production with an artificial neural network. *Int. J. Hydrogen Energy* **2020**, *45*, 24355–24369. [CrossRef]
42. Madani, S.S.; Shabeer, Y.; Allard, F.; Fowler, M.; Ziebert, C.; Wang, Z.; Panchal, S.; Chaoui, H.; Mekhilef, S.; Dou, S.X.; et al. A Comprehensive Review on Lithium-Ion Battery Lifetime Prediction and Aging Mechanism Analysis. *Batteries* **2025**, *11*, 127. [CrossRef]

https://doi.org/10.3390/batteries12030078

batteries

MDPI

Article

Performance Improvement of a Honeycomb Battery Thermal Management System Based on Fin–Casing Synergistically Enhanced Heat Transfer

Liang Tong [1], Xin Gong [2], Shenglin Su [2], Linzhi Xu [3,*], Min Liu [4], Lingyu Chen [4], Qianqian Xin [5], Tianqi Yang [6,*], Hengyun Zhang [7] and Jinsheng Xiao [6]

[1] State Key Laboratory of Maritime Technology and Safety, Wuhan University of Technology, Wuhan 430063, China; tongliang2@whut.edu.cn
[2] School of Automotive Engineering, Wuhan University of Technology, Wuhan 430070, China
[3] School of Naval Architecture, Ocean and Energy Power Engineering, Wuhan University of Technology, Wuhan 430063, China
[4] Research Institute of State Grid Zhejiang Electric Power Co., Ltd., Hangzhou 310006, China
[5] School of Mechanical Engineering, Wuhan Vocational College of Software and Engineering, Wuhan 430205, China
[6] State Key Laboratory of Light Superalloys, Wuhan University of Technology, Wuhan 430070, China
[7] School of Mechanical and Automotive Engineering, Shanghai University of Engineering Science, Shanghai 201620, China
* Correspondence: xulinzhi@whut.edu.cn (L.X.); tqyang@whut.edu.cn (T.Y.)

Abstract

With the continuous rise in the energy density of power batteries, battery heat generation has become an increasingly severe issue. Particularly under extreme conditions combining high summer temperatures and high discharge rates, battery thermal safety is facing tremendous challenges. To address this problem, this study proposes a honeycomb liquid cooling–PCM hybrid battery thermal management system (BTMS) based on fin–casing synergistic heat transfer enhancement. We analyzed the effects of the longitudinal fins and thermal conductive casing on the thermal characteristics of the system, further investigated the influence patterns of key factors including fin number, battery spacing and contact thermal resistance on the thermal performance of the honeycomb BTMS, and clarified the action mechanisms of each structure and parameter on battery temperature rise and temperature uniformity. The results show that the fin structure enhances longitudinal heat conduction, improves liquid cooling efficiency, and effectively reduces the maximum battery temperature, while the thermal conductive casing significantly improves battery temperature uniformity. The BTMS with fin–casing synergistic heat transfer enhancement can control the maximum battery temperature and temperature difference within 60 °C and 5 °C, respectively, under extreme operating conditions.

Keywords: lithium-ion battery; honeycomb structure; battery thermal management system; fins-casing synergy; heat transfer

1. Introduction

The performance of lithium-ion batteries is closely correlated with operating temperature. Typically, the operational temperature range for lithium-ion batteries spans from −20 °C to 60 °C [1], with strict control required to maintain a maximum temperature difference (ΔT_{max}) within 5 °C across individual cells in a module and on cell surfaces [2,3].

Exceeding thermal safety thresholds may lead to irreversible battery degradation, underscoring the criticality of efficient battery thermal management systems (BTMSs) for ensuring the safety and performance of electric vehicles (EVs).

Current BTMS methodologies encompass air cooling [4], liquid cooling [5], phase change material (PCM) cooling [6], and hybrid cooling systems [7,8]. Air cooling, characterized by a simple structure, low cost, and zero leakage risk, has been widely adopted in early EV models and low-power energy storage devices [9]. However, air's low specific heat capacity and thermal conductivity render air-cooled systems insufficient for dissipating high heat flux during high-rate charge/discharge cycles, often resulting in poor thermal uniformity [10].

Liquid cooling regulates battery temperature through the convective heat transfer of liquid media, primarily implemented via cold-plate channel structures [11] or immersion designs [12,13]. The mini-channel design for liquid cooling systems can significantly increase the heat transfer specific surface area [14]. Nevertheless, liquid cooling systems rely on active pump-driven circulation, leading to complex system architectures, a delayed transient response to high thermal loads, and challenges in achieving efficient thermal uniformity within confined spaces [15].

PCM, as a passive cooling medium, suppresses temperature rise by absorbing latent heat during solid–liquid phase transitions [16]. However, pure PCM suffers from low thermal conductivity [17], limiting heat diffusion into deeper regions and reducing material utilization efficiency. Additionally, once melted, pure PCM requires auxiliary cooling mechanisms to re-solidify and restore its thermal storage capacity.

To address PCM's low thermal conductivity, three enhancement strategies are commonly employed: incorporating high-conductivity nanosuspensions, integrating porous media composites [18,19], and embedding metal foams or fins to construct high-conductivity pathways. Swamy et al. [20] demonstrated that CuO or Al_2O_3 nanoparticles significantly improve PCM thermal conductivity, albeit at the cost of exponential viscosity increases. Vali et al. [21] successfully maintained battery module peak temperatures within safety limits during 3C discharge by introducing multi-walled carbon nanotubes and graphene nanoplatelets. Zhou et al. [22] found that 20 wt% expanded graphite (EG) forms a continuous thermal conduction framework, enhancing thermal conductivity by 418.5%. Yang et al. [23] developed a composite PCM–liquid cooling honeycomb structure with 12% EG content, reducing the maximum battery temperature by 4.39 °C compared to pure PCM-based BTMS. Zang et al. [24] achieved a thermal conductivity of 4.75 W/(m·K) using paraffin–EG and aluminum foam composites. Keyhani-Asl et al. [25] confirmed that copper foam can multiply the equivalent thermal conductivity, with over 90% porosity effectively suppressing temperature rise during phase transitions. However, nanoparticle agglomeration and sedimentation, potential corrosion risks from sulfur residues in carbon-based material synthesis, and the high manufacturing costs/weight of metal foams remain critical challenges.

Fin-integrated structures for constructing thermal conduction frameworks focus on fin geometry innovation and hybrid system topology optimization. Luo et al. [26] designed fractal snowflake fins with high perimeter–area ratios, enabling deep PCM matrix penetration and achieving temperature differences below 3 °C under 3C conditions. Shen et al. [27] and Wu et al. [28] proposed web-like and gear-shaped fins, respectively, which enhanced isotropic thermal networks and expanded solid–liquid phase interfaces to eliminate hotspots and accelerate phase-transition propagation. Esmaeili et al. [29] demonstrated the irreplaceable advantages of fin–PCM systems over air cooling in high-load pulse scenarios, combining conductive pathways with PCM thermal buffering capacity. Wang et al. [30] integrated fins with heat pipes, leveraging the latter's ultra-high thermal conductivity to

https://doi.org/10.3390/batteries12030094

instantaneously transfer heat from battery surfaces to remote fin regions, ideal for space-constrained prismatic battery modules. These studies confirm that a fin-enhanced BTMS offers structural simplicity, cost control, and stable thermal performance across diverse battery configurations.

However, most published studies have focused primarily on ambient temperatures below 40 °C, while the National Standard GB38031-2020 [31] Safety Requirements for Traction Battery Packs and Systems of Electric Vehicles stipulates that the maximum allowable discharge temperature for cylindrical lithium-ion batteries is 60 °C. In actual driving processes, vehicles operate under working conditions such as rapid acceleration, climbing and full load, all of which demand high-rate discharge of batteries. In high-temperature regions in summer, the ground surface temperature can usually exceed 60 °C; during charging and discharging, batteries generate a large amount of heat on the one hand, and are exposed to baking by high-temperature ambient air from the ground on the other. If heat fails to be dissipated in a timely manner, the battery temperature will most likely exceed the safe temperature [32,33]. Furthermore, although the incorporation of metal fins into PCM can enhance heat transfer, most relevant studies have focused primarily on the regulation of the maximum or average battery temperature by fin structures in cylindrical BTMSs, whereas relatively little attention has been paid to their effects on novel configurations such as honeycomb-structured BTMSs and battery temperature uniformity. Honeycomb-structured BTMSs not only feature a compact layout, but also can effectively suppress the leakage of liquid PCM [34] and mitigate the hazards caused by battery thermal runaway [35], thus exhibiting prominent application advantages. In addition, a large internal temperature difference in the battery pack is prone to induce uneven current distribution and the generation of thermal stress, which in turn degrades battery performance and shortens its service life [36].

According to the background, this study addresses the extreme harsh working condition of 5C high-rate battery discharge at an ambient temperature of 50 °C and proposes a honeycomb-structured liquid cooling–PCM hybrid BTMS based on the synergistic heat transfer enhancement of longitudinal fins and thermal conductive casing. Based on the COMSOL Multiphysics 6.2 platform [37], four numerical models of a honeycomb BTMS with different combinations of longitudinal fins and a thermally conductive casing were developed. Numerical simulations were conducted to investigate the effects of the fin structures and conductive casing on the system heat dissipation performance, battery temperature uniformity, and PCM phase change behavior under ambient temperatures of 30, 40, and 50 °C and counter-flow coolant configurations. Subsequently, the single-factor analysis method was adopted to investigate the influences of battery spacing and contact thermal resistance on the thermal performance, battery temperature uniformity and module grouping efficiency of the honeycomb-structured BTMS with synergistic heat transfer enhancement by longitudinal fins and a thermal conductive casing.

2. Numerical Model

2.1. Geometric Model and Thermophysical Parameters

Figure 1 illustrates the structure and simplified model of the honeycomb BTMS. Cylindrical battery cells are arranged in a staggered configuration within the module, with each cell surrounded by six liquid-cooled tubes (inner diameter: 3 mm, wall thickness: 1 mm). Adjacent liquid-cooled tubes are connected via thermal conductive fins, and the internal cavities of the tubes are filled with PCM, forming a honeycomb unit structure, as shown in Figure 1a.

Based on the symmetry of the battery module, the module is simplified to a single-cell model, which comprises a cylindrical battery, PCM, liquid-cooled tubes, and their thermal

https://doi.org/10.3390/batteries12030094

conductive plates. The implementation of staggered counter-flow cooling fluid enhances temperature uniformity [14], as depicted in Figure 1b.

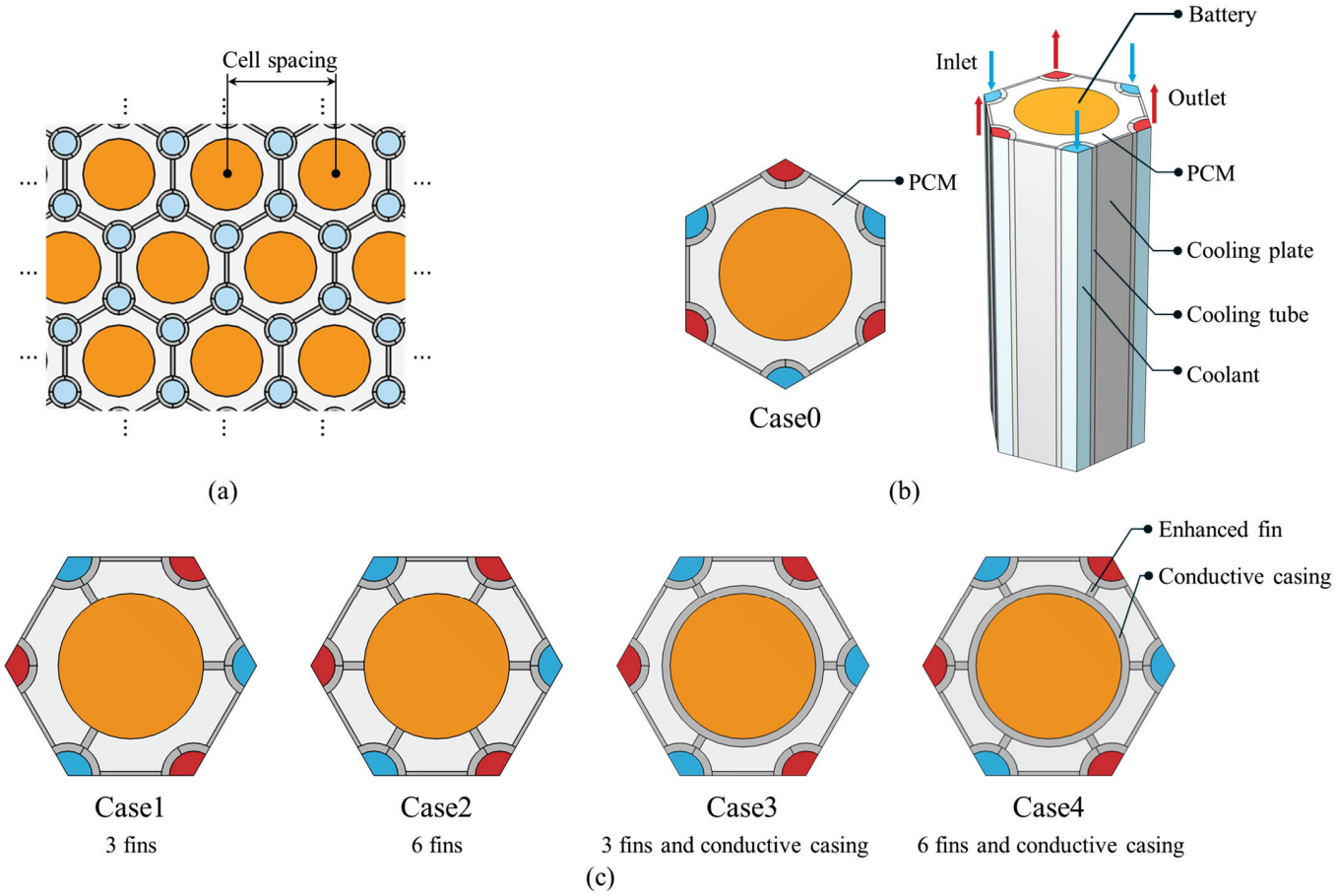

Figure 1. Schematic of the honeycomb BTMS: Structural diagram of the battery module (**a**); simplified model (**b**); enhanced model with longitudinal fins and thermal conductive casing (**c**).

In this study, on the basis of the simplified honeycomb BTMS, longitudinal fins with a thickness of 1 mm and a thermal conductive casing are introduced to strengthen the internal heat transfer of the module, and four models are constructed, as presented in Figure 1c. The INR18650/25P cylindrical lithium-ion battery is adopted in this research, which has a rated capacity of 2500 mAh, supports high-rate discharge, and exhibits an allowable operating temperature range of −20 °C to 60 °C for discharge. High-purity paraffin RT54HC was adopted in this study, with a solid–liquid phase change temperature of 53–54 °C. The detailed physical properties of the battery, PCM and aluminum alloy are summarized in Table 1.

Table 1. Thermophysical properties of the battery and key materials.

Material	Property	Value	Unit
INR18650/25P	Nominal Capacity	2500	mAh
	Nominal Voltage	3.6	V
	Battery Height	65.00 ± 0.15	mm
	Battery Diameter	18.35 ± 0.10	mm
	Battery Weight	48	g
	Density	2755.9	kg/m^3
	Specific Heat Capacity	1129.95	J/(kg·K)
	Thermal Conductivity	Radial 1.6; Axial 27	W/(m·K)

https://doi.org/10.3390/batteries12030094

Table 1. *Cont.*

Material	Property	Value	Unit
RT-54HC	Melting Point	53–54	°C
	Density	800	kg/m^3
	Specific Heat Capacity	2000	J/(kg·K)
	Thermal Conductivity	0.2	W/(m·K)
	Latent Heat	200	kJ/kg
Water	Density Liquid	998	kg/m^3
	Dynamic Viscosity	1.01×10^{-3}	kg/(m·s)
	Specific Heat Capacity	4180	J/(kg·K)
	Thermal Conductivity	0.599	W/(m·K)
Aluminum	Density	2719	kg/m^3
	Specific Heat Capacity	871	J/(kg·K)
	Thermal Conductivity	238	W/(m·K)

2.2. Governing Equations

2.2.1. Heat Generation and Heat Transfer Model of Lithium-Ion Batteries

In this study, the battery is assumed to be a homogeneous solid with a constant specific heat capacity. The thermal conductivities in the radial, axial, and circumferential directions are anisotropic but constant, and the internal heat generation rate of the battery is assumed to be uniform.

The battery heat generation model adopted in this study is based on the heat generation rates obtained from the research group's previous work, which were used to simulate the internal heat generation during battery discharge. Specifically, the dynamic internal resistance of the battery was measured using the hybrid pulse power characterization (HPPC) method under various discharge rates, including 5C, over a state-of-charge (SOC) range from 0.1 to 1.0. The nonlinear dependence of internal resistance on discharge rate and SOC was thus characterized. Subsequently, constant-current discharge temperature-rise experiments were conducted, during which real-time data of the current, terminal voltage, and surface temperature were recorded throughout the entire discharge process at different discharge rates.

Based on these measurements, the classical Bernardi heat generation equation [38] was employed to calculate the total heat generation, which was decomposed into two components: irreversible heat generated by ohmic and polarization effects, and reversible heat associated with the entropy change in electrochemical reactions. By integrating the resistance–voltage correlation data obtained from the HPPC tests with the experimentally measured transient data from the temperature-rise experiments, and further utilizing the conversion relationship between SOC and discharge time, the volumetric heat generation rate of the battery over the entire SOC range at different discharge rates was accurately determined. Finally, sixth-order polynomial expressions describing the variation in battery heat generation rate with discharge time under different discharge rates were obtained by curve fitting [23].

The governing equations for the heat transfer process of the battery are as follows:

$$\rho_{\mathrm{b}} C_{p,\mathrm{b}} \frac{\partial T_{\mathrm{b}}}{\partial t} = \nabla \cdot \left(\begin{pmatrix} \lambda_{\mathrm{bx}} & 0 & 0 \\ 0 & \lambda_{\mathrm{by}} & 0 \\ 0 & 0 & \lambda_{\mathrm{bz}} \end{pmatrix} \nabla T_{\mathrm{b}} \right) + Q_v \quad (1)$$

where ρ_{b} denotes the density of the battery, in units of kg/m^3; $C_{p,\mathrm{b}}$ represents the specific heat capacity of the battery, in units of J/(kg·K); λ_{bx}, λ_{by}, and λ_{bz} are the thermal conduc-

https://doi.org/10.3390/batteries12030094

tivities of the battery in three orthogonal directions; and Q_v denotes the heat generated by the battery, in units of W/m^3.

2.2.2. PCM Model

In this study, PCM is assumed to be a homogeneous medium with thermal conductivity in all directions. The thermophysical properties of the solid and liquid phases, including density, specific heat capacity, and thermal conductivity, are assumed to be identical and temperature-independent constants. The liquid phase region is simplified as an incompressible fluid, and natural convection is neglected [39].

The energy conservation equation is expressed as follows:

$$\rho_{\mathrm{PCM}} C_{p,\mathrm{PCM}} \frac{\partial T_{\mathrm{PCM}}}{\partial t} = \nabla \cdot (\lambda_{\mathrm{PCM}} \nabla T_{\mathrm{PCM}}) - \rho_{\mathrm{PCM}} L \frac{\partial \beta}{\partial t} \tag{2}$$

$$\beta = \begin{cases} 0, & T \le T_{\mathrm{sol}} \\ \dfrac{T - T_{\mathrm{sol}}}{T_{\mathrm{liq}} - T_{\mathrm{sol}}}, & T_{\mathrm{sol}} < T < T_{\mathrm{liq}} \\ 1, & T \ge T_{\mathrm{liq}} \end{cases} \tag{3}$$

where T_{PCM} denotes the temperature of PCM, in units of K; ρ_{PCM} is the density of the PCM, in units of kg/m^3; $C_{p,\mathrm{PCM}}$ represents the specific heat capacity of the PCM, in units of J/(kg·K); λ_{PCM} and L are the thermal conductivity (W/(m·K)) and latent heat (J/kg) of the PCM, respectively. The last term on the right-hand side of Equation (2) characterizes the release or absorption of latent heat during the phase change process of the PCM. The liquid volume fraction β is defined as a function of temperature, as illustrated in Equation (3).

2.2.3. Liquid Cooling Model

In this study, a pipe-type liquid cooling structure is adopted, with water as the coolant, which is treated as an incompressible fluid. Calculations show that the Reynolds number (Re) of the fluid in all simulation cases is lower than the critical laminar–turbulent value (2300) [23]; thus, the flow in the fluid domain is solved using the laminar flow model. The fluid flow and heat transfer processes are governed by the equations of mass conservation, momentum conservation, and energy conservation, as presented below:

$$\frac{\partial \rho_{\mathrm{c}}}{\partial t} + \nabla \cdot \left(\rho_{\mathrm{c}} \vec{u} \right) = 0 \tag{4}$$

$$\rho_{\mathrm{c}} \frac{\partial \vec{u}}{\partial t} + \rho_{\mathrm{c}} \left(\vec{u} \cdot \nabla \right) \vec{u} = -\nabla p + \nabla \left[\mu \left(\nabla \vec{u} + \left(\nabla \vec{u} \right)^T \right) \right] \tag{5}$$

$$\rho_{\mathrm{c}} C_{p,\mathrm{c}} \frac{\partial T}{\partial t} + \nabla \cdot \left(\rho_{\mathrm{c}} c_{p,\mathrm{c}} \vec{u} T \right) = \nabla \cdot (\lambda_{\mathrm{c}} \nabla T) \tag{6}$$

where ρ_{c} is the density of the coolant (kg/m^3), $\vec{u}$ is the velocity vector (m/s), and p is the static pressure (Pa); $C_{p,\mathrm{c}}$ and λ_{c} are the specific heat capacity (J/(kg·K)) and thermal conductivity (W/(m·K)) of the coolant, respectively; μ denotes the dynamic viscosity($N \cdot s/m^2$).

2.3. Initial and Boundary Conditions

The honeycomb BTMS exhibits geometric symmetry in its arrangement. Thus, symmetric boundary conditions are applied to the side surfaces of both the solid and fluid domains in the simplified model. The top and bottom surfaces of the model were treated as adiabatic boundaries, and the effect of natural convection with the ambient air was

https://doi.org/10.3390/batteries12030094

neglected. The heat exchange between the battery, PCM, fin structure, and cooling water is dominated by thermal conduction and thermal convection, with the specific expressions provided below:

$$-\lambda_{\mathrm{b}}\frac{\partial T_{\mathrm{b}}}{\partial n_{\mathrm{b}}} = -\lambda_{\mathrm{PCM}}\frac{\partial T_{\mathrm{PCM}}}{\partial n_{\mathrm{PCM}}} \tag{7}$$

$$-\lambda_{\mathrm{b}}\frac{\partial T_{\mathrm{b}}}{\partial n_{\mathrm{b}}} = -\lambda_{\mathrm{Al}}\frac{\partial T_{\mathrm{Al}}}{\partial n_{\mathrm{Al}}} \tag{8}$$

$$-\lambda_{\mathrm{PCM}}\frac{\partial T_{\mathrm{PCM}}}{\partial n_{\mathrm{PCM}}} = -\lambda_{\mathrm{Al}}\frac{\partial T_{\mathrm{Al}}}{\partial n_{\mathrm{Al}}} \tag{9}$$

$$-\lambda_{\mathrm{Al}}\frac{\partial T_{\mathrm{Al}}}{\partial n_{\mathrm{Al}}} = h_c(T_{\mathrm{Al}} - T_{\mathrm{c}}) \tag{10}$$

where λ_{b}, λ_{PCM}, and λ_{Al} are the thermal conductivities of the battery, PCM, and fin structure, respectively, in W/(m·K); h_c is the convective heat transfer coefficient between cooling water and the liquid-cooled tube wall, in W/(m^2·K); T_{b}, T_{PCM}, T_{Al}, and T_{c} denote the temperatures of the battery, PCM, fin structure, and cooling water, respectively, in K.

In addition, the initial conditions were set as $T = T_{am}$ and $v = v_0$, where T_{am} denotes the initial temperature of the BTMS and v_0 represents the inlet velocity of the coolant. A velocity-inlet boundary condition was applied at the inlet, while a pressure-outlet boundary condition was specified at the outlet. According to relevant studies, a coolant flow velocity of 0.1 m/s can generally meet the heat dissipation requirement with low pump power consumption [27,40]. Therefore, 0.1 m/s is selected as the inlet flow velocity of the coolant.

2.4. Model Verification

The simplified baseline honeycomb BTMS model adopted in this study is derived from the pre-validated work of the research group [23]. The simulation results based on the COMSOL platform demonstrate that the proposed model can accurately reproduce the dynamic temperature-rise behavior of the battery under discharge rates ranging from 1C to 5C. In comparison with the experimental data, the maximum relative error of the simulation results is approximately 4%, and the root mean square errors (RMSEs) at different discharge rates are maintained at low levels of 0.45, 0.60, 0.75, and 0.38, respectively, indicating that the model accuracy satisfies the requirements for numerical simulation.

In addition, grid independence verification was conducted for the six-fin model with a thermal conductive casing under an ambient temperature of 50 °C, involving six groups of meshes with the number ranging from 5940 to 175,000. As shown in Figure 2, the maximum battery temperature exhibits a convergence trend of first increasing and then stabilizing with the increase in mesh number: in the sparse mesh regime (mesh number < 109,200), the calculation results are significantly affected by the mesh density. When the mesh number increases from 109,200 to 121,600, the maximum battery temperature rises by only 0.002 °C, with a relative deviation of less than 0.01%, indicating that the numerical solution satisfies the grid independence criteria. Further mesh refinement to 175,000 thereafter results in only negligible temperature variations. Considering both solution accuracy and computational cost, the meshing scheme with 109,200 mesh elements was selected for the subsequent studies in this work, and the mesh distribution is presented in Figure 3.

https://doi.org/10.3390/batteries12030094

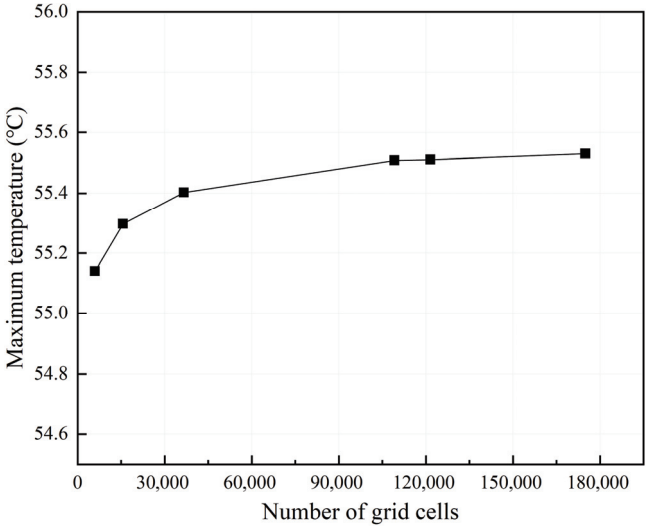

Figure 2. Grid independence verification.

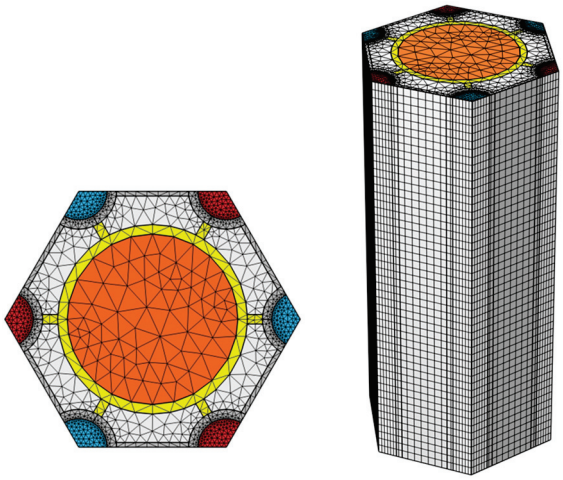

Figure 3. Meshing of the BTMS Model.

3. Results and Discussion

3.1. Thermal Performance Analysis of Honeycomb BTMS with Fins

Adding fins can improve the heat dissipation performance of the BTMS. In this section, the honeycomb BTMS without fins is taken as the baseline (Case 0). Case 1 and Case 2 are equipped with three and six longitudinal aluminum fins, respectively, and all fins are directly connected to the side surfaces of the battery cells and the liquid-cooled tube wall, as shown in Figure 4. The effects of fin configuration on the system heat dissipation performance, battery temperature uniformity, and PCM phase-transition process are investigated. Three ambient temperatures of 30 °C, 40 °C, and 50 °C are set for the simulations, with the battery discharged at a constant current of 5C and the coolant flow rate fixed at 0.1 m/s.

Figure 5 displays the temperature contour plots of the central cross-sections for the fin configuration models under three ambient temperatures. Case 0 exhibits concentric circular isotherms, with heat accumulating at the battery center to form a high-temperature region. Case 1 forms three low-temperature nodes at the fin connections, presenting a "triangular" contour pattern; in contrast, Case 2 displays a "petal-like" temperature field, where six low-temperature nodes are created at the interfaces between the six fins and the battery, dividing the high-temperature region into six smaller areas. Compared with Case

https://doi.org/10.3390/batteries12030094

0, both Case 1 and Case 2 have a higher proportion of low-temperature color scales in their contour plots, indicating a reduction in battery temperature.

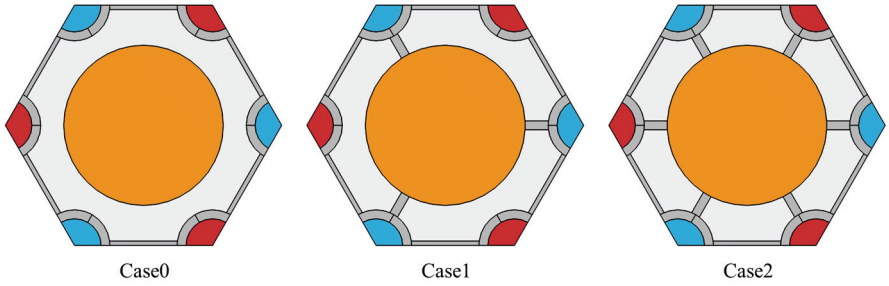

Figure 4. Schematic of the honeycomb BTMS with longitudinal fins: Case 0 (baseline, without fins), Case 1 (3 fins), and Case 2 (6 fins).

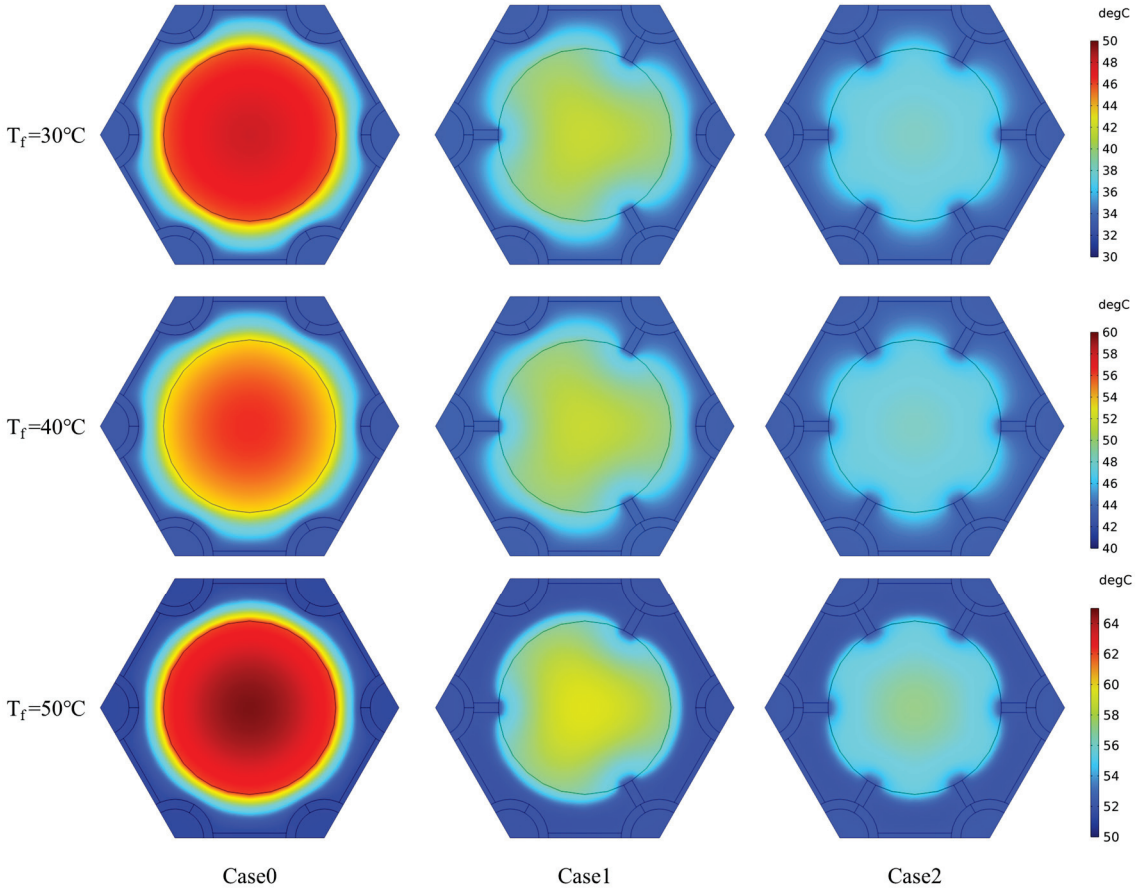

Figure 5. Temperature distribution of the central cross-section of the BTMS for Cases 0, 1 and 2 under different ambient temperatures.

Figure 6 presents the temperature variation curves of the battery under different ambient temperatures. After adding fins, the maximum temperature of the battery decreases significantly, with Case 2 (six fins) achieving the largest reduction. Conversely, ΔT_{max} of the battery increases sharply with the introduction of fins, rapidly exceeding the uniformity requirement of 5 °C. Notably, ΔT_{max} of Case 2 is lower than that of Case 1, demonstrating that increasing the number of fins can partially mitigate the non-uniformity of battery temperature distribution, yet fails to meet the minimum uniformity requirement.

https://doi.org/10.3390/batteries12030094

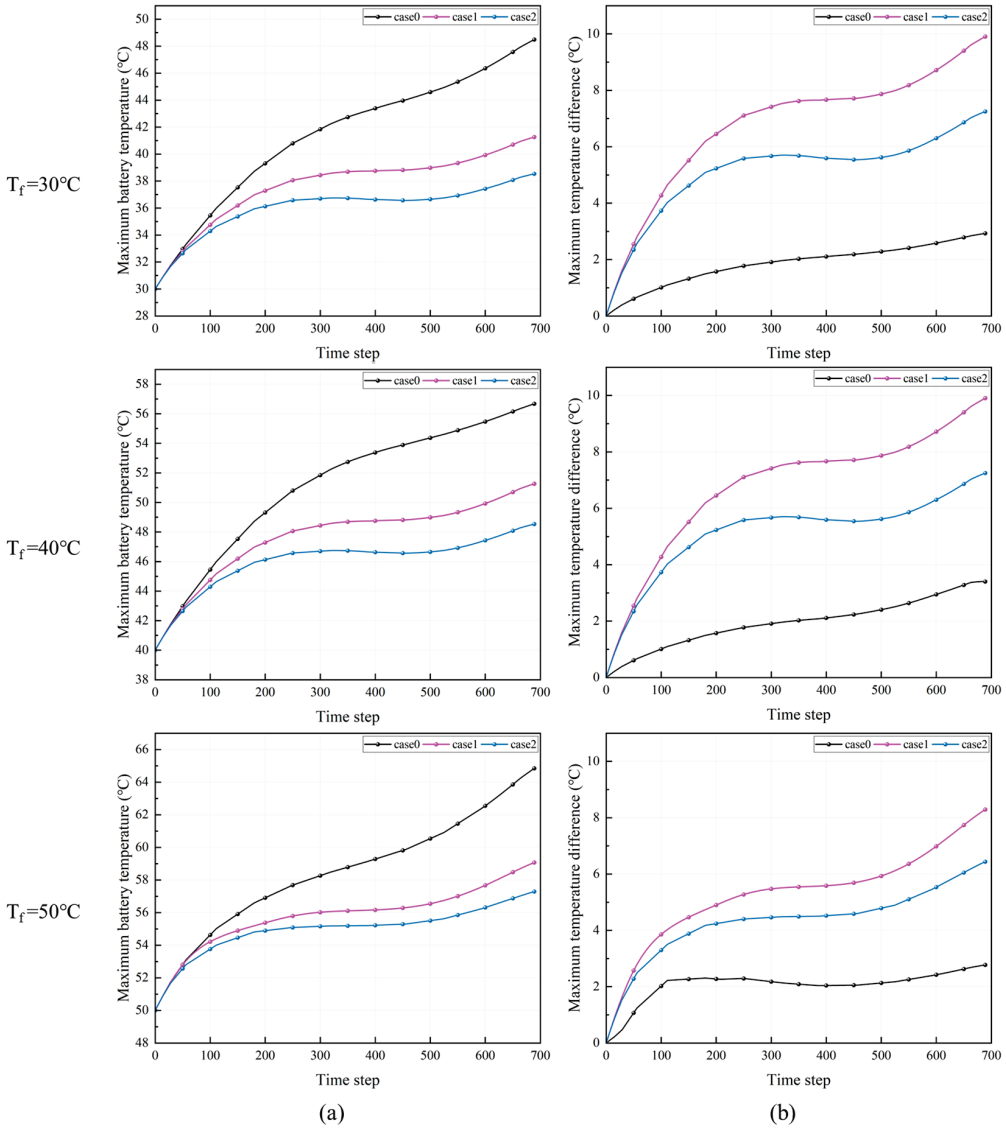

Figure 6. Maximum battery temperature (**a**) and maximum temperature difference in the battery (**b**) during the discharge process of Cases 0, 1 and 2 under different ambient temperatures.

Figure 7 summarizes the maximum temperature and the maximum temperature difference in the batteries in three honeycomb BTMS configurations at the end of discharge. As shown in Figure 7a, under conventional operating conditions with ambient temperatures of 30 °C and 40 °C, all three configurations can maintain the maximum battery temperature within the safe range. In contrast, under the extreme condition of 50 °C, the maximum temperature of Case 0 increases to 64.8 °C, exceeding the discharge safety limit of 60 °C specified by GB 38031-2020.

With the introduction of fin structures, the maximum temperature of Case 1 under the 50 °C condition is reduced to 59.1 °C, corresponding to a temperature decrease of 5.7 °C, which represents an approximately 8.8% reduction. Case 2 further lowers the maximum temperature to 57.3 °C, achieving a decrease of 7.5 °C, equivalent to a reduction of about 11.6%. These results indicate that the fin structures significantly enhance the heat dissipation capability of the system, with Case 2 exhibiting the most pronounced cooling performance.

https://doi.org/10.3390/batteries12030094

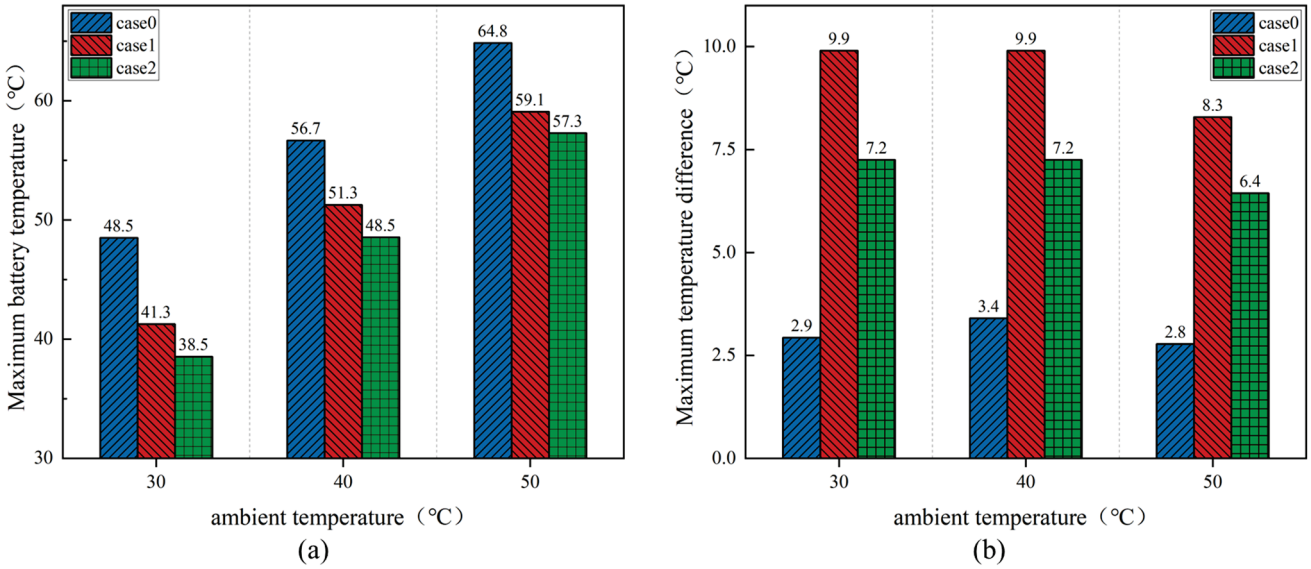

Figure 7. Maximum battery temperature (**a**) and maximum temperature difference in the battery (**b**) for Case 0, 1 and 2 at the end of discharge.

The results of the maximum temperature difference shown in Figure 7b reveal that, under the 30 °C and 40 °C conditions, the maximum temperature differences in Case 1 and Case 2 increase by approximately 7.0 °C and 4.3 °C, respectively, compared with Case 0, indicating that the fin structures adversely affect temperature uniformity. Under the 50 °C condition, although the maximum temperature difference decreases slightly, it still increases by 5.5 °C and 3.6 °C relative to Case 0, corresponding to increments of as high as 196% and 129%, respectively. Further comparison shows that both the maximum temperature and the maximum temperature difference in Case 2 are consistently lower than those of Case 1, suggesting that increasing the number of fins can enhance heat dissipation while partially alleviating temperature non-uniformity. Overall, although fin structures can effectively reduce the maximum battery temperature, they simultaneously lead to a significant deterioration in the temperature uniformity of the system.

For Case 0 without fins, the heat transfer pathway consists of the battery outer surface, PCM, honeycomb framework, liquid cooling tube wall, and coolant, forming a purely series thermal resistance network. By comparing the thermal conductivities of each component, it can be found that the PCM contributes to the dominant thermal resistance, resulting in a relatively high overall thermal resistance of the system. Consequently, the heat generated by the battery cannot be effectively transferred to the liquid cooling side in a timely manner, leading to limited heat dissipation performance. Under the extreme condition of 50 °C, this drawback becomes particularly pronounced, and the maximum temperature of Case 0 rises to 64.8 °C. On the other hand, since the battery is uniformly surrounded by homogeneous PCM in the circumferential direction, the radial thermal resistance distribution is nearly uniform, which contributes to good temperature uniformity. As a result, the maximum temperature difference in the battery does not exceed 3.4 °C under all three ambient temperature conditions.

For Case 1 and Case 2 with fins, parallel heat conduction pathways composed of fins and PCM are established between the battery surface and the honeycomb framework as well as the liquid cooling tubes. Owing to the much higher thermal conductivity of the fins compared with that of PCM, the equivalent thermal resistance of the parallel configuration is significantly reduced relative to that of pure PCM, leading to a substantial decrease in the overall thermal resistance of the BTMS. Consequently, the heat generated by the battery can be rapidly transferred through the low-resistance fin pathways, thereby

https://doi.org/10.3390/batteries12030094

effectively enhancing the heat dissipation performance. Under the 50 °C condition, the maximum temperatures of Case 1 and Case 2 decrease to 59.1 °C and 57.3 °C, respectively, corresponding to reductions of 5.7 °C and 7.5 °C compared with Case 0, which significantly improves the cooling performance under high ambient temperatures.

However, the parallel heat conduction structure also results in a non-uniform circumferential distribution of thermal resistance. Low-resistance pathways are formed in the regions connected to the fins, while the PCM regions between adjacent fins retain relatively high thermal resistance. The pronounced contrast between these regions generates large temperature gradients along the battery surface, thereby deteriorating temperature uniformity. As a result, the maximum temperature differences in Case 1 and Case 2 are consistently much higher than that of Case 0 under all operating conditions. In particular, under the 50 °C condition, they reach 8.3 °C and 6.4 °C, representing increases of 196% and 129%, respectively, relative to Case 0.

Under the ambient temperature of 50 °C, phase change occurs in the PCM of Case 0, Case 1, and Case 2, as illustrated in Figure 8. The PCM undergoes uniform phase change melting along the circumferential direction of the battery without fins. After adding fins, a large amount of heat is conducted out through the fins, and the region where the PCM is completely melted is significantly reduced. In addition, with the increase in the number of fins, the liquid fraction of PCM near the liquid-cooled tube increases, which reduces the distribution difference in the solid–liquid phases of the PCM and improves the distribution uniformity.

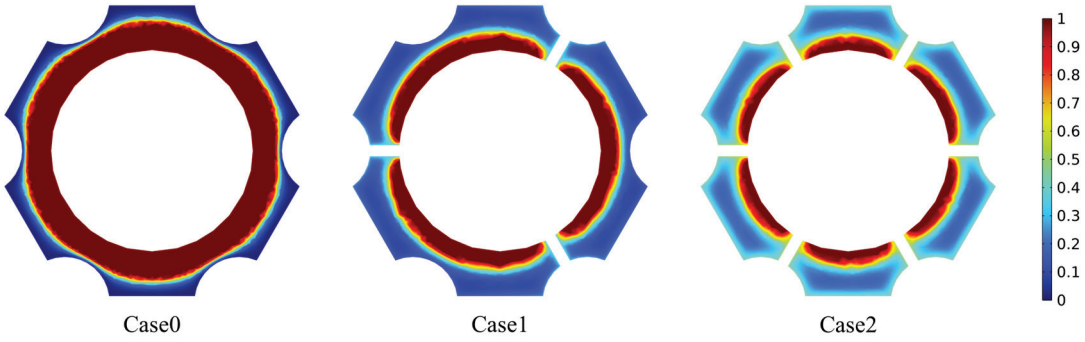

Figure 8. Distribution of the liquid fraction of PCM at the central cross-section of Cases 0, 1, and 2 at the end of discharge under an ambient temperature of 50 °C.

Figure 9 presents the time evolution curve of the average liquid fraction of the PCM: after the addition of fins, the liquid fraction of the PCM is reduced by nearly half. This means that more PCM remains in the solid state, storing more latent heat, which enhances the thermal safety redundancy of the system and provides an effective buffer against battery temperature rise under extreme operating conditions or thermal accumulation during long-term cycling. Mechanistically, the increase in the number of fins expands the contact area between the fins and the PCM, and improves the heat transfer in the PCM along the circumferential direction, resulting in a more uniform temperature distribution of the PCM. This facilitates the stable and full utilization of the latent heat absorption capacity of the PCM under subsequent thermal loads.

In summary, the addition of fins alone gives rise to a contradiction between heat dissipation performance and temperature uniformity. While fins can effectively suppress the maximum battery temperature and delay the latent heat consumption of PCM, they significantly deteriorate the temperature uniformity of the BTMS. This phenomenon is primarily attributed to the non-uniform distribution of local thermal resistance between the fin-contact region and the non-contact region. Therefore, enhancing the circumferential

https://doi.org/10.3390/batteries12030094

thermal conductivity of the battery surface could, in theory, maintain the efficient heat dissipation of fins while balancing the circumferential thermal resistance distribution. This hypothesis will be verified in the subsequent section of this study.

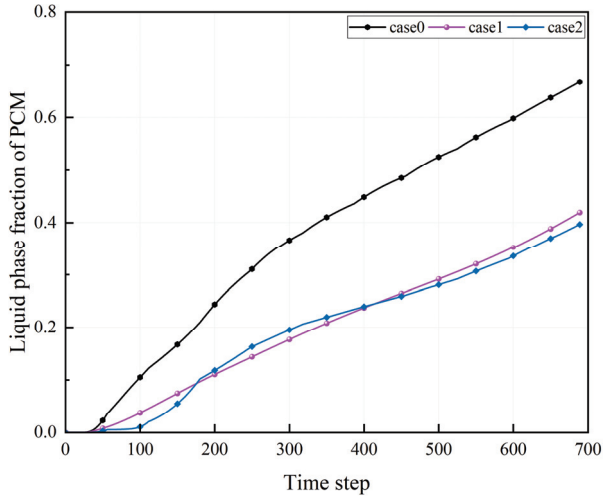

Figure 9. Average liquid-phase fraction of PCM in Cases 0, 1, and 2 during the discharge process at an ambient temperature of 50 °C.

3.2. Thermal Performance Analysis of Fin—Casing Honeycomb BTMS

Previous research in the preceding section indicated that adding fins causes an excessive maximum temperature difference in the honeycomb BTMS. In this section, a high-thermal-conductivity aluminum alloy casing with a thickness of 1 mm is introduced to evaluate its effect on the comprehensive heat dissipation performance of the system in the fin-integrated honeycomb BTMS. As shown in Figure 10, the thermal casing is tightly wrapped around the surface of the cylindrical battery, with both ends of the fins connected to the casing and the liquid-cooled tube, respectively. All other simulation conditions remain consistent with those in the preceding section.

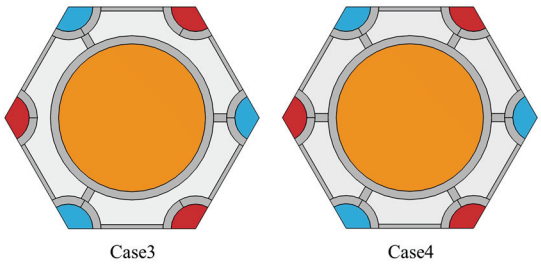

Figure 10. Schematic diagram of the honeycomb BTMS with longitudinal fins and a thermal conductive casing: Case 3 (3 fins) and Case 4 (6 fins).

As shown in the temperature cloud maps of the central cross-section in Figure 11, after adding the high-thermal-conductivity casing, the temperature distribution of the BTMS exhibits a concentric circular pattern for both the 3-fin and 6-fin configurations, with the highest temperature at the battery center and heat transferring uniformly outward. This is attributed to the fact that the aluminum alloy casing constructs a fully contacted heat conduction path on the battery surface. Heat is transferred from the battery surface to the low-thermal-resistance aluminum casing, where it is rapidly distributed evenly, and then transmitted to the fins uniformly, eliminating the thermal resistance difference on the battery surface caused by direct fin contact. Compared with Case 3, Case 4 features a smaller temperature gradient and superior heat dissipation performance.

https://doi.org/10.3390/batteries12030094

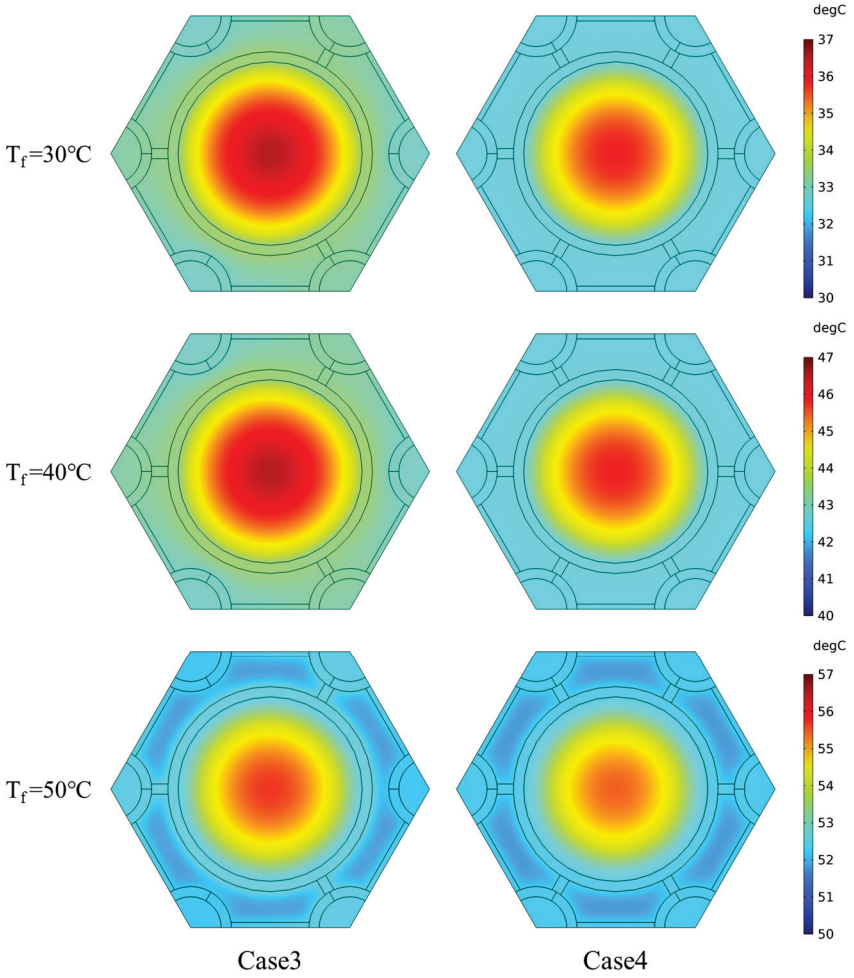

Figure 11. Temperature distributions on the central cross-section of the BTMS for Cases 3 and 4 at different ambient temperatures.

Figure 12 presents the temperature-time curves of four honeycomb BTMS configurations, namely Cases 1, 2 from Figure 6 and Cases 3, 4 in this section. After adding the casing, the maximum battery temperature in Cases 3 and 4 further decreases, and the maximum temperature difference is strictly controlled below 5 °C, verifying that the thermal conductive casing can significantly improve the temperature uniformity of the battery. In particular, the maximum temperature difference in Case 3 is lower than that of Case 2, indicating that the introduction of the thermal conductive casing has a better effect on improving uniformity than simply increasing the number of fins.

Figure 13a shows that Case 4 achieves the best cooling effect; however, the cooling gain brought by the configuration upgrade shows a decreasing trend, and the temperature drop amplitude of the maximum battery temperature from Case 1 to Case 4 gradually weakens, which indicates that the main thermal resistance affecting the system heat dissipation has shifted from the external heat dissipation path resistance to the internal radial thermal resistance of the cell. Figure 13b further illustrates that at an ambient temperature of 50 °C, the introduction of the thermal conductive casing reduces ΔT_{max} from 6.4 °C in Case 2 to 4.3 °C in Case 3; while the difference in ΔT_{max} between Case 3 and Case 4 is only within 0.5 °C, demonstrating that the introduction of the casing has a significant effect on reducing the maximum temperature difference in the battery, whereas the influence of the number of fins on the battery uniformity is significantly weakened.

https://doi.org/10.3390/batteries12030094

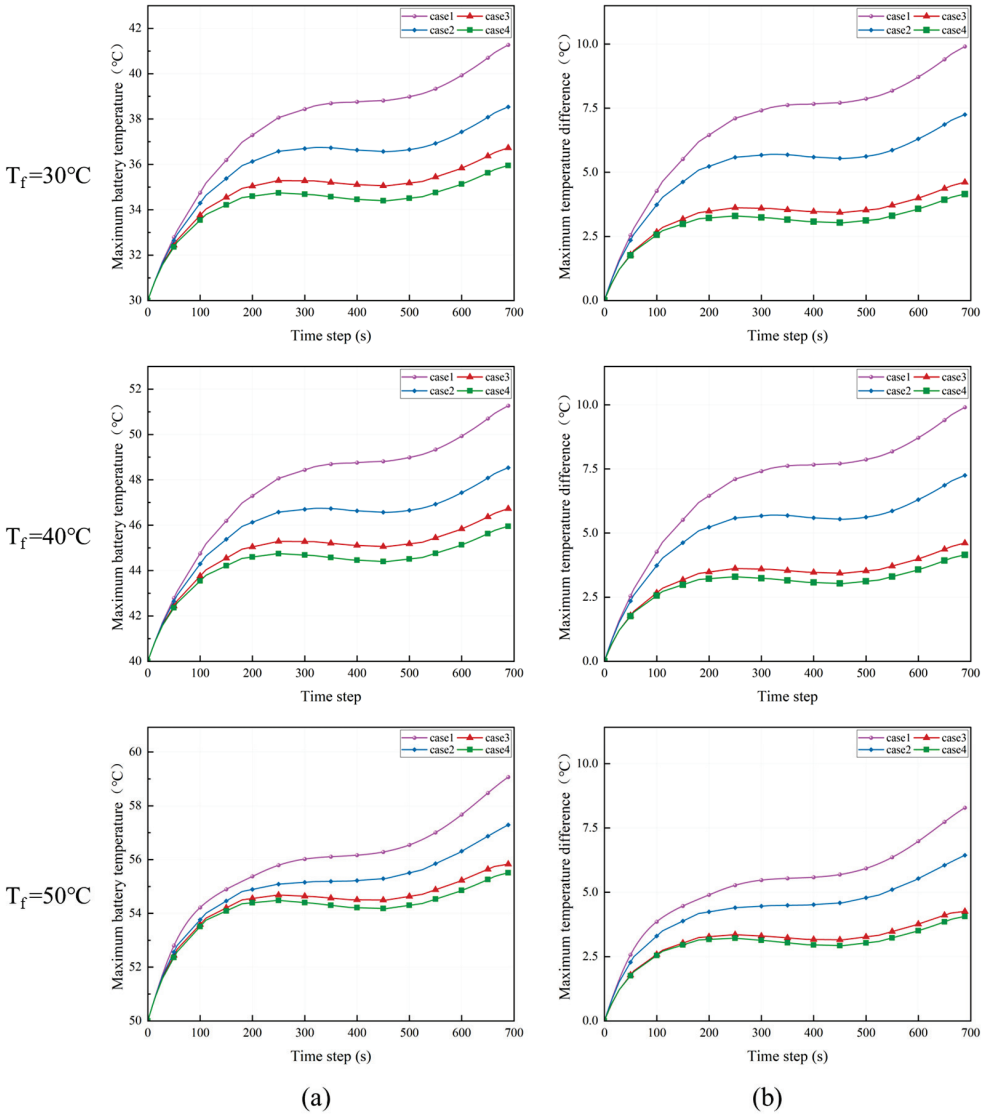

Figure 12. Maximum battery temperature (**a**) and maximum temperature difference in the battery (**b**) during discharge for Cases 1, 2, 3 and 4 under different ambient temperatures.

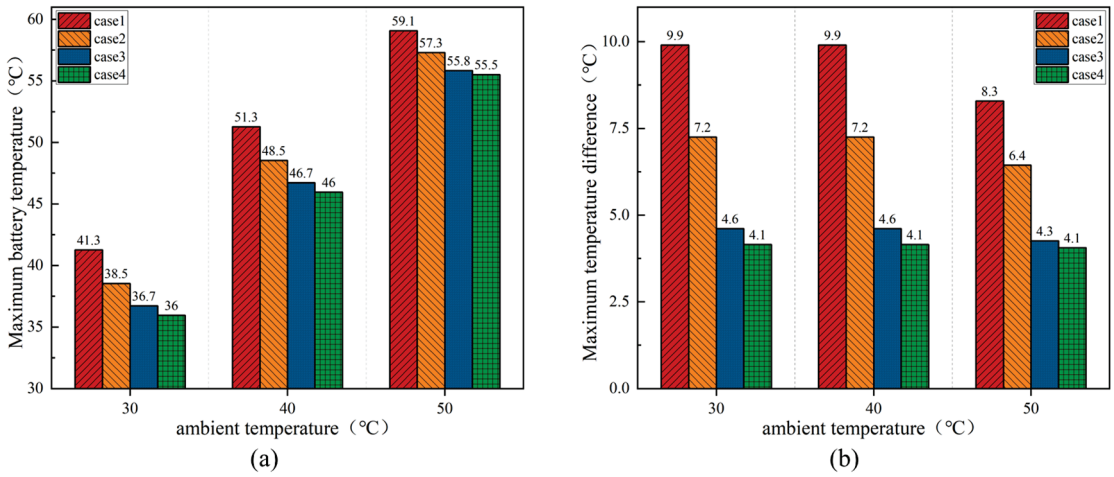

Figure 13. Maximum battery temperature (**a**) and maximum temperature difference in the battery (**b**) of Cases 1, 2, 3, and 4 at the end of discharge under different ambient temperatures.

https://doi.org/10.3390/batteries12030094

In Case 3 and Case 4, the internally generated heat of the battery is first transferred from the battery surface to the low-thermal-resistance aluminum alloy casing. Owing to the high thermal conductivity of aluminum alloy and its excellent temperature equalization capability, heat can rapidly diffuse along the circumferential direction, resulting in a more uniform temperature distribution on the battery surface. Consequently, the temperature difference induced by the direct contact between the fins and the battery is substantially mitigated. Under the 50 °C condition, the maximum temperature differences in Case 3 and Case 4 are only 4.3 °C and 4.1 °C, respectively, which are reduced by approximately 48% and 36% compared with 8.3 °C in Case 1 and 6.4 °C in Case 2, indicating a remarkable improvement in temperature uniformity.

Similar trends are also observed under the 30 °C and 40 °C conditions, where the maximum temperature differences in Case 3 and Case 4 consistently remain below 4.6 °C, which are significantly lower than those of the configurations with direct fin–battery contact. These results convincingly demonstrate the effectiveness of the aluminum alloy casing in reducing circumferential thermal resistance disparities and enhancing the surface temperature uniformity of the battery.

Figure 14a integrates the time-course curves of the average PCM liquid fraction of the five honeycomb BTMS configurations, including those in Figure 9 (Cases 0, 1, and 2) and Cases 3 and 4 in this section. Figure 14b summarizes the liquid fraction values at the end of discharge. The results indicate that the introduction of fins significantly suppresses the melting process of PCM. Furthermore, when the thermal conductive casing is added, the liquid fraction can be further reduced, with Case 4 achieving the minimum liquid fraction value. Figure 14c presents the cross-sectional distribution of the PCM liquid fraction at the end of battery discharge. Case 4 exhibits a highly uniform distribution in the circumferential direction, with no local regions of high liquid fraction concentration. This result visually indicates that the design of Case 4, with the thermal conductive casing providing uniform circumferential heating and six fins efficiently dissipating heat, maximizes the retention of the solid-state latent heat storage capacity of PCM.

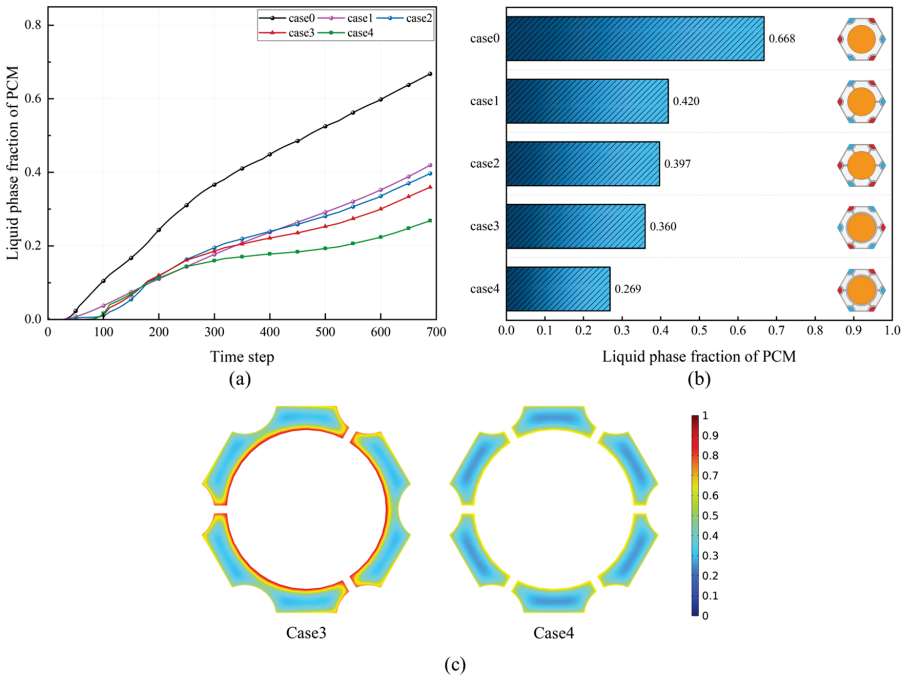

Figure 14. Average liquid fraction of PCM for five Cases during discharge at an ambient temperature of 50 °C (**a**), PCM liquid fraction at the end of discharge (**b**), and cross-sectional distribution of PCM liquid fraction for Cases 3 and 4 at the end of discharge (**c**).

https://doi.org/10.3390/batteries12030094

As shown in Figure 15, when the fin thickness increases from 1 mm to 5 mm, the variation in the maximum battery temperature under both Case 3 and Case 4 conditions does not exceed 0.3 °C, and the overall temperature remains nearly unchanged, indicating that fin thickness has a negligible influence on the maximum battery temperature. Meanwhile, with increasing fin thickness, the variation in the maximum temperature difference under both operating conditions remains below 0.25 °C and exhibits no evident decreasing trend, suggesting that thickening the fins does not significantly improve the temperature uniformity of the system.

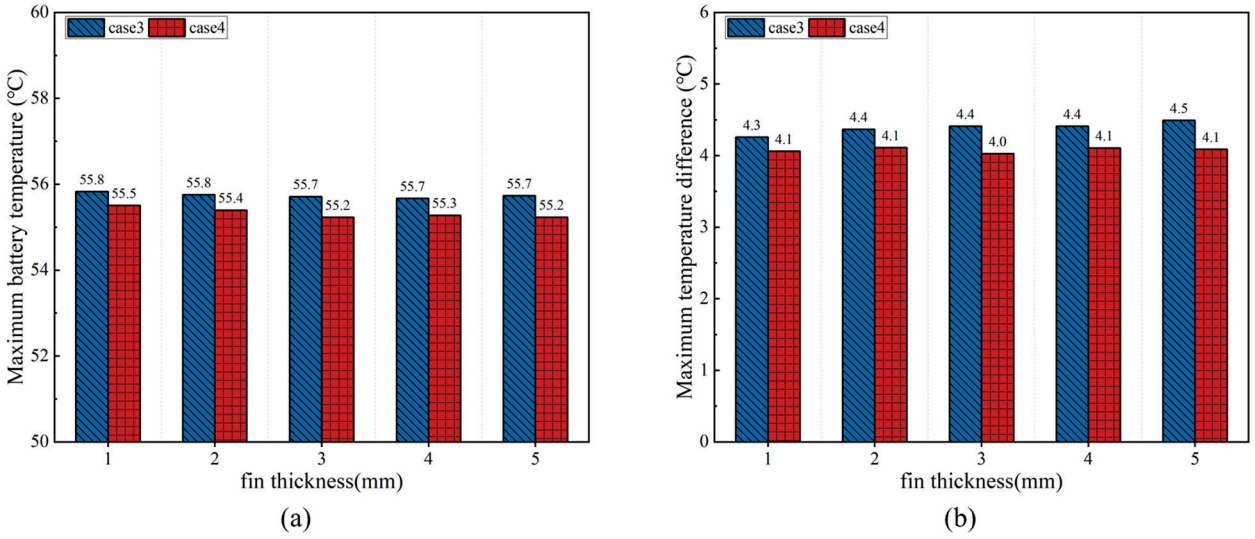

Figure 15. Maximum battery temperature (**a**) and maximum temperature difference in the battery (**b**) of Cases 3 and 4 with different fin thicknesses at the end of discharge under an ambient temperature of 50 °C.

Based on the above results and considering the high thermal conductivity of aluminum alloy fins, which is 238 W/(m·K), it can be concluded that the heat conduction requirement can already be satisfied at relatively small fin thicknesses, and further increasing the thickness is unlikely to yield a noticeable improvement in the overall thermal performance of the BTMS. In addition, thicker fins occupy a larger volume of PCM, thereby reducing the effective latent heat storage capacity of the system, while also increasing the total mass, which is detrimental to lightweight design. Therefore, while ensuring adequate thermal performance, and considering structural mass, PCM utilization, as well as practical manufacturing constraints and mechanical strength requirements, a fin thickness of 1 mm represents a near-minimum yet reasonable design choice. Accordingly, 1 mm is selected as the optimal fin thickness in this study.

In summary, the introduction of a high-thermal-conductivity aluminum alloy casing with heat-conducting fins effectively improves the temperature uniformity of the fin-integrated honeycomb BTMS. Specifically, the maximum temperature difference in all casing-equipped configurations (Case 3 and Case 4) is controlled within 5 °C. However, restricted by the radial thermal resistance inside the battery, the inhibitory effect of increasing the number of fins on the maximum temperature exhibits a trend of diminishing marginal returns. Meanwhile, the fin–casing structure further reduces the liquid fraction of the PCM, thereby retaining more solid-phase latent heat storage capacity.

Under the working conditions of this study, Case 4 exhibits the optimal heat dissipation performance, the lowest battery temperature difference, and the smallest PCM liquid fraction. In contrast, Case 3 ensures satisfaction of temperature uniformity requirements, while the maximum battery temperature of Case 3 is slightly higher than that of Case

https://doi.org/10.3390/batteries12030094

4. Moreover, Case 3 features a more simplified structure and achieves a favorable balance between thermal performance and manufacturing cost, making it equally worthy of consideration.

3.3. Effect of Battery Spacing on the Thermal Performance of the Fin—Casing Honeycomb BTMS

In battery modules, the center-to-center spacing between adjacent cells is a key parameter governing the thermal management performance and space utilization efficiency of a Battery Thermal Management System. As the spacing increases, the storage capacity of PCM rises, while the heat conduction paths of the fins are elongated, leading to an increase in thermal resistance for heat conduction. In addition, the volumetric packing efficiency of the module decreases significantly. Therefore, under the operating conditions of an ambient temperature of 50 °C and a cooling fluid flow rate of 0.1 m/s, this section simulates Cases 3, 4 with cell spacings ranging from 25 mm to 32 mm to investigate the effects of cell center-to-center spacing on the thermal performance of the BTMS and volumetric packing efficiency.

Figure 16 presents the temperature contours along the fin cross-section of the two fin–casing honeycomb BTMS configurations. Increasing the cell spacing enlarges the thickness of the PCM filling layer and elongates the heat conduction paths of the fins. Both configurations maintain excellent temperature uniformity across all cell spacing conditions.

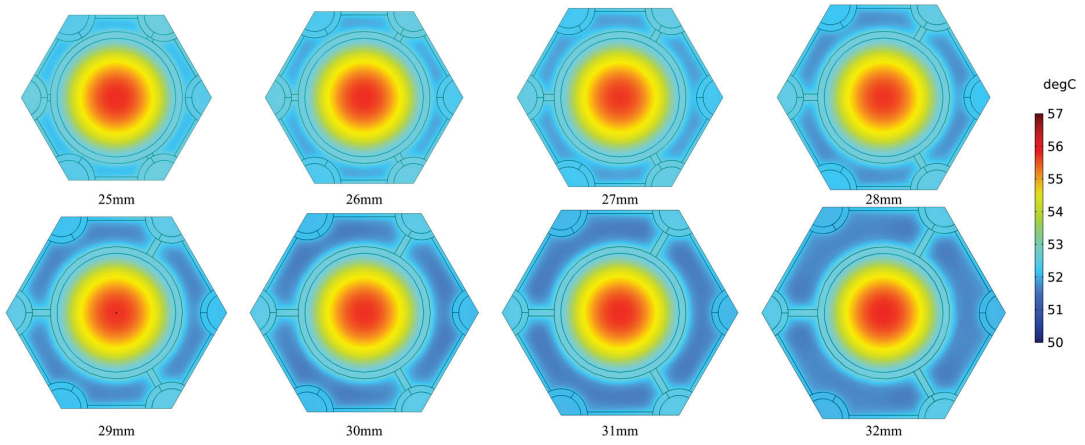

(Case3)

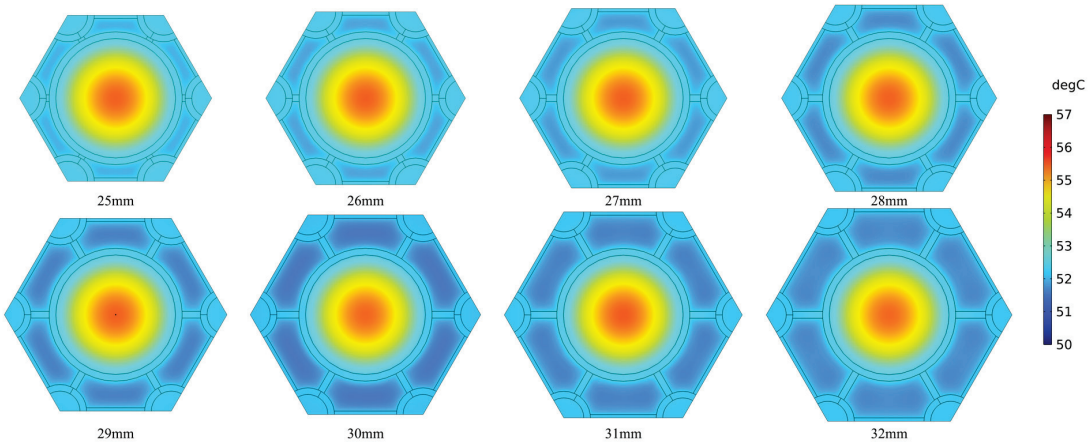

(Case4)

Figure 16. Temperature distribution on the central cross-section of the BTMS for (Cases 3) and (Case 4) with different battery spacings under an ambient temperature of 50 °C.

https://doi.org/10.3390/batteries12030094

Figure 17 illustrates the influence of variations in cell spacing on the thermal performance and packing efficiency of the two honeycomb BTMS. The maximum temperatures of Cases 3 and 4 stabilize at approximately 55.8 °C and 55.5 °C, respectively. In contrast to the trend of the maximum temperature, the maximum temperature difference in the cells shows a monotonic decrease with increasing spacing. This phenomenon is attributed to two factors: first, the elongated heat conduction paths of the fins caused by larger cell spacing reduce the heat transfer efficiency of the liquid cooling loop; second, the increased thickness of the PCM elevates its thermal resistance. As the overall thermal resistance of the BTMS rises with increasing cell spacing and approaches that of the cell, the heat transfer efficiency between the battery's interior and exterior is balanced, leading to a continuous decline in the maximum temperature difference. Meanwhile, the heat capacity of the PCM increases accordingly, enabling it to absorb more heat through latent heat storage and thus maintain the stability of the battery's maximum temperature. This further indicates that increasing the PCM thickness strengthens its thermal buffering effect, which is conducive to improving the circumferential temperature uniformity of the cells.

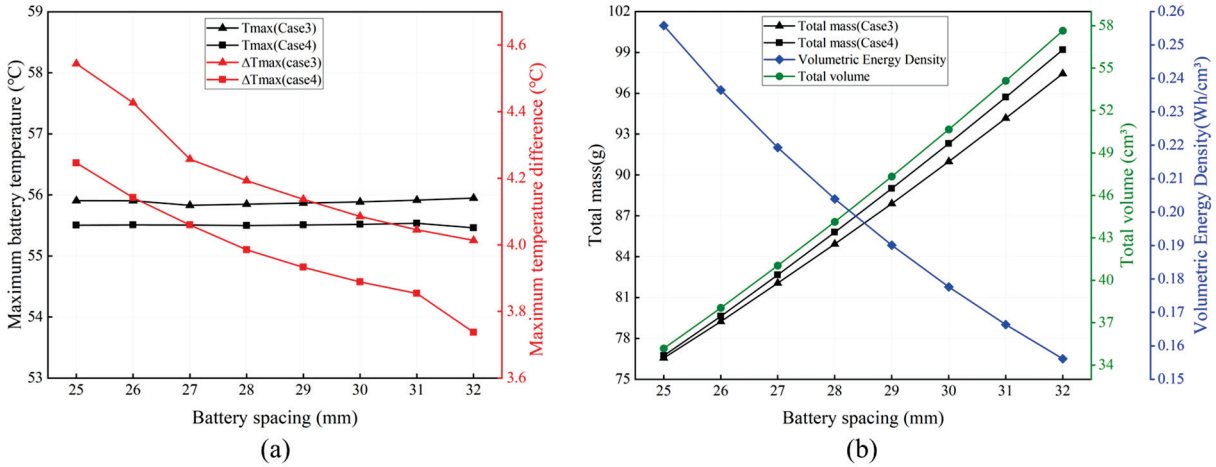

Figure 17. Maximum battery temperature and maximum temperature difference in the battery of Cases 3 and 4 at different battery spacings under an ambient temperature of 50 °C (**a**); mass, volume and volumetric energy density of the BTMS (**b**).

As illustrated in Figure 17a,b, with increasing battery spacing, both the total volume and total mass of the honeycomb BTMS exhibit pronounced nonlinear growth trends, while the volumetric energy density correspondingly shows a nonlinear decline. Quantitative analysis indicates that when the battery spacing increases from 25 mm to 32 mm, the total volume of the thermal management system rises from 35.2 cm^3 to 57.6 cm^3, corresponding to a cumulative increase of 63.8%. Meanwhile, the volumetric energy density decreases cumulatively by 39%, demonstrating that enlarging the battery spacing significantly deteriorates the spatial utilization efficiency of the system.

In terms of mass, the total mass of both Case 3 and Case 4 increases with increasing battery spacing, with cumulative increments of 27.3% and 29.3%, respectively. Moreover, under identical battery spacing conditions, the total mass of Case 4 is consistently slightly higher than that of Case 3.

However, from the perspective of battery temperature uniformity, the performance enhancement achieved by increasing battery spacing is relatively limited. As the battery spacing increases, the maximum temperature differences in Case 3 and Case 4 decrease by only approximately 11%. This reduction is not only substantially lower than the growth rates of system volume and mass, but also smaller than the decline in volumetric energy density. Further analysis reveals that when the battery spacing exceeds 27 mm, each addi-

https://doi.org/10.3390/batteries12030094

tional increase of 1 mm leads to an improvement in the maximum temperature difference of less than 0.1 °C, whereas the system volume and mass continue to increase rapidly in a nonlinear manner.

Considering multiple factors, including system volume, mass, volumetric energy density, and battery temperature uniformity, both Case 3 and Case 4 satisfy the temperature uniformity requirements under all investigated operating conditions. Therefore, from the perspectives of overall performance and engineering practicality, a battery spacing of 25–27 mm is recommended as the optimal design range for the honeycomb BTMS.

This section demonstrates that for the fin–casing honeycomb BTMS (Cases 3 and 4), increasing the battery spacing can further improve the temperature uniformity inside the module, while simultaneously reducing the module packing efficiency. Considering the sensible heat and thermal buffering benefits of the (PCM as well as the requirements of volumetric energy density, this study recommends 25–27 mm as the optimal design range. Within this range, the volume increment of the system can be controlled within 20%, effectively avoiding volume redundancy and thereby maximizing the volumetric energy density of the system.

3.4. Effect of Contact Thermal Resistance on the Thermal Performance of the Fin—Casing Honeycomb BTMS

Considering the inevitable microvoids at solid–solid contact interfaces in practical engineering applications, this section selects the contact thermal resistance R_c as the variable and sets five different values to investigate the effect of contact thermal resistance on the thermal performance of the fin–casing honeycomb BTMS. The cell spacing is set to 27 mm, and the cooling fluid flow velocity is set to 0.1 m/s for the simulation.

The contact thermal resistance values selected in this section cover a range from 10^{-3} to 10^{-6} $m^2 \cdot K/W$, which can comprehensively represent practical operating conditions under different assembly tolerances and interfacial treatment methods. For a typical assembly gap of 50 μm, the corresponding contact thermal resistance is on the order of 10^{-3} $m^2 \cdot K/W$ when air is present at the interface, whereas it decreases to approximately 10^{-5} $m^2 \cdot K/W$ when thermal grease is used as the interfacial material [41]. Furthermore, when a graphite-based composite thermal interface material is applied, the contact thermal resistance can be further reduced to the order of 10^{-6} $m^2 \cdot K/W$ [42].

Figure 18 presents the temperature field cross-sections of the BTMS under four orders of magnitude. When the contact thermal resistance 10^{-3} $K \cdot m^2/W$, severe heat accumulation occurs inside the cell, forming an obvious temperature stratification between the interior and exterior of the cell, which seriously impairs the heat dissipation performance of the BTMS. As the contact thermal resistance decreases from 10^{-3} to 10^{-6} $K \cdot m^2/W$, the temperature distribution of the two honeycomb BTMS configurations becomes increasingly uniform with the reduction in the magnitude.

Figure 19a,b illustrate the cell temperatures at different contact thermal resistances R_c at the end of discharge. When the contact thermal resistance R_c is at the level of 10^{-4} $K \cdot m^2/W$, both the maximum cell temperature and the maximum temperature difference remain stable, and the BTMS maintains high-efficiency heat dissipation. In contrast, when the contact thermal resistance exceeds the level of 10^{-4} $K \cdot m^2/W$, the maximum cell temperature rises sharply, while the maximum temperature difference continues to decrease. Combined with the results in Figure 18, it can be concluded that when R_c is at the level of 10^{-4} $K \cdot m^2/W$ or lower, the heat inside the cell is rapidly transferred to the liquid-cooled tube. However, when the contact thermal resistance increases to 10^{-3} $K \cdot m^2/W$, a large amount of heat accumulates inside the cell and cannot be transferred across the contact interface, which reduces the temperature gradient inside the cell and leads to an increase in the maximum temperature.

https://doi.org/10.3390/batteries12030094

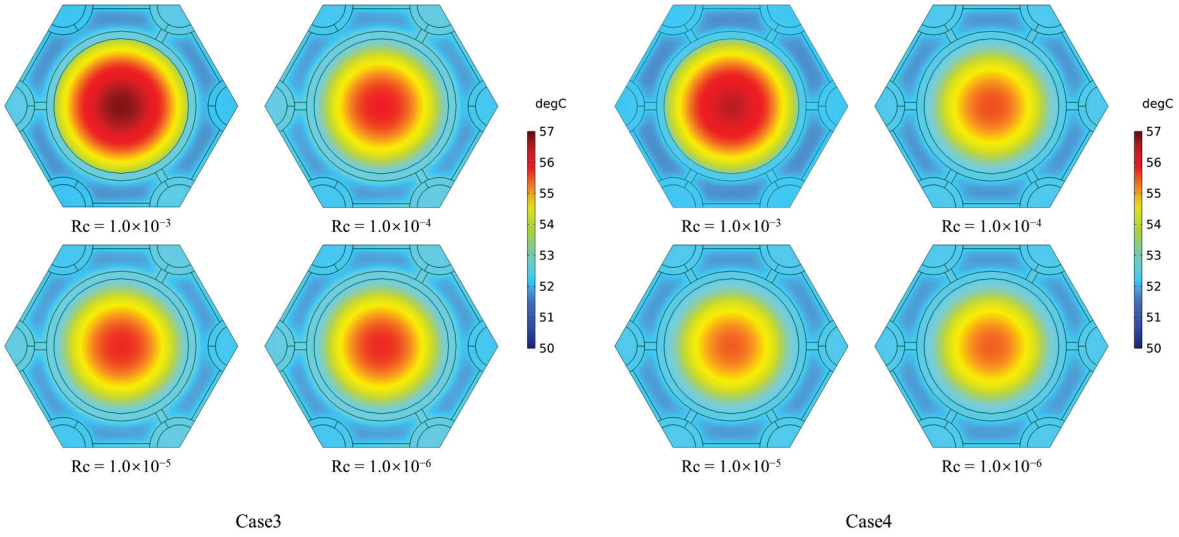

Figure 18. Contour distributions of temperature on the central cross-section of the BTMS for (Case 3) and (Case 4) under different contact thermal resistances.

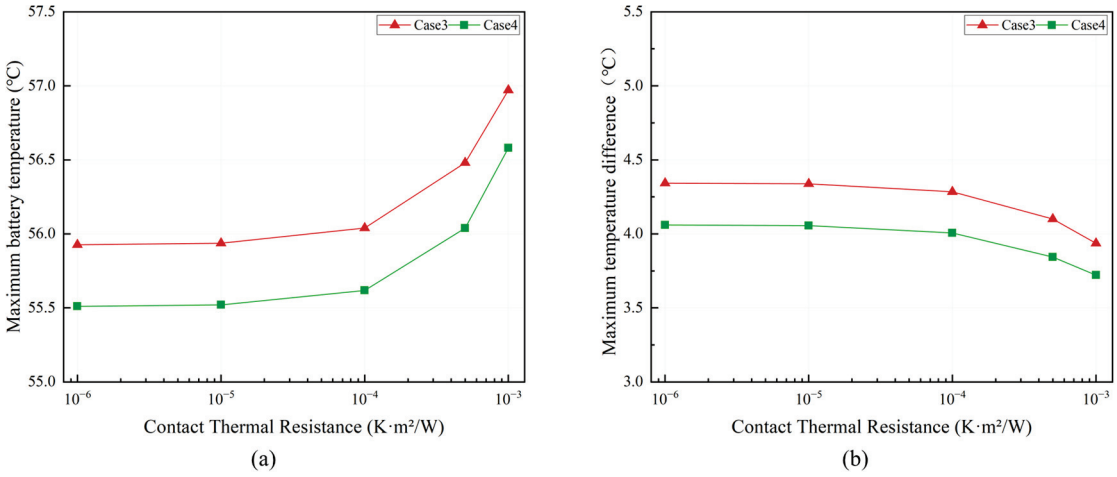

Figure 19. Maximum battery temperature (**a**) and maximum temperature difference in the battery (**b**) for Cases 3 and 4 under different contact thermal resistances.

In summary, the magnitude of contact thermal resistance has a significant influence on the maximum battery temperature and the maximum temperature difference. Excessively high contact thermal resistance causes a sharp increase in the maximum battery temperature; meanwhile, it exhibits a temperature equalization effect, which leads to a reduction in the maximum temperature difference. The findings indicate that when the contact thermal resistance is at the order of 10^{-4} K·m^2/W or lower, its adverse impact on the heat dissipation performance is negligible.

4. Conclusions

In this study, numerical simulations were conducted on the fin–casing honeycomb BTMS under conditions of 5C high-rate discharge and an ambient temperature of 50 °C. By comparing the thermal performance of five configurations, two optimized cases that meet the heat dissipation requirements were selected. Furthermore, the influence patterns of battery spacing and contact thermal resistance on the system's heat transfer characteristics were analyzed. The main conclusions are as follows:

https://doi.org/10.3390/batteries12030094

(1) The addition of longitudinal fins can significantly suppress the temperature rise in the battery and delay the phase change process of PCM, with a more pronounced effect achieved as the number of fins increases. However, the installation of fins leads to an increase in the internal temperature difference in the battery due to the uneven distribution of circumferential thermal resistance.
(2) The introduction of a battery thermal conductive casing effectively resolves the issue of excessive internal temperature difference in the battery caused by the fin structure, further enhances the heat dissipation capability of the system, and delays the phase change process of PCM.
(3) The battery spacing affects the temperature uniformity and grouping efficiency of battery modules. Increasing spacing raises the latent heat of PCM and improves the temperature uniformity of the battery but has a negligible effect on the maximum temperature and leads to a decline in the grouping efficiency of the BTMS. Considered comprehensively, a battery spacing of 25–27 mm is optimal.
(4) The contact thermal resistance between the battery and the thermal conductive casing is a key parameter influencing the heat dissipation efficiency and temperature uniformity of the battery. Excessively high contact thermal resistance exacerbates heat accumulation inside the battery and raises the maximum temperature. When the contact thermal resistance is controlled below 10^{-4} K·m^2/W, its adverse impact on the system heat dissipation can be neglected.

The numerical simulations conducted in this study aim to investigate the effects of fin structures and a thermally conductive casing on the thermal performance of the honeycomb BTMS, thereby providing optimized design guidelines for subsequent experimental investigations. In the present work, a simple longitudinal fin configuration is adopted. In future studies, different fin geometries and advanced optimization strategies will be further explored. In addition, the natural convection of liquid-phase PCM will be taken into consideration, and a quantitative evaluation of the liquid-cooling pump power and BTMS cost will be conducted.

Author Contributions: Conceptualization, L.X. and T.Y.; methodology, L.T. and X.G.; software, S.S. and Q.X.; validation, M.L. and L.C.; formal analysis, H.Z. and J.X.; investigation, X.G. and S.S.; resources, L.X. and T.Y.; data curation, M.L. and L.C.; writing—original draft preparation, L.T. and X.G.; writing—review and editing, L.X. and T.Y.; visualization, L.T. and Q.X.; supervision, H.Z. and J.X.; project administration, L.X. and T.Y.; funding acquisition, Q.X. and H.Z. All authors have read and agreed to the published version of the manuscript.

Funding: This research is funded by the Natural Science Foundation of Hubei Province of China (2025AFD087, 2025AFB665), and the National Natural Science Foundation of China (52476079).

Data Availability Statement: The original contributions presented in this study are included in the article. Further inquiries can be directed to the corresponding authors.

Conflicts of Interest: Liang Tong, Xin Gong, Shenglin Su, Linzhi Xu, Qianqian Xin, Tianqi Yang, Hengyun Zhang, Jinsheng Xiao have no conflicts of interest. Min Liu and Lingyu Chen work for Research Institute of State Grid Zhejiang Electric Power Co., Ltd.

References

1. Kang, D.; Lee, P.Y.; Yoo, K.; Kim, J. Internal thermal network model-based inner temperature distribution of high-power lithium-ion battery packs with different shapes for thermal management. *J. Energy Storage* **2020**, *27*, 101017. [CrossRef]
2. Paul, S.; Diegelmann, C.; Kabza, H.; Tillmetz, W. Analysis of ageing inhomogeneities in lithium-ion battery systems. *J. Power Sources* **2013**, *239*, 642–650. [CrossRef]
3. Rao, Z.; Qian, Z.; Kuang, Y.; Li, Y. Thermal performance of liquid cooling based thermal management system for cylindrical lithium-ion battery module with variable contact surface. *Appl. Therm. Eng.* **2017**, *123*, 1514–1522. [CrossRef]

https://doi.org/10.3390/batteries12030094

4. Liu, Y.; Zhang, J. Design a J-type air-based battery thermal management system through surrogate-based optimization. *Appl. Energy* **2019**, *252*, 113426. [CrossRef]
5. Qian, Z.; Li, Y.; Rao, Z. Thermal performance of lithium-ion battery thermal management system by using mini-channel cooling. *Energy Convers. Manag.* **2016**, *126*, 622–631. [CrossRef]
6. Zou, D.; Liu, X.; He, R.; Zhu, S.; Bao, J.; Guo, J.; Hu, Z.; Wang, B. Preparation of a novel composite phase change material (PCM) and its locally enhanced heat transfer for power battery module. *Energy Convers. Manag.* **2019**, *180*, 1196–1202. [CrossRef]
7. Yang, Y.; Xu, X.; Zhang, Y.; Hu, H.; Li, C. Synergy analysis on the heat dissipation performance of a battery pack under air cooling. *Ionics* **2020**, *26*, 5575–5584. [CrossRef]
8. Jang, D.S.; Yun, S.; Hong, S.H.; Cho, W.; Kim, Y. Performance characteristics of a novel heat pipe-assisted liquid cooling system for the thermal management of lithium-ion batteries. *Energy Convers. Manag.* **2022**, *251*, 115001. [CrossRef]
9. Akinlabi, A.H.; Solyali, D. Configuration, design, and optimization of air-cooled battery thermal management system for electric vehicles: A review. *Renew. Sustain. Energy Rev.* **2020**, *125*, 109815. [CrossRef]
10. Luo, J.; Zou, D.; Wang, Y.; Wang, S.; Huang, L. Battery thermal management systems (BTMs) based on phase change material (PCM): A comprehensive review. *Chem. Eng. J.* **2022**, *430*, 132741. [CrossRef]
11. Wu, C.; Sun, Y.; Tang, H.; Zhang, S.; Yuan, W.; Zhu, L.; Tang, Y. A review on the liquid cooling thermal management system of lithium-ion batteries. *Appl. Energy* **2024**, *375*, 124173. [CrossRef]
12. Ali, A.M.; Angelino, M.; Rona, A. Numerical analysis on the thermal performance of microchannel heat sinks with Al_2O_3 nanofluid and various fins. *Appl. Therm. Eng.* **2021**, *198*, 117458. [CrossRef]
13. Patil, M.S.; Seo, J.H.; Lee, M.Y. A novel dielectric fluid immersion cooling technology for Li-ion battery thermal management. *Energy Convers. Manag.* **2021**, *229*, 113715. [CrossRef]
14. Wiriyasart, S.; Hommalee, C.; Sirikasemsuk, S.; Prurapark, R.; Naphon, P. Thermal management system with nanofluids for electric vehicle battery cooling modules. *Case Stud. Therm. Eng.* **2020**, *18*, 100583. [CrossRef]
15. Akbarzadeh, M.; Kalogiannis, T.; Jaguemont, J.; Jin, L.; Behi, H.; Karimi, D.; Beheshti, H.; Van Mierlo, J.; Berecibar, M. A comparative study between air cooling and liquid cooling thermal management systems for a high-energy lithium-ion battery module. *Appl. Therm. Eng.* **2021**, *198*, 117503. [CrossRef]
16. Chen, S.; Peng, X.; Bao, N.; Garg, A. A comprehensive analysis and optimization process for an integrated liquid cooling plate for a prismatic lithium-ion battery module. *Appl. Therm. Eng.* **2019**, *156*, 324–339. [CrossRef]
17. Oliveski, R.D.; Becker, F.; Rocha, L.A.; Biserni, C.; Eberhardt, G.E. Design of fin structures for phase change material (PCM) melting process in rectangular cavities. *J. Energy Storage* **2021**, *35*, 102337. [CrossRef]
18. Gulfam, R.; Zhu, W.; Xu, L.; Cheema, I.I.; Sheng, P.; Zhao, G.; Deng, Y. Design, fabrication and numerical analysis of compact thermal management system integrated with composite phase change material and thermal bridge. *Energy Convers. Manag.* **2018**, *156*, 25–33. [CrossRef]
19. Zhao, Y.; Jin, L.; Zou, B.; Qiao, G.; Zhang, T.; Cong, L.; Jiang, F.; Li, C.; Huang, Y.; Ding, Y. Expanded graphite–paraffin composite phase change materials: Effect of particle size on the composite structure and properties. *Appl. Therm. Eng.* **2020**, *171*, 115015. [CrossRef]
20. Swamy, K.A.; Verma, S.; Bhattacharyya, S. Experimental and numerical investigation of nanoparticle assisted PCM-based battery thermal management system. *J. Therm. Anal. Calorim.* **2024**, *149*, 11223–11237. [CrossRef]
21. Vali, P.M.; Murali, G. Experimental study on thermal management of nano-enhanced phase change material integrated battery pack. *ASME J. Heat Mass Transfer* **2024**, *146*, 032401. [CrossRef]
22. Zhou, D.; Xiao, S.; Liu, Y. The effect of expanded graphite content on the thermal properties of fatty acid composite materials for thermal energy storage. *Molecules* **2024**, *29*, 3146. [CrossRef]
23. Yang, T.; Su, S.; Xin, Q.; Zeng, J.; Zhang, H.; Zeng, X.; Xiao, J. Thermal management of lithium-ion batteries based on honeycomb-structured liquid cooling and phase change materials. *Batteries* **2023**, *9*, 287. [CrossRef]
24. Zhang, Y.; Huang, J.; Cao, M.; Du, G.; Liu, Z. A novel sandwich structured phase change material with well impact energy absorption performance for Li-ion battery application. *J. Energy Storage* **2021**, *40*, 102769. [CrossRef]
25. Keyhani-Asl, A.; Perera, N.; Lahr, J.; Hasan, R. Innovative hybrid battery thermal management system incorporating copper foam porous fins and layers with phase change material and liquid cooling. *Appl. Therm. Eng.* **2025**, *268*, 125848. [CrossRef]
26. Luo, M.; Zhang, Y.; Wang, Z.; Niu, Y.; Lu, B.; Zhu, J.; Zhang, J.; Wang, K. Thermal performance enhancement with snowflake fins and liquid cooling in PCM-based battery thermal management system at high ambient temperature and high discharge rate. *J. Energy Storage* **2024**, *90*, 111754. [CrossRef]
27. Shen, X.; Zhang, X.; Chen, M.; Chen, D. Thermal management performance of spiderweb-like fins enhanced phase change material cooling system for lithium-ion batteries. *J. Energy Storage* **2024**, *97*, 112973. [CrossRef]
28. Wu, Y.; Lv, L.; Wu, F.; Wei, L.; Li, H.; Zhou, H. Numerical simulation of phase change material-assisted liquid cooling with gear-shaped fins for battery thermal management. *Appl. Therm. Eng.* **2025**, *284*, 128983. [CrossRef]

https://doi.org/10.3390/batteries12030094

29. Esmaeili, Z.; Vahidhosseini, S.M.; Rashidi, S.; Karimi, N.; Yan, W.M. Thermal management of lithium-ion batteries: Numerical evaluation of phase change materials and fin designs against air cooling. *Int. J. Therm. Sci.* **2026**, *219*, 110194. [CrossRef]
30. Wang, J.; Yu, Y.; Song, L.; Yue, Y.; Zeng, W.; Mei, W.; Wang, Q. Thermal management performance and optimization of a novel system combining heat pipe and composite fin for prismatic lithium-ion batteries. *Energy Convers. Manag.* **2024**, *302*, 118106. [CrossRef]
31. *GB 38031-2020*; Electric Vehicles Traction Battery Safety Requirements. State Administration for Market Regulation & Standardization Administration of China: Beijing, China, 2020.
32. Azizi, Y.; Sadrameli, S.M. Thermal management of a LiFePO4 battery pack at high temperature environment using a composite of phase change materials and aluminum wire mesh plates. *Energy Convers. Manag.* **2016**, *128*, 294–302. [CrossRef]
33. Wu, W.; Liu, J.; Liu, M.; Rao, Z.; Deng, H.; Wang, Q.; Qi, X.; Wang, S. An innovative battery thermal management with thermally induced flexible phase change material. *Energy Convers. Manag.* **2020**, *221*, 113145. [CrossRef]
34. Liu, F.; Wang, J.; Liu, Y.; Wang, F.; Yang, N.; Liu, X.; Liu, H.; Li, W.; Liu, H.; Huang, B. Performance analysis of phase change material (PCM) in battery thermal management with biomimetic honeycomb fin. *Appl. Therm. Eng.* **2021**, *196*, 117296. [CrossRef]
35. Weng, J.; He, Y.; Ouyang, D.; Yang, X.; Chen, M.; Cui, S.; Zhang, G.; Yuen, R.K.; Wang, J. Honeycomb-inspired design of a thermal management module and its mitigation effect on thermal runaway propagation. *Appl. Therm. Eng.* **2021**, *195*, 117147. [CrossRef]
36. Yang, X.G.; Zhang, G.; Wang, C.Y. Computational design and refinement of self-heating lithium ion batteries. *J. Power Sources* **2016**, *328*, 203–211. [CrossRef]
37. *COMSOL Multiphysics®*, version 6.2; COMSOL AB: Stockholm, Sweden, 2023. Available online: www.comsol.com (accessed on 5 March 2026).
38. Bernardi, D.; Pawlikowski, E.; Newman, J. A general energy balance for battery systems. *J. Electrochem. Soc.* **1985**, *132*, 5. [CrossRef]
39. Kermani, J.R.; Taheri, M.M.; Shafii, M.B.; Moosavi, A. Analytical solution, optimization and design of a phase change cooling pack for cylindrical lithium-ion batteries. *Appl. Therm. Eng.* **2023**, *232*, 120963. [CrossRef]
40. Xin, Q.; Xiao, J.; Yang, T.; Zhang, H.; Long, X. Thermal management of lithium-ion batteries under high ambient temperature and rapid discharging using composite PCM and liquid cooling. *Appl. Therm. Eng.* **2022**, *210*, 118230. [CrossRef]
41. Lewis, J.S.; Perrier, T.; Barani, Z.; Kargar, F.; Balandin, A.A. Thermal interface materials with graphene fillers: Review of the state of the art and outlook for future applications. *Nanotechnology* **2021**, *32*, 142003. [CrossRef]
42. Sharma, M.; Chung, D.D.L. Solder–graphite network composite sheets as high-performance thermal interface materials. *J. Electron. Mater.* **2015**, *44*, 929–947. [CrossRef]

https://doi.org/10.3390/batteries12030094

batteries

MDPI

Article

Degradation of a Lithium-Ion Battery Cell for Enhanced First and Second Life: Effects of Temperature, Orientation, C-Rate and State of Charge

Ejikeme Raphael Ezeigwe [1], Sivert A. Woll [1], Lene T. B. Erichsen [1], Simon B. B. Solberg [1], Gareth M. Hughes [2], Wenjia Du [3], Jacob J. Lamb [1], Julia Wind [4], Torleif Lian [5], Paul R. Shearing [3], Odne Stokke Burheim [1,3,*] and Preben J. S. Vie [1]

[1] Department of Energy and Process Engineering, Norwegian University of Science and Technology, 7491 Trondheim, Norway; lene.erichsen@gmail.com (L.T.B.E.); pjvie@ntnu.no (P.J.S.V.)
[2] Department of Materials, University of Oxford, Oxford OX1 3PH, UK
[3] Department of Engineering Science, University of Oxford, Oxford OX1 3PJ, UK
[4] Institute for Energy Technology, 2027 Kjeller, Norway
[5] Norwegian Defence Research Establishment (FFI), 2027 Kjeller, Norway
* Correspondence: burheim@ntnu.no; Tel.: +47-91707856

Abstract

Lithium-ion batteries (LIBs) can considerably improve their lifespan by optimising operating conditions. This may entail ensuring optimal operating temperature, limiting the state-of-charge (SoC) window, reducing cycling current, and changing the physical orientation of the uncompressed LIB cell. In this study, we examine how these four conditions and some of their combinations impact degradation in both 1st life as well as in second life. The cell analysed in this investigation was the Xalt 31 HE cell, an energy-optimised Li-ion pouch cell with a capacity of 31 Ah and an NMC433-graphite chemistry. As a follow-up study of previously reported results, a total of 18 cells were investigated. We report results focusing on improving cycle life and ensuring safety before second life. The optimal conditions for first-life cycling in the full SoC window were found at room temperature, when cycled with a lower current and the cells oriented horizontally. We observed that under the same cycling conditions, a vertical alignment of cells resulted in an increased degradation rate compared to horizontal alignment. The best second-life capacity retention was found for cells initially cycled at room temperature, then later cycled with a reduced SoC window, at a lower current and in a horizontal orientation. If the cells were cycled at an elevated temperature in first life, the second-life compatibility was reduced considerably. An incremental capacity analysis (ICA) of the first-life ageing data revealed a possible indicator for ensuring safety and cycleability into second-life use.

Keywords: lithium-ion battery; degradation modes; second-life cycling; temperature; incremental capacity analysis

1. Introduction

The demand for lithium-ion batteries (LIBs) has been increasing significantly, driven by the global transition towards more sustainable energy systems. As an example, the International Energy Agency (IEA) reported that the total volume of batteries reached over 2000 gigawatt-hours (GWh) in 2023, four times the amount reported in 2020 [1]. Out of this, electric vehicles (EVs) are expected to demand a significant share of LIBs, and

their sustained rapid growth is projected to exceed forecasts for 2030 [1]. The increasing demand for and utilisation of EVs will lead to the availability of retired batteries with terawatt-hour (TWh) capacities in the coming decades. These batteries will no longer meet the performance criteria required within most EV applications, as their output will have declined to below 80% of their nominal capacity [2,3]. However, these batteries can potentially still serve sectors other than the EV sector, for example within the Battery Energy Storage System (BESS) sector. When considering the repurposing of batteries, it is essential to improve understanding of both lifetime expectancy and safety.

For LIBs, there are several traditional safety aspects readily studied (e.g., material-related fire hazards and environmental and operational aspects [3–6]). Batteries taken out of service in their original applications can have their life extended by being put into service within other less-demanding applications (second life), thereby providing a potential solution for environmental, economic, and sustainability issues [3,6–16]. From these examples, the environmentally benign effects are unequivocal. They further indicate that the transition toward a renewable-energy-based society must deepen in order to achieve substantial economic profitability. Moreover, they highlight the need for additional experimental data concerning degradation mechanisms associated with second-life applications. To determine a battery's potential second-life applicability, the evaluation of the battery's performance and safety is essential. A state-of-health (SoH) threshold of 80% is commonly cited as the criterion marking the end of first-life applications [14,17,18]. While this holds for some segments, many daily examples have shown other user practices where, for example, cars and consumer electronics are used up to a point where operation is no longer feasible. Despite this, some studies do target measurement campaigns for second life. Martinez-Laserna et al. reported on the degradation of 20 Ah NMC-carbon cells and degradation under both first- and second-life conditions. Their study includes different temperatures above 25 °C, currents ranging 0.5–2 C, and first-life capacity ending above 90% capacity [19]. Wang et al. studied 5.2 Ah LFP-graphite cylindrical cells at different SOC windows at 25 °C [20]. Timke et al. cycled 5 Ah NMC(622)-graphite pouch cells at 20 °C for the purpose of second-life application [21]. Beyond this, several recent reviews target the use of batteries in light of technical and economic feasibility [22–28], and most recently Nazim and Elavarasan published a review with special attention around machine learning and predicting the second-life use of batteries [29]. As such, experimental battery degradation studies targetting second-life use and degradation of larger cell sizes, as well as colder temperatures, are required.

In terms of batteries, degradation is the loss of capacity as a battery ages. Batteries can degrade or age both at rest (calendar ageing) and during cycling (cyclic ageing) [30–33]. One of the most common ways to describe battery degradation is to track the evolution of the battery's state of health (SoH) as a function of time or the summarized capacity a battery has delivered (normalized cycles) [34]. The SoH is typically defined as the remaining capacity (Ah) relative to the initial capacity of a pristine battery at a given temperature and cycling rate (e.g., 0.05 C). Note that the SoH can be reported relative to the cell's rated (nominal) capacity or its measured initial capacity. Typical factors influencing cyclic ageing are the deployed cycling rates and temperature. The rate deployed is most commonly reported as the C-rate, which corresponds to current divided by the nominal cell capacity or the change in SOC divided by time in hours, (e.g., a current giving a discharge time of 20 h between 100 and 0%SOC would correspond to a C-rate of C/20 or 0.05 C) [35]. Another factor that is of importance for cyclic ageing is the upper and lower state-of-charge (SoC) limits. When a battery cell is cycled within a limited SoC window, it effectively goes through partial cycles. As such, cyclic degradation studies typically report SoH versus full equivalent cycles (FEC), sometimes also referred to as equivalent full cycles (EFC). As an example,

https://doi.org/10.3390/batteries12040121

if a cell is cycled within a SoC window of 25–75%, this equates to 0.5 FEC. In reporting degradation, performance loss can also be examined using other electrochemical methods, such as self-discharge, impedance rise, differential voltage analysis (DVA), incremental capacity analysis (ICA), voltage change, and capacity fade [36–41].

In an LIB, many internal reactions within the battery can lead to performance loss and thereby loss in (available) capacity [34]. Moreover, depending on storage conditions and operational patterns, different parasitic reactions occur that can contribute separately or in combination with its degradation. However, identifying and analysing the individual prevalent degradation mechanisms is challenging due to their highly complex dependencies on not only the specific battery chemistry (including not only active materials but also additives, electrolyte composition, and impurities), electrode (e.g., thicknesses, porosity, tortuosity) and cell designs [38] but also the operational conditions like temperature, heat management systems, cell pretension, SoC window, and C-rate.

A degradation mode represents changes to a battery's capacity based on degradation mechanisms causing similar changes to measurable quantities in the battery [42]. This can be illustrated by the two very different degradation mechanisms: SEI growth and Li-metal plating. Both mechanisms cause a loss of cycleable lithium deposited on the anode and are both represented by the degradation mode called loss of lithium inventory (LLI). The other two degradation modes are conductivity loss (CL) and loss of active material (LAM) [38,43,44].

Research indicates that most temperature-related effects are linked to the chemical reactions occurring within the batteries, following the relationship described by the Arrhenius equation [45,46]. Furthermore, temperature significantly affects the materials used in batteries and the ionic conductivities of both the electrodes and electrolytes [47].

At low operating temperatures, the viscosity of the electrolyte increases, resulting in reduced ionic conductivity and higher internal resistance due to increased impedance of ion movement [47]. Advances in additives and electrolytes with low freezing points have been explored to mitigate these effects [48–50]. Additional challenges in low-temperature operation include higher charge-transfer resistance at the electrode–electrolyte interface and slower lithium-ion diffusion within the electrodes [51,52]. Lithium plating can occur at low temperatures, where metallic lithium deposits on the anode surface. This process leads to a significant loss of active lithium, resulting in capacity fade. Additionally, plating is associated with an increased risk of internal short circuits, thereby raising safety concerns [53,54]. At elevated temperatures, chemical and structural changes within the battery accelerate, resulting in higher degradation rates. Enhanced growth of the solid electrolyte interphase (SEI) at the anode primarily contributes to loss of lithium inventory (LLI). At the same time, changes in the structure and morphology of the active material result in loss of active material (LAM). Together, LLI and LAM increase internal resistance and reduce battery capacity [55]. Additionally, electrolyte decomposition can lead to gas release and battery volume expansion [56].

Several methodologies have been deployed in the literature to identify and quantify various degradation modes for batteries operated under different conditions. Sun et al. [57] conducted a quantitative study on degradation modes at 25 °C and 45 °C, and analysed the effects of charging current rates using electrochemical impedance spectroscopy (EIS). As ageing progressed, they identified three degradation modes, with LLI and LAM being more pronounced than CL at elevated temperatures. LLI was attributed to SEI growth on the anode, while LAM was attributed to mechanical stress from cycling across a wide SoC range. CL was influenced by the interfacial processes at the current-collector–electrolyte interface. However, charging current within the tested range (0.5 C–1 C) did not significantly affect these modes. More specifically, no differences in LLI were observed, as the applied currents

were insufficient to accelerate electrolyte reduction reactions responsible for SEI growth. A study by Alcaide et al. [55] investigated the degradation of commercial cylindrical graphite-SiOx/NCA cells subjected to different cycling temperatures of 10 °C, 25 °C and 45 °C. The lowest degradation rate was observed for cells cycled at 25 °C. LAM and an increase in cell resistance were factors attributed to degradation at 45 °C, and lithium plating was observed to be accelerated at 10 °C.

Zhu et al. [58] analysed the degradation mechanisms of 18650-type cells comprised of 42 wt.% NMC and 58 wt% NCA as cathode and graphite as anode. Using AC impedance and differential voltage analysis (dV/dQ) under various operating conditions, they identified LLI and loss of active cathode material as the dominant factors of battery degradation. Additionally, varying degradation rates were observed at 0 °C and 25 °C. Wittman et al. [59] reported that LLI was the dominant degradation mode for both NMC and NCA chemistries. In the NMC cell, lithium plating occurred at 15 °C, transitioning to SEI growth at 35 °C, along with significant LAM on the cathode. The NMC cells exhibited a stronger temperature dependence compared to NCA in their cyclic ageing and material degradation.

As summarised so far, advancements in research consist of extensive investigation of the degradation mechanisms of LIBs using advanced electrochemical and material characterisation techniques under specific operating conditions. This study broadens the scope to examine how first-life operating conditions, particularly temperature dependency, affect the batteries' performance during second-life usage. The batteries were experimentally analysed under various cycling conditions, and the resulting data were compared to identify the optimal conditions for their second-life operation. This work studies degradation modes and evaluates their impact on battery performance and safety. Results from incremental capacity analysis (ICA) and complementary diagnostic techniques offer valuable insights into the viability and limitations of LIBs for extended second-life applications, particularly under temperature-dependent conditions. Moreover, this paper presents post-mortem studies, including SEM (Scanning Electron Microscopy) inspections supported by material ARC (accelerated rate calorimetry) testing, XCT (X-ray Computer aided Tomography) and FIB (Focused Ion Beam), EDX/EDS (Energy Dispersive X-ray Spectroscopy) and SIMS (Secondary Ion Mass Spectroscopy).

2. Experimental

This section gives the experimental and methodological procedures for the applied investigation of first-life, second-life, and post-mortem studies.

2.1. Cell and Testing Infrastructure

The cell used in this study was the XALT 31 HE pouch cell, with a nominal capacity of 31 Ah and a specific energy of 160 Wh/kg. The cell's active electrode materials were NMC433 on the cathode (16 double-sided and 2 single-sided electrode sheets) and graphite on the anode (17 double-sided electrode sheets). These LIB cells were purchased in 2015 and were classified as an energy optimised cell at the time. Results from this cell have previously been published [60–63].

A total of 18 cells were used in this study. Fourteen of these cells were cycled as part of a large cycle life study in the period from 2015 to 2017 and later stored at 50% SoC and ∼5 °C until used in the second-life cycling from 2016, 2019 or 2022 . The remaining 4 cells were "pristine", meaning they had been stored at a low temperature (∼5 °C) and never been charged or discharged until used in 2022. Table 1 offers detailed information about the cycling conditions applied during the cells first- and second-life cycling and when they were tested. The cells are labelled with specific identifiers, indicating each cell as well as the temperature for first-life cycling and their orientation (H = horizontal,

V = vertical) during both first- and second-life testing. The cycling of the first 14 cells was conducted from 2015 to 2017 using testers from PEC (SBT-0550 or ACT-0550), while the remaining 4 cells were tested with an Arbin LBT21084 battery tester. All second-life cycling tests and measurements were conducted with the same battery tester used for the first-life measurement, expect for cells 45V-1-H, 25H-10-H and 25V-13-H, which were cycled using the Arbin LBT21084 battery tester for the second-life testing. All cycling was done in temperature-controlled chambers. Note that all cells were tested without any mechanical constraints, allowing the cells to swell and contract during cycling.

Table 1. Overview of all tested cells and their cycling conditions during the 1st-life and 2nd-life testing. The test conditions were temperature, orientation (H = horizontal, V = vertical), C-rate, SoC window, and which year(s) the cells were tested. The cell label has the format of TTO-N-O, where TTO is the 1st-life cycle temperature and orientation, N is the cell number, and the final O represents the possible orientation during 2nd-life cycling.

Cell Label	Cycling Conditions During 1st Life					Cycling Conditions During 2nd Life				
	Temp (°C)	Orientation	C-Rate	SoC (%)	Year(s)	Temp (°C)	Orientation	C-Rate	SoC (%)	Year(s)
45V-1-H	45	V	1	0–100	2015–2016	25	H	0.25	10–70	2022–2023
45H-2-H	45	H	1	0–100	2022–2024	25	H	0.25	10–70	2023–2024
45H-3-H	45	H	1	0–100	2022–2024	25	H	0.25	10–70	2023–2024
45V-4	45	V	1	0–100	2015–2016	–	–	–	–	–
45V-5	45	V	1	0–100	2015–2016	–	–	–	–	–
25V-6	25	V	1	0–100	2016–2017	–	–	–	–	–
25V-7-V	25	V	1	0–100	2016–2017	25	V	0.25	10–70	2019–2023
25V-8-V	25	V	1	0–100	2016–2017	25	V	0.25	10–70	2019–2023
25H-9	25	H	1.5	0–100	2016–2017	–	–	–	–	–
25H-10-H	25	H	1.5	0–100	2016–2017	25	H	0.25	10–70	2022–2023
25V-11-V	25	V	1.5	0–100	2015–2016	25	V	0.25–0.5 *	0–100	2016–2017
25V-12	25	V	1.5	0–100	2015–2016	–	–	–	–	–
25V-13-H	25	V	1.5	0–100	2015–2016	25	H	0.25	10–70	2022–2023
5H-14	5	H	1	0–100	2022	–	–	–	–	–
5H-15	5	H	1	0–100	2022	–	–	–	–	–
5V-16	5	V	1	0–100	2015	–	–	–	–	–
5V-17	5	V	1	0–100	2015	–	–	–	–	–
5V-18	5	V	1.5	0–100	2015	–	–	–	–	–

* Cell 25V-11-V went through a different 2nd-life test than the other cells; 1st life with 1.5 C, 2nd life with C/2 current, and later C/4 current, all in the full SoC window.

2.2. Cycle Life Testing and Characterisation

All cells in this study were cycled in their first life within a SoC window from 0 to 100% at different temperatures (5, 25 and 45 °C), C-rates and orientations, as presented in Table 1. Second-life cycling was performed at 25 °C, with reduced C-rate or in combination with a reduced SoC window. All charge and discharge steps were finished with an OCV period of a minimum of 5 min. The OCV period was prolonged if necessary to enable the cell to cool down to at least 1 °C above the set cycle temperature. All charging of the cells was finished with a constant voltage (CV) hold at the specified SoC levels of 100% or 70% SoC after the constant current charge (CC) until the current dropped below either 0.1 C (2015–2017) or 0.05 C (>2019).

All cells were characterised at 25 °C by measuring the remaining capacities at three different currents (1 C, 0.5 C, 0.1 C) in addition to a high-pulse-power characteristic (HPPC) test to assess changes in the internal resistance. For the cells tested after 2017, an additional 0.05 C cycle was included in the characterisation test. Characterisation tests were performed every 200 cycles, every 1 month, or if the capacity decreased by more than 5%, depending on which condition occurred first. The capacity evaluation was based on the charge capacity measured during the 0.05 C cycle (0.1 C for cells tested before 2017). In the HPPC test, the applied current pulses and their corresponding responses on the cell voltage were analysed. Especially for this paper, the voltage relaxation after the current pulses was analysed to

https://doi.org/10.3390/batteries12040121

find the DC resistance 50 ms after the current pulse was finished. This DC resistance is denoted as "internal resistance" . Typically, we report the evolution of how this resistance changes at 50% SoC.

Note that the Arbin LBT21084 battery tester has a maximum charge and discharge current of 30 A, which corresponds to 0.97 C. For simplicity, we will still refer to this rate as 1 C to facilitate easier comparisons with the older studies performed at 31 A, despite this being a 3% deviation from the nominal 1 C current.

Further details on the experimental setup, as well as cell characteristics, are provided in Appendix A.

2.3. Diagnostics

Incremental capacity (IC) (dQ/dV) curves were calculated from the 0.05 C charge and discharge cycles (0.1 C before 2017). A smoothing algorithm was applied to the voltage and capacity data as described previously [60]. Feature peaks of interest on the IC curves (FOIs) were identified by extracting the values and locations of two local maxima during charging. The voltage shift was calculated by subtracting the actual potential of the maxima from the potential of the maxima at 100% SoH. In combination with the peak height, changes in features were studied and compared under different cycling conditions. The data analysis of the IC curves was conducted using a set of simulated degradation maps established in our previous work [60].

2.4. Post-Mortem Analysis

Several tests were performed on selected cells and their parts when the testing of cells in first life and second life was finished. Two aged cells at 5 °C were opened and scrutinised for electrode morphology, material safety of the anode, and remaining lithium metal in the anode. As a reference, one uncycled cell was also opened. Before dismantling a cell, it was discharged to the lower voltage limit of 2.7 V (0% SoC) at a low C-rate (0.05 C) and left overnight at rest. The cells were then disassembled in an argon-filled glove box ($H_2O \leq 0.1$ ppm, $O_2 \leq 0.1$ ppm) and separated into cathode, anode, and separator sheets.

The material safety of the anode material was studied in an accelerated rate calorimetry (ARC) test of the material, as ARC testing for the full cell was not possible due to the lack of an appropriate setup. The material was obtained by scraping the surface of one side of a double-coated anode sheet aged at 5 °C using a scalpel. The material was tested with a heat–wait–seek (HWS) stepwise procedure of 5 °C steps using the ES-ARC instrument from THT. A stainless-steel bomb/tube (ARC-ES-1750), 5.5 cm long with 0.15 mm wall thickness and one side welded shut, was filled with 0.7 g of anode material and 0.27 mL 1.0 M $LiPF_6$ in EC/DMC (ϕ-factor of 3). The sensitivity of the selected method was 0.02 °C/min.

The morphology, as well as chemical composition of samples from an anode sheet from the cell cycled at 5 °C, was examined using SEM (scanning electron microscopy), EDX (energy Dispersive X-ray), and SIMS (Secondary Ion Mass Spectroscopy), supported by FIB (Focused Ion Beam) for making cross sections. The setup is as described in great detail by Sun et al. [64]. The samples investigated were mounted in a glove box and subsequently put into an air tight transfer chamber so that the sample would not be exposed to air (neither oxygen nor humidity) before subjected to the investigation methods described in this paragraph.

To extend the investigation beyond the capabilities of the extended SEM analysis, a piece of the same anode was subjected to investigation by X-ray computed tomography (XCT). The XCT was performed using a Zeiss Versa 630 machine and with focuses providing

voxels with cubical pixels of approximately 1.67 μm and 0.33 μm. The apparatus and procedure are described further in [65] and the references therein.

Two samples for analysing the remaining lithium content in the electrodes were prepared by soaking selected anode sheets in deionised water. A full electrode sheet was taken from a pristine cell, whereas the the other sheet was taken from cell 5H-14 cycled to 65% SOH at 5 °C. After soaking in water, the solutions were filtered. Reference potential curves were established using standard solutions with varying lithium concentrations, prepared by weighing lithium metal (0.01–0.4 g) and adding it to 100 mL of distilled water. Additionally, 0.1 g of lithium chloride was added to both the sample and standard solutions to improve conductivity and enhance the sensitivity of the ion-selective electrode. The potentials were measured using a DX207-Li ISE half-cell (Mettler Toledo) with an Ag/AgCl reference electrode preconditioned in a potassium chloride solution.

3. Results and Discussion

This section presents the results of the experiments described in Section 2, along with discussions and important considerations for their interpretation. The development of the capacity loss for the Xalt 31HE cell was assessed under different cycling conditions. In this paper, we begin our investigation by examining the general trends in capacity loss over the cells' two separate ageing conditions in first and second lives.

3.1. Capacity Development

In this section, the effect of how different operating conditions affected capacity loss in both the first life and second life is presented for the Xalt 31HE cell. The different operating conditions are presented in Table 1. The different cycle life outcomes are presented in Figure 1, shown as how the remaining capacity (SoH) changes with the number of full equivalent cycles (FEC) for the tested cells. In Figure 1a, the evolution of SoH in first-life cycling is presented. Cells operated at 25 °C showed the lowest loss in capacity, with longer usable life and slower degradation. Cells cycled at 45 °C demonstrated a reduced total cycle life, with a short period of slower capacity loss up to ∼500 FEC. For the cells cycled at 5 °C, an almost instantaneous loss in capacity was observed, with a maximum cycle life of only 25 FEC (see inset in Figure 1a). This was most likely caused by considerable lithium metal plating on the anode and will be further discussed later. An improved effect on cycle life was also observed by reducing the cycle current from 1.5 C to 1 C during first-life cycling.

In addition to the effects of temperature and current, we studied the effect of cell orientation (i.e., vertical vs horizontal) on cycle life. In general, vertical orientation during cycling led to an increased capacity loss. This effect was most pronounced in the cells cycled at 25 °C and 1.5 C, where a vertical orientation reduced the cycle life by more than 50% compared to a horizontal orientation. The effect of orientation was less apparent at 45 °C, with a reduced cycle life of approx 30% for the vertical cells. A vertical orientation has been found to promote non-uniform cell ageing in EV battery packs [66]. This effect is also documented and recently reported for cylindrical cells [67]. The effect of orientation observed here is for cells cycled without any mechanical compression. Also, a significant difference between cylindrical cells and poach cells is the volume in the core of the cylindrical cells, where there is space for residual electrolyte to flow in and out depending on the SOC. Note that some capacity loss variability between cells cycled in different orientations reported herein may also be attributed to manufacturing differences for individual cells.

The ageing trajectory of the cells cycled into second life is illustrated in Figure 1b, with the colours representing the first-life temperatures the same as those presented in Figure 1a, while the first-life part is now grey. Most second-life cells were cycled at 25 °C with a

https://doi.org/10.3390/batteries12040121

reduced SoC window and at a reduced C-rate (see Table 1 for detailed conditions). We observe a prolonged cycle life for all cells, with an improved ageing slope, even if the cell's second-life cycling was started after the cell had reached the "knee-point" in the ageing curve [68,69]. The cycle life extension due to the second-life cycling resulted in more than a doubling of the total FEC for the majority of the investigated cells, with, on average, only 5–10 percentage points additional drop in the SoH.

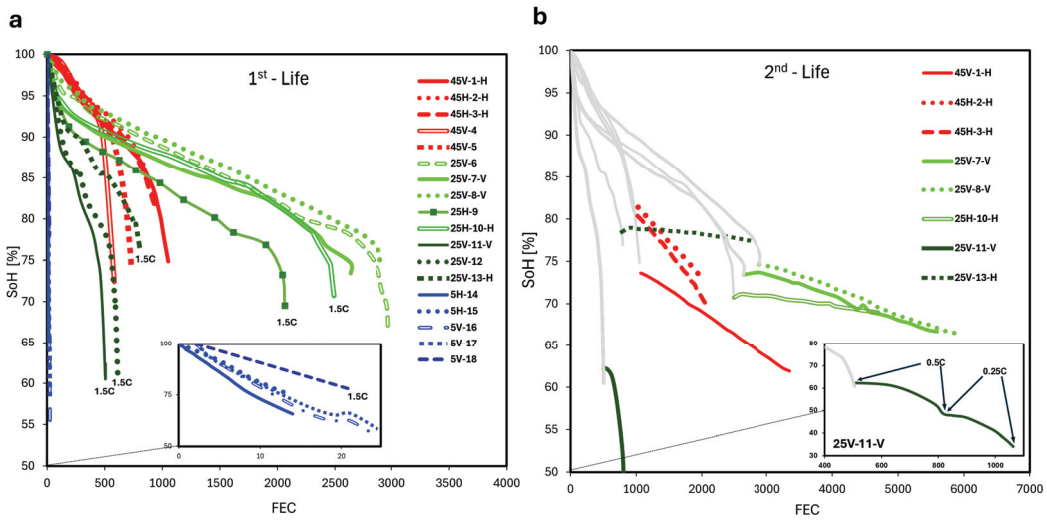

Figure 1. SoH as a function of FEC for cells cycled at different temperatures, C-rates, and orientations. The specific test conditions for all cells are presented in Table 1. The cell label discloses cycle temperature in 1st life as well as orientation in both 1st- and 2nd-life cycling in addition to a specific cell number. In 1st-life cycling (**a**), all cells were cycled in the full SoC window and at 1 C current, except those where 1.5 C is indicated at the end of the lines. In 2nd-life cycling (**b**), all cells were cycled at 25 °C in a reduced SoC window of 10 to 70% and at a C-rate of 0.25 C, except for cell 25V-11-V, which was cycled from 0 to 100% SoC, first at 0.5 C and then at 0.25 C.

The ageing behaviour during second-life cycling may depend both on the history and conditions for cycling in the first life, as well as for the new cycling conditions used in the second life. The main factor improving cycle life in the second-life is the reduction of the SoC window. This is apparent when comparing the ageing trajectory of the only cell that was not cycled in a limited SoC window (25V-11-V). This cell experienced a continued rapid drop in cycle life, with only a minor improvement in cycle life when using the stepwise reduction of the cycling current (see insert in Figure 1b). This behaviour can possibly be attributed to a shift in electrode balance and local higher electrode voltages. In particular, when the cathode is at high SoC and the anode at low SoC, local elevated electrode potentials that are thermodynamically and kinetically unfavourable can be reached. At high SoC, the cathode may operate at higher potentials than at BoL, potentially facilitating parasitic reactions, such as electrolyte oxidation, transition metal dissolution, and lattice structural degradation, that compromise the integrity of the cathode–electrolyte interface [70]. At low SoC, the anode is subjected to highly reducing potentials that can potentially cause instability of the SEI [71]. These parasitic reactions could have contributed to the intensified degradation observed for the cell in 25V-11-V.

The second important factor affecting the second-life cycle life is the temperature that the cells were exposed to in the first life. Cells previously cycled at 25 °C exhibited a slower second-life decline in SoH compared to the cells that were originally cycled at 45 °C. In general, more demanding first-life cycling led to faster capacity loss during second life. This indicates that ageing at higher temperatures triggers ageing mechanisms that possibly cannot be reversed by changing cycling conditions in the second life.

https://doi.org/10.3390/batteries12040121

As for the effects of C-rate and cell orientation in the first life, there was no clear trend on how they affected the ageing trajectory into the second life. The capacity loss of 45V-1-H, which was initially cycled vertically and then horizontally for the second life is lower per FEC than the two cells that were originally cycled horizontally at the same temperature. For 25 °C, the opposite is observed. The cells cycled horizontally in the second life, 25H-10-H and 25V-13-H, degraded more slowly than the two cells cycled vertically, despite also being cycled at 1.5 C in the first life.

3.2. Resistance Development

During ageing, the cell's DC resistance increased considerably depending on its ageing conditions. The DC resistance was derived from the HPPC current pulses. The changes in DC resistance at 50% SoC are presented in Figure 2. For the first-life cycling illustrated in Figure 2a, all cells exhibited an overall increase in resistance as the SoH declined, which is consistent with typical LIB degradation characteristics for older-generation LIB cells. The cells cycled at 45 °C displayed a steeper increase in resistance as the SoH is lowered. In contrast, the 25 °C cells displayed a small initial drop in resistance accompanied by a more moderate, steadier increase in resistance with decreasing SoH. The 5 °C cells maintained a near-flat slope, reflecting minimal resistance growth for the very few cycles that the cells achieved.

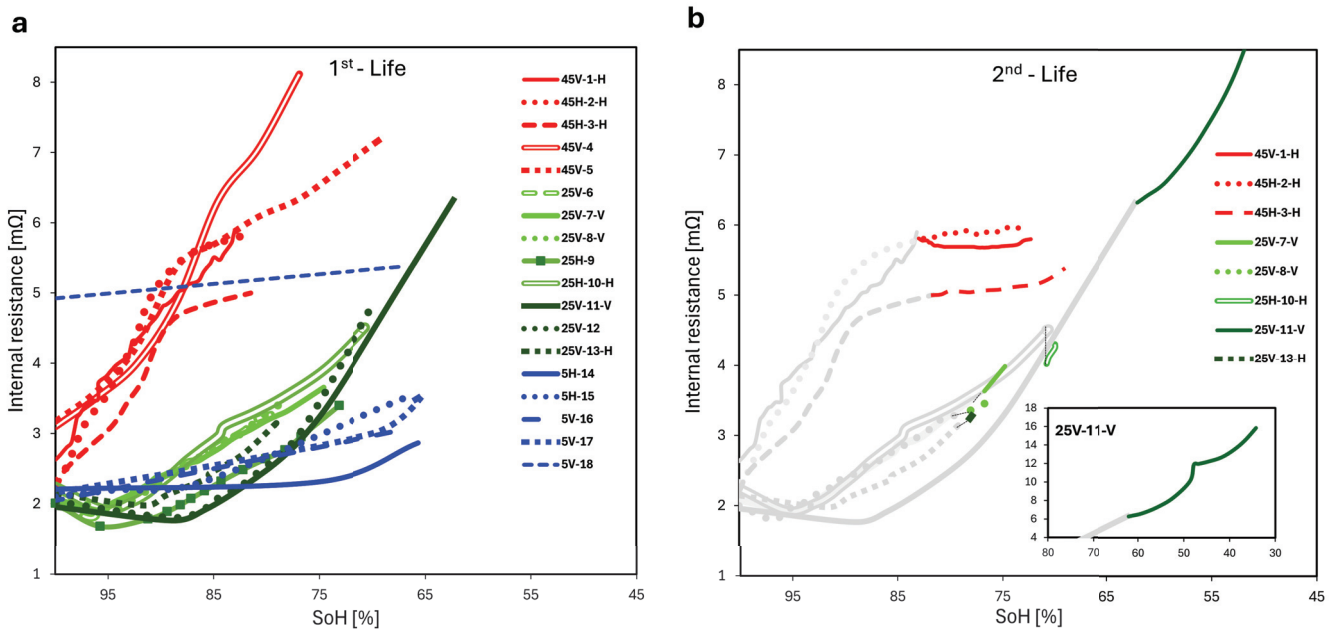

Figure 2. Plot of the DC resistance at 50% SoC as a function of SoH for cells cycled under different temperatures and C-rates during (**a**) 1st-life and (**b**) 2nd-life cycling. For information on test conditions and cell labels, see Table 1 and Figure 1.

Notably, cell 5V-18, cycled at 1.5 C, has a higher initial absolute resistance value compared to all other cells, but still has the same near-flat slope in its resistance curve as the other cells cycled at 5 °C. The authors believe the discrepancy of the initial resistance value was due to an inconvenient location for a voltage sensor/connector and that the resistance difference (3 mΩ) is merely an additional contact resistance. The slightly improved cycle life for cell 5V-18 can potentially be attributable to additional internal heat generation at the higher C-rate for this cell, which has slightly mitigated some low-temperature degradation mechanisms, e.g., lithium plating. From the superimposed graphics in Figure 1a, cell 5V-18 has a slightly lower degradation rate than the other cells cycled at 5 °C. This cell was cycled at a 50% higher C-rate than the other cells at this temperature. It is worth noting

that when we look at the difference between the cell surface temperature and the chamber temperature, ΔT_{C-A}, the 5 °C cells at 1 C had an end of cycle ΔT_{C-A} of around 8 °C and the cell cycled at 1.5 C had a ΔT_{C-A} of around 16 °C. In the light of the other SoH (FEC) curves at different temperatures, this is a probable reason for the slightly lowered degradation rate for cell 5V-18 versus the other cells cycled at 5 °C. Much of its cycling was thus above the low temperatures that initiate and drive the capacity loss in the rest of the 5 °C cells.

In the second-life cycling (Figure 2b), the rate of increase in resistance with respect to the SoH within the cells is significantly reduced for the cells tested at 45 °C cells in the first life, but not in the same manner for the 25 °C cells. The cells tested at 45 °C in the first life retain relatively high resistance values but display a reduced slope. In contrast, the cells tested at 25 °C begin their second lives with a lower resistance value but gradually increase in resistance again as their SoH declines. However, the number of additional cycles achieved is much larger for all cells aged at 25 °C in their second life compared to those aged at 45 °C.

The inset of (Figure 2b) highlights that the resistance behaviour of cell 25V-11-V exhibited a notably steeper increase in resistance with declining SoH, indicative of the onset of accelerated degradation processes. This behaviour is consistent with the corresponding capacity data, which showed rapid capacity deterioration under full SoC cycling during second-life cycling. Additionally, it reinforces the statement already made that operating across the full SoC range, even at moderate temperatures and C-rates, accelerates resistance growth. This highlights the critical role of reducing the SoC window in mitigating degradation and preserving capacity and resistance characteristics into second-life cycling.

3.3. Changes in Incremental Capacity Curves

Beyond reporting SoH and electric resistance as a function of FEC, we investigate how the incremental capacity (IC) curves change as the batteries experience capacity loss at the different operating conditions. The incremental capacity (IC) curves for selected cells at different temperatures during their the first-life cycling are presented by plotting them as functions of the cell potential in Figure 3. In this study, we focused the analysis on two feature peaks in relation to SoH, indicated as reference points labelled F1 and F2 for the IC signal at 100% SoH and shown by the black solid baseline in Figure 3a,b.

In Figure 3a, the dQ/dV plots from cells at a SoH ranging between 91 and 95% depict several trends related to the cycling conditions. The cells cycled at higher temperature exhibited little voltage shift in the F1 peak position, while the F2 shifted to a higher potential value. Additionally, a reduction in intensity was observed for both peaks. For the cell cycled horizontally at 25 °C, the F1 peak shifted to a higher potential while maintaining its intensity, whereas F2 shifted to a higher potential with reduced intensity. A different behaviour was observed for cells cycled at 25 °C but at a higher C-rate and different orientation. The F1 peak shifted to a higher potential with an increase in intensity, while F2 also shifted to a higher potential but with a reduction in intensity. The cell cycled at low temperature had the largest shift to higher potential and the highest increase in intensity for F1 and a shift to lower potential and the lowest intensity for F2.

The SoH levels shown in Figure 3b represent the data after the last cycle in the first-life cycling procedure. To understand the trends in greater detail, we analyse the variation of the F1 and F2 peak positions (potential) and intensities (dQ/dV) as functions of SoH. The potential shift and peak intensity of the two features, F1 and F2, as a function of the SoH of the cells cycled at different temperatures at first- and second-life cycling is shown in Figure 4.

https://doi.org/10.3390/batteries12040121

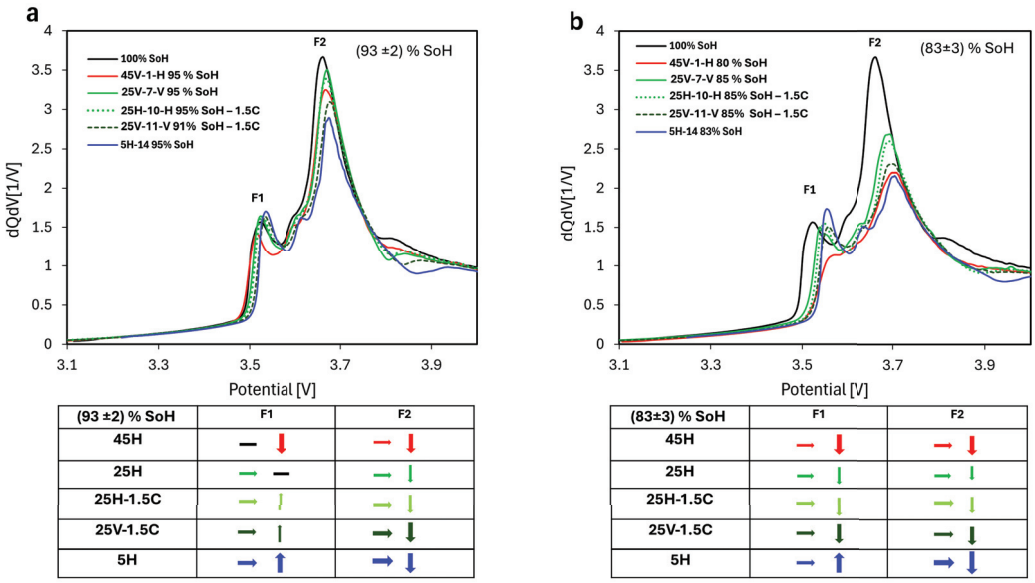

Figure 3. Incremental Capacity Aanalysis (ICA) presented as dQ/dV during charge as a function of cell voltage at 0.05 C for cells during their first life for selected cells aged at different temperatures. In (**a**), the IC curves for the cells range from a SoH of 91 to 95%. In (**b**), the SoH ranges from 81 to 85%. Below each of the plots, (**a**,**b**), arrows or bars indicate the trends of change in potential (**left**) and dQ/dV (**right**) for each peak from 100% SoH, as well as the cycling condition and corresponding plot colours (For the arrows; the color red, green and blue indicate 45, 25, and 5 °C, respectively, and dash bar no significant change.).

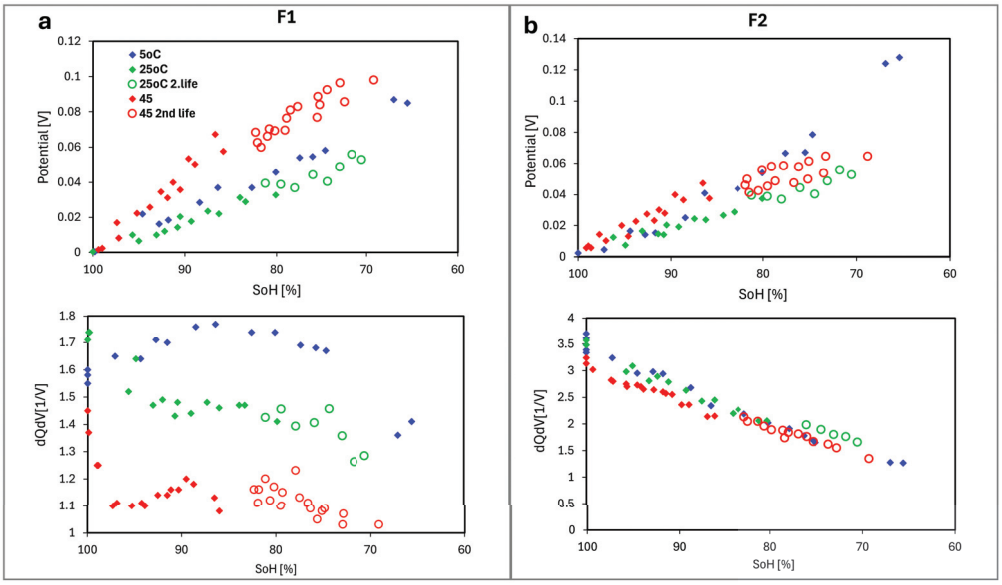

Figure 4. Potential (**top**) and intensity (**bottom**) shifts of (**a**) F1 and (**b**) F2 versus SoH for cells cycled at different temperatures (5 °C, 25 °C, and 45 °C) under1st-life and 2nd-life cycling conditions. Second-life data points are indicated with open markers.

In Figure 3b, we show the dQ/dV plots at SoH values ranging between 80 and 86%. Due to the measurement procedure, where the cells go through 100 cycles or whenever the SoH decreased by 5%—depending on which condition occurred first—and ICA measurements are taken in between, the cells subject to ICA naturally reach slightly different SoHs. For peak F1, all cycled cells displayed a shift towards higher potentials. Notably, the low-temperature-cycled cell exhibited higher peak intensity, while the 45 °C cell had a significantly diminished peak, nearly collapsing in amplitude. For the F2 peak, all cycling

https://doi.org/10.3390/batteries12040121

conditions result in a shift to higher potential, accompanied by an apparent reduction in peak intensity. Notably, the F1 peak exhibits the most significant drop in intensity for the high-temperature-cycled (45 °C) cell.

The shift in the voltage (potential) of F1 for all the cells (see Figure 4a) shows a clear correlation with SoH, increasing progressively as the SoH declines. This behaviour is observed across all temperatures, with the most significant shift observed for cells cycled at 45 °C, while the shift at 25 °C is smaller. A similar relationship is observed during the second-life phase. The F1-intensity for the 25 °C cells decreases with a slight initial drop followed by a gradual flattening (see Figure 4a). However, this behaviour is not observed in cells cycled at 45 °C and 5 °C. For the 45 °C cells, the F1 intensity initially drops significantly before being more or less stable from SOHs of around 97% and lower. The 5 °C cells show a distinctly different behaviour, the F1 intensity remains higher than in cells aged at other temperatures and initially increases as the SoH decreases. After the SoH drops below 80%, the intensity begins to decline, followed by a significant drop at lower SoH levels. Upon second-life cycling, all cells demonstrated a proportional decline in intensity for the F1 peak with a decrease in SoH.

The shifts in potential and intensity of the F2 peak for all cells (see Figure 4b) correlate with the SoH. The F2 potential increases consistently as the SoH decreases in all temperature conditions, with the most considerable shift observed in cells cycled at 5 °C. The F2 intensity decreases as the SoH decreases, showing slight variation among the different temperature conditions. This indicates that the intensity of F2 decreases linearly with capacity loss, irrespective of the cycling temperature. The second-life data exhibit similar trends, following the same relationship between SoH and both the potential and intensity shifts of F2, as observed during first-life cycling. Compared to the resistance measurements in Figure 2, observing the shift to higher potentials of F2 for the cells cycled at low temperatures indicates that losing capacity does not necessarily lead to increased resistance in the same manner.

Analysis of the F1 and F2 feature peaks at different temperatures provides insight into the dominant degradation mode. For high-temperature cells (45 °C), the potential shift and intensity drops in F1 are indicators of LAM at both electrodes (LAMdePE and LAMdeNE) and accelerated SEI formation [60]. The thickening of the SEI layer consumes cyclable lithium, leading to LLI and a rise in internal resistance [38]. For low-temperature cells (5 °C), there is little change in the F1 intensity, but F2 intensity drops strongly, suggesting LLI as the primary degradation mode, potentially due to irreversible lithium plating [60].

To this point, we have examined the impact of temperature, SoC, C-rate, and orientation on degradation behaviour in first-life and second-life cycling. Next, we will focus on post-mortem analyses to further elucidate temperature-specific degradation. In particular, we will investigate cells aged at 5 °C using material ARC, SEM, EDX, SIMS, and lithium leaching. These methods provide insight into thermal offset changes, morphological changes in the anode material, and the potential presence of lithium plating.

3.4. (Material) ARC Testing

Accelerated rate calorimetry (ARC) is a valuable tool for understanding the safety of batteries, as it indicates the temperature at which LIB cells or materials extracted from them become unstable and prone to initiating a thermal runaway. ARC used in degradation studies can also indicate the degree of suitability for second-life applications, as in this case, where the interest lies in understanding whether first-life cycling conditions have an impact on second-life high-temperature thermal stability. Note that ARC is a destructive method, so once an LIB is investigated after first life using ARC it is no longer available for second-life testing. As the cells in this study were mostly subjected to second-life

testing, except for the cells cycled at 5 °C, we have also presented relevant ARC results for a different cell type (LFP cells) that underwent only first-life cycling. These results are shown to give a comparison to the 5 °C cycled cells of the present study that were subject to the material ARC testing.

Material ARC was conducted to qualitatively assess the thermal behaviour of the anode material extracted from the 5 °C cell by measuring its self-heating rate as a function of temperature. While the comparison is limited compared to full-cell ARC results, this analysis aims to provide supporting context for interpreting changes in thermal stability associated with low-temperature cycling. Figure 5 illustrates the measured heating rate as a function of temperature. The provided results are for the anode material (material ARC) of the cell cycled at 5 °C (light blue), along with experimental data from [72] for a commercial LFP cell (full-cell ARC) cycled at 5 °C (dark blue), 25 °C (green) and 45 °C (red), as well as for an uncycled cell (grey). The cycled LFP cells had SoHs ranging from 72% to 81% when subjected to the ARC test. The anode material cycled at 5 °C exhibits a self-heating onset at 74 °C, and the reaction rate accelerates rapidly between 130 °C and 144 °C, ultimately reaching thermal runaway at 144 °C. The result of the material ARC test is similar to the reported data for the commercial LFP cell cycled at 5 °C in [72], corroborating the understanding that low-temperature cycling lowers the thermal runaway temperatures for both thermal onset and thermal runaway, increasing reactivity, and that this hazardous effect is related to anode degradation processes during cycling at low temperatures.

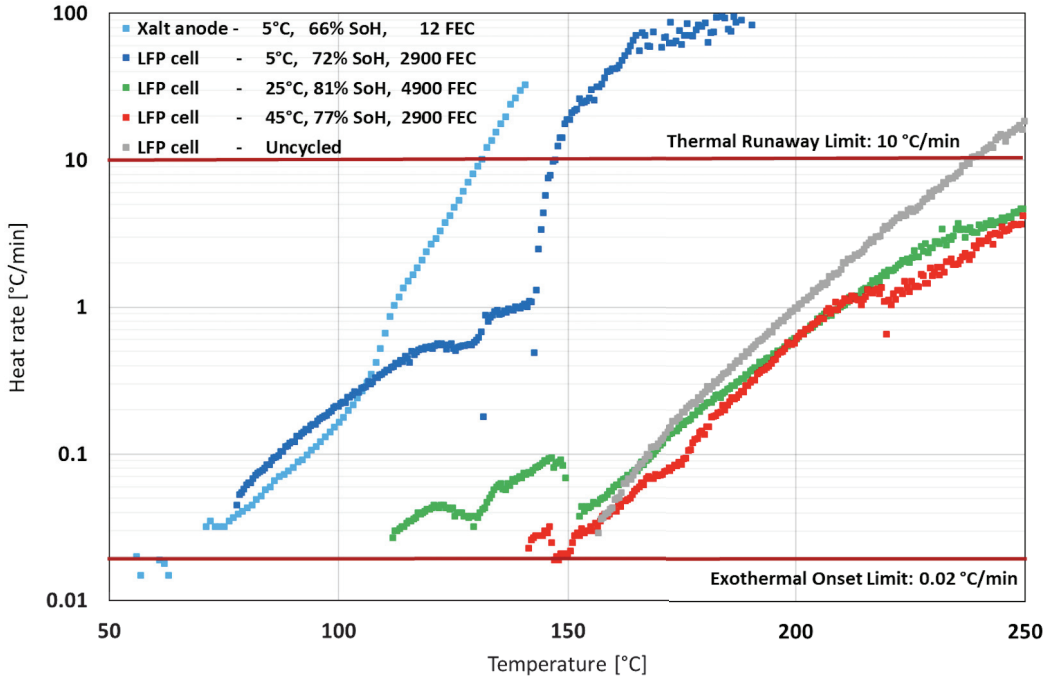

Figure 5. ARC test of the cycled anode material from a 5 °C cell, with reference data from [72].

3.5. Investigation of Anodes Cycled at Low Temperatures (5 °C)

As so far seen in this article, the cells cycled at 5 °C had an extremely rapid loss in capacity during cycling. It is also observed that this relates to the anode, considering the results of the material ARC testing. As such, it is interesting to look at what happened to the anodes during cycling.

The anodes from the low-temperature cycling were dissected and subjected to various tests after the reported cycling. The details of this investigation are reported in the Appendices B–F, and only the highlights are presented here.

The first significant observation is from visual inspection of these anodes. The anodes were slightly larger than the cathodes, so that in the cell stacking, the anodes' edges would always be around 2 mm outside the cathodes. This is commonly referred to as an overhang and is common in many battery stacks to avoid local overcharge at the edges. An edge strip is shown using digital imaging in Figure 6 (lower centre). From this, one can see that the overhang has a distinctly different colour to the part of the anode that was underlying the cathode. Whereas the overhang part was black and looked like a pristine anode, the underlying area was beige or silver-like. When exposed to air, the underlying area reacted and changed in colour and topography, and the changes were clearly visible to the eye. These changes are documented further in the supporting materials.

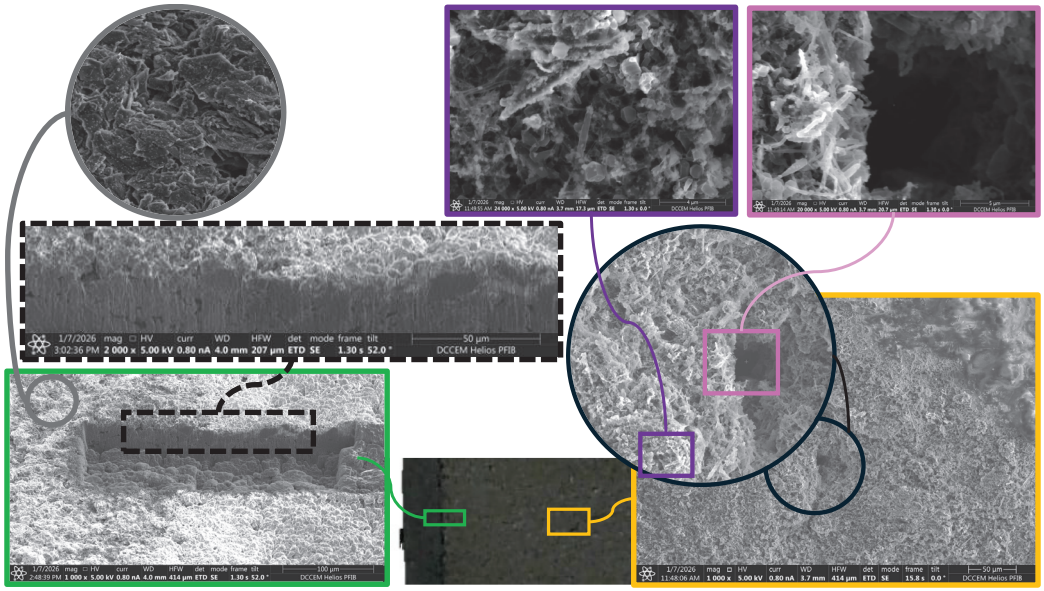

Figure 6. The figure shows a sample of an anode examined by SEM, FIB-SIMS and SEM-EDX. In the lower centre, one can observe the sample (optical picture) of a section of the anode. Two characteristic sections of the anode where inspected further; the transition between overhang and cathode underlay anode (green) and well into the actively cycled anode (light orange). From these two SEM images (green and orange framed), one can see the three types of layers (i), (ii), and (iii). (i) is visible in the left part of the green-framed micrograph, (ii) is visible in the right of the green-framed micrograph and in the majority of the orange-framed figure, and (iii) is visible in the upper right part of the orange-framed micrograph. Further, layer type (ii) was found to have surface (purple framed) and pit/hole (pink framed) characteristics.

The anode sample was then examined using SEM, FIB-SIMS, and EDX. From SEM micrographs, one can see that the anode had three different characteristic surface appearances: type (i), the overhang that appeared like uncycled anodes; type (ii), crystals on the surface; and type (iii), a smooth layer that partly covered the second characteristic surface. For the overhang, it can be seen in the upper left corner of Figure 6. The transition zone between the overhang and the underlying area is shown in the lower left of Figure 6. By deploying FIB etching, one can see how the crystal-based surface layer is present in larger pores and more open areas near the surface, as well as just in the surface layer on top of the anode. At the top surface, one can see the characteristics of type (ii) and (iii) surface coatings via the yellow-framed SEM micrograph. In that micrograph, type (iii) is recognised in the upper right corner and type (ii) is seen in the remaining area. Using EDX, the type (iii) characteristic areas were found to contain very large portions of phosphorous and fluorine, in molar proportions of one to six, indicating residual PF_6^-. Here, carbon and lithium (by SIMS) were also detected. This suggests this layer being composed of residual electrolyte that was not sufficiently cleaned from the electrodes. Similarly, materials with

https://doi.org/10.3390/batteries12040121

same composition were also found deeper in the anode pores, further supporting the type (iii) layer being residual electrolyte. Type (ii) coatings were found to be very rich in lithium (SIMS indications), as well as having large portions of oxygen, indicating that this could have been lithium metal oxidized by trace levels of oxygen in the glove box (which is never truly zero). Looking further at the type (ii) coating, it appears as a highly porous structure constituted of crystals. These crystals were seen to be needle-like in deeper pores and more cubic, hexagonoids, or dendritic together-grown lumps on the top surface. This is a strong indication of lithium electro-deposited structures grown under diffusion-limited concentration gradients.

X-ray computed tomography (XCT) was also included in this study. A summary of the visualisations is provided in Figure 7. In contrast to the SEM approaches, it was not possible to document any differences between the three typical surface layers: type (i), (ii), and (iii). What can be observed instead is that the carbon in the anode region, typically coated by layers of type (ii) and (iii), appears swollen compared to the carbon at the overhang (under surface layer type (i)). From the semicircle focus, where the pixels are 5 times smaller than the other XCT images and where the zone between the cathode overlay region (left) and the anode overhang (right) is shown, one can see this difference in carbon swelling particularly well, as well as the gradual change.

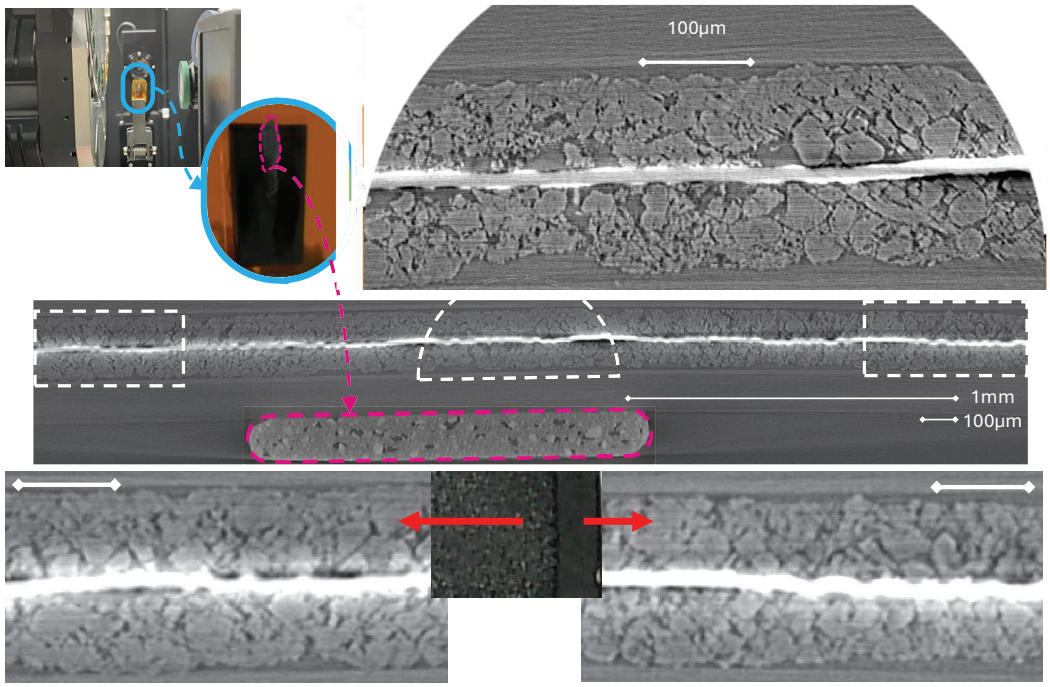

Figure 7. Illustration of the X-ray setup (**upper left**) and a slice cut through the battery anode thickness direction (**centre**). Also, a picture of the electrode near the end is displayed (**lower middle**), with enlarged XCT images of under surface coating type (ii)/(iii) (**left**) and under type (i) (**right**). In the upper-right semicircle, XCT images of the transition zone between the active cathode overlay region and the anode overhang region, oriented accordingly, are shown. Images include 100 µm bars for indication of dimensions, as well as one 1 mm bar in the centre picture. The anode current collector can be recognised as the bright centreline or region.

Despite not directly documenting the type (ii) or (iii) surface layers by studying Figure 7, one can see that the top layer of the cathode underlay region has a distinct reduced porosity in comparison to the overhang region. The region at the part of the anode that has been facing the cathode and the electrolyte is more dense. In light of the SEM investigation, this layer can thus be interpreted as layer (ii) or (iii), but it is difficult to argue this independently of the SEM investigation. Moreover, from the XCT analysis and

particularly regarding the bulk part of the anode, this densification is at least partly due to the anode active graphite particles being more swollen.

The observations shown here via SEM, FIB, SIMS, EDX, and XCT are representative of what was typically seen by investigating several different sites on an anode. Further details and additional documentation are provided in the supporting materials.

As much as lithium in combination with various elements, either oxygen or PF_6^-, is recorded and documented, even in very metallic like structures, this does not prove that the deposit is actually metallic lithium. Since lithium metal is indeed very difficult to record and report, the samples were subject to testing for the purpose of developing a leaching test. This can be viewed as a novel approach to detecting lithium. The main conclusion is that only a small percentage of the lost capacity could be detected in this manner. It also remains unclear why the deposited material would not leach, but two possibilities remain: either metallic lithium reacted with air into lithium oxide that would not dissolve in water, or the surface layer is an organic lithium or carbide compound that will not dissolve in the chosen water solution.

4. Conclusions

In this study, we cycled 18 NMC(433)-graphite 31Ah LIB cells to understand the prospects for a second life, focusing on their remaining life potential and safety. The cells underwent various first-life cycling conditions by changing the temperature, SoC window, C-rate, and orientation. This was followed by standardised second-life cycling at fixed temperature, with further variation in the SoC window, C-rate, and cell orientation. From the experimental results, we draw the following conclusions:

- By changing cycling conditions at a SoH of around 75%, the amount of added full equivalent cycles can double before reaching 70% SOH.
- Cycling cells at room temperature provides lower degradation rates than cycling cells at 5 and 45 °C.
- Increasing the ambient operation temperature in first life from 25 to 45 °C will increase the degradation rate of second-life cycling, despite the second-life operation temperature being lowered back to 25 °C.
- For second-life cycling, reducing the SoC window (by 40%) is more important than lowering the C-rate (by 1/3) (for the selected cells).
- First-life cycling in room-temperature air (25 °C) gives lower degradation rates as well as lower cell resistance compared to elevated air temperatures (45 °C). These two effects positively contribute to the lower degradation rate in second-life cycling.
- Vertically oriented cells (standing) experienced higher degradation than horizontally oriented (lying) cells when not under pretension. Vertically oriented cells at 1C degrade at similar rates to horizontal cells at 1.5 C, for the selected cells in the first life in this study.
- Cycling cells at excessively high C-rates and low temperatures (1 C and 5 °C) leads to the most extreme degradation rates (tenfold higher than other temperatures) in this study.
- In the ICA analysis, and for the two selected features (most distinct positive peaks at 100% SOH), feature 1 (F1, lower cell potential) was the one peak that most strongly indicated compatibility with a second life, considering both safety and lowered degradation rates.

Author Contributions: Conceptualization, O.S.B. and P.J.S.V.; methodology, All Authors; validation, G.M.H., W.D., S.B.B.S., O.S.B. and P.J.S.V.; investigation, E.R.E., O.S.B., P.J.S.V., S.B.B.S., W.D., G.M.H., J.W., T.L., S.A.W. and L.T.B.E.; data curation, E.R.E., O.S.B., S.A.W., L.T.B.E. and T.L.; writing—original

draft preparation, E.R.E., S.B.B.S., J.W., P.J.S.V. and O.S.B.; writing—review and editing, All Authors; visualisation, E.R.E., S.B.B.S., W.D., T.L., G.M.H. and O.S.B.; supervision, E.R.E., P.J.S.V. and O.S.B.; project administration, O.S.B., P.J.S.V. and J.W.; funding acquisition, O.S.B., P.J.S.V. and J.W. All authors have read and agreed to the published version of the manuscript.

Funding: The authors would like to acknowledge funding under the Research Council of Norway, grant numbers: 320760, 281005, 228739, and 350373. W.D. and P.R.S. acknowledge financial support from the Oxford Martin School (for Circular Battery Economies).

Data Availability Statement: The data presented in this study are available on request from the corresponding author.

Acknowledgments: Arnstein Røskar Nisja is acknowledged for contributions to the measurements in the Appendix B regarding ICA, cycling, and the confidence therein.

Conflicts of Interest: The authors declare no conflicts of interest.

Appendix A. Experimental Details of the Battery and First-Life Testing Conditions

The Xalt battery underwent all tests in standard thermal chambers with fan-circulated air. During the first life, some of the cells were lying down (horizontal), whereas others were in an upright position (vertical). The upright position was achieved by standing the cells on their lower end towards a plexiglass (polycarbonate) sheet, with the tabs (clamped to leads and sensing wires) on the top, while leaning gently on a line support. In detail, a plexiglass sheet with large rectangular end-rounded holes, at least twice the thickness of the cells, were supporting the cells so that they would stand up. The setup is illustrated in Figure A1. The details of the cell specifications are given in Table A1.

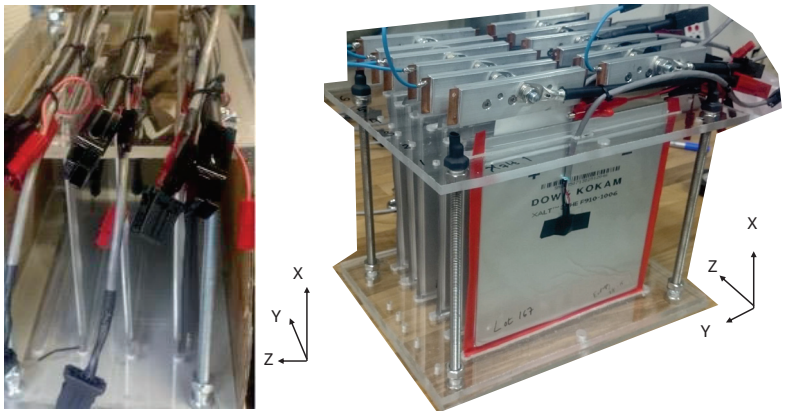

Figure A1. The battery cell holder for the standing (vertical) cells. Three cells are displayed, with lead connections at the top.

Table A1. Factory specification sheets of the Xsalt cell.

Specifications	Range
Capacity (C/2)	31 Ah
Voltage range (nominal voltage)	2.7–4.2 V (3.7 V)
Continuos max charge and disch.	2 C and 5 C
Temperature window, charge and disch.	0–45 °C and −20–60 °C

Appendix B. ICA First Life Comparison and Confidence Considerations

In this study, we have presented a large variation of cycling conditions for an NMC-graphite 31 Ah cell. This large variation also means that replicas of specific cycling conditions are scarce and that the confidence level towards conclusions appears low. One of

the main discussion points relates to how we can separate, particularly the feature height (dQ/dV-value) of F1, in relation to the cycling temperature in the first life and consequently relate these to safety concerns regarding the battery cells in their second lives.

In Figure 4, there are not that many cells that provide information about the first- and second-life ICA feature peaks for the three first-life cycling temperatures. Our discussion revolves around the signature of feature F1 and the dQ/dV value, organised by temperature groups. To somehow improve the validity of these temperature groupings is therefore essential. Here (Appendix B), we attempt this by two means. For all the temperatures we have added ICA recorded at C/10, and for the short-lived low-temperature measurements we have also cycled an extra cell, recording the ICA after each cycle under the same conditions as those for cells 5H-14 and 5H-15.

The data sets used to improve the validity of the results discussed in the main manuscript were collected over an extended period. It is worth noting that some earlier-recorded ICA curves were obtained at C/10 rather than C/20. In Figure A2, one can see first-life cycling data for cells where the ICA feature peaks are gathered at 25 °C at C/20 (circles) and C/10 (squares) and where the first-life ambient-air cycling temperatures were 5 °C (blue), 25 °C (green), and 45 °C (red).

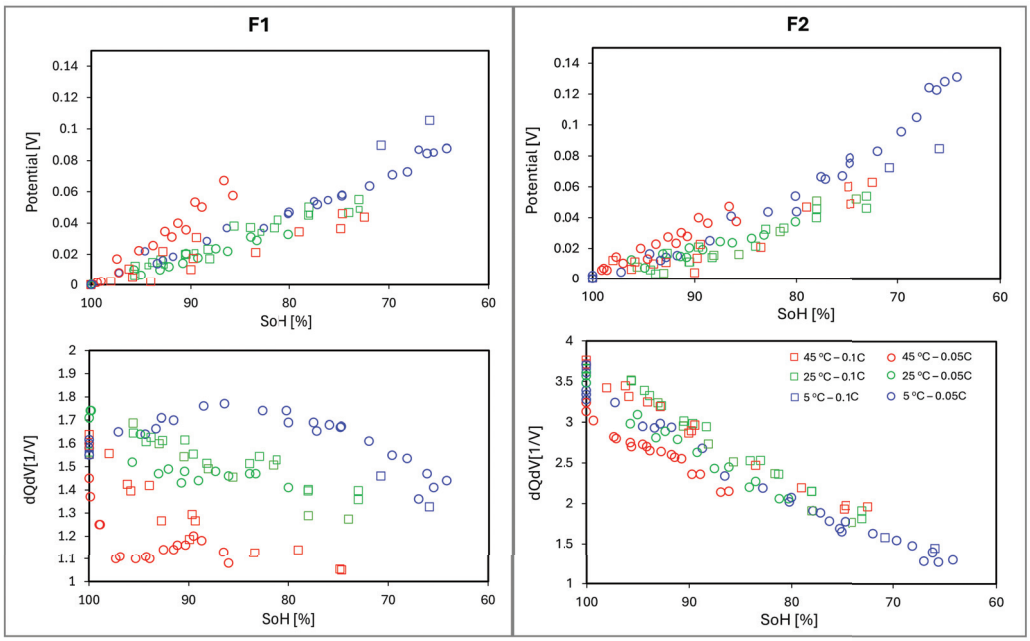

Figure A2. Overview of 1st-life ICA and feature peaks (F1 and F2) obtained at C/20 (circle) and C/10 (square). In comparison to Figure 4, we have added ICA data recorded at C/10 as well as C/20 ICA data for a cell cycled at 5 °C.

Generally, one can see that for feature F2, there is no significant difference in the dQ/dV or the potential (V) as functions of state of health (SOH) when examining the cycling temperature dependency. This also goes for the V value as a function of SOH for feature F1. It is for feature F1 and when looking at the dQ/dV value as a function of SOH that the results tend to group distinctly differently for the three different cycling temperatures, thus demonstrating an interesting feature for considering second-life usefulness.

Looking more carefully at feature F1 dQ/dV as a function of SOH, the higher cycling temperature (45 °C) leads to a more rapid drop for F1 dQ/dV data, the medium temperature (25 °C) leads to a slower drop in F1 dQ/dV values over time, and the lower cycling temperature (5 °C) leads to an initial slight increase and later lowering in F1 dQ/dV as a function of SOH.

https://doi.org/10.3390/batteries12040121

In comparing the results in Figure 4 to Figure A2, we can see that the first-life feature peak coordinates as a function of SOH remain similar with respect to cycling temperature. However, this comparison is challenging because the ICA cycling rates (C/10 and C/20) lead to an adjusted voltage change due to the ohmic potential drop being slightly larger at C/10 compared to C/20. For the dQ/dV, this is even more complicated; however, generally and theoretically, the dQ/dV peak should have lower values when recorded at faster C-rates. The expected shifts in voltage and dQ/dV values when comparing C/20 to C/10 in this study appear random at best. Thus, it is not considered valid to discuss this point further here, other than stating that the temperature trends observed in Figure 4 are not significantly different from those seen in Figure A2, thereby increasing the conformity of knowledge drawn from Figure 4. The information with most importance for improving validity that is presented in Figure A2 compared to Figure 4 is the extra cell cycled at low temperature where the dQ/dV(SOH) trend is further verified.

Appendix C. Visual Inspection in Air

The anode of the cells cycled at 5 °C turned out to be very sensitive to air exposure. Depending on the air in the room, the time response differed a lot. In Figure A3, one can see the visual changes of the electrode at different air exposure times. The air in the room location where these images were captured was relatively still, and it is worth noting that under other air flow conditions around the sample the visual response was sometimes observed to be almost ten times faster.

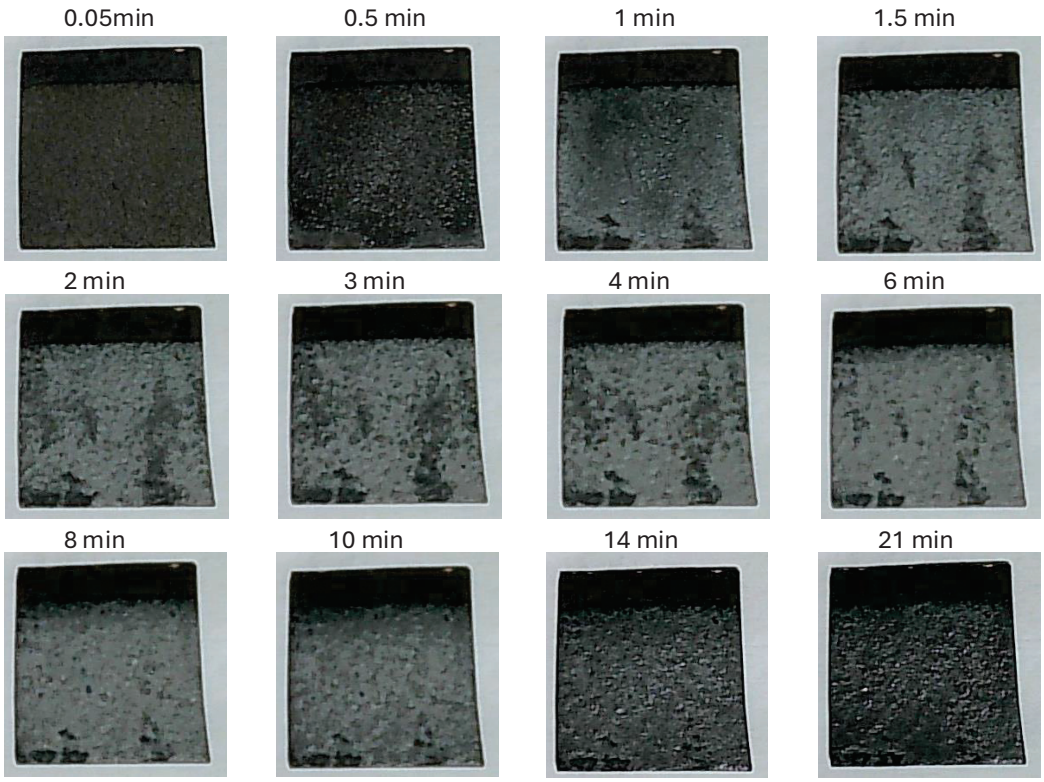

Figure A3. Figure showing photographs of a piece of an anode exposed to air for different lengths of time. The electrodes are pieces of an anode (ca 15 mm by 15 mm) cycled at 5 °C, and the time stamps indicate air exposure times.

Looking at the anodes taken from the 5 °C cycled cells, when in a glove box, one can clearly see the overhang of the anodes, i.e., the area that would not have been aligned within or covered by the cathode. This area was black, similar in appearance to an uncycled anode or an anode cycled at higher temperatures. The area covered by the cathode had a

https://doi.org/10.3390/batteries12040121

lighter colour, beige or light brown, and this colour changed a lot during air exposure, first turning light grey and then turning dark or almost black again. This rather reactive layer was included in the anode material ARC tests described in the main manuscript, although it was collected and placed in a sealed test holder using glove boxes.

The reactive layer described in this study caught the attention of the researchers participating in the study, and several attempts were made to understand or document the nature of this material. One experiment was to leave the electrodes in water and measure a lithium response electrochemically, see Appendix F. Other experiments involved transferring electrodes in argon from a glove box into an SEM-FIB-SIMS-EDX instrument, Appendix D, as well as an X-ray computer tomography (XCT) device.

Appendix D. SEM, FIB, EDX, and SIMS Example Investigations

In the main part of the manuscript (Section 3.5) a brief description of the electrode extended SEM investigation is provided, which was a result of a broader investigation. Here, a more detailed SEM investigation is described, whereby SEM is supported by the use of EDX, SIMS and/or FIB sectioning.

Looking first at the top view of the electrode in Figure A4, one can see the characteristic surface coatings, the porous crystal layer (type (ii)) and the smooth coating (type (iii)). To assist the reader in comparing the different graphics in Figure A4, dashed white grid lines are added consistently applied throughout the graphics. From EDX elemental composition analysis (excluding Li), it was found that the general composition of fluorine and phosphorus was very close to 6:1, indicating residual electrolyte salt, $LiPF_6$, was present at the surface. It can also be seen that in the region where the type (iii) layer is present, oxygen appears to be absent. Oxygen can be seen as a sign of lithium deposits that, over time, have adsorbed and reacted with even the small amounts of oxygen in a glove box. Carbon is also observed in relation to the type (ii) layer. Generally, from the EDX mapping, it appears that the topography of the type (ii) layer gives a topographic shadowing effect on the left and the upper side of the structure sticks out slightly more. Where holes are absent (e.g., lower middle of the lower middle sections and the lower middle of the upper left section), the EDX signal also appears to be absent. This indicates that carbon is present in the crystalline layer characteristic of type (ii). As such, it is difficult to argue that the type (ii) layer is lithium metal alone; it could also be lithium–carbon that is oxidised to hold oxygen. Examination by FIB and SIMS can provide further details on this. Thus, this is a point of discussion that needs to be understood from the FIB milled cross-section inspection discussed in the following paragraphs.

The smooth type (iii) coating appears to weaken the signal of all elements, suggesting this layer is neither of the investigated elements. The lack of response for all four elements in the type (iii) layer makes it very difficult to assess what this is. It could be electrolyte organic solvent compounds; however, this should then also include the electrolyte salt ($LiPF_6$), which is simultaneously less visible. It was noted that this type of layer would react to become porous and cracked when exposed to the electron beam for a longer period or at a higher intensity, further suggesting that this could be an organic material, for example electrolyte solvent.

Having investigated the surface topography and composition, the study further delves into the subsections underneath. This is done via FIB etching and the use of EDX and partly SIMS. Looking at Figure A5, one can see a picture of piece of an anode (similar to those in Figure A3) in the lower centre. Two places were investigated: along the edge (yellow frames) where the piece was cut out of the anode sheet, and an area well into the material where it was unaffected by the cutting (red frames).

https://doi.org/10.3390/batteries12040121

Looking at the edge investigation (yellow- and black-framed images in Figure A5), one can see that the material cutting has led to delamination, as well as being covered by the type (ii) layer. One can see that the hole in the electrode (likely from the manufacturing) has a very different type of crystal pattern from the surface, as discussed previously. It follows that the surface structure in this image is covered by the FIB redeposition of sputtered material, so the type (ii) top view crystals no longer appear with their original structure, now being more volumetric in shape. Those in the pit or hole are shielded from this scatter and have retained their more needle-like shape.

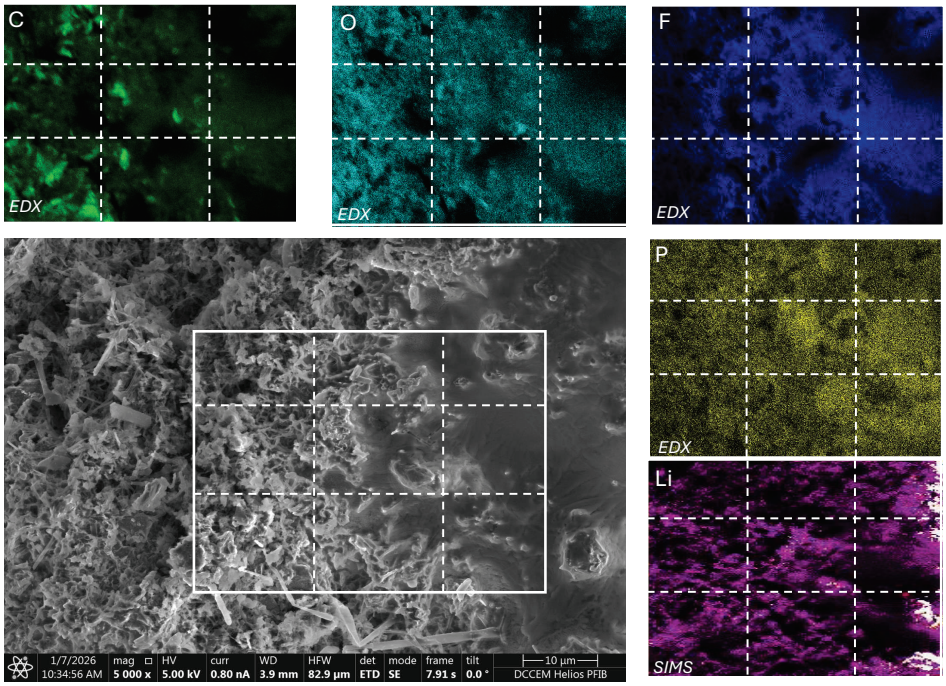

Figure A4. SEM micrograph of a typical top view of the anodes cycled at 5 °C (lower left), 4 EDX elemental intensity maps for carbon (C), oxygen (O), fluorine (F), and phosphor (P), and a SIMS lithium (Li) intensity map.

Looking at the micrographs taken well into the material (red- and purple-framed pictures in Figure A5), one can get a view of both the top view (red frame) as well as the cross-sectional view (purple frame) of the material. In the top view, the purple line indicates the site of the FIB cross section. Prior to milling, a block of platinum was deposited to preserve and protect the surface detail in the cross section. The platinum deposit can be recognised in the purple frame image and as a grey line on top. In the cross-sectional view, it can be seen more clearly how the type (ii) surface layer has grown in what were initially empty surface pores. An EDX line scan was taken along a pore from relatively deep into an area that is clearly coated with a type (ii) layer. This line scan is indicated using a blue line, and it was approximately 45 µm long. The elemental composition was then plotted in the graph in the uppermost right corner of Figure A5. This plot shows the ratio of fluorine to phosphorus (F:P in purple) as well as the carbon content (red line). In the lower part of the pore, one can see more than 80% carbon, which reflects less than 20% porosity for carbon. One can also see that this region has a presence of fluorine that is much higher than 6 (consider PF_6^-), and this can be attributed to a mixture of carbon black and fluorine rich binder, like PVDF. In the region where the pore was likely more open, deposits of $LiPF_6$ salt can be considered, given that the fluorine–phosphorus ratio is closer to 6. At the outer end of the pore, one can see that the type (ii) surface layer is predominant. Using SIMS and

https://doi.org/10.3390/batteries12040121

EDX, this layer was rich in both lithium and oxygen. One can also see that this layer is rich in carbon, so it is not solely lithium or oxidized lithium.

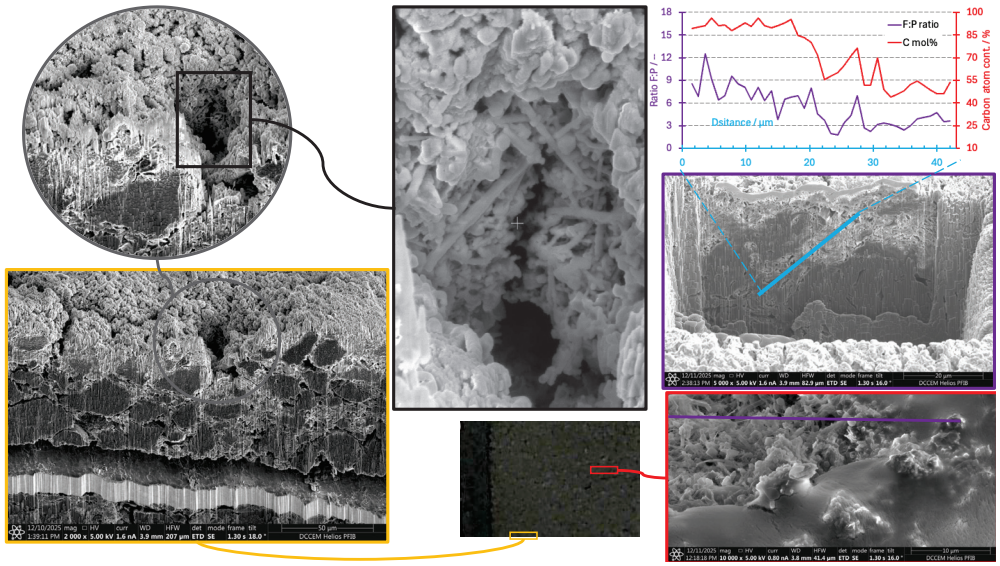

Figure A5. SEM views of sections subject to FIB milling and EDX/SIMS investigation. Images on the left show FIB milling into an edge of an anode sample. Images of the right show a surface FIB milled section (lower) with indication of the line area subject to FIB front (purple line) and the through-plane section SEM view (right middle purple frame), where in turn an EDX line scan through a pore (blue line is indicated) and atomic percentage of carbon (red) and F:P molar ratio (light purple) are further plotted graphically (upper right).

Here, we provide further documentation for some of the statements given in relation to Figure 6, the transition zone between type (i) and type (ii) surface characteristics. This is the transition zone between the anode overhang and cathode underlying anode, and it is shown here with EDX maps and as a table. This can be seen in Figure A6. The SEM micrograph (same section as in Figure 6) indicates the EDX mapped region using a white line that can also be seen in the elemental intensity pictures. The first thing to note is how strong the linkage is between the type (ii) coating and oxygen and inversely so for carbon. Recall the discussion from five paragraphs above in relation to the top view of Figure A4 around the visibility of carbon and other elements. In the combination of Figure A4 and Figure 6, one can conclude that the top view carbon signal is essentially from the EDX signal penetrating though the surface coating, making carbon seemingly appear together with oxygen and, likely, also lithium, which is thus not the case. In fact, from views of FIB milled cross sections, supported by EDX and SIMS oxygen coincides with lithium and oppositely so with carbon. Oxygen and carbon appear to be not simultaneously present. Fluorine and phosphorus have a similar trend. It is therefore important to display local composition as well as the overall average elemental composition, and to point out the relationship between fluorine and phosphorus and how close their stoichiometric ratio is to 6. This is an indication that $LiPF_6$ is present in the type (ii) surface layer. It can also be seen that this ratio is present well into the pores in the deeper layers of the anode; however, it occurs much more in the type (ii) surface layer, which also coincides with the presence of oxygen.

https://doi.org/10.3390/batteries12040121

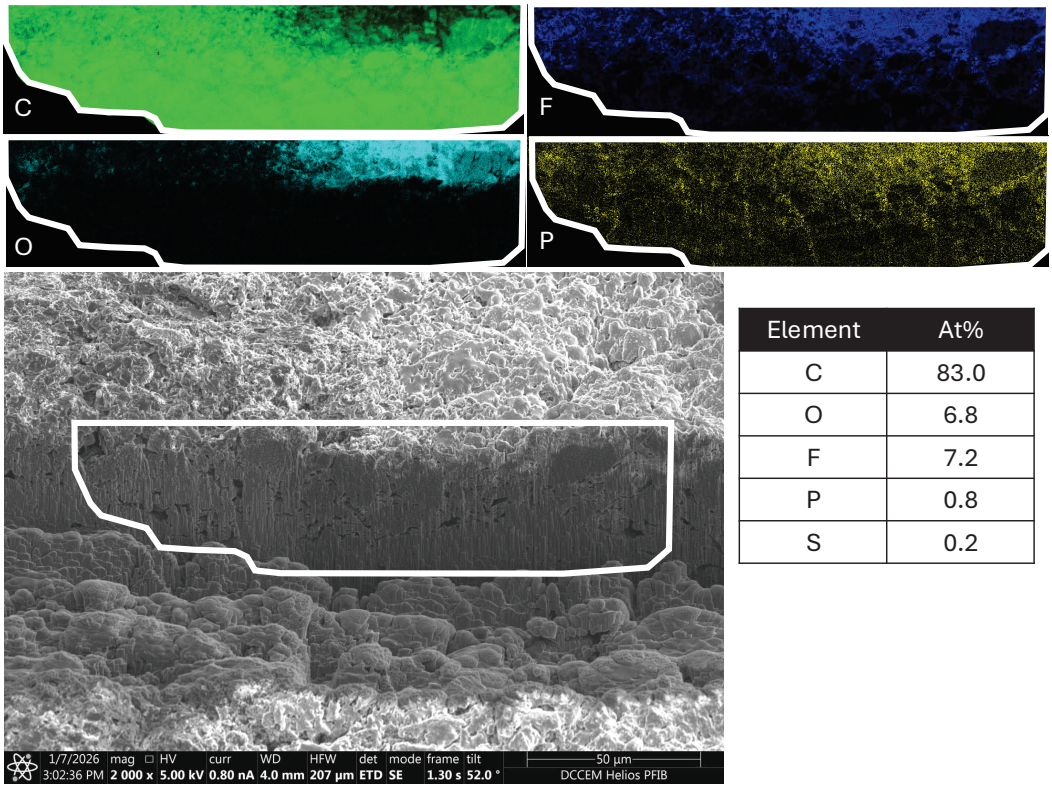

Element	At%
C	83.0
O	6.8
F	7.2
P	0.8
S	0.2

Figure A6. SEM micrograph of a region subject to FIB milling, where the anode overhang transcends into the cathode underlying area, corresponding to Figure 6. EDX intensity plots of relevant elements are also shown. A tabulated overview of EDX-scanned total atomic composition is also shown.

Appendix E. XCT Visualisation and Porosity

As described in the main section, the porosity of the overhang region appears to visually differ from the part of the anode overlayed by the cathode. Using XCT, it is possible to quantify the volume fraction of the active graphite material and thus make considerations about the state of the graphite particles in the two regions. This is because the resolution of the XCT is not sufficiently fine to include detecting carbon black and binder materials. Figure A7 shows how this is done in volumetric boxes in parallel with the overlay–overhang transition edge zone. The volumes analysed for graphite filling degree consisted of over 10.5 million (1151 × 100 × 92) voxels (ca 500 × 33 × 33 µm^3), creating a high degree of accuracy for each data point. The smaller variation between each volume is assumed to be natural variation between them. Moreover, if considering that there is a transition zone and dividing them into two, Figure A7 indicates that there are two regions with fairly constant graphite fillings. One can see that this is a distinct shift around 450 µm in the graph in Figure A7, but one can also see that this shift is challenging to argue the significance of, at least with a sigma two (95%) confidence.

Furthermore, porosity in a classical sense of gas volume is not actually possible using the present XCT resolution. If considering a solid content of 66%, it would indicate a porosity of 34%. This is however not the case, as the reported graphite content of Figure A7 only accounts for graphite (active material) and not for other materials (binders and carbon black). If, however, approximately 10% additional solid volume is added by these other materials in the anode (pristine), graphite (only) contents of 62, 65, and 68% would correspond to electrode porosities (graphite, carbon black, and binder) of 32, 29, and 25%.

https://doi.org/10.3390/batteries12040121

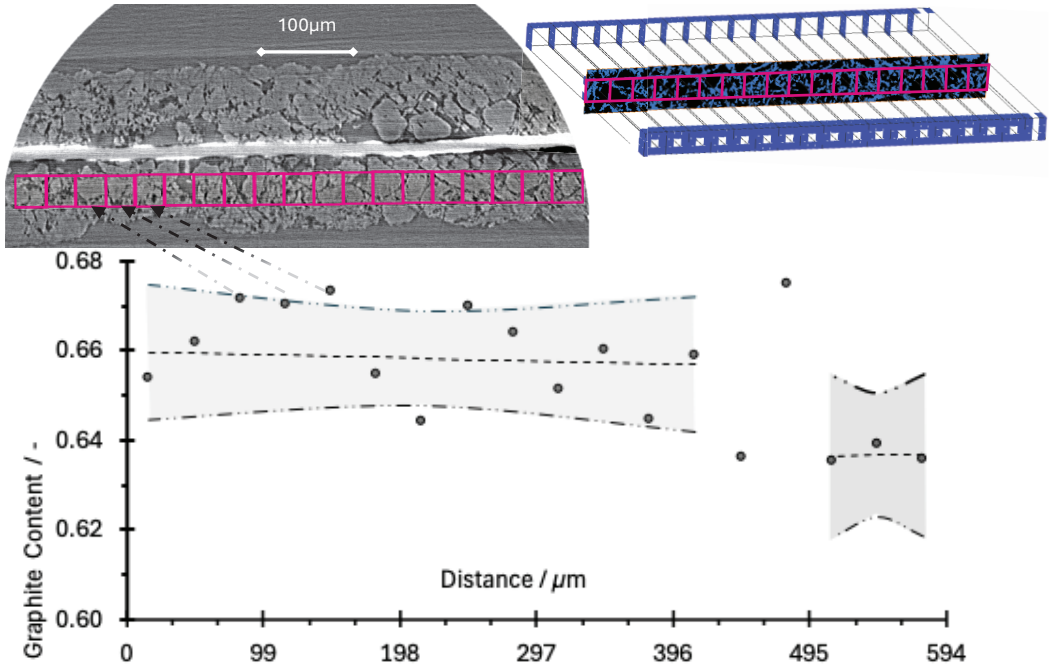

Figure A7. The graphite volume counting. To the upper left, an XCT cross-section reconstruction is shown while indicating the voxels used for the volumes (upper right) that in turn provide the graphite volume content shown graphically (lower).

Appendix F. Lithium Leaching

For the cells cycled at 5 °C, we saw an extremely fast loss of capacity under cycling and that a distinct layer (particularly type (ii)) is formed on the top of the anode. We have also observed that this layer increases reactivity. As this material can not decisively be concluded to be lithium metal, however lithium rich it is. We are curious to see whether it deviates from metallic lithium in other ways too. The comparison between lithium metal and the type (ii) layer reported in this study involves placing lithium metal and the anode sheets in separate water solutions and then measuring the dissolved lithium concentration by detecting the potential using reference electrodes.

All voltage values measured for standard solutions and solutions obtained from dissolving lithium plated on anode sheets are shown in Figure A8. Using a standard regression curve fitted to the voltage results at known concentrations, the concentrations of the unknown samples are estimated. The lithium concentration amount recorded (from the concentration) by immersing the double-sided anode in water for the uncycled cell was 1.65 mmol. For the cycled anode sheet, the recorded amount of lithium was 1.91 mmol. This means that the amount of lithium released to water caused by the cycling at low temperature (by immersing a double-sided anode sheet) was around 0.26 mmol.

If the battery has 31 Ah capacity, 34 double-sided anode sheets, and all LLI plates as metal on the anode, then a double-layered anode aged to 65% SoH should leach 68.0 mmol more lithium compared to the uncycled sheet. In the present case, we observe that the amount of lithium released in relation to the ΔSoH was just above 1% of what it maximally could have been. Since we do not see much lithium release during the water immersion of the anode compared to the ΔSoH, we reason that we cannot argue that the deposited type (ii) layer material on the anode is classic lithium metal plating.

From the results presented in this section, it appears that the deposited layer is not metallic lithium. This, however, does not mean that the layer does not contain lithium. The deposited layer could, for example, be lithium organic compounds, where lithium is chemically bound to carbon and hydrocarbons, as often seen in SEI layers. With the

https://doi.org/10.3390/batteries12040121

available tools, we have not been able to trace where and in what form the lost capacity of the cells cycled at 5 °C ended up. It is not unreasonable that a large portion of this lithium ended up trapped in the observed type (ii) layer; however, the results of this study are not suited to documenting it quantitatively or confirming that it is metallic lithium.

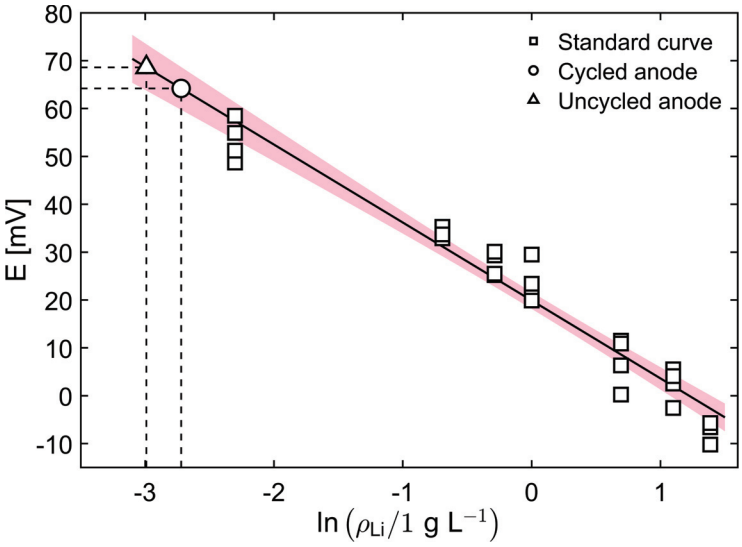

Figure A8. The measured voltage, E, of the Li^+ selective electrode vs. Ag/AgCl as a function of the mass concentration of Li, ρ_{Li}. A standard regression curve (solid line) with a 95% confidence interval (red shaded area) fitted to measurements with known concentrations (squares) is shown. The regression curve, given by $E = 20 - 16 \ln \rho_{Li}$, is used to estimate the Li concentration in solutions obtained from cycled (circle) and uncycled (triangle) anode sheets. Dashed lines show the measured values for the unknown concentrations.

References

1. International Energy Agency (IEA). Batteries and Secure Energy Transitions. 2024. Available online: https://www.iea.org/reports/batteries-and-secure-energy-transitions (accessed on 18 February 2026).
2. Shahjalal, M.; Roy, P.K.; Shams, T.; Fly, A.; Chowdhury, J.I.; Ahmed, M.R.; Liu, K. A review on second-life of Li-ion batteries: Prospects, challenges, and issues. *Energy* **2022**, *241*, 122881. [CrossRef]
3. Martinez-Laserna, E.; Gandiaga, I.; Sarasketa-Zabala, E.; Badeda, J.; Stroe, D.I.; Swierczynski, M.; Goikoetxea, A. Battery second life: Hype, hope or reality? A critical review of the state of the art. *Renew. Sustain. Energy Rev.* **2018**, *93*, 701–718. [CrossRef]
4. Farrington, M.D. Proposed amendments to UN ST/SG/AC.10/11: Transport of dangerous goods—Lithium batteries. *J. Power Sources* **1999**, *80*, 278–285. [CrossRef]
5. Shen, H.; Zhang, Y.; Wu, Y. A comparative study on air transport safety of lithium-ion batteries with different SOCs. *Appl. Therm. Eng.* **2020**, *179*, 115679. [CrossRef]
6. Haram, M.H.S.M.; Lee, J.W.; Ramasamy, G.; Ngu, E.E.; Thiagarajah, S.P.; Lee, Y.H. Feasibility of utilising second life EV batteries: Applications, lifespan, economics, environmental impact, assessment, and challenges. *Alex. Eng. J.* **2021**, *60*, 4517–4536. [CrossRef]
7. Eleftheriadis, P.; Leva, S.; Gangi, M.; Rey, A.V.; Borgo, A.; Coslop, G.; Groppo, E.; Grande, L.; Sedzik, M. Second Life Batteries: Current Regulatory Framework, Evaluation Methods, and Economic Assessment: Reuse, refurbish, or recycle. *IEEE Ind. Appl. Mag.* **2024**, *30*, 46–58. [CrossRef]
8. Neigum, K.; Wang, Z. Technology, economic, and environmental analysis of second-life batteries as stationary energy storage: A review. *J. Energy Storage* **2024**, *103*, 114393. [CrossRef]
9. Rallo, H.; Casals, L.C.; De La Torre, D.; Reinhardt, R.; Marchante, C.; Amante, B. Lithium-ion battery 2nd life used as a stationary energy storage system: Ageing and economic analysis in two real cases. *J. Clean. Prod.* **2020**, *272*, 122584. [CrossRef]
10. Koh, S.; Smith, L.; Miah, J.; Astudillo, D.; Eufrasio, R.; Gladwin, D.; Brown, S.; Stone, D. Higher 2nd life Lithium Titanate battery content in hybrid energy storage systems lowers environmental-economic impact and balances eco-efficiency. *Renew. Sustain. Energy Rev.* **2021**, *152*, 111704. [CrossRef]
11. Vullum-Bruer, F.; Galteland, O.; Gouis, M.; McDougall, N.; Tenhunen-Lunkka, A. Existing and Upcoming Challenges for Extending Electric Vehicle Battery Lifetime Through 2nd Life Applications. *J. Circ. Econ.* **2024**, *2*. [CrossRef]
12. Casals, L.C.; García, B.A.; Canal, C. Second life batteries lifespan: Rest of useful life and environmental analysis. *J. Environ. Manag.* **2019**, *232*, 354–363. [CrossRef]

13. Lee, H.; Lim, D.; Lee, B.; Gu, J.; Choi, Y.; Lim, H. What is the optimized cost for a used battery?: Economic analysis in case of energy storage system as 2nd life of battery. *J. Clean. Prod.* **2022**, *374*, 133669. [CrossRef]
14. Hossain, E.; Member, S.; Murtaugh, D.; Mody, J.; Mansur, H.; Faruque, R.; Sunny, S.H. A Comprehensive Review on Second-Life Batteries: Current State, Manufacturing Considerations, Applications, Impacts, Barriers and Potential Solutions, Business Strategies, and Policies. *IEEE Access* **2019**, *7*, 73215–73252. [CrossRef]
15. Wewer, A.; Bilge, P.; Dietrich, F. Advances of 2nd life applications for lithium ion batteries from electric vehicles based on energy demand. *Sustainability* **2021**, *13*, 5726. [CrossRef]
16. Iqbal, H.; Sarwar, S.; Kirli, D.; Shek, J.K.; Kiprakis, A.E. A survey of second-life batteries based on techno-economic perspective and applications-based analysis. *Carbon Neutrality* **2023**, *2*, 8. [CrossRef]
17. Neubauer, J.; Pesaran, A. The ability of battery second use strategies to impact plug-in electric vehicle prices and serve utility energy storage applications. *J. Power Sources* **2011**, *196*, 10351–10358. [CrossRef]
18. Viswanathan, V.V.; Kintner-Meyer, M. Second use of transportation batteries: Maximizing the value of batteries for transportation and grid services. *IEEE Trans. Veh. Technol.* **2011**, *60*, 2963–2970. [CrossRef]
19. Martinez-Laserna, E.; Sarasketa-Zabala, E.; Sarria, I.V.; Stroe, D.I.; Swierczynski, M.; Warnecke, A.; Timmermans, J.M.; Goutam, S.; Omar, N.; Rodriguez, P. Technical viability of battery second life: A study from the ageing perspective. *IEEE Trans. Ind. Appl.* **2018**, *54*, 2703–2713. [CrossRef]
20. Wang, C.; Lin, D.; Zhao, B.; Zhang, X.; Wang, Y.; Wang, Y.; Cao, W.; Jiang, F. State estimation and aging mechanism of 2nd life lithium-ion batteries: Non-destructive and postmortem combined analysis. *Electrochim. Acta* **2023**, *443*, 141996. [CrossRef]
21. Timke, B.; Winter, M.; Niehoff, P. Impact of State of Health (SOH) on the Thermal Safety of Lithium Ion Cells for Long 1st Life and 2nd Life Applications. *J. Electrochem. Soc.* **2024**, *171*, 100526. [CrossRef]
22. Hu, X.; Deng, X.; Wang, F.; Deng, Z.; Lin, X.; Teodorescu, R.; Pecht, M.G. A review of second-life lithium-ion batteries for stationary energy storage applications. *Proc. IEEE* **2022**, *110*, 735–753. [CrossRef]
23. Li, J.; He, S.; Yang, Q.; Wei, Z.; Li, Y.; He, H. A comprehensive review of second life batteries toward sustainable mechanisms: Potential, challenges, and future prospects. *IEEE Trans. Transp. Electrif.* **2022**, *9*, 4824–4845. [CrossRef]
24. Salek, F.; Resalati, S.; Babaie, M.; Henshall, P.; Morrey, D.; Yao, L. A review of the technical challenges and solutions in maximising the potential use of second life batteries from electric vehicles. *Batteries* **2024**, *10*, 79. [CrossRef]
25. John, J.; Kudva, G.; Jayalakshmi, N. Secondary life of electric vehicle batteries: Degradation, state of health estimation using incremental capacity analysis, applications and challenges. *IEEE Access* **2024**, *12*, 63735–63753. [CrossRef]
26. Roslan, M.; Satpathy, P.R.; Prasankumar, T.; Ramachandaramurthy, V.K.; Mansor, M.; Walker, S.L. Second-life battery energy storage system for energy sustainability: Recent advancements, key takeaways and future perspectives. *J. Energy Storage* **2025**, *123*, 116808. [CrossRef]
27. Shen, J.; Zhou, M.; Liu, W.; Shi, Y.; Tang, W.; Deng, Y.; Liu, R.; Zuo, Y.; Zhang, J. Advanced direct recycling technology enables a second life of spent lithium-ion battery. *Energy Storage Mater.* **2025**, *74*, 103964. [CrossRef]
28. Gu, X.; Bai, H.; Cui, X.; Zhu, J.; Zhuang, W.; Li, Z.; Hu, X.; Song, Z. Challenges and opportunities for second-life batteries: Key technologies and economy. *Renew. Sustain. Energy Rev.* **2024**, *192*, 114191. [CrossRef]
29. Nazim, M.S.; Elavarasan, R.M. Extending battery lifecycles: A holistic review of second-life lithium-ion technology in sustainable energy systems from assessment to emerging trends. *Renew. Sustain. Energy Rev.* **2026**, *233*, 116848. [CrossRef]
30. Redondo-Iglesias, E.; Venet, P.; Pelissier, S. Calendar and cycling ageing combination of batteries in electric vehicles. *Microelectron. Reliab.* **2018**, *88-90*, 1212–1215. [CrossRef]
31. Uddin, K.; Chouchelamane, G.H.; Pastor-fern, C.; Widanage, W.D.; Marco, J. A Comparison between Electrochemical Impedance Spectroscopy and Incremental Capacity-Differential Voltage as Li-ion Diagnostic Techniques to Identify and Quantify the Effects of Degradation Modes within Battery Management Systems. *J. Power Sources* **2017**, *360*, 301–3018. [CrossRef]
32. Gordon, I.J.; Genies, S.; Larbi, G.S.; Boulineau, A.; Daniel, L.; Alias, M. Original implementation of Electrochemical Impedance Spectroscopy (EIS) in symmetric cells: Evaluation of post-mortem protocols applied to characterize electrode materials for Li-ion batteries. *J. Power Sources* **2016**, *307*, 788–795. [CrossRef]
33. Choi, W.; Shin, H.c.; Kim, J.M.; Choi, J.y.; Yoon, W.s. Modeling and Applications of Electrochemical Impedance Spectroscopy (EIS) for Lithium-ion Batteries. *J. Electrochem. Sci. Technol.* **2020**, *11*, 1–13. [CrossRef]
34. Spitthoff, L.; Shearing, P.R.; Burheim, O.S. Temperature, Ageing and Thermal Management of Lithium-Ion Batteries. *Energies* **2021**, *14*, 1248. [CrossRef]
35. Burheim, O.S.; Lamb, J.J. *Engineering Energy Storage*; Academic Press: Cambridge, MA, USA, 2024.
36. Bloom, I.; Cole, B.W.; Sohn, J.J.; Jones, S.A.; Polzin, E.G.; Battaglia, V.S.; Henriksen, G.L.; Motloch, C.; Richardson, R.; Unkelhaeuser, T.; et al. An accelerated calendar and cycle life study of Li-ion cells. *J. Power Sources* **2001**, *101*, 238–247. [CrossRef]
37. Dubarry, M.; Qin, N.; Brooker, P. Calendar aging of commercial Li-ion cells of different chemistries—A review. *Curr. Opin. Electrochem.* **2018**, *9*, 106–113. [CrossRef]

38. Vetter, J.; Novák, P.; Wagner, M.R.; Veit, C.; Möller, K.C.; Besenhard, J.O.; Winter, M.; Wohlfahrt-Mehrens, M.; Vogler, C.; Hammouche, A. Ageing mechanisms in lithium-ion batteries. *J. Power Sources* **2005**, *147*, 269–281. [CrossRef]
39. Broussely, M.; Herreyre, S.; Biensan, P.; Kasztejna, P.; Nechev, K.; Staniewicz, R.J. Aging mechanism in Li ion cells and calendar life predictions. *J. Power Sources* **2001**, *97–98*, 13–21. [CrossRef]
40. Dubarry, M.; Anseán, D. Best practices for incremental capacity analysis. *Front. Energy Res.* **2022**, *10*, 1023555. [CrossRef]
41. Bloom, I.; Christophersen, J.; Gering, K. Differential voltage analyses of high-power lithium-ion cells: 2. Applications. *J. Power Sources* **2005**, *139*, 304–313. [CrossRef]
42. Dubarry, M.; Truchot, C.; Liaw, B.Y. Synthesize battery degradation modes via a diagnostic and prognostic model. *J. Power Sources* **2012**, *219*, 204–216. [CrossRef]
43. Edge, J.S.; O'Kane, S.; Prosser, R.; Kirkaldy, N.D.; Patel, A.N.; Hales, A.; Ghosh, A.; Ai, W.; Chen, J.; Yang, J.; et al. Lithium ion battery degradation: What you need to know. *Phys. Chem. Chem. Phys.* **2021**, *23*, 8200–8221. [CrossRef]
44. Birkl, C.R.; Roberts, M.R.; McTurk, E.; Bruce, P.G.; Howey, D.A. Degradation diagnostics for lithium ion cells. *J. Power Sources* **2017**, *341*, 373–386. [CrossRef]
45. Troxler, Y.; Wu, B.; Marinescu, M.; Yufit, V.; Patel, Y.; Marquis, A.J.; Brandon, N.P.; Offer, G.J. The effect of thermal gradients on the performance of lithium-ion batteries. *J. Power Sources* **2014**, *247*, 1018–1025. [CrossRef]
46. Lin, X.; Khosravinia, K.; Hu, X.; Li, J.; Lu, W. Lithium Plating Mechanism, Detection, and Mitigation in Lithium-Ion Batteries. *Prog. Energy Combust. Sci.* **2021**, *87*, 100953. [CrossRef]
47. Ma, S.; Jiang, M.; Tao, P.; Song, C.; Wu, J.; Wang, J.; Deng, T.; Shang, W. Progress in Natural Science: Materials International Temperature effect and thermal impact in lithium-ion batteries: A review. *Prog. Nat. Sci. Mater. Int.* **2018**, *28*, 653–666. [CrossRef]
48. Yang, B.; Zhang, H.; Yu, L.; Fan, W.; Huang, D. Lithium difluorophosphate as an additive to improve the low temperature performance of LiNi0.5Co0.2Mn0.3O2/graphite cells. *Electrochim. Acta* **2016**, *221*, 107–114. [CrossRef]
49. Wang, H.; Zhang, H.; Cheng, Y.; Feng, K.; Li, X.; Zhang, H. All-NASICON LVP-LTP aqueous lithium ion battery with excellent stability and low-temperature performance. *Electrochim. Acta* **2018**, *278*, 279–289. [CrossRef]
50. Hong, Z.; Tian, H.; Fang, Z.; Luo, Y.; Wu, H.; Zhao, F.; Li, Q.; Fan, S.; Wang, J. Challenges and Advances in Wide-Temperature Electrolytes for Lithium-Ion Batteries. *ChemElectroChem* **2024**, *11*, e202300759. [CrossRef]
51. Zhang, S.S.; Xu, K.; Jow, T.R. The low temperature performance of Li-ion batteries. *J. Power Sources* **2003**, *115*, 137–140. [CrossRef]
52. Zhang, S.S.; Xu, K.; Jow, T.R. A new approach toward improved low temperature performance of Li-ion battery. *Electrochem. Commun.* **2002**, *4*, 928–932. [CrossRef]
53. Gunawardhana, N.; Dimov, N.; Sasidharan, M.; Park, G.J.; Nakamura, H.; Yoshio, M. Suppression of lithium deposition at sub-zero temperatures on graphite by surface modification. *Electrochem. Commun.* **2011**, *13*, 1116–1118. [CrossRef]
54. Petzl, M.; Kasper, M.; Danzer, M.A. Lithium plating in a commercial lithium-ion battery—A low-temperature aging study. *J. Power Sources* **2015**, *275*, 799–807. [CrossRef]
55. Alcaide, F.; Álvarez, G.; Bekaert, E.; Bonilla, F.; Gucciardi, E.; Urdampilleta, I.; Vicedo, R.; Ayerbe, E. Exploring the Influence of Temperature on Anode Degradation in Cycling-Aged Commercial Cylindrical Graphite-Si | NCA Cells. *J. Electrochem. Soc.* **2023**, *170*, 80523. [CrossRef]
56. Zhu, Y.; Zhu, J.; Jiang, B.; Wang, X.; Wei, X.; Dai, H. Insights on the degradation mechanism for large format prismatic graphite/$LiFePO_4$ battery cycled under elevated temperature. *J. Energy Storage* **2023**, *60*, 106624. [CrossRef]
57. Sun, H.; Jiang, B.; You, H.; Yang, B.; Wang, X.; Wei, X.; Dai, H. Quantitative Analysis of Degradation Modes of Lithium-Ion Battery under Different Operating Conditions. *Energies* **2021**, *14*, 350. [CrossRef]
58. Zhu, J.; Dewi Darma, M.S.; Knapp, M.; Sørensen, D.R.; Heere, M.; Fang, Q.; Wang, X.; Dai, H.; Mereacre, L.; Senyshyn, A.; et al. Investigation of lithium-ion battery degradation mechanisms by combining differential voltage analysis and alternating current impedance. *J. Power Sources* **2020**, *448*, 227575. [CrossRef]
59. Wittman, R.; Dubarry, M.; Ivanov, S.; Juba, B.W.; Romàn-Kustas, J.; Fresquez, A.; Langendorf, J.; Grant, R.; Taggart, G.; Chalamala, B.; et al. Characterization of Cycle-Aged Commercial NMC and NCA Lithium-ion Cells: I. Temperature-Dependent Degradation. *J. Electrochem. Soc.* **2023**, *170*, 120538. [CrossRef]
60. Spitthoff, L.; Vie, P.J.S.; Wahl, M.S.; Wind, J.; Burheim, O.S. Incremental capacity analysis (dQ/dV) as a tool for analysing the effect of ambient temperature and mechanical clamping on degradation. *J. Electroanal. Chem.* **2023**, *944*, 117627. [CrossRef]
61. Richter, F.; Kjelstrup, S.; Vie, P.J.S.; Burheim, O.S. Thermal conductivity and internal temperature profiles of Li-ion secondary batteries. *J. Power Sources* **2017**, *359*, 592–600. [CrossRef]
62. Hua, J.; Vie, P.J.S.; Wind, J. Methods for faster estimation of the entropy profile of a lithium-ion battery: A comparison of accelerated potentiometry and the estimation of entropy through thermal signatures. *Electrochim. Acta* **2025**, *509*, 145289. [CrossRef]
63. Wind, J.; Vie, P.J.S. Entropy Profiles for Li-Ion Batteries—Effects of Chemistries and Degradation. *Entropy* **2025**, *27*, 364. [CrossRef]

64. Sun, Y.; Hughes, G.M.; Bu, J.; Liu, J.; Grovenor, C.R.; Grant, P.S. Visualizing the Li distribution in an all-solid-state battery composite electrode using combined plasma focused-ion beam microscopy and secondary-ion mass spectroscopy. *Micron* **2025**, *190*, 103746. [CrossRef]
65. Scott, S.; Du, W.; Horwood, R.; Lei, C.; Shearing, P.; Abbott, A.P. An Assessment of Blended Short Loop Recycled Graphite Electrodes Using X-Ray Micro-Computed Tomography. *Adv. Energy Mater.* **2025**, *15*, 2403498. [CrossRef]
66. Milojevic, Z.; Attidekou, P.S.; Muhammad, M.; Ahmeid, M.; Lambert, S.; Das, P.K. Influence of orientation on ageing of large-size pouch lithium-ion batteries during electric vehicle life. *J. Power Sources* **2021**, *506*, 230242. [CrossRef]
67. Solchenbach, S.; Tacconis, C.; Martin, A.G.; Peters, V.; Wallisch, L.; Stanke, A.; Hofer, J.; Renz, D.; Lewerich, B.; Bauer, G.; et al. Electrolyte motion induced salt inhomogeneity–a novel aging mechanism in large-format lithium-ion cells. *Energy Environ. Sci.* **2024**, *17*, 7294–7317. [CrossRef]
68. Attia, P.M.; Bills, A.; Brosa Planella, F.; Dechent, P.; dos Reis, G.; Dubarry, M.; Gasper, P.; Gilchrist, R.; Greenbank, S.; Howey, D.; et al. Review—"Knees" in Lithium-Ion Battery Aging Trajectories. *J. Electrochem. Soc.* **2022**, *169*, 60517. [CrossRef]
69. You, H.; Zhu, J.; Wang, X.; Jiang, B.; Wei, X.; Dai, H. Nonlinear aging knee-point prediction for lithium-ion batteries faced with different application scenarios. *eTransportation* **2023**, *18*, 100270. [CrossRef]
70. Laszczynski, N.; Solchenbach, S.; Gasteiger, H.A.; Lucht, B.L. Understanding Electrolyte Decomposition of Graphite/NCM811 Cells at Elevated Operating Voltage. *J. Electrochem. Soc.* **2019**, *166*, A1853. [CrossRef]
71. Zhu, J.; Knapp, M.; Sørensen, D.R.; Heere, M.; Darma, M.S.D.; Müller, M.; Mereacre, L.; Dai, H.; Senyshyn, A.; Wei, X.; et al. Investigation of capacity fade for 18650-type lithium-ion batteries cycled in different state of charge (SoC) ranges. *J. Power Sources* **2021**, *489*, 229422. [CrossRef]
72. Lian, T.; Vie, P.J.S.; Gilljam, M.; Forseth, S. (Invited) Changes in Thermal Stability of Cyclic Aged Commercial Lithium-Ion Cells. *Electrochem. Soc. Trans.* **2019**, *89*, 73–81. [CrossRef]

MDPI AG
Grosspeteranlage 5
4052 Basel
Switzerland
Tel.: +41 61 683 77 34

Batteries Editorial Office
E-mail: batteries@mdpi.com
www.mdpi.com/journal/batteries

Academic Open
Access Publishing

mdpi.com

ISBN 978-3-7258-7624-2